Large Eddy Simulation of separating flows from curved surfaces

Temmerman, L.

Large Eddy Simulation of separating flows from curved surfaces

by

L. Temmerman

Department of Engineering

Queen Mary University of London

Mile End Road

London E1 4NS, United Kingdom

This thesis is submitted for the degree of Doctor of Philosophy of the University of London

March 2004

Abstract

The capabilities and limitations of LES in predicting separation from curved surfaces at high Reynolds number are at the centre of this Thesis. Issues of particular interest are mesh resolution, subgrid–scale modelling and near–wall approximations aiming to reduce the computational cost.

Two cases are examined: a flow separating in a channel with streamwise periodic constrictions (*hills*), and the flow around a single–element, high–lift aerofoil at a Reynolds number of $2.1 \cdot 10^6$. Prior to these studies, fully–developed channel–flow simulations are considered. These show substantial differences among subgrid–scale models in terms of the subgrid–scale viscosity magnitude and its wall–asymptotic variation. Modelling and numerical errors appear to counteract each other, thus reducing the total error. Wall functions are shown to be a cost–effective approach, providing a reasonably accurate approximation in near–equilibrium conditions. Adequate resolution remains critical, however, in achieving successful simulations.

In the *hill* flow, separation occurs downstream of the hill crest, reattachment takes place about half-way between two consecutive hills and partial recovery occurs prior to a re-acceleration on the following hill. A highly–resolved simulation, performed to produce benchmark data, permits an extensive study of the flow properties. Coarser mesh simulations are then compared with the former. These highlight the influence of the streamwise discretisation around the separation point and the role played by the implementation details of the wall treatments, while the subgrid-scale models influence is less significant.

The aerofoil, which features transition and separation, is extremely challenging and at the edge of current LES capabilities. None of the simulations reproduce

the experimental data well. Indications on the sensitivity to various parameters, including the numerical scheme, the mesh resolution and the spanwise extent, are extracted, however. The studies indicate the need for a structured mesh of about 80 million nodes to achieve the required accuracy. For the present study, this was unaffordable.

Acknowledgements

First of all, I would like to express my profound gratitude to my supervisor, Prof. Michael Leschziner, for giving me the opportunity to carry out the research presented in this Thesis, for his continuous and patient support, for many hours of rich discussions that made this a fruitful and enjoyable relationship and for helping me to bring this manuscript into a readable form. With the initial funding of this project only available for two years, I am also very thankful to him for securing fundings for a follow-up project, the results of which are not part of this work, but which allowed me to pay my bills.

This research was made possible with the financial support of the European Community through the LESFOIL project (reference number BRPR-CT97-0565), part of the Framework V Brite-Euram initiative. The simulations reported in the present work required a substantial amount of computing power, and access to the CSAR service in Manchester was granted by EPSRC through the consortium LESUK II (grant GR/M050539). I am very grateful to EPSRC for this as well as all the people behind the CSAR service who, while providing a very reliable service, were also very helpful. With my work having spanned over three different UK universities, UMIST in Manchester, Queen Mary University of London and Imperial College London, I am grateful to all the support people in these institutions, who provided the environment necessary to carry the present Thesis.

I would not have applied to the Research Assistant position within which the present research was undertaken without the encouragements from my friend, Dr. Georges Barakos. I would also like to thank Prof. Dimitris Drikakis for supporting my application.

Many thanks goes to Dr. Raphael Lardat for his patience in introducing me to the code he wrote, and many interesting discussions. I would also like to thank Dr. Mike Ashworth and Dr. David Emerson for their hospitality at the Daresbury Laboratory and for introducing me to the world of parallel computing. The work on the role played by numerical and modelling errors in LES of a channel flow resulted from discussions with Prof. Bernard Geurts from Twente University (The Netherlands) during his stay as a visiting professor at Queen Mary University of London.

The hill-flow chapter benefited from an extensive and very fruitful collaborative effort with Dr. Christopher Mellen, Dr. Jochen Fröhlich and Prof. Wolfgang Rodi from the University of Karlsruhe, Germany.

During the course of the LESFOIL project, many discussions arose between the different members of the consortium either through e-mail exchanges or during the meetings, and these contributed greatly to this work. I am especially indebted to Dr. Simon Dählstrom, Dr. Christopher Mellen and Dr. Jochen Fröhlich for endless discussions, among other helpful interactions.

My profound gratitude goes to Dr. Anne Dejoan who, in addition to sharing the office space with me for the last two years, proved to be a willing and well-informed discussion partner on the subjects of LES, turbulence and many others. My apologies goes to my two other colleagues, Dr. Yong-Jun Jang and Dr. Chen Wang, who were subjected to an almost permanent French chatter. However, they never missed an opportunity to contribute to the occasionally chaotic, but always well-humoured atmosphere of our common space.

I am also very grateful to my other past and present colleagues, Dr. David Apsley, Dr. Hughes Loyau, Dr. Francois Mallinger, Dr. Georges Barakos, Dr. Aldo Bonfiglioli, Dr. Yongmann Chung, Mr. Pierre Humbert, Dr. Ken-Ichi Abe, Dr. Xu Zhou, Dr. Xi Jiang, Dr. Eldad Avital, Dr. Sylvain Lardeau and Dr. Richard Wilden for many enriching discussions, some of which contributed to this Thesis, others absolutely not related, but nevertheless interesting, as well as for their friendship, encouragements and sharing the odd beer.

During the course of this Thesis, I had the opportunity to meet many new peo-

ple, some of them are now my friends, while keeping strengthening older friendships. Thanks goes thus to all my friends, particularly among them Dr. Marianna Grammatika, Fabrice Plançon, Dr. Patrice Bouche, Dr. Roland Pietsch, Corrado di Pisa, Gaétan Masson, Simon Morren, Laurent Mampaey, Benoit Denet, Bernard Languillier and Renaud Hendricé for the many encouragements I received from them and for the special moments we shared, among many other things. A membership to the Anglo-Belgian Society provided for a some time much needed escape to other worlds and the opportunity to visit some very impressive venues in London in always kind and interesting company. Special thanks goes to Mrs. Françoise Vermeylen who kindly provided a sometimes much needed ear.

These acknowledgements would not be complete without mentioning the very strong support I received from my parents, Colette and Edouard Temmerman and my sister, Charlotte, who while far away, most of the time, were close in spirit.

Last but not least, the very loving presence of my companion, Miss Anne Hermans, as well as her patience, greatly contributed to my ability to complete this Thesis.

Contents

List of Figures

List of Tables

Nomenclature

Roman

a_{ij}	anisotropy stress tensor
A	flatness parameter for the anisotropy stress tensor b_{ij}
A^+	constant in the van Driest damping function
b_{ij}	dimensionless anisotropy stress tensor
c	chord length
C_M	constant in the Mixed-Scale model
C_s	Smagorinsky constant
C_w	constant in the WALE model
C	Dynamic coefficient
CD	convective and diffusive terms in the Navier-Stokes equations
CFL	Courant-Friedrich-Lewis number ($CFL = u\Delta t/\Delta$)
D_{ij}	viscous diffusion for the turbulent stress ij
E_{ij}	energy spectra for the ij velocity pair
E	energy spectra
f_c	cut-off frequency
f	frequency
g_{ij}	gradient-velocity tensor
G	filtering kernel
h	channel half width, also hill height
II	second invariant of the tensor b_{ij}
III	third invariant of the tensor b_{ij}

k	turbulence energy
k_c	cut-off wave-number
l_d	van Driest damping function
L_i	domain extent in the i-direction
n	normal direction
N_i	number of cells in the i-direction
p	pressure
P_{ij}	production of the turbulent stress ij
q	subgrid-scale energy
Q	second invariant of the velocity-gradient tensor
R_{ij}	two-point correlation for the ij velocity pair
Re	Reynolds number
Re_b	Reynolds number based on bulk velocity U_b and channel half width h ($Re_b = U_b h/\nu$)
Re_c	Reynolds number based on chord length c and free-stream velocity U_0 ($Re_c = U_0 c/\nu$)
Re_h	Reynolds number based on hill height h and bulk velocity U_b at the hill crest ($Re_h = U_b h/\nu$)
Re_{L_y}	Reynolds number based on the channel height L_y and bulk velocity U_b ($Re_{L_y} = U_b L_y/\nu$)
Re_λ	Reynolds number based on inter-hill distance λ and bulk velocity U_b at the hill crest ($Re_\lambda = U_b \lambda/\nu$)
Re_τ	Reynolds number based on wall shear velocity U_τ and channel half width h ($Re_\tau = U_b h/\nu$)
S_{ij}	strain rate tensor
t	time
T_{ij}	turbulence transport for the turbulent stress ij
$\mathbf{x}$	vector position
u, v, w	Cartesian components of the velocity
u_τ	wall shear velocity ($u_\tau = \sqrt{\tau_w/\rho}$)
u_c	centreline velocity

u_i	Cartesian components of the velocity
U_0	freestream velocity
U_b	bulk velocity
x_i	Cartesian coordinates
x, y, z	Cartesian coordinates

Greek

α_i	ratio between the test-filter width $\overline{\Delta_i}$ and the grid-filter width $\overline{\hat{\Delta}_i}$ in the i-direction
β	blending factor
δ_{ij}	Kronecker symbol
Δ	discriminant of the characteristic equation of the velocity-gradient stress tensor
Δt	time-step
Δx	cell size in the x-direction
Δy	cell size in the y-direction
Δz	cell size in the z-direction
ϵ	dissipation
ϵ_d	discretisation effect
ϵ_{ij}	dissipation rate for the turbulent stress ij
ϵ_m	modelling effect
ϵ_t	total effect
η	Kolmogorov length scale
κ	von Karman constant
λ_2	second eigenvalue of $S_{ik}S_{kj} + \Omega_{ik}\Omega_{kj}$
λ	inter-hill distance for wavy terrain
ν	kinematic viscosity
ν_t	subgrid-scale viscosity
ϕ	flow variable
$< \phi >$	mean component of the flow variable ϕ

ϕ'	fluctuating component of the flow variable ϕ
$\overline{\phi}$	filtered flow variable ϕ
$\hat{\phi}$	test-filtered flow variable ϕ
Π_{ij}	velocity-pressure gradient interaction term for the turbulent stress ij
ρ	density
τ_{ij}	subgrid-scale stresses
τ_w	wall shear stress
ω	vorticity vector
ω_i	Cartesian components of the vorticity vector
Ω_{ij}	vorticity tensor

Subscripts

1	indicates the first cell near the wall
crest	located at the top of the hill
i, j, k	tensor directions, varying from 1 to 3
max	maximum
reat	reattachment
sep	separation
wake	relative to the wake region

Superscripts

+	indicates that the related variable is expressed in wall units
$n-1$	instant n-1
$n+1$	instant n+1
n	instant n

Abbreviations

CDS	Central Difference Scheme

DES	Detached Eddy Simulation
DNS	Direct Numerical Simulation
DSM	Dynamic Smagorinsky Model
LDSM	Localized Dynamic Smagorinsky Model
LES	Large Eddy Simulation
LL2	Two-Layer Log-Law
LL2-i	integrated form of the Two-Layer Log-Law
LL3	Three-Layer Log-Law
LLK	Two-Layer Log-Law based on the turbulence energy k
MILES	Monotone Integrated Large Eddy Simulation
MKM	Moser, Kim and Mansour
MPI	Message Passing Interface
MSM	Mixed-Scale Model
NS	No-Slip condition
NSGS	No Subgrid-Scale Model
PS	Pressure Side
r.m.s.	root mean square
RANS	Reynolds-Averaged Navier-Stokes
SGS	Subgrid-Scale
SM	Smagorinsky Model
SS	Suction Side
UPWIND	Upwind scheme
WALE	Wall-Adapted Local Eddy-viscosity
WW	Werner-Wengle Wall law
WW-p	pointwise form of the Werner-Wengle wall law

Chapter 1

Introduction

1.1 Large Eddy Simulation - Motivation and Rationale

The predictive capabilities of Computational Fluid Dynamics (CFD) are challenged by many physical processes, the most difficult among them being turbulence. This difficulty arises from the *chaotic* or unpredictable behaviour of the phenomenon and the wide range of spatial and temporal scales involved, typically covering several orders of magnitude at the high Reynolds numbers encountered in practice.

Because turbulence is responsible for the mixing of momentum, heat and chemical species, it has, in most circumstances, a major impact on the distribution of velocity, temperature and species concentrations. It also exerts a strong influence on flow separation, re-attachment and recovery. It governs chemical reactions and frictional losses. In addition, turbulence is responsible for structural vibrations and the creation and propagation of noise.

The numerical representation of turbulent flows can be achieved via a number of different techniques, each yielding a different level of detail. Statistical modelling approaches provide the least detail. They are based on Reynolds-averaging, which assumes the following decomposition of the flow variables:

$$u(\mathbf{x},t) = \underbrace{\langle u(\mathbf{x})\rangle}_{steady} + \underbrace{u'(\mathbf{x},t)}_{fluctuation} \tag{1.1}$$

with the time-averaging operator $< \cdot >$ defined as:

$$\langle u(\mathbf{x})\rangle = \frac{1}{T}\int_0^T u(\mathbf{x},t)\,dt \tag{1.2}$$

where T is the period of time over which the averaging is made and is significantly larger than the longest time-scale associated with the turbulent motion. After introducing the decomposition (1.1) for the velocity and the pressure, the operator (1.2) is applied to the Navier-Stokes equations. In other words, the equations are time-averaged. The result is a new set of equations, the Reynolds-averaged Navier-Stokes (RANS) equations, which describe the spatial evolution of the mean velocity and pressure fields. This process results in the appearance of turbulent velocity fluctuations $\langle u_i' u_j' \rangle$, referred to as the (kinematic) Reynolds stresses. These are unknown quantities and require modelling in terms of known determinable quantities.

Over the past six decades, a wide variety of turbulence models have been formulated. These range from algebraic relationships (Prandtl [182], Van Driest [222], Cebeci and Smith [29] among others), linking the stresses and the strains to multi-equations transport closures consisting of evolution equations for the individual Reynolds stresses (Launder et al [115], Speziale et al [214], Craft and Launder [42] among others). Although the generality of even the most complex models is limited, the key advantage of the RANS strategy is computational economy, arising from the absence of the requirement to resolve the details of the turbulent motion. This method is therefore widely used in engineering for predictive studies within design loops, especially when extensive parametric investigations are necessary.

An inherent limitation of the RANS approach, associated with the Reynolds decomposition (1.1), is that it only provides an ensemble- or time-averaged picture of the flow. Hence, it is not useful when the focus is on the resolution of temporal features associated with the structural and temporal details of the turbulent motion. This includes free transition, noise, unsteady pressure, instabilities, unsteady loads and heat transfer extrema. In some circumstances, the RANS method is used to

resolve flows that contain a periodic, low-frequency motion which is not part of the turbulence spectrum. Here, the objective is not merely to resolve the mean motion, but also its periodic behaviour. This practice is referred to as unsteady RANS (URANS). Examples of flows to which URANS is applied are vortex shedding behind bluff bodies (Bosch and Rodi [19]), Rayleigh-Bénard convection (Hanjalić and Kenjereš [81]), flapping flows (Barakos and Drikakis [11]), wake-blade interaction in turbomachinery (Fan and Lakshminarayana [57]) and piston-cylinder flows in IC engines (Behzadi and Watkins [14]). In all such cases, a key requirement for a meaningful application of the RANS method is a clear gap between the turbulent motions over which the decomposition (1.1) is applied and the frequency of the periodic component. In other words, this period must be significantly larger than the time-period T introduced in (1.2). Even when this requirement is satisfied, however, there remains a significant level of uncertainty in this approach, even when it is applied in $3D$ mode, as it should be, regardless of whether or not the flow is statiscally two-dimensional. RANS and URANS methods are reviewed in detail in Wilcox [236], Leschziner [122], Spalart [210].

The most fundamental approach to resolving turbulence and its effects is Direct Numerical Simulation (DNS). In DNS, the unsteady Navier-Stokes equations are discretised and solved in time so to resolve all the turbulent scales, down to the smallest eddies dissipated by viscosity. Thus, a fully three-dimensional and unsteady representation of the flow is obtained. DNS allows the extraction of any flow quantity of interest and is a very important tool in the study of turbulent flows, giving access to quantities often beyond reach via experiments. It is, however, extremely resource-intensive and requires the use of accurate high-order schemes, limiting the geometric complexity of a problem that can be simulated.

As all scales have to be resolved, the number of nodes required is proportional to the ratio between the largest and the smallest eddy. This ratio is proportional to $Re^{3/4}$, where Re is a Reynolds number based on length and velocity characteristic of the largest scales. Hence, the number of nodes in a numerical grid required to resolve all scales rises with $Re^{9/4}$. Correspondingly, the time-step must be small enough so that all the temporal scales of turbulence are resolved. This results in a Reynolds

number dependance of the CPU of $O(Re^3)$.For example, the simulation of a fully-developed channel flow within a domain $2\pi h \times 2h \times 4\pi h$ at $Re = 6600$, based on mean velocity and half channel height, requires around $2 \cdot 10^6$ nodes and 40 CPU hours on a 150 MFlops computer. DNS is therefore not an economically tenable approach to engineering flow at the high Reynolds numbers encountered in practice. It is, however, extremely valuable for studying fundamental features of turbulence and validating new turbulence modelling proposals, at least at relatively low Reynolds numbers. The subject is reviewed in more details in Moin and Mahesh [160] and Sandham [198].

An intermediate technique between DNS and RANS, which is at the heart of the present work, is Large Eddy Simulation (LES). In LES, only the large, most energetic scales are directly computed, while the effect of the small scales is modelled. The expectation is that, in contrast to the RANS approach, the models will be relatively simple, since the small, unresolved scales tend to be more universal and homogeneous, and are, therefore, less affected by the mean strain and the boundaries. The separation between the resolved and unresolved fields is effected by applying a spatial filter on the variable field. The filter width is (or should be) chosen so that the cut-off occurs in the inertial subrange of the turbulent energy spectrum, that is between the generation and the dissipative ranges but preferably close to the latter. Thus filtering entails the decomposition:

$$u(x,t) = \underbrace{\overline{u(\mathbf{x},t)}}_{filtered} + \underbrace{u'(\mathbf{x},t)}_{unresolved} \tag{1.3}$$

where the filtered quantity is obtained via the application of convolution integral:

$$\overline{u(\mathbf{x},t)} = \int_D G(\mathbf{x},\mathbf{x}')\, u(\mathbf{x}',t)\, d\mathbf{x}' \tag{1.4}$$

with G, the filtering function.

The application of the filter to the flow governing equations leads to a new set of equations, the filtered Navier-Stokes equations, which describes the motion of the large scales. The influence of the small, unresolved scales is represented by the subgrid-scale stresses, which are similar to the Reynolds stresses and need to be

approximated. While the subgrid-scale stresses are intended to constitute a minor proportion of the respective resolved components, the relative levels depend greatly on the coarseness of the grid. As the grid becomes coarser, at a given Reynolds number, the cut-off limit is shifting towards the low-frequency, large-scale features, and an increasing burden is placed on the subgrid-scale model to represent an increasingly larger proportion of the effects of turbulence. Hence, the nature of the subgrid-scale model can become influential. Simple models, formulated principally to dissipate the turbulence energy cascading down the inertial subrange, may become inadequate. The dependence of the simulated solution on subgrid-scale modelling is one of the issues pursued in the research documented in this Thesis.

Because LES resolves the majority of scales associated with the turbulence dynamics, it allows the interaction between periodic components and turbulence to be captured realistically and unsteady features associated with the larger scales, usually the ones of practical interest, to be predicted. On the negative side, LES is costly, albeit much less than DNS, and it is not likely to become an engineering approach for some years to come. According to Reynolds [185], the resolution requirement away from the wall rises as $Re^{0.5}$. As a wall is approached, however, the large scales diminish in size, eventually approaching the dissipation scale (Kolmogorov) in the viscous sublayer. This leads to near-wall resolution requirements rising with $Re^{2.4}$. Yet, further factors adversely affecting the economy of LES are the need for low aspect ratio grid cells, low level of grid skewness and high numerical accuracy, the last, requiring the use of non-diffusive, energy conserving schemes. As in DNS, the time-step is constrained by the need to compute even the lowest temporal scale of the resolved turbulent field. As an example, Wang and Moin [230] recently performed a LES of a trailing edge at a chord Reynolds number of $2.15 \cdot 10^6$ on a grid of over $7 \cdot 10^6$ points. The complete simulation required over 1000 CPU-hours on a CRAY C90.

With the number of nodes increasing as $Re^{2.4}$ near the walls, the resolution requirements constitute a major obstacle to the exploitation of LES at high Reynolds numbers. This is especially so in flows separating from curved surfaces, in which the near-wall flow structure can become very influential. Overcoming this obstacle,

by way of approximate near-wall practices employed in the RANS environment is an objective pursued vigorously at the time this Thesis is being written, and a substantial proportion of the research pursued here addresses this challenge. Detailed reviews on LES are available in Sagaut [193], Lesieur and Métais [124] or Moin [158].

1.2 Objectives of the research

As noted under Section 1.1, LES faces a number of challenges in respect of accuracy and economy, which impinge on the potential of LES as a predictive tool within a design environment. Three issues of particular concerns are the resolution afforded by the numerical grid, the adequacy of subgrid-scale modelling and the quality of the near-wall resolution. These three issues are at the heart of the present research. The emphasis of the research is on separated flows at high Reynolds number, specifically a flow separating from a hill-shaped constriction in a streamwise periodic channel segment and the flow around a single element high-lift aerofoil at chord Reynolds number of $2.1 \cdot 10^6$. Preceding these studies, however, are investigations for plane channel flows at shear Reynolds number ranging from 180 to 1050, undertaken with the aim of gaining insight into a number of fundamental aspects associated with grid support, resolution, model sensitivity and performance of near-wall approximations. To perform these studies effectively, an efficient LES algorithm was developed for massively parallel systems. This has been implemented on several architectures, the principal one being a 816 processors Cray T3E computer. This Thesis therefore also reports on computational-performance characteristics to survey resource issues and the effectiveness of parallelisation.

1.3 Outline of the thesis

The remainder of this thesis is divided into 8 Chapters. Chapter 2 reviews the relevant areas of LES, identifying the current state-of-the-art on several fronts. The review starts with an historical survey until the 1980's when LES became established as a research tool. A more detailed review of the most recent efforts then focuses

separately on subgrid-scale modelling, near-wall representation and numerical techniques.

In Chapter 3, the governing equations for LES are expanded and details are given of the subgrid-scale models and near-wall approximations employed in the course of this research.

The numerical framework and solution algorithm are explained in Chapter 4, together with the description of the parallel-computing strategy. The final part of the Chapter reports the outcome of computational tests on various parallel platforms. Aspects such as efficiency, scalability and limitations as regard problem size and the parallel/algorithmic strategy adopted are discussed.

Chapter 5 documents a range of post-processing and analysis tools employed in the course of this work for investigating flow features and specific statistical properties.

Chapter 6 deals with the first of three geometries considered, namely a fully-developed plane-channel flow. This geometrically simple and well-documented case allows important insight to be gained into numerical and modelling issues. Aspects discussed include subgrid-scale model performance, sensitivity to grid resolution, effectiveness of near-wall approximation, based on a log-law representation, at moderate Reynolds numbers and the influence of numerical and modelling errors.

Chapter 7 presents results of simulations for the second of the three geometries studied, a separated spanwise-homogeneous flow in a periodic segment of an infinitely long channel with periodic hill-shaped bumps on one wall. This case can be regarded as an infinite sequence of hills separated by a constant distance, and it will be referred as the *hill flow*, henceforth. The hill flow is characterized by separation occurring from the leeward surface, re-attachment taking place at approximately half the distance between two successive hills, partial recovery along a plane-wall portion between the hills and, finally, re-acceleration due to the windward slope of the following hill. As done in the previous Chapter for the case of the channel flow, a wide range of simulations are reported in an effort to identify the dependence of the results on grid density, subgrid-scale modelling and near-wall approximations. A highly-resolved (quasi-DNS) simulation employing $4.6 \cdot 10^6$ nodes was performed,

providing benchmark data against which coarser-grid simulations could be compared. Turbulent stresses, kinetic energy budgets and other statistical quantities were extracted from this simulation, and these are discussed in this Chapter.

In Chapter 8, a separated flow over a single element, high-lift aerofoil is investigated. This geometry, conventionally referred as the A(érospatiale)-aerofoil, is extremely challenging for LES, because of the very high Reynolds number ($Re_c = 2.1 \cdot 10^6$) of the flow, the large computational domain requiring the grid to extend to 10 chord lengths away from the aerofoil, and the variety of phenomena taking place on the aerofoil including transition and separation. The reported simulations extend the investigations of some of the modelling issues studied in the previous Chapters for different grid densities and spanwise extent, with the objective of identifying the current capabilities and limitations of LES for high-Reynolds-number flows in the context of external aerodynamics.

Chapter 9 presents the conclusions for the range of simulations undertaken in the course of this research, identifying limits and capabilities of LES for separated flows at high Reynolds numbers. Proposals for further research are then put forward to resolve open issues which could not be answered or addressed in the present research effort.

Chapter 2

Large Eddy Simulation - A Review

2.1 Overview

Large Eddy Simulation (LES), briefly introduced in Chapter 1, is reviewed in the present chapter in terms of its main building blocks and applications. In a first section, the governing equations for LES are derived, alongside a discussion of the assumptions that lead to them. This derivation is necessary to create a foundation against which to discuss a variety of issues pertinent to LES. Major topics considered are subgrid-scale modelling, near-wall treatments, numerical methodologies and related accuracy and resolution issues. The objective of the above is to create the appropriate backdrop against which to review representative applications rejecting current capabilities and limitations. This is done largely in qualitative terms with details pertinent to the present research delegated to the following chapters.

2.2 The governing equations for LES in physical space

The dynamics of an incompressible non-reacting flow for a Newtonian fluid are described by the conservation laws for mass and momentum, the latter known as the Navier-Stokes equations:

$$\begin{cases} \dfrac{\partial u_i}{\partial x_i} = 0 \\ \dfrac{\partial u_i}{\partial t} + \dfrac{\partial u_i u_j}{\partial x_j} = -\dfrac{1}{\rho}\dfrac{\partial p}{\partial x_i} + \nu \dfrac{\partial^2 u_i}{\partial x_j^2} \end{cases} \tag{2.1}$$

where ρ is the fluid density, p is the pressure, ν is the laminar viscosity (assumed constant), u_i is the velocity component in the i^{th} direction and x_i is the Cartesian coordinate in the i^{th} direction with $i = 1, 2, 3$.

If U_o is a characteristic velocity for the considered problem and L, a characteristic length scale of the flow then the system of equations (2.1) can be written in terms of the following non-dimensional variables:

$$t^* = \frac{tU_o}{L}\ ,\ x^* = \frac{x}{L}\ ,\ u_i^* = \frac{u_i}{U_o}\ ,\ p^* = \frac{p}{\rho U_o^2}\ ,\ Re = \frac{U_o L}{\nu}\ . \tag{2.2}$$

where Re is the Reynolds number. The Navier-Stokes equations may hence be written as follows:

$$\begin{cases} \dfrac{\partial u_i^*}{\partial x_i^*} = 0 \\ \dfrac{\partial u_i^*}{\partial t^*} + \dfrac{\partial u_i^* u_j^*}{\partial x_j^*} = -\dfrac{\partial p^*}{\partial x_i^*} + \dfrac{1}{Re}\dfrac{\partial^2 u_i^*}{\partial x_j^{*2}} \end{cases} \tag{2.3}$$

For the sake of simplicity, the superscript $*$ in the system of equations (2.3) will be omitted henceforth, and all variables are considered as expressed in a dimensionless form, unless otherwise specified.

The governing equations for LES are obtained by applying a spatial filter to the system of equations (2.3) by means of a convolution product:

$$\overline{f(\mathbf{x}, t)} = \int_D f(\mathbf{x}', t)\, G(\mathbf{x}, \mathbf{x}')\, dx' \tag{2.4}$$

where $f(\mathbf{x}', t)$ is the function to be filtered and $G(\mathbf{x}, \mathbf{x}')$, the filtering function which must satisfy $G(\mathbf{x}, \mathbf{x}') = \int_D G(\mathbf{x}, \mathbf{x}')\, dx' = 1$. The filter must obey the following properties:

- conservation of a constant:

$$\overline{a} = a \tag{2.5}$$

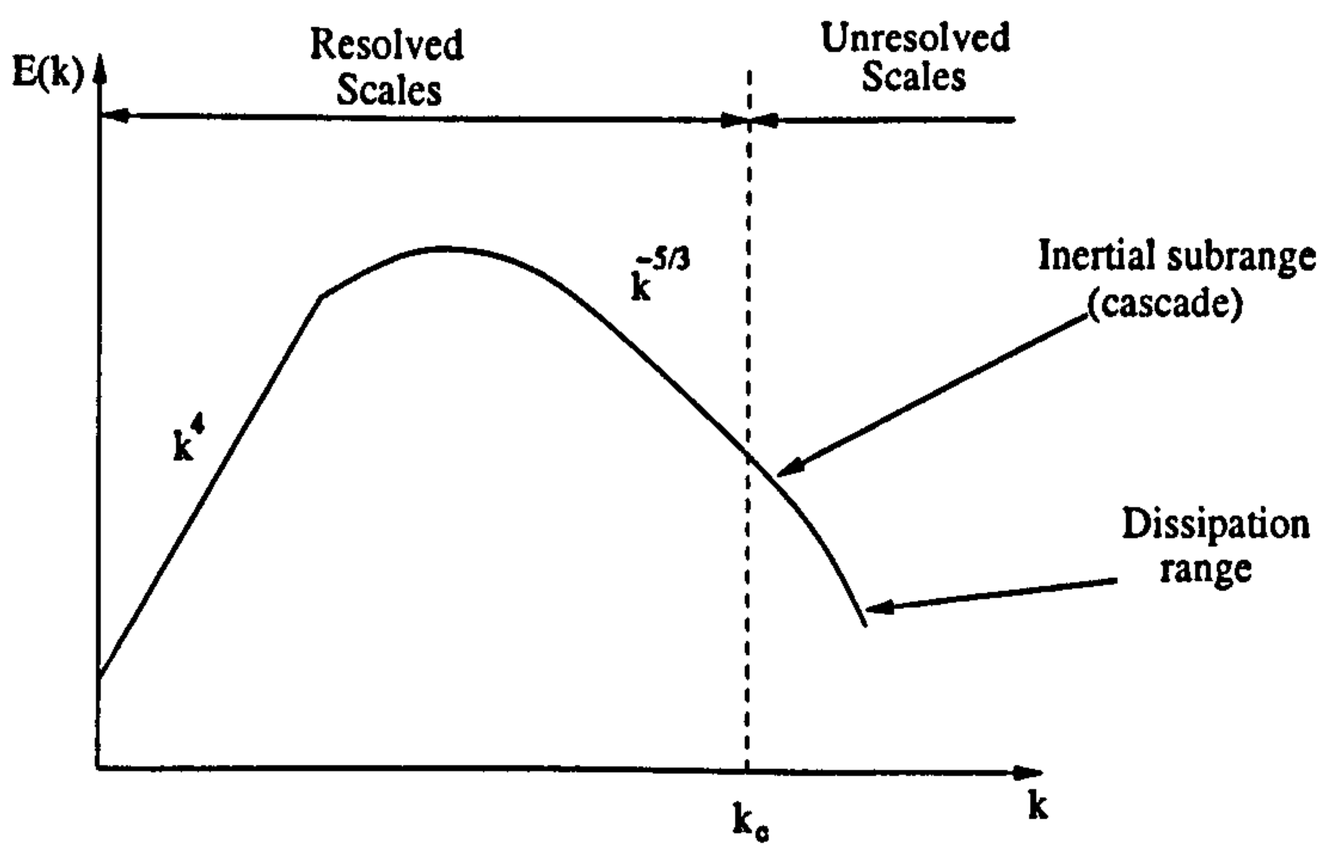

Figure 2.1: Principle of the cut-off in the 1D energy spectrum (k is the wavenumber).

- linearity:

$$\overline{f+g} = \overline{f} + \overline{g} \tag{2.6}$$

- commutativity with respect to the derivatives in space and time:

$$\overline{\frac{\partial f}{\partial \xi}} = \frac{\partial \overline{f}}{\partial \xi} \tag{2.7}$$

Typical filters used in LES are the Box Filter, the Gaussian Filter and the Cut-Off Filter which are described in Appendix A.

In practical terms, the application of a filter on any variable f leads to the decomposition of this variable into two terms. One is related to the large energetic scales of the turbulence spectrum, while the other pertains to the relatively small, more isotropic and universal scales. This decomposition, expressed as:

$$f(\mathbf{x},t) = \underbrace{\overline{f(\mathbf{x},t)}}_{resolved\,scales} + \overbrace{f'(\mathbf{x},t)}^{unresolved\,scales} \tag{2.8}$$

is shown schematically in Figure 2.1, the left partition containing the resolved scales and the right, the unresolved scales. If the filtering operation satisfies the conditions (2.5)-(2.7), Equations (2.3) become:

$$\begin{cases} \dfrac{\partial \overline{u_i}}{\partial x_i} = 0 \\ \dfrac{\partial \overline{u_i}}{\partial t} + \dfrac{\partial \overline{u_i u_j}}{\partial x_j} = -\dfrac{\partial \overline{p}}{\partial x_i} + \dfrac{2}{Re}\dfrac{\partial \overline{S_{ij}}}{\partial x_j} \end{cases} \tag{2.9}$$

where $\overline{S_{ij}} = 0.5\,(\partial\overline{u_i}/\partial x_j + \partial\overline{u_j}/\partial x_i)$. Equations (2.9) govern $\overline{u_i}$ and $\overline{p}$. However, they cannot be solved in this form because the correlation $\overline{u_i u_j}$ is unknown. If u_i is decomposed into its resolved and subgrid-scale parts ($u_i = \overline{u_i} + u_i'$), then $\overline{u_i u_j}$ can be expressed as:

$$\overline{u_i u_j} = \overline{\overline{u_i}\,\overline{u_j}} \underbrace{+\overline{\overline{u_i} u_j'} + \overline{u_i' \overline{u_j}}}_{C_{ij}} + \underbrace{\overline{u_i' u_j'}}_{R_{ij}} = \overline{\overline{u_i}\,\overline{u_j}} - \tau_{ij} \tag{2.10}$$

where $\tau_{ij} = C_{ij} + R_{ij}$ represent the subgrid-scale stresses and require modelling. C_{ij} are the cross-term stresses representing the interaction between large and small scales. R_{ij}, known as the subgrid-scale Reynolds stresses, represent the interaction between the small scales.

Expression (2.10) poses two problems. First, the term $\overline{\overline{u_i}\,\overline{u_j}}$ is not computable from (2.9). Second, the subgrid-scale stresses are unknown. This latter issue will be addressed in details in Section 2.3.

In early LES (Deardorff [49], Smagorinsky [208]), the first term on the right hand-side of Equation (2.10) was approximated by:

$$\overline{\overline{u_i}\,\overline{u_j}} \approx \overline{u_i}\,\overline{u_j} \tag{2.11}$$

Leonard [120] revisited the principles of decomposition with the objective of avoiding assumption (2.11). Following Equation (2.10), the subgrid-scale stress tensor is:

$$\tau_{ij} = C_{ij} + R_{ij} = \overline{u_i u_j} - \overline{\overline{u_i}\,\overline{u_j}} \tag{2.12}$$

and the filtered Navier-Stokes equations therefore become:

$$\frac{\partial \overline{u_i}}{\partial t} + \frac{\partial \overline{\overline{u_i}\,\overline{u_j}}}{\partial x_j} = -\frac{\partial \overline{p}}{\partial x_i} + \frac{2}{Re}\frac{\partial \overline{S_{ij}}}{\partial x_j} - \frac{\partial \tau_{ij}}{\partial x_j} \tag{2.13}$$

To address the term $\overline{\overline{u_i}\,\overline{u_j}}$, Leonard [120] proposed the following decomposition:

$$\overline{\overline{u_i}\,\overline{u_j}} = \underbrace{\left(\overline{\overline{u_i}\,\overline{u_j}} - \overline{u_i}\,\overline{u_j}\right)}_{L_{ij}} + \overline{u_i}\,\overline{u_j} \tag{2.14}$$

where L_{ij}, the Leonard stress tensor, represent the interactions between the large scales. This decomposition, known as the *triple decomposition* or the *Leonard decomposition*, leads to the subgrid-scale stresses arising as:

$$\tau_{ij} = \underbrace{\overline{\overline{u_i}\,\overline{u_j}} - \overline{u_i}\,\overline{u_j}}_{L_{ij}} + \underbrace{\overline{\overline{u_i}\,u'_j} + \overline{\overline{u_j}\,u'_i}}_{C_{ij}} + \underbrace{\overline{u'_i u'_j}}_{R_{ij}} = L_{ij} + R_{ij} + C_{ij} = \overline{u_i u_j} - \overline{u_i}\,\overline{u_j} \quad (2.15)$$

Introducing this decomposition into the filtered Navier-Stokes equations (2.10) now leads to:

$$\frac{\partial \overline{u_i}}{\partial t} + \frac{\partial \overline{u_i}\,\overline{u_j}}{\partial x_j} = -\frac{\partial \overline{p}}{\partial x_i} + \frac{2}{Re}\frac{\partial \overline{S_{ij}}}{\partial x_j} - \frac{\partial \tau_{ij}}{\partial x_j} \quad (2.16)$$

Combined with the filtered continuity equation, Equations (2.16) form the governing equations for LES as they are solved today.

An important property of the governing equations of LES is highlighted by Speziale [213]. He showed that, as is the case with the Navier-Stokes equations, the LES equations are Galilean-invariant. This means that the description of the physics is identical irrespective of the frame of reference. While this is also true for the Reynolds-stress term and the sum of the Leonard and the cross stresses, the latter two are not individually Galilean-invariant. This observation has important implications when subgrid-scale models represent explicitly each of these terms. It imposes the constraint that each part has to be Galilean invariant for the model to be physically consistent.

2.3 Subgrid-scale modelling

2.3.1 Overview

The procedure and assumptions described in the previous section lead to the governing equations for LES and result in the presence of correlations of small-scale motions referred to as the subgrid-scale stresses. These extra terms are unknown and requires modelling. Their principal role is to extract the turbulence energy that is *cascading* from the large resolved scales across the cut-off as indicated in

Figure 2.1. In effect, the model mimics the dissipative drain occuring at the high end of the wave number band.

The area of subgrid-scale modelling has seen many developments since Smagorinsky's pioneering work in the 60's and it remains a very active area of research in LES. The purpose of the present section is to give a broad overview of the variety of models available in the literature. A brief statement is given on the general requirements that a subgrid-scale model must satisfy, followed by a discussion of the principles of various subgrid-scale model groups.

Sagaut [193] proposes that an appropriate model must satisfy the following conditions:

- Galilean invariance;
- physical consistency;
- adherence to known concepts of turbulence physics;
- numerical stability when implemented;
- computational economy.

Ghosal [68] also discusses further possible conditions that need to be considered in the course of constructing a subgrid-scale model, namely symmetry and realizability, the latter concerned with physical plausibility.

Once a model has been formulated to satisfy these requirements, its properties can be investigated via *a-priori* and *a-posteriori* tests. In a-priori tests, fully resolved DNS data (e.g. Clark et al [39], Mcmillan and Ferziger [144], Vreman et al [227]) or experimental data (Meneveau [152], Liu et al [130]) are first filtered in conformity with the LES filter size. The subgrid-scale stresses are then extracted from the filtered data. With the filtered field of motion inserted in the subgrid-scale model, the modelled subgrid-scale stresses are obtained. The correlation between the *prediction* of the model and the stresses derived from the data gives then a statement of how well the model represents the stresses. This approach, while relatively simple and economical, suffers from the fact that the numerical effects, resulting

from the solution of the LES equations, are not taken into account as well as the two-way interaction between the LES solution and the subgrid-scale stresses. It is thus occasionally observed that models giving good results in *a-priori* tests, perform poorly in real LES computations. A well-known example is the scale-similarity model proposed by Bardina et al [12], which displays a high correlation in *a-priori* tests, results in instability in actual LES computations because of its non-dissipative properties. The reverse observation has also been made as some of the most commonly used models in LES are known to correlate rather badly in *a-priori* tests. One example is the Smagorinsky model [208] which performs badly in *a-priori* tests (Mcmillan and Ferziger [144]), but is one of the most widely employed subgrid-scale models in LES, and is often adequate if all that is required is the dissipation of the turbulence energy.

A-posteriori testing consists of introducing the model in a LES code and performing a computation, with subsequent examination of the full solution and possibly of the subgrid-scale stresses. This is a more expensive process. However, it provides the definitive statement on whether the model is suitable for LES or not and constitutes the ultimate test of the model's characteristics.

There exists a wide variety of formulations for the subgrid-scale stresses, some formulated in physical space, others in spectral space, some isotropic and others anisotropic, some based on the eddy-viscosity concepts and others based on non-diffusive principles. The formulations range from relatively simple algebraic expressions to models involving transport equations. All models involve numerical coefficients. Models may be distinguished between those which employ coefficients that are fixed by calibration and others which automatically (dynamically) adjust the coefficients to the flow conditions. Models in the latter categorie are referred to as *dynamic*.

The calibration of constants for subgrid-scale models usually involves simulating freely decaying isotropic homogeneous turbulence: energy spectra are obtained at different locations in a direct numerical simulation of the flow. Large eddy simulations are then performed with the considered model and various values of the constant(s) until the correct spectra are reproduced (see Nicoud and Ducros [167],

Shur et al [206], Kosović et al [109]). Constant calibrating is also carried on other types of flow, such as channel flow (Mason and Callen [143], Deardorff [49]) or the flow over a backward-facing step (Sagaut [192]), among others.

2.3.2 Subgrid-scale eddy-viscosity

Eddy-viscosity formulations rely on the assumption that the anisotropic part of the stress tensor is proportional to the strain tensor via a proportionality coefficient known as the turbulent viscosity ν_t, by analogy to the viscous stresses. Hence, the subgrid-scale stresses τ_{ij} are expressed as:

$$\tau_{ij} - \frac{\delta_{ij}}{3}\tau_{kk} = -2\nu_t \overline{S_{ij}} \tag{2.17}$$

where $\overline{S_{ij}} = 0.5\left(\partial\overline{u_i}/\partial x_j + \partial\overline{u_j}/\partial x_i\right)$ is the strain tensor.

Based on the knowledge of turbulence properties, various models for the subgrid-scale viscosity may be derived. Alternative formulations can be based on considerations in physical space or in spectral space. Most models are *homogeneous*, in the sense that they only depend on a single filter width $\overline{\Delta}$. Anisotropy can be obtained by modifying the filter size (Scotti et al [203]). Other formulations involve a viscosity tensor, instead of a scalar coefficient pertaining to all stresses (Abba et al [1]).

While the previously cited approaches are all constructed from considerations in physical space, models based on spectral properties have also been proposed (see Lesieur and Métais [124] for a complete review of such models) and indeed succesfully applied to a wide range of flows such as the mixing layer or backward-facing step (see Lesieur and Métais [124] for examples of applications).

For some of the eddy-viscosity models, the design is that the eddy-viscosity formulation describes the energy drain in the cascade part of the turbulence spectrum for isotropic turbulence. These models thus involve numerical constants which are tuned to one set of conditions and therefore are not universal. In other models, the viscosity is adjusted dynamically following the procedure proposed by Germano et al [65]. In practice, this is achieved by making the constant of the eddy-viscosity model a time/space-dependent coefficient, based on continuous scrutiny of the re-

solved field. As this procedure also applies to other models than those based on an eddy-viscosity approach, it is the subject of a separate Section 2.3.5.

The extensive use of eddy-viscosity subgrid-scale models is due to the simplicity of their implementation and the advantageous impact they have on numerical stability, owing to their dissipative properties.

All subgrid-scale models employed in the course of this work are of the eddy-viscosity type, and their details are presented in Chapter 3.

2.3.3 Scale similarity models

The eddy-viscosity approach is very popular among LES practitioners owing to dissipative properties of the related models and their numerically stabilising properties. These models rely on the assumption of equilibrium which has a limited validity especially when the filter is large relative to the dynamically dominant scales (e.g. near the wall). Alternative formulations have therefore been proposed to circumvent these limitations and so give a better representation of the subgrid-scale processes.

Bardina et al [12] proposed a model that assumes the unresolved scales to behave in a similar way to the smallest resolved scales. This assumption is known as the *similarity hypothesis*. This model is obtained by a repeated application of the LES filter, assuming that $\overline{u_i u_j} = \overline{u_i}\,\overline{u_j}$ and $\overline{\overline{u_i} u'_j} = \overline{\overline{u_i}}\,\overline{u'_j}$. By replacing these in Relation 2.15, one obtains:

$$\tau_{ij} = \overline{\overline{u_i}\,\overline{u_j}} - \overline{\overline{u_i}}\,\overline{\overline{u_j}} \tag{2.18}$$

The resulting model has been found to perform well in *a-priori* tests, but its lack of dissipative properties made it unsuitable for use in actual LES computations. Its major advantage is, however, its ability to represent backscatter, i.e. the transfer of energy from small to larger scales. The lack of dissipative properties was ultimately solved by linearly combining this model with the Smagorinsky model to add the lacking dissipative properties (Bardina et al [12], McMillan et al [145]).

An alternative to the scale-similarity model of Bardina et al [12], uses a second filter with a width twice as large as the one used in the original scale-similarity

model (Liu et al [130]). The resulting model writes as:

$$\tau_{ij} = c_L L_{ij} = c_L \left(\widetilde{\overline{u_i u_j}} - \widetilde{\overline{u_i}}\,\widetilde{\overline{u_i}} \right) \tag{2.19}$$

where $\bar{\cdot}$ represents the grid filter and $\tilde{\cdot}$ the second filter (the test filter) with a width twice as large as the width of the grid filter.

Shah and Ferziger [205] observed that if the definition of the real subgrid-scale stresses is considered ($\tau_{ij} = \overline{u_i u_j} - \overline{u_i}\,\overline{u_j}$), the scale-similarity model can be derived by replacing u_i by $\overline{u_i}$. The scale-similarity model is however unable to provide enough dissipation which, according to Shah and Ferziger, is due to $u_i \approx \overline{u_i}$ not being an accurate enough representation of the complete field. Hence, they proposed to include higher order terms for the representation of the resolved field, leading to the model being written as:

$$\tau_{ij} = \widehat{u_i^* u_j^*} - \widehat{u_i^*}\,\widehat{u_j^*} \tag{2.20}$$

where u_i^* is the new approximation for u_i and is the solution of a partial differential equation defined as:

$$L(u_i^*) = \overline{u_i} \tag{2.21}$$

with $L = L_x L_y L_z$ where L_x, L_y and L_z are differential operators defined as $L_\psi = 1 + C_1 \partial/\partial\psi + C_2 \partial^2/\partial\psi^2$ with $\psi = x, y, z$. The filtering operation $\widehat{\cdot}$ is defined in a similar way: $\widehat{u_i^*} = M(u_i^*)$ with $M = M_x M_y M_z$ and $M_\psi = 1 + D_1 \partial/\partial\psi + D_2 \partial^2/\partial\psi^2$. The constants C_1, C_2, D_1 and D_2 are the constants of the model. They regulate the level to which the small scales are used in the model. Shah and Ferziger determined these constants by reference to a Taylor serie approximation of the Box Filter.

More recent proposals include the subgrid-scale estimation model of Domaradzki and Loh [52] and the approximate deconvolution procedure of Stolz and Adams [216]. Both approaches attempt at reconstructing the unresolved unknown field of motion by extrapolation from the known field. In the subgrid-scale estimation model, a first step involves the inversion of the filter operator to obtain an estimate of the total velocity field. A second stage consists of generating a range of subgrid-scales

on a mesh twice smaller than the LES mesh by using a non-linear operator. The approximate deconvolution procedure of Stolz and Adams [216] is similar. In this case, the unresolved field is estimated via a truncated serie expansion of the inverse filter expansion. Again, these models contain constants, the values of which are either fixed by the user or obtained via the dynamic procedure of Germano et al [65] (see Section 2.3.5 for more details).

2.3.4 Models based on transport equations

A widely used approach to RANS involves the use of transport equations for the Reynolds stresses, the turbulence energy and the turbulence dissipation rate. These are derived from the Navier-Stokes equations and their time-averaged form, but require closure to eliminate unknown correlations. Similarly, transport equations can be written for the subgrid-scale stresses, the subgrid-scale energy and the subgrid-scale dissipation. Here too, modelling is required to eliminate unknown terms.

A first proposal of this kind was made by Deardorff [50] for a model of transport equations for the subgrid-scale stresses, using the filter width as characteristic length scale. This model was recently investigated by Fureby et al [63] for forced isotropic turbulence and channel flow. They observed improved performances relative to simpler models and noted that the use of a subgrid-scale stress transport model is better suited to deal with the anisotropy of the grids as it does not assume the isotropy of the scales, assumption which is at the heart of most models. Most transport models proposed for LES are, however, limited to the use of a subgrid-scale energy transport equation. In these models, the dissipation term is approximated by $\epsilon = C_\Delta k^{3/2}/\overline{\Delta}$ except for the model by Dejoan [51] which solves, in addition to the subgrid-scale transport equation, a transport equation for the subgrid-scale dissipation. Such one-equation models were proposed by Schumann [200], Yoshizawa [240] or Dejoan [51] among others. Transport-equation models with dynamic features were also proposed by Ghosal et al [69] and Menon et al [154], following the procedure proposed by Germano et al [65] and described in the next section. The DES proposal of Spalart et al [212], which leans on the RANS one-equation model of Spalart and Allmaras [211],

is another model in this category, with the pecularity that the transport equation governs the subgrid-scale viscosity rather than the subgrid-scale energy.

Models based on transport equations are clearly more complex and involve more equations. Because these models are non local, they are claimed to require fewer grid nodes than simpler algebraic models for similar accuracy. Indeed, Menon et al [154] have shown that, for isotropic turbulence, as the grid was coarsened, the level of correlations for the subgrid-scale stresses predicted by a one-equation model with those predicted by DNS remained higher than the level of correlations resulting from the use of less complex models such as the scale-similarity model or the dynamic Smagorinsky model whose performances worsened a lot more with the loss of resolution. Another argument put forward in favour of using transport equation models is that the cost of solving additional transport equations for the subgrid-scale quantity is comparatively small, when compared to the cost of solving LES equations [63]. On the other hand, Piomelli [139], among others, argues that the benefits are small relative to the additional cost.

2.3.5 The dynamic procedure

The dynamic procedure, proposed by Germano et al [65], aims to circumvent the need for using a fixed constant in the subgrid-scale model. While initially applied in the context of eddy-viscosity modelling, specifically to the Smagorinsky model [208], this procedure can be extended to all models. Examples are the dynamic mixed-scale model of Zang et al [242], based on the mixed model of Bardina et al [12], and the one equation-transport model for the turbulence energy of Menon et al [154]. The approach is based on a relationship between the subgrid-scale stresses and the resolved turbulent stresses at two different levels of filtering. By using the same model to represent both subgrid-scale stress tensors, constants can be eliminated or, rather, become dependent on the flow properties. In specific terms, two levels of filtering are considered: the first is the LES filter, the grid filter, with a filter width being equal to the grid size and denoted by $\overline{(\cdot)}$; the second filter, the test-filter, has a width twice that of the grid filter and is denoted by $\widehat{(\cdot)}$ (see Figure 2.2). The

application of the grid-filter to the Navier-Stokes equations leads, as noted earlier, to the LES Equations (2.16). The test-filter can similarly be applied to Equation (2.16), and this leads to:

$$\frac{\partial \widehat{\overline{u_i}}}{\partial t} + \frac{\partial \widehat{\overline{u_i}}\,\widehat{\overline{u_j}}}{\partial x_j} = -\frac{\partial \widehat{\overline{p}}}{\partial x_i} + \frac{2}{Re}\frac{\partial \widehat{\overline{S_{ij}}}}{\partial x_j} - \frac{\partial T_{ij}}{\partial x_j} \tag{2.22}$$

where $T_{ij} = \widehat{\overline{u_i u_j}} - \widehat{\overline{u_i}}\,\widehat{\overline{u_j}}$ represents the subgrid-scale stress tensor at the test-filtered level. The resolved turbulent stresses are:

$$L_{ij} = \widehat{\overline{u_i}\,\overline{u_j}} - \widehat{\overline{u_i}}\,\widehat{\overline{u_j}} \tag{2.23}$$

and can be reformulated as a function of the subgrid-scale stresses τ_{ij} and T_{ij} by what is known as the *Germano identity*:

$$L_{ij} = T_{ij} - \widehat{\tau_{ij}} \tag{2.24}$$

If the same model is used to relate T_{ij} and τ_{ij} to their respective strain fields, that is if one assumes similarity between T_{ij} and τ_{ij}, the constant appearing in the selected model can be extracted from (2.24).

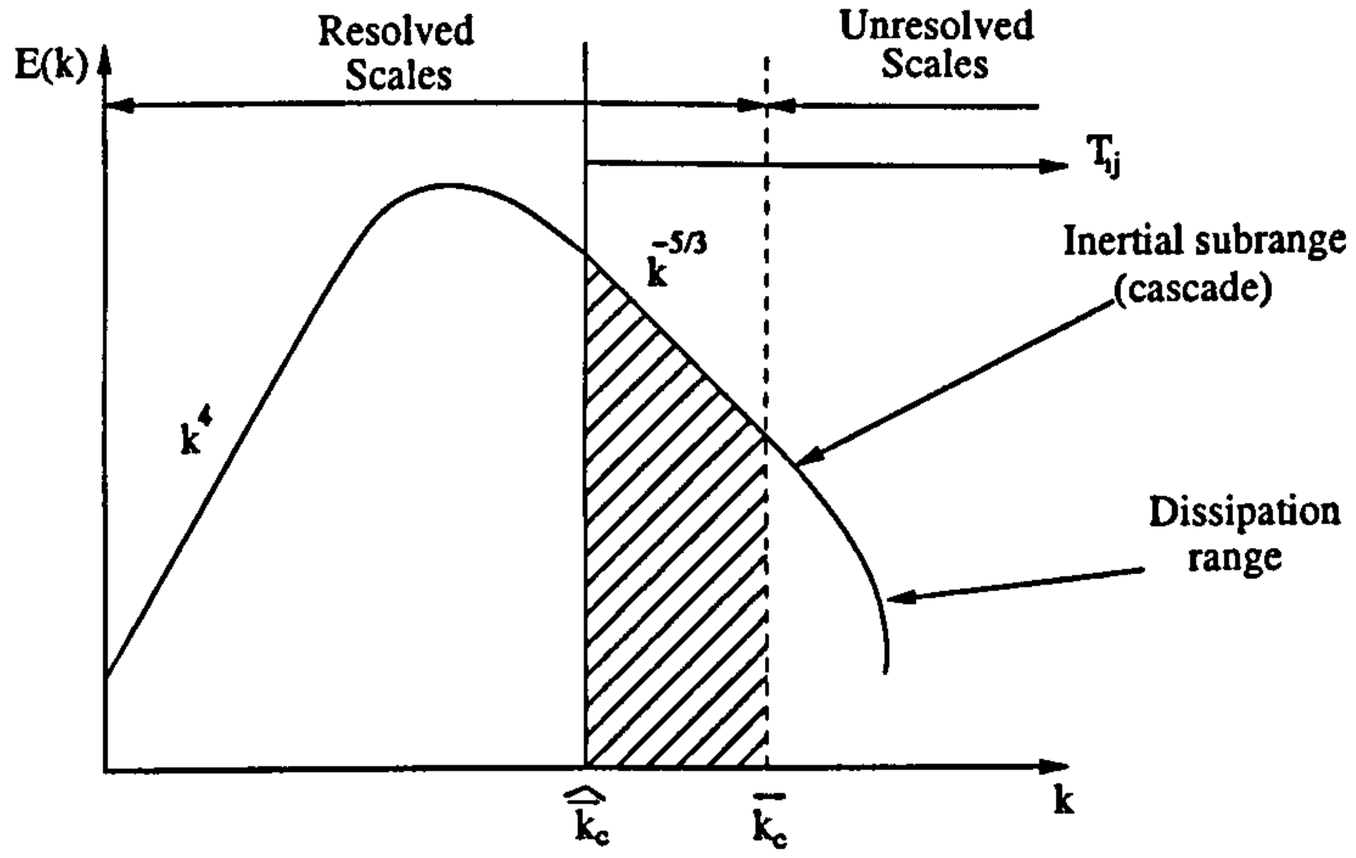

Figure 2.2: Position of the filters cut-off for the dynamic model.

A desirable consequence of the above methodology is that the subgrid-scale stresses vanish in the absence of turbulent motion and also decay to zero as the wall is approached. The dynamic procedure admits, in principle, backscatter which is the transfer of energy from small to large scales. This is reflected by negative

values of the coefficient extracted from (2.24). However, this renders the numerical solution unstable. Indeed, the coefficient extracted from (2.24) often varies at extremely high rates, which is also destabilizing, even if the coefficient is limited to positive values. This problem is usually addressed by introducing some kind of averaging process and limiters which restrict the range within which the coefficient is allowed to vary.

2.3.6 Implicit subgrid-scale modelling

The traditional approach to large eddy simulation consists, as described in the previous sections, of resolving the filtered Navier-Stokes equations in conjunction with a subgrid-scale model. An alternative approach is to employ certain classes of discretisation schemes which have the pecularity of introducing a numerically dissipative mechanism broadly equivalent to that of a subgrid-scale model, making the subgrid dissipation implicit. The effects of the smallest, unresolved scales of the motion are then taken into account by the truncation error of the discretisation scheme, mimicking the role of energy drain normally played by the subgrid-scale stresses. This approach is also often referred to as MILES (Monotone Integrated Large Eddy Simulation) (see Boris et al [18], Margolin and Rider [141]). An argument occasionally put forward in favour of MILES is that it removes all empiricism which is inherent in a subgrid-scale model. However, it is obvious that the linkage between the truncation error and the physics of subgrid-scale dissipation is at best obscure if not absent. Concerns regarding the use of these methods were summarised by Spalart [210] who argues that implicit dissipation will affect a wider band of the spectrum than is done by a conventional subgrid-scale model. In addition, Galilean invariance is not conserved due to the numerical scheme and the dissipative mechanism being asymmetric. Yet another concern relates to the near-wall layer which can only be simulated by the LES approaching a DNS. The MILES method remains controversial, but has been shown, over the years, to work on various flows with some degrees of success, making it difficult to reject it, as argued by Fureby et al [62, 63] and Mary and Sagaut [142], among others.

2.4 Initial and boundary conditions

2.4.1 Initial condition

In Large-Eddy Simulations, the initial conditions are rarely of importance (or rather should be unimportant). Usually, the initial condition consists of a guessed velocity field onto which a small random perturbation field is superimposed. This has little influence in flows for which an inflow is prescribed, provided that the integration-time is long enough. In the case of flows in which one direction is homogeneous (e.g. channel flows), the nature of the perturbation can become influential, and the flow can approach a laminar state if the perturbation does not create enough unstable modes.

2.4.2 Inflow boundary condition

Inflow conditions must be prescribed, in principle, in terms of the entire spectral state. This is rarely possible, and an approximate state must be specified. It is important in this case that the approximate condition is physically consistent and meaningful, otherwise the realism of the simulations may be seriously affected. A variety of routes have been proposed:

- Ducros et al [53], when computing a spatially developping boundary layer, used a time-constant field onto which a random perturbation is imposed;
- a variant consists of selecting the perturbation in a way that certain moments or spectral features are reproduced (Lee et al [119]);
- another approach consists of extracting a time serie of instantaneous velocity from a precursor periodic simulation and feeds them into the final simulation (e.g. a periodic channel flow could be used as a precursor for generating the inflow condition for the flow over a cube [235]);
- a variant of the latter approach is proposed by Li et al [126] who proposed to extract such a time serie over a period equal to the integral time scale of the

flow and to make it periodic by a windowing technique before feeding it into the actual simulation;

- Lund et al [136] devised a procedure in which the velocity from a plane near the exit is extracted, rescaled and, then, reintroduced as inflow.

Although the need for unsteady inflow condition does not arise in the present work, the issue is potentially very influential in terms of its impact on the quality of LES solutions. More details on the use of inflow boundary conditions in LES can be found in Sagaut [193] and Li et al [126].

A way to circumvent the use of inflow (and outflow) boundary conditions is to exploit periodicity whenever it exists, and this has indeed been widely done in LES and DNS for channel flow (Moin and Kim [159], Deardorff [49] among others), square ducts (Huser et al [89]), river flows (Bradbrook et al [20]), flows over wavy walls (De Angelis et al [47]) and many other geometries. The use of periodic conditions is a mean to a substantial diminution of the spatial size of the computational domain. Care must be taken, however, to ensure that the domain remains large enough for decorrelation to be maintained between the motions at the periodic boundaries, contained within the domain. Jiménez and Moin [97] demonstrated that the lower order statistics can be still obtained with acceptable accuracy in a channel flow with the domain size being as small as about 100 wall units in the streamwise direction and 300 wall units large in the spanwise extent. This geometry is referred as the minimal channel.

2.4.3 Outflow

Typically in LES, the flow is highly unsteady, vortical and involves large spatial gradients. This situation is very different from what is encountered in RANS modelling in which often statistically fully-developed conditions can be assumed with good accuracy. This is equivalent to suppose that the gradient of any variable in the direction normal to the outflow boundary is zero:

$$\frac{\partial \phi}{\partial n} = 0 \tag{2.25}$$

where n is the direction normal to the boundary. The use of this approach in LES is, however, not recommended especially in the presence of vortical structures. The application of (2.25) indeed prevents the propogation of the pressure waves across the boundary which, then, reflects these waves inside the domain, leading to the contamination of the flow by spurious oscillations, and, eventually, the destabilisation of the computation (Esfahani [56]).

When incompressible flows are considered, an approach first proposed by Pauley et al [170] is often used. Mathematically, for any variable ϕ convected through the boundary, this is expressed as follows:

$$\frac{\partial \phi}{\partial t} + u_c \frac{\partial \phi}{\partial n} = 0 \tag{2.26}$$

where n is the direction normal to the boundary, and u_c represents a convective velocity scale. Several choices for u_c can be envisaged, such as the mean velocity along the local boundary. Pauley et al [170] have shown that this choice has little influence on the results. In DNS and LES of incompressible flows, expression (2.26) is very often applied (Le et al [118], Kaltenbach et al [103] among others). Another way of deriving (2.26) is to apply the characteristic method to the compressible Navier-Stokes equations in the direction normal to the boundary, that is in the direction in which the waves propagate (see Poinsot and Lele [179], Thompson [220]). If the flow is then assumed incompressible, adiabatic and inviscid at the boundary and, in addition, if the considered boundary is far enough so that a condition of constant pressure at infinity can be used, one obtains (2.26).

2.5 Near-wall treatment

At high Reynolds numbers, LES cannot resolve the eddies in the semi-viscous near-wall region, unless a very fine mesh is used. Even if such a fine mesh can be tolerated normal to the wall, accuracy requirements impose constraints on the mesh aspect ratio, and normal-to-wall refinement implies the need for equivalent refinements in the other two directions. This is not tenable on economic grounds and necessitates the adoption of an approximate treatment which bridges the near-wall layer. Alter-

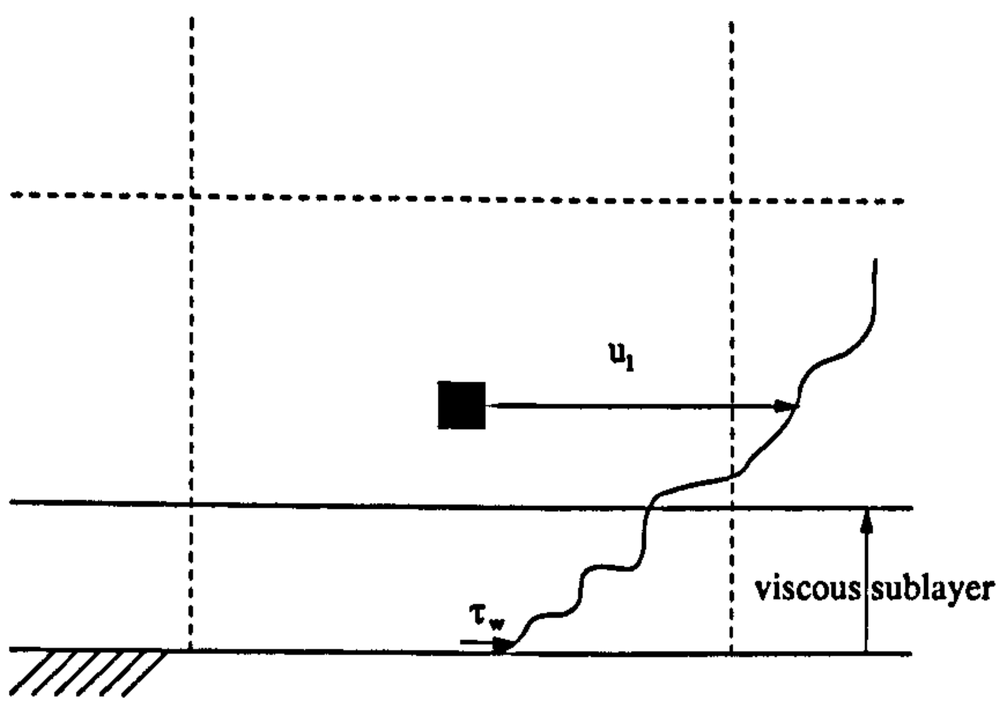

Figure 2.3: Relationship between wall shear stress and tangential velocity.

native approaches are based on the use of conventional low-Re turbulence models or semi-analytical *wall laws*. The latter route is investigated in the present work.

In essence, a wall-law approximation is required to return the correct instantaneous wall shear stress corresponding to the known instantaneous velocity at the wall-nearest computational node which is (normally) outside the semi-viscous sublayer (see Figure 2.3). The wall-shear stress is then used as the wall boundary condition (in conjunction with the impermeability condition). This approach requires an assumption to be made on how the instantaneous velocity varies within the bridged near-wall region. Alternatives include log-law and power-law distributions. Other wall-law formulations also available, but not tested in the present work, were proposed by Schumann [200], Grötzbach [74] and Piomelli et al [177]. The Schumann-Grötzbach approach proposes that the velocity at the first grid point should be in phase with the instantaneous wall stress, while Piomelli et al [177] modified this approach by introducing an empirical shift to the near-wall horizontal velocity and wall shear stress to take into account the effect of the near-wall structures.

Alternatives routes to wall functions include the use of a simplified set of the Navier-Stokes equations in the form known as the thin boundary layer equations (see Balaras et al [10] and Cabot and Moin [25]). Other approaches are based on coupling or interfacing RANS and LES sub-domains, with the interface of the two regions either arbitrarily specified or dictated by a grid-related criterion. An example for the former is presented by Davidson and Peng [46] who solved a k-ω RANS model near the wall and the LES in the outer region using a one-equation

subgrid-scale model for k (see also Temmerman et al [218]). An example for the latter approach is the Detached Eddy Simulation (DES) of Spalart et al [212] based on the Spalart-Allmaras one-equation model [211] applied to both domains. In this case, the *switching* between the RANS and the LES domain is effected upon a comparison between the grid filter size $\overline{\Delta}$ and the length-scale returned by the RANS model, essentially the distance from the wall, which delimits the RANS and LES regions.

In the present study, different formulations, based on log-law formulations, are investigated and will be discussed in details in Section 3.3.

2.6 Resolution requirements

The quality of the solution in a LES computation strongly depends on the choice of the time-step and the definition of the mesh. These choices strongly depend on the problem considered, the numerical strategy adopted (see Section 2.7), the modelling approach employed (see Section 2.3) and the amount of computing power available.

A first aspect is the choice of the time-step. Assuming that it satisfies the criteria for numerical stability, the time-step must be chosen so that it remains smaller than the time-scale of the smallest resolved eddies. Choi and Moin [33] showed, in DNS of channel flows, that the time-step had a strong influence on the quality of the statistics, with too large time-steps even leading to the computed flow relaminarizing after an initial turbulent state.

The grid choice, both with respect to its density and topology, is the second important aspect. The density of the grid must be adequate enough to resolve the energy-carrying scales in all the directions. As the internodal distance dictates the filter width, it must in effect be small enough to ensure that the cut-off occurs in the inertial subrange of the energy spectrum. Bagget et al [8] estimated that the grid size needed to be ten times smaller than the local integral dissipation scale defined by $L = k^3/\epsilon$ where $k = \overline{u_i u_i}$, and ϵ is the energy dissipation rate. As discussed in Section 1.1, this leads to the number of cells rising as $Re^{0.5}$ away from the wall and $Re^{2.4}$, near the wall (Reynolds [185]). This also implies that, near the wall, the grid

employed is very similar to the grid used in a DNS with typical sizes, in wall units, of order $\Delta x^+ \approx 50-150$, $\Delta y^+ \leq 2$, $\Delta z^+ \approx 15-40$ [61]. These constraints originate from the need to resolve the near-wall structures. Typically, an elongated near-wall hairpin vortex is 100 wall units long, while 50 wall units separate, in the spanwise direction, the boundary layer streaks.

Regarding other grid properties, low aspect ratio, high orthogonality, low skewness and low stretching are all desirable properties in LES. In terms of aspect ratio, the cell should be ideally perfectly cubic, as this guarantees that the solution is well-resolved in all directions, and that there is no contamination from the badly resolved solution in one direction to a well resolved solution in another direction. This strongly affects the accuracy of the spatial discretisation scheme, which depends on the grid properties. The aspect ratio also plays an important role in securing that the subgrid-scale model works to its full potential. Highly stretched grids result in the addition of extra terms in the equation that will also need to be modelled (Geurts and Leonard [66]). As shown by Mellen et al [148], the impact of grid stretching on the accuracy of LES in turbulent channel flow is important in so far as stretching and compression imply the need for energy transfer from the resolved to the modelled ranges and vice-versa.

2.7 Numerical methods

LES computations are characterized by the rapid variations of the flow properties in space and time. This places heavy demands on the numerical approximations, and on the computational cost of a solution. In DNS, the need to resolve accurately all the scales leads naturally to the use of high-order schemes. The range of problems considered in LES includes some very complex geometries which may force to consider the use of methods which can deal with these geometries but also whose accuracy are smaller in order to limit the cost of a simulation to a reasonnable level. The present section aims at summarising the numerical techniques available for use in a LES procedure.

When it comes to selecting a numerical strategy for the LES of incompressible

flows, four different aspects have to be considered:

- the spatial discretisation;
- the time-integration method;
- the coupling between the pressure and the velocity fields;
- the solution of algebraic systems.

As regards the basis for spatial discretisation, spectral, finite-difference, finite-volume and finite-element methods are all applied in current LES practice. In spectral methods, the spatial derivatives are evaluated in Fourier space. This allows a very accurate representation of all the turbulent scales, which is maintained throughout the complete spectrum [157], with errors declining exponentially with grid density. However, the method is limited to simple geometries which can be covered by uniform spaced grid cells, rendering a poor choice for general LES procedure in contrast to DNS (Kim et al [106], Rogers and Moser [190]).

A more popular variant of the above in LES is the pseudo-spectral method. Here, the convective term in the governing equations is first evaluated in the physical space, then its derivatives are computed using a Fourier transform. A common practice is to combine a pseudo-spectral method in the homogeneous directions with a finite-difference scheme in the wall-normal direction, as is done, for example, by Moin and Kim [159] for a channel flow.

Pseudo-spectral and spectral methods alike suffer from aliasing errors (see Section 2.8 for more details on aliasing errors) that can severely affect the solution of a computation. Methods to suppress them or, at least, control them exist, however.

In finite difference methods, the computational domain is represented by lines of nodes. At each node (line intersection), the partial differential form of the governing equations is written and discretised as a function of the neighbouring nodes. If the geometry is complex, curvilinear coordinates are used, and the physical space is projected onto a rectilinear computational space. These methods are simple to use and implement, robust, can attain a high degree of accuracy and deal with complex geometries. For these reasons, finite-difference methods are regularly used

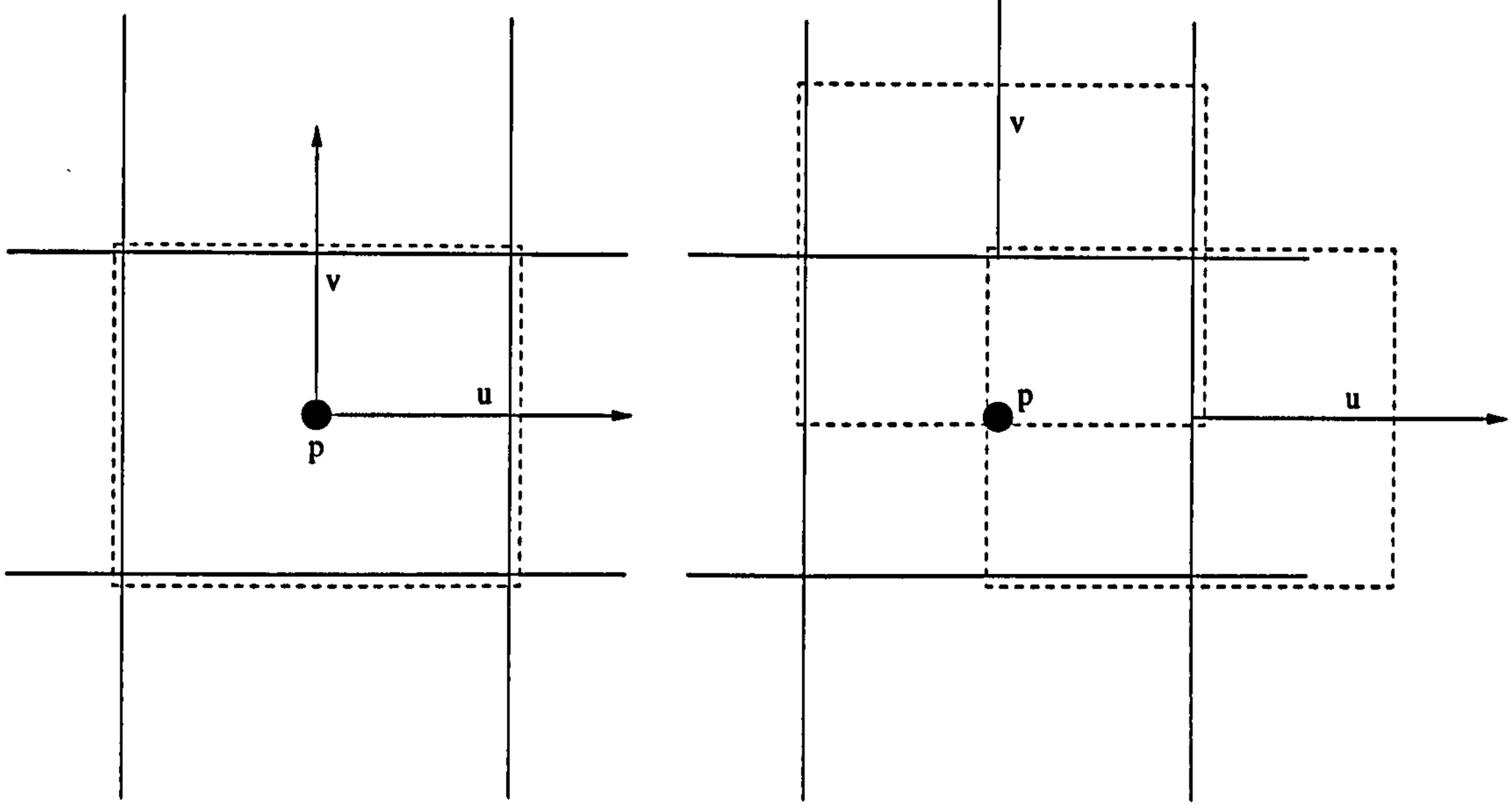

Figure 2.4: Alternative finite-volume arrangements: Left - colocated arrangement; Right - staggered arrangement. The continuous lines indicated define cells associated with the pressure while the dashed ones relate to the cells associated with the velocities or momentum components.

in LES. Finite-difference methods require considerably more grid nodes than spectral methods for similar accuracy even if the order of discretisation is as high as 8 or 10. Typically, a DNS using a second-order central difference scheme would require up to 6 times more grid points than a Fourier spectral method in order to compensate the loss of accuracy due to the use of a lower order scheme (Moin and Mahesh [160]). Numerous examples of LES and DNS that use finite-difference methods can be found in the literature. Some of the many examples of DNS that use finite-difference methods are the backward-facing step of Le et al [118] or the compressible boundary layer of Wasistho [231]. Examples of LES are the channel flow computed by Deardorff [49], the impinging jets of Olsson and Fuchs [168], and a flow over obstacle computed by Yang and Ferziger [239].

The finite volume method is a very popular technique in LES. It distinguishes itself by an exact satisfaction of the conservation principles embedded in the integral form of the governing LES equations. The computational domain is subdivided into small volumes or cells known as control volumes. Two principal arrangements are

employed depending on the variable storage location: colocated or staggered storages as shown in Figure 2.4. In the colocated arrangement, pressure and velocities are all located at the centroids of a single set of volumes, while in the staggered arrangement, the velocities are placed at the cell faces of the primary set of volumes and at the centroids of which the pressure is stored. Often, the staggered arrangement is preferred to the colocated one as spurious pressure oscillations are observed when the latter is used. These oscillations originate from the fact that linear interpolation of the nodal velocity field, effected to derive the cell-face velocities which are needed to impose mass-conservation, results in a decoupling between the velocity and pressure fields and, hence, in oscillatory solutions [169]. This is responsible for a numerical decoupling of the pressure from the velocities. A special interpolation practice proposed by Rhie and Chow [186] allows the coupling to be re-established, but introduced a measure of artificial dissipation which leads to a violation of the energy conservation principle. Despite its disadvantages, the co-located option is highly attractive and preferred in complex geometries because of its simplicity and its storage economy.

The finite volume method involves two levels of spatial approximations when discretising the governing equations:

- surface and volume integrals are evaluated by use of quadrature formulae such as the trapeze and Simpson rules;
- interpolation of nodal variables is used to determine variable values at locations where they are not computed.

Both the quadrature formulae and the interpolation scheme affect the order of accuracy of the method, and it is, in practice, difficult to construct methods with accuracy higher than order two, which is generally held to be adequate for LES. On the other hand, finite-volume methods are easy to implement efficiently, are suited to complex geometries and satisfy, inherently, the conservation principle. Finite-volume methods are widely used in RANS scheme in research and industries alike and are also very popular in LES both in staggered and collocated formulation. Breuer [21] used a collocated finite-volume code to compute flows over cylinders.

Confined coaxial jets were computed with finite-volume and a staggered arrangements subsequently by Akselvoll and Moin [4] and by Pierce and Moin [174]. Other LES applications of colocated finite-volume methods include airfoil computations by Weber and Ducros [232] or jets in cross-flow (Jones and Wille [98, 99]).

In the finite-element method, the computational domain is divided into elements with the computational nodes located at the corners and possibly also on the element edges and interior. The variables and their derivatives are evaluated at these nodes. In between the nodes, interpolation functions, termed *shape functions*, determinate the variation of the variables. The shape functions are only valid on the considered element and are usually not continuous from one element to another. The order of the method is determined by the number of nodes forming an element. The set of governing equations is then multiplied by some weighting function and then written in its integral form, and this then leads to a system of algebraic equations. Finite-element methods are mathematically more complex than finite-volume methods and therefore more difficult to implement. Their mathematical properties are well understood and documented, however. Their main field of application is solid mechanics, but they have gained a degree of popularity in fluid dynamics. Some applications of the finite-element method to LES are encountered in the literature, although much less frequently than the other methods. Examples include works by Chalot et al [30] for aerodynamic applications and the work by Rollet-Miet et al [191] on tube bundles.

An important comment to be made, at this point, relates to the presence or not of numerical dissipation in the spatial discretisation scheme. This is of particular importance to the question of whether the scheme is energy-conserving. It has been explained in Section 2.3.6 that some LES practitioners will use the dissipative properties of the numerical scheme to replace the subgrid-scale model. Except for this particular case, it is normally considered that LES must use non-dissipative schemes in order for the energy of the scales to be conserved. Indeed, it has been shown that dissipative schemes, such as QUICK (Leonard [121]) and other upwind schemes destroy the medium and small scales which ougth to be resolved, giving highly inaccurate solutions (Breuer [21], Mittal and Moin [156], Kravchenko and

Moin [111]). There are circumstances in which numerical dissipation is exploited in an effort to avoid unacceptable numerical problems arising from fully centred, non-dissipative discretisations. The most frequent reason is the need to damp unphysical oscillations resulting from various sources (reflection from the boundaries, check-boarding). Recent LES computations on an high-lift aerofoil at high Reynolds use a zonal approach (Dahlström and Davidson [44]), another approach used a numerical sensor which introduces upwinding locally (Mary and Sagaut [142]). Finally, simulations in which shocks occur necessitate dissipative schemes. Such LES computations have been performed by Held and Fuchs [83] for a NACA 0012 wing in the transonic regime and by Ducros et al [54] for $3D$ shock/turbulence interaction. Both codes used central schemes with additional second and fourth order artificial dissipations.

The next issue is the selection of the time-integration scheme. This has a substantial impact on both the efficiency and accuracy of the solver. Two principal strategies are used in LES. Explicit methods evaluate directly the variables from the previous time-step using only the information possible from that time-step. These methods are algorithmically straightforward, but impose severe stability-related restrictions on the time- step. Favourites explicit schemes in LES are the Adams-Bashfort (second order) and Runge-Kutta (third and fourth order) methods. The former only requires one evaluation of the convective and diffusive terms per time-step, while Runge-Kutta requires as many evaluations of these terms as the order of the method. The advantage of using the latter is that the constraint on the time-step is less stringent than for Adams-Bashfort. The alternative is to use an implicit method, such as the Cranck-Nicholson scheme, which also employ the unknown variable fields at the forward time-level to obtain the solution, hence requiring a matrix-inversion algorithm. Against the increase in complexity of the implementation and the extra cost coming from the need to inverse a matrix at each time- step is the advantage that these methods do not suffer from stability-related limitation on the time-step, hence allowing the use of a larger time-step.

In LES, explicit approaches are often preferred for advancing the convective fluxes as accuracy constraints demand that the time-step be smaller than the cha-

racteristic time-scale of the smallest resolved eddies. These constraints are more limiting than the convective stability limit ($CFL = u\Delta t/\Delta < 1$) imposed by the scheme. Economical arguments do, therefore, justify the use of explicit methods. The stability argument associated with the diffusive fluxes is usually far more constraining ($\Gamma\Delta t/\Delta^2 < 1/4$ for uniform 2D mesh as shown in Hirsch [85], p320) than the CFL criterion, especially near the walls, where the cell sizes become very small. The use of an explicit scheme for the diffusive term may be more justified, in term of coherence, if such a scheme is already used for the convective term. However, economical considerations may motivate the use of an implicit approach as, for example, at high Reynolds number in a near-wall region, cells are small and viscous processes play an important role, and the time-step dictated by the stability analysis may be extremely small. In practice, a variety of methods are used. For example, Kravchenko and Moin [111] used a third-order Runge-Kutta for the convective term and the second order Crank-Nicholson method for the diffusive term, Jones and Wille [98, 99] preferred an implicit approach based on the Crank-Nicholson scheme, while Breuer [21] applied the third-order Runge-Kutta method to both diffusive and convective terms.

The third issue considered in the present section relates to the pressure-velocity coupling strategy. When computing incompressible flows, the absence of a time-derivative in the continuity equation renders the system of equations elliptic, requiring the solution of an implicit problem which links velocity and pressure and rendering the use of a fully-explicit method, as it is done for compresible flows, impossible. This need for coupling arises from the fact that mass-conservation must be satisfied to a high level of accuracy at any time level. As mass-conservation is dictated by the pressure field, the implication is the need to solve the elliptic pressure Poisson equation, or a related equation, implicitly at the forward time level. Alternative approaches are: pressure-Poisson or pressure-correction methods, fractional-step or projection methods and artificial compressibility methods.

Pressure-correction methods (SIMPLE [28], SIMPLER [169], PISO [90]) involve the solution of a Poisson equation for the pressure correction field at the forward time-level, driven by cell-specific mass residuals which express the lack of satisfaction

of zero-divergence. The pressure correction is then added to the provisional pressure field used to determine a first estimate of the velocity field. Inner iterations are needed at any given time-step until both the pressure and the velocity field satisfy continuity and momentum simultaneously up to the desired accuracy. SIMPLE and related algorithms were used by Breuer [21], Jones and Wille [98, 99] and Dahlström and Davidson [44] among others.

The fractional-step method (Chorin [37]), popular both in DNS and LES, consists of splitting the momentum equations into two parts. In the first step, an intermediate velocity is evaluated using the convective and diffusive operators. At this intermediate level, mass conservation is not satisfied. The second step consists of solving a Poisson problem for the pressure obtained by imposing the zero-divergence condition. Once the new pressure is obtained, the intermediate velocity field is updated to give the velocity field at the new time-step. The fractional-step is certainly the most widely used of the velocity-pressure coupling technique for solving the governing equations of LES (Deardorff [49], Moin and Kim [159], Zang et al [243] among others).

The artificial-compressibility method (Chorin [36]) solves the incompressible flow problem as a pseudo-compressible problem with an artificial relationship between density and pressure. A time-derivative for the density is thus introduced into the continuity equation, making the system hyperbolic and allowing the use of methods employed for the resolution of compressible problems. Mass conservation is not satisfied until this artificial term in the continuity equation has vanished. For unsteady flows, this requires an inner iteration procedure. Again, this method has been applied with success to LES (Kim and Menon [107]) although much less frequently.

The use of an implicit approximation scheme inevitably leads to a coupled system of algebraic equations. Such a system arises from the pressure (or the pressure correction) which is the solution of a Poisson equation. This also arises when implicit schemes are used for the advancement in time of the solution. There is, therefore, a need to carefully consider the choice of the solution algorithm as it represents a major component of the LES solution in term of computing resources. A wide

variety of techniques can be applied and they can essentially be separated into two families: the direct methods and the iterative methods (e.g. Ferziger and Perić [59] for a review). In direct methods, the solution is directly extracted from the algebraic system by performing a serie of permutations between the different lines or columns of the matrix. Methods like the Gauss elimination, the Thomas algorithm for tri-diagonal matrices or the cyclic reduction method are very efficient solvers and are often used in LES and DNS (Dejoan [51], Kim et al [106] among others).

When the number of equations becomes very large, the equations become non-linear or the mesh is non-uniform, iterative procedures are often preferred to direct methods as their requirements in memory storage are lower and they often gives a better accuracy. Their principle consists of guessing a first solution which is then used to obtain a new one, and so on until the variation between two successive solutions becomes smaller than a given criterion. The solution is then said to have *converged*. The simplest iterative method is the point-Jacobi method which used the solution at time (n) to obtain a new solution at time $(n+1)$. It parallelises very well but its convergence is poor. It is, however, often used in combination with other approaches. A faster method is the Gauss-Seidel method in which the solution is calculated from the solution at time (n), and as it becomes available, the solution at time $(n+1)$. The method is more complex, but its convergence is twice as fast as the point-Jacobi method. An alternative method to Gauss-Seidel is the SOR approach (successive over-relaxation) in which an over-relaxation factor is introduced. This leads to further improvement in the convergence rate. More advanced solvers include the SIP method (Strongly Implicit Method) from Stone [217] which has a very good convergence rate and constitute an excellent basis as a preconditionner for other methods or a smoother for multigrid algorithms. Breuer [21, 22], among others, uses SIP. Conjugate gradient method (Golub and van Loan [72]), which is limited to symmetric matrices, biconjugate gradient (Fletcher [60]) and CGSTAB (Conjugate Gradient Squared Stabilized, Van den Vorst [221]) methods are also excellent methods (Wille [237], Jones and Wille [98, 99], Moin et al [40]). These last methods however require a preconditionner i.e. a method that provides a smooth enough initial guess of the solution.

Additionally, a serie of strategies exists that are often used in combination with the algorithms mentionned in the previous paragraph to accelarate the convergence to the solution: the multigrid method, the colored method and the zebra method. The multigrid approach consists of determining the solution of the problem using a solver (the smoother) on the initial grid (the fine grid), building a coarser grid, usually by removing one node (one cell) every two nodes (cells) in a given direction, then restricting on the coarser grid the solution obtained on the fine grid before applying the smoother on that coarse grid. This coarsening operation can be repeated until there is no more coarse grid available. The solution of the coarse grid is then interpolated on the previous fine grid the problem solution updated, and this operation is repeated until the finest grid among all is finally reached. The colored method consists of separating neighbouring nodes into groups of different colors, and to solve the points of one color at a time using the points of the other colors. In the zebra method, first the odd lines are solved then, the even ones.

A major component in the high cost of LES computations comes from the need to use very large numbers of grid nodes. Substantial economy can be achieved via the use of particular meshing strategies which gives more flexibility to the practitionner with regard to the grid nodes location by using zonal grids (see Mary and Sagaut [142], Kravchenko et al [112] for example) or unstructured meshes (Jansen [92, 93], Chalot et al [30]). Applying these techniques significantly reduce the number of grid nodes. Drawbacks however exist and are an increase in the complexity of the solver, question marks regarding the proper definition of the filter and the way information has to be transferred without loss between zones of different cell densities.

2.8 Source of errors in LES

While some aspects presented here may have already been discussed earlier, the intention of the present section is to summarise and discuss more carefully the source of errors encountered in LES. There exists a substantial body of theoritical work on this subject (Ghosal [67, 68], Kravchenko and Moin [110], Geurts and Leonard [66]).

However, practical LES procedures rarely take explicitely into account the impact of these errors and attempt to control or quantify them. They are present, and efforts are generally being made to secure acceptable accuracy via high mesh quality and the use of non-diffusive schemes. It is nevertheless important to understand the nature of possible errors and to appreciate their possible impact. Errors are listed and discussed below separately.

The commutativity error

In deriving the governing equations for LES, it is assumed that partial derivatives commute with the filter. This assumption holds for homogeneous turbulent flow because, the filter width is not varying in the homogeneous directions and the convolution operator commutes with respect to the differentiation. In non-homogeneous flows however, the filter width will vary in space, because the size of the smallest eddies is varying according to the region of the flow considered. In general, a filter with a variable width will not commute with respect to the differentiation. In the conventional approach for LES, the discrete nature of the equations is supposed to act as the filter. This approach is known as implicit filtering. The consequence is that errors resulting from the non-commutation between differentiation and filtering will have to be compensated by the subgrid-scale model which has not been designed for that purpose. Commutation errors can however be controlled by explicit filtering and commutating filters with variable width have been proposed (Ghosal and Moin [70], Vasilyev et al [223]). The introduction of explicit filtering as proposed by Ghosal [68] into a solution procedure has numerous advantages including the freedom for the user to choose the filter width and gain better control on the numerical error (Vasilyev et al [223]). This has been seldom put into application (see Jordan [100] for such example), however, because of the increase in complexity in the code implementation and the significant increase in CPU cost.

The modelling error

The difference between the subgrid-scale stresses and their modelled counter-part can be quite large because of the interaction of the model with the numerics for which the model may not have been designed (Vreman et al [228]). These aspects have been dealt extensively in Section 2.3.

The truncation error

This is one of the two errors that constitute the numerical error in LES. It indicates the level of accuracy with which derivatives are evaluated in their discrete form. Often, a second-order centred scheme is considered good enough for LES. However, it has been shown that the truncation error for schemes of order 2 is not negligible when it is compared to the subgrid-scale terms (Kravchenko and Moin [110]) and can strongly influence the solution (Vreman et al [228]). Another aspect concerns the nature of the truncation error which, in some case, is used to act as the subgrid-scale model (see Sections 2.3.6 and 2.7) but has equally an important impact on the resolved scales.

The aliasing error

This constitutes the second part of the numerical error. Because of the discretisation of the non-linear terms of the governing equations on a grid, the transfer of energy between the Fourier modes, for which these terms are responsible, is wrongly represented. The aliasing error can be removed in simulations performed with spectral methods. If the aliasing error is small relative to the truncation error, it can be neglected. When the aliasing error is not negligible, and dealiasing is ignored, the flow features can be seriouly misrepresented (see Rogallo and Moin [189] and Kravchenko and Moin [110]). Another influential aspect is the particular form of the non-linear terms. For example, $\partial\left(u_i u_j\right)/\partial x_j$ and $u_j \partial u_i/\partial x_j$ are not identical when expressed in a discrete form (Zang [241]). Most of the work done on the control of aliasing error has been directed towards spectral methods. Kravchenko and Moin [110] considered the question for finite-difference methods and showed the skew-symmetric form of

the non-linear terms to reduce the most the aliasing error. They also showed that, for low-order finite-difference methods, the aliasing error was considerably smaller than the trucation error, but was increasing with the scheme order. This has, however, been rarely put into practical applications in finite-difference and finite-volume methods (see Weber and Ducros [232]).

Overall, user control on the errors is rather limited, and errors are often not taken into account when considering complex geometries (except for the truncation error) as most of the uncertainty lies in the choice of the subgrid-scale and near-wall models (Spalart [210]). An interesting attempt toward identifying the relative importance of the numerical and modelling errors in LES was made by Vreman et al [228] for a mixing layer. They defined the total error as the sum of the modelling error (concerned with the errors due to the modelling of the subgrid-scale stresses) and the numerical error (which originates from the scheme choice and the grid discretisation). Their studies, using a variety of numerical schemes and subgrid-scale models, show that these errors can cancel each others, attenuating the total error or have the opposite effect, amplifying the total error.

2.9 Practical applications of large eddy simulations.

While the previous sections describe the techniques of large eddy simulations and focus on its theoretical and practical aspects, the present section surveys the range of applications and flow conditions to which it has so far been applied. Also considered are the facts that had led to the ever-increasing use of LES as a research tool in the academic world and the attention it has attracted from the industrial users.

The range of applications to which LES has been applied is strongly linked to the development of computers and their availability. Computing power is doubling roughly every two years (see Figure 2.5) while its associated cost has been dropping exponentially since the begin of the 1980's.

Initially, LES was used in the 1960's to compute meteorological flows (Smagorin-

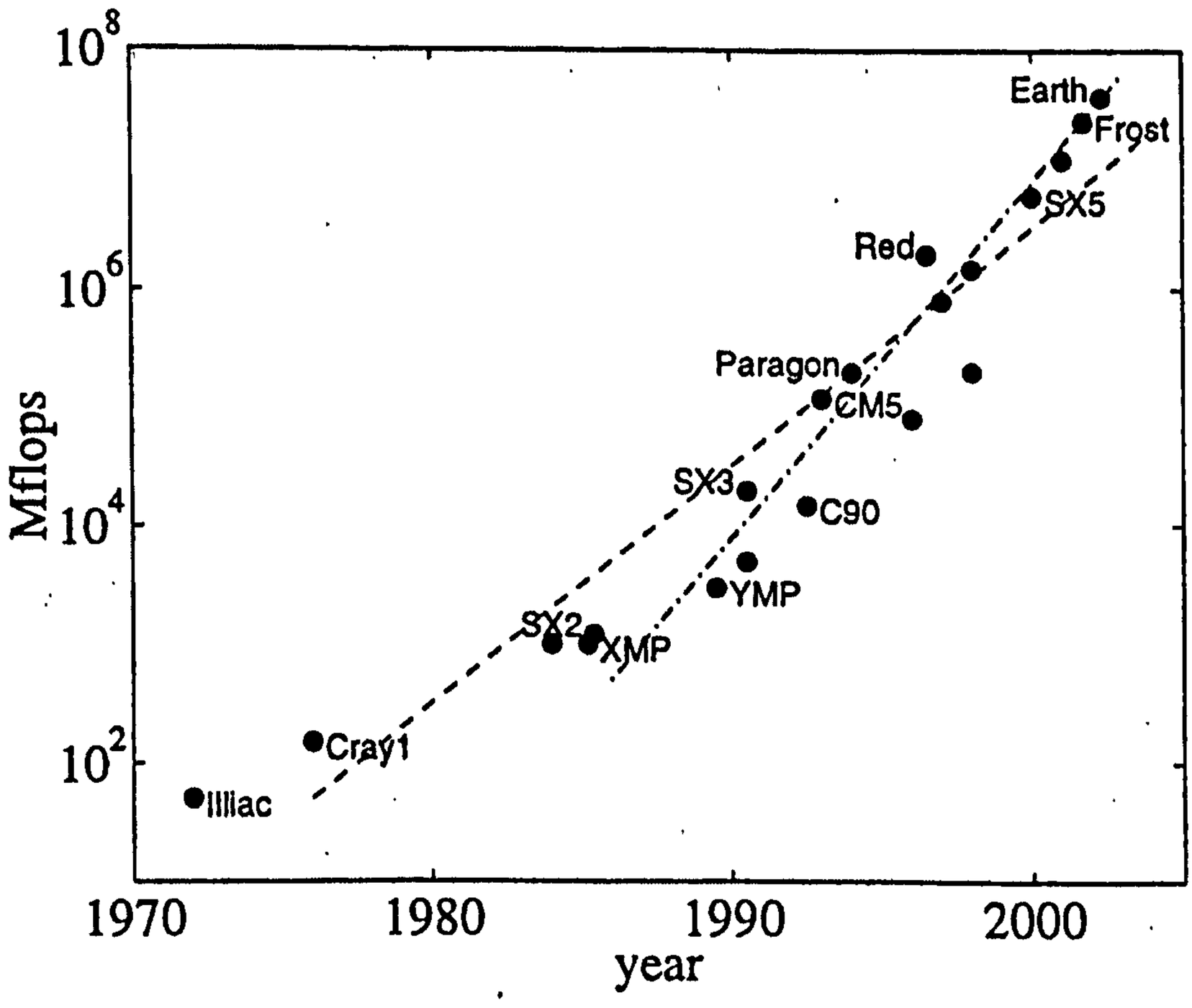

Figure 2.5: Increase in computing power in recent years (Jiménez [96]).

sky [208]). Soon, the technique attracted the attention of engineers and, at the beginning of the 1970's, it was successfully applied to a variety of *simple* flows, such as channel, duct and annular flows (Deardorff [49], Schumann [200], Grötzbach and Schumann [75], the latter studies including an interest to temperature fields and heat transfer), isotropic turbulence (Ferziger et al [58], McMillan and Ferziger [144]).

The 1980's saw steady increase in the number of LES practitioners as well as the applications treated, as the cost of computer decreased. However, CPU power still remained significantly lower than that needed to treat realistic engineering applications. Therefore, the range of flow, while broadening, still remained simple and oriented towards fundamental issues.

Thus, computations performed continued to include channel flows (Moin and Kim [159], Mason and Callen [143], Piomelli et al [177]), isotropic turbulence (Bardina et al [12], Lesieur and Rogallo [125]) or pipes and annuli (Grötzbach [74]). Other somewhat more complex flows were also being computed, including rotating channel flows (Kim [105]), flow over square ribs (Werner and Wengle [234]) and over periodic arrangements of cube (Murakami et al [162]), backward-facing step

(Schmitt and Friedrich [199]) and jets (Baron and Laurence [13]). The primary objectives of most of these studies was to gain a better understanding of turbulence phenomena.

Since the start of the 1990's, computers have become widely available and powerful enough to perform simulations similar to those of Deardorff [49] and Schumann [200] on desktop machines. At the same time, numerical techniques have reached a degree of maturity allowing demanding LES computations to be undertaken with confidence. Continued developments on theoritical issues of LES, a major one being the development of the dynamic procedure by Germano et al [65], have encouraged an increase in the number of applications and flow conditions treated with LES. Phenomena that are now studied with LES include strongly 3D flows around complex geometries, compressible flows, some featuring shocks, reacting flows, multiphase flows, heat transfer, and fluid/structure interaction.

Numerous recent applications reflect the current status of LES and include straight and curved ducts (Breuer and Rodi [23]), square ducts (Balaras and Benocci [9]), cavity flows (Zang et al [242], Avital [7]), rotating flows (Piomelli and Liu [178], Squires and Piomelli [215]), flows over bluff bodies (Breuer [21, 22], Mittal and Moin [156], Kravchenko and Moin [111]), flows in tube bundles (Rollet-Miet et al [191]), flows over obstacles such as a cube (Werner and Wengle [235]), 2D and 3D bumps (Wu and Squires [238]), separating flows in a diffuser (Kaltenbach et al [103]) or the backward-facing step (Silveira-Neto et al [207], Akselvoll and Moin [2], Cabot and Moin [25]), flow over electronic components (Chung et al [38]), piston-cylinder assembly for IC engine (Verzicco et al [225], Haworth and Jansen [82], Meinke and Krause [146]), stirred tank (Verzicco et al [224]), turbine blade (Raverdy et al [183]), gas turbine combustor (Mahesh et al [137]), environmental flows such as a river (Bradbrook et al [20]), high-Reynolds number flow of near-stall aerofoil (Jansen [92, 93], Weber and Ducros [232], Dahlström and Davidson [44], Mary and Sagaut [142]), coaxial jets with passive scalar and with swirling (Pierce and Moin [174]) or without (Akselvoll and Moin [4]), jets in cross-flow (Jones and Wille [98, 99]), control of turbulence (Neumann and Wengle [166]), impinging jets (Olsson and Fuchs [168]), aero-accoustic (Mankbadi et al [138], Seror et al [204]), reacting flows (Gao and

O'Brien [64], Cook and Riley [41], Reveillon and Vervisch [184]) and flows with particles (Portella and Oliemans [181]), shock/turbulence interaction (Ducros et al [54], Held and Fuchs [83]), fluid/structure interaction (example of a control rod in nuclear power generation by Longatte et al [131]).

While a number of questions remains open in many of the above applications, specifically in relation to accuracy and model realism, the list nevertheless conveys the message that LES has progressed to a stage at which it is becoming an engineering tool supplementing RANS methods and this trend is set to continue.

Chapter 3

Aspects of modelling

3.1 Introduction

As noted in Chapter 2, modelling in large eddy simulation is required in two areas:

- the subgrid-scale stresses in the filtered equations need to be approximated;
- unaffordable requirements at high Reynolds number may dictate the near-wall layer to be bridged by an approximate model.

In Section 3.2, a complete description of the subgrid-scale models employed in the current research is given. These models are all based on the concept of eddy-viscosity and were selected because they represent current state-of-the-art and are routinely applied in practice. Near-wall modelling, by means of wall-function approximations, is discussed in Section 3.3, where four specific model variants are presented.

The performance of the above models is investigated in Chapter 6, 7 and 8 for a range of geometries and flow conditions, with each successive flow featuring increasingly demanding turbulence phenomena.

3.2 Subgrid-scale modelling

3.2.1 Subgrid-scale viscosity

The most common approach to modelling the subgrid-scale stresses is based on the eddy-viscosity concept:

$$\tau_{ij} - \frac{\delta_{ij}}{3}\tau_{kk} = -2\nu_t\overline{S_{ij}} \tag{3.1}$$

where ν_t is the subgrid-scale viscosity. The deviatoric part of the subgrid-scale stress tensor τ_{kk} is traditionally incorporated in the pressure term and is, therefore, not accounted for explicitly. For positive viscosity, this formulation possesses desirable (although not necessarily correct) dissipative properties, but provides, as is the case with RANS-based eddy-viscosity formulations, a poor representation of subgrid-scale transport. This latter weakness is not especially important when the subgrid-scale eddies are small, relative to the resolved range of energetic eddies which tend to strongly dominate turbulence transport, but can be seriously detrimental to accuracy when the resolved range is narrow, i.e. when the grid is (locally or globally) coarse. On the practical side, these models are easily implemented although the expression of the subgrid-scale viscosity ν_t can be, for some models, rather complex to implement.

All the models investigated in this research are based on this concept of eddy-viscosity and are described in the following subsections. These models are:

- the Smagorinsky model (SM) (Smagorinsky [208]);
- the dynamic Smagorinsky model (DSM) (Germano et al [65]);
- the localized dynamic Smagorinsky model (LDSM) (Piomelli and Liu [178]);
- the mixed-scale model (MSM) (Sagaut [192]);
- the wall-adapted local eddy-viscosity model (WALE) (Ducros et al [55]);

These models were chosen because of their common use in LES practice.

3.2.2 The Smagorinsky model

The Smagorinsky model [208] is probably the most widely used subgrid-scale model and, historically, the first to have appeared. It may be written as:

$$\tau_{ij} - \frac{\delta_{ij}}{3}\tau_{kk} = -2\left(C_s\overline{\Delta}\right)^2 \left|\overline{S}\right| \overline{S_{ij}} = -2\nu_t\overline{S_{ij}} \tag{3.2}$$

where $\left|\overline{S}\right| = (2S_{ij}S_{ij})^{1/2}$, $\overline{\Delta}$ represents the filter width defined as $(\Delta x\Delta y\Delta z)^{1/3}$, essentially, a length scale of the subgrid eddies, and C_s is a constant. This constant is determined following a proposal by Lilly [128]. This proposal assumes that the cut-off ($k_c = \pi/\Delta$) lies in the inertial range of the turbulent spectrum (see Figure 2.1). In that case, C_s can be selected so that the ensemble-averaged subgrid-scale kinetic-energy dissipation is equal to the dissipation ϵ, hence:

$$\epsilon \approx 2\nu \int_0^{k_c} k^2 E(k)\, dk \tag{3.3}$$

with the energy spectrum in the Kolmogorov cascade [108] being expressed as:

$$E(k) = C_k \epsilon^{2/3} k^{-5/3} \tag{3.4}$$

This leads to the constant C_s being written as:

$$C_s \approx \frac{1}{\pi}\left(\frac{3C_k}{2}\right)^{-0.75} \tag{3.5}$$

Experiments by Champagne et al [31] have shown $C_k \approx 1.4$, leading to $C_s \approx 0.18$. For the channel flow, Deardorff [49] preferred to use $C_s = 0.1$. Larger coefficients appeared to make the model too dissipative, hence suppressing the turbulence unduly and leading to a laminar solution.

The Smagorisnky model is based on the assumption that the small scales are in equilibrium and entirely and instantaneously dissipate the energy received from the resolved scales. While the model is attractively simple, and hence widely used in LES, it contains several defects. It is unconditionally dissipative and cannot account for backscatter. A constant value for C_s is unrealistic and does not even represent correctly the dissipative process. The subgrid-scale viscosity does not vanish for

laminar conditions and does not provide the requisite asymptotic near-wall decay in proportion to y^{+3}. One route to securing a broadly correct near-wall behaviour of the Smagorinsky model is to introduce a damping function l_d as a multiplier of the Smagorinsky constant. A number of alternative forms have been proposed on the basis of fits to empirical data. These are usually variants of the van Driest [222] formulation (denoted by WD):

$$l_d = 1 - e^{-y^+/A^+} \tag{3.6}$$

which is used in the present work, with y^+ being the distance to the nearest wall, expressed in wall units, and A^+, a constant in the range 5 to 25.

3.2.3 The dynamic Smagorinsky model

The dynamic procedure, proposed by Germano et al [65], and described in Section 2.3.5, was applied by these authors to the Smagorinsky model, effectively allowing the coefficient C_s, which is a constant, to vary both in time and space.

As shown in Section 2.3.5, it exists a relationship, known as the Germano identity, between the subgrid-stresses at grid and test levels:

$$L_{ij} = \widehat{\overline{u_i}\,\overline{u_j}} - \widehat{\overline{u_i}}\,\widehat{\overline{u_j}} = T_{ij} - \widehat{\tau_{ij}} \tag{3.7}$$

where $\widehat{\cdot}$ represents the test filter, τ_{ij} are the subgrid-scale stresses at grid level and T_{ij} are the subgrid-scale stresses at test level.

By assuming that the same subgrid-scale model (the Smagorinsky model in this case) can represent both the grid- and test-filtered subgrid-scale tensors, Expression (3.7) becomes:

$$L_{ij} = T_{ij} - \widehat{\tau_{ij}} = -2C\alpha_{ij} + 2\widehat{C\beta_{ij}} \tag{3.8}$$

with $\alpha_{ij} = \widehat{\overline{\Delta}}^2 |\widehat{\overline{S}}| \widehat{\overline{S_{ij}}}$ and $\beta_{ij} = \overline{\Delta}^2 \left|\overline{S}\right| \overline{S_{ij}}$. With the additional assumption that the coefficient C varies locally smoothly in space and time, C can be extracted from the test-filtering operation in the second term on the right hand side of Equation (3.8) which then becomes:

$$L_{ij} = -2C\widehat{\overline{\Delta}}^2 |\widehat{\overline{S}}|\widehat{\overline{S}_{ij}} + 2C\overline{\Delta}^2 \widehat{|\overline{S}|\,\overline{S}_{ij}} = 2CM_{ij} \tag{3.9}$$

with L_{ij} and M_{ij}, both determinable. With Equation (3.9) being a tensorial expression, it forms an over-determined system for the scalar C and Germano et al [65] chose to contract using $\overline{S_{ij}}$:

$$C = 0.5\frac{L_{ij}\overline{S_{ij}}}{M_{ij}\overline{S_{ij}}} \tag{3.10}$$

The denominator in Equation (3.10) may vanish, making this expression singular which leads to numerical instabilities. This observation lead Lilly [129] to propose an alternative method of extracting C by first contracting (3.9) with M_{ij}:

$$L_{ij}M_{ij} = 2CM_{ij}M_{ij} \tag{3.11}$$

and then taking the square of the error ($Q = (L_{ij}M_{ij} - 2CM_{ij}M_{ij})^2$) and minimising it ($\partial Q/\partial C = 0$). This then results in:

$$C = 0.5\frac{L_{ij}M_{ij}}{M_{ij}M_{ij}} \tag{3.12}$$

The denominator of (3.12) only becomes zero if all elements of M_{ij} vanish simultaneously so that the chance of (3.12) becoming singular is very small. Expression (3.12) however strongly varies both in space and time (as does (3.10)) and this is a further source of numerical instabilities. This problem is alleviated by averaging both numerator and denominator in the homogeneous directions. When no such a direction exists, alternative strategies such as time-filtering (Breuer and Rodi [23]) or time averaging over fluid path (Meneveau et al [153]). This latter approach effectively leads to a Lagrangian dynamic Smagorinsky model.

A potential advantage of the model is that the coefficient C can become negative, simulating backscatter. Numerical stability precludes the use of negative eddy-viscosity. Hence, the positivity of the total viscosity ($\nu + \nu_t$) is in practice enforced.

In the initial work of Germano et al [65], test-filtering was only applied in the homogeneous directions (as it will be the case in the present work). Nothing prevents

it from being applied in other directions although some care has to be taken because of the grid clustering and presence of the wall.

Practically, filters used for test filtering are the Box filter, the Gaussian filter and the Fourier Cut-Off filter (see Appendix A). While these are easily implemented in the procedure for spectral methods, they require to be expressed in a discrete form when working with finite-difference and finite-volume methods (described in Appendix A):

$$\widehat{f} = \frac{1}{2\overline{\Delta}} \int_{-\overline{\Delta}}^{\overline{\Delta}} \overline{f}\,(x')\,dx' \tag{3.13}$$

with the test filter being twice that of the grid filter width. Through numerical integration, the filter is expressed in a discrete manner (Najjar and Tafti [165]). Various alternatives consist of:

- the Trapeze rule:

$$\widehat{f} = \frac{1}{4}\left(f_{i-1} + 2f_i + f_{i+1}\right) \tag{3.14}$$

- the Simpson rule:

$$\widehat{f} = \frac{1}{6}\left(f_{i-1} + 4f_i + f_{i+1}\right) \tag{3.15}$$

- local averaging over the neighbouring cells:

$$\widehat{f} = \frac{1}{3}\left(f_{i-1} + f_i + f_{i+1}\right) \tag{3.16}$$

Strictly speaking the use of these filters should be limited to orthogonal uniform grid. However, in practice, for reasons of simplicity, these filters are applied for all cases. This is justified by the fact that large-eddy simulation grids usually consist of low-aspect ratio cells and are nearly orthogonal in most cases. Multi-dimensional filters are obtained by applying the discrete filter successively in the different considered directions (Zang et al [242]). Discrete filters have been designed for complex

geometries and non-uniform, non-orthogonal grids exist (Vasilyev et al [223], Sagaut and Grohens [194]), but their implementation is more complex.

The choice of the ratio $\alpha_i = \widehat{\Delta_i}/\overline{\Delta_i}$ between the filter widths at both levels of filtering is, in this model, the only parameter that needs to be fixed. Germano et al take it equal to 2 for a test-filter twice as large as the grid-filter while, if both filters are equal, $\alpha_i = 1$. Vreman [226] demonstrates that, to maintain the consistency between the integration rule and the filter width, a Top-Hat filter approximated by the Trapeze rule (3.14) requires $\alpha_i = \sqrt{5}$. Lund [135] proposes to use, for the Trapeze rule (3.14), a similar value of $\alpha_i = \sqrt{6}$ and, for the Simpson rule (3.15),

Many variations of the dynamic Smagorinsky model, aiming at removing some of the initial inconsistencies and improving the stability of the computations, have been proposed and one of these improvements is considered in the following subsection. The present model, in its original formulation or in some of its variations, has been applied to a wide range of flows: channel flow (Germano et al [65]), the flow around cylinders (Breuer [21]), the flow in a diffuser (Kaltenbach et al [103]), coaxial jets (Akselvoll and Moin [3]), and airfoil flow (Jansen [93]).

3.2.4 The Localized Dynamic Smagorinsky Model

This model, proposed by Piomelli and Liu [178], is a variation of the model proposed by Germano et al [65] and described in the previous subsection and aims at removing some inconsistencies of the previous formulation. As noted earlier, the coefficient C, obtained with (3.12) rapidly varies in time and space, contradicting the assumption that it can be considered locally constant and hence being extracted from the test-filtering operation in (3.8). The retention of the coefficient C in the test-filter leads to (3.8) being rewritten:

$$L_{ij} = T_{ij} - \widehat{\tau_{ij}} = 2C\alpha_{ij} + 2\widehat{C\beta_{ij}} \tag{3.17}$$

with $\alpha_{ij} = \widehat{\overline{\Delta}}^2 |\widehat{\overline{S}}| \widehat{\overline{S_{ij}}}$ and $\beta_{ij} = \overline{\Delta}^2 \left|\overline{S}\right| \overline{S_{ij}}$. Equation (3.17) is then contracted with α_{ij} and C, extracted by minimising the least mean square error as done by Lilly [129] (see also (3.12)):

$$C = -\frac{1}{2}\frac{\left(L_{ij} - 2\widehat{C^*\beta_{ij}}\right)\alpha_{ij}}{\alpha_{mn}\alpha_{mn}} \tag{3.18}$$

Expression (3.18) is implicit in C and the coefficient present under the test-filter on the right hand side is denoted as C^* as it represents an approximation of C. Piomelli and Liu [178] proposed three routes to estimate C^*, all leading to similar results. The simplest route, used in this work, consists of taking $C^* = C^{n-1}$ where $n-1$ indicates the previous time-step. The denominator in the above expression is positive definite and, unlike in (3.8), does not involve a difference between two terms of the same order of magnitude. As C can become negative, the constraint of positive total viscosity is imposed: $\nu + \nu_t \geq 0$. To further improve the numerical stability and increase the smoothness of the coefficient variation, C is averaged over a few neighbouring cells.

3.2.5 The mixed-scale model

Sagaut [192] proposes a model that arises as a weighted geometric average of two subgrid-scale viscosities. The first is extracted from the Smagorinsky formulation $\nu_t = (C_s\Delta)^2 \left|\overline{S}\right|$ and is assumed to appertain to the large scales and the second, $\nu_t = C_q\overline{\Delta}\, q^{0.5}$ with q, the subgrid-scale energy, is relating to the small scales. Its name, the mixed-scale model originates from this use of both the small and large scales. The model thus arises as:

$$\nu_t = C_M \left|\overline{S}\right|^{\alpha} q^{1-\alpha}\overline{\Delta}^{1+\alpha} \tag{3.19}$$

where α is a weighting factor in the range 0 to 1 and C_M is a constant, taken here equal to 0.1.

The subgrid-scale energy, not directly available, can be estimated by using the assumption of scale-similarity (Bardina et al [12]), which states that, structurally, unresolved scales can be estimated from the smallest resolved scales. Practically, this assumption introduces, as in the dynamic Smagorinsky model of Germano et al [65], two levels of filtering. The subgrid-scale energy q is thus approximated by:

$$q = \frac{1}{2}\overline{u_i}'\overline{u_i}' \tag{3.20}$$

with $\overline{u_i'} \approx (\overline{u_i})' = \overline{u_i} - \widehat{\overline{u_i}}$.

In practice, a test-filtering operation, as in the dynamic model (Equation (3.12)), is performed. This model is considerably simpler than the Germano model and does not require the assumption of commutativity between the test and grid filters despite the use of a test-filtering operation. It also insures that the subgrid-scale viscosity vanishes near the wall.

3.2.6 The WALE Model

The WALE model (wall-adapted local eddy-viscosity), proposed by Nicoud and Ducros [167], is constructed on an operator based on the square of the gradient velocity tensor $g_{ij} = \partial u_i / \partial u_j$:

$$S_{ij}^d = \frac{1}{2}\left(g_{ij}^2 + g_{ji}^2\right) - \frac{1}{3}\delta_{ij} g_{kk}^2 \tag{3.21}$$

where $g_{ij}^2 = g_{ik}g_{kj}$.

The reasons of the choice behind (3.21) are the following:

- the willingness to take into account the effects of the strain rate and the rotation rate of the smallest resolved scales;
- the need of an operator which vanishes in the near-wall region.

Nicoud and Ducros demonstrate that these properties are met by the properties built on the operator (3.21) while operators built on S_{ij} as in the Smagorinsky model do not retain this characteristic.

Scaling considerations lead Nicoud and Ducros [167] to propose the following model:

$$\nu_t = C_w \Delta_{eq}^2 \frac{\left(S_{ij}^d S_{ij}^d\right)^{3/2}}{\left(\overline{S_{ij}S_{ij}}\right)^{5/2} + \left(S_{ij}^d S_{ij}^d\right)^{5/4}} \tag{3.22}$$

where $\overline{S_{ij}} = 1/2\left(\partial\overline{u_i}/\partial x_j + \partial\overline{u_j}/\partial x_i\right)$ is the strain-rate tensor. The constant C_w takes the value 0.1 and $\Delta_{eq} = (\Delta_x \Delta_y \Delta_z)^{1/3}$ is the filter width. Additional characteristics of this model are that it only uses local information and is invariant to

any change of co-ordinate. Nicoud and Ducros [167] also report the model ability to handle transition.

3.3 Near-wall treatment

3.3.1 Rationale and overview

With the cost of computation of wall-bounded flows rapidly increasing with the Reynolds number (see Section 1.1), a way of limiting the expense is to apply a wall condition that bridges the near-wall region where a high number of grid nodes would otherwise be required. The route, chosen in the present research, exploits semi-empirical relationships linking the near-wall velocity at the first grid node with the wall shear stress (see Figure 3.1). These are referred to as *wall-law*. Other routes exist and were briefly introduced in Section 3.3.

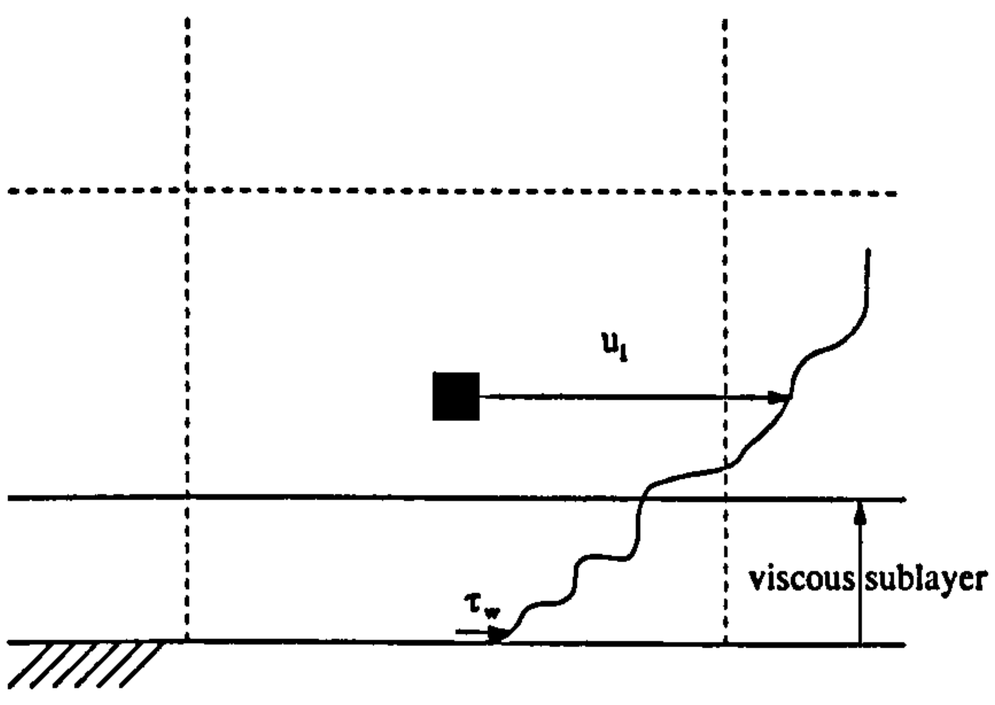

Figure 3.1: Relationship between wall shear stress and tangential velocity.

All wall-laws employed in the present work directly relate the resolved motion at the first grid node to the wall shear stress and are alternative representations of the log-law (see Figure 3.2). Four different formulations are considered in the present research and are described in the related subsections to follow:

- a two-layer log-law (LL2), using the shear velocity as the velocity scale;
- a three-layer log-law (LL3), which accounts for the smooth transition between the fully-viscous and fully-turbulent layers and is otherwise identical to the previous formulation;

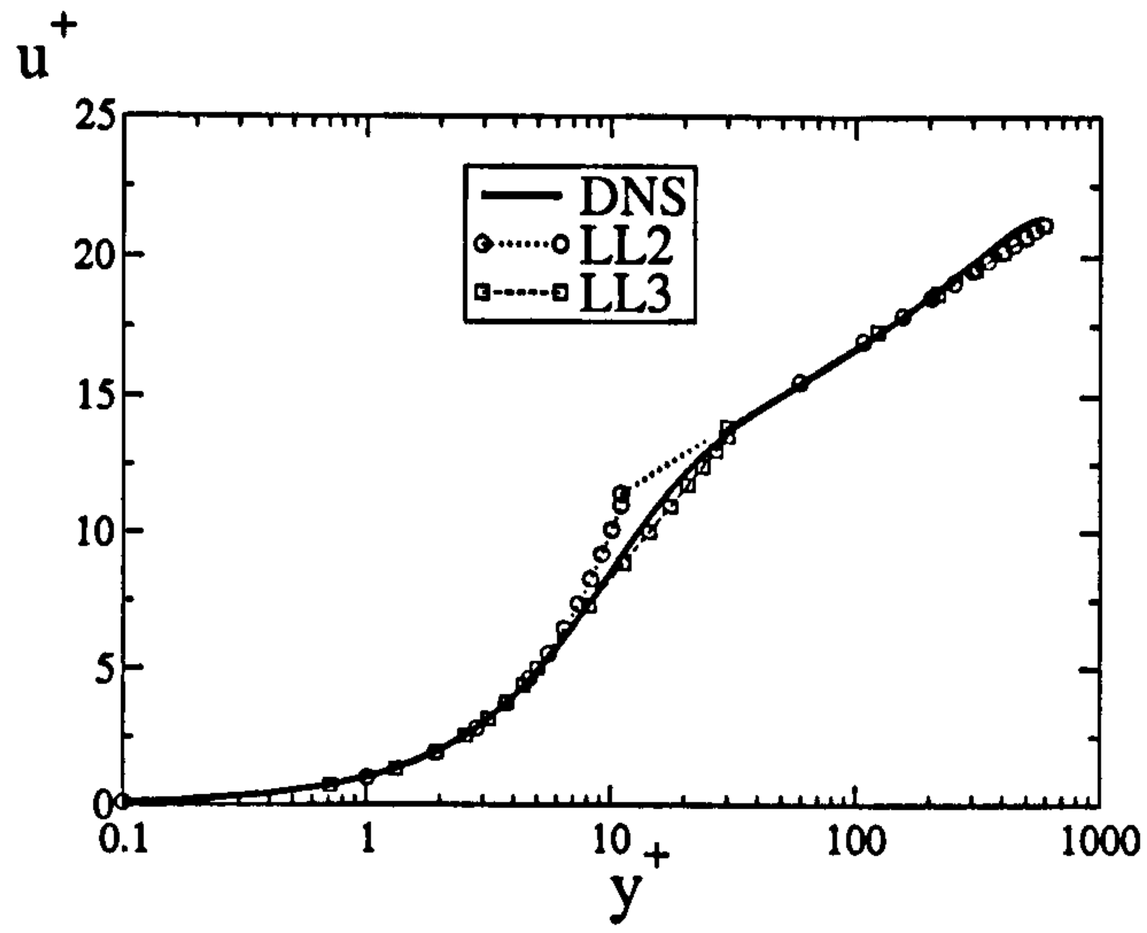

Figure 3.2: Velocity in wall co-ordinates for a turbulent channel flow.

- a two-layer log-law (LLK) with the resolved turbulence energy as a velocity scale;

- a $1/7^{th}$ power-law-based formulation in combination with a linear near-wall law (WW).

3.3.2 Log-law based approximations

The simplest formulation is based on the assumption that the near-wall layer consists, instantaneously, of a fully viscous sublayer and a fully turbulent layer above it with the interface defined by $y^+ \leq 11$, where the subscript 1 identifies the first node from the wall at which the velocity is resolved:

$$u_1^+ = \begin{cases} y_1^+ & \text{if} \quad y_1^+ \leq 11 \\ \\ \frac{1}{\kappa} ln\left(E y_1^+\right) & \text{if} \quad y_1^+ > 11 \end{cases} \tag{3.23}$$

with the von Karman constant $\kappa = 0.42$, $E = 9.8$, $u_1^+ = u_1/u_\tau$ (u_1 is the tangential resolved velocity to the wall taken at the wall-nearest point), $u_\tau = \sqrt{\tau_w/\rho}$ is the instantaneous wall-shear velocity and $y_1^+ = y_1 u_\tau/\nu$. Relation (3.23) is assumed to hold instantaneously and allows the deduction of the instantaneous shear stress.

The profile (3.23) evidently exhibits an unrealistic discontinuity in the slope at $y^+ = 1$, as shown on Figure 3.2. To account for the smooth transition between the

linear and the logarithmic regions, Breuer and Rodi [24] have proposed a smooth fit, resulting in a three-layer log law (LL3):

$$u_1^+ = \begin{cases} y_1^+ & \text{if} \quad y_1^+ \leq 5 \\ Aln\left(y_1^+\right) + B & \text{if} \quad 5 < y_1^+ \leq 30 \\ \frac{1}{\kappa} ln\left(Ey_1^+\right) & \text{if} \quad y_1^+ > 30 \end{cases} \tag{3.24}$$

with $A = (ln(30\,E)\,/\,\kappa - 5)/ln(6)$ and $B = 5 - A\,ln(5)$.

In relations (3.23) and (3.24), the velocity scale in y^+ is formed with the wall shear stress. This establishes a rigid linkage between the near-wall velocity and the wall-shear stress and can give a seriously erroneous wall-shear stress if the near-wall departs from the state of turbulence-energy equilibrium. In RANS computations, the turbulence energy has been used to scale y rather than the shear velocity, extending the range of validity of the log-law. This substitution, based on the equivalence $u_\tau^2 = C_\mu^{0.5} k$, is only strictly valid when the assumption of turbulence energy equilibrium is verified (Launder and Spalding [116]). This concept can be extended to LES (Murakami et al [163]) with $k = k_1$ being the resolved turbulence energy at the wall-nearest computational point. With this approach, the universal wall distance thus arises as:

$$y_1^+ = \frac{y_1 C_\mu^{1/4} k_1^{1/2}}{\nu} \tag{3.25}$$

where $C_\mu = 0.09$ and

$$k_1 = \frac{1}{2} < (u_i - < u_i >)_1 (u_i - < u_i >)_1 > = \frac{1}{2} (< u_i u_i > - < u_i >< u_i >)_1 \tag{3.26}$$

where u_i is the instantaneous resolved velocity and $< \cdot >$ indicates an averaging operator in time and in any homogeneous direction. The formulation of this log-law otherwise remains identical to expression (3.23).

A disadvantage of this formulation is the need to obtain the resolved turbulence energy by progressive averaging as the simulation goes on. However, the turbulence stabilises quickly, and the extra cost is compensated by the fact that the wall shear

stress can be extracted directly, rather than through an iterative procedure, as it is the case when the wall-shear velocity is used as scale velocity.

3.3.3 Werner-Wengle wall law

The log-law, if used exclusively with the shear velocity, is transcendental and requires an iterative inversion for the wall shear stress. On the other hand, the alternative of using k in y^+ renders the wall law quasi-explicit, but requires the evaluation of the resolved turbulence energy. Both forms are computationally cumbersome. A simpler two-layers approximation, proposed by Werner and Wengle [235], is based on the assumption of a $1/7^{th}$ power-law outside the viscous sublayer, interfaced with the linear profile in the viscous sublayer. Thus:

$$u_1^+ = \begin{cases} y_1^+ & \text{if} \quad y_1^+ \leq 11.81 \\ \\ A(y_1^+)^B & \text{if} \quad y_1^+ > 11.81 \end{cases} \tag{3.27}$$

where $A = 8.3$ and $B = 1/7$. By integrating the velocity distribution over the height of the first grid element, an analytical expression linking the tangential velocity to the wall and the wall shear stress can be obtained:

$$|\tau_w| = \begin{cases} \frac{2\mu|u_1|}{\Delta y} & \text{for} \quad |u_1| \leq \frac{\nu}{2\Delta y} A^{2/1-B} \\ \\ \rho \left[\frac{1-B}{2} A^{(1+B)/(1-B)} \left(\frac{\nu}{\Delta y} \right)^{1+B} + \frac{1+B}{A} \left(\frac{\nu}{\Delta y} \right)^{B} |u_1| \right]^{2/1+B} & \\ \\ & \text{for} \quad |u_1| > \frac{\nu}{2\Delta y} A^{2/1-B} \end{cases} \tag{3.28}$$

This constitutes the original formulation proposed by Werner and Wengle [235]. An alternative approach consists of extracting u_τ as a function of u_1 and y_1 directly from (3.27) in the same way it is done to LL2.

3.4 Concluding remarks

The present chapter has described the nature of the subgrid-scale models and near-wall approximations used in the simulations to follow. In essence, both are needed

in partial compensation for the lack of resolution that has to be accepted when simulating high-Reynolds-number flows.

Ideally, the effect of the subgrid-scale modelling would strictly be confined to the removal of the turbulence energy at the dissipative end of the energy spectrum, with the simulation resolving the remainder, including the entire inertial subrange. This is not possible in practice and the subgrid-scale model has also to account for a part of the inertial subrange. Thus, the quality of the subgrid-scale model, as a mean of representing the subgrid-scale activity, can be important. Therein lies the rationale of examining a range of models, as it is done in the computations to follow, among them, dynamic formulations that are held to be state-of-the-art model in practical LES. Whatever model is adopted, it is important to identify the contribution of the subgrid-scale stresses in comparison to the resolved components, and this is done in the simulations to follow.

Near-wall approximations are required when wall-resolved simulations are simply untenable on grounds of excessive resource requirements. In the present research, a number of log-law-type wall laws have been examined, and their nature has been summarised in the present chapter. An important objective of many of the simulations to follow is to identify the limitations and penalties associated with the use of what are inevitably tenuous practices known to rest on physically weak assumptions such as the existence of an instantaneous log-law. This will be done by performing both wall-resolved and wall-law computations at moderate Reynolds numbers for which proper wall resolution is possible, albeit at high computational costs. Such computations allow conclusions to be drawn which hopefully extrapolate at very high Reynolds numbers for which wall-resolved computations are not possible. While the writer is aware of the current efforts to use low-Reynolds number turbulence models within zonal RANS/LES strategies, these are still embryonic and, it is fair to say, as controversial as wall laws in terms of both fundamental foundation and predictive performances.

Chapter 4

Computational and implementation issues

4.1 Introduction

Numerical strategies and discretisation techniques for large eddy simulations are described and compared in Chapter 2. Among the methods reviewed, the finite-volume method, incorporating a collocated variable storage arrangement was selected for the present research in combination with a projection method with an explicit time-marching scheme. This combination leads to an efficient numerical algorithm which uses a low amount of memory storage, is easily parallelisable, and is well-suited for complex geometries and the very large number of grid points that will be required to compute the flows considered in the present research.

In Section 4.2, the finite-volume approach is described in detail. Section 4.3 introduces the fractional-step method and the details of the time-marching scheme. The details of the time-step control are then given in Section 4.4. Aspects of the spatial discretisation are described in Section 4.5. The pressure solver, the most complex part of the procedure, is detailed in Section 4.6. Section 4.7 deals with the parallel implementation, while Section 4.8 introduces the boundary conditions for the velocity and pressure, including a general description of the implementation of the wall-treatment. The parallel performance of the code is then assessed in

Section 4.9 for a variety of flows and computing platforms.

4.2 The finite-volume formulation

The finite-volume approach uses the integral form of the governing equations. In the present case, these equations are the filtered Navier-Stokes equations, derived in Section 2.2 of Chapter 2. With Ω representing the integration volume, the equations to be solved are:

$$\int_{\Omega} \frac{\partial \overline{u_i}}{\partial x_i} d\Omega = 0 \tag{4.1}$$

$$\int_{\Omega} \frac{\partial \overline{u_i}}{\partial t} d\Omega = \underbrace{-\int_{\Omega} \frac{\partial \overline{u_i}\,\overline{u_j}}{\partial x_i} d\Omega}_{C} - \int_{\Omega} \frac{\partial \overline{p}}{\partial x_i} d\Omega + \underbrace{\int_{\Omega} \left(\frac{2}{Re} \frac{\partial \overline{S_{ij}}}{\partial x_j} + \frac{\partial \tau_{ij}}{\partial x_j} \right) d\Omega}_{D} \tag{4.2}$$

In the present approach, the domain is anyone of the contiguous finite volumes that, put together, form the flow domain. A computational node is associated with each finite-volume centroid. The flow properties values at this location are held to represent the averaged values over the cell. The volume integrals are converted into surface integrals using the Gauss-Divergence theorem and, these are then approximated using quadrature formulae. As the discrete form of the surface integral require knowledge of the variable values at the cell face, these are interpolated from the computational nodes located at the cell centre. Among the advantages of a finite-volume approach are the ease of accommodating complex geometries, the fact that the method is conservative by construction and relatively easy to understand and implement. A disadvantage is the difficulty of constructing high-order methods (Lilek and Perić [127]) beyond second order as finite-volume methods requires two levels of approximations:

- quadrature formulae to evaluate the surface integrals;
- interpolations of the variables on the cell faces.

The use of a collocated arrangement also requires less memory storage than a staggered arrangement. However, it leads to the generation of spurious oscillations, reflecting pressure-velocity decoupling, and special interpolation practices are required to suppress them.

4.3 Solution strategy and time discretisation

The present strategy uses a fractional-step method (Chorin [37]), a very popular method for large-eddy and direct numerical simulations (Kim and Moin [106], Le et al [118], Mittal and Balachandar [155], Olsson and Fuchs [168], Zang et al [242]). The fractional-step method, also known as the projection method, consists of splitting the momentum equations (4.2) into two parts. In the first step, an intermediate velocity field is derived by stepping the solution to the forward time and taking into account the convective and diffusive fluxes. This field does not satisfy the mass conservation and will need to be corrected. In the second step, the pressure is obtained. Using the newly obtained pressure, the final divergence-free velocity field is then obtained from the intermediate one.

The time derivative in Equation (4.2) is approximated using a second order backward Euler scheme:

$$\frac{\partial \overline{u_i}}{\partial t} = \frac{3\overline{u_i}^{n+1} - 4\overline{u_i}^{n} + \overline{u_i}^{n-1}}{2\Delta t} \tag{4.3}$$

In what follows, the convective and diffusive terms in Equation (4.2) are, respectively, denoted by C and D. These terms are advanced in time by means of the explicit second-order Adams-Bashfort scheme. This consists of extrapolating to time $n+1$ the fluxes at time levels n and $n-1$ as follows:

$$CD^{n+1} = 2CD^{n} - CD^{n-1} \tag{4.4}$$

The approximated form of the momentum equation (4.2) therefore becomes:

$$\frac{3\overline{u_i}^{n+1} - 4\overline{u_i}^{n} + \overline{u_i}^{n-1}}{2\Delta t} = -\frac{\partial \overline{p}^{n+1}}{\partial x_i} + 2CD^{n} - CD^{n-1} \tag{4.5}$$

The application of the fractional-step method leads to Equation (4.5) being split into two parts. Thus, an intermediate $\overline{u_i}^*$ arises upon the application of the first step:

$$\frac{3\overline{u_i}^* - 4\overline{u_i}^n + \overline{u_i}^{n-1}}{2\Delta t} = 2CD^n - CD^{n-1} \tag{4.6}$$

and this is then updated by:

$$\frac{3\overline{u_i}^{n+1} - 3\overline{u_i}^*}{2\Delta t} = -\frac{\partial \overline{p}^{n+1}}{\partial x_i} \tag{4.7}$$

This first step is fully explicit, its implementation, relatively simple and its computational cost, low.

With the intermediate Cartesian velocity u_i^* being known, the intermediate contravariant velocity C_i^* can be computed. In the present case, this is achieved through linear interpolation (see Figure 4.1 which shows the location of the various velocity vectors):

$$C_i^* = L(u_i^*)S_i \tag{4.8}$$

where L is the interpolation operator and S_i is the surface of the cell face concerned in the i-direction.

Before the second step taking place, the normal component of the intermediate contravariant velocity must be specified on the boundary. This is done here by taking:

$$C_i^{n+1} n_i = C_i^* n_i = Const \tag{4.9}$$

In order to obtain a well posed problem for the second step, overall mass conservation on the domain boundary must be satisfied:

$$\int_\Gamma \mathbf{C}^* \cdot \mathbf{n}\, d\Gamma = 0 \tag{4.10}$$

where Γ represents the domain boundary.

The intermediate contravariant velocity is now projected onto the space of divergence-free vector field by adding the gradient of a scalar function which is the pressure:

$$\frac{3}{2\Delta t}(C_i^{n+1} - C_i^*) = -\frac{\partial \overline{p}^{n+1}}{\partial x_i} \tag{4.11}$$

Because of the boundary condition (4.9), the pressure gradient normal to the boundary has to vanish:

$$\nabla p^{n+1} \cdot \mathbf{n} = \frac{3}{2\Delta t}(\mathbf{C}^{n+1} - \mathbf{C}^*) \cdot \mathbf{n} = 0 \tag{4.12}$$

By applying the divergence operator on (4.11) and taking mass conservation ($\nabla \cdot \mathbf{C}^{n+1} = 0$) into account, the following system is obtained:

$$\left.\begin{array}{l} \dfrac{\partial^2 \overline{p}^{n+1}}{\partial x_i^2} = \dfrac{3}{2\Delta t} C_i^* \\ \dfrac{\partial \overline{p}^{n+1}}{\partial x_i} n_i = 0 \end{array}\right\} \tag{4.13}$$

System (4.13) is implicit and its solution is a very expensive operation, accounting for up to 80% of the total cost of a computation. The method used to resolve the system (4.13) is described in Section 4.6.

The pressure p^{n+1} is now known and the contravariant velocity C_i^* is updated through (4.11) while the Cartesian velocity u_i^* is computed through a similar expression:

$$\frac{3}{2\Delta t}(u_i^{n+1} - u_i^*) = -\frac{\partial \overline{p}^{n+1}}{\partial x_i} \tag{4.14}$$

Equations (4.11) and (4.14) only differ in the form of the discrete pressure gradient they use. It is staggered when the contravariant velocity is considered and collocated for the cell-centred velocity. The use of these two different discrete gradients when updating the velocity is equivalent to the application of the Rhie and Chow [186] procedure which aims at eliminating the checkboarding problem. A consequence of this is that, at the end of the time-step, Relation (4.8) is not satisfied anymore.

Once the Cartesian velocity u^{n+1} is known, the boundary conditions are applied on it (see Section 4.8 for more details).

4.4 Control of the time-step

In addition to the physical constraints imposed by the physics of the flow (see Section 2.6 for more details), there are limitations resulting from the choice of the time-marching scheme. In the solution of the Navier-Stokes equations (filtered or not), two criteria limit the time-step and have to be taken into account in order for the numerical process to remain stable:

- the CFL (Courant-Friedrich-Lewis) condition requires that $\Delta t \leq CFL\Delta/u$, where CFL is a limit and depends on the numerical scheme, Δ is a local cell-related distance and u is the local velocity;

- the viscous condition for which $\Delta t \leq D_n\Delta^2/\nu$, where D_n is also a limit depending on the numerical scheme ($D_n = \infty$ for implicit schemes).

The use of the Adams-Bashfort scheme imposes fairly stringent limits on both conditions ($CFL < 1$ and $D_n < 0.5$) to avoid numerical instabilities (Hirsch [85]). Both conditions need to be satisfied as the solution evolves and the most restrictive one will dictate the magnitude of the time-step which is re-evaluated at each iteration.

Because the time-marching scheme determines the fields at time $n+1$ from the known fields at time n and $n-1$ and the time-step is determined at each iteration and may vary as the computation goes on, the time discretised momentum equations writes as:

$$\sigma_1 u_i^{n+1} + \sigma_2 u_i^n + \sigma_3 u_i^{n-1} = -\frac{\partial p^{n+1}}{\partial x_i} + \underbrace{\sigma_4 CD^n + \sigma_5 CD^{n-1}}_{CD^{n+1}} \tag{4.15}$$

where

$$\sigma_1 = \frac{2\Delta t^n + \Delta t^{n-1}}{\Delta t^n(\Delta t^n + \Delta t^{n-1})} \quad \sigma_2 = -\frac{\Delta t^n + \Delta t^{n-1}}{\Delta t^n \Delta t^{n-1}} \quad \sigma_3 = \frac{\Delta t^n}{\Delta t^{n-1}(\Delta t^n + \Delta t^{n-1})}$$
$$\sigma_4 = \frac{\Delta t^n + \Delta t^{n-1}}{\Delta t^{n-1}} \qquad \sigma_5 = -\frac{\Delta t^n}{\Delta t^{n-1}} \tag{4.16}$$

The coefficients σ_i are obtained through a Taylor serie expansion.

4.5 Spatial discretisation

With the subgrid-scale stresses approximated by (3.1), Equation (4.2) may be written as:

$$\int_\Omega \frac{\partial \overline{u_i}}{\partial t} d\Omega = -\int_\Omega \frac{\partial \overline{u_i}\,\overline{u_j}}{\partial x_i} d\Omega - \int_\Omega \frac{\partial \overline{p}}{\partial x_i} d\Omega + \int_\Omega \frac{\partial \left[(2/Re + 2\nu_t)\,\overline{S_{ij}} + \frac{1}{3}\delta_{ij}\tau_{kk} \right]}{\partial x_j} d\Omega \tag{4.17}$$

In practice, the deviatoric part of the subgrid-scale stress tensor is merged into the pressure gradient. Equation (4.17) then becomes:

$$\int_\Omega \frac{\partial \overline{u_i}}{\partial t} d\Omega = -\int_\Omega \frac{\partial \overline{u_i}\,\overline{u_j}}{\partial x_i} d\Omega - \int_\Omega \frac{\partial \overline{p}}{\partial x_i} d\Omega + 2\int_\Omega \frac{\partial \left(\nu_{tot}\overline{S_{ij}} \right)}{\partial x_j} d\Omega \tag{4.18}$$

where $\overline{p}$ is $\overline{p} - 1/3\delta_{ij}\tau_{kk}$ and $\nu_{tot} = 1/Re + \nu_t$.

The convective term in Equation (4.18) is approximated by first applying the Gauss divergence theorem:

$$\int_\Omega \frac{\partial \overline{u_i}\,\overline{u_j}}{\partial x_i} d\Omega = \int_S (\overline{u_i}\,\overline{u_j})\; n_j dS \tag{4.19}$$

The surface integral in Equation (4.19) is then approximated using the second-order midpoint rule:

$$\int_S (\overline{u_i}\,\overline{u_j})\; n_j dS = \sum_{c=e,w,n,s,t,b} \overline{u_i}^c\,\overline{u_j}^c S_j = \sum_{c=e,w,n,s,t,b} \overline{u_i}^c C^c \tag{4.20}$$

where n_j is the j-component of the vector normal to the cell face c ($c = e$ - east, w - west, n - north, s - south, t - top, b - bottom). C^c represents the mass flux through the cell face c, $C^c = \overline{u_j}^c S_j^c$. $\overline{u_i}^c$ is the i^{th} component of the quantity convected through the cell face c. The variable arrangement chosen being collocated, the quantities on the cell faces must be interpolated. Here, the value of the variable at a given cell face e is obtained trough a linear interpolation using the neighbouring cell centres P and E (see Figure 4.1). The second-order derivatives constituting the diffusive terms and the Laplace problem for the pressure in two steps. First, the Gauss theorem is applied on the volume integral:

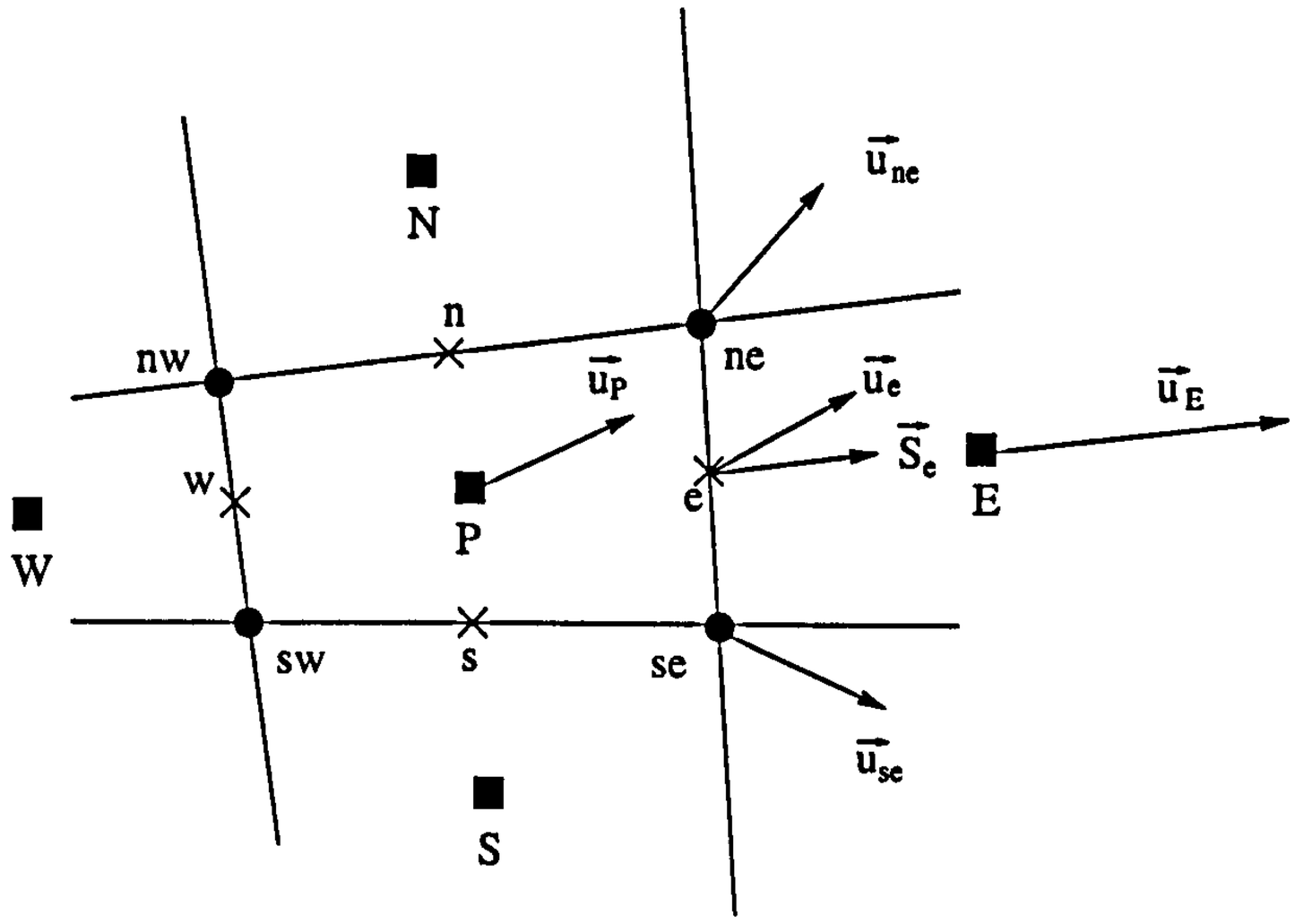

Figure 4.1: Control volume for the discretisation of centred and staggered gradients.

$$\int_\Omega \frac{\partial^2 \overline{u_i}}{\partial x_j^2} d\Omega = \int_S \frac{\partial \overline{u_i}}{\partial x_j} n_j dS \tag{4.21}$$

As in Equation (4.20), the midpoint rule is then applied:

$$\int_S \frac{\partial \overline{u_i}}{\partial x_j} n_j dS = \sum_{c=e,w,n,s,t,b} \left(\frac{\partial \overline{u_i}}{\partial x_j} \right)_c S_{x_j} \tag{4.22}$$

In the second step, the gradient centred on the cell face c (staggered) is written as a volume integral. The Gauss theorem is then applied, and the midpoint rule allows the discrete form of the staggered gradient to be derived. In the following example, the discretisation of the gradient centred on the east (e) face of the cell is presented (see Figure 4.1):

$$\left(\frac{\partial \overline{u_i}}{\partial x_j} \right)_c = \frac{1}{\Omega_c} \int_{\Omega_c} \left(\frac{\partial \overline{u_i}}{\partial x_j} \right)_c d\Omega_c = \frac{1}{\Omega_c} \int_{S_c} \overline{u_i}^c S_{x_j}^c \tag{4.23}$$

The geometric parameters at the cell centre are evaluated by averaging the cell parameters. For example, $S_x^P = (S_x^e + S_x^w)/2$ where S_x represents the x-component of the surface vector located in P and oriented in the direction WE. The variables at the vertices of the cell are obtained by averaging the values of the variable taken at the surrounding cell centres. For example, $u_e = (u_P + u_{ne} + u_{se} + u_E)/4$.

4.6 Pressure solver

4.6.1 Principles

The pressure p at the time $(n+1)$ is the solution of the system (4.13). This is an implicit Poisson problem requiring a coupled solution. The algorithm used here employs a partial diagonalisation and a $2D$ V-cycle multigrid algorithm combined with a Successive-Line-Over-Relaxation (SLOR) in alternate directions.

4.6.2 The partial diagonalisation

Partial diagonalisation is used to accelerate the resolution of the Poisson problem by reducing the $3D$ problem into a set of $2D$ subproblems. If the domain consists of $N_x \times N_y \times N_z$ cells and the z-direction is orthogonal to the x-y plane, the problem can be partially diagonalised. In other words, if the grid and boundary conditions are given, the eigenvalues and eigenvectors of the Laplacian operator can be found in the z-direction. By going into the base formed by the eigenvectors, the operator in the z-direction becomes a diagonal matrix made of the eigenvalues. N_z uncoupled $2D$ problems, each of them corresponding to one of the eigenvalues, then replace the $3D$ problem. Because of the class of problems considered in the present research, the current implementation is limited to periodic conditions in the z-direction divided into an even number N_z of uniform cells. However, other types of boundary conditions can be implemented (Schumann and Sweet [202]). The procedure can also be extended to non-uniform grids and an odd number of cells (Lardat [113]). The derivation of the eigenvalues and eigenvectors for the present case is described in Appendix B.1.

The procedure can be summarised symbolically by first writing the discrete form of system (4.13) in a matrix form:

$$L\mathbf{x} = \mathbf{S} \tag{4.24}$$

where L represents the discrete Laplace operator, $\mathbf{S}$ is the right hand side of (4.13) and $\mathbf{x}$, the unknown vector (the pressure). If $\Lambda = T^{-1}LT$ is the diagonal matrix

made of the eigenvalues and T is the transfer matrix and consists of the eigenvectors. The unknown vector $\mathbf{y}$ in the base formed by the eigenvectors is defined by $\mathbf{x} = T\mathbf{y}$. The solution proceeds as follows:

1. compute $T^{-1}L\mathbf{x} = T^{-1}LT\mathbf{y} = \Lambda\mathbf{y} = T^{-1}\mathbf{S}$;

2. solve the $2D$ problem by the multi-grid algorithm which is, for the z-direction, $\mathbf{y} = \Lambda^{-1}T^{-1}\mathbf{S}$;

3. return into the physical base: $\mathbf{x} = T\mathbf{y} = T\Lambda^{-1}T^{-1}\mathbf{S}$.

Because of the symmetry of L, $T^{-1} = T^T$ if T is constituted of the unit eigenvectors.

4.6.3 The multi-grid algorithm

The present algorithm uses a V-cycle with line-relaxation and bi-linear interpolation and solves step 2 of the sequence given in Section 4.6.2. Because the problem is $2D$, the discrete Laplace equation only involves 9 coefficients denoted: a_P ,a_E ,a_W ,a_N ,a_S ,a_{en} ,a_{es} ,a_{wn} ,a_{ws} (see Figure 4.1). These coefficients are computed and stored at the start of a computation. The eigenvalue is then added to the coefficient a_P. The discrete form of the problem to be solved may be written as:

$$L\phi_g^{(k)} = \mathbf{S}_g \tag{4.25}$$

where $\phi_g^{(k)}$ is the solution at the (k) iteration of the multigrid cycle on the g grid (g varying between 1, the finest grid and, N_g, the coarsest grid), L is the discrete Laplace operator and $\mathbf{S}_g$, the right hand side term. The algorithm may be summarised as a sequence of the following steps:

1. initialise $\mathbf{S_1}$ to the right hand side coming from the partial diagonalisation and $\phi_1^{(0)}$ to the previous solution;

2. perform one iteration with the line solver;

3. compute the residual defined as $\mathbf{e_1} = \mathbf{S_1} - L\phi_1^{(0)}$;

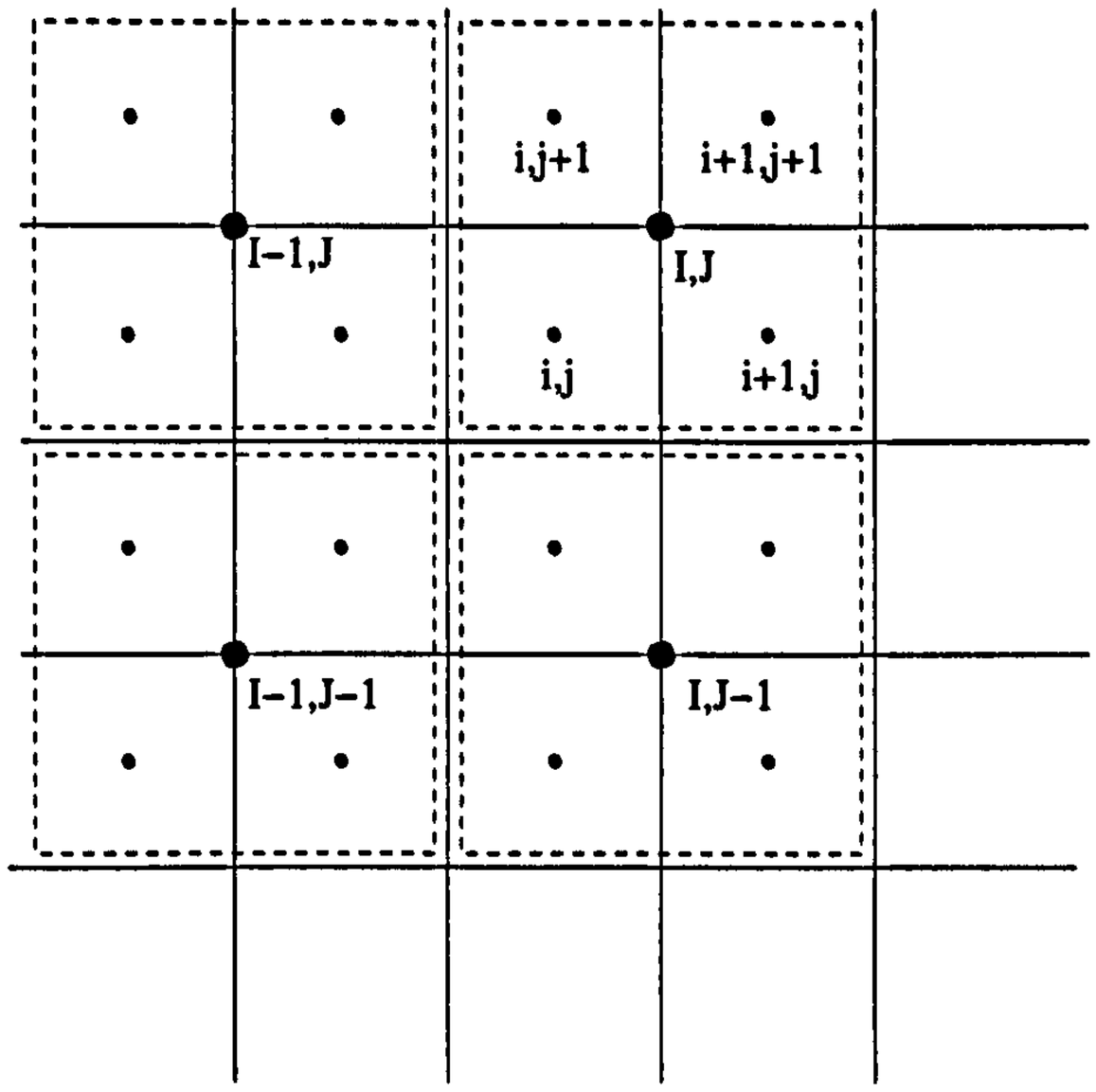

Figure 4.2: Transfer from one grid level to the other.

4. if convergence is reached (i.e. the residual is below a set limit), end the multi-grid algorithm;

5. compute the right hand-side term $\mathbf{S}_{g+1}$ by agglomerating the residual $\mathbf{e}_g$ over the four fine cells of the grid g constituting a coarse cell of the grid $g+1$ (see Figure 4.2):

$$(V_{g+1}S_{g+1})_{I,J} = (V_g e_g)_{i,j} + (V_g e_g)_{i+1,j} + (V_g e_g)_{i,j+1} + (V_g e_g)_{i+1,j+1} \qquad (4.26)$$

6. initialise $\phi_g^{(k)}$ to zero as the problem is now posed on the error to the solution;

7. perform N_c steps with the line solver;

8. compute the new residual $\mathbf{e}_{g+1} = \mathbf{S}_{g+1} L\phi_{g+1}^{(k)}$

9. if the coarsening sequence is not completed ($g < N_g$), go back to step 5;

10. compute the new solution on the finer grid from the previous solution at the same grid level and the solution from the coarser grid by bilinear interpolation:

$$\phi_g^{(k+1)}|_{i,j} = \phi_g^{(k)}|_{i,j} + \frac{1}{8}\left[5\phi_{g+1}^{(k+1)}|_{I,J} + \phi_{g+1}^{(k+1)}|_{I,J-1} + \phi_{g+1}^{(k+1)}|_{I-1,J} + \phi_{g+1}^{(k+1)}|_{I-1,J-1}\right] \tag{4.27}$$

11. perform N_r steps with the line solver;

12. if the refining sequence is not completed ($g > 1$), go back to step 10;

13. compute the residual **e** and finish the algorithm if convergence is reached. Otherwise, return to step 5.

4.6.4 The line solver

The solution of the system (4.25), for any grid level g, requires the inversion of L. This is achieved by using a line over-relaxation and an ADI* technique in which the solution is computed by sweeping alternatively in the x- and y-directions with the variable along x- or y-oriented lines solved by the Thomas algorithm. If, for example, the sweep takes place in the West-East direction, the equation for any node P is:

$$\begin{aligned} a_W\phi_W^{l+1} + a_P\phi_P^{l+1} + a_E\phi_E^{l+1} &= (1-\omega)\left(a_W\phi_W^{l} + a_P\phi_P^{l} + a_E\phi_E^{l}\right) \\ &+\omega\left[S_P - \left(a_N\phi_N^{l} + a_S\phi_S^{l+1} + a_{en}\Phi_{en}^{l} + a_{es}\Phi_{es}^{l} + a_{ws}\Phi_{ws}^{l}\right)\right] \end{aligned} \tag{4.28}$$

where ω is the relaxation factor and l, the iteration number of the solver. For non-orthogonal meshes, a value of $\omega = 1$ is highly recommended while, for orthogonal and nearly-orthogonal grids, higher values (up to 1.5) can be chosen so that a better convergence is achieved.

In the case of a periodic domain, the grid lines form closed *loops* and extra terms appear in the upper-left and lower-right corners of the matrix. The inversion of this matrix is achieved by using the sweeping method of Samarskii and Nikolaev [196, 197] which is more expensive than the Thomas algorithm as it requires two matrix inversions but is nevertheless implemented in the present code (see Appendix B.2).

*ADI = Alternate Direction Implicit

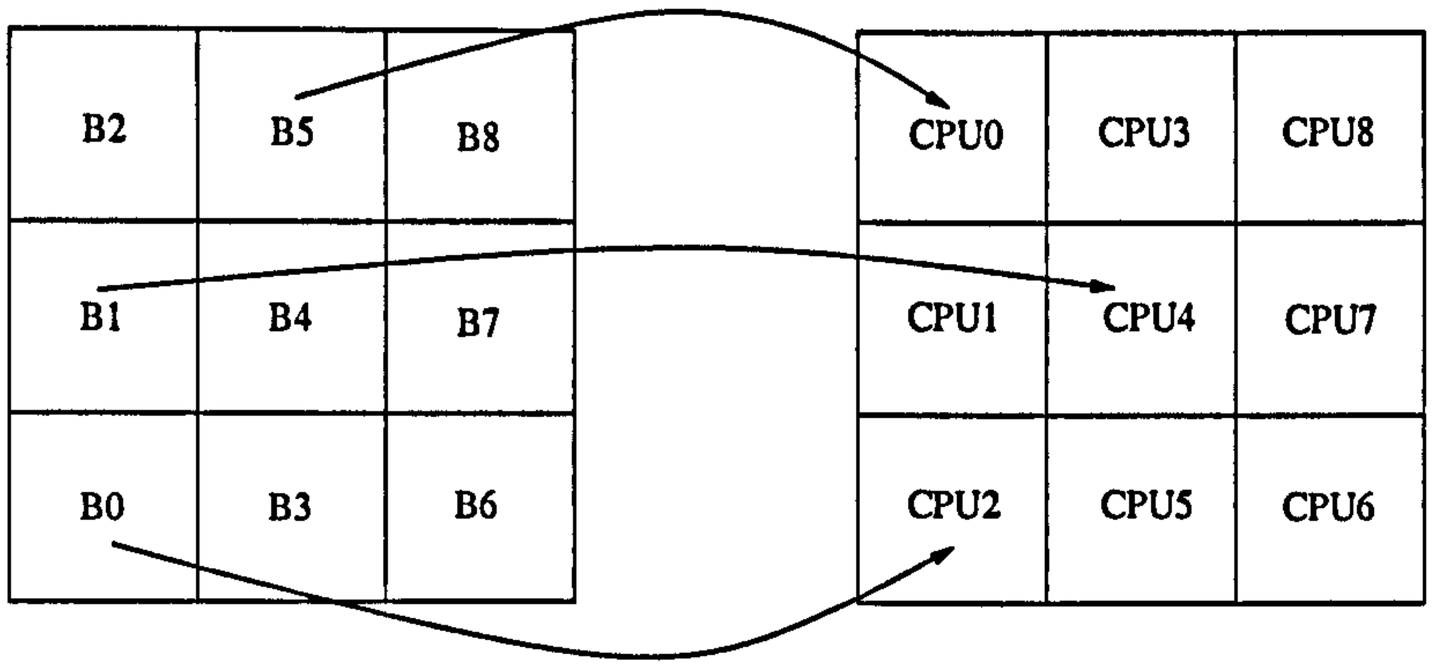

Figure 4.3: Domain decomposition and allocation to processors.

4.7 Parallelisation issues

4.7.1 Overview

The code uses two levels of parallelisation. The first level employs domain decomposition wherein sub-domains are designated to processes. The second level is related to the method used to solve the pressure problem. It relies on the partial diagonalisation technique introduced in Section 4.6.2 and allows the decomposition of the $3D$ problem into N_z uncoupled $2D$ problems which offers a natural route to parallelisation. These two aspects are discussed in separate subsections to follow.

The parallelisation uses the MPI[†] libraries to manage the communications between the processors [209].

4.7.2 Domain decomposition

The computational domain is divided into N_B blocks (see Figure 4.3), and each of these blocks is associated with one of the N_P processors used to solve the complete problem. At various stages of the solution procedure, one block requires informations from neighbouring blocks. To accommodate this, each block is supplemented by extra layers of cells (halo cells) penetrating into neighbouring blocks. These are updated at different stages of the computing sequence by allowing the processes to communicate between each other. These halo layers include the corner cells and lines (see Figure 4.4).

[†]MPI = Message Passing Interface

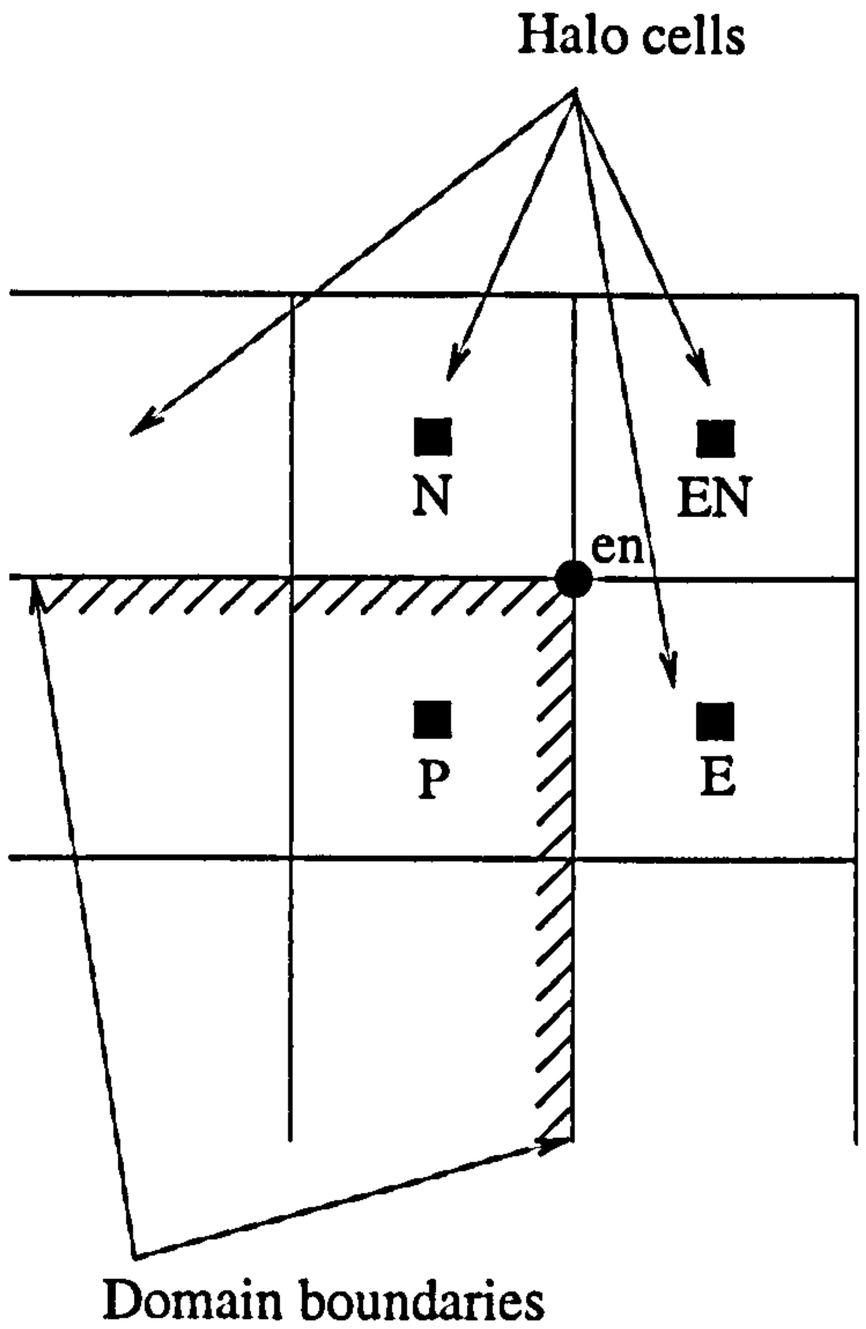

Figure 4.4: Halo layer at a corner region (example with one layer).

Block boundaries and associated halo-layer treatments may be of three different types:

- the block boundary is a domain boundary, in which case, the halo layer lies outside the solution domain and is used to specify the boundary conditions (see Section 4.8);

- the domain is periodic in the considered direction and covered by one block only, the exchange of data is then purely internal to the process:

  $\phi_0 = \phi_n$ and $\phi_{n+1} = \phi_1$ where ϕ is the considered variable (see Figure 4.5);

- the block boundary is purely internal to the computational domain. The exchange is:

  $\phi_{0,eb} = \phi_{n,wb}$ and $\phi_{n+1,wb} = \phi_{1,eb}$ (see Figure 4.6).

Using halo layers to impose the boundary conditions on a block simplify the code implementation as the interior and the exterior part of the block do not need to be distinguished in the solution procedure.

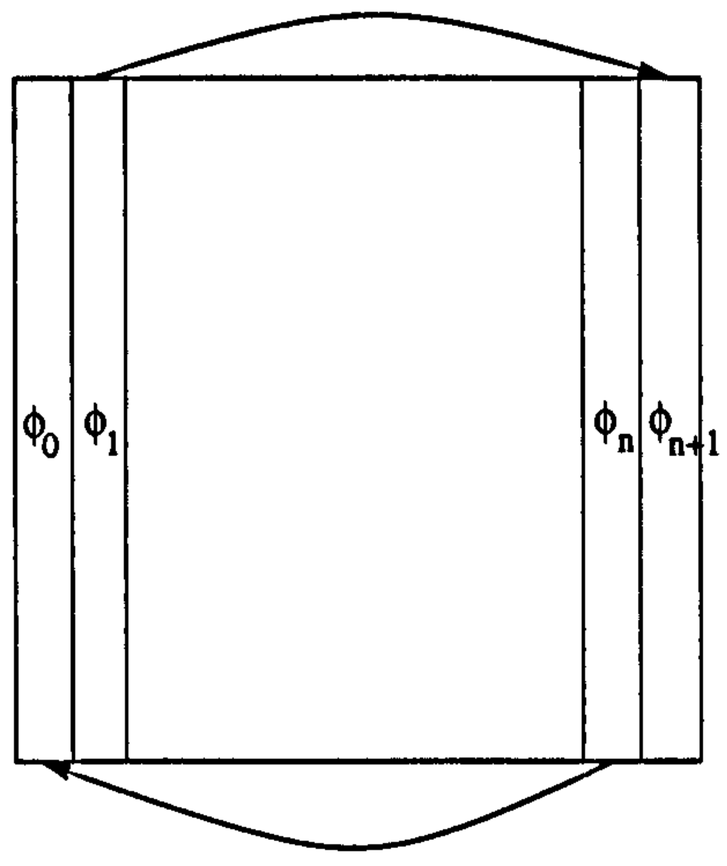

Figure 4.5: Periodic domain spanning on a single block.

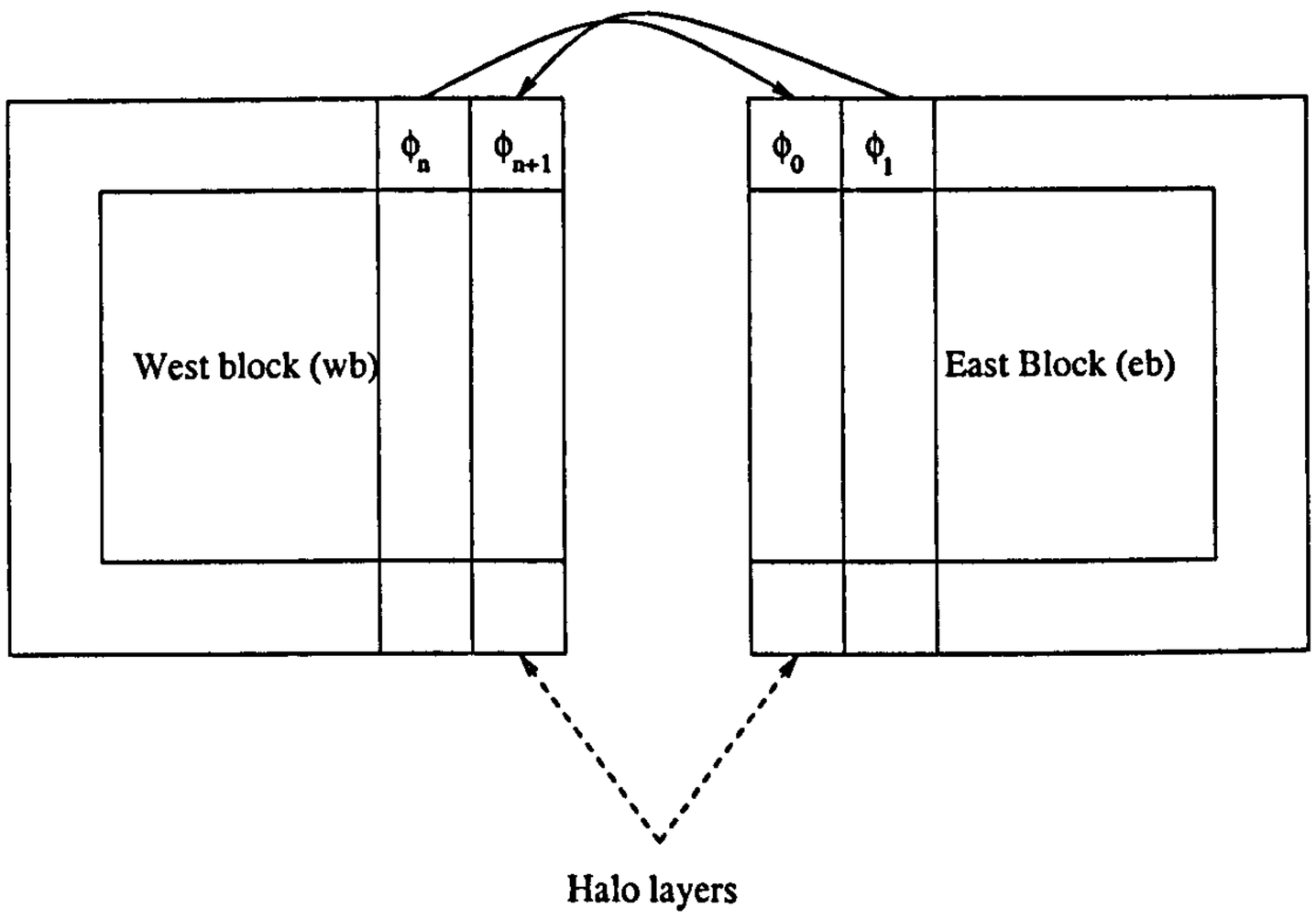

Figure 4.6: Boundaries between two neighbouring blocks.

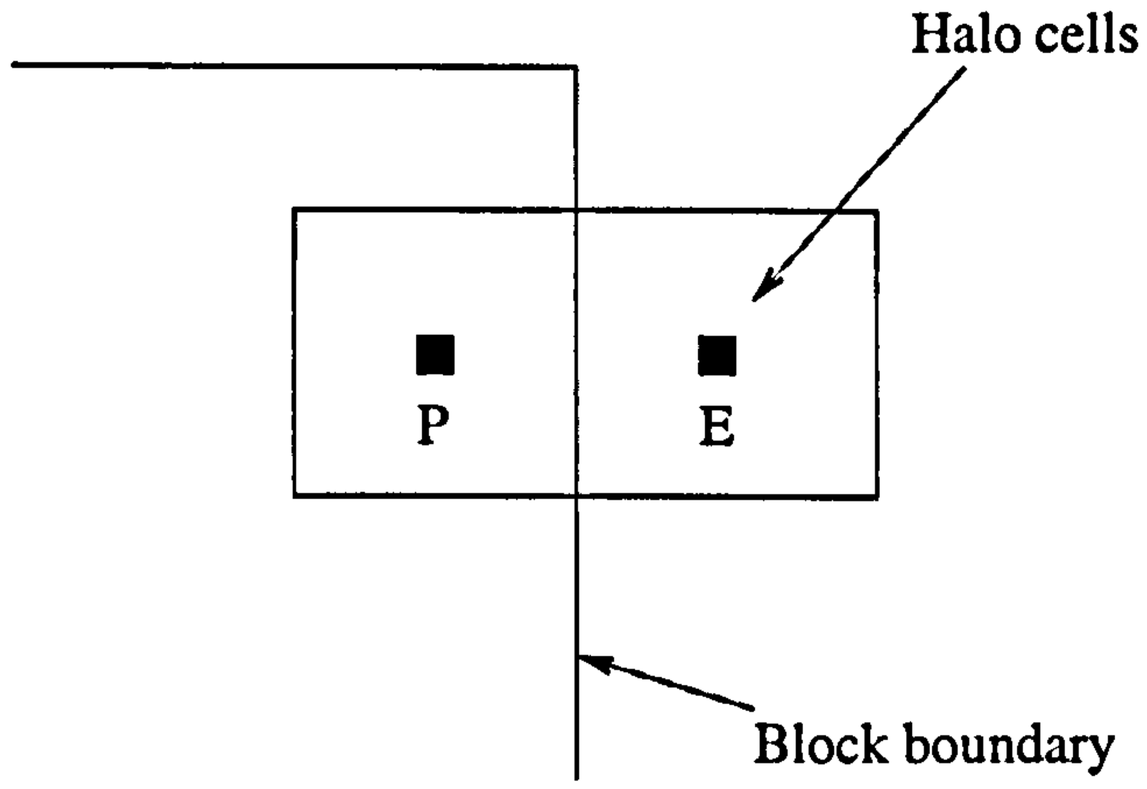

Figure 4.7: Interblock boundary for the pressure.

4.7.3 Parallelisation associated with partial diagonalisation

In Section 4.6, the details of the partial diagonalisation algorithm are given. This technique is used to replace $3D$ pressure problem ($N_x \times N_y \times N_z$) by a set of N_z $2D$ problems. In the present code, each $2D$ problem is associated with one sub-set of processors. Thus, if N_P processors are used, each $2D$ problem will be solved on N_P/N_z processors.

4.7.4 Inter-block boundary condition for the pressure

In the case of an internal block boundary (see Figure 4.7) for the pressure, a virtual Dirichlet condition is prescribed at the said boundary. This condition is:

$$\frac{\phi_P^{(k+1)} + \phi_E^{(k+1)}}{2} = \frac{\phi_P^{(k)} + \phi_E^{(k)}}{2} \tag{4.29}$$

where k is the iteration counter in the line solver. Once the system has been inverted by the line solver, the true $\phi_E^{(k+1)}$ is replaced by the value computed in the neighbouring block by updating the content of the halo layers. The simpler Dirichlet boundary condition $\phi_E^{(k+1)} = \phi_E^{(k)}$ was found to lead to numerical instability (Lardat and Leschziner [114]).

4.8 Boundary constraints

4.8.1 Overview

The domain boundaries are imposed by using the halo cells (see Section 4.7.2). Three different conditions are applied:

1. the boundary condition on the mass fluxes which is applied before the solution of the Poisson equation;

2. the boundary condition on the Cartesian velocity which is applied at the end of the time-step;

3. the boundary condition on the pressure gradient which is partially implemented when constructing the Laplace operator.

4.8.2 Mass-flux constraint

The mass flux on the domain boundary must always be defined as a Dirichlet condition:

$$\mathbf{C}^* \cdot \mathbf{n} = \mathbf{C}^{n+1} \cdot \mathbf{n} = \mathbf{a} \cdot \mathbf{n} \tag{4.30}$$

where $\mathbf{a}$ is a velocity vector that can be either prescribed once at the start of a computation or updated through it.

In the present work, the outflow conditions have been treated in one of two ways:

- the boundary velocity gradient was set to zero:

$$\frac{\partial \mathbf{a}}{\partial \xi} = 0 \tag{4.31}$$

with ξ, the normal direction to the computational domain;

- a convective boundary condition was used (Pauley et al [170]):

$$\frac{\partial \mathbf{a}}{\partial t} + U_c \frac{\partial \mathbf{a}}{\partial \xi} = 0 \tag{4.32}$$

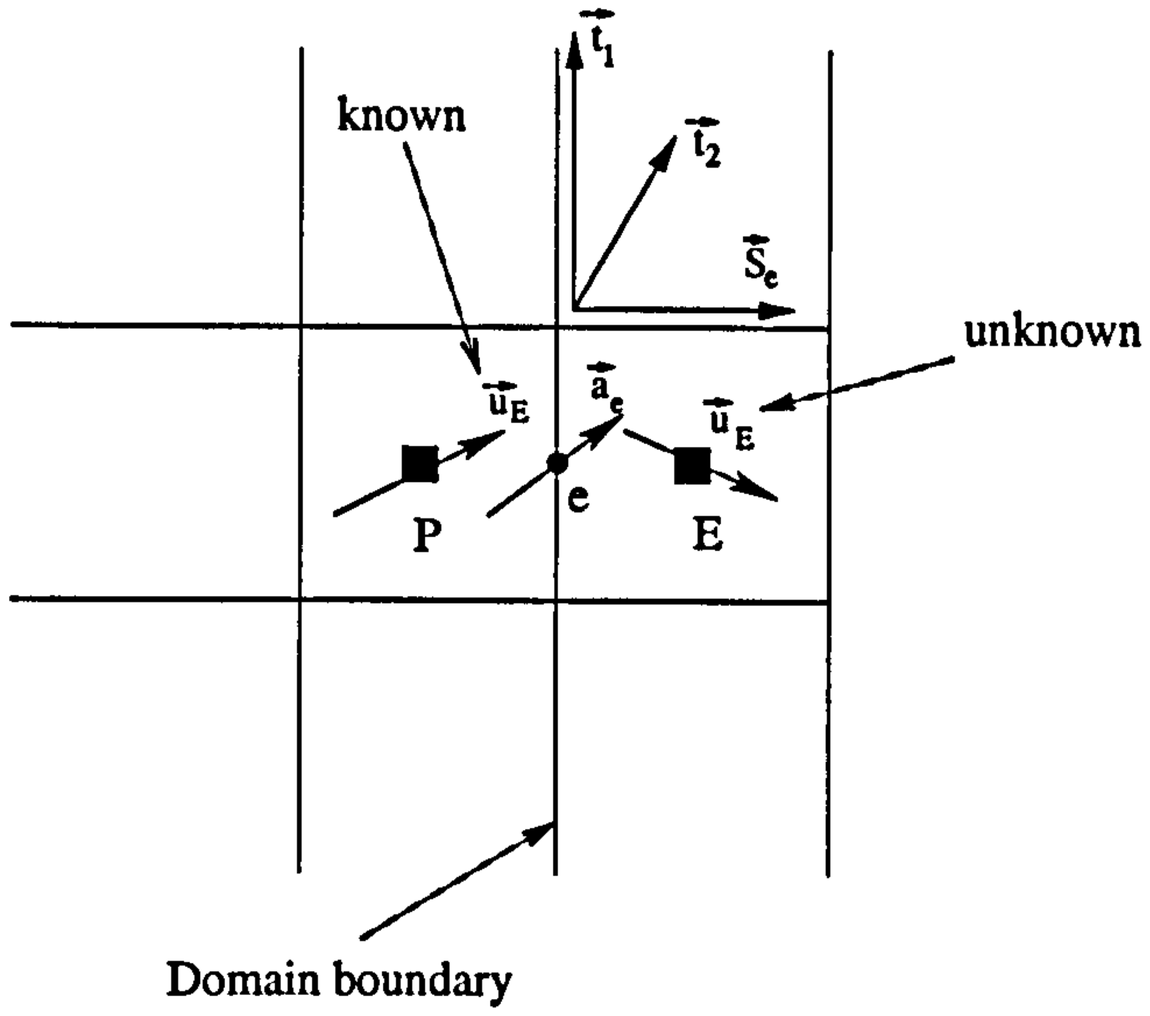

Figure 4.8: Halo cells for the Cartesian velocity.

with ξ being the direction normal to the domain boundary and U_c being a convective velocity scale which can be taken equal to the local convective velocity, the mean exit velocity or a representative scale such as the free-stream velocity. As shown by Pauley et al [170], this choice is not influential.

4.8.3 Boundary condition on the Cartesian velocity

The boundary conditions on the Cartesian velocity are imposed at the end of the time-step by using the halo cells next to the domain border. Their content is determined from the Cartesian velocity inside the domain and the type of boundary considered for the tangential components of the velocity to the domain boundary. In three-dimensions, the halo cell content is obtained by solving for each of them a 3×3 linear system.

If P marks the centre of the cell inside the domain on the eastern border and E is the centre of the corresponding halo cell on the outside domain (see Figure 4.8), and if $\mathbf{S_e}$ is the vector normal to the e face and $\mathbf{t_1}$ and $\mathbf{t_2}$ are some tangential vectors defined as:

$$\mathbf{S_e} \cdot \mathbf{t_1} = 0 \quad \text{and} \quad \mathbf{S_e} \times \mathbf{t_1} = \mathbf{t_2} \tag{4.33}$$

then:

- for Dirichlet boundary conditions on the tangential components of the Cartesian velocity:

$$\left.\begin{aligned} \mathbf{S}_e \cdot \frac{\mathbf{u}_P + \mathbf{u}_E}{2} &= \mathbf{S}_e \cdot \mathbf{a}_e \\ \mathbf{t}_1 \cdot \frac{\mathbf{u}_P + \mathbf{u}_E}{2} &= \mathbf{t}_1 \cdot \mathbf{a}_e \\ \mathbf{t}_2 \cdot \frac{\mathbf{u}_P + \mathbf{u}_E}{2} &= \mathbf{t}_2 \cdot \mathbf{a}_e \end{aligned}\right\} \tag{4.34}$$

where $\mathbf{a}_e$ is the given velocity vector on the boundary, $\mathbf{u}_P$ is the known velocity vector at P and $\mathbf{u}_E$ is the unknown velocity vector;

- Neumann boundary conditions on the tangential velocities of the tangential components of the Cartesian velocity:

$$\left.\begin{aligned} \mathbf{S}_e \cdot \frac{\mathbf{u}_P + \mathbf{u}_E}{2} &= \mathbf{S}_e \cdot \mathbf{a}_e \\ \mathbf{t}_1 \cdot (\mathbf{u}_P - \mathbf{u}_E) &= 0 \\ \mathbf{t}_2 \cdot (\mathbf{u}_P - \mathbf{u}_E) &= 0 \end{aligned}\right\} \tag{4.35}$$

The two last equations of the system (4.35) are Neumann homogeneous boundary conditions. These can be used for slip and symmetry conditions.

The treatment of the domain corner also need to be considered and is different from the other halo cells. In Figure 4.4, the upper right corner of the domain, denoted by EN is considered. If at least one of two of the domain boundary involves a Dirichlet condition then the value $\mathbf{a}_{en}$ at the node en must be provided and the velocity value in the halo cell EN is extracted from:

$$\frac{\mathbf{u}_P + \mathbf{u}_E + \mathbf{u}_N + \mathbf{u}_{EN}}{2} = \mathbf{a}_{en} \tag{4.36}$$

When the conditions at both boundaries are of the Neumann type for the tangential components of the velocity, the halo cell velocity in EN is obtained from the resolution of the following system:

$$\left.\begin{aligned} \mathbf{S}_e \cdot \frac{\mathbf{u}_N + \mathbf{u}_E N}{2} &= \mathbf{S}_e \cdot \mathbf{a}_e \\ \mathbf{S}_n \cdot \frac{\mathbf{u}_E + \mathbf{u}_E N}{2} &= \mathbf{S}_n \cdot \mathbf{a}_n \\ \mathbf{t} \cdot (\mathbf{u}_P - \mathbf{u}_{EN}) &= 0 \end{aligned}\right\} \tag{4.37}$$

where $\mathbf{t} = \mathbf{S}_e \times \mathbf{S}_n$.

4.8.4 Alternative wall boundary conditions

In Section 3.3, a number of alternative near-wall approximations have been described. These wall functions return a value of the wall shear stress τ_w based on the value of the tangential velocity $\mathbf{u}_1$ at the centre of the near-wall cell centre (see Figure 4.9).

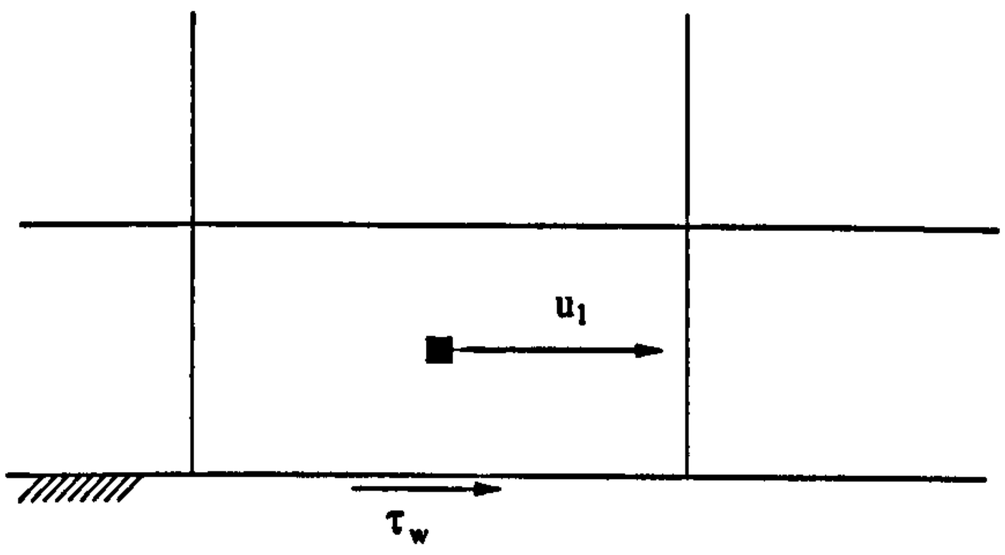

Figure 4.9: Imposing an approximate boundary condition by replacing the momentum fluxes.

Once the wall shear stress is known, any momentum flux through the cell face coinciding with the wall is replaced by:

- $\tau_{w,x} S_{tot}$ for the x-momentum equation;
- $\tau_{w,y} S_{tot}$ for the y-momentum equation;
- $\tau_{w,z} S_{tot}$ for the z-momentum equation;

where $S_{tot} = \sqrt{S_x^2 + S_y^2 + S_z^2}$ is the surface of the cell face lying on the domain boundary.

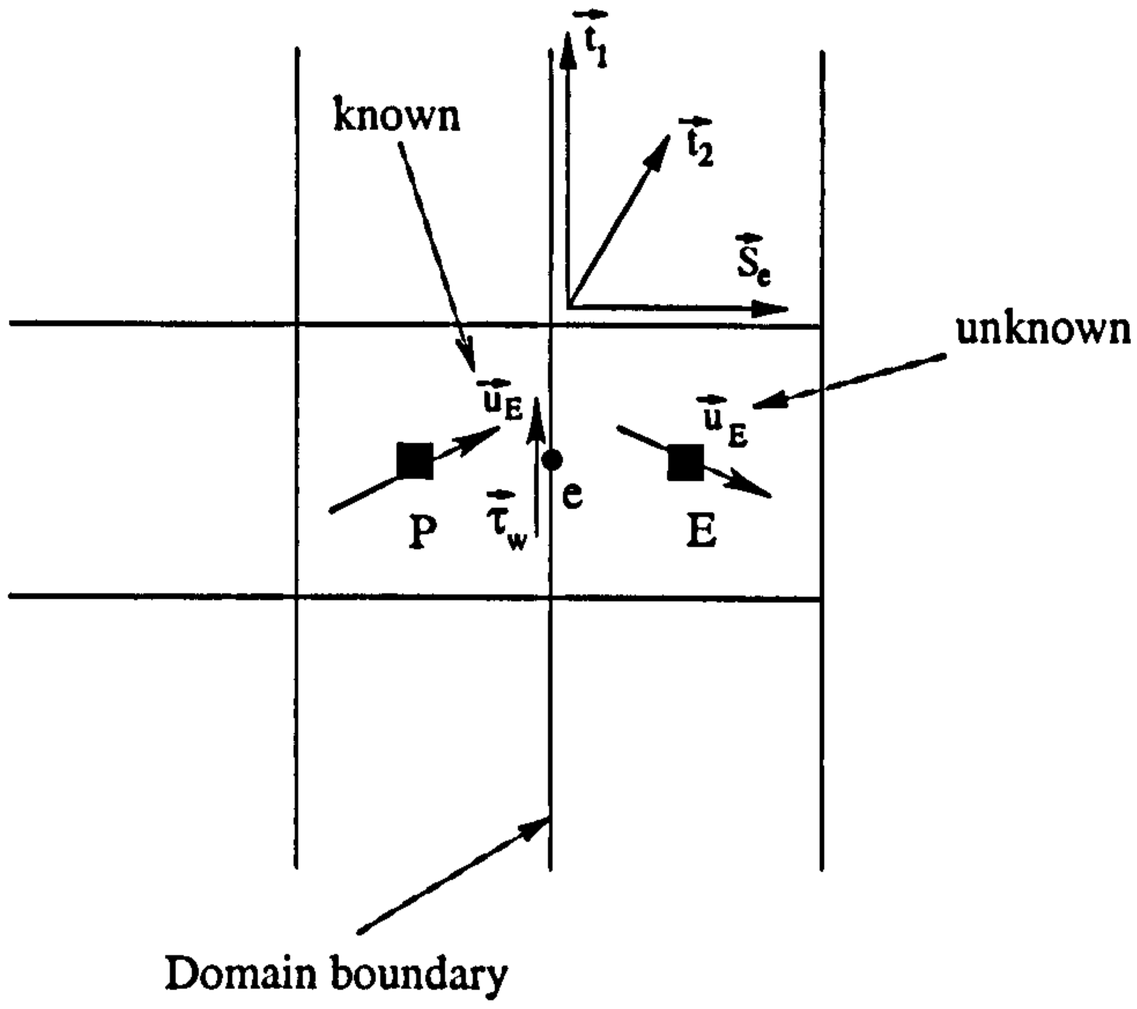

Figure 4.10: Imposing an approximate boundary condition through the halo cells.

A possible alternative route (not used here) is to introduce these boundary conditions via non-homogeneous Neumann boundary conditions for the Cartesian velocities with system (4.35) being rewritten as follows if the eastern border of the domain is considered (see Figure 4.10):

$$\left.\begin{aligned} \mathbf{S}_e \cdot \frac{\mathbf{u}_P + \mathbf{u}_E}{2} &= \mathbf{S}_e \cdot \mathbf{a}_e \\ \mathbf{t}_1 \cdot (\mathbf{u}_P - \mathbf{u}_E) &= \mathbf{t}_1 \cdot \tau_w \\ \mathbf{t}_2 \cdot (\mathbf{u}_P - \mathbf{u}_E) &= \mathbf{t}_2 \cdot \tau_w \end{aligned}\right\} \tag{4.38}$$

4.8.5 Boundary condition for the pressure

The boundary condition for the pressure on the domain is a homogeneous Neumann condition (see system (4.13):

$$\frac{\partial \overline{p}^{n+1}}{\partial x_i} n_i = 0 \tag{4.39}$$

This condition results from the requirement that the overall mass must be conserved on the domain boundary. In this code, condition (4.39) is built in the Laplace equation at the start of a computation when the stencils of the discrete Laplace problem are evaluated.

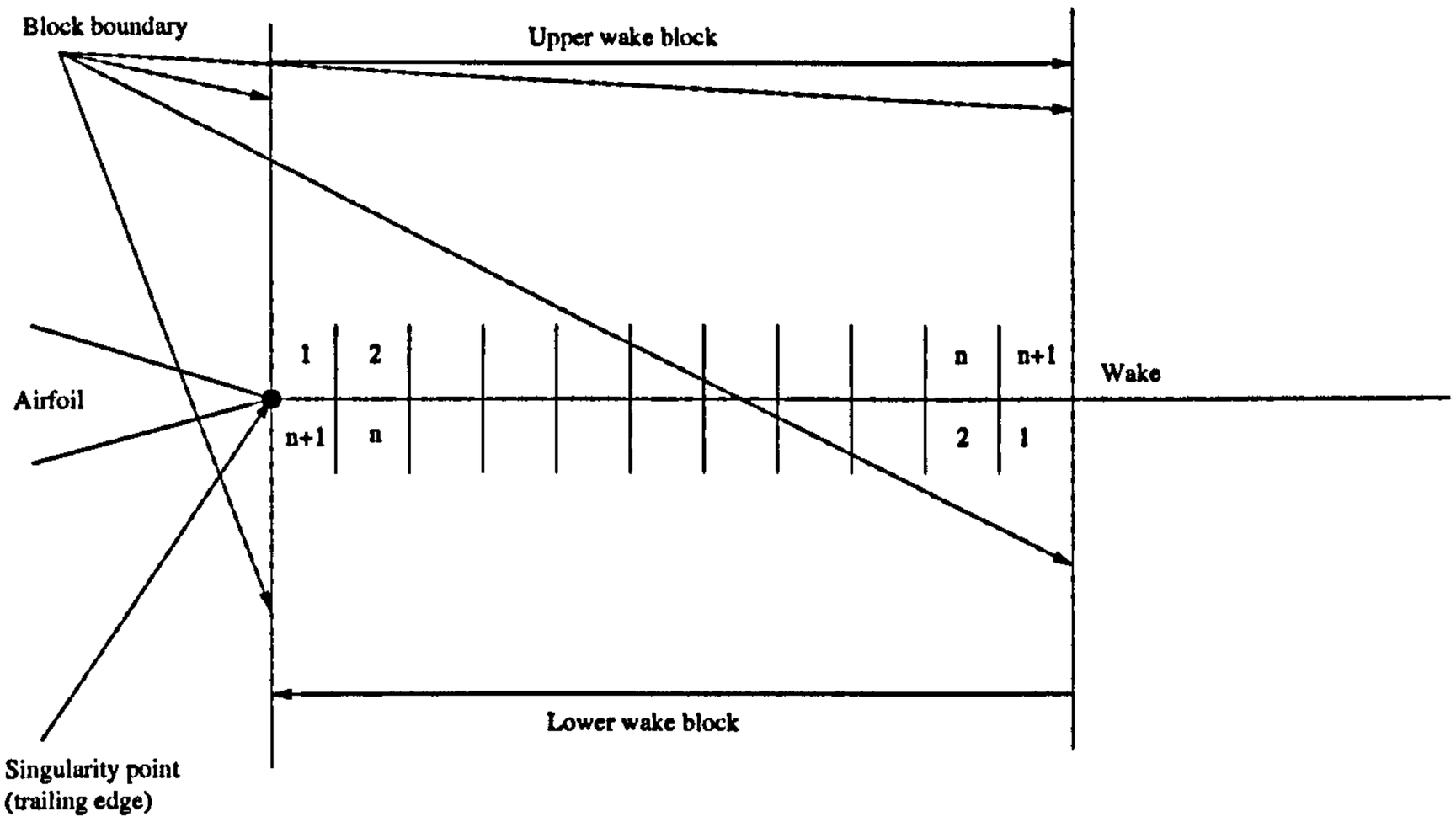

Figure 4.11: Treatment of the block interface in the aerofoil wake.

For a non-orthogonal mesh, the solver needs the nodal value of the pressure on the boundary. This value is computed by using the content of the halo cells. The halo cells values are determined using a linear extrapolation from the domain inside (as recommended by Bernard and Kapitza [16]). The linear interpolation, assuming that the eastern face of the domain is considered (see Figure 4.1), writes:

$$p_E = 2p_P - p_W \tag{4.40}$$

4.8.6 C-grid capability

The present code has been designed to compute flows around airfoils with a sharp trailing-edge and has, therefore, a C-grid capability in which the domain is *folded* in such a way that one part of a boundary collapses to another part of the same boundary. The domain being structured, special care has to be taken when updating the halo cells of two blocks with common interfaces originating from different parts of the same boundary. As shown in Figure 4.11, a consequence of a folded boundary is that the cells $1 \ldots n$ of one block connect to cells $n \ldots 1$ of the neighbouring block. The procedure to update the halo cells is as follows. First, the halo cells are updated as described in Section 4.7.2. Second, the order of the halo cells is inversed so that its content corresponds to the content of the associated cell inside the domain.

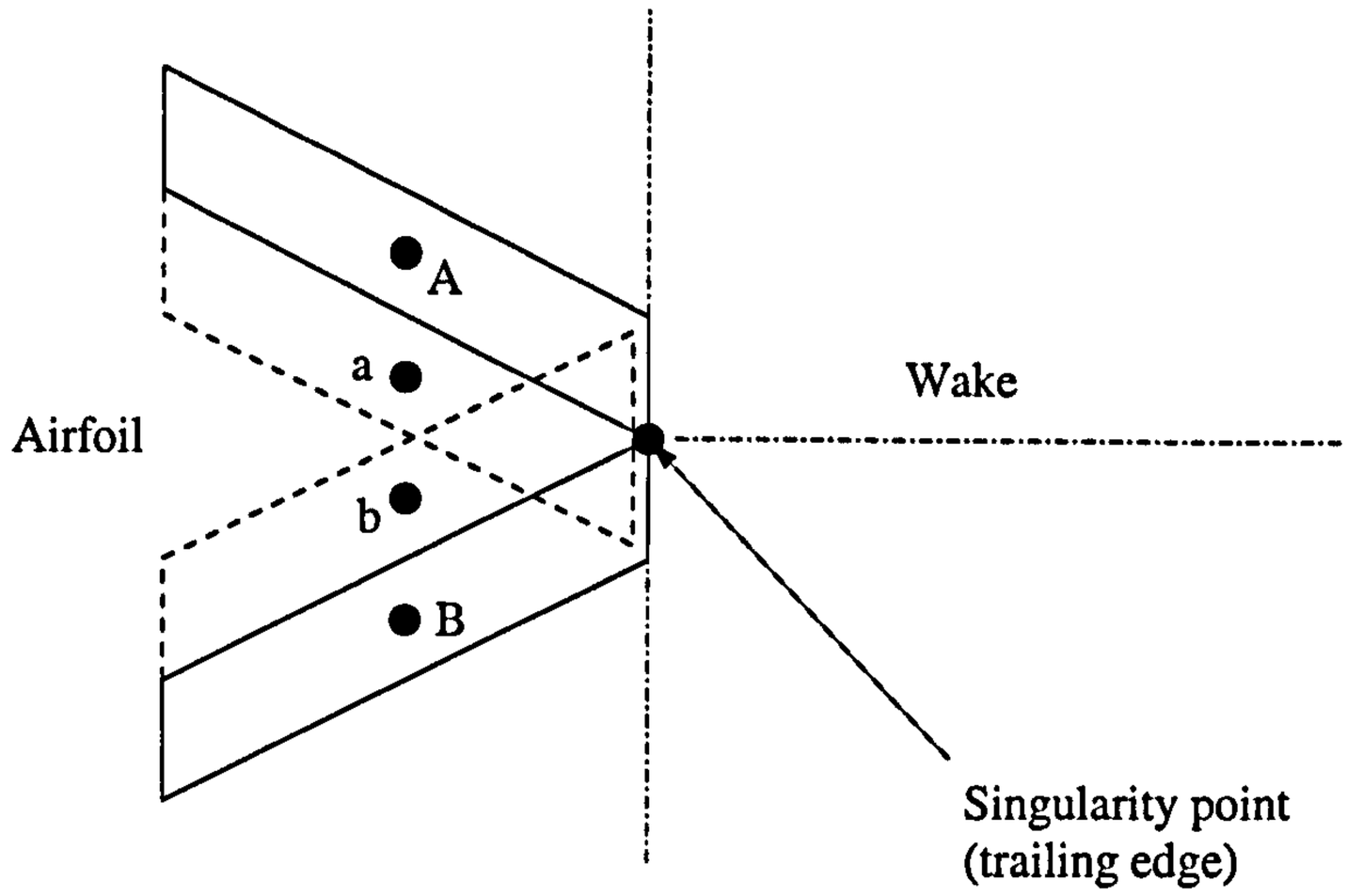

Figure 4.12: Discretisation in the trailing edge (singularity point) region.

A current requirement of the code is that the vertex located at the trailing edge must be located on a block interface as shown in Figure 4.11. The multigrid solver also requires that the trailing edge vertex belongs to each grid used in the multigrid cycle.

4.8.7 Singularity point

The aerofoil considered in this work presents a sharp trailing edge on which a node is located (see Figure 4.11). This particular point is a singular point and the code needs the value for the pressure and the Cartesian velocities at this particular location. For the Cartesian velocities, one is imposing that:

$$\mathbf{u}_{node,sing} = \mathbf{0} \tag{4.41}$$

The nodal pressure value is computed by considering the near-wall cells next to the trailing-edge and their corresponding halo cells (see Figure 4.12). The nodal pressure is obtained by taking the average of the pressure at the centroid of these four cells as follows:

$$\phi_{node,sing} = \frac{1}{4}\left(\phi_A + \phi_B + \phi_a + \phi_b\right) \tag{4.42}$$

This is applied at each level of the multigrid procedure, hence the use of ϕ rather than $\overline{p}$ to represent the pressure.

4.9 Code performance on parallel platforms

4.9.1 Hardware characteristics

The code was developed and ported to four different architectures:

- a Cray T3D with 512 DEC Alpha 21064 processors having a cycle rate of 150 MHz and 64 MB of memory;
- a Cray T3E 1200E with 788 processors Alpha 21164 having a cycle rate of 600 MHz and 256 MB of memory;
- a 32 processors Intel Pentium III system (Beowulf II), each processor having a cycle-rate of 450 MHz with 256 MB of memory and interconnected via Fast Ethernet;
- a Compaq system (Loki) made of 16 Alpha EV67(21264A) dual-processors, having a cycle rate of 667 MHz and 512 MB of memory with communication achieved by the QSW high performance interconnect.

Communications-related information is given in Table 4.1.

Platform	Communication software	Latency	Maximum bandwidth
Beowulf system	LAM MPI	$100\mu s$	10 MBs
Loki system	MPICH	$20\mu s$	160 MBs
Cray T3D	MPI	$92\mu s$	110 MBs
Cray T3E	MPI	$10\mu s$	220 MBs

Table 4.1: System communication characteristics.

Beowulf systems are very cost-effective computing platforms. Their communications, often effected through Ethernet, is their weak point. Other interconnect

options offering better communications exist, but are generally too expensive for modest systems.

4.9.2 Parallel performance for the channel flow

The first benchmark case selected is the turbulent periodic channel flow. The computational domain has the dimensions $2\pi h \times 2h \times \pi h$ (h is the channel half width) and the Reynolds number (based on h, laminar viscosity ν and bulk velocity U_b) is equal to 10935. Each simulation started from an unitary velocity field and ran over a period of 1000 time-steps. All computational parameters are kept constant, while the domain decomposition is varied. Two different grids are employed:

- a medium size grid of $96 \times 64 \times 4$ cells;
- a large size grid of $384 \times 256 \times 4$ cells.

Figure 4.13 shows the solution time in seconds for 1000 iterations on partitions of 4 to 32 processors for the smallest of the two problems on three of the platforms described previously: the Beowulf system, the Loki system and the Cray T3E 1200E. Among these platforms, the Loki system appears to give the best overall performance. It has the fastest processors, and its communications are also fast, with a low-latency which is nearly as good as the Cray T3E. Fast communications with low-latency are desirable for iterative algorithms on parallel systems. In this respect, the Beowulf system is clearly disadvantaged (see Table 4.1).

For the same problem, Figure 4.14 shows the scalability to be similar for all platforms, with the Cray T3E performing a little better due to its better communication network, despite the fact that its processors are slower than those of the Beowulf and Loki systems.

In Figure 4.15, the larger problem is considered. The speed-up curve is shown for the Beowulf system and the Cray T3E. In this case, a virtually linear speed-up is achieved on both machines. Indeed, a super-linear behaviour is observed for the Cray T3E for the 32 processors case. This feature, quite common on such machines indicates an especially effective cache utilisation.

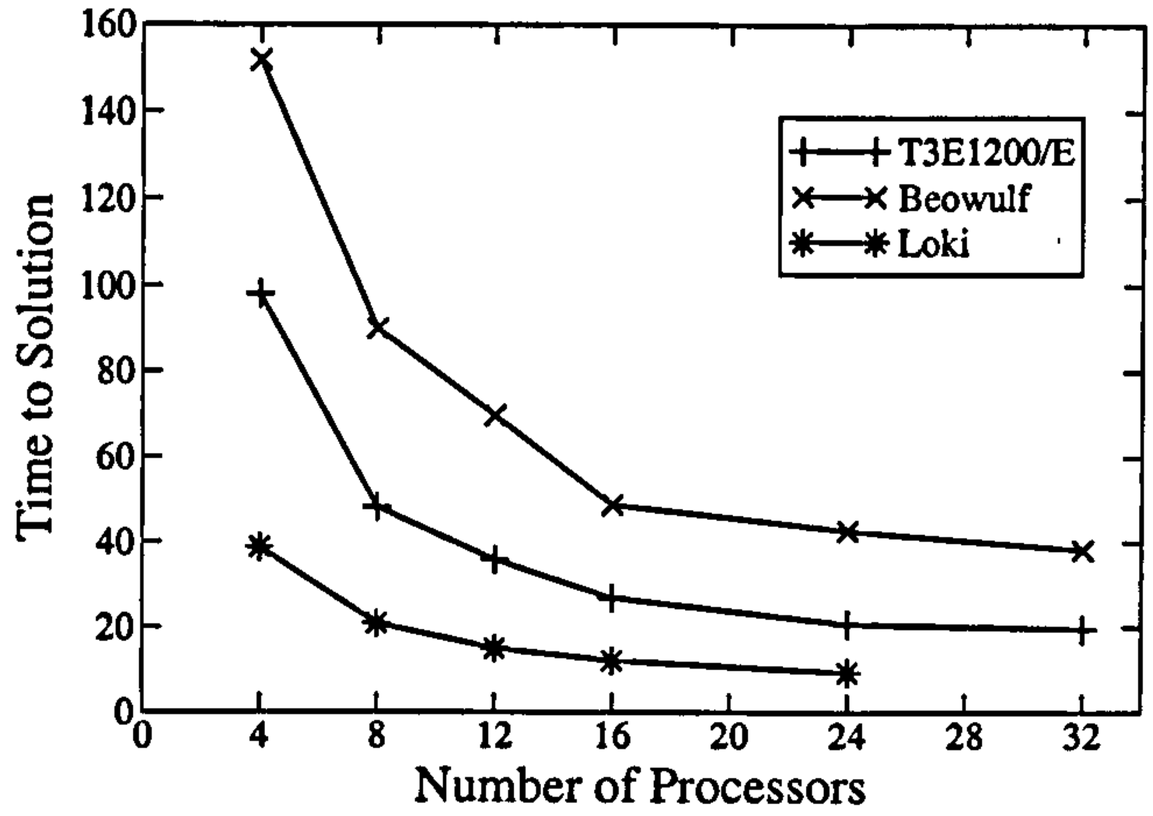

Figure 4.13: Time to solution for the channel problem. $96 \times 64 \times 4$ cells.

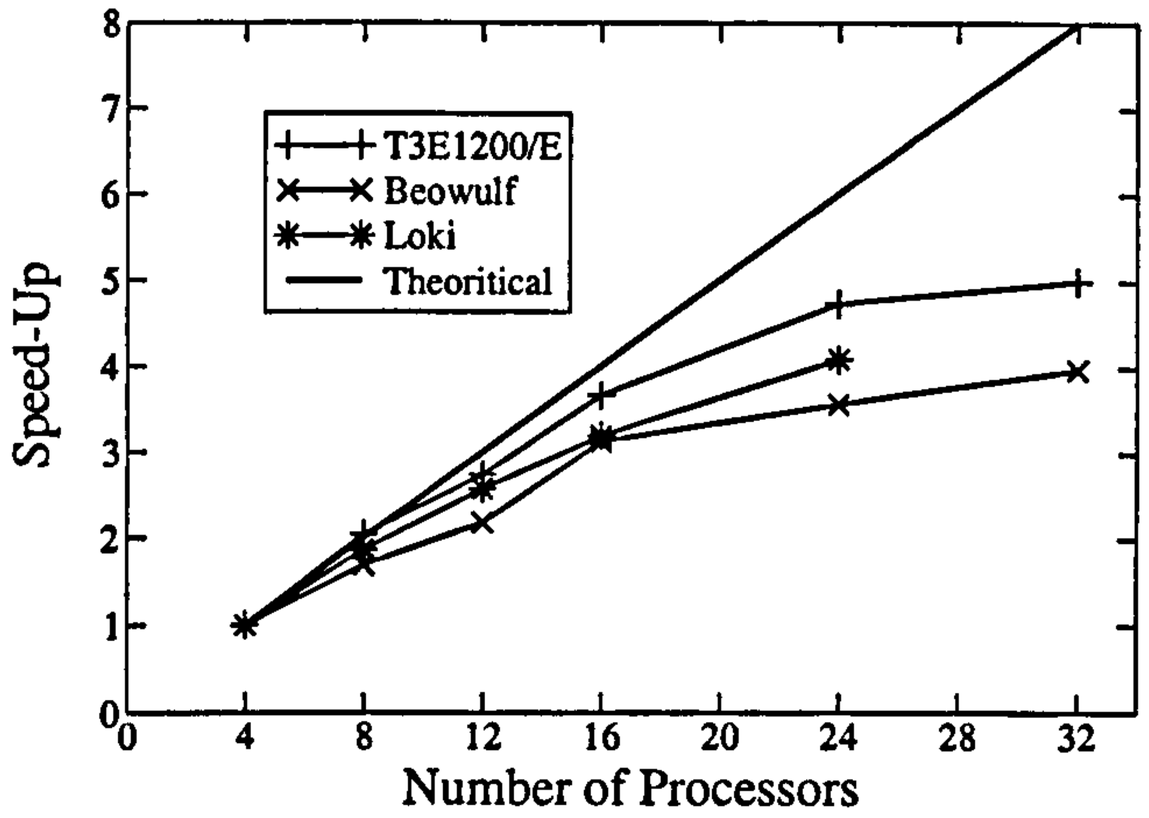

Figure 4.14: Speed-up curve for the channel problem. $96 \times 64 \times 4$ cells.

The relative importance of the communication to the total computational cost is indicated in Figures 4.16 and 4.17. The communication times are identified by reference to the different variables that are exchanged between processors, i.e. pressure, velocities and viscosity. The first observation is that the solution of the pressure requires the lion's share of the communications, especially for small problems with large number of blocks. As the problem size increases, the relative contribution of the communications to the total computational cost diminishes. The processors are spending more time calculating than exchanging informations. This explains why the larger problem scales much better on the Cray T3E and on the Beowulf system. For the latter, this is especially influential as the communications characteristics are

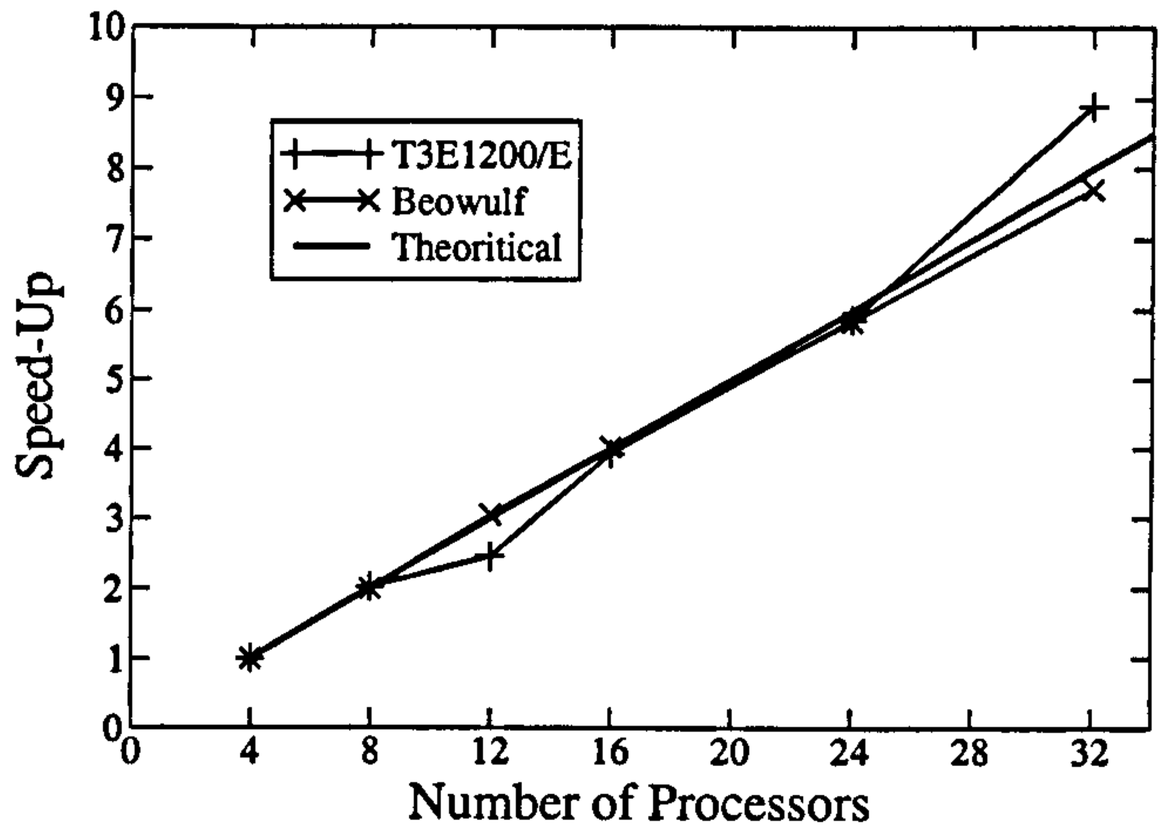

Figure 4.15: Speed-up curve for the channel problem. $384 \times 256 \times 4$ cells.

rather poor.

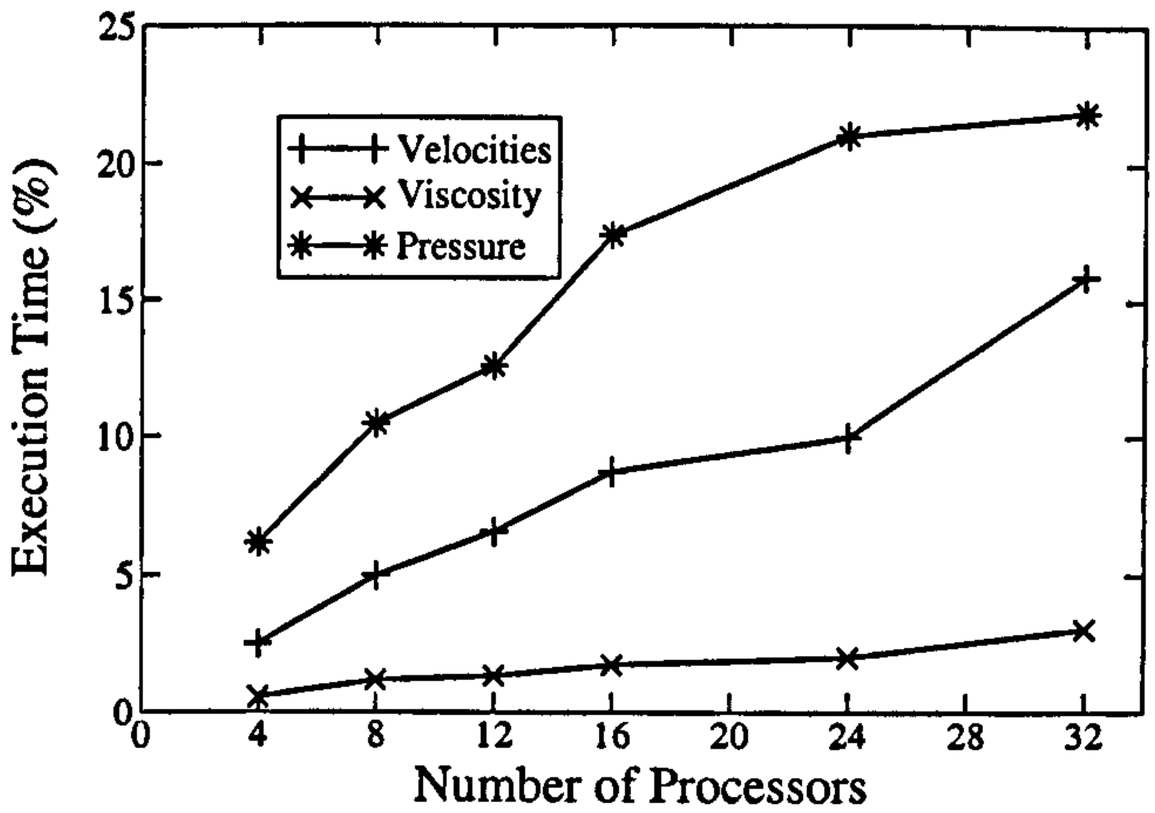

Figure 4.16: Communications time expressed as a fraction of the total execution time for the Cray T3E and the channel problem. $96 \times 64 \times 4$ cells.

4.9.3 Parallel performance for the Aerofoil

The problem considered here is a single element high-lift aerofoil (Aérospatiale-A [77, 78]) at 13.3^o angle of attack and a Reynolds number of 2×10^5, based on chord length and free-stream velocity. The spanwise extent of the aerofoil was chosen to be 0.23% of the chord. The grid consists of $320 \times 64 \times 32$ cells. The results were obtained on two of the four platforms considered: the Cray T3D [114] and the Cray

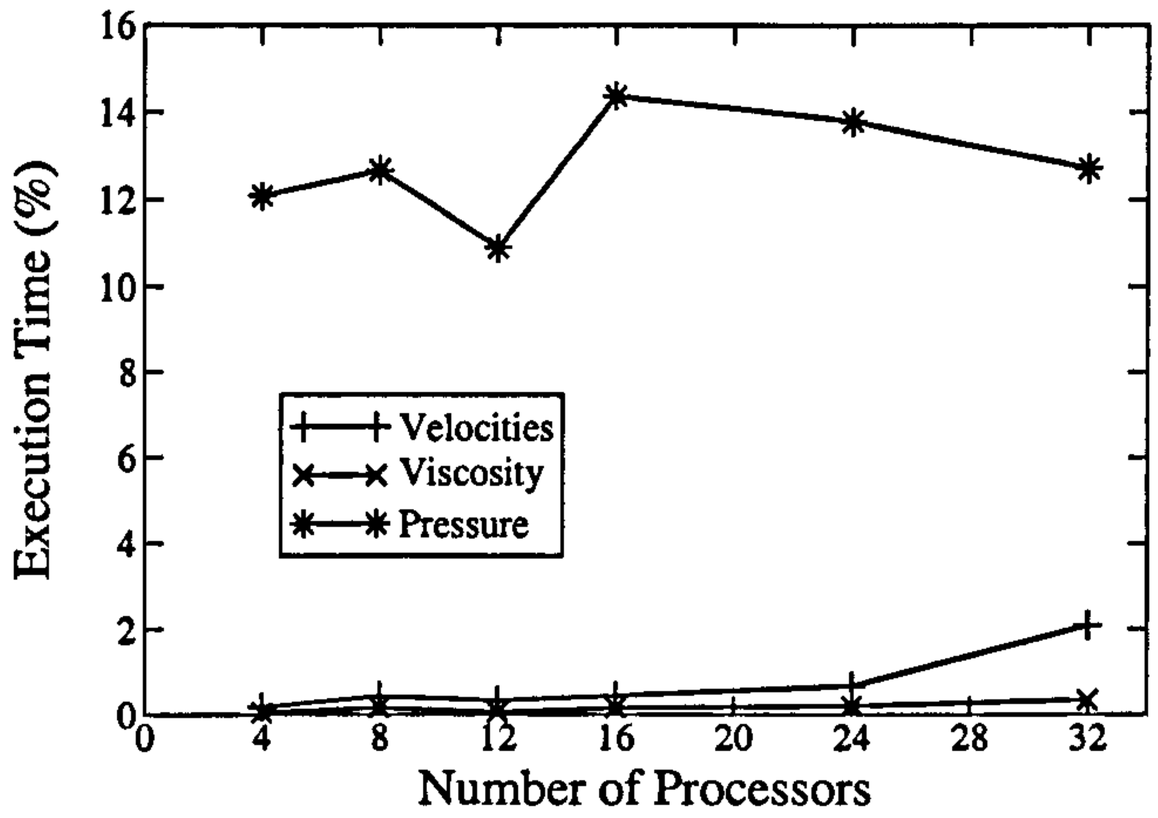

Figure 4.17: Communications time expressed as a fraction of the total execution time for the Cray T3E and the channel problem. $384 \times 256 \times 4$ cells.

T3E 1200E. The initial problem is decomposed into 32 blocks, and tests are carried out for 32, 64, 128, 256 and 512 blocks.

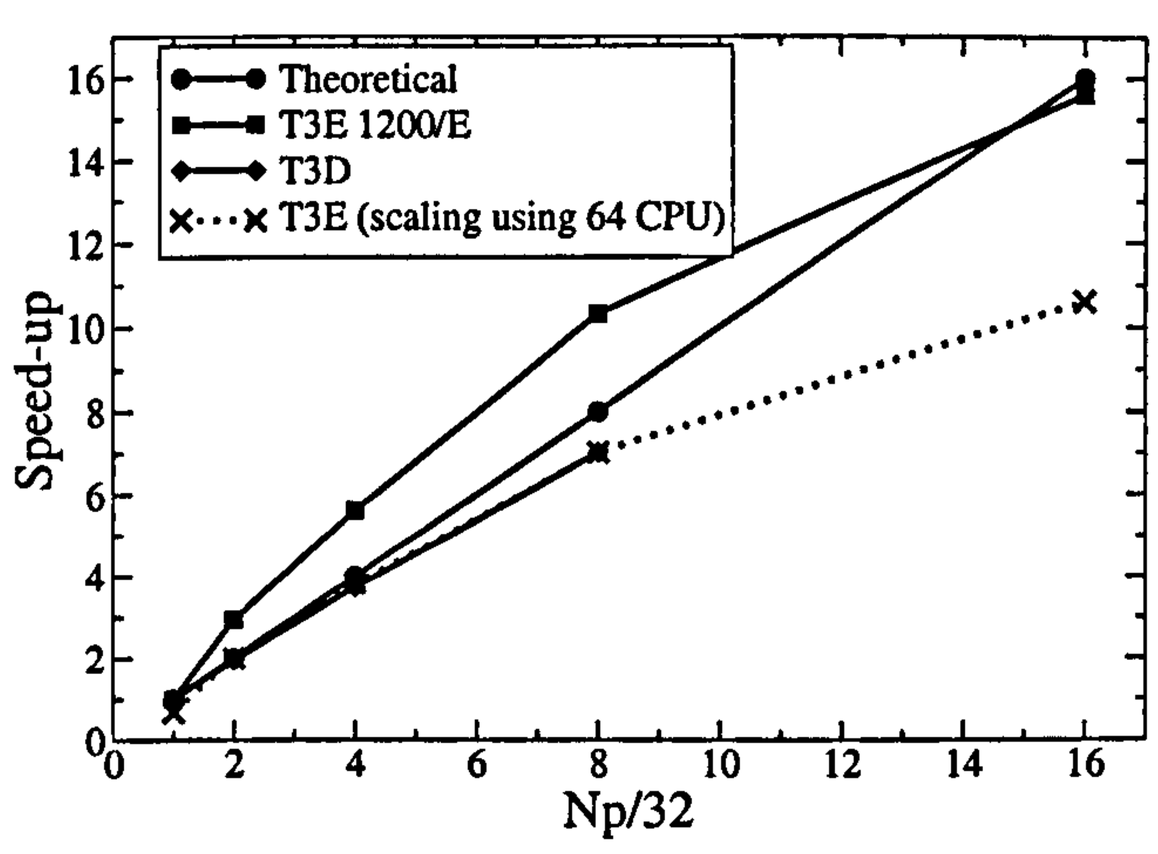

Figure 4.18: Speed-up curve for aerofoil flow. $320 \times 64 \times 32$ cells.

The speed-up curves obtained on both platforms are shown in Figure 4.18 for up to 256 processors for the Cray T3D and 512 processors for the Cray T3E, respectively. The scalability on both machines is good, but diminishes rapidly beyond 256 processors simply because the problem is too small for the largest partitions. For the Cray T3E, the scaling is made using 32 processors and 64 processors as references. A substantial gain in performances was observed when increasing the number of processors from 32 to 64 for the Cray T3E. The super-linearity, achieved by the

T3E indicates a poor cache utilization with 32 processors. Beyond 64 processors, each block fits in the cache, giving a better and faster access of the data to the processor.

Chapter 5

Flow analysis

5.1 Introduction

The phenomena of turbulence are very complex and their study, interpretation and understanding require the use of a range of mathematical tools. The aim of this chapter is to describe the tools that have been used in the present work to interpret results and extract useful data from the simulations.

Section 5.2 is concerned with basic aspects of the statistical description of turbulence. Sections 5.3 and 5.4 consider, respectively, the RANS equations which govern the mean velocity field and feature the Reynolds stress tensor and the equations dictating the transport of the Reynolds stresses. Section 5.5 introduces the anisotropy of the Reynolds-stress tensor and some post-processing tools which relate to this. Two-point correlations are defined in Section 5.6, while Section 5.7 is concerned with the study of turbulence in spectral space. Finally, Section 5.8 deals with approaches characterising instantaneous features of the flow, with particular emphasise on criteria for identifying vortical structures.

5.2 Statistical description

The study of the instantaneous turbulence fields offers the opportunity to extract from them certain structural features and statements on extreme events. Otherwise, a quantitative analysis of such fields is unproductive because they are non-repetitive.

To undertake a quantitative analysis of turbulence, attention has thus to focus on statistical properties. As these properties are also the focus of turbulence modelling, or the outcome resulting from the application of models to particular flow problems, the extraction of the statistical properties is often one of the principal objectives of a simulation. Such data allow closure approximations to be tested and mechanisms to be identified. This, in turn, aids model improvements. Statistical data also provide a benchmark for model validation.

The statistical analysis of turbulence is almost invariably based on time- or ensemble-averaging, here used interchangeably:

$$< \phi(\mathbf{x}) >= \lim_{T \to \infty} \frac{1}{T} \int_0^T \phi(\mathbf{x}, t) dt \tag{5.1}$$

where ϕ is any property of the turbulent field, and T indicates the period over which the average is performed. If a flow is statistically homogeneous in a certain direction, a spatial averaging operator can be usefully defined in that direction. If z is that direction, the averaging operator is as follow:

$$< \phi(x, y, t) >= \lim_{L_z \to \infty} \frac{1}{L_z} \int_0^{L_z} \phi(\mathbf{x}, t) dz \tag{5.2}$$

where L_z indicates the spatial extent of the averaging of the z-direction. Operators (5.1) and (5.2) can be combined, and this is advantageous in simulations that contain a homogeneous direction as it helps reduce the time necessary to obtain fully-converged statistical properties. As a simulation returns the fields at discrete space and time locations, the averaging operators have to be written in a discrete form such as:

$$< \phi >= \frac{1}{N} \sum_{i=1}^{N} \phi_i(\mathbf{x}, t) \tag{5.3}$$

where N represents the number of samples recorded. The introduction of the averaging operator then allows any instantaneous flow property ϕ to be separated into two components, a mean value and an instantaneous fluctuation:

$$\phi =< \phi > +\phi' \tag{5.4}$$

where $< \cdot >$ indicates the averaging operator. Representation (5.4) is known as *Reynolds decomposition.*

In addition to the mean value of ϕ, it is interesting to quantify the properties of the fluctuations, in a statistical sense, around that mean value by considering the average of the different powers of ϕ', the *moments.* The first moment $< \phi' >$ is, by definition of the mean, equal to zero. The second moment, defined as $\sigma^2 =< \phi'\phi' >$, is known as the *variance*, although its square root is often used, representing the standard deviation from the mean value.

5.3 The RANS equations

The introduction of decomposition (5.4) into the governing equations of an incompressible flow in the absence of body forces (described by the Navier-Stokes equations (2.1)), combined with the application of an averaging operator to these equations lead to a new set of equations known as the Reynolds-Averaged Navier-Stokes equations (*RANS*):

$$\rho\frac{\partial < u_i >}{\partial t} + \rho\frac{\partial < u_i u_k >}{\partial x_k} = -\frac{\partial < p >}{\partial x_i} + \mu\frac{\partial^2 < u_i >}{\partial x_k^2} - \rho\frac{\partial < u_i' u_k' >}{\partial x_k} \qquad (5.5)$$

Equation (5.5) governs the mean motion and its last term, $\rho < u_i' u_k' >$, is the Reynolds-stress tensor and its components identify the primary statistical properties of the turbulence field. The components $i = k$ are the normal Reynolds stresses while, for $i \neq k$, the Reynolds shear stresses arise. Equation (5.5) can be rewritten in terms of the dimensionless variables (2.2) as:

$$\frac{\partial < u_i >}{\partial t} + \frac{\partial < u_i u_k >}{\partial x_k} = -\frac{\partial < p >}{\partial x_i} + \frac{1}{Re}\frac{\partial^2 < u_i >}{\partial x_k^2} - \frac{\partial < u_i' u_k' >}{\partial x_k} \qquad (5.6)$$

and this is in this form that the RANS equations will be used in what follows.

5.4 Turbulence transport equations

In the previous section, it is shown that the mean velocity $< u_i >$ is linked to or is affected by $< u_i' u_j' >$. This stress tensor is, in fact, the only link between the mean field and the turbulence properties. Hence, $< u_i' u_j' >$ and the processes governing its behaviour are of principal interest. To understand the mechanisms which govern $< u_i' u_j' >$, it is necessary to derive further equations which describe the evolution of this tensor. As will be seen, these equations contain higher-order moments, and like $< u_i' u_j' >$, they too can be extracted from simulations. The higher moments provide rich information on the constituents of the transport equations and the mechanisms driving the stresses themselves.

Equations of transport for the Reynolds stresses and the turbulence energy, defined as half the sum of the normal stresses ($k = 0.5 < u_k' u_k' >$), may be derived from the Navier-Stokes equations. First, the RANS equations (5.6) are subtracted from the Navier-Stokes equations (2.3). Equations for the turbulent velocity components are thus obtained:

$$\frac{\partial u_i'}{\partial t} + < u_k > \frac{\partial u_i'}{\partial x_k} = -\frac{\partial p'}{\partial x_i} + \frac{1}{Re}\frac{\partial^2 u_i'}{\partial x_k^2} - \frac{\partial < u_i' u_k' >}{\partial x_k} - u_k' \frac{\partial u_i'}{\partial x_k} - \frac{\partial u_i' u_k'}{\partial x_k} \tag{5.7}$$

After multiplication of (5.7) by u_j', and averaging, the result is:

$$\begin{aligned} < u_j' \frac{\partial u_i'}{\partial t} > + < u_j' u_k' \frac{\partial < u_i >}{\partial x_k} > + < u_j' < u_k > \frac{\partial u_i'}{\partial x_k} > + < u_j' u_k' \frac{\partial u_i'}{\partial x_k} > \\ = - < u_j' \frac{\partial p'}{\partial x_i} > + \frac{1}{Re} < u_j' \frac{\partial^2 u_i'}{\partial x_k^2} > + < u_j' \frac{\partial < u_i' u_k' >}{\partial x_k} > \end{aligned} \tag{5.8}$$

and with i and j reversed:

$$\begin{aligned} < u_i' \frac{\partial u_j'}{\partial t} > + < u_i' u_k' \frac{\partial < u_j >}{\partial x_k} > + < u_i' < u_k > \frac{\partial u_j'}{\partial x_k} > + < u_i' u_k' \frac{\partial u_j'}{\partial x_k} > \\ = - < u_i' \frac{\partial p'}{\partial x_j} > + \frac{1}{Re} < u_i' \frac{\partial^2 u_j'}{\partial x_k^2} > + < u_i' \frac{\partial < u_j' u_k' >}{\partial x_k} > \end{aligned} \tag{5.9}$$

The sum of (5.8) and (5.9) leads to the transport equation for the Reynolds stresses:

$$\frac{D < u_i' u_j' >}{Dt} = P_{ij} + T_{ij} + D_{ij} + \Pi_{ij} + \epsilon_{ij} \tag{5.10}$$

where

$$\frac{D < u_i' u_j' >}{Dt} = \frac{\partial < u_i' u_j' >}{\partial t} + < u_k > \frac{\partial < u_i' u_j' >}{\partial x_k} \tag{5.11}$$

represents the substantial derivative. The group of terms

$$P_{ij} = - < u_j' u_k' > \frac{\partial < u_i >}{\partial x_k} - < u_i' u_k' > \frac{\partial < u_j >}{\partial x_k} \tag{5.12}$$

is the production of the turbulent stress $< u_i' u_j' >$. It represents the influence of the mean flow straining on the turbulent stresses, thus linking mean flow and turbulent quantities. These terms are normally positive and will increase the stresses, but can also be negative in certain unusual strain fields. The dissipation rate is:

$$\epsilon_{ij} = -\frac{2}{Re} < \frac{\partial u_i'}{\partial x_k} \frac{\partial u_j'}{\partial x_k} > \tag{5.13}$$

and expresses the transfer of turbulence energy to heat. This term always diminishes the turbulent stresses. The term

$$T_{ij} = -\frac{\partial < u_i' u_j' u_k' >}{\partial x_k} \tag{5.14}$$

is the turbulence transport rate and expresses the spatial redistribution of any turbulent stress by the turbulence itself. Viscous diffusion is expressed by

$$D_{ij} = \frac{1}{Re} \frac{\partial^2 < u_i' u_j' >}{\partial x_k^2} \tag{5.15}$$

This term is usually very small, except in the viscous sublayer. Finally, the term

$$\begin{aligned} \Pi_{ij} &= - < u_i' \frac{\partial p'}{\partial x_j} > - < u_j' \frac{\partial p'}{\partial x_i} > \\ &= - \frac{\partial < p' u_i' >}{\partial x_j} - \frac{\partial < p' u_j' >}{\partial x_i} + < p' \frac{\partial u_j'}{\partial x_i} > + < p' \frac{\partial u_i'}{\partial x_j} > \end{aligned} \tag{5.16}$$

is the velocity pressure-gradient interaction term. It can be decomposed, as done above, into two constituents: the pressure diffusion term and the pressure-strain

term. The latter tends to redistribute the turbulence energy among the normal stresses, steering turbulence toward isotropy.

The transport equation for the turbulence energy is obtained by contracting Equation (5.10):

$$\frac{Dk}{Dt} = P_k + T_k + D_k + \Pi_k + \epsilon_k \tag{5.17}$$

where

$$\frac{Dk}{Dt} = \frac{\partial k}{\partial t} + < u_k > \frac{\partial k}{\partial x_k} \tag{5.18}$$

$$P_k = - < u_i' u_j' > \frac{\partial < u_i >}{\partial x_j} \tag{5.19}$$

$$T_k = -0.5 \frac{\partial < u_i' u_i' u_j' >}{\partial x_j} \tag{5.20}$$

$$D_k = \frac{1}{Re} \frac{\partial^2 k}{\partial {x_j}^2} \tag{5.21}$$

$$\Pi_k = - \frac{\partial < p' u_j' >}{\partial x_j} \tag{5.22}$$

$$\epsilon_k = - \frac{1}{Re} < \frac{\partial u_i'}{\partial x_j} \frac{\partial u_i'}{\partial x_j} > \tag{5.23}$$

Note that the pressure-strain term vanishes as a consequence of the mass-conservation constraint (for incompressible flow, $\partial u_i'/\partial x_i = 0$). This clarifies the earlier interpretation that this term describes the redistribution of turbulence energy k among the normal stresses and thus does not alter the level of turbulence energy.

5.5 Turbulence anisotropy and related post-processing

The anisotropy represents the deviatoric part of the Reynolds stresses and is obtained by substraction from the Reynolds stresses the isotropic contribution ($-2/3\delta_{ij} <$

$u'_k u'_k >$), i.e.:

$$a_{ij} =< u'_i u'_j > -\frac{2}{3}\delta_{ij} < u'_k u'_k > \tag{5.24}$$

where δ_{ij} is the Kronecker symbol*. The anisotropy tensor (5.24) is usually considered in the dimensionless form:

$$b_{ij} = \frac{< u'_i u'_j > -\frac{2}{3}\delta_{ij} < u'_k u'_k >}{2 < u'_k u'_k >} \tag{5.25}$$

The tensor b_{ij} is thus traceless, i.e. its first invariant is equal to zero, and this allows the study of its properties by considering only two parameters: its second invariant, defined as $II = -b_{ij}b_{ij}/2$, and its third invariant, $III = b_{ij}b_{jk}b_{kj}/3$. A consequence of this tensor being traceless is that the sum of its eigenvalues λ_1, λ_2 and λ_3 (the eigenvalues also represent the stresses in principal axis) is also zero, hence $\lambda_3 = -\lambda_1 - \lambda_2$, and the eigenvalues of b_{ij} can also be used to characterise b_{ij}. This constraints all eigenvalues to be no smaller than $-1/3$ (this corresponds to the vanishing of the related component) and none can be larger than $2/3$, in which case, the two other components vanish. Hence, any physically realizable turbulent state is constrained to lie in a zone delimited by the above extrema or the corresponding invariant values. Table 5.1 shows the limiting values that can be attained by the invariants and the eigenvalues, while Figure 5.1 shows graphically these limits. This plot is known as the *anisotropy invariant map* or the *Lumley triangle* (Lumley and Newman [134], Lumley [133]). This triangle describes the various physically realistic states that can be attained by a turbulent flow. For any turbulent flow, each point has to lie inside or on these boundaries, for otherwise it will be unphysical (non-realizable). The Lumley triangle is often used in RANS modelling to verify that a turbulence model does not violate realizability constraints.

A parameter also often employed is the *flatness*:

$$A = 1 + 9(II + 3III) \tag{5.26}$$

*$\delta_{ij} = 1$ if $i = j$ and $\delta_{ij} = 0$ if $i \neq j$

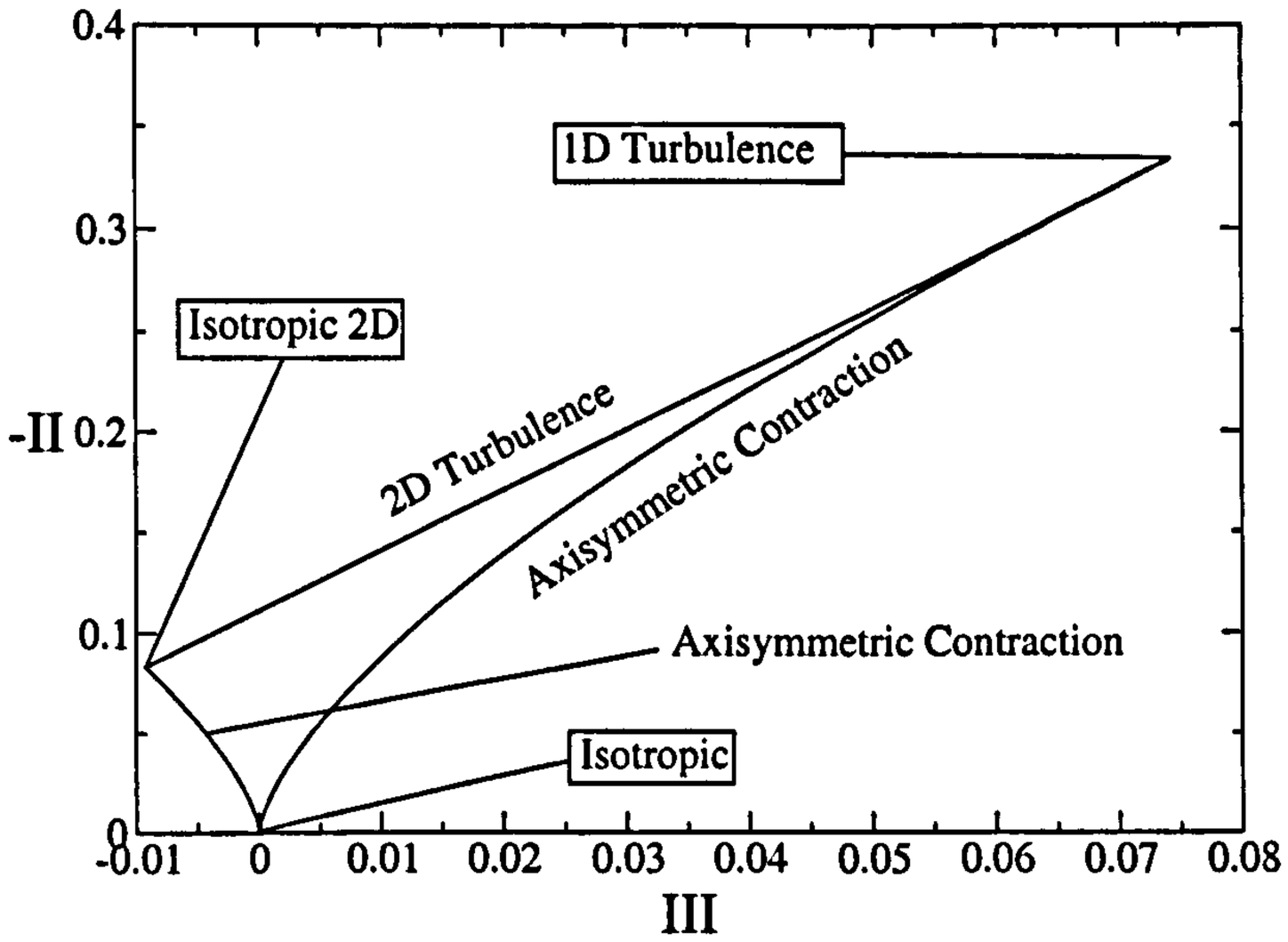

Figure 5.1: Anisotropy invariant map

This parameter characterises, as best as a single scalar can do, the range of turbulence states spanning from the state of isotropy to two-components turbulence corresponding, to $A = 1$ and $A = 0$, respectively. This fact is often taken advantage of in RANS modelling to secure the limiting behaviour at walls and fluid interfaces (Hanjalić and Jakirlić [79], Craft and Launder [42]).

Eigenvalues	Invariant values	State of turbulence
$\lambda_1 = \lambda_2 = \lambda_3 = 0$	$-II = 0$	Isotropic turbulence
	$III = 0$	
$\lambda_1 = \lambda_2 = 1/6$	$-II = 1/12$	Isotropic two-dimensional
	$III = -1/108$	turbulence
$\lambda_1 = 2/3$	$-II = 1/3$	One-dimensional turbulence
$\lambda_2 = \lambda_3 = -1/3$	$III = 2/27$	
$-1/3 \leq \lambda_1 = \lambda_2 \leq 0$	$III = 2(-II/3)^{3/2}$	Axisymmetric contraction (one large eigenvalue) straining the flow in one direction and contracting it in the two others
$0 \leq \lambda_1 = \lambda_2 \leq 1/6$	$III = -2(-II/3)^{3/2}$	Axisymmetric expansion (one small eigenvalue) caused by straining the flow equally in two orthogonal directions and contracting it in the third
$\lambda_1 + \lambda_2 = 1/3$	$1/9 + II + 3III = 0$	Two-dimensional turbulence

Table 5.1: Limits to the state of turbulence.

5.6 Two-point correlations

Two-point correlations are coefficients which identify the degree of correlation between the fluctuations at two different spatial or temporal locations. In what follows, ξ will represents the time or any of the three spatial coordinates x, y, z. Thus, for $\phi(\xi)$, the correlation coefficient relating to a separation $\Delta\xi$ is:

$$R(\xi, \Delta\xi) = \frac{<\phi'(\xi)\phi'(\xi + \Delta\xi)>}{<(\phi'(\xi))^2>} \tag{5.27}$$

If $\Delta\xi = 0$, there is no separation in the ξ-direction, and, evidently, $R(\Delta\xi = 0) = 1$. If $\Delta\xi$ becomes sufficiently large then $R(\Delta\xi)$ drops to zero and the flow variables are said to be uncorrelated. Note that if the flow is statistically homogeneous in the ξ-direction, then R is independent of ξ. Two-point correlations can be used as a mean of testing whether a computational box is large enough to contain all the turbulent scales (even the largest) in a statistically homogeneous direction. However, Jiménez and Moin [97] have shown, for a channel flow, that adequate first and second-order statistics could be obtained with a box size significantly lower than a decorrelated flow would require. This concept is known as the *minimal flow unit*. Nevertheless, the application of (5.27) is useful in guiding the choice of the computational box.

5.7 Energy and velocity-spectra

In a turbulent flow, where the random signal $u(\xi)$ is periodic (ξ can be the time-variable or any of the spatial coordinates x, y, z), the two-point velocity correlation (5.27) and its spectrum form the Fourier transform pair:

$$R_{jk}(\xi) = \int_{-\infty}^{+\infty} E_{jk}(\omega) e^{-i\omega\xi} d\omega \tag{5.28}$$

and

$$E_{jk}(\omega) = \frac{1}{2\pi} \int_{-\infty}^{+\infty} R_{jk}(\xi) e^{i\omega\xi} d\xi \tag{5.29}$$

where R_{jk} is the two-point correlation for the jk velocity pair and E_{jk} is the associate spectrum. ω represents the frequency, if ξ is the time-variable, and the wave-number,

if ξ is any of the spatial coordinates.

Velocity-spectra are thus defined for each pair of velocities $u_j u_k$ and provide informations on the spectral interaction between these two variables and only them. In most studies of turbulence, attention is restricted to the turbulence energy spectrum, defined as the half-sum of the velocity-spectra E_{11}, E_{22} and E_{33}. Velocity and energy spectra provide information on the mechanisms of energy transfer between different wave-numbers and frequencies. In the context of numerical simulation, the spectrum of k also provides a statement on the quality of the numerical resolution.

5.8 Identification of turbulent structures

The structure of turbulent flows is of much interest, as it provides insight into the fundamental formation and interaction of the vortices which constitute the turbulent motion. The presence of *quasi-periodic repeating patterns of coherent motions in the flow* (Robinson [187]) has been observed for many years, and it is sought that these coherent motions (also referred to as *coherent structures*) are the cause for the maintenance of the turbulence. Most of the knowledge on these structures comes from the study of low-Reynolds-number flows, but little of this knowledge has so far been embedded into closure models. The main reasons for the study of turbulence structures are the need and the wish to understand the dynamical phenomena associated with the statistical properties.

Coherent structures are usually identified from visualising iso-surfaces of certain instantaneous flow properties. The choice of the threshold at which these iso-surfaces are drawn is a matter of trial and error and is dictated by the ability of the observer to *see* these structures within the particular flow property field examined. Coherent structures are associated with vortex cores. An intuitive approach is to consider regions where pressure minima occur. Another is based on associating a vortex core with a region of high rotation rate and thus with regions of high enstrophy, defined as the modulus of the vorticity ($\omega = \nabla \times \mathbf{u}$), or regions of high ω_x, ω_y or ω_z. As noted by Jeong and Hussain [94], an inherent problem of using the vorticity is that it assumes high values in sheared regions even in the absence of vortices. Thus, more

rigorous criteria are needed to identify vortical structures.

One criterion, proposed by Chong et al [34], is based on the assumption that a vortex core is a region of the flow where the eigenvalues of the velocity-gradient tensor ($A_{ij} = \partial u_i/\partial x_j$) are complex. This implies that the local streamlines are closed. Mathematically, this can be expressed by considering the characteristic equation of A_{ij}:

$$\lambda^3 - P\lambda^2 + Q\lambda - R = 0 \tag{5.30}$$

where $P = \partial u_i/\partial x_i$ (= 0 for incompressible flows), $Q = -1/2\,(\partial u_i/\partial x_j)\,(\partial u_j/\partial x_i)$ and $R = det(A_{ij})$. For an incompressible flow, all the eigenvalues are complex if the discriminant of (5.30) is positive:

$$\Delta = \frac{Q^3}{27} + \frac{R^2}{4} > 0 \tag{5.31}$$

Coherent structures are thus regions of the flow where Δ is positive.

Another proposal, made by Hunt et al [88], defines a vortex core as a region where the second invariant Q of A_{ij} is positive and, at the same time, where the local pressure has a lower value than the ambient.

More recently, Jeong and Hussain [94] proposed a criterion based on the eigenvalues of $S_{ik}S_{kj} + \Omega_{ik}\Omega_{kj}$. They consider that this tensor identifies local pressure minima associated with vortical motions. They define a vortex core as a region where two of the eigenvalues of $S_{ik}S_{kj} + \Omega_{ik}\Omega_{kj}$ are negative. Assuming these eigenvalues are $\lambda_1 \geq \lambda_2 \geq \lambda_3$, a vortex core is thus a region of the flow where $\lambda_2 < 0$.

Note that, contrary to the vorticity, the Δ and λ_2 criteria vanish at the wall where shear is high, but vortices are weak.

Other but less popular approaches include the kinematic vorticity number (Melander and Hussain [147]) or the use of instantaneous streamlines (Lugt [132]). Detailed lists of criteria, with applications, can be found in Kasagi et al [104], Lesieur et al [123] and Hanjalić and Kenjereš [80]. In the present work, the only criteria used to identify the coherent structures are: the pressure, the Δ-criterion, the second-invariant criterion and the λ_2-criterion.

Chapter 6

Channel flow computations

6.1 Overview

Fully developed turbulent channel flow is the first and most studied generic configuration of engineering interest in LES research (Deardorff [49], Moin and Kim [159], Piomelli [175] among others). The simplicity of the geometry shown in Figure 6.1, the statistical homogeneity of the flow in the streamwise and spanwise directions and the option of adopting periodic conditions in these two directions make this flow an ideal test case for investigating the near-wall behaviour of LES, the performance of subgrid-scale models and the adequacy of near-wall approximations at high Reynolds numbers. Furthermore, it allows the various post-processing tools described in the previous chapter to be examined. These tools will be applied to analyse more complex flows.

In this chapter, channel flow at three Reynolds numbers Re_τ, based on the wall shear velocity u_τ and the channel half width h, are considered, namely 180, 590 and 1050. A summary of the test cases is given in Section 6.2. In Section 6.3, the performance of the subgrid-scale models described in Section 3.2 will be investigated for the case $Re_\tau = 590$. Section 6.4 deals with the adequacy of the near-wall approximations described in Section 3.3 for the cases $Re_\tau = 590$ and $Re_\tau = 1050$. Section 6.5 is concerned with the study of numerical and modelling errors based on a procedure developed by Vreman et al [228] for mixing layers, and adapted, in the

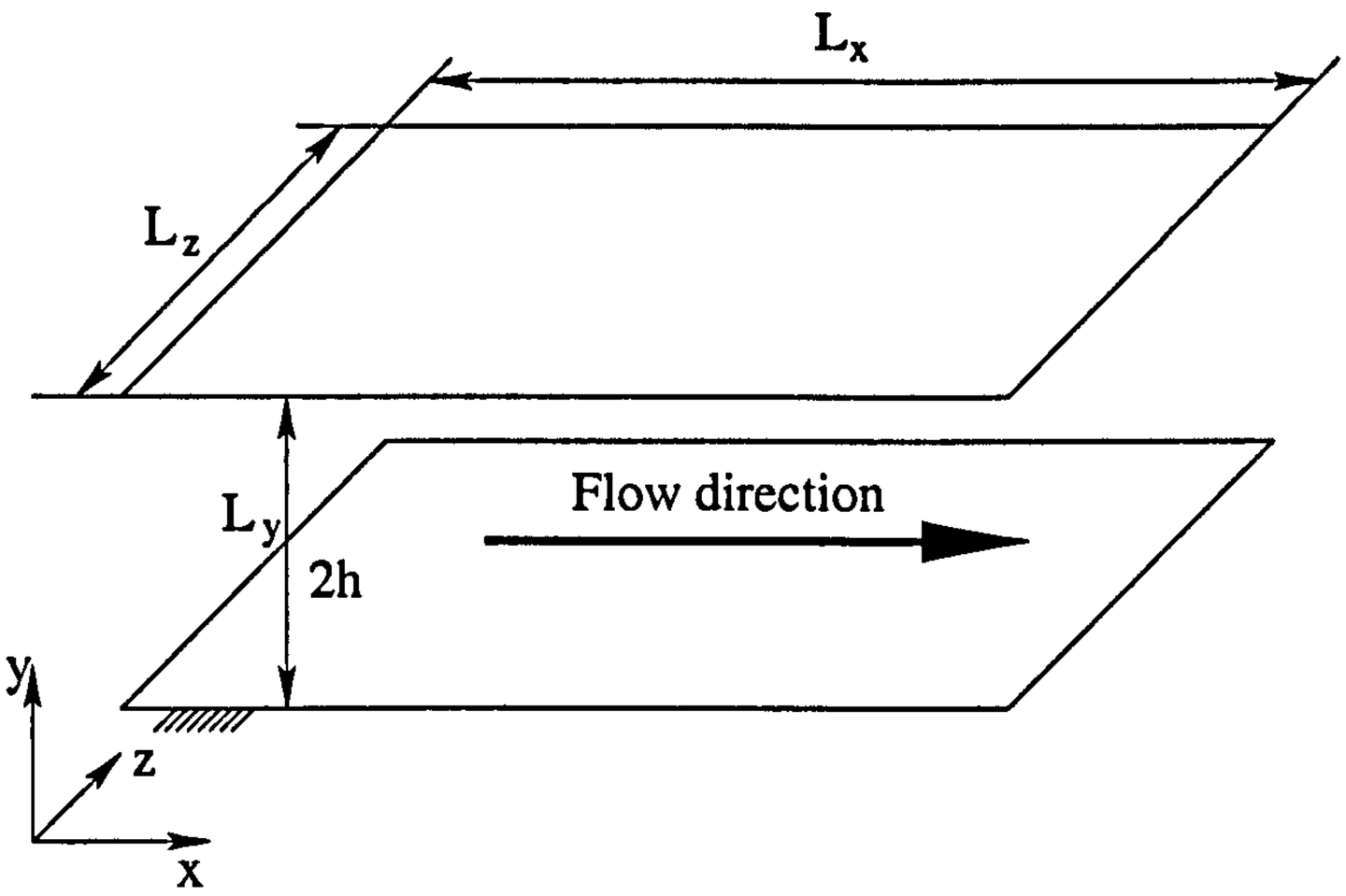

Figure 6.1: Geometry of the channel flow, with L_x and L_z being periodic segments.

present work, to the case of the turbulent periodic channel flow. Mathematical tools, used to study turbulence and presented in Chapter 5, are tested in Section 6.6 in order to validate the correctness of their implementation and to construct the basis that will enable a better understanding to be gained of the phenomena studied later in Chapters 7 and 8. Finally, Section 6.7 summarises the observations made during the studies presented in this chapter, and draws lessons to be applied to the more complex flows studied in the chapters to follow.

6.2 Summary of the test cases

Three different periodic channel flows at three Reynolds numbers, Re_τ, have been considered. The first two cases correspond, respectively to $Re_\tau = 180$ and $Re_\tau = 590$, for which an extensive DNS database* is available (Moser et al [161]). The third case, at $Re_\tau = 1050$, corresponds to a high-Reynolds number LES performed by Piomelli [175]. For each case, a range of box sizes and grids have been used, and these are summarised in Table 6.1.

*http://www.tam.uiuc.edu/faculty/moser/

Ref.	Re_τ	Re_b	Box dimensions $L_x \times L_y \times L_z$	Discretisation $N_x \times N_y \times N_z$	Δx^+	Δy^+	Δz^+
CM1	180	2800	$2\pi h \times 2h \times \pi h$	$96 \times 64 \times 64$	12	$1.2 - 19.3$	8.8
CM2	590	10935	$2\pi h \times 2h \times \pi h$	$64 \times 32 \times 32$	58	37	58
CM3	590	10935	$2\pi h \times 2h \times \pi h$	$72 \times 48 \times 32$	51.5	$10 - 37.1$	58
CM4	590	10935	$2\pi h \times 2h \times \pi h$	$96 \times 64 \times 64$	38.6	$2 - 42.2$	29
CM5	590	10935	$2\pi h \times 2h \times \frac{2\pi h}{3}$	$96 \times 64 \times 64$	38.6	$2 - 42.2$	19.3
CM6	590	10935	$2\pi h \times 2h \times \pi h$	$96 \times 64 \times 96$	38.6	$2 - 42.2$	19.3
CM7	1050	21351	$\frac{5\pi h}{2} \times 2h \times \frac{\pi h}{2}$	$50 \times 20 \times 10$	165	105	165

Table 6.1: Summary of the channel flow cases.

6.3 Influence of the subgrid-scale model

Simulations undertaken in this section aim to investigate the performance of the subgrid-scale models (and some of their variants) described in Section 3.2. The task of a subgrid-scale model is to compensate for the loss of the turbulence scales associated with grid coarseness. If it were possible to avoid numerical errors, the performance of subgrid-scale models could be examined unambiguously by recording the associated LES to represent the appropriately filtered DNS solution. However, numerical errors cannot be avoided, and the solution error is therefore a non-separable amalgam of subgrid-scale model and numerical and resolution errors. Hence, in the present investigation, the central issue is an examination of the ability of subgrid-scale models, relative to others, to provide a solution which is close to the benchmark. All simulations were performed for the case $Re_\tau = 590$ for which DNS data are available (Moser et al [161]). Three different meshes, designated CM3, CM4 and CM6, and described in Table 6.1, were used. Cases CM4 and CM6 are wall-resolved in the sense that $\Delta y^+(1) \leq 2$. Case CM3, with $\Delta y^+(1) \approx 10$, is not wall-resolved and was chosen to assess whether some models were able to compensate better than others for the loss of near-wall resolution. In all cases, a no-slip boundary condition was used. The ratio between the grid-filter width $\overline{\Delta}$ and the cell size was chosen equal to 1. Statistics were collected over a period of 12 flow-through times, for

all non-dynamic subgrid-scale models, and 24 flow-through times for the dynamic subgrid-scale models, sufficient to ensure fully converged statistical properties. In total, 11 modelling practices, including variations of models, were examined, these are summarised in Table 6.2. Their performance was judged by reference to mean velocity, friction Reynolds number and Reynolds-stress components, all relative to DNS solutions.

For the series of computations performed on the wall-resolving mesh CM4, none of the models returns the universal velocity distribution especially well, as shown in Figure 6.2. While the log slope is correctly reproduced in most cases, the errors in the level of the log-law region are not insignificant and appear to be associated with the representation of the buffer region and the predicted level of the wall shear stress for a prescribed mean velocity, as shown in Table 6.3. Figure 6.3 demonstrates that different models return substantially different subgrid-scale viscosity distributions. In the core region of the flow, the maximum viscosity levels vary within the range of one order of magnitude, between 0.1 and 1 times the fluid viscosity, with the WALE model returning the lowest value and the localised dynamic model (LDSM) the highest. As the subgrid-scale transport is only a small portion of the resolved transport in the log-law region, this difference is not influential. However, the viscosity level in the upper part of the buffer layer, as well as the asymptotic behaviour of the subgrid-scale viscosity, can be more important because the resolved contribution declines rapidly as the wall is approached. The theoretical asymptotic behaviour of the subgrid-scale viscosity is cubic in y^+ and is represented by the straight line in Figure 6.3. Only the WALE model and the dynamic variants return the asymptotic behaviour well. The substantial variations in the subgrid-scale viscosity can be identified to cause corresponding variations in the mean velocity. In the region $10 < y^+ < 20$, a high subgrid-scale viscosity tends to depress the velocity in the buffer and log regions below the DNS variation, while the reverse occurs when the viscosity in this region is low.

Model Designation	Model Description
SM	Smagorinsky Model ($Cs = 0.1$)
SM + WD1	Smagorinsky Model ($Cs = 0.1$) + Wall-Damping Function 1 ($A^+ = 5$)
SM + WD2	Smagorinsky Model ($Cs = 0.1$) + Wall-Damping Function 2 ($A^+ = 25$)
MSM1	Mixed-Scale Model (Sagaut [192]) ($C_M = 0.01$ - $\alpha = 0.5$)
MSM2	Mixed-Scale Model (Sagaut [192]) ($C_M = 0.1$ - $\alpha = 0.5$)
GDSMT	Dynamic eddy-viscosity model (Germano et al [65]), filtering using the trapeze rule $\widehat{\Delta_x}/\Delta_x = \sqrt{6}$
DSMT	Dynamic eddy-viscosity model (Germano et al [65]-Lilly [129]), filtering using the trapeze rule $\widehat{\Delta_x}/\Delta_x = \sqrt{6}$
DSMS	Dynamic eddy-viscosity model (Germano et al [65]-Lilly [129]), filtering using the Simpson rule $\widehat{\Delta_x}/\Delta_x = 2$
DSMTN	Dynamic eddy-viscosity model (Germano et al [65]-Lilly [129]), filtering using the trapeze rule $\widehat{\Delta_x}/\Delta_x = \sqrt{6}$ no planar averaging
NSGS	No subgrid-scale model
WALE	WALE Model ($Cw = 0.1$) (Nicoud and Ducros [167])
LDSM	Localised Dynamic eddy-viscosity model (Piomelli and Liu [178])

Table 6.2: Subgrid-scale models used in channel flow computations.

SGS Model	Re_τ	Error	u_c/U_b	Error
DNS	584	-	1.1418	-
SM	617	+5.6 %	1.1533	+1.00 %
MSM1	565	-3.3 %	1.1461	+0.04 %
MSM2	605	+3.6 %	1.1411	-0.06 %
SM + WD1	595	+1.8 %	1.1444	+0.23 %
SM + WD2	538	-7.8 %	1.1319	-0.86 %
GDSMT	520	-10.8 %	1.1216	-1.77 %
DSMT	523	-10.3 %	1.1239	-1.57 %
DSMTN	537	-8.1 %	1.1230	-1.6 %
DSMS	529	-9.3 %	1.1298	-1.05 %
WALE	542	-7.1 %	1.144	+0.2 %
LDSM	520	-10.8 %	1.1221	-1.73 %
NSGS	541	-7.4 %	1.1428	+0.09 %

Table 6.3: Predictions of wall shear stress and centreline velocity for case CM4.

Figures 6.4 to 6.7 show, respectively, profiles of r.m.s. velocity fluctuations in the streamwise, wall-normal and spanwise directions and of the shear stress. Away from the wall, the streamwise intensity, shown in Figure 6.4, is correctly returned or slightly underestimated for all cases, except MSM2 for which it is overestimated. Near the wall, all models overestimate the peak in fluctuating velocity in the streamwise direction. On the other hand, Figures 6.5 and 6.6 show that the wall-normal and spanwise intensity are too low, indicating that the energy repartition between the three directions is not correctly resolved, thus suggesting that mesh resolution in the spanwise extent and possibly also in the streamwise and wall-normal directions contributes to the differences between all LES results and the DNS reference data. This makes it difficult to judge the subgrid-scale model performance. Figure 6.7 shows the resolved shear stress to be well predicted for all cases. As the wall is approached, differences appear between the predictions given by the different models, indicating the part a model is playing in representing the subgrid scales.

Figure 6.8 shows the distributions of the subgrid-scale viscosity, highlighting

the variation in magnitude and shape that the models considered lead to. Overall, the best results in this set of tests were obtained using the WALE, SM and MSM1 models, although the last two models do not present the proper near-wall asymptotic behaviour for the subgrid-scale viscosity. It is furthermore noteworthy that those models returning the lowest subgrid-scale viscosity yield results closest to the DNS reference solution. This might be taken to indicate that the models *double-count* the effects of subgrid-scale motion, with numerical resolution errors providing another mechanism. However, the fact that using no subgrid-scale model does not yield a satisfactory solution indicates that a subgrid-scale model representing the scales removed by the application of the LES filter, is necessary.

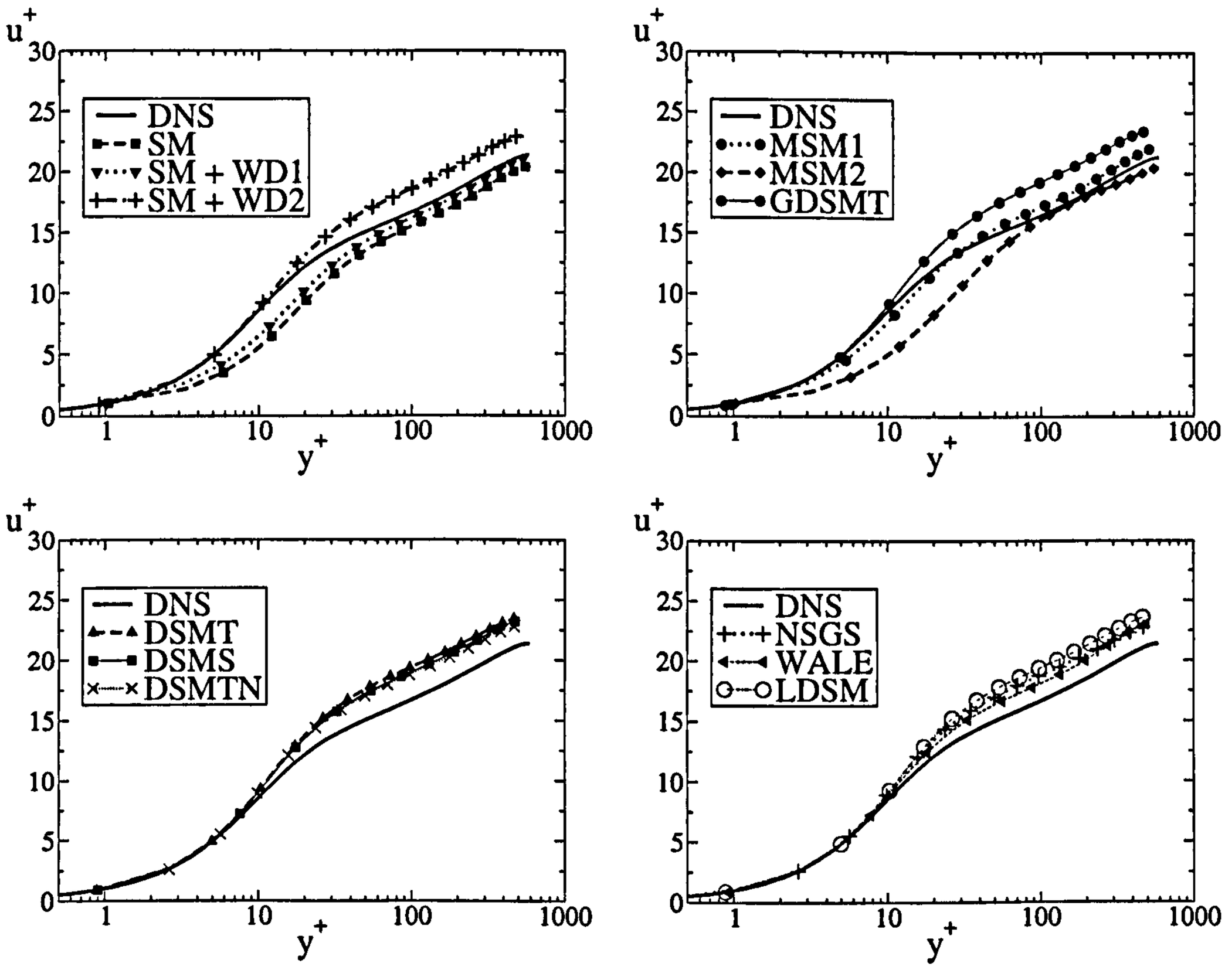

Figure 6.2: Streamwise velocity for channel flow for case CM4.

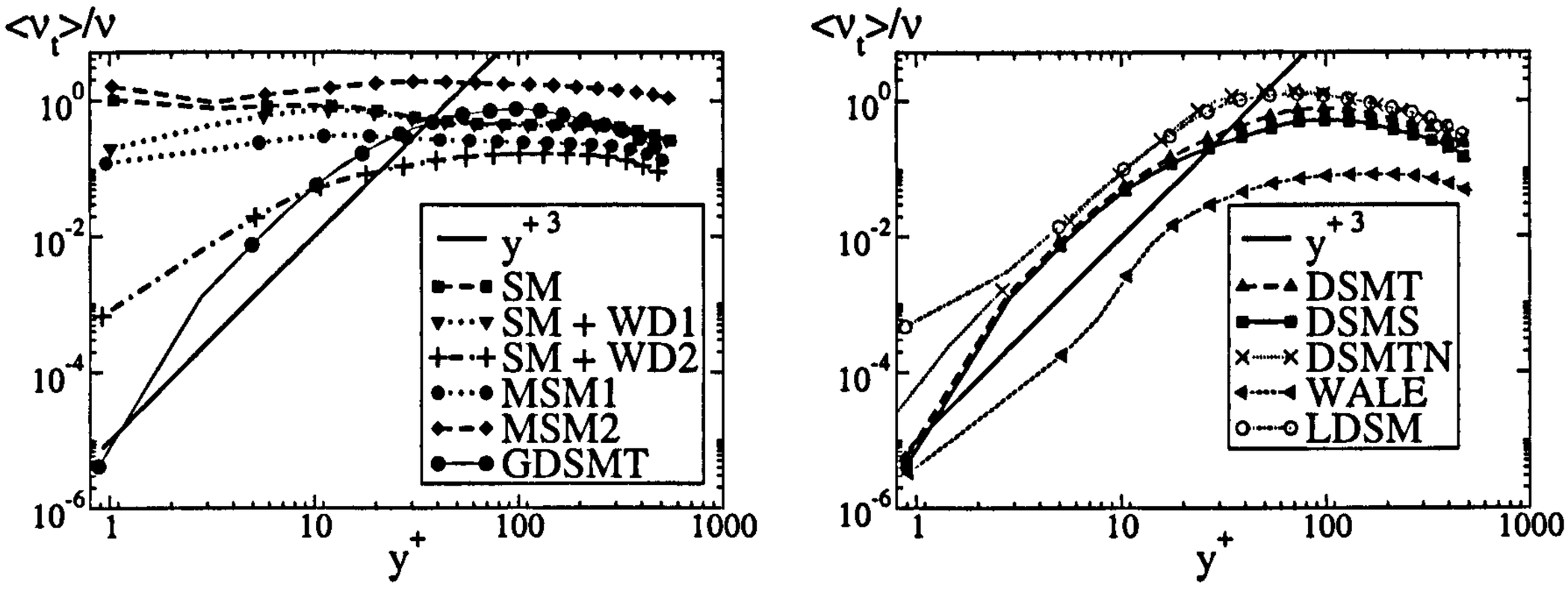

Figure 6.3: Distribution of subgrid-scale viscosity $< \nu_t > /\nu$ in wall units for case CM4.

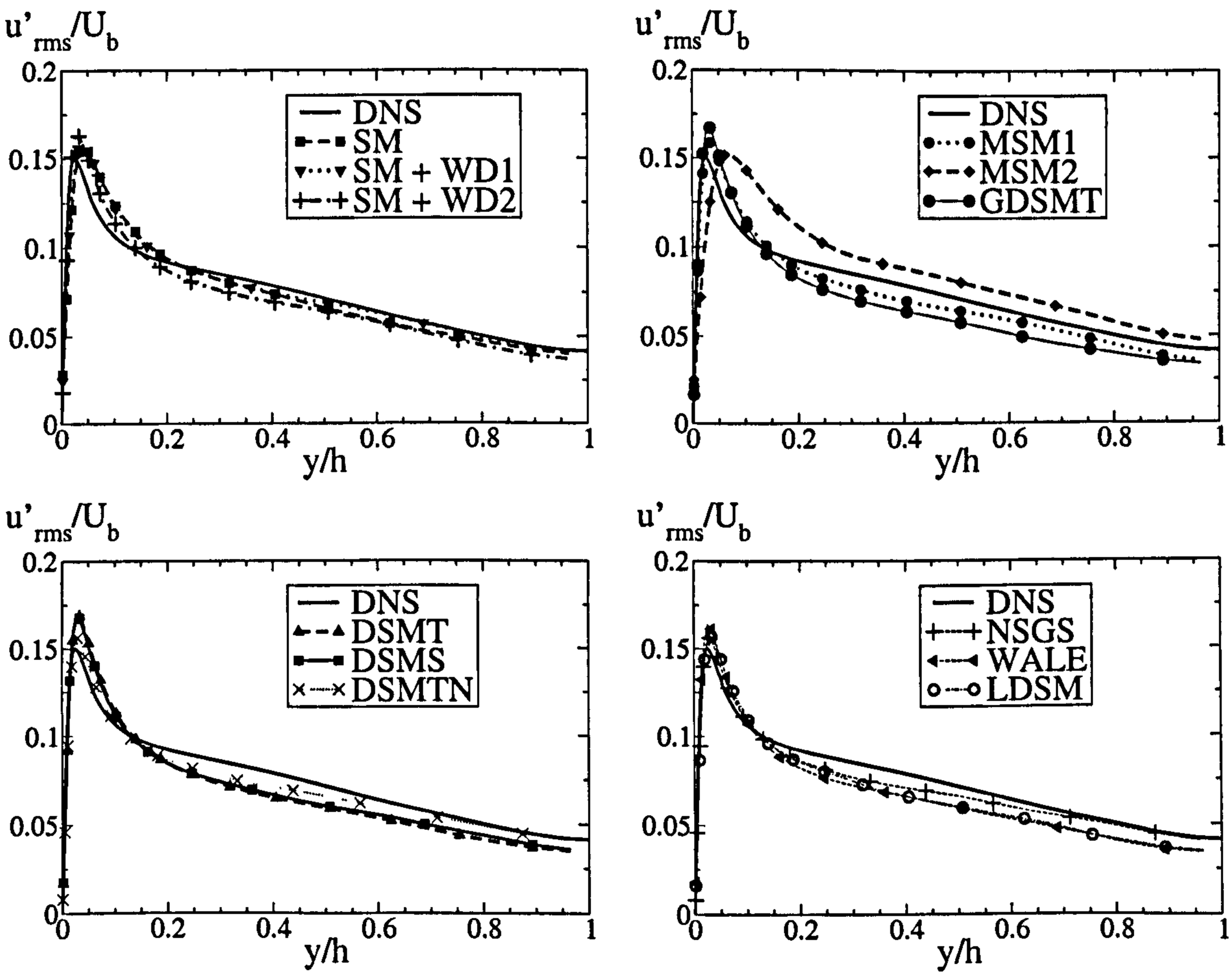

Figure 6.4: Distribution of r.m.s. streamwise velocity for case CM4.

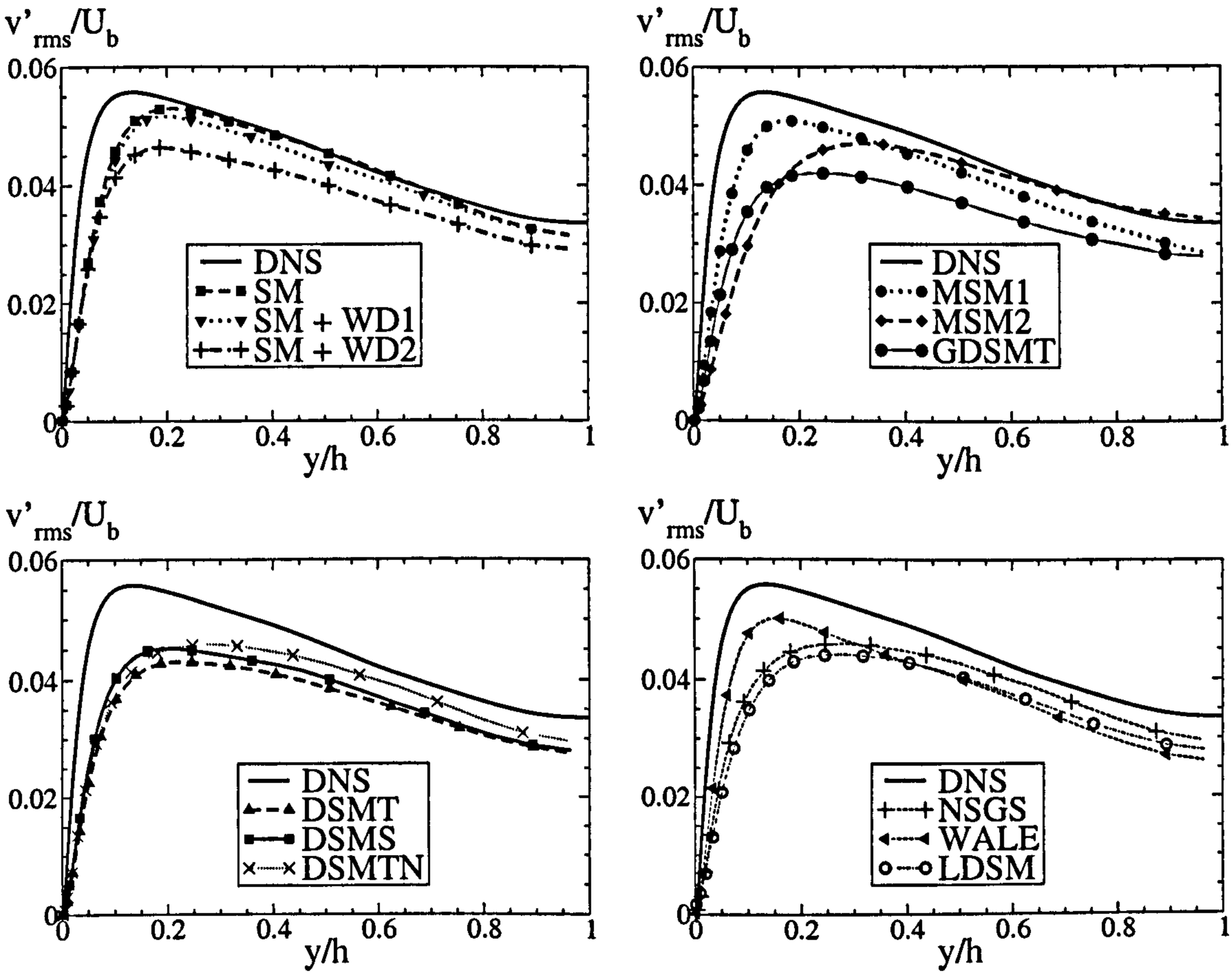

Figure 6.5: Distribution of r.m.s. wall-normal velocity for case CM4.

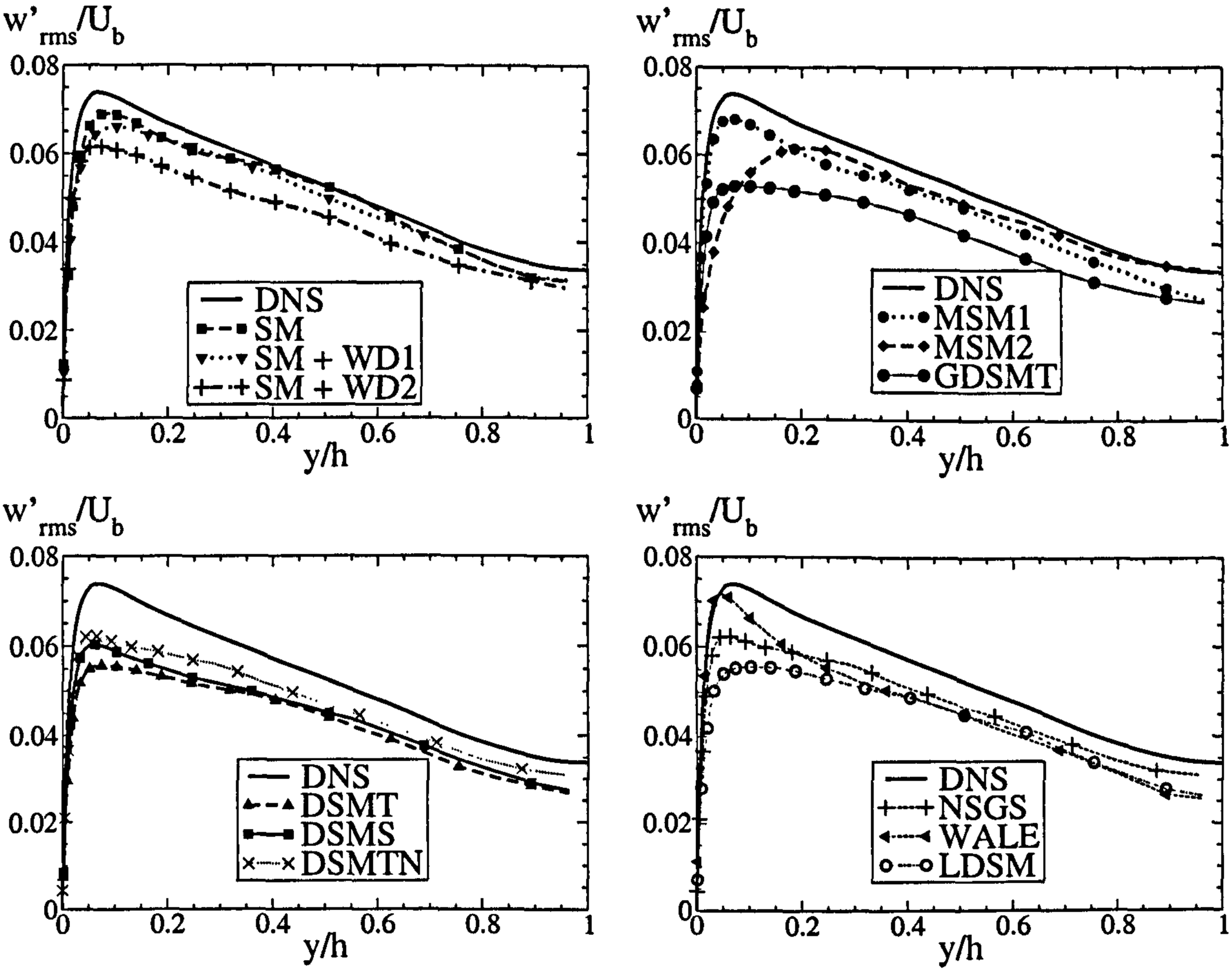

Figure 6.6: Distribution of r.m.s. spanwise velocity for case CM4.

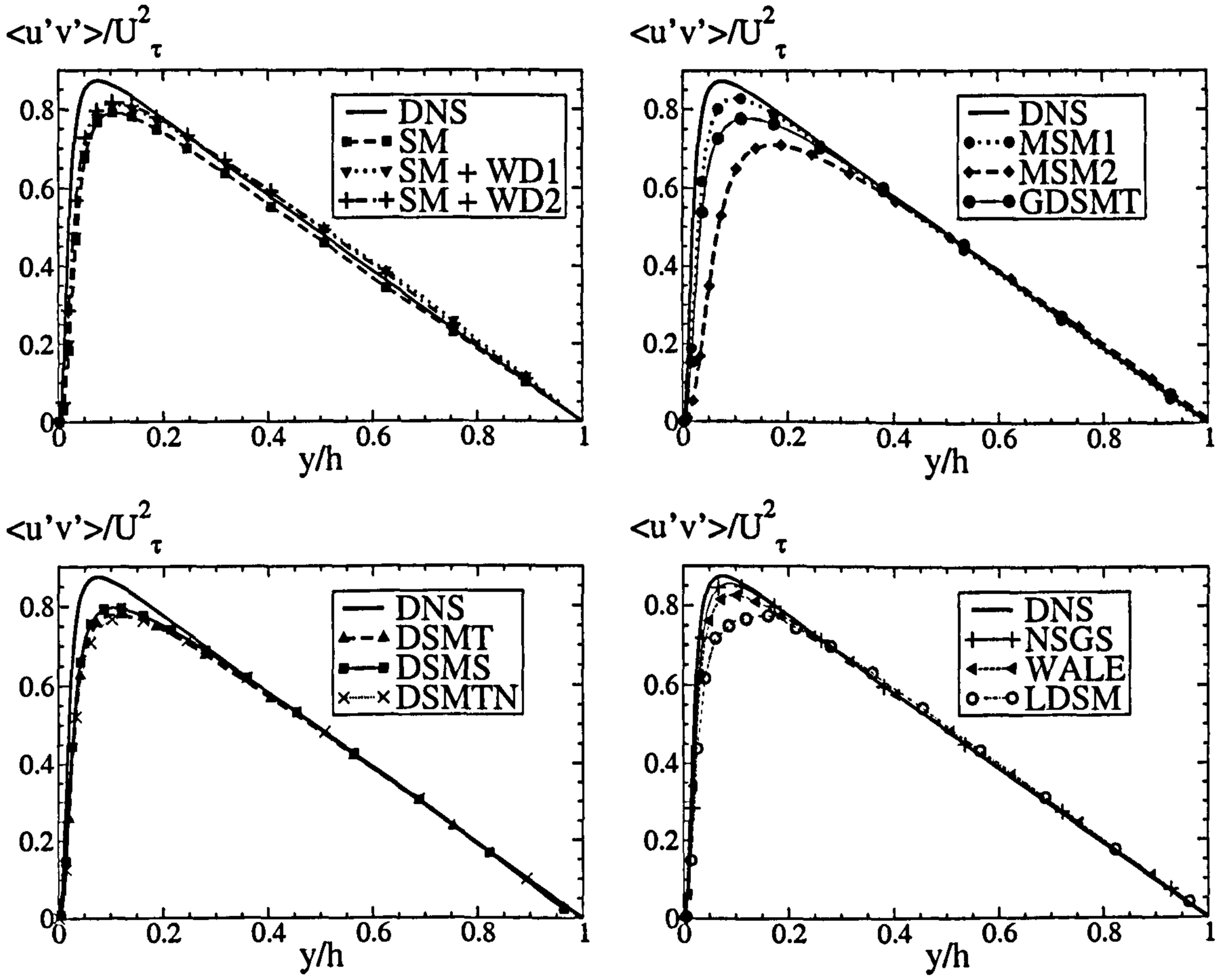

Figure 6.7: Distribution of shear stress for case CM4.

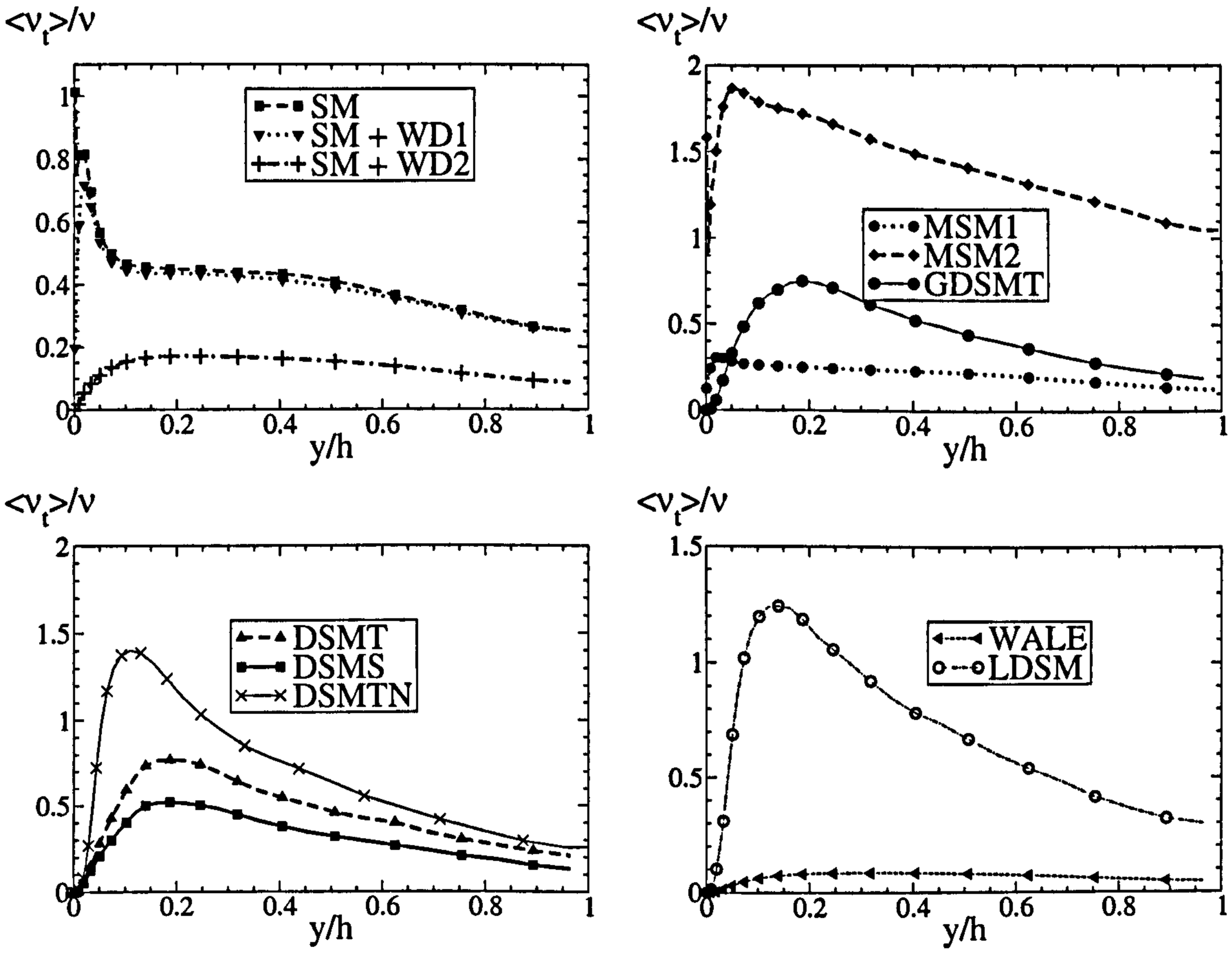

Figure 6.8: Distribution of subgrid-scale viscosity $< \nu_t > /\nu$ for case CM4.

SGS Model	Re_τ	Error	u_c/U_b	Error
DNS	584	n.a.	1.1418	n.a.
GDSMT	463	-20.5 %	1.1165	-2.22 %
DSMT	467	-19.8 %	1.1231	-1.64 %
DSMTN	469	-19.5 %	1.1232	-1.63 %
WALE	474	-18.6 %	1.1257	-1.41 %
NSGS	481	-17.5 %	1.1234	-1.61 %

Table 6.4: Predictions of wall-shear stress and centreline velocity for case CM3.

A second set of numerical experiments was undertaken on a coarser mesh than CM4, namely CM3 which contains $72 \times 48 \times 32$ cells, with $\Delta y^+(1) = 10$. Simulations were performed with 5 of the models considered previously, with the aim of investigating the ability of these models to respond to the lack of near-wall resolution in the absence of near-wall modelling.

Table 6.4 shows that the wall shear stress and centreline velocity are strongly underestimated. In fact, it appears that the best prediction is obtained when no subgrid-scale model is used. These results are not surprising as the grid is of poor quality for a wall-resolving LES, which requires $\Delta y^+ \leq 2$. Figure 6.9 shows that, with all subgrid-scale models, the log-law is misrepresented, primarily because of the underestimation of the friction velocity. The streamwise turbulence intensity, shown in Figure 6.10, is overestimated, with the near-wall peak being located further away from the wall than expected. Conversely, the wall-normal intensity is consistently underestimated, while depending upon the model the spanwise intensity is too low (DSMT, GDSMT, DSMTN) or too high (WALE, NSGS) in the near-wall region. For all models, the intensity is too low in the channel-centre region. The effect of the under-resolution appears also in Figure 6.11, which shows the resolved shear stress. Indeed, in the near-wall region, the profiles obtained from the LES significantly depart from the DNS solution. Thus, use of the coarse near-wall grid CM3 leads generally to poor results. Poor resolution manifests itself in excessive streamwise stress and too low wall-normal and spanwise stresses.

Figure 6.12 show profiles of subgrid-scale viscosity for the four models tested

with grid CM3, both in linear and logarithmic axis. The first observation is the increase in magnitude of the subgrid-scale viscosity when compared with the levels produced on grid CM4 and shown in Figure 6.8. The second observation concerns the decay of the subgrid-scale viscosity as the wall is approached. The rate of decay is close to y^{+3}, as observed in the course of the simulations made on CM4, indicating that the models are responding as they should do to the presence of the wall.

To summarise, none of the models was able to deliver accurate or close to accurate predictions of the averaged quantities using the coarse mesh CM3 and no-slip boundary condition, although they responded to the lack of resolution by an increase in the subgrid-scale viscosity, as they should do. As in the set of computations performed on CM4, a test was made without any subgrid-scale model, leading to results very similar, this time, to those obtained with a subgrid-scale models. This points again at the complexity of the relationship between the models and the numerics, which will be further investigated in Section 6.5. The issue of the representation of the wall by mean other than the no-slip condition is addressed in Section 6.4.

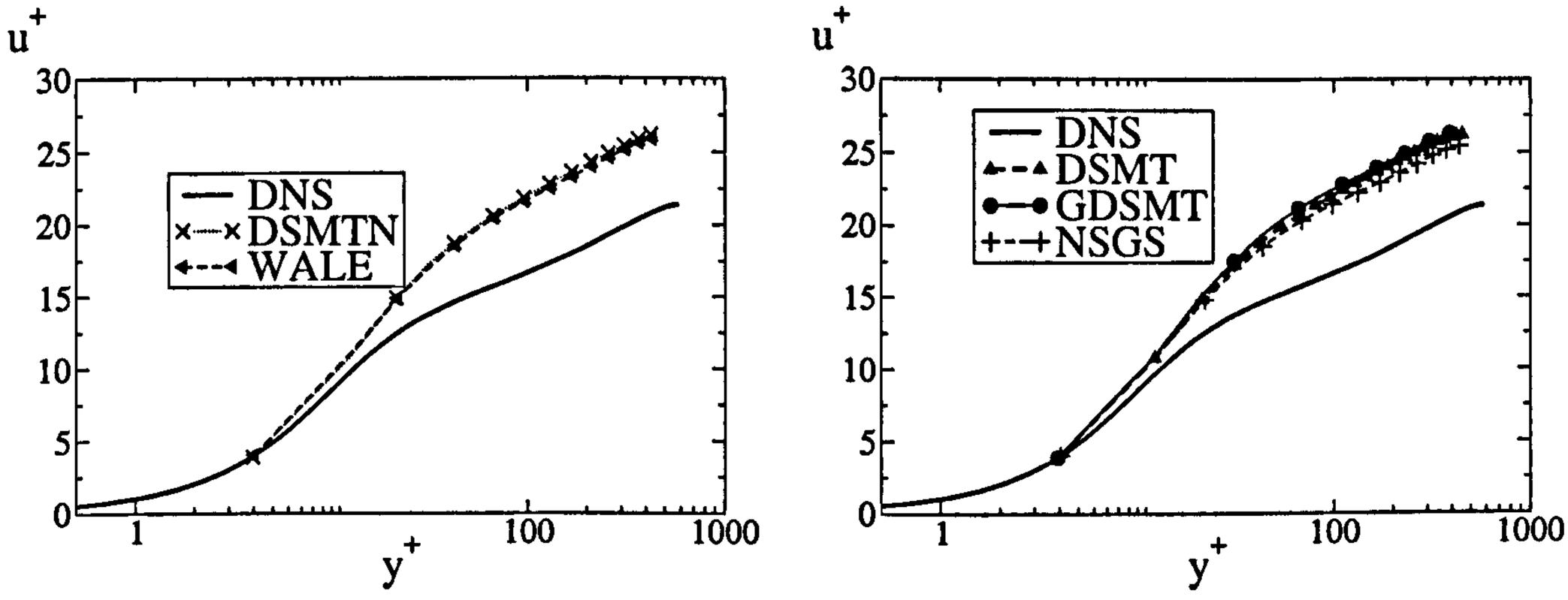

Figure 6.9: Streamwise velocity for case CM3.

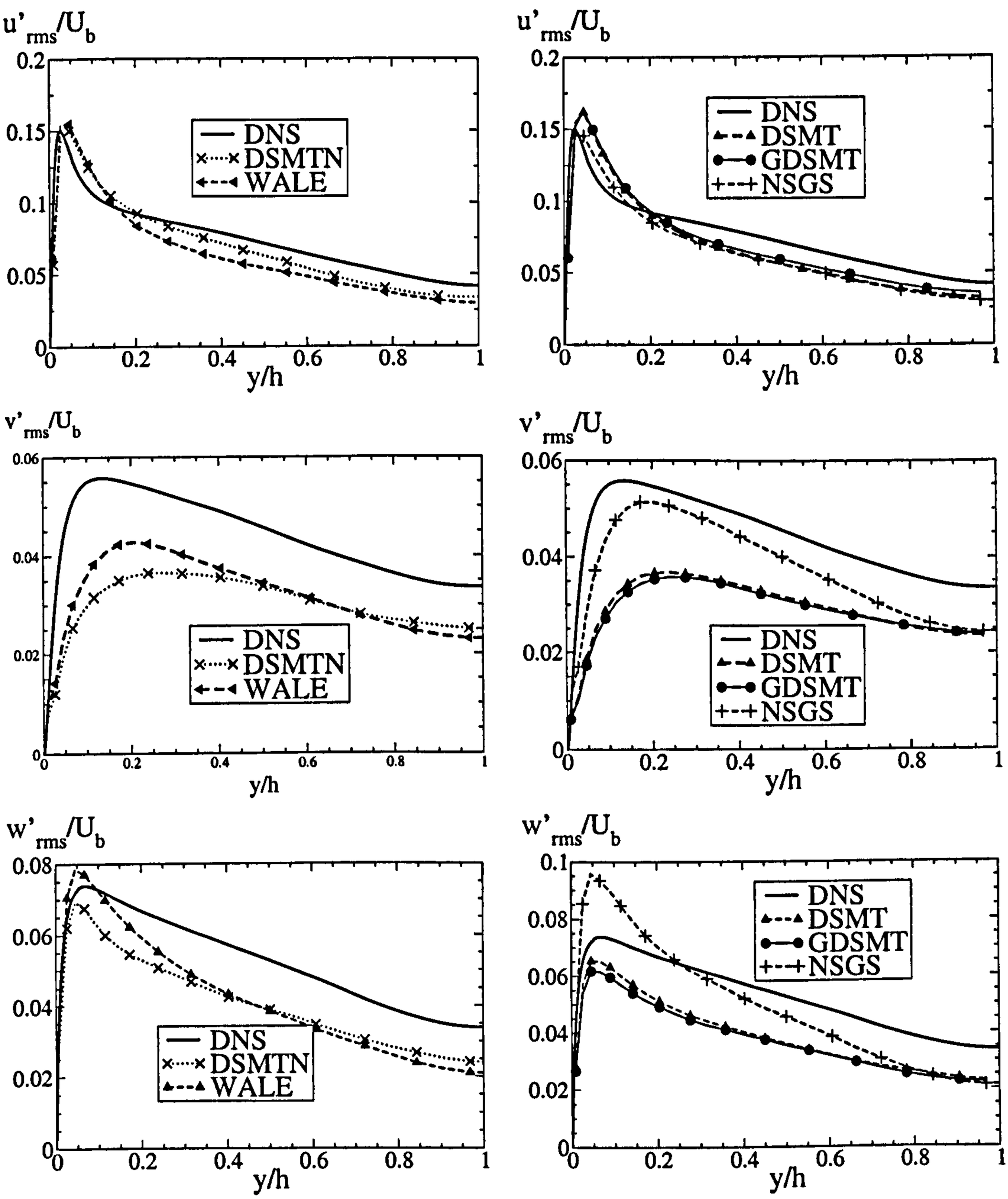

Figure 6.10: Distribution of r.m.s. velocities for case CM3.

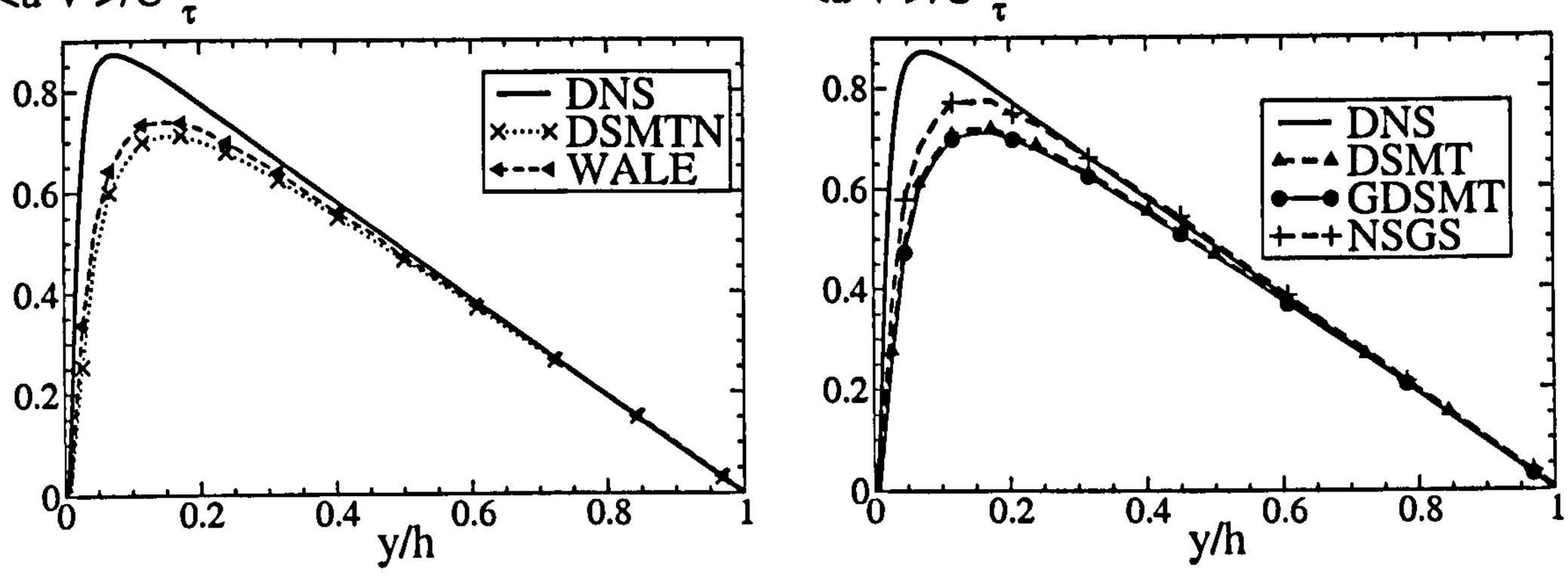

Figure 6.11: Distribution of resolved shear stress for case CM3.

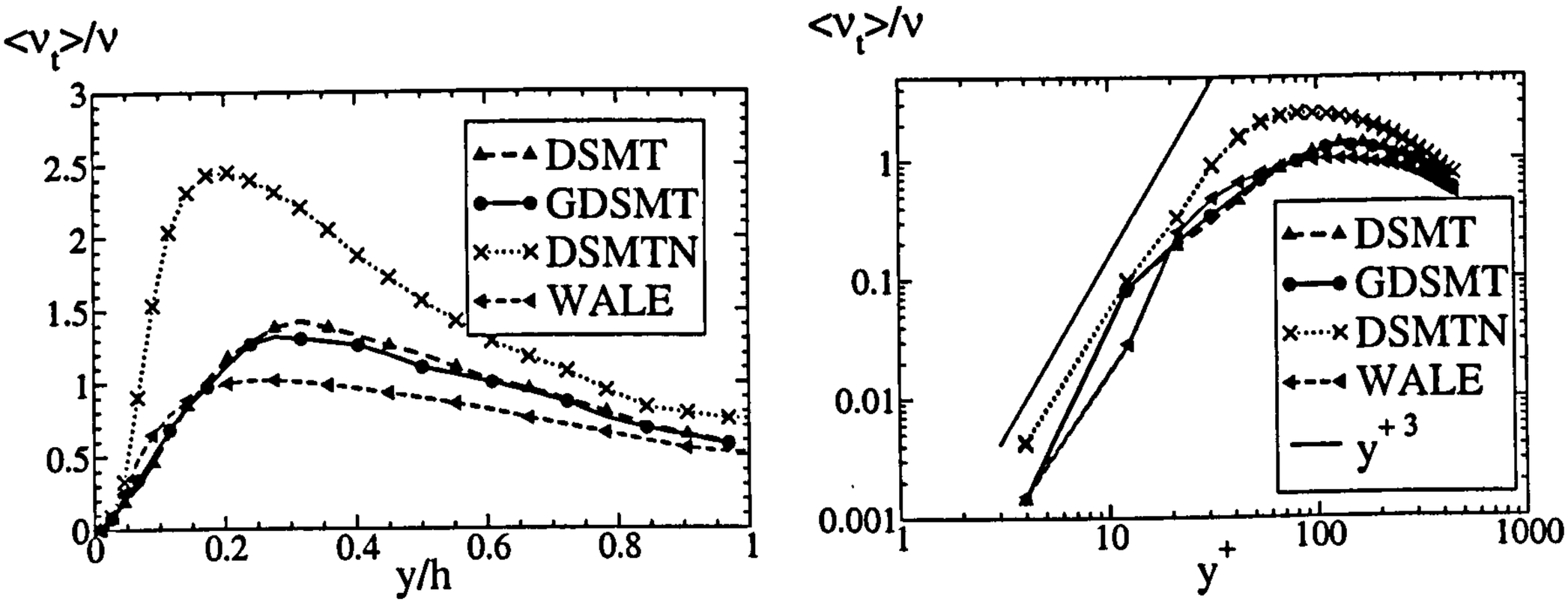

Figure 6.12: Subgrid-scale viscosity for case CM3.

Grid	Re_τ	Error	u_c/U_b	Error
DNS	584	n.a.	1.1418	n.a.
CM3	467	-19.8 %	1.1231	-1.64 %
CM4	523	-10.3 %	1.1239	-1.57 %
CM6	551	-5.6 %	1.1253	-1.45 %

Table 6.5: Predictions of wall shear stress and centreline velocity for different grids with the dynamic model DSMT.

The foregoing set of numerical experiments presented in this section focuses on the influence of the grid density beyond that associated with near-wall resolution. Here, a single subgrid-scale model is used, namely a version of the dynamic Smagorinsky model (DSMT), for different grids. Table 6.5 and Figure 6.13 quantify the influence of the grid changes on global and local quantities. The switch from CM3 to CM4 leads to a strong improvement in the predictions, primarily because of the increase in grid density in the near-wall region. The increase in resolution, from CM4 to CM6, is only effective in the spanwise direction, and again gives marked improvements in the predictions. As the grid resolution increases, more small scales are resolved, the log-law is progressively better represented, with a more accurate value for the wall shear stress being obtained, and the turbulent intensity is getting closer to the DNS solution. With more scales being resolved, the burden put on the subgrid-scale model decreases, and the magnitude of the subgrid-scale viscosity decreases. A comparison of these results with those obtained on mesh CM4, presented earlier in this section, tends to indicate that dynamic models require a much higher resolution, specially in the near wall-region, than their non-dynamic counterparts in order to achieve the same representation of the statistical properties of the flow.

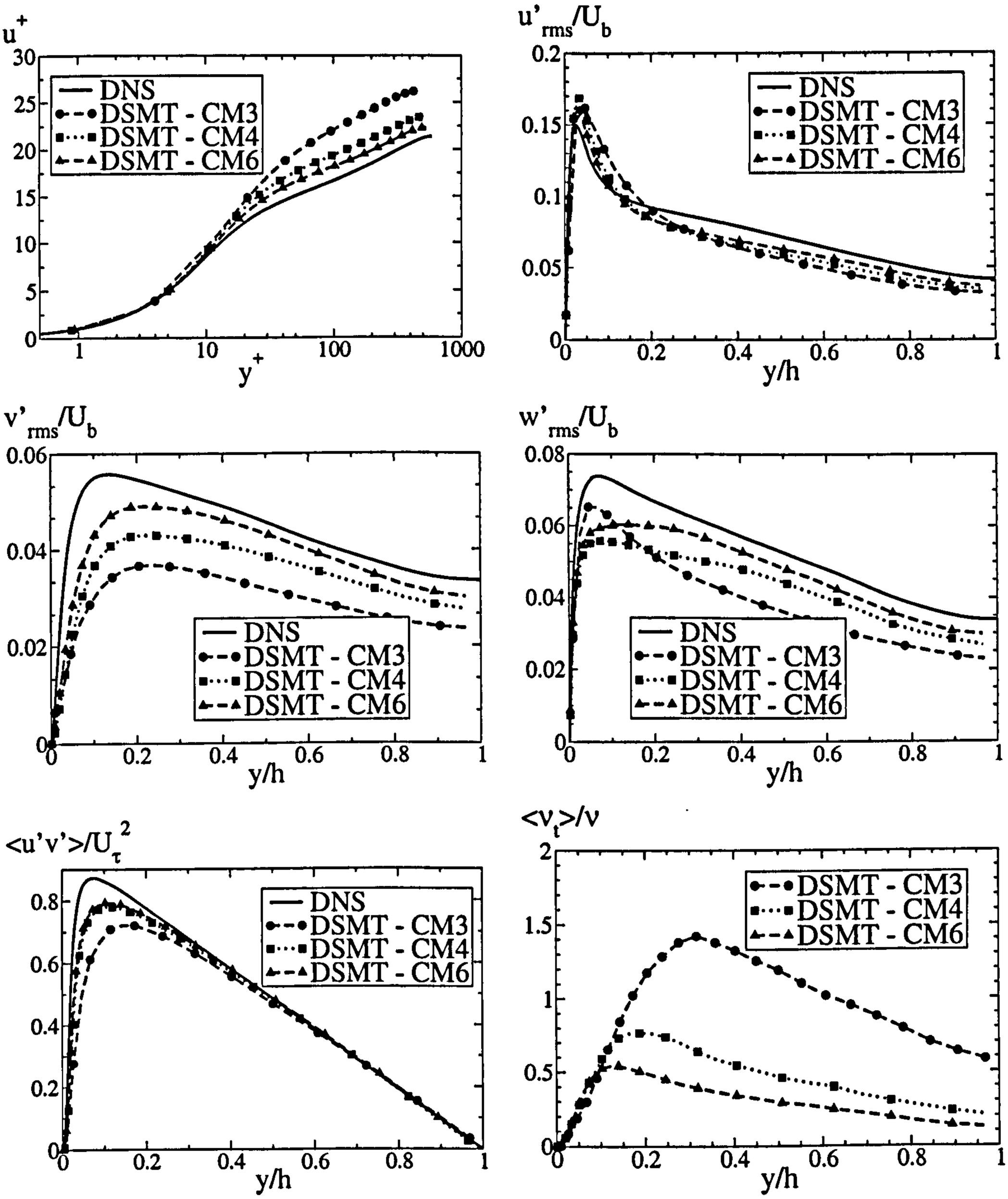

Figure 6.13: Effect of the variation of the grid density with the model DSMT.

6.4 Influence of the near-wall treatment

The performance of the wall laws, described in Section 3.3 and summarised in Table 6.6, is examined here for two different channel flows. The first case is similar to the one considered in the previous section, at $Re_\tau = 590$, but with a somewhat coarser grid, denoted CM2 in Table 6.1, while the second case, denoted CM7 in Table 6.1, is at $Re_\tau = 1050$. The results of the simulations for CM7 will be compared with the results of a LES computation performed by Piomelli [175]. All computations presented in this section used the WALE model.

Denomination	Description
LL2	Instantaneous 2-layers Log-Law
LL3	Instantaneous 3-layers Log-Law
LLK	2-layers Log-Law using k
WW	Werner-Wengle

Table 6.6: Summary of wall-treatments used in the channel computations.

For case CM2, Table 6.7 gives errors in terms of friction Reynolds number and centreline velocity relative to the DNS, while Figures 6.14 and 6.16 show velocity and turbulence intensity profiles, respectively. Despite the coarseness of the grid used, the results are certainly not disappointing, especially in terms of the resolution of the velocity and turbulence intensity away from the wall, over 80% of the channel width. Table 6.7 shows that the three-layers log-law formulation slightly underpredicts the friction velocity, leading to the log-law profile lying slightly above the DNS solution as shown in Figure 6.14, while the Werner-Wengle formulation returns the opposite behaviour, but gives results quite close to the DNS solution. A degree of uncertainty arises here from the fact that the log-law based wall-treatments were implemented so as to yield the wall-shear stress using, directly, the velocity u_1 at the wall-nearest node y_1, while the Werner-Wengle model involved cell integration, as described in Section 3.3.3. This may have caused the offset in the wall-nearest velocity seen in Figure 6.14. The turbulence intensity, shown in Figure 6.16, is reasonably well

SGS Model	Re_τ	Error	u_c/U_b	Error
DNS	584	-	1.1418	-
WALE + LL2	558.5	-4.4 %	1.12	-1.91 %
WALE + LL3	557.8	-4.5 %	1.118	-2.08 %
WALE + LLK	537.6	-7.9 %	1.13	-1.03 %
WALE + WW	598.4	2.5 %	1.133	-0.08 %

Table 6.7: Predictions of wall shear stress and centreline velocity for the channel flow using different wall treatments for $Re_\tau = 590$ (Case CM2).

predicted, although, oscillatory features are observed in the near-wall region. This behaviour is characteristic of a collocated finite-volume scheme when used on coarse cells which give high local Peclet numbers. Overall, for this set of simulations, the Werner-Wengle formulation was judged to give the best results.

Further tests were then conducted with the same wall-law formulations at the higher Reynolds number, $Re_\tau = 1050$, on a much coarser grid (Case CM7). Table 6.8 gives errors in terms of friction Reynolds number and centreline velocity, relative to a LES computation performed by Piomelli [175]. Velocity profiles are shown in Figure 6.15, while turbulence intensity profiles are presented in Figure 6.17. Velocity profiles, centreline velocity and wall-shear stress are reasonably well predicted for all cases. In term of the turbulence intensity, shown in Figure 6.17, the predictions agree well with the reference data, considering the differences that exist. The oscillatory behaviour observed in Figure 6.16 is also present here and is again rooted in the use of a co-located scheme. These observations are similar to those made for the lower Reynolds number case CM2, although it is now difficult to judge which of the wall laws perform best.

The above set of simulations thus demonstrate the attraction of using simple wall treatments, which allow major flow features to be represented with a reasonable degree of realism, while drastically reducing the computational cost. The penalty is, however, that too coarse meshes lead to the loss of near-wall details and an oscillatory behaviour which can contaminate the solution.

SGS Model	Re_τ	Error	u_c/U_b	Error
Expected	1050	-	1.11	-
WALE + LL2	1160	+10.5 %	1.10	0.9 %
WALE + LL3	1090	+3.8 %	1.12	0.9 %
WALE + LLK	1127	+7.3 %	1.11	0.0 %
WALE + WW	1166	+11.0 %	1.103	0.6 %

Table 6.8: Predictions of wall shear stress and centreline velocity using different wall functions for $Re_\tau = 1050$ (Case CM7).

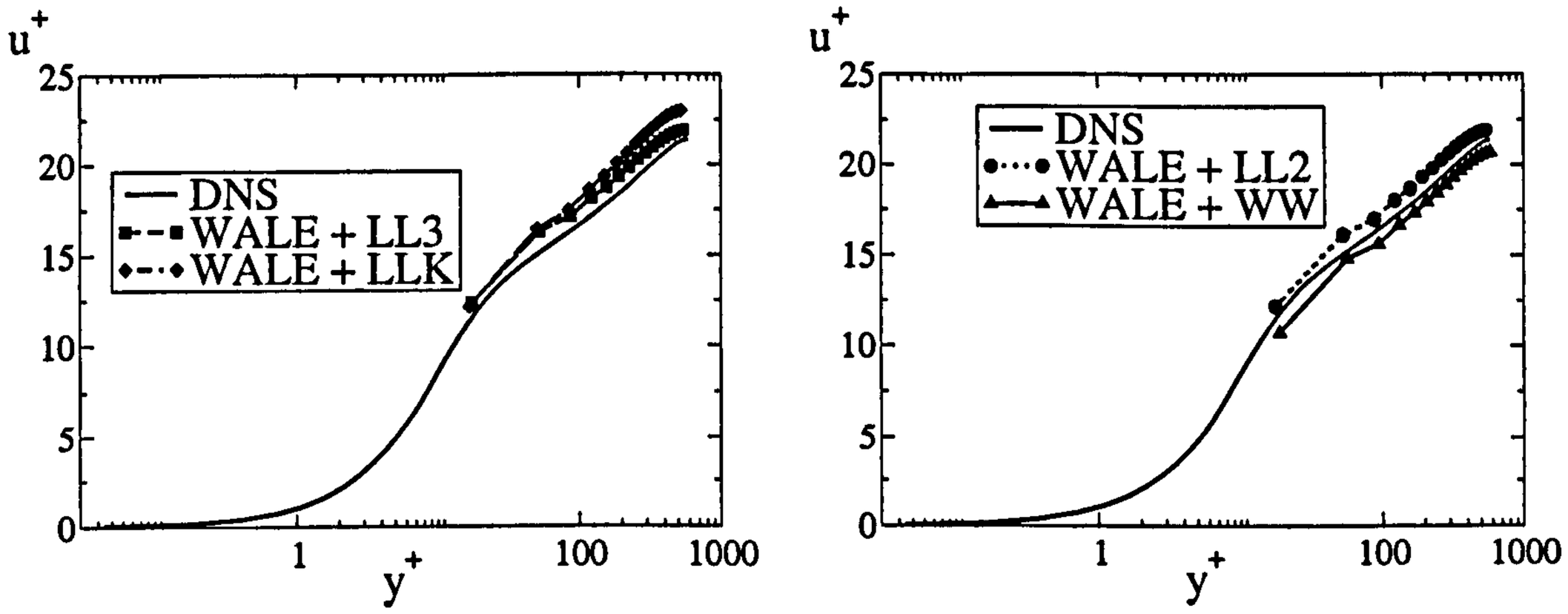

Figure 6.14: Streamwise velocity for channel flow ($Re_\tau = 590$), sensitivity to near-wall modelling (Case CM2).

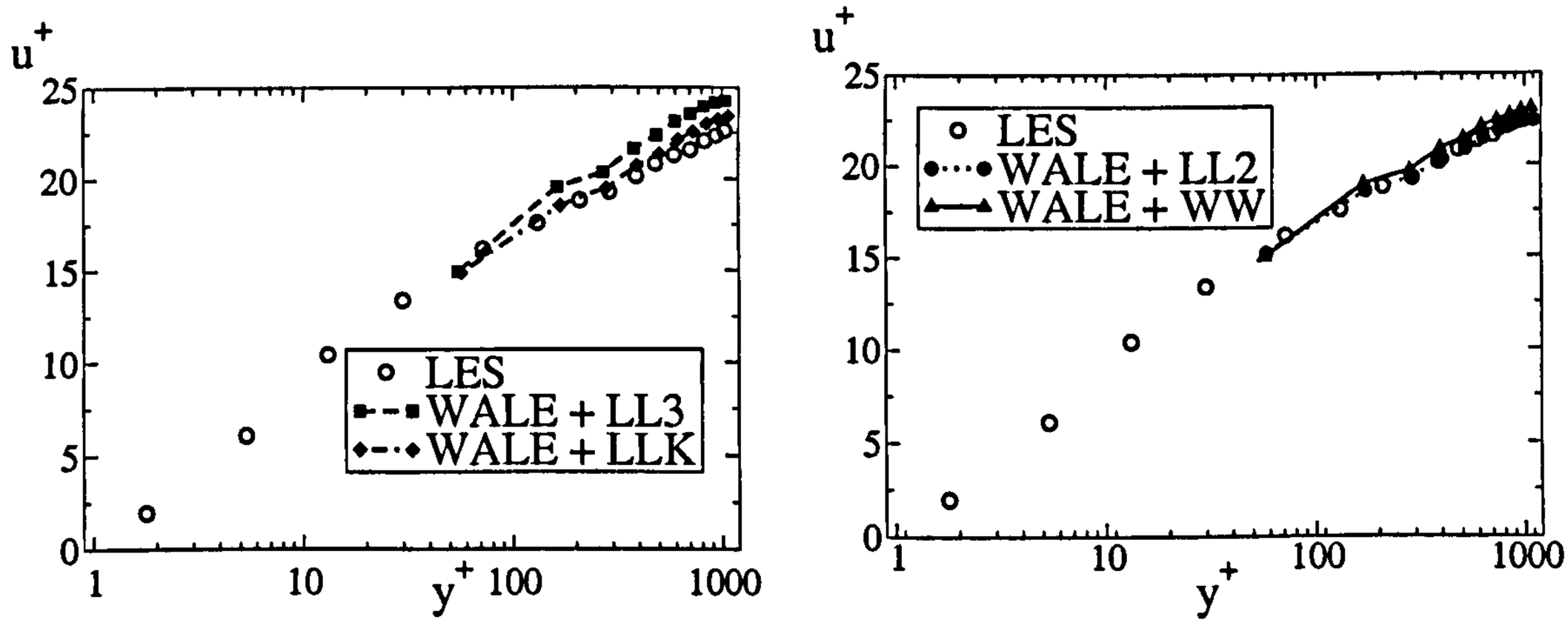

Figure 6.15: Streamwise velocity for channel flow ($Re_\tau = 1050$), sensitivity to near-wall modelling (Case CM7).

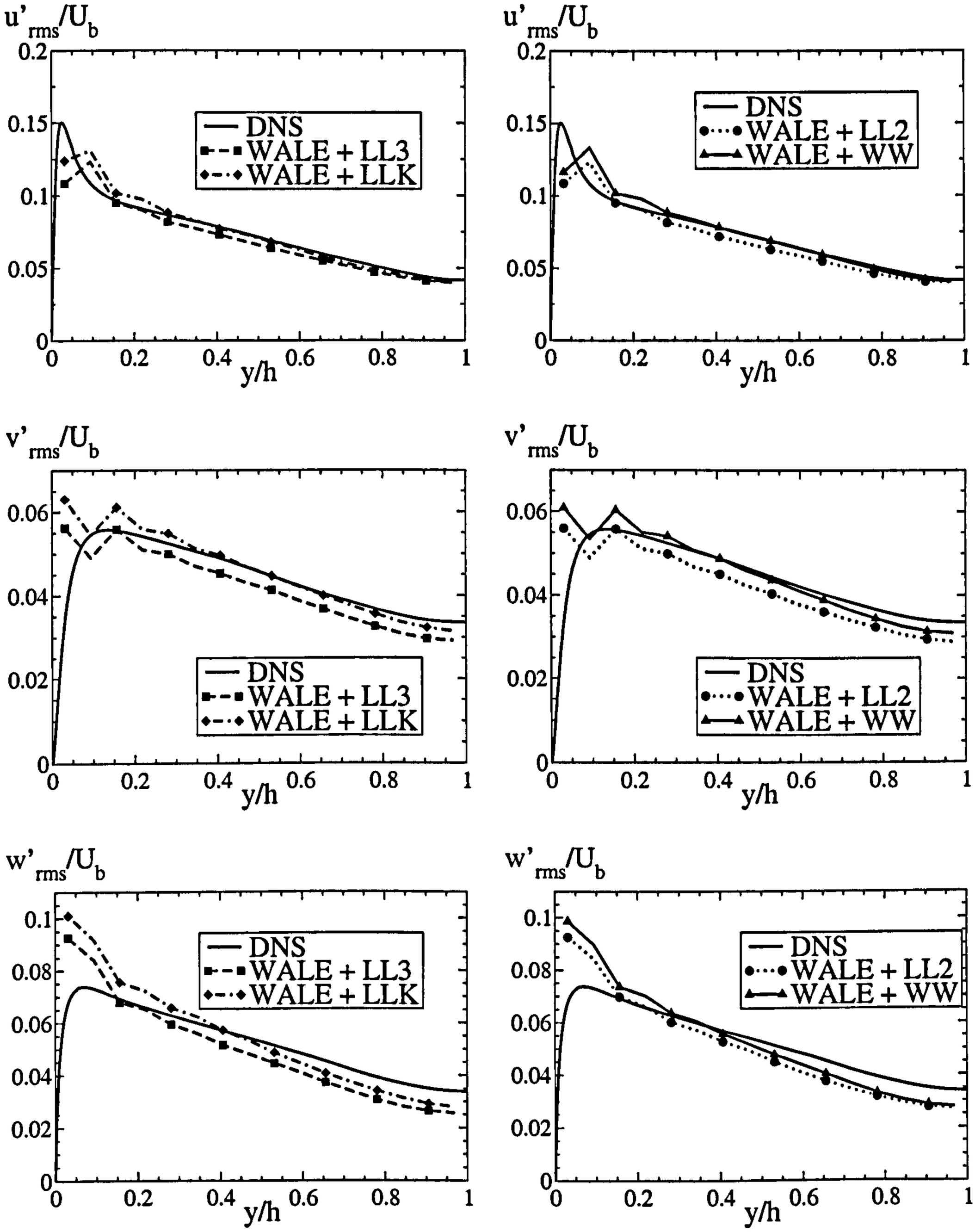

Figure 6.16: Turbulence intensity for channel flow ($Re_\tau = 590$), sensitivity to near-wall modelling (Case CM2).

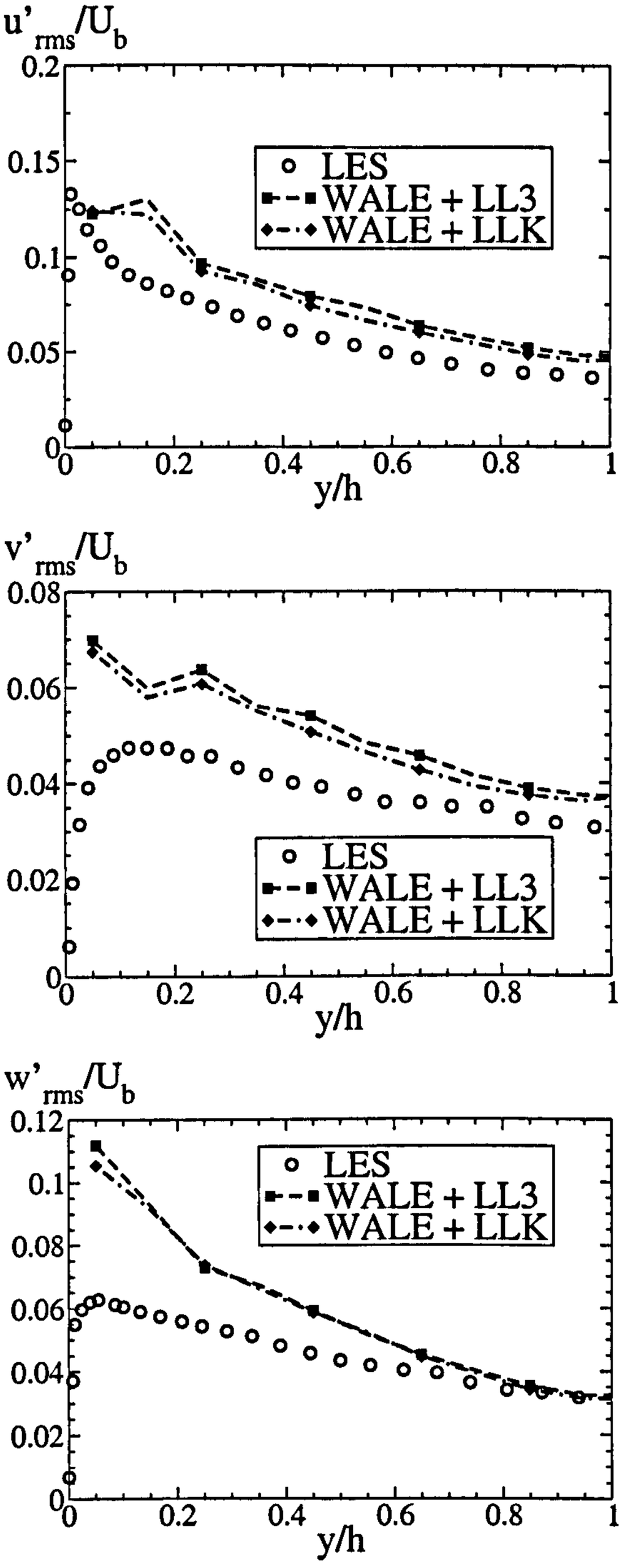

Figure 6.17: Turbulence intensity for channel flow ($Re_\tau = 1050$), sensitivity to near-wall modelling (Case CM7).

6.5 Error analysis

As noted earlier, the differences between the LES and DNS solutions are due to a combination of numerical and modelling errors. The relative contributions of these are investigated in this section with the aid of a procedure first introduced by Vreman et al [228]. The procedure involves computing the same flow with three different levels of discretisation. The first level corresponds to a DNS, i.e. the flow is computed on a high-density grid, so that no modelling is needed. The two others are LES computations performed on two different grids. The denser is obtained from the initial DNS grid by removing alternate grid lines. The same procedure is applied to obtain the coarser grid from the medium grid. Both LES computations use the same subgrid-scale model, with the grid-filter width $\overline{\Delta}$ being kept constant. Thus, if h is the characteristic cell size, $\overline{\Delta}/h = 1$ for the coarse-grid LES and $\overline{\Delta}/h = 2$ for the dense-grid LES.

With the above solutions obtained, discretisation error and modelling error can, following Vreman [226], be separated from each other, at least approximately. The discretisation error is estimated by considering the difference between the two LES computations for which it is assumed that the model, having the same filter width, plays the same role. Thus, for any time-fluctuating quantity, Q, the discretisation effect is represented by:

$$\epsilon_d = Q_{LES-2} - Q_{LES-1} \tag{6.1}$$

Assuming that LES-1 does not suffer from the discretisation error, i.e. the grid density is high enough, the effect of the modelling error is obtained from:

$$\epsilon_m = Q_{LES-1} - Q_{LF-1} \tag{6.2}$$

where LF-1 indicates the DNS solution filtered with the same filter width as LES-1. The sum of (6.1) and (6.2) gives the total error:

$$\epsilon_t = \epsilon_d + \epsilon_m = Q_{LES-2} - Q_{LF-1} \tag{6.3}$$

Ref.	$N_x \times N_y \times N_z$	Δx^+	Δy^+	Δz^+
DNS	$128 \times 128 \times 128$	29	$1 - 21$	14.5
LES-1	$64 \times 64 \times 64$	58	$2 - 42$	29
LES-2	$32 \times 32 \times 32$	116	$4 - 84$	58

Table 6.9: Description of the different levels of discretisation for a channel flow, error analysis.

Vreman et al [228] applied their procedure to a compressible mixing layer for a range of spatial discretisation schemes and subgrid-scale models. In the present work, attention will be limited to two variations of the same subgrid-scale model: the Smagorinsky model with $C_s = 0.1$ and denoted by SM, and the same model using the near-wall damping function (3.6) with $A^+ = 25$, this variant being denoted SM + WD2. For both convective and diffusive terms, the spatial discretisation scheme is second-order centred (see Chapter 4 for more details). The test case is a periodic channel flow at $Re_\tau = 590$. The size of the computational box is $2\pi h \times 2h \times \pi h$. For this case, DNS data are available for comparison (see Moser et al [161]). Table 6.9 gives the description of the meshes. The filter width, for both subgrid-scale models, is taken equal to the grid size of the coarsest mesh. Hence, it is defined as $\overline{\Delta} = \overline{\Delta}_{LES-2} = 2\overline{\Delta}_{LES-1}$ where $\overline{\Delta} = (\Delta x \Delta y \Delta z)^{1/3}$. All the computations were started from an instantaneous velocity field obtained from the DNS computation once it has reached a statistically steady state. The field was then filtered to coincide with the filter width used in the LES computations. The DNS and the LES computations were then restarted from these fields and ran over a period of 24 flow-through-times before statistics and time-dependent signals were recorded for a further 12 flow-through-times.

The relative importance of numerical and modelling errors is evaluated by considering steady and unsteady quantities in an attempt to separate the contributions of the numerical and modelling errors to the total error in the different regions of the flow. In addition to the statistics (mean velocity and turbulent intensity components), the time evolution of several flow quantities is recorded. These quantities

Ref.	SGS Model	Re_τ	Error	u_c/U_b	Error
MKM	n.a.	584	n.a.	1.1418	n.a.
DNS	n.a.	594.7	1.83 %	1.141	-0.07 %
LES-1	SM	698.2	+19.55 %	1.155	+1.16 %
LES-2	SM	658.1	+12.69 %	1.155	+1.16 %
LES-1	SM + WD2	545.2	-6.64 %	1.107	+3.07 %
LES-2	SM + WD2	515.0	-11.82 %	1.117	-2.17 %

Table 6.10: Predictions of wall shear stress and centreline velocity for the channel flow, error analysis.

are:

- the global kinetic energy defined by $E = \frac{1}{2} \int u_i u_i \, dx \, dy \, dz$ where x, y and z respectively indicate the streamwise, wall-normal and spanwise directions;
- a global measure of the fluctuating velocity, defined by $R = \frac{1}{2} \int_{\omega_j} (u_i - < u_i >)^2 \, dx \, dz$ where ω_j is the j^{th} horizontal plane (plane made of the streamwise and spanwise directions) and $< \cdot >$ is the spatial averaging operator over the plane ω_j.

The total kinetic energy is used to investigate the global effect of each source of errors while R, the norm of the fluctuating velocity, can give an insight into localised features.

The first stage of the procedure thus consists of generating the DNS data. The results are compared with existing DNS data for the same case by Moser et al [161]. Table 6.10 shows the values of the predicted friction Reynolds number and centreline velocity to be in very good agreement. In Figure 6.18, mean velocity, turbulence intensity and shear stress profiles are all seen to compare well with the reference DNS. The small differences possibly indicate that the resolution may not be high enough in both the spanwise and streamwise directions. These data are nevertheless considered sufficiently accurate for the present purpose.

The next step consists of generating the LES data. Table 6.9 contains the predicted values of the wall shear Reynolds numbers and centreline velocities for the LES computations. Figures 6.19 and 6.20 show, for both LES computations, the velocity, turbulence intensity and shear stress profiles compared with the DNS data filtered at the same filter width as the LES. Figure 6.21 shows the same results as in Figures 6.19 and 6.20, all grouped together. Overall, the computation using SM+WD2 returns better predictions of the filtered DNS data. Figure 6.22 shows the effect of keeping the filter width constant in the subgrid-scale model in the LES simulations. The level of subgrid-scale viscosity does not vary if the grid is changed, indicating the modelling contribution in LES-1 and LES-2 is essentially the same, and that the differences between the two computations are thus rooted in the numerics.

The next task is to quantify the two contributions to the total error. Figure 6.23 presents a global view. When the SM model is used, the largest contribution to the total error arises from the modelling part. In agreement with the finding of Vreman et al [228], the contribution of the discretisation error is negative which, therefore, tends to reduce the total error. By introducing a damping function (model SM+WD2), the subgrid-scale viscosity generated by the model is forced to decrease to zero toward the wall. This results in a significant reduction of the modelling error, which is now of the same order of magnitude as the discretisation error. Interestingly, the discretisation error has now become positive, and this contribution increases the magnitude of the total error. Compared to the other case where the SM model is used, the total error has significantly decreased as a consequence of the more realistic near-wall region modelling.

Figures 6.24 to 6.26 show the evolution in time of the errors in fluctuating velocity, R, at different wall-normal locations. The plots on the left-hand-side of each figure show the magnitude of the errors, while the right-hand-side plots compare their relative contribution to the total error. When SM is used, the modelling error is seen to be dominant and large in magnitude in comparison with the discretisation error. For each location, the modelling contribution to the total error remains negative, in agreement with the observations made in Figure 6.23. When the damping

function (WD2) is introduced, it is observed that, near the wall, the discretisation error is the major contributor to the total error. At the other locations considered, modelling and discretisation errors weight similarly in their contribution to the total error.

In summary, the method developed by Vreman et al [228] to assess the importance of errors in LES has been fruitfully employed for the present case of a periodic channel flow. Although the present results are approximate because of the coarseness of the grids used, they are qualitatively similar to those obtained by Vreman et al [228] for the case of the mixing layer, and this inspires confidence in their validity. Overall, it has been demonstrated that modelling and discretisation errors can, subject to the choice of subgrid-scale models, vary significantly and that the details of the subgrid-scale modelling in the near-wall region play an important role in respect of the total error in near-wall flows.

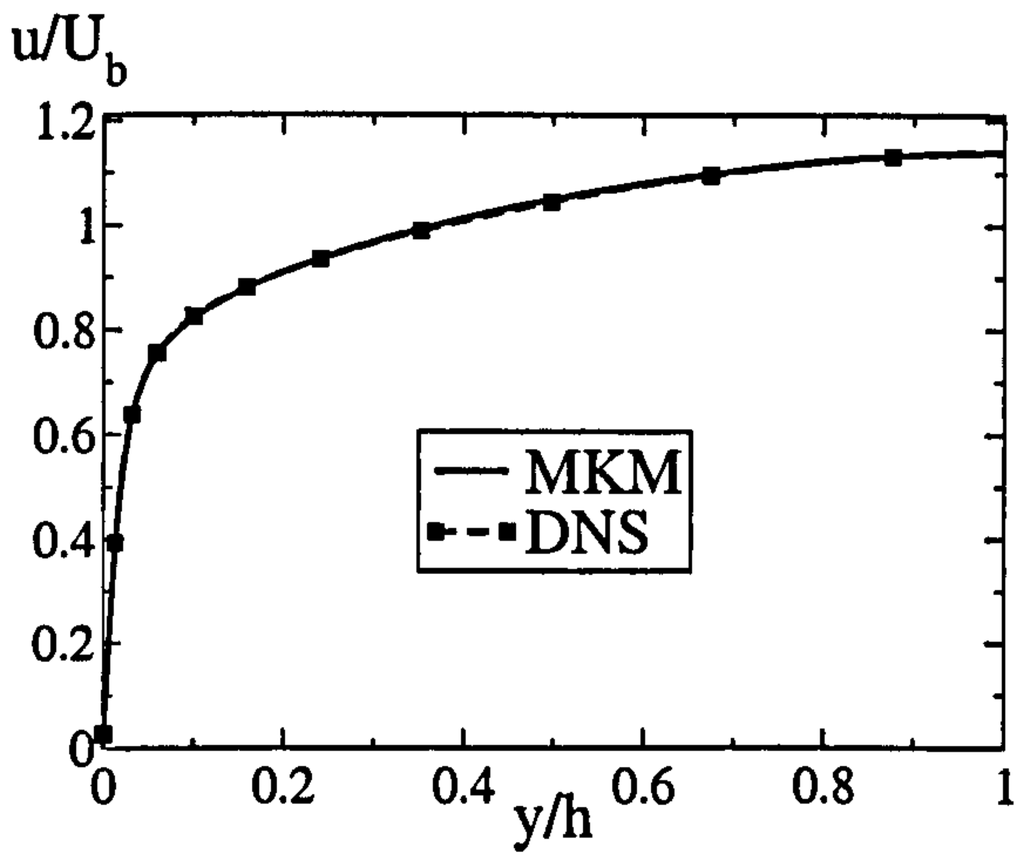

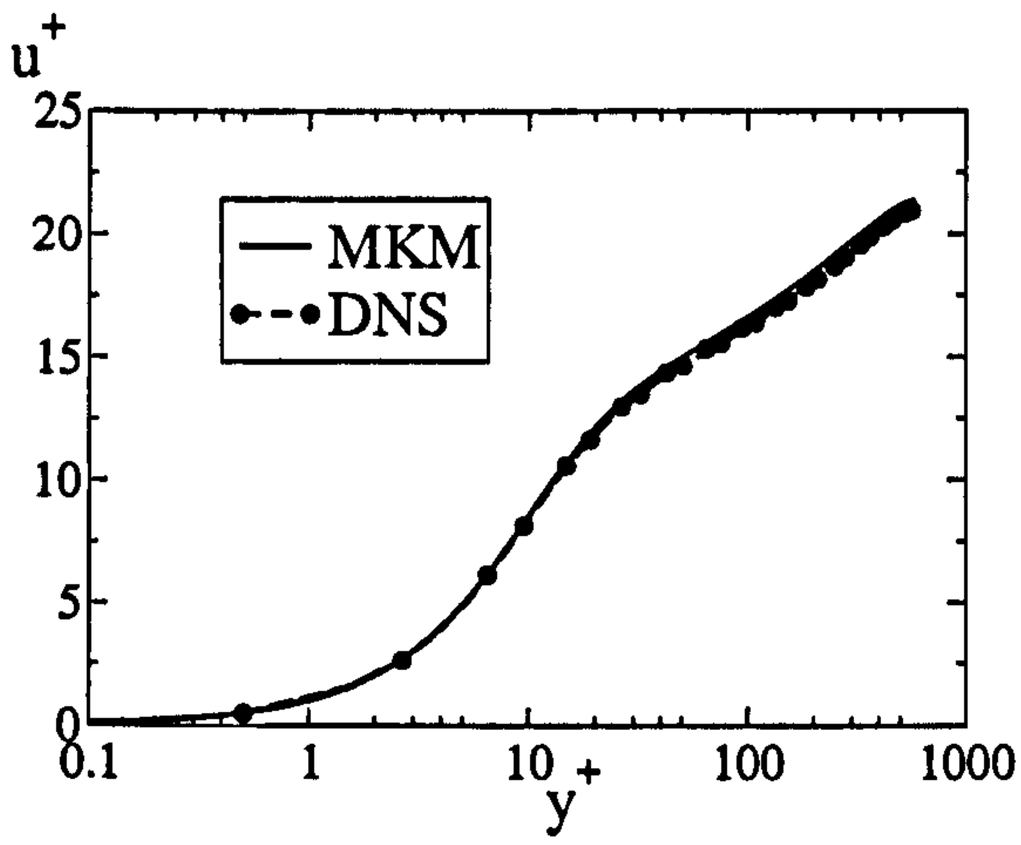

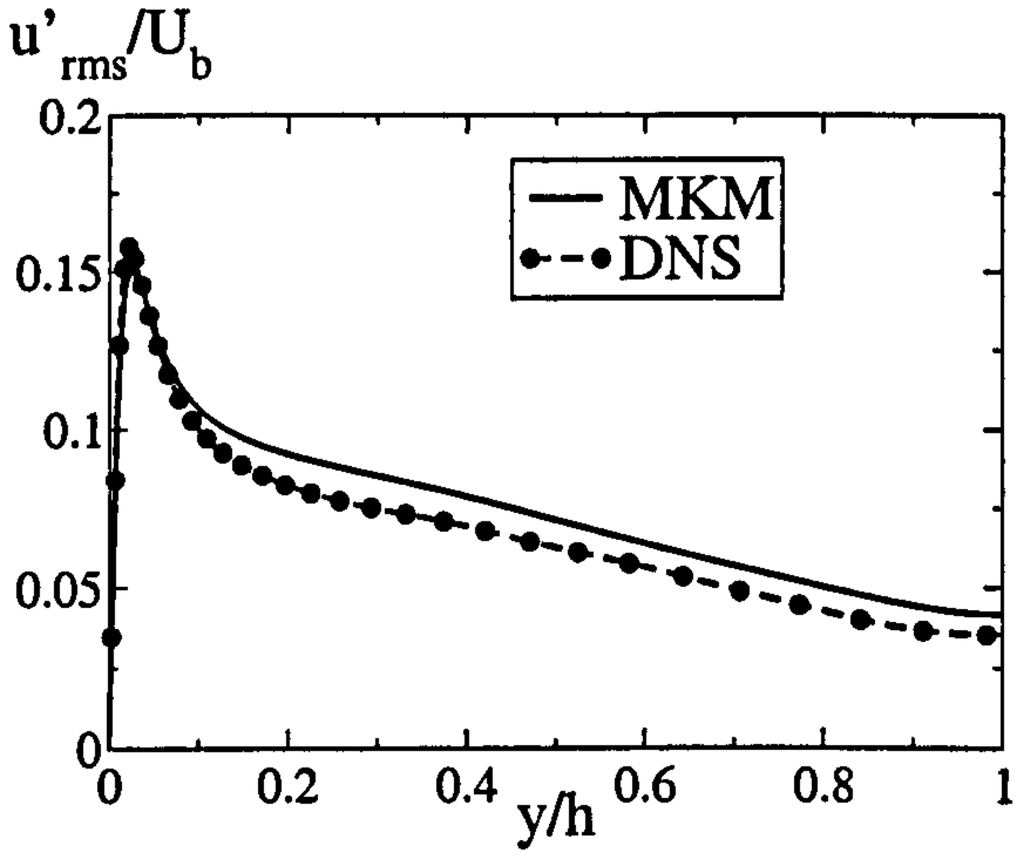

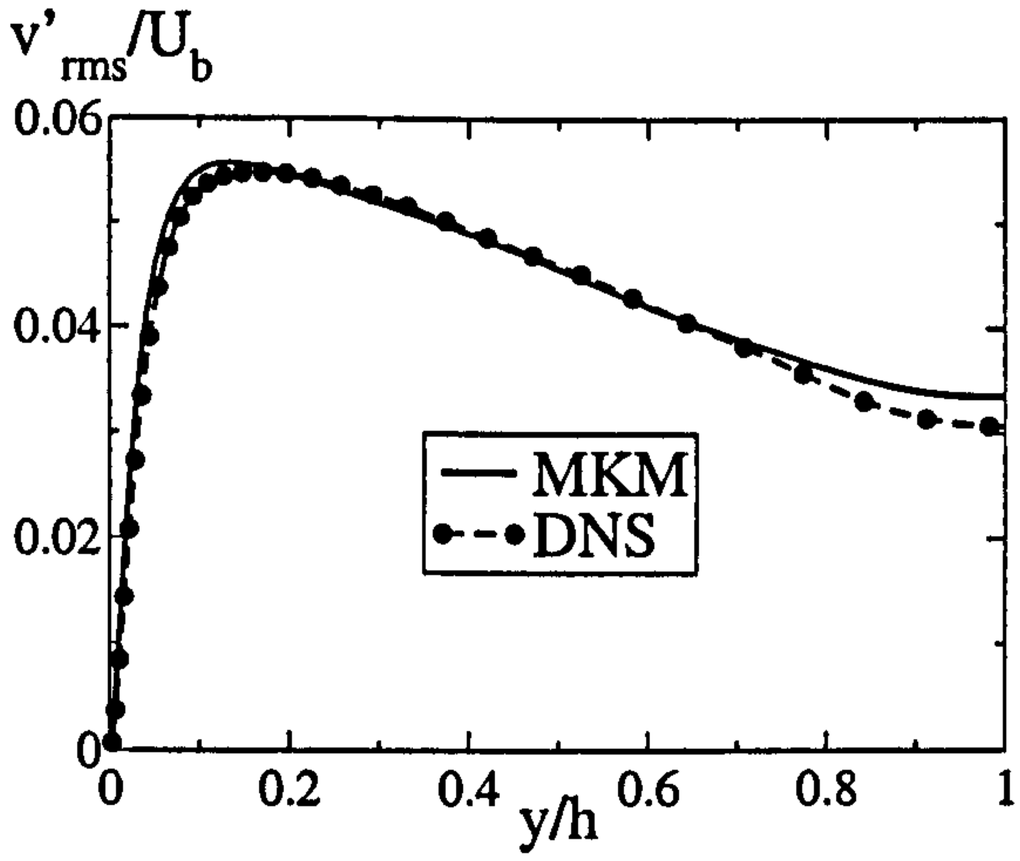

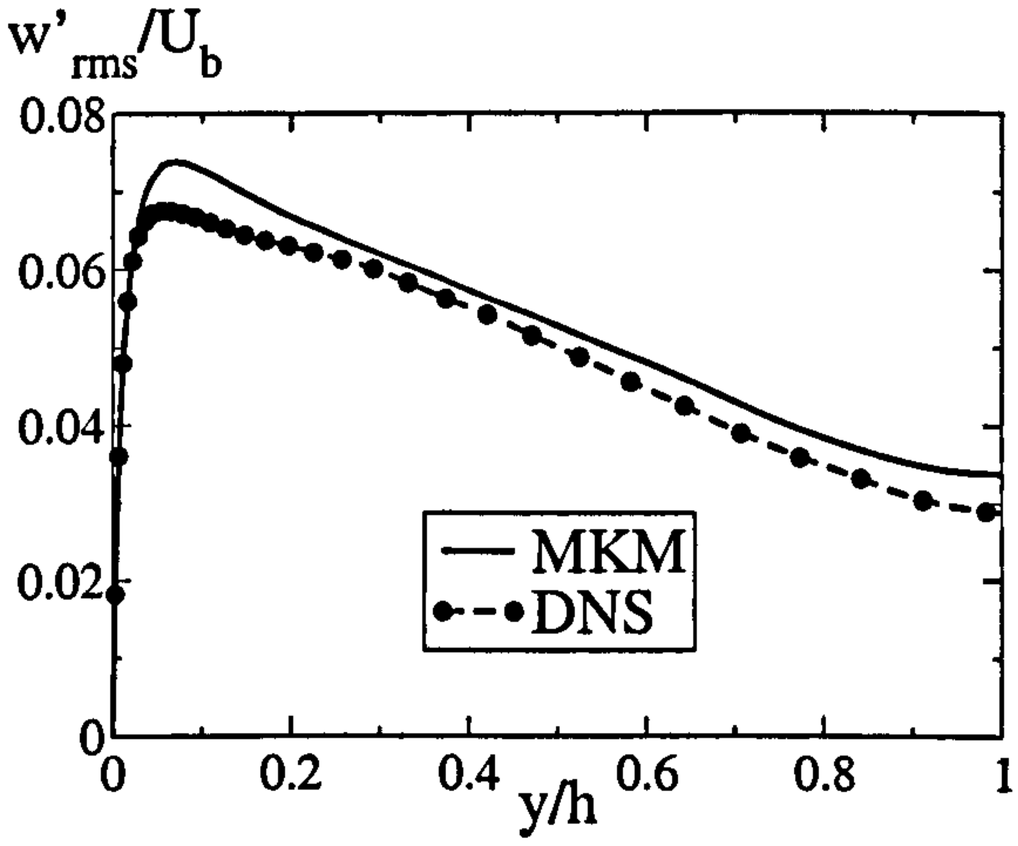

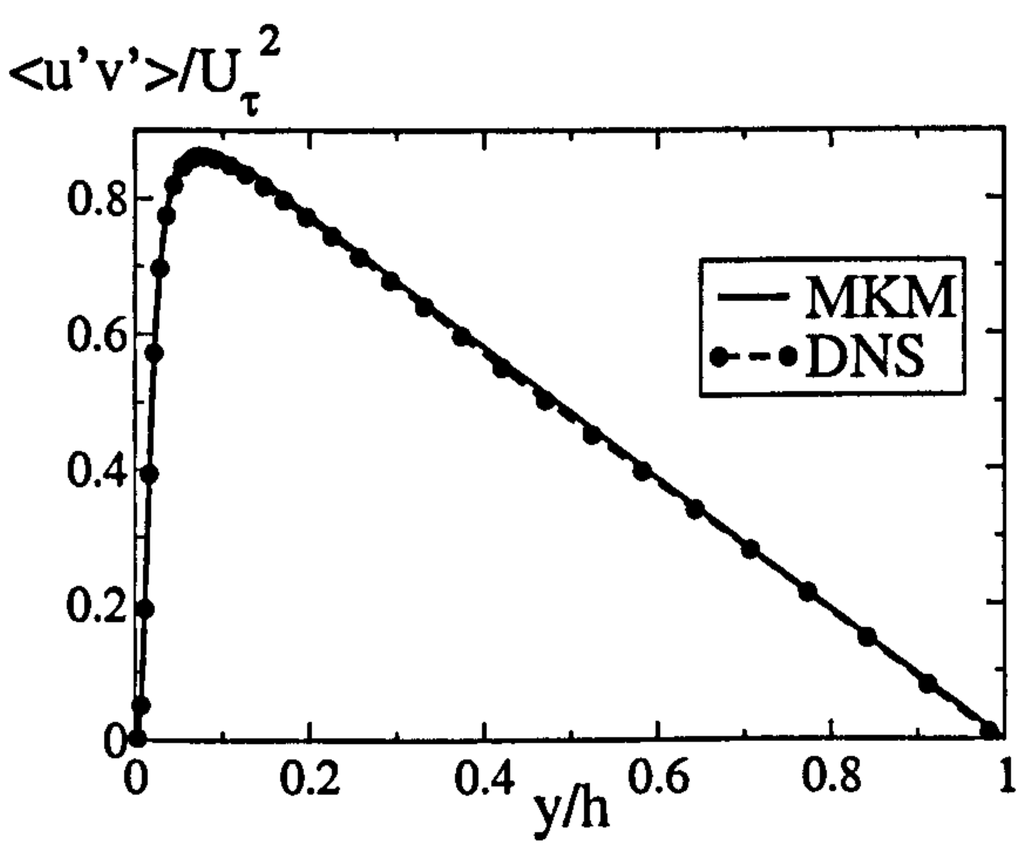

Figure 6.18: Comparison of the present DNS computation to that of Moser et al [161].

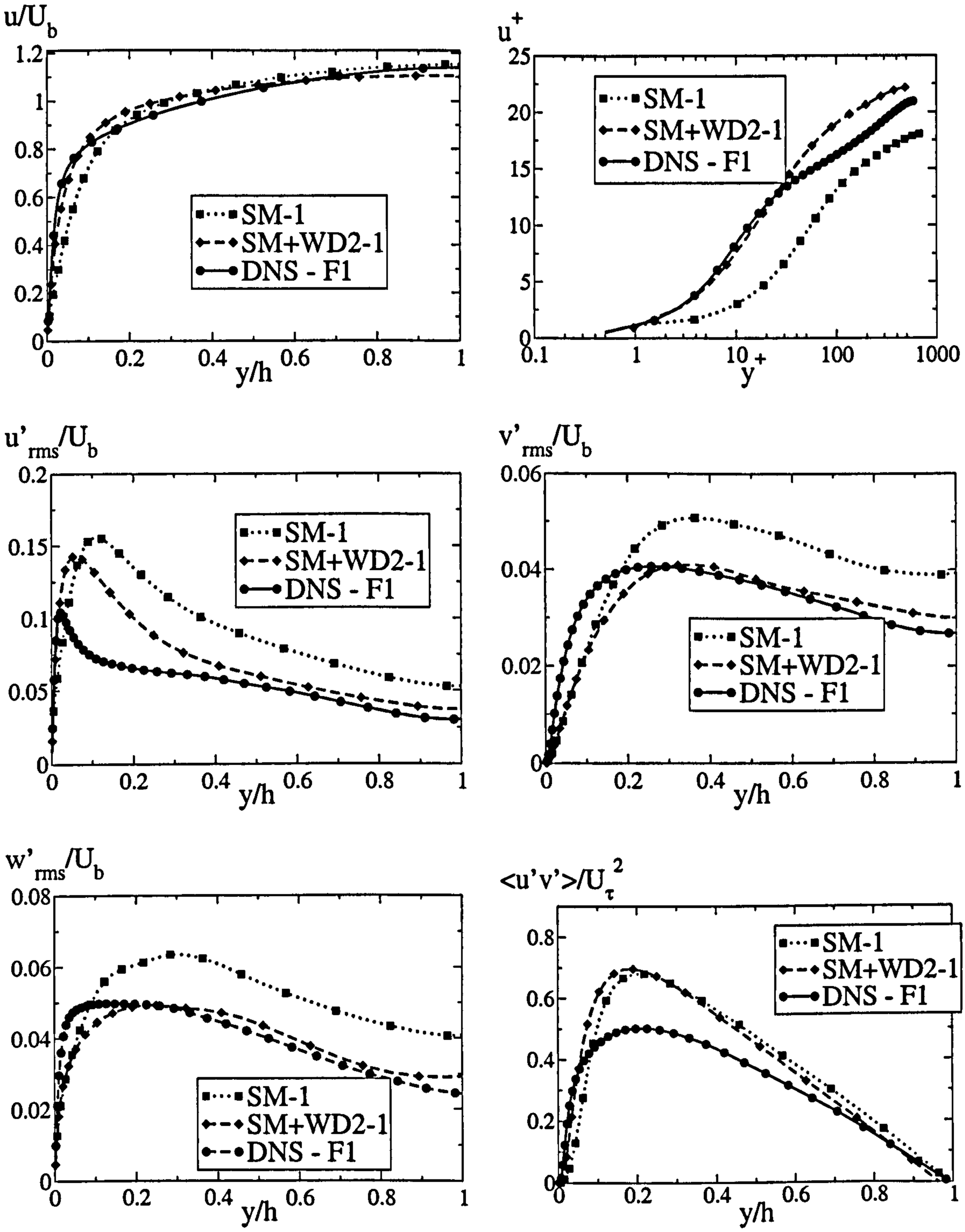

Figure 6.19: Large eddy simulation on the medium grid using SM and SM + WD2, comparison with filtered data.

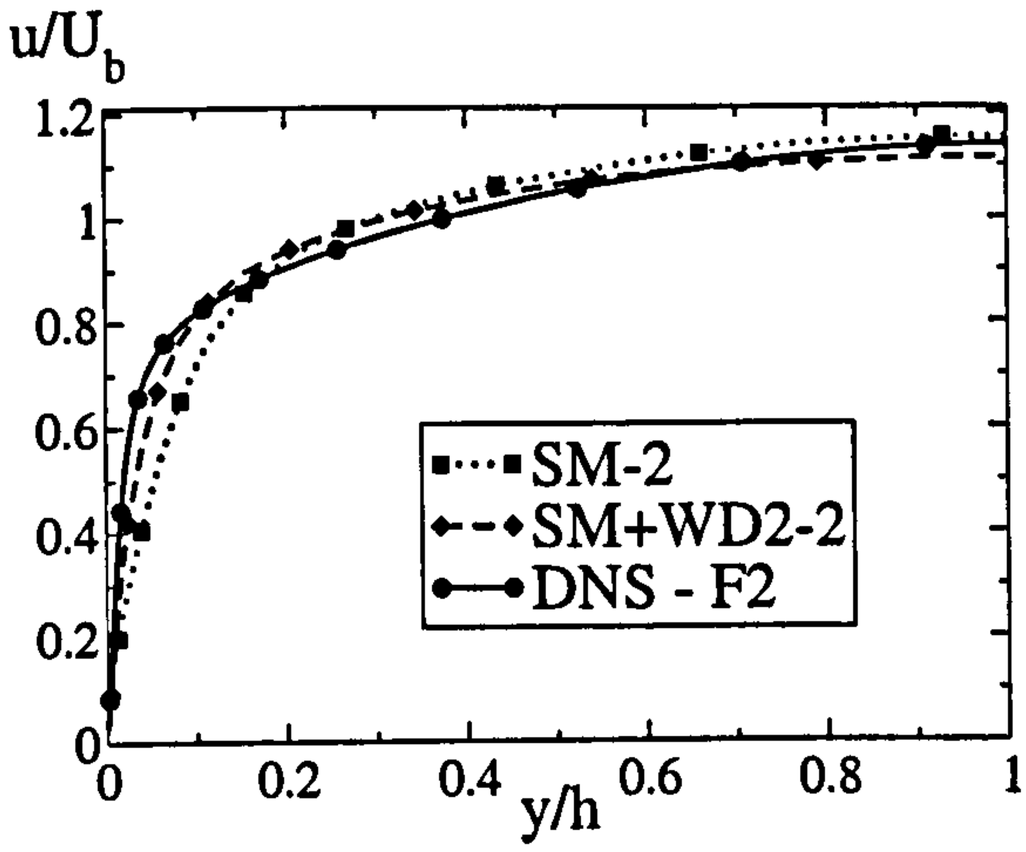

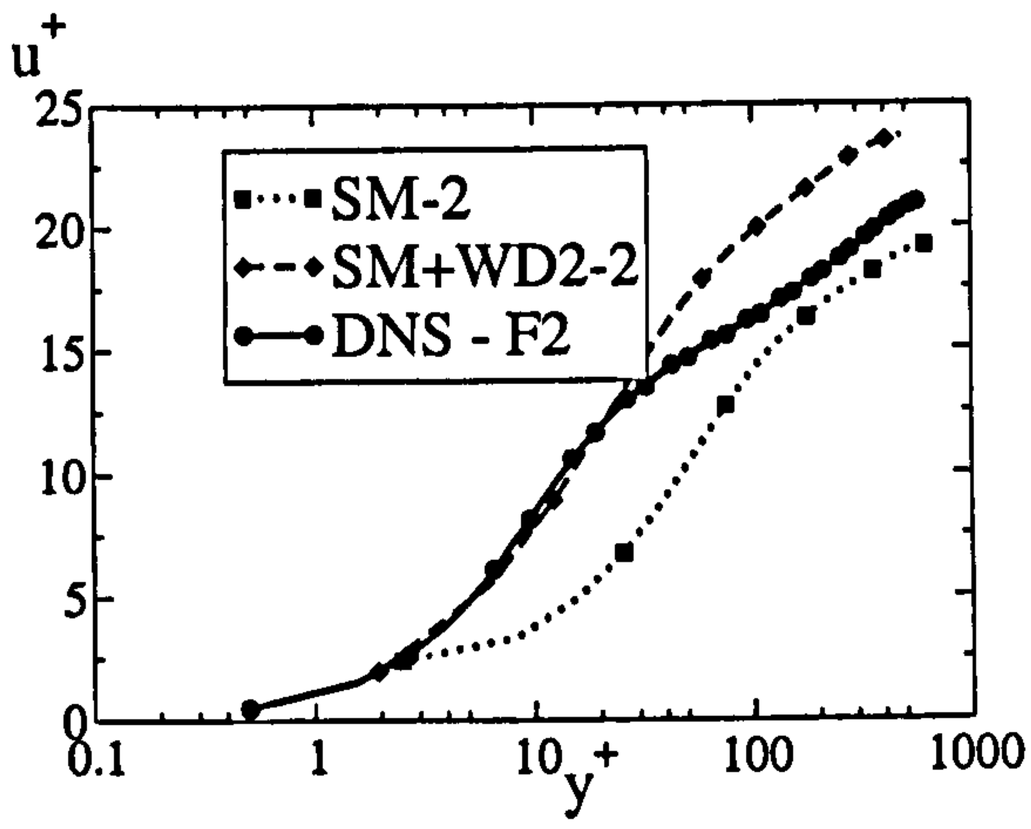

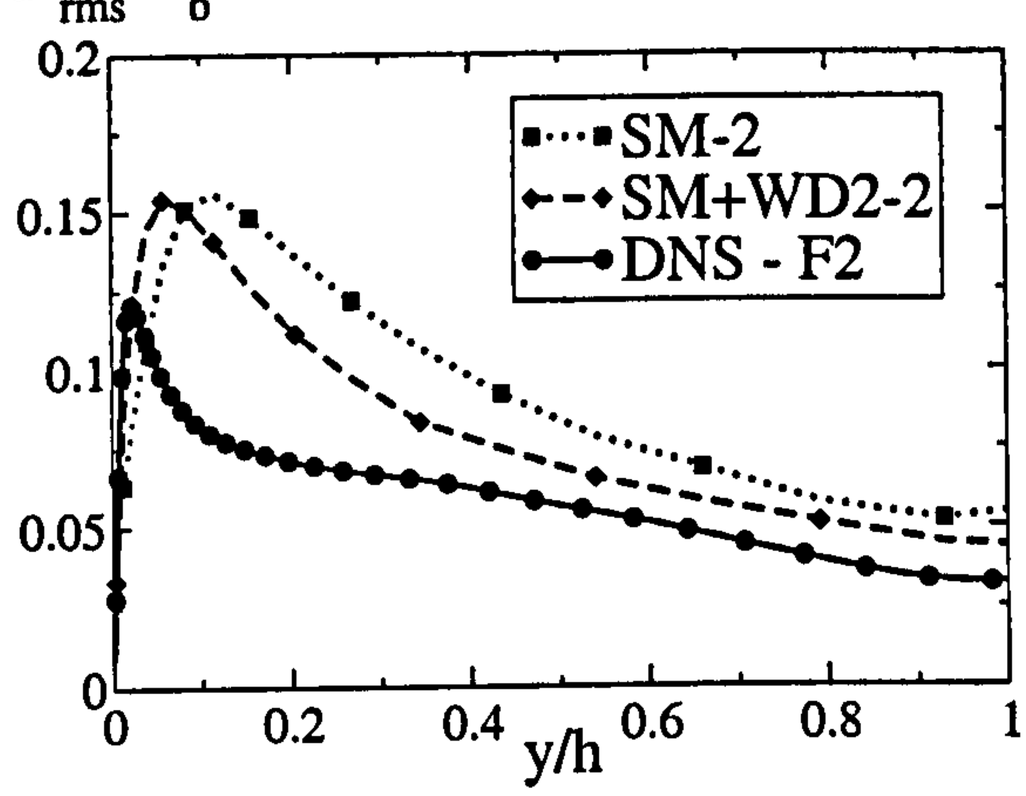

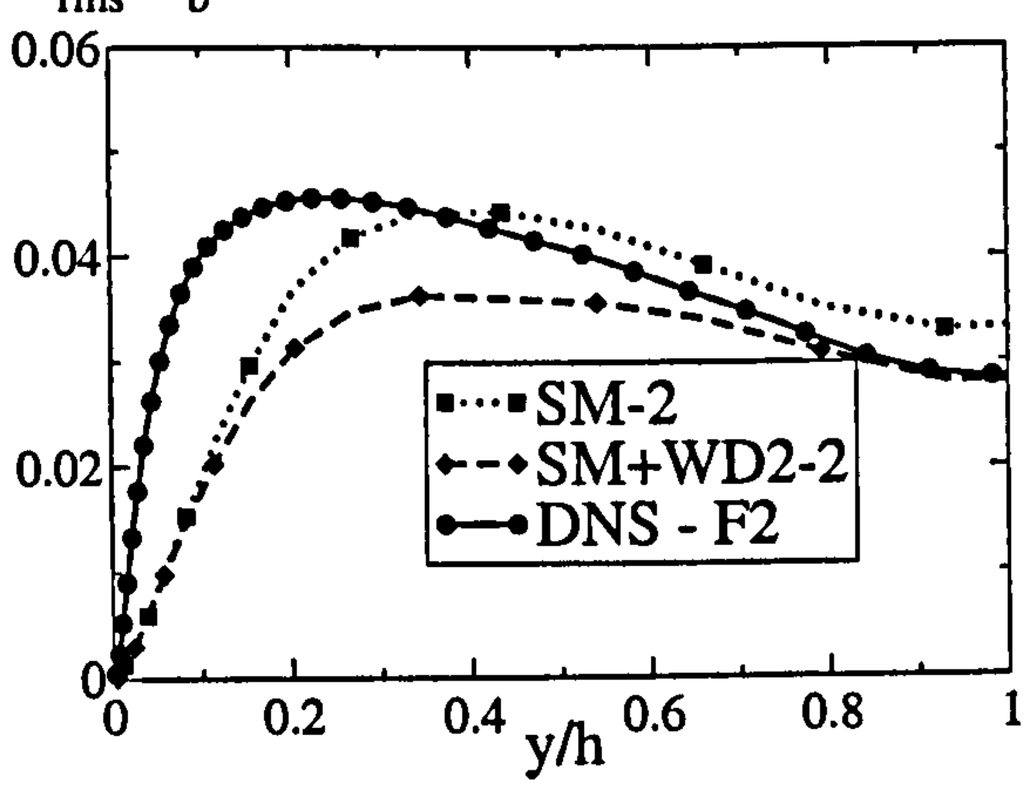

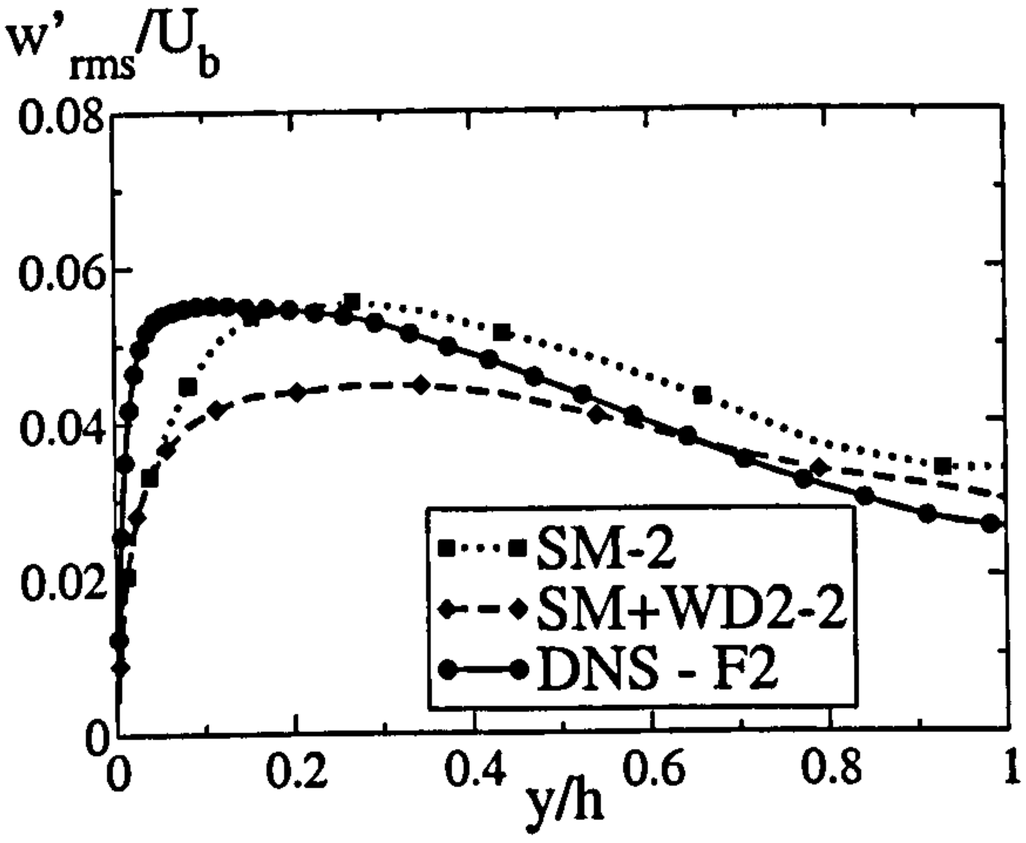

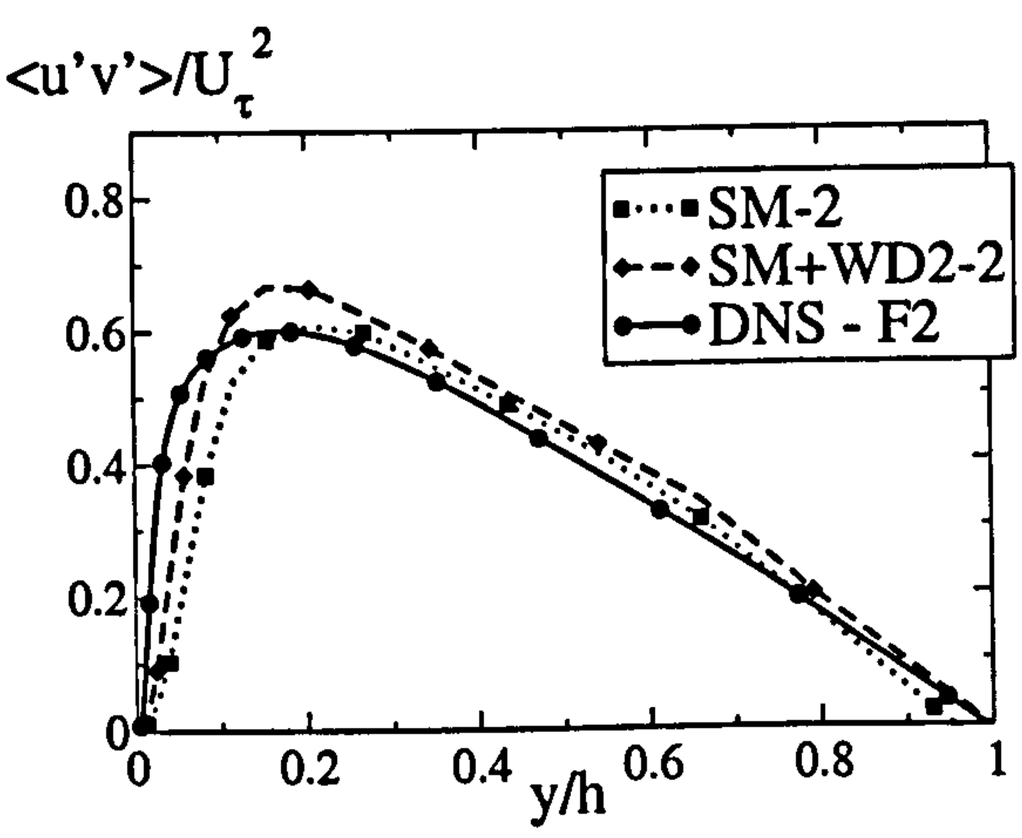

Figure 6.20: Large eddy simulation on the coarsest grid using SM and SM + WD2, comparison with filtered data.

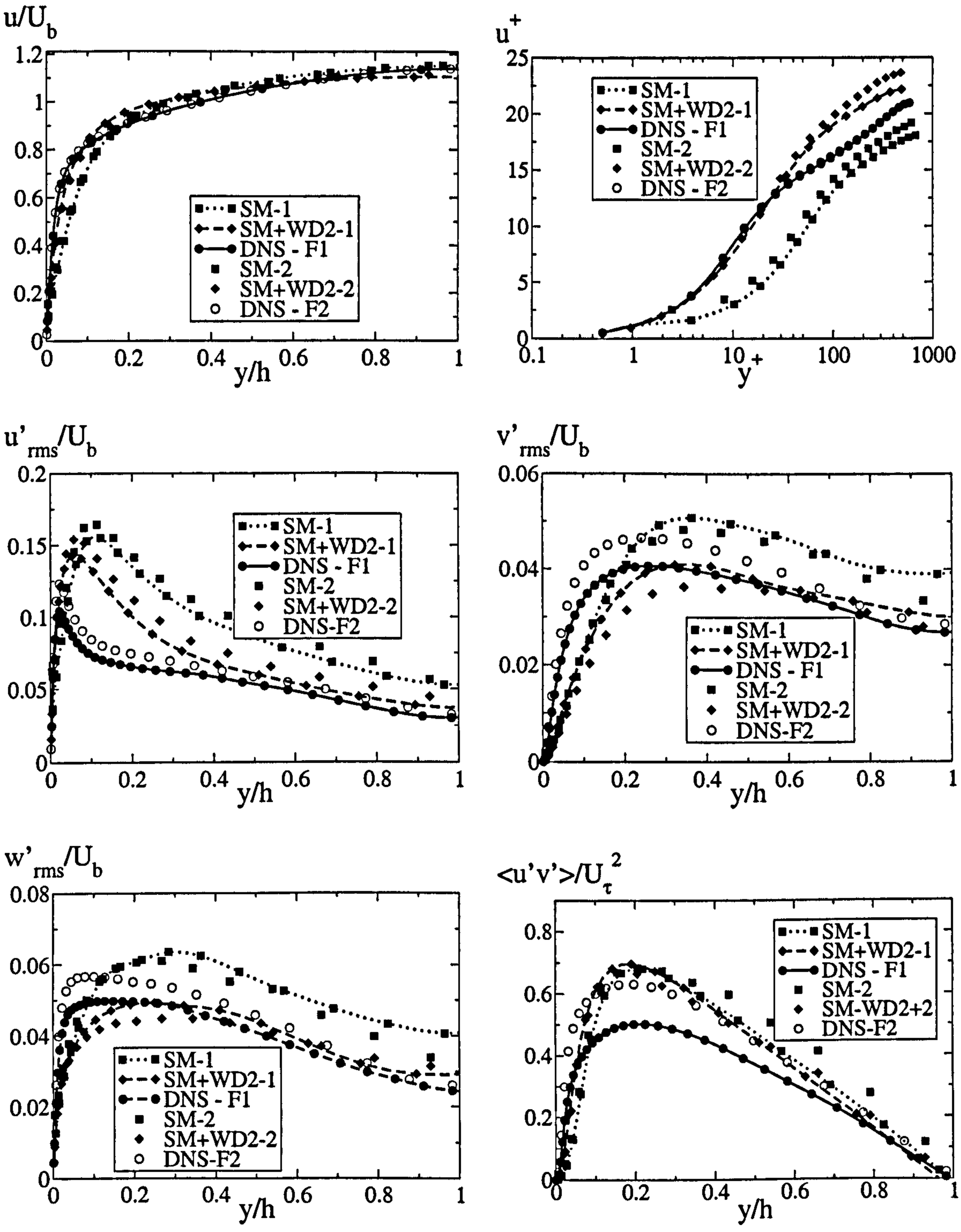

Figure 6.21: Large eddy simulation on the coarsest grid and on the medium grid using SM and SM + WD2, comparison with filtered data.

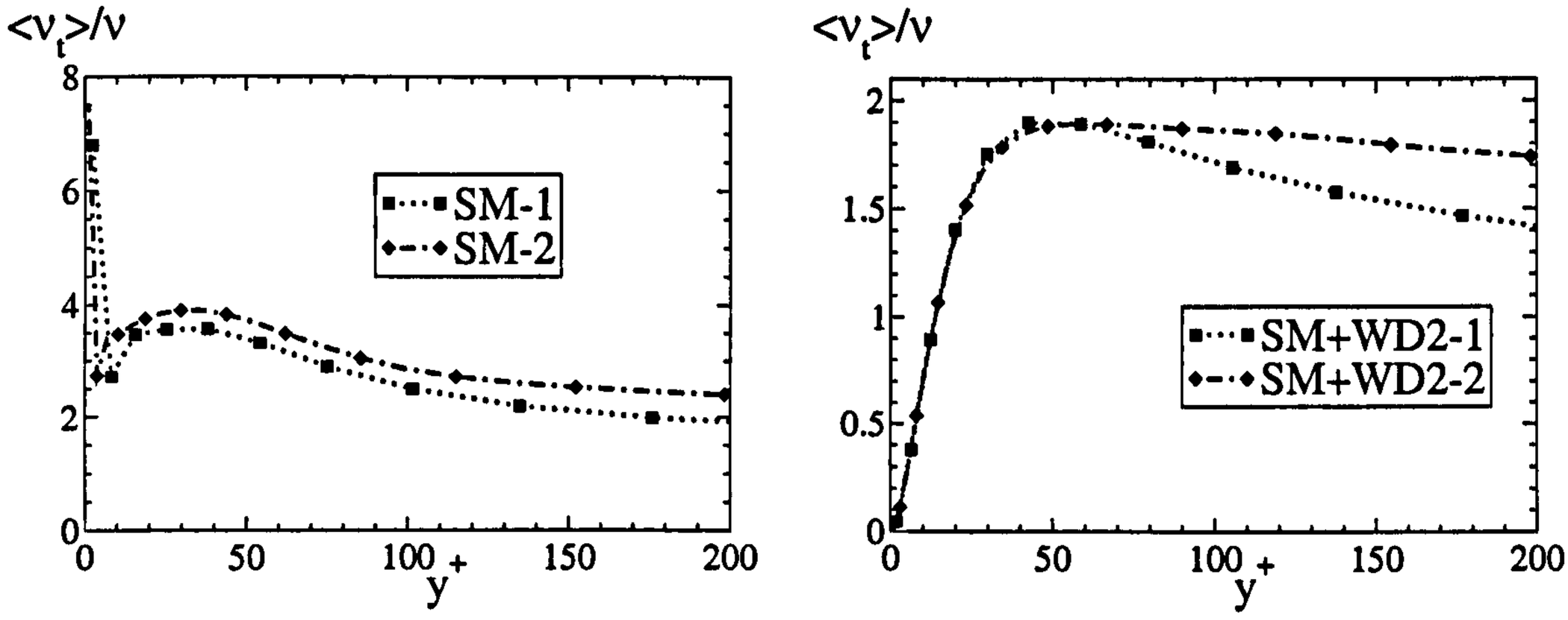

Figure 6.22: Subgrid-scale viscosity obtained with a constant filter width for SM and SM + WD2.

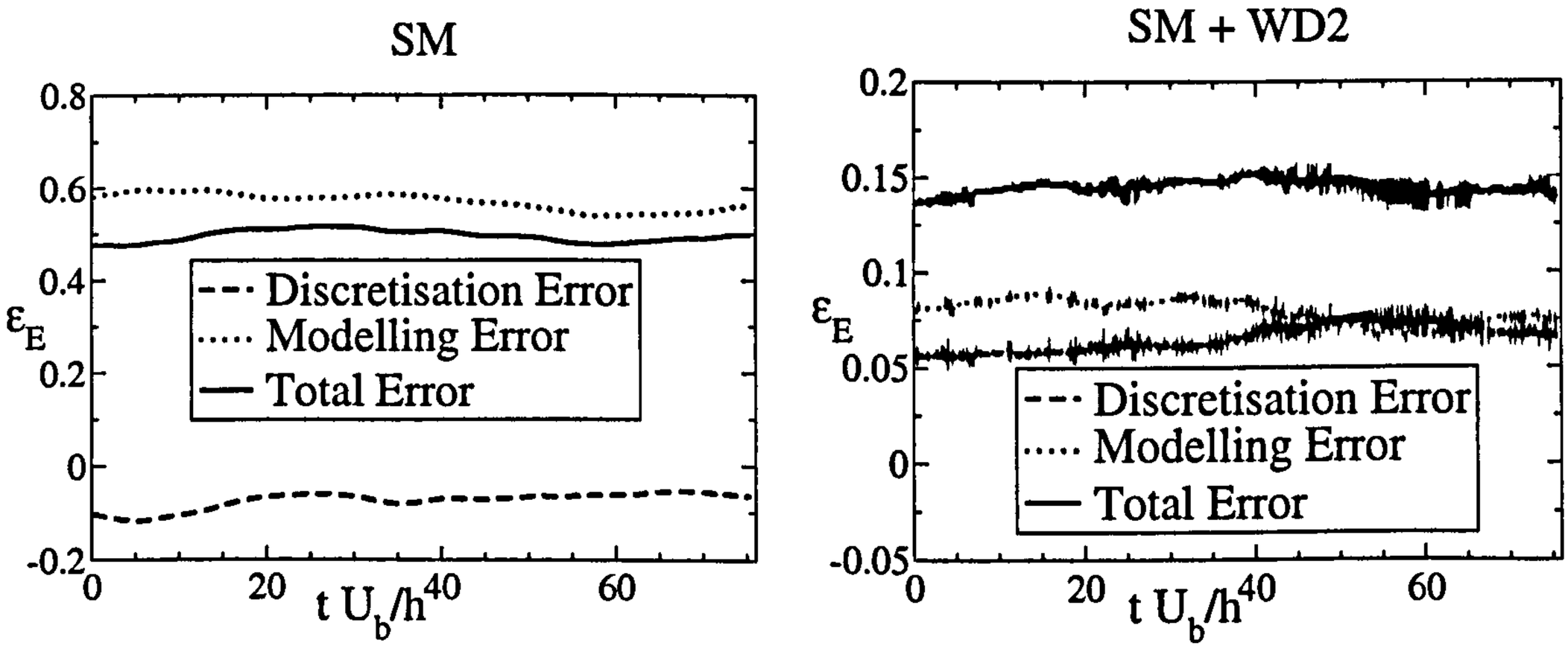

Figure 6.23: Contributions to error in global kinetic energy.

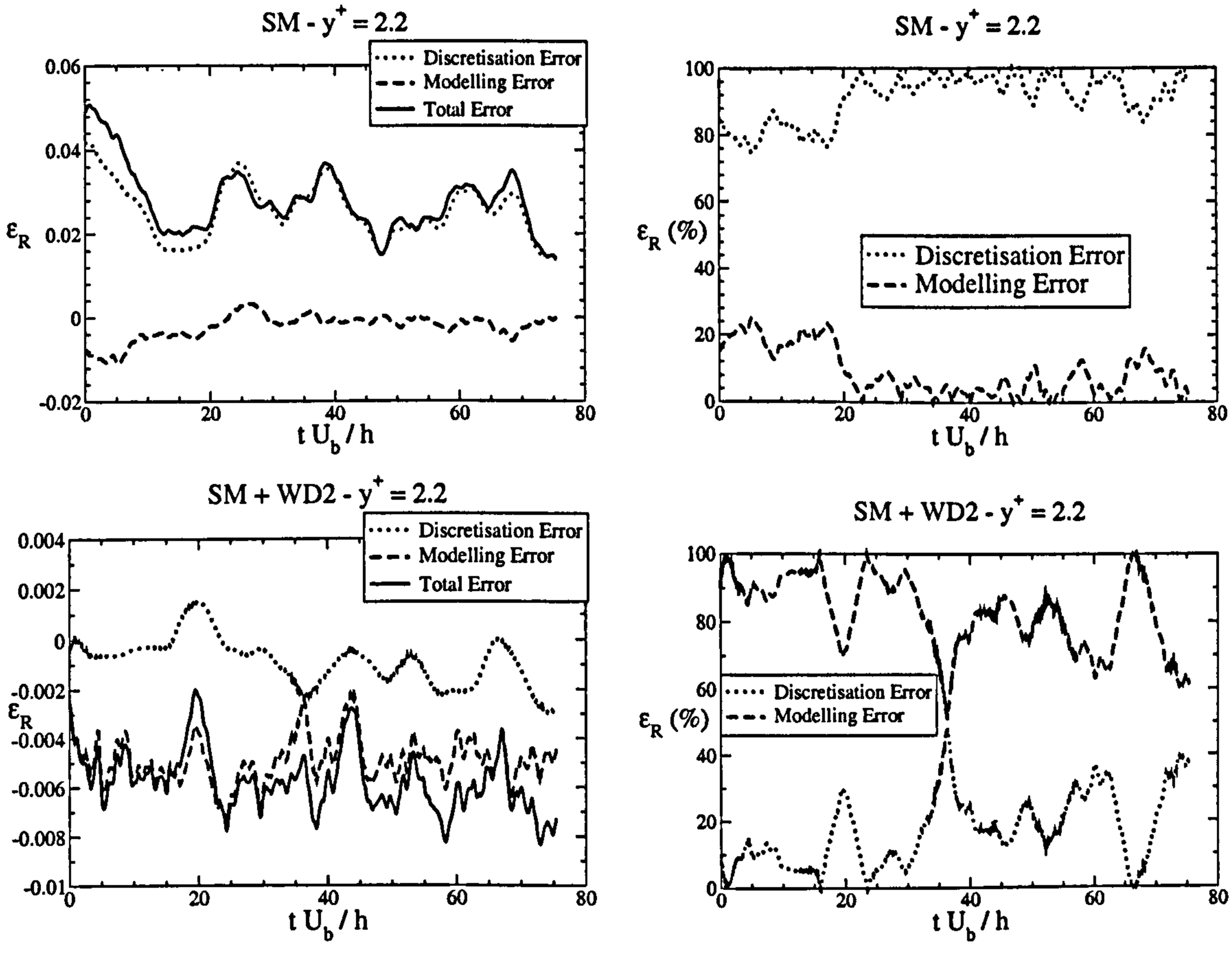

Figure 6.24: Contributions to error in fluctuating velocity at $y^+ = 2.2$.

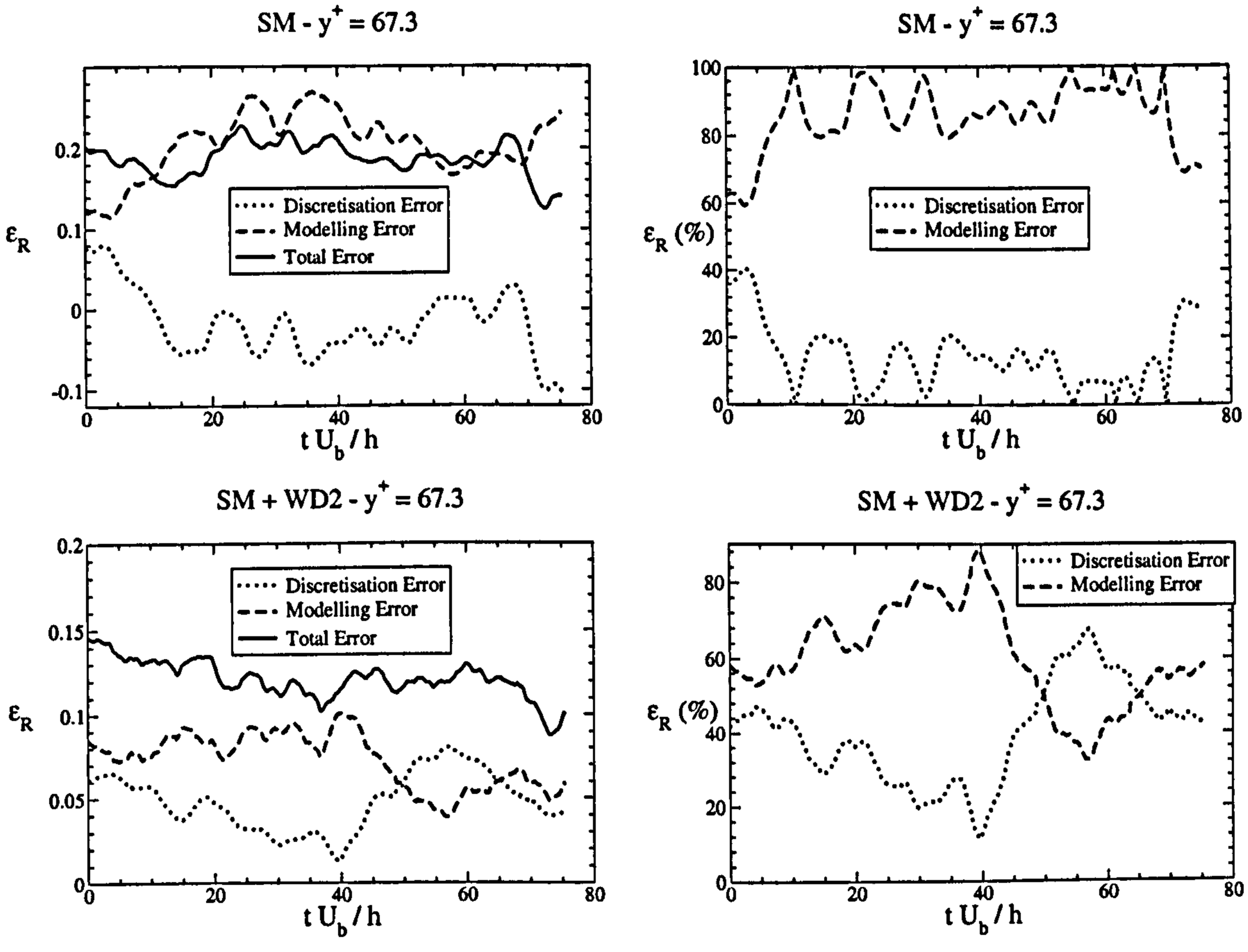

Figure 6.25: Contributions to error in fluctuating velocity at $y^+ = 67.3$.

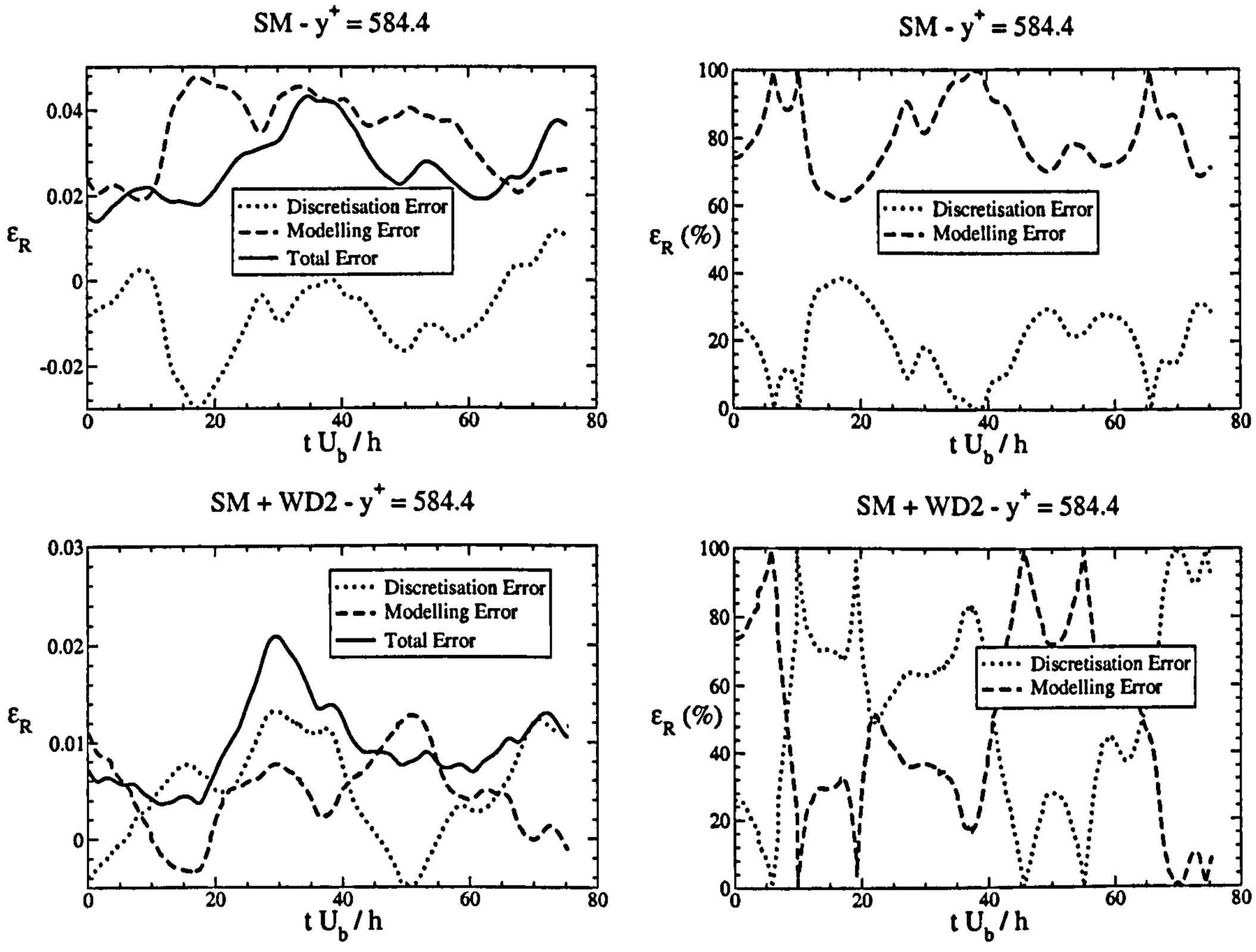

Figure 6.26: Contributions to error in fluctuating velocity at $y^+ = 548.4$.

6.6 Analysis of physics of the turbulent channel flow

6.6.1 Overview

Chapter 5 described a wide range of tools used for the analysis of turbulence. The present section sees these tools put into application on the case of the periodic turbulent channel flow with two main objectives. First, the numerical implementation of these tools has to be validated. Second, the present application provides a good basis for interpreting the information derived from the tools before they are used on other more complex flows considered later.

In Subsection 6.6.2, the turbulence anisotropy, its invariants and realisability are considered. Reynolds-stress and turbulence energy budgets are then examined in Subsection 6.6.3. Two-points spatial correlations and spectra in wave-number space are investigated in Subsection 6.6.5, while Subsection 6.6.4 deals with the spectra in the frequency domain. Finally, Subsection 6.6.6 deals with coherent-structure identification.

In Subsections 6.6.2 to 6.6.3, the case examined corresponds to CM1 in Table 6.1 for which DNS data reported by Moser et al [161] are available for comparison. As CM1 is a LES computation, a subgrid-scale model is employed, here chosen to be the WALE model with $C_w = 0.1$. Statistics were collected over a period of 20 flow-through times.

6.6.2 Anisotropy-invariants map

Figure 6.27 shows the anisotropy-invariants map for the present channel flow case. The map is a plot of $II = -b_{ij}b_{ij}/2$ vs. $III = b_{ij}b_{jk}b_{kj}/3$, as proposed by Lumley [133] who shows that any turbulent state within the triangular domain is realisable. In agreement with the observations made by Mansour et al [140], the turbulence state varies from nearly isotropic at the channel centre, $II = III = 0$, to the two-component state, $II = -III - 1/9$, close to the wall. Up to $y^+ \approx 9$, the wall suppresses the normal component of the velocity to an extent rendering turbu-

lence to contain almost only fluctuations parallel to the wall. This is consistent with kinematic considerations which show that $v'v' = O(y^4)$ while $u'u' = w'w' = O(y^2)$. Further away, the turbulence behaves in accord with a process identified as axisymmetric expansion, until the centre of the channel where turbulence approaches an isotropic state.

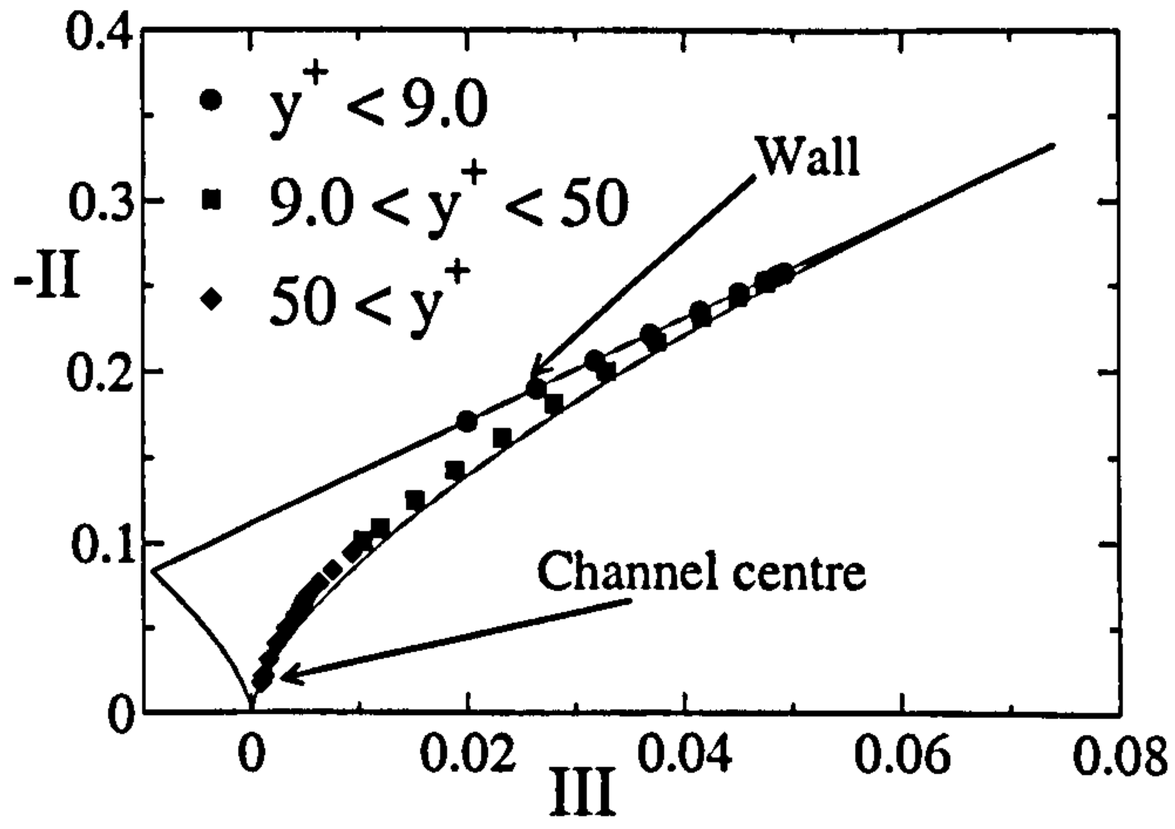

Figure 6.27: Anisotropy invariants map for a channel flow ($Re_\tau = 180$).

6.6.3 Turbulence-energy and Reynolds-stress budgets

In the present subsection, the energy and Reynolds-stress budgets, described in Section 5.4, are assembled. Details of the precise data-recording and processing methodology are given in Appendix C. The different terms for the budgets presented in this subsection are scaled by u_τ^4/ν. The results are then compared with DNS data reported by Moser et al [161].

Figures 6.28 and 6.29 show the various contributions to the turbulence-energy budget. All terms evaluated from the LES compare well with the corresponding terms obtained from the DNS data. Production balances dissipation away from the wall. At the wall, the maximum dissipation occurs because, although the turbulence energy vanishes, the fluctuating strain does not. There, the dissipation is only balanced by the viscous diffusion, all other terms approaching zero. Mansour et al [140] observe that, at the wall, the dissipation attains the value of 0.166.

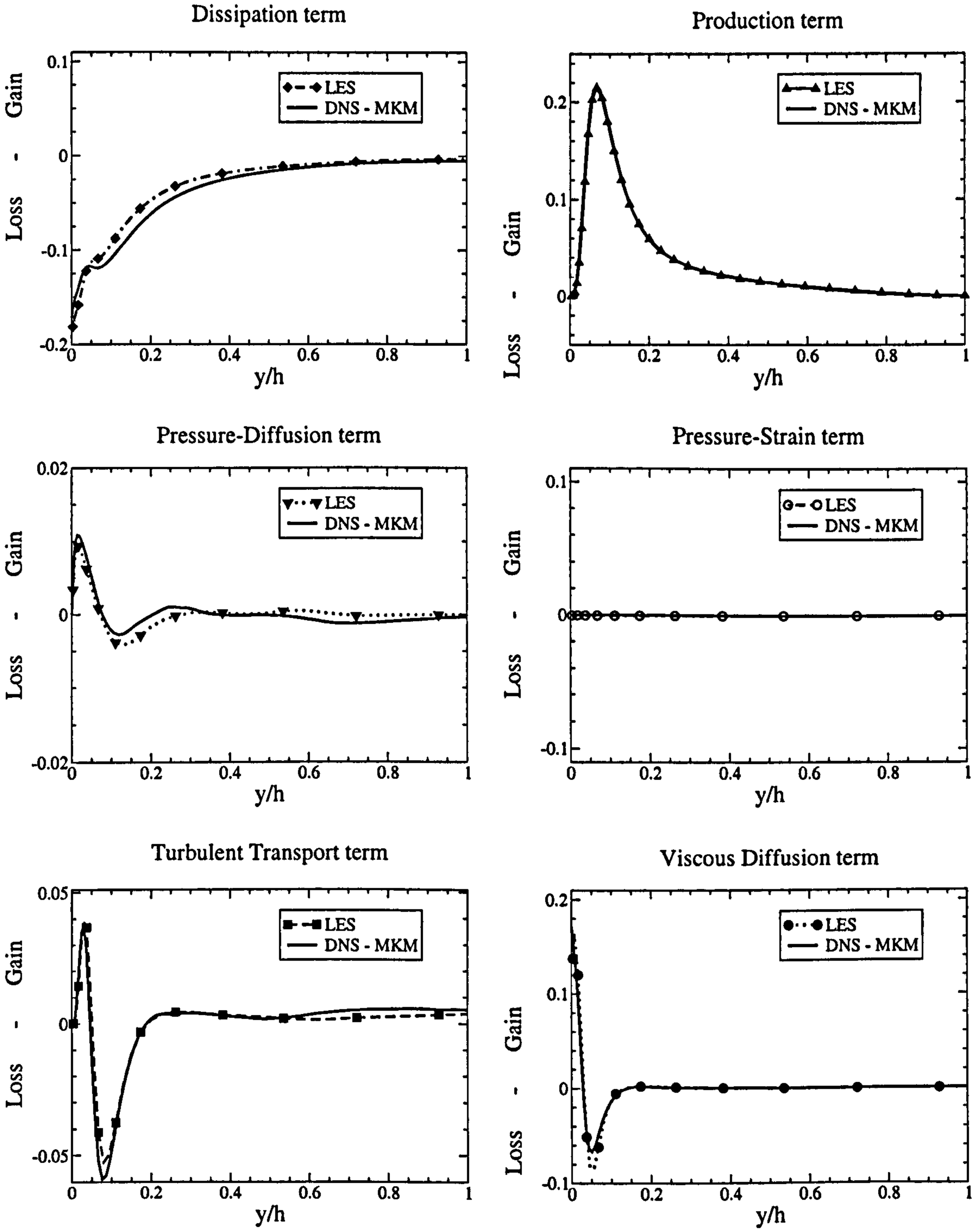

Figure 6.28: Terms forming the turbulence energy budget for a channel flow at $Re_\tau = 180$.

In the present computation, this value is approximatively 0.18. At approximatively $y^+ \approx 12$, a peak in production is reached which is only partially removed by the dissipation, the rest being removed by turbulence transport which moves turbulence energy towards the wall. Noteworthy is the fact that the production peak, located at $y^+ \approx 12$, corresponds to the point where viscous and shear stresses are equal. Figure 6.29 shows that the balance is not completely satisfied mainly because of the inaccurate evaluation of the dissipation, which is associated with the smallest scales.

Figure 6.30 shows the different terms contributing the budget for the streamwise stress, while Figures 6.31 to 6.33 show the budgets for the three normal stresses. The shear stress budget is presented Figure 6.34. The data plotted in Figure 6.30 again agree well with the data of the DNS performed by Moser et al [161]. This observation also applies to the wall-normal, spanwise and shear stresses budgets, and a term-by-term comparison is not therefore included.

In the streamwise-stress budget (Figures 6.30 and 6.31), the main gain term above the viscous layer is the production which, above the buffer layer, is balanced principally by the dissipation. There is no production in the two other normal stresses, as shown in Figures 6.32 and 6.33, and these stresses are elevated by the pressure-strain terms which transfer turbulence energy from the streamwise component to the other two. For the streamwise-stress budget (Figure 6.31), it is also observed that, towards the wall, the rise in turbulent transport is such that it becomes a gain term, compensating the increase in dissipation. Towards the wall, the production decreases smoothly towards zero while the dissipation is now balanced by viscous diffusion, which has, now, become the main gain term. The pressure-diffusion plays an insignificant role while the pressure-strain term is draining energy from the streamwise stress. For the wall-normal stress budget presented in Figure 6.32, the absence of production term has already been noted, and the dominant gain term is, away from the wall, the pressure-strain, which mostly balances the dissipation and, partially also the pressure-diffusion and the turbulent transport. In the near-wall region, pressure-diffusion, now the gain term, is balanced by pressure-strain, which has become a loss term. At the wall, all terms vanish. Figure 6.33 shows the spanwise-stress budget. The absence of production has been already

noted. The main loss term is the dissipation which, away from the wall, is balanced by the pressure-strain term and, very close to the wall, by viscous-diffusion. Figure 6.34 shows the contributions to the shear stress ($- < u'v' >$) budget. Away from the wall, the dominating term is the production, balanced by pressure-strain, with the dissipation being minimal. Towards the wall, the dominant terms are now pressure-strain and pressure-diffusion, and these balance each other, while the other terms vanish.

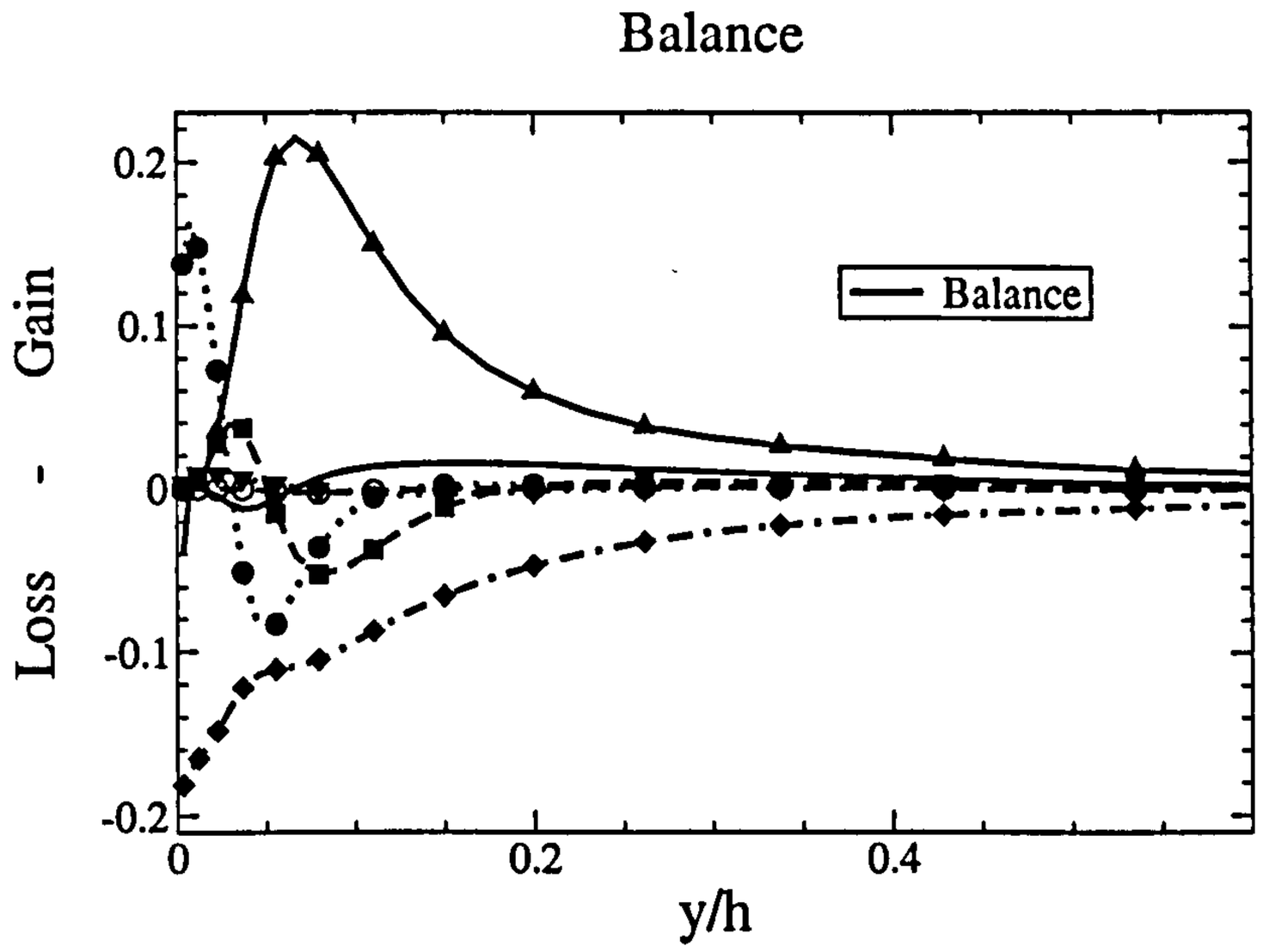

Figure 6.29: Turbulence-energy budget for a channel flow ($Re_\tau = 180$). For the symbols meaning, see Figure 6.28

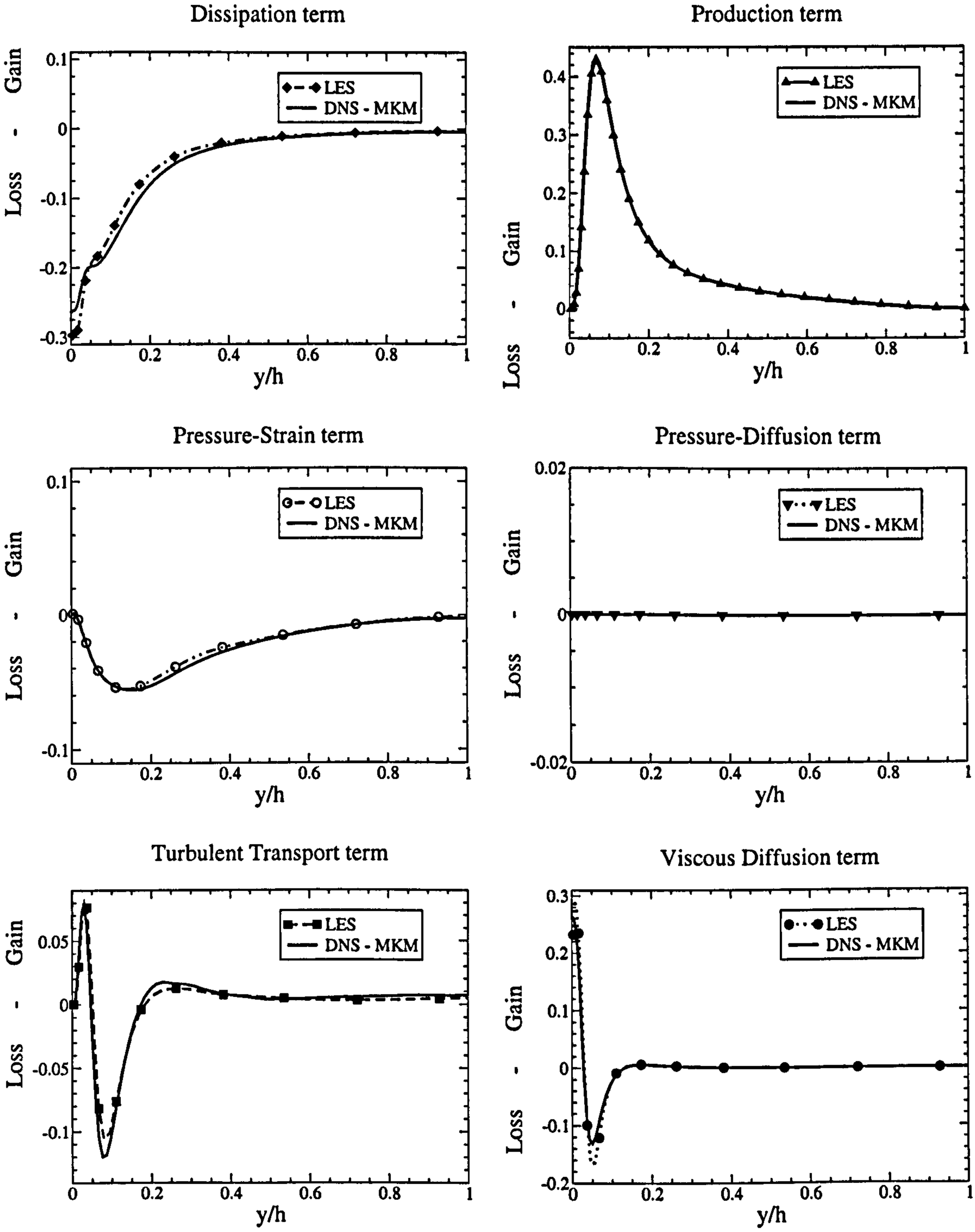

Figure 6.30: Terms forming the streamwise-Reynolds-stress budget for a channel flow ($Re_\tau = 180$).

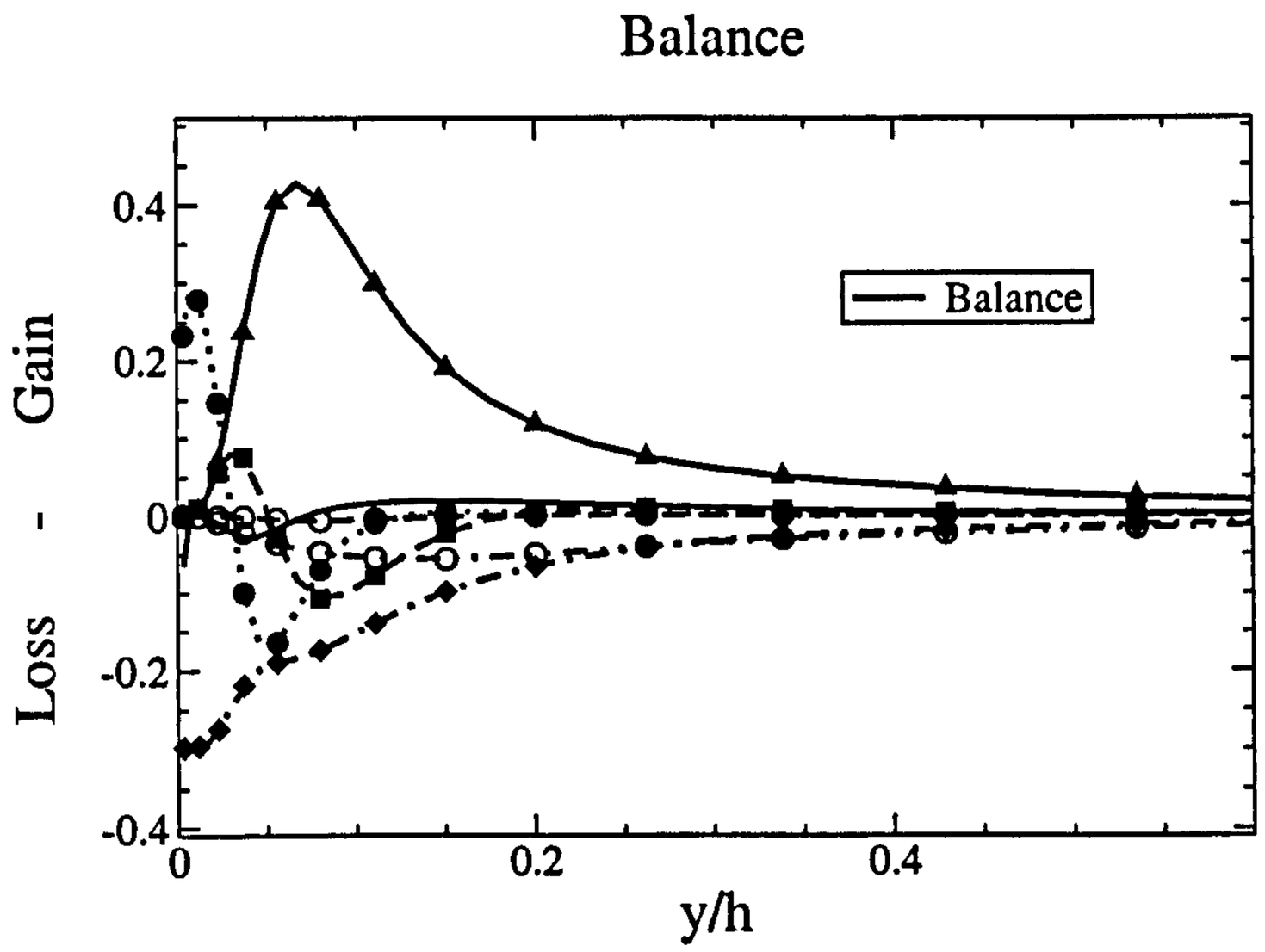

Figure 6.31: Streamwise-Reynolds-stress budget for a channel flow ($Re_\tau = 180$). For the symbols meaning, see Figure 6.30

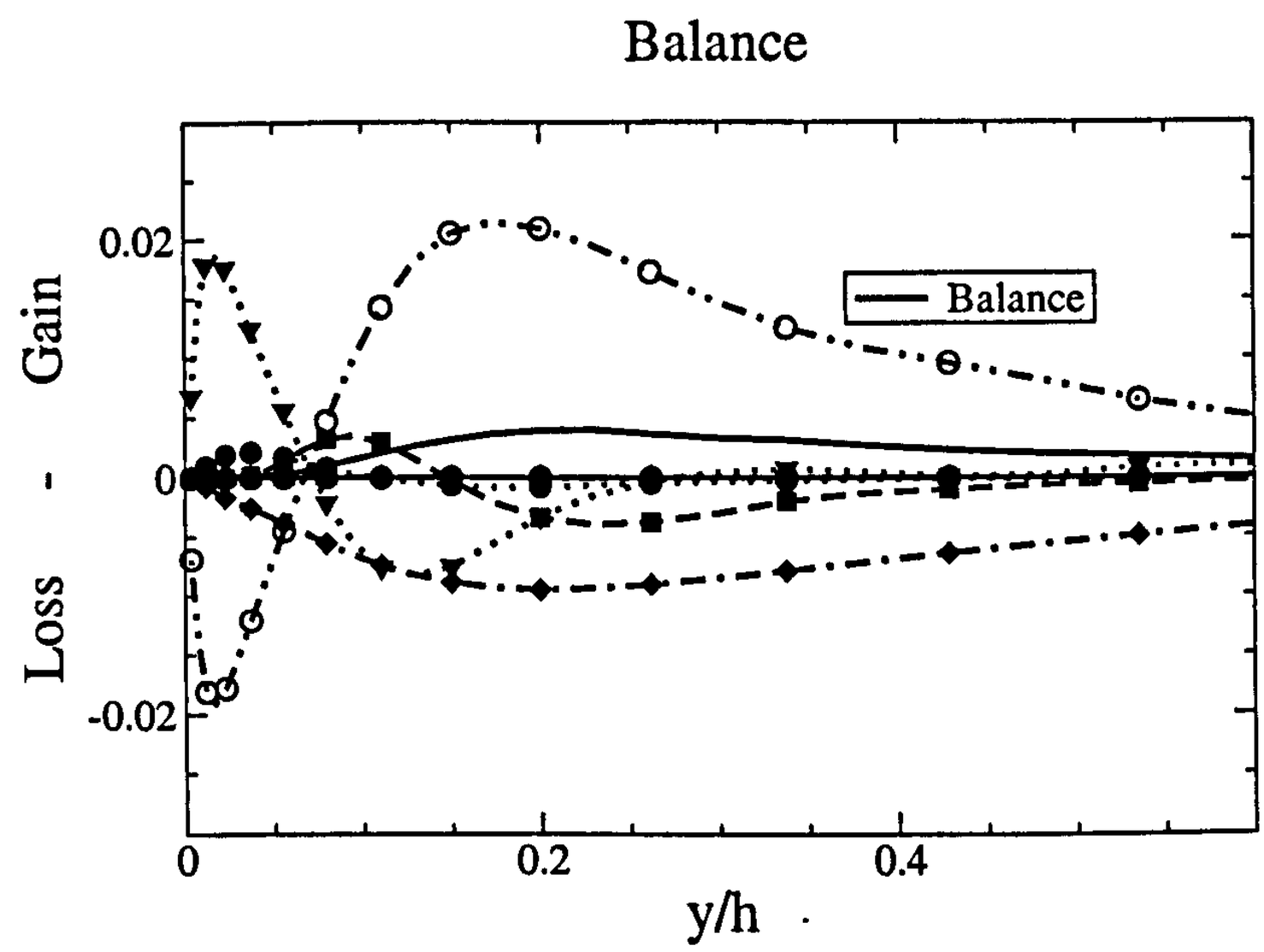

Figure 6.32: Wall-normal Reynolds-stress budget for a channel flow ($Re_\tau = 180$). For the symbols meaning, see Figure 6.30

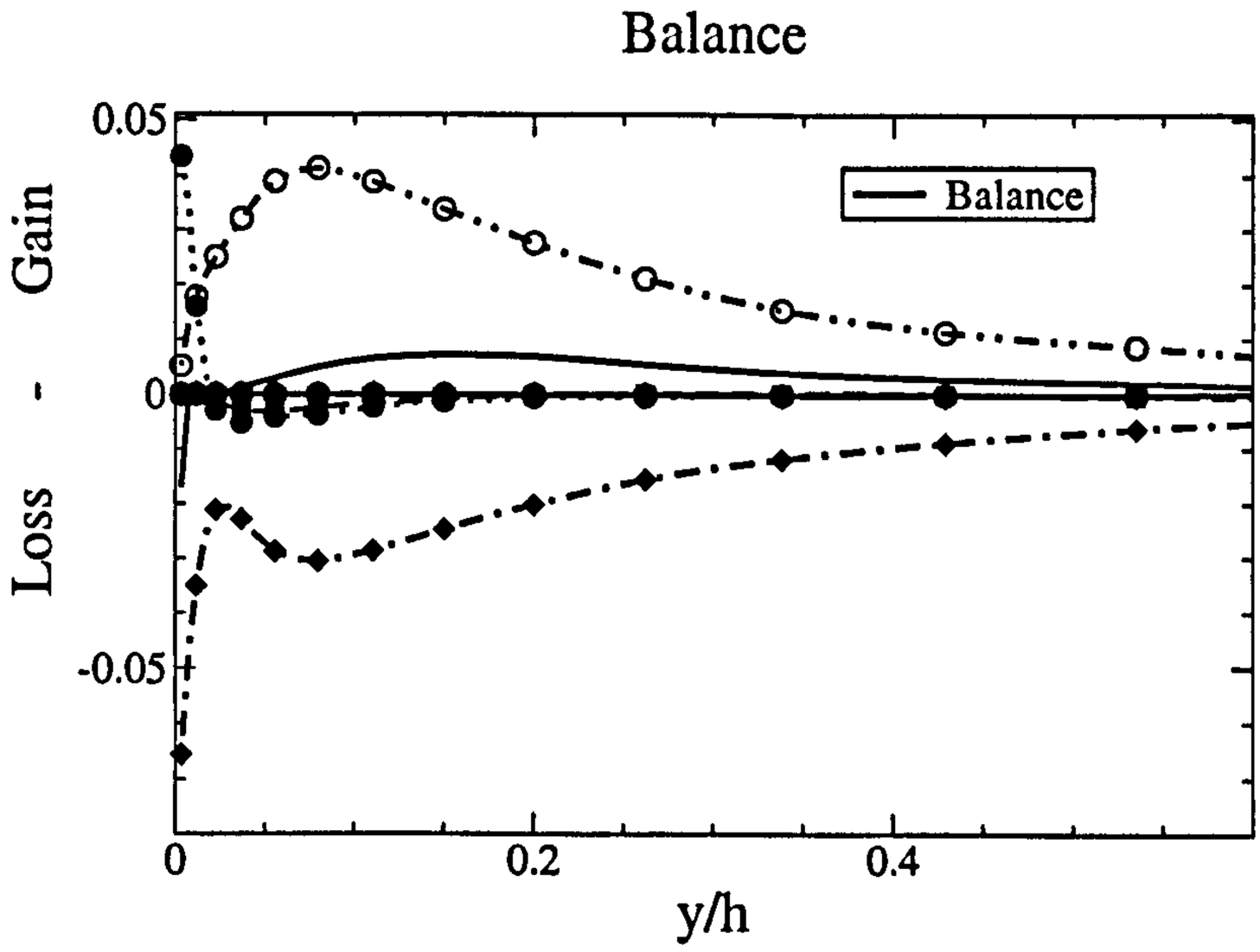

Figure 6.33: Spanwise-Reynolds-stress budget for a channel flow ($Re_\tau = 180$). For the symbols meaning, see Figure 6.30

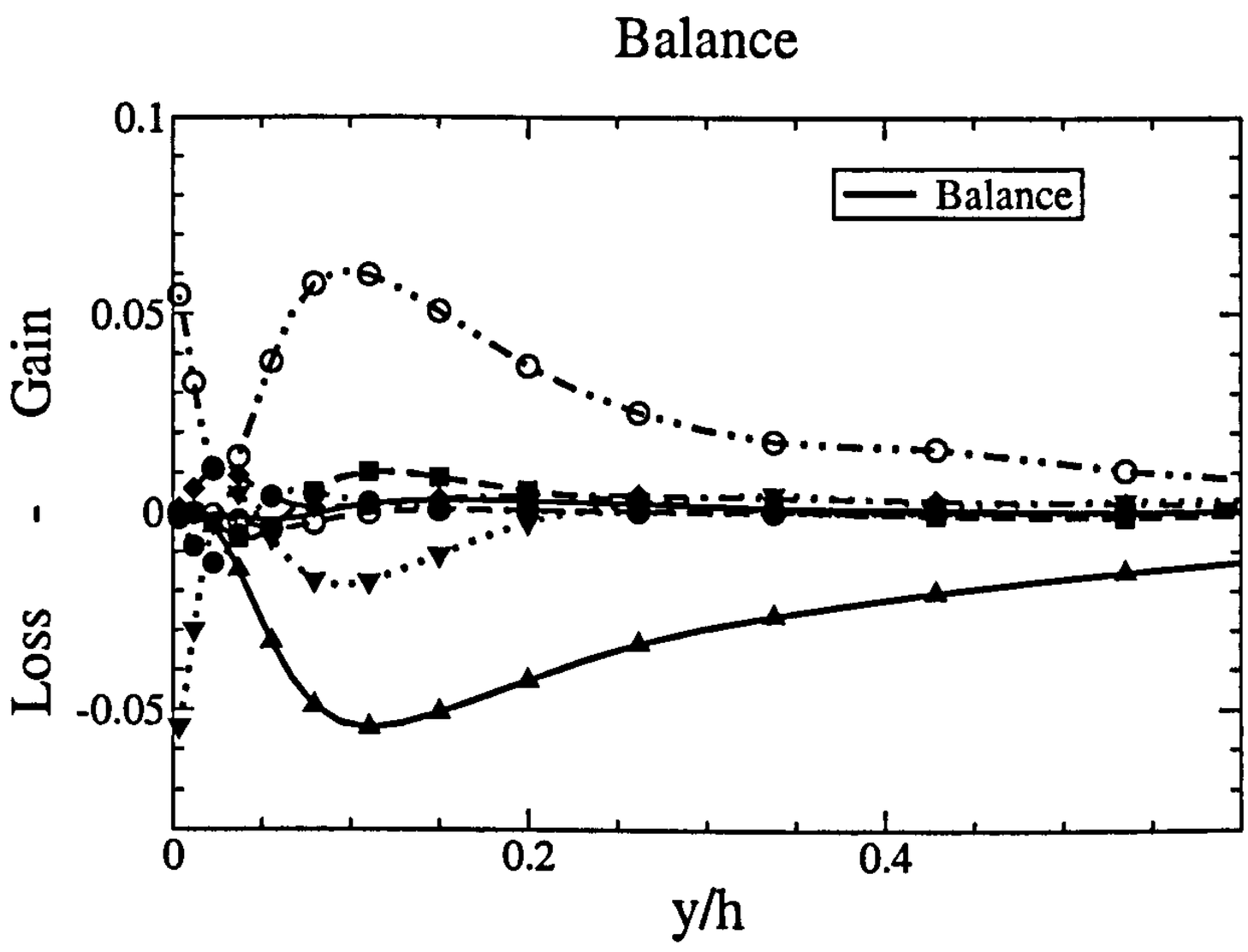

Figure 6.34: Shear-stress budget for a channel flow ($Re_\tau = 180$). For the symbols meaning, see Figure 6.30

6.6.4 Spectral analysis in the frequency domain

Time-signals were recorded at various wall-normal locations over a period of 12 flow-through-times with a time-step $\Delta t = 0.001$ ($t = h/U_b$). A Fourier transform was performed on these signals and the resulting spectra are plotted in Figure 6.35 for four locations. These spectra are expressed in terms of frequency, and can, in principle, be related to the spatial spectra through Taylor's hypothesis. This is only possible, however, if the local mean velocity is much larger than the corresponding fluctuating velocity. Hence, the equivalence is not valid in near-wall regions.

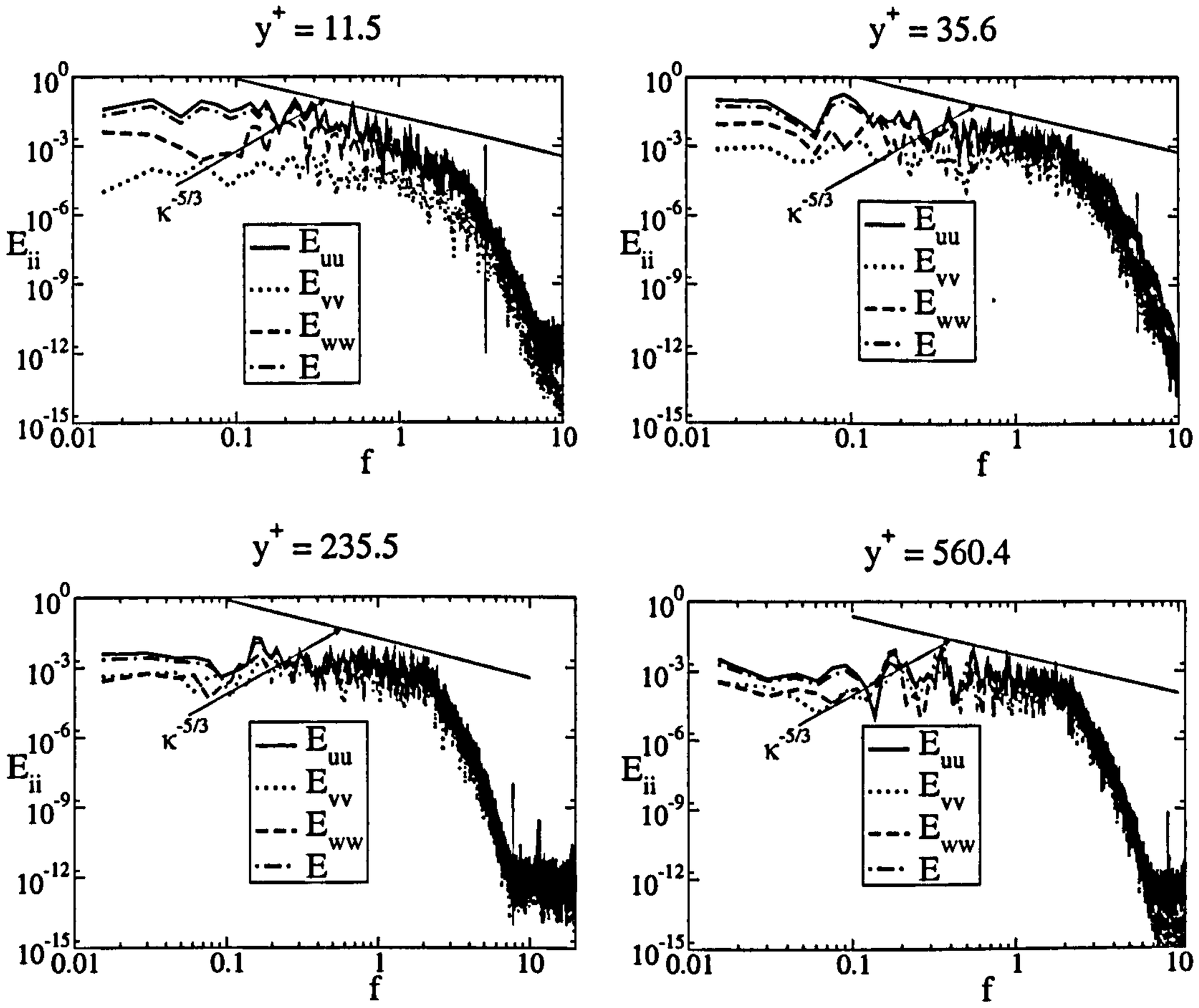

Figure 6.35: Velocity and energy spectra in the frequency space at four different locations for the channel flow.

The maximum cut-off frequency is determined by $f_c = < u > /2\Delta_x$ A short vertical line indicates the location of the cut-off for each of the spectra presented in Figure 6.35. For the spectra located at $y^+ = 11.5$ and $y^+ = 35.6$, the ratio $< u > /u_{rms}$ are equal to 3.1 and 5.6, respectively. Hence, Taylor's hypothesis may not be ap-

plicable for these two cases. For the two other locations, this ratio is higher than 10.

6.6.5 Spatial two-point correlations and spectra in wave-number space

Two-point correlations and spectra were introduced in Sections 5.6 and 5.7, respectively. The two-point correlations allow an assessment of whether the size of a computational domain is large enough to include all the resolved scales. They also provide informations on how well the near-wall streaks are resolved. Energy spectra help understanding the way in which the turbulence energy is distributed and transferred among the different scales. It is also useful in judging the quality of the grid resolution.

The data presented here were generated using meshes CM4 and CM5 (see Table 6.1) and with the Smagorinsky model ($C_s = 0.1$). Statistics were collected over a period of 12 flow-through-times, and results are compared with the data of Moser et al [161]. The difference between CM4 and CM5 is the spanwise extent which, in the case of CM5, is one third smaller than for CM4. With 64 spanwise planes used in both cases, the resolution in CM5 is correspondingly lower.

Figures 6.36 and 6.37 show streamwise and spanwise two-points correlations for all three components of the fluctuating velocity components at two different wall-normal locations. As Δx and Δz increase, the correlation levels rapidly decrease toward zero well before the mid-box locations in both directions. As expected, R_{uu} decreases at the lowest rate, reflecting the fact that the streamwise length scale of the energetic eddies are considerably larger in this direction than others, especially near the wall. The results thus demonstrate that the computational box is large enough in both homogeneous directions, so that even the largest eddies are well-contained within the computational domain. The fact that this is also true for the box with a smaller spanwise extent shows this box size, used in many other simulations discussed in the present Chapter, to be conservative. Thus, if the need arises, the computational costs can be reduced by reducing the box size without

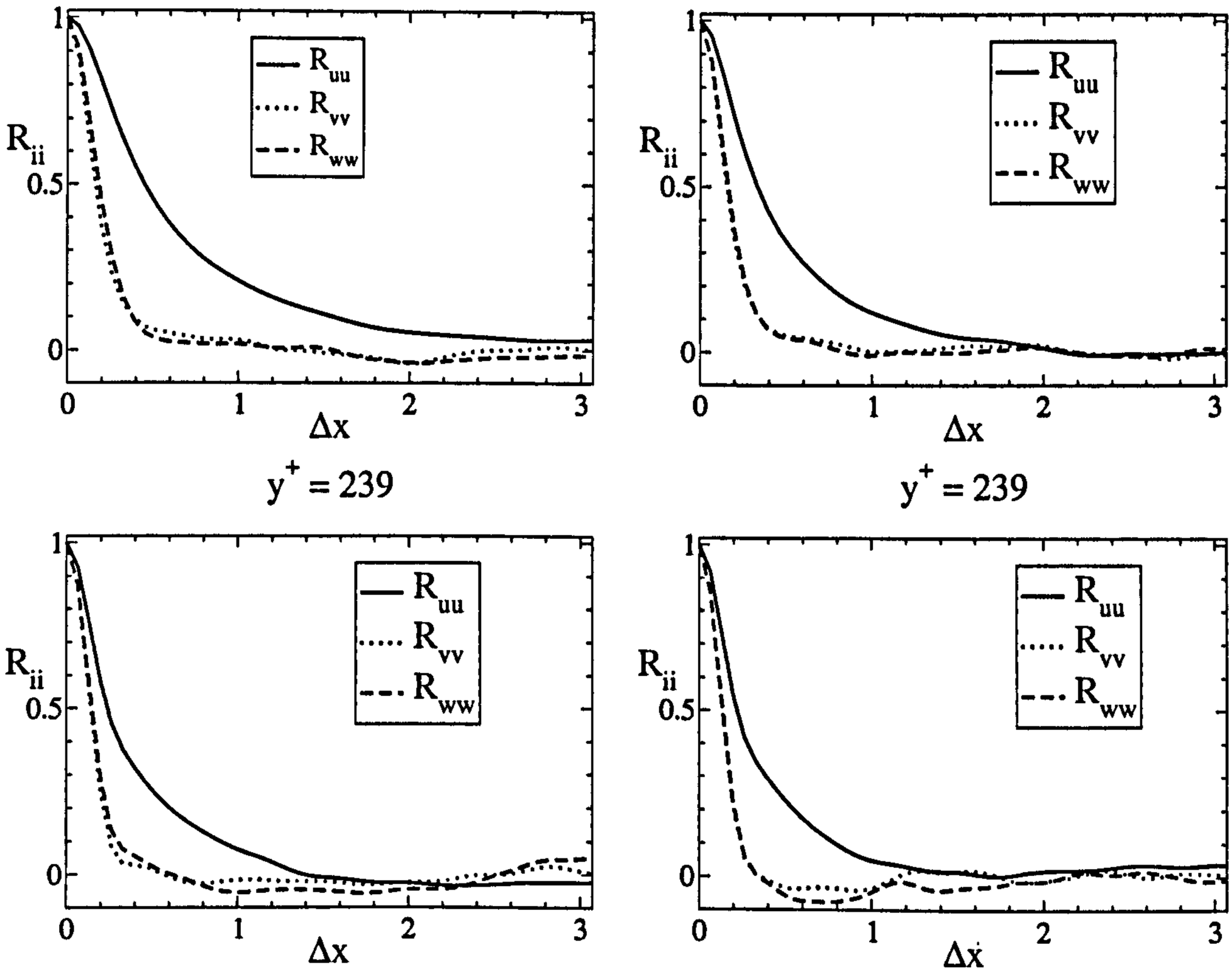

(a) Larger box

(b) Smaller box

Figure 6.36: Two-point correlations in the streamwise direction for the channel flow ($Re_\tau = 590$).

undue effect to the extent of decorrelation.

Figure 6.38 shows the two-point correlations plotted at $y^+ = 11.7$ for both computational boxes with the separation distance expressed in wall units (Δz^+). For the smallest of the two boxes, R_{uu}, R_{vv} and R_{zz} reach a minimum at $\Delta z^+ \approx 85$, $\Delta z^+ \approx 35$ and $\Delta z^+ \approx 65$, respectively. The location of the first minimum corresponds to the mean distance between high and low-speed fluids. The mean spacing between the streaks (regions of relatively slow moving fluids, with a velocity about half of the local mean) corresponds to twice this distance. This distance is larger than $\Delta z^+ \approx 100$, however, which is the usual distance separating two streaks (see Kim et al [106]). As in the computation of Moin and Kim [159], lack of resolution is to blame for the streaks spacing being too large. Kim et al [106] associate the

minimum in R_{vv} with the presence of streamwise vortical structures, $\Delta z^+ \approx 35$ corresponding to the streamwise vortices averaged diameter. Again, this value is somewhat larger than the one recorded by Kim et al [106]. The minimum in R_{ww}, located at $\Delta z^+ \approx 65$, compared to $\Delta z^+ \approx 50$ as recorded by Kim et al [106], may indicate the presence of counter-rotating vortex pairs or may be due to the splatting effect that can be caused by a single vortex impinging on the wall. For the larger box, this pattern, although present, is more difficult to identify, due to the lack of adequate spanwise resolution.

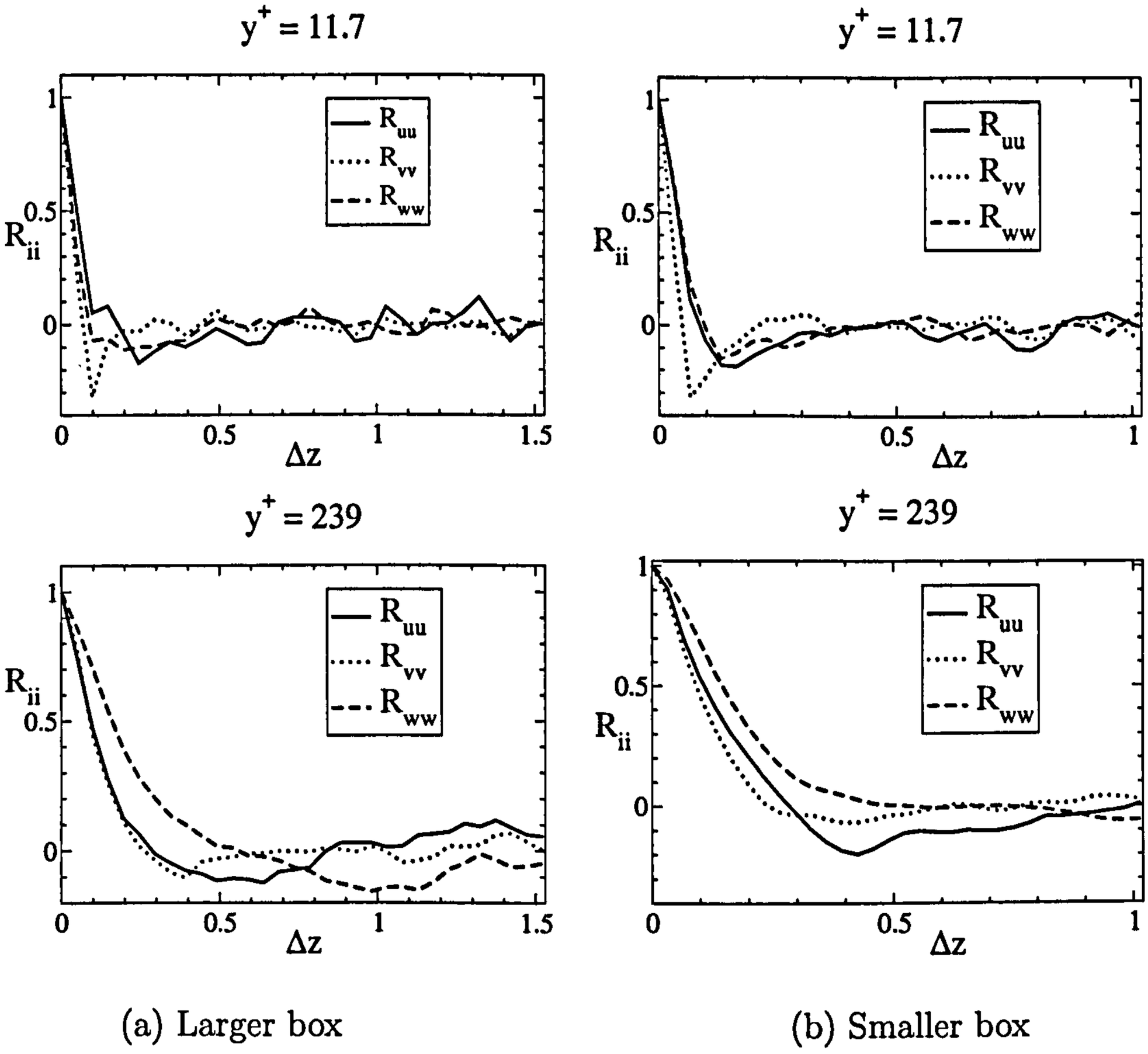

(a) Larger box (b) Smaller box

Figure 6.37: Two-point correlations in the spanwise direction for the channel flow ($Re_\tau = 590$).

Figures 6.39 and 6.40 show one-dimensional spectra for the energy and its three components in the wave-number space at two wall-normal locations. Also plotted is

a straight line with a *-5/3* slope which indicates the inertial range in which energy is transfered from larger to smaller scales. The simulation clearly returns this range.

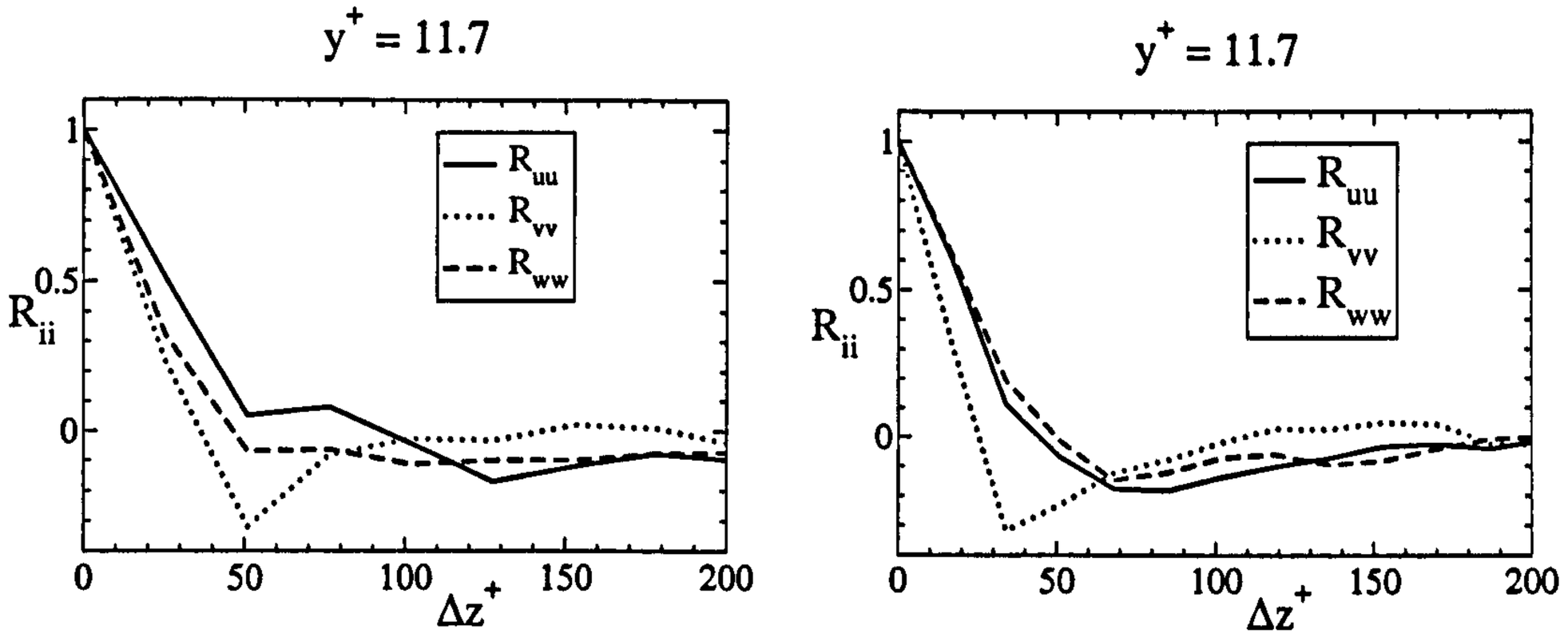

(a) Larger box

(b) Smaller box

Figure 6.38: Two-point correlations in the near-wall region in the spanwise direction for the channel flow ($Re_\tau = 590$) in wall units.

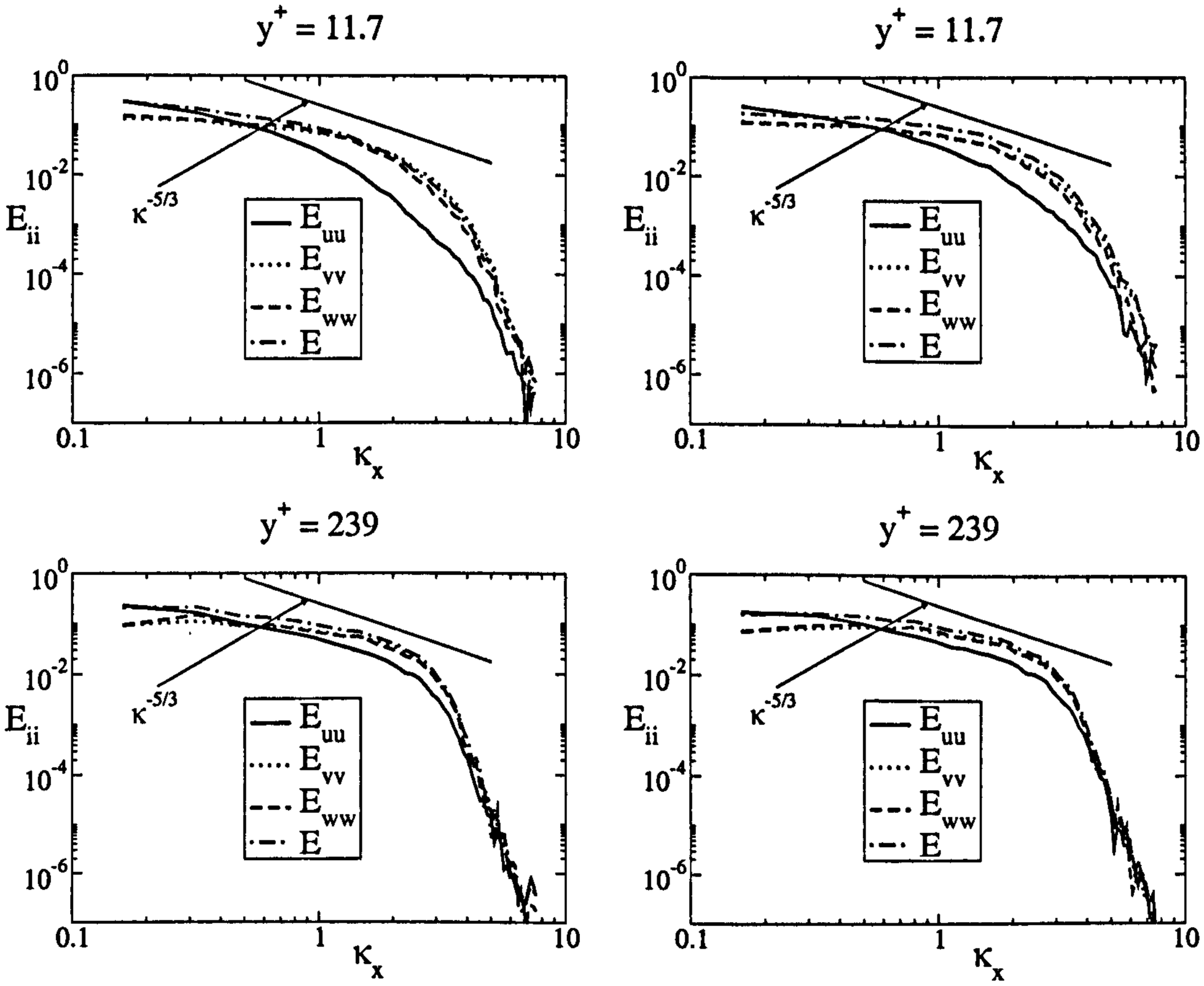

(a) Larger box

(b) Smaller box

Figure 6.39: Velocity and turbulence-energy spectra in the streamwise direction for the channel flow ($Re_\tau = 590$).

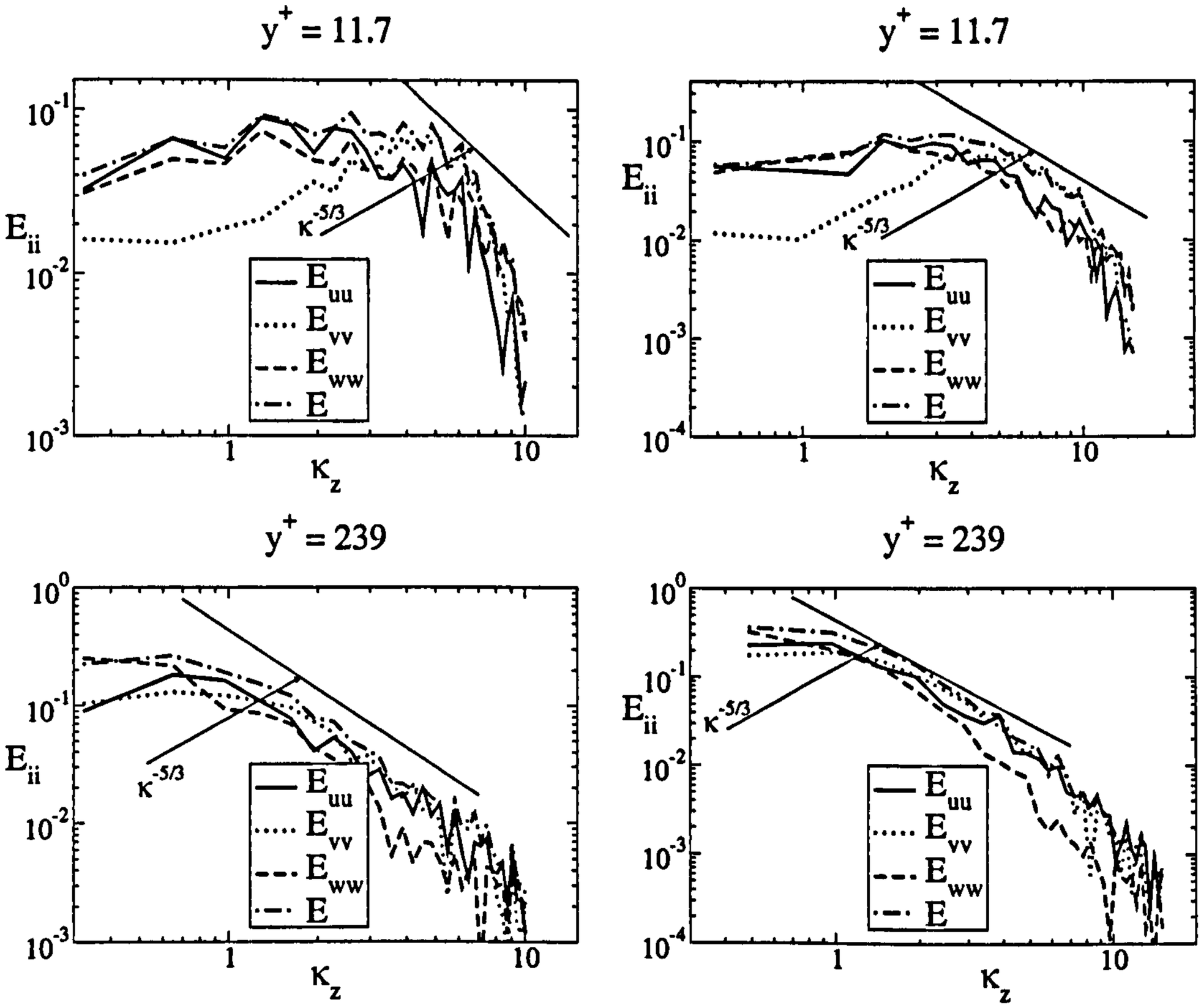

(a) Larger box (b) Smaller box

Figure 6.40: Velocity and turbulence-energy spectra in the spanwise direction for the channel flow ($Re_\tau = 590$).

6.6.6 Coherent structures identification

A variety of criteria designed to identify coherent structures were introduced in Section 5.8. Their performance and characteristics are here illustrated by reference to an instantaneous field of a DNS computation performed by CERFACS[†], a contribution to the European-funded project LESFOIL [45]. Based on the friction velocity and channel half-width, the Reynolds number of the flow is 180. The use of these DNS data, rather than others originating from one of the LES simulations performed in this chapter, was motivated by the intention to make direct comparisons with observations reported previously.

Figure 6.41 shows near-wall structures identified by way of pressure iso-surfaces. Contours of the discriminant criterion Δ, proposed by Chong et al [34], are shown in Figure 6.42 and are seen to yield a similar result. A third criterion examined in Section 5.8 is the second invariant Q of the tensor A_{ij} for which coherent structures are associated with positive Q. Contours of Q are shown in Figure 6.43. The last criterion considered is the λ_2 criterion of Jeong et Hussain [94], and results of the application of this criterion are given in Figure 6.44. The contours shown on Figures 6.41 to 6.44 delimit zones in which the values of the criterion considered are smaller than the threshold value represented by the contours.

The choice of the threshold at which the contours are plotted is based on the experience of the observer in efforts to obtain the best *looking* visualisation rather than any *rigorous* criterion. Figures 6.41 to 6.44 show very similar pictures of the flow. Essentially, they shows structures aligned with the streamwise direction, parallel to the wall in the near-wall region and inclined upwards at an angle of approximately 45°, the structures having a length of approximately 200 wall units. This is in agreement with the observations made by Blackburn et al [17], Chong et al [35] and Jeong et al [95]. Figure 6.41 shows far fewer structures, but those picked out are of a smoother nature and somewhat larger size than those in Figures 6.42 to 6.44. This is in agreement with the observations made by Lesieur et al [123] that pressure fluctuations used as criterion would give smoother, bigger shapes.

[†]Centre Européen de Recherche et de Formation Avancée en Calcul Scientifique

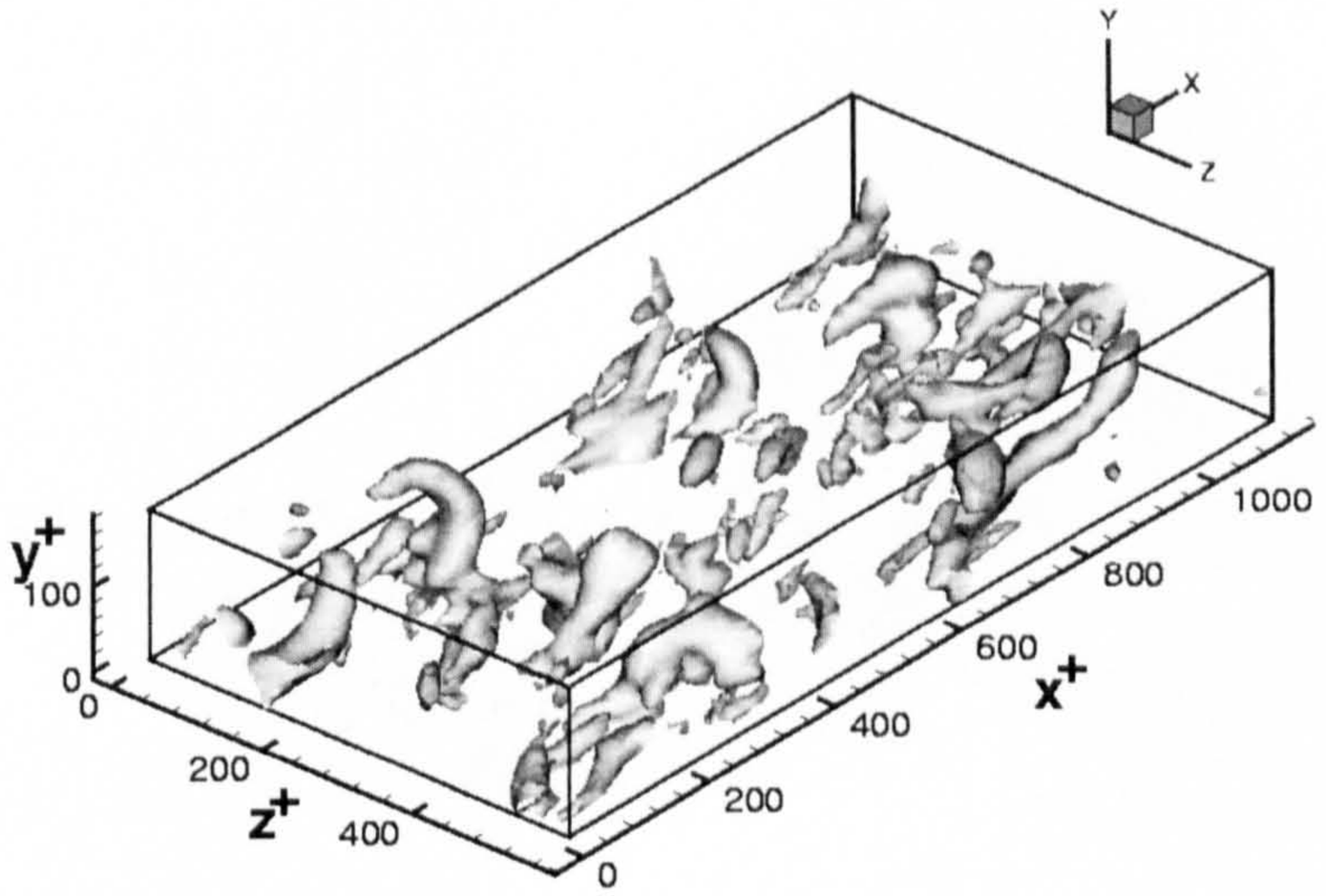

Figure 6.41: Fluctuating pressure iso-contour ($p' = -0.22$).

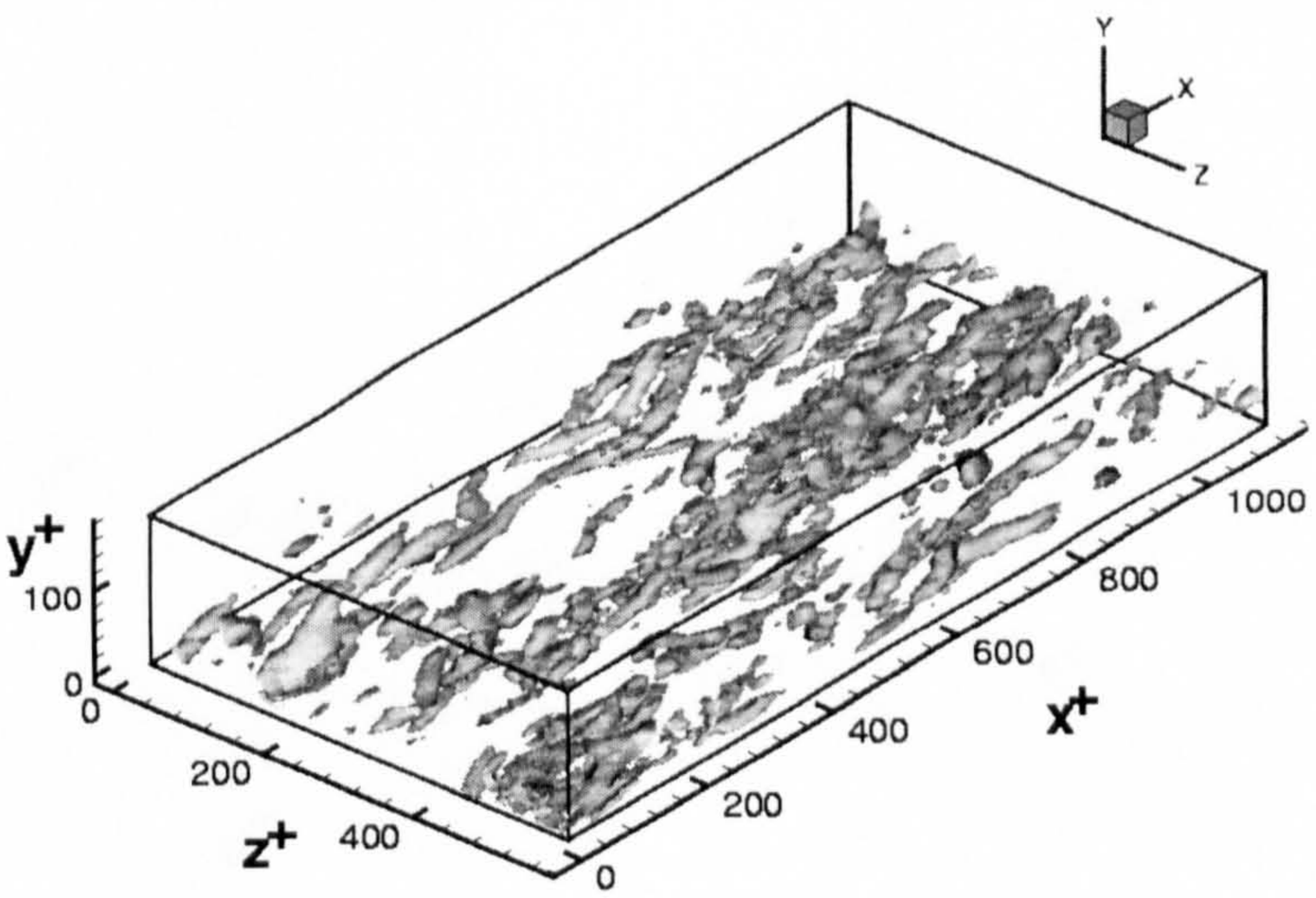

Figure 6.42: Discriminant Δ iso-contour ($\Delta = 0.099$).

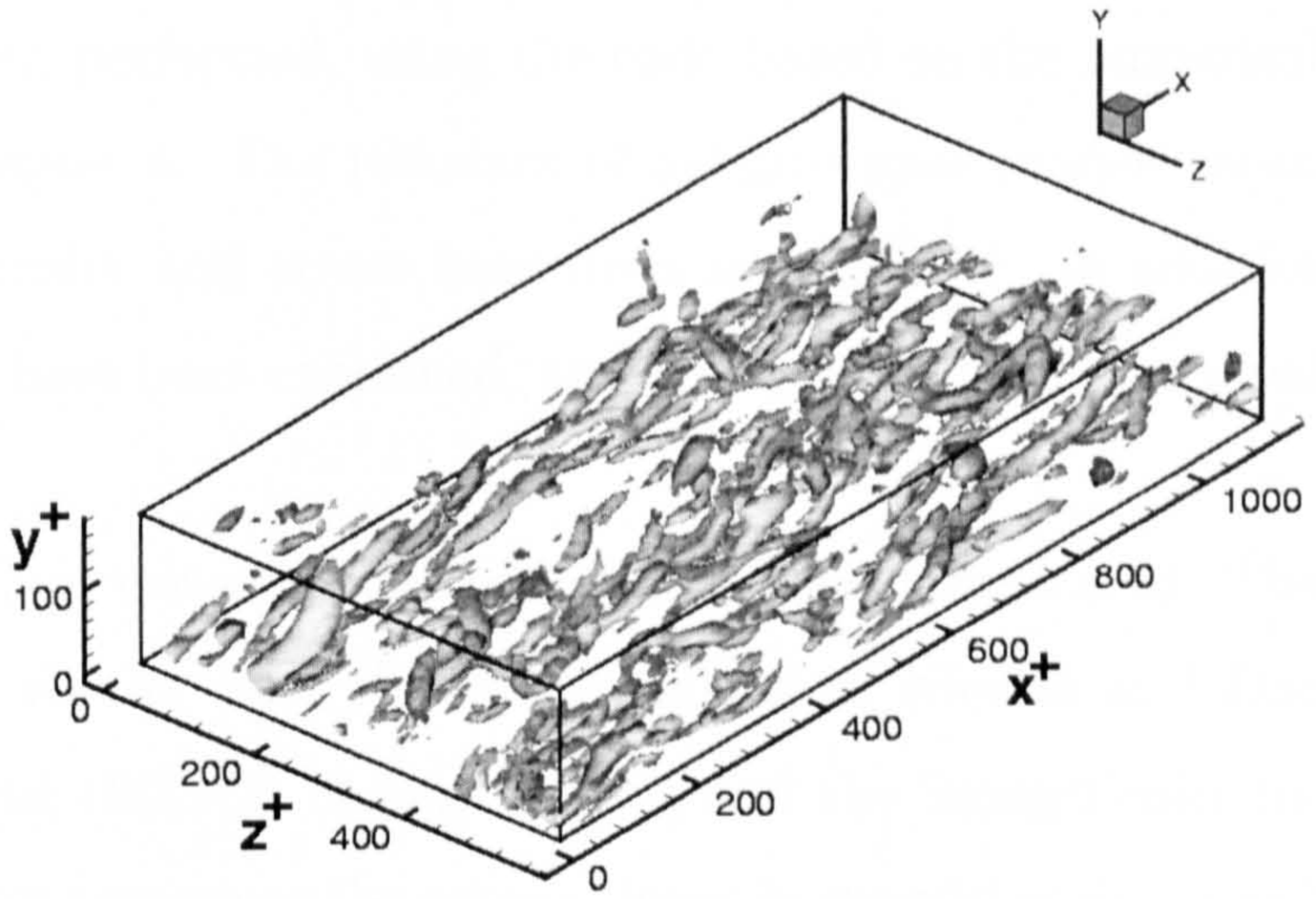

Figure 6.43: Second invariant iso-contour ($Q = 0.008$).

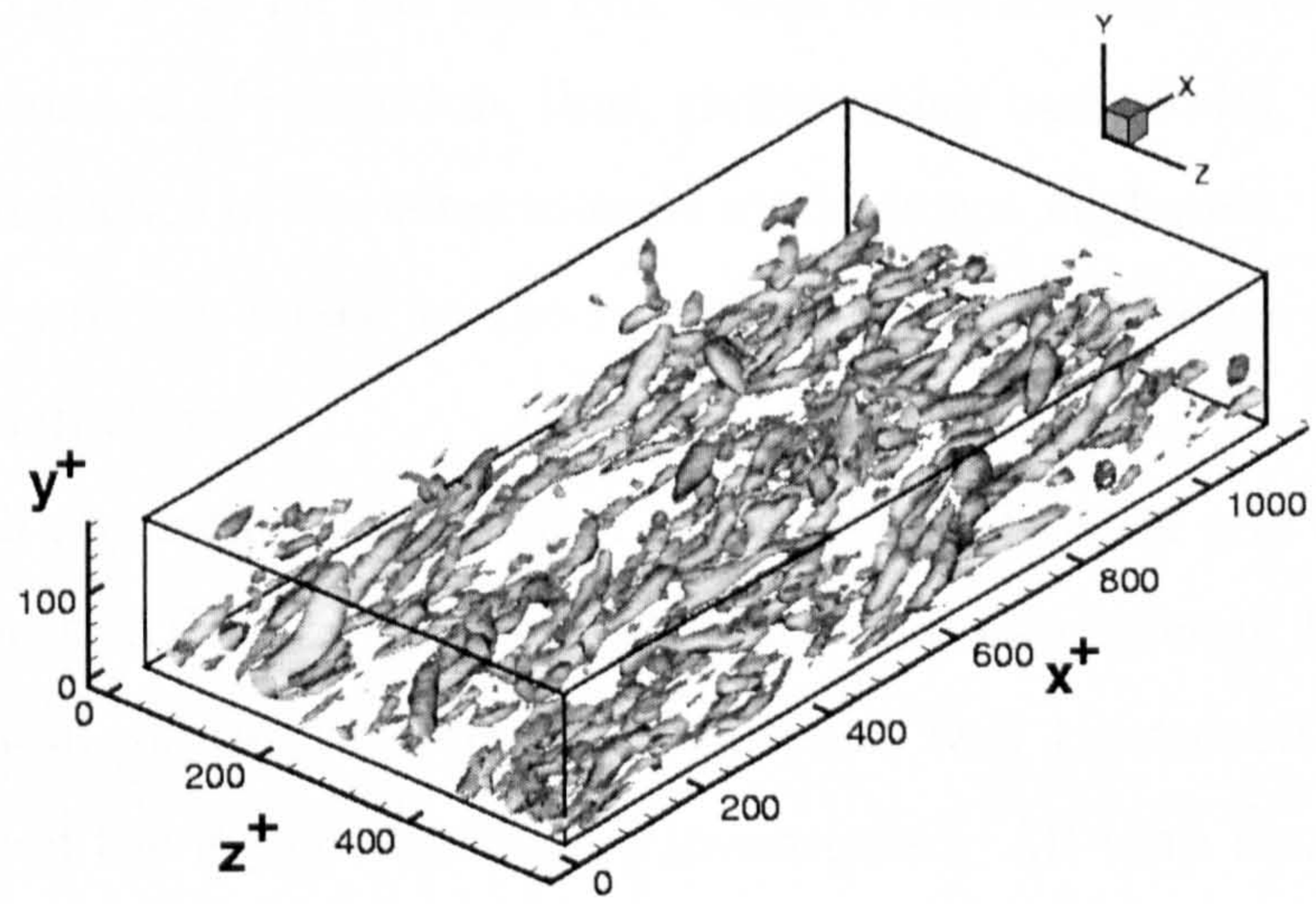

Figure 6.44: λ_2 iso-contour ($\lambda_2 = -0.006$).

6.7 Concluding remarks

In this chapter, simulations for a number of fully-developed turbulent flows in a channel have been performed, using the code based on the numerical methodology described in Chapter 4. The influence of subgrid-scale models, near-wall approximations, grid density and errors have been investigated. In addition, a variety of physical aspects have been examined, and results have been compared with those in the literature.

In Section 6.3, a variety of subgrid-scale models were tested. The model giving the best overall results were the WALE model of Nicoud and Ducros [167], the mixed-scale model (MSM1) of Sagaut [192] and the Smagorinsky model, although the last two do not reproduce the correct decay in subgrid-scale viscosity towards the wall. Dynamic models were observed to require higher near-wall grid densities than non-dynamic variants to produce similar predictions. These simulations highlighted the importance of having the subgrid-scale quantities decaying, if possible, at the correct rate and the particular impact subgrid-scale modelling has on the buffer region. The importance of grid resolution, especially in the near-wall region, was shown by performing simulations with five different models and the no-slip condition on a mesh with $\Delta y^+ = 10$ for the first cell. None of the models tested were able to compensate for this loss of resolution, thus, giving rather bad results. Overall, it was shown that the influence of the subgrid-scale model is not negligible, but difficult to quantify as it is strongly linked to the role played by the numerics and the errors introduced through them.

The near-wall representation by other means than adequate grid resolution was investigated in Section 6.4 by performing simulations at two different Reynolds numbers with near-wall approximations. Four different wall treatments, all based on simple functions of the log-law type, were investigated. All were found to perform, in a similar manner, although it was noted that for the lowest of the two Reynolds number, the Werner-Wengle approach (Werner and Wengle [235]) gave slightly better predictions than the three other variants. The use of such approach to represent the near-wall flow resulted in a significant reduction in the computational resources.

This, however, came at the price of a reduction in the accuracy of the predictions, especially for the turbulence quantities near the walls. A second limiting factor is the occurrence of oscillations caused by the combined use of a co-located scheme and too coarse meshes, which leads to the solution becoming numerically contaminated.

A methodology proposed by Vreman et al [228] to distinguished between the contributions of the numerical and modelling errors was applied to the case of the periodic turbulent channel flow in Section 6.5.

The simulations were carried out using a second-order centred scheme in space and two subgrid-scale models: the Smagorinsky model and the Smagorinsky model with wall-damping. The results, while more qualitative than quantitative due to a lack of resolution in the simulations, lead to conclusions similar to those of Vreman et al [228] for the combination of the second-order centred scheme and the Smagorinsky model. Thus, the numerical error was found to counteract the modelling error, reducing the total error. The introduction of wall-damping in the Smagorinsky model lead to a significant reduction in the modelling error, the influence of the wall being better taken into account, the result being a significant drop in the total error. The method of Vreman et al [228] gave an interesting insight into the interplay of the errors and their influence on the results. It must be pointed, however, that the present method is limited to low-Reynolds number flows, for which the production of a highly-resolved simulation is feasible.

Section 6.6 considers the application of a variety of mathematical tools intended for the analysis of turbulent flows. The results presented all reproduce well others observed in the many studies of the periodic channel flow. This demonstrates that the analysis tools are properly implemented and, more importantly, that the code described in Chapter 4 correctly simulates turbulent flows. With this established, a firm basis has been created for studying more complex flows in chapters to follow.

Chapter 7

Separated flow in a streamwise periodic channel constriction

7.1 Introduction

Flows that involve separation from curved surfaces occur in numerous applications, including wings, turbine blades, car-like bodies, shaped constrictions and obstructions in pipes. Unfortunately, the satisfactory computation of flows in such geometries is difficult to achieve, regardless of the computational methodology. RANS schemes, in particular, are problematic in the sense that different turbulence models can return very different solutions.

A particularly challenging property to determine is the mean location at which a flow separates from any curved surface. Indeed, this location varies greatly in space and time and the dynamics of turbulence can be expected to greatly influence the mean separation location. However, this is invariably outside the scope of most closure approximations used in current RANS schemes. If, as a consequence, the separation is misrepresented, the flow is usually badly predicted further downstream.

In order to improve existing models, both in RANS and LES methods, the role played by the physical processes in these flows requires careful analysis. There are few extensive sets of data available, however, which cover the turbulence characteristics and flow structures in the near-wall region around the separation point, in

the separated shear layer, in the reattachment region and in the subsequent recovery zone. While numerous experimental studies on separated flows exist, they have yielded, in most cases, sparse data which do not provide significant insight into the flow mechanisms. Experimental limitations, such as the difficulty of achieving true spanwise homogeneity and streamwise periodicity and the presence of a spanwise confinement, often introduce non-negligible uncertainties in the data.

In principle, DNS is the ideal tool to study separated flows. However, DNS is limited to relatively simple geometries and low Reynolds number, as the computational costs become prohibitive when the complexity of the geometry and the Reynolds number approach engineering conditions. In such circumstances, the only reasonable approach is to perform a high-quality LES in geometries which have been carefully designed to yield extensive data on the mechanics of a separated flow in conditions representative of engineering conditions. Such simulations must be carried out with care so that any approximations introduced into the LES do not affect the quantities of interest. This also means that the flow must be highly-resolved. Such data help not only to gain insight into the flow physics, but also serve to form a benchmark against which RANS calculations and less-resolved LES can be assessed.

One objective of the work presented in this chapter is to provide such data and to conduct a thorough investigation of the mechanisms of a particular separated flow. A second objective is to investigate, by reference to the highly-resolved data previously generated, the predictive qualities of the subgrid-scale models and wall treatments described in Chapter 3 on the same geometry, undertaken with coarse-grid LES.

The geometry of the flow under consideration is shown in Figure 7.1. It comprises a channel with periodically arranged hill-shaped constrictions on one wall. The simulation domain extends from one hill crest to the next (or, in one case, over two periodic segments). The spanwise direction is deliberately prescribed to be statistically homogeneous so as to secure statistical two-dimensionality. Streamwise periodicity and spanwise homogeneity thus divorce the simulations from uncertainties arising from boundary conditions, except for those at the upper and lower walls. The inter-hill distance is chosen so that the flow reattaches well upstream of the fol-

lowing hill, permitting some recovery before the acceleration on the windward side of that hill. The choice of this geometry was inspired by a number of experimental and simulation studies on related configurations. In the former category, a series of investigations by Almeida et al [5] was of particular influence. These were concerned with separation from single and periodically-arranged hill-shaped, nominally 2D obstacles on a wall in a large duct. The experiments were, however, affected by 3D contamination arising from spanwise confinement and, in the multiple-hill configuration, by incomplete streamwise periodicity. Moreover, the breadth and resolution of the experimental data are limited and do not permit fundamental mechanisms to be studied. Thus, although the data have formed the basis for extensive RANS validation studies [188], there is considerable uncertainty about their reliability when assessing 2D solutions.

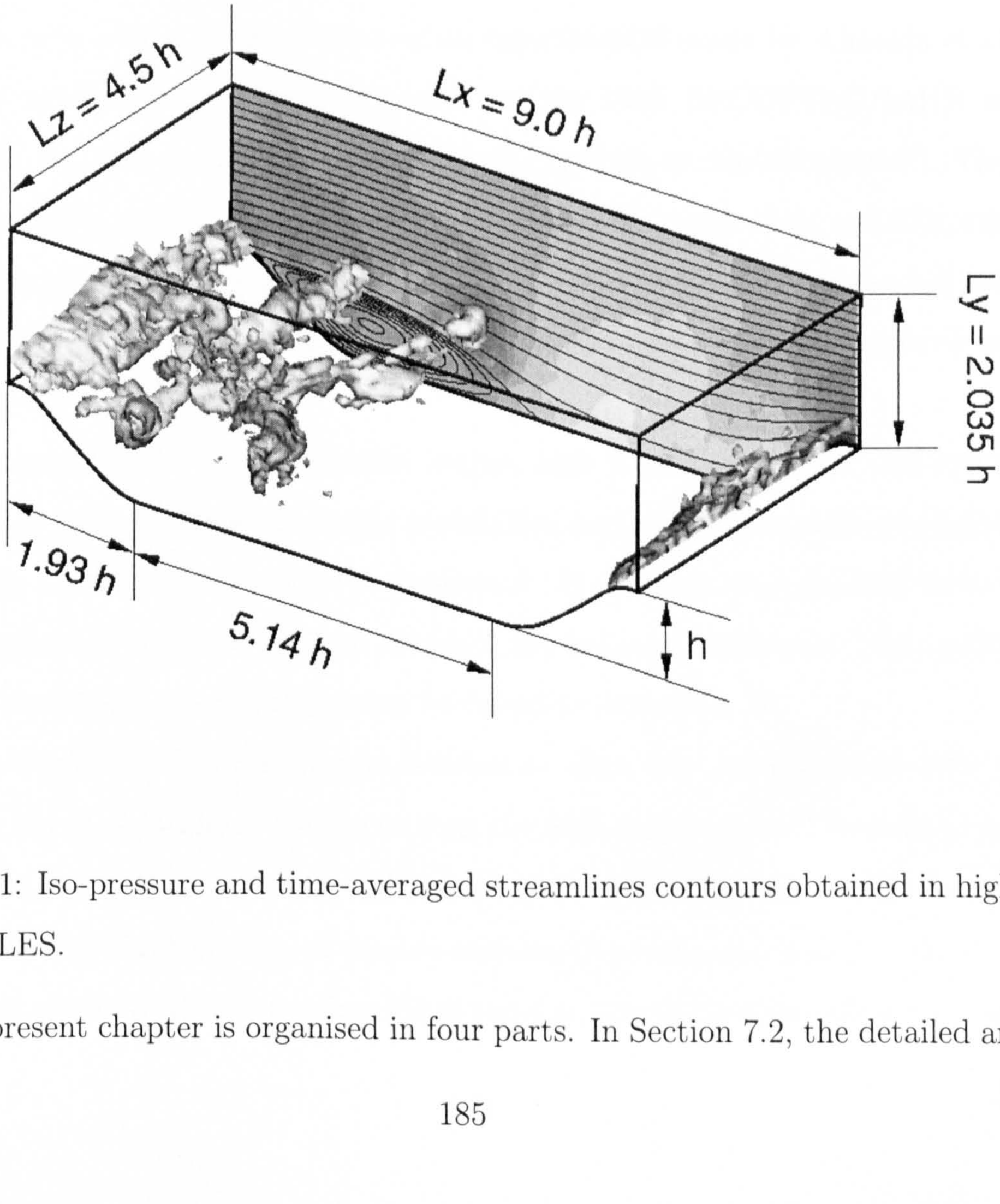

Figure 7.1: Iso-pressure and time-averaged streamlines contours obtained in highly-resolved LES.

The present chapter is organised in four parts. In Section 7.2, the detailed argu-

ments justifying the choice of the geometry used in the present work and shown in Figure 7.1, are presented. Past studies on related configurations are also reviewed in this section. Section 7.3 presents and analyses the results of the highly-resolved LES, which serves as a foundation for judging coarser-grid simulations. Included in this section, are mean–flow and second-moment fields, the budgets for the turbulent stresses and energy and spectra. Section 7.4 focuses on simulations on substantially coarser grids, with the highly-resolved simulation serving as a benchmark. In particular, the sensitivity of the solutions to subgrid-scale modelling, grid density and approximate near-wall treatments is investigated. Finally, conclusions are contained in Section 7.5.

7.2 The simulated configuration

This section provides arguments for the choice of the geometry shown in Figure 7.1. A related geometry was the subject of an experimental study by Almeida et al [5]. This was previously used as a test case for the 1995 ERCOFTAC/IAHR workshop [188] (see also `http://fluindigo.mech.surrey.ac.uk/database/`). The geometry features periodic constrictions with a channel height of $L_y = 6.07h$, successive hills being separated by a distance of $L_x = 4.5h$, with h being the hill height. The Reynolds number of this flow, based on the hill height and bulk velocity above the hill crest, was 60000.

The combination of large channel height, high Reynolds number and spanwise confinement was concluded to imply prohibitive computing demands especially if a sufficiently resolved LES was to be generated. It was therefore decided to modify the configuration with the original shape of the hill being retained. The analytical function describing the hill shape can be found in Appendix D.

First, the Reynolds number was reduced to allow the use of a *quasi-DNS* resolution at the lower wall, in the sense that the SGS and near-wall modelling would have no impact on the solution. This reduction in the Reynolds number was not seen as a major disadvantage, as the key features of a separated flow are only weakly dependant of the Reynolds number if not too low. Based on bulk velocity U_b at the

hill crest and hill height h, the Reynolds number was chosen to be $Re_h = 10595$. Second, while the shape of the hills was retained, the distance separating two successive hills was increased to $L_x = 9h$ and the channel height, reduced to $L_y = 3.035h$. Thus, based on L_y, the channel height between the hills, the Reynolds number Re_{L_y} is 21560. These modifications in height and length of the channel, favoured streamwise decorrelation and permitted the reattachment to occur on a planar portion, thus, allowing a post-reattachment recovery region prior to the flow reaccelerating on the next hill. With reattachment allowed to occur in a region unrestricted by the geometry of the next hill, the predicted structure of the flow becomes more sensitive to the quality of the simulation. Third, the geometry was made periodic in the spanwise direction, with the spanwise extent being $L_z = 4.5h$. This could ideally have been chosen larger. However, test computations with larger dimensions (Temmerman et al [219]) demonstrated that the present choice had only a very small impact on the quality of the computed statistics. It must also be noted that this choice is significantly less restrictive than the one implied by the *minimal flow unit* of Jiménez and Moin [97].

Past simulations for geometries broadly akin to that considered here focused on flow over wavy terrain at relatively low Reynolds numbers and with coarse grids. These configurations are characterised by the lower wall having a sinusoidal shape with wave-length λ. Related DNS were performed by De Angelis et al [47] and Cherukat et al [32], matching the experimental conditions of Hudson et al [87], namely $h/\lambda = 0.1$ and a Reynolds number $Re_\lambda = 6760$ corresponding to $Re_h = 676$. The domain height was chosen equal to the inter-hills distance. LES for similar configurations, again at these low Reynolds numbers, are reported in Calhoun and Street [27], Henn and Sykes [84] and Armenio and Piomelli [6]. The statistical data obtained from such simulations matched the experiments fairly well, as shown by the compilation of Armenio and Piomelli [6]. Apart from the low Reynolds number, reattachment always occurred on the up-slope of the next hill, so that there was no post re-attachment recovery region. Hence, these simulations are substantially different from those performed in the present study.

At higher Reynolds number, DNS is no longer an option, and only LES can

be carried out. A simulation of the flow over a sinusoidal wall at $Re_\lambda = 4.2 \cdot 10^5$ was conducted by Salvetti et al [195]. Although the use of a very coarse grid in combination with a no-slip condition, as employed in this case, is a questionable practice, the computed averaged velocity field agreed well with the experiments of Gong et al [73]. However, no information was provided on the turbulence quantities. This study also investigated the influence of wave slope and Reynolds number, but no detailed analysis of the flow in the recirculation region and in the near-wall region was included. LES reported by Henn and Sykes [84] and Armenio and Piomelli [6] are concerned with the experimental situation studied by Hudson et al [87] for the case $h/\lambda = 0.2$ and $Re_\lambda = 2 \cdot 10^4$. The mean flow and turbulent fluctuations obtained agreed well with the experimental data, although the mean location of the separation was predicted to occur somewhat too far upstream, the consequence being that the separation bubble was too long.

All the *wavy terrain* simulations noted above focused on the influence of the wavy wall on the boundary layer above the wave crests without any relaxation of the disturbed flow between the waves. None included a detailed analysis of the properties and structure of the separated region. This is precisely where the emphasis of the present study is put.

7.3 Highly-resolved simulation

7.3.1 Overview

As argued in the previous section, a new target geometry had to be defined, appropriate to the objective of studying separation from a curved surface at moderate Reynolds number and tenable computational expenses. The main constraint is posed by the requirement that at least one simulation can be performed on a grid dense enough to render the results insensitive to resolution and modelling approximations. Such a simulation would then allow the physics of the separated flow to be studied in detail and would provide benchmark data against which to judge other computations. The present section is concerned with this highly-resolved simulation.

An unusual, but advantageous aspect of the present configuration is that a simulation performed by Mellen et al [150], contemporaneously, with the present research effort for the same flow conditions and mesh, allows the verification of the validity of the present computation. That simulation was done entirely independently, using a different code and a different SGS model. Because of the high grid density employed, the latter difference was expected to be of little consequence.

Case		SGS	Wall	$(x/h)_{sep}$	$(x/h)_{reat}$
31	Present	WALE	NS	0.22	4.72
32	Mellen et al [150]	DSM	NS	0.20	4.56

Table 7.1: Comparison of the highly-resolved simulations.

The results presented here were obtained on a mesh of $196 \times 128 \times 186 \approx 4.6 \cdot 10^6$ cells. This mesh, shown in Figure 7.2 and designated *Grid 3* in the discussion to follow, is close to orthogonal and is of low aspect ratio over most of the domain. Near the lower wall, where the no-slip condition was applied, the mesh was made sufficiently fine so that a near-DNS could be attained. At the upper wall, the Werner-Wengle wall function [235] was applied, because the details of the flow in that region were not of interest, while its gross development and role on the other regions of the flow could be adequately handled with lower resolution. In the spanwise direction, the cells were uniformly distributed.

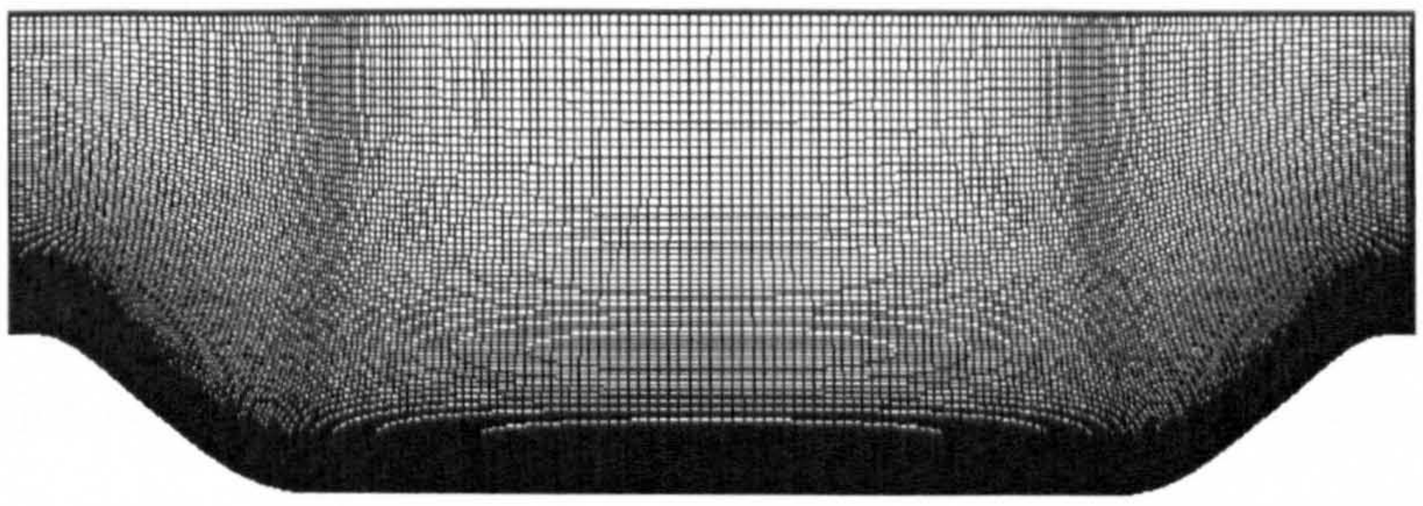

Figure 7.2: Cut in the $x - y$ plane through the grid (Grid 3) used to perform the highly-resolved LES.

Throughout this chapter, the reference quantities for length and velocity will be

h, the hill height, and U_b, the bulk velocity at the crest, respectively. The present computation was performed using the code described in Chapter 4, in conjunction with the WALE model for which $C_w = 0.1$. The CFL number was limited to 0.2. The computation was run over 23 flow-through times (L_x/U_b) before statistics were collected for a further 55 flow-through times. Averaging over the spanwise direction was also performed. The computational effort required to assemble these statistics amounted to 55000 CPU hours on a Cray T3E-1200E. The companion computation, performed by Mellen et al [150], used similar computational parameters. However, it used the dynamic Smagorinsky model to capture the SGS processes.

7.3.2 Resolution assessment

The quality of the resolution is first judged by considering the streamwise distributions of the cell dimensions in the layer closest to the wall. These distributions, in terms of wall units, are shown in Figure 7.3. That designated $\Delta y^+/2$ gives the wall-normal distance of the nodes closest to the wall.

The centre of the first cells are located at $\Delta y^+/2 \approx 0.5$ along most of the wall. The streamwise and spanwise cell dimensions are below 25 and 10, respectively. These values are much lower than those commonly recommended for a wall-resolved LES: $y_1^+ < 2$, $\Delta x^+ = 50 - 150$ and $\Delta z^+ = 15 - 40$ (Piomelli and Chasnov [176]). Figure 7.3 also shows that, along the upward slope of the hill, the mesh size, expressed in wall units, increases, because of the steep increase in wall shear stress, associated with acceleration. The maximum values reach $\Delta y^+/2 = 2$, $\Delta x^+ = 50$ and $\Delta z^+ = 30$, which are well within the recommended range. Near the upper wall, the grid is considerably coarser: $\Delta x^+ = 12 - 35$, $\Delta z^+ = 10 - 15$ and $\Delta y^+/2 = 12 - 17$. These values are typical of wall-function computations (Fröhlich and Rodi [61]).

In the interior of the flow, the resolution can be assessed by comparing the cell size Δ to an estimate of the Kolmogorov length scale η, which characterises the length scale of the dissipative motion. The latter scale can be obtained from the dissipation rate ϵ via the relation:

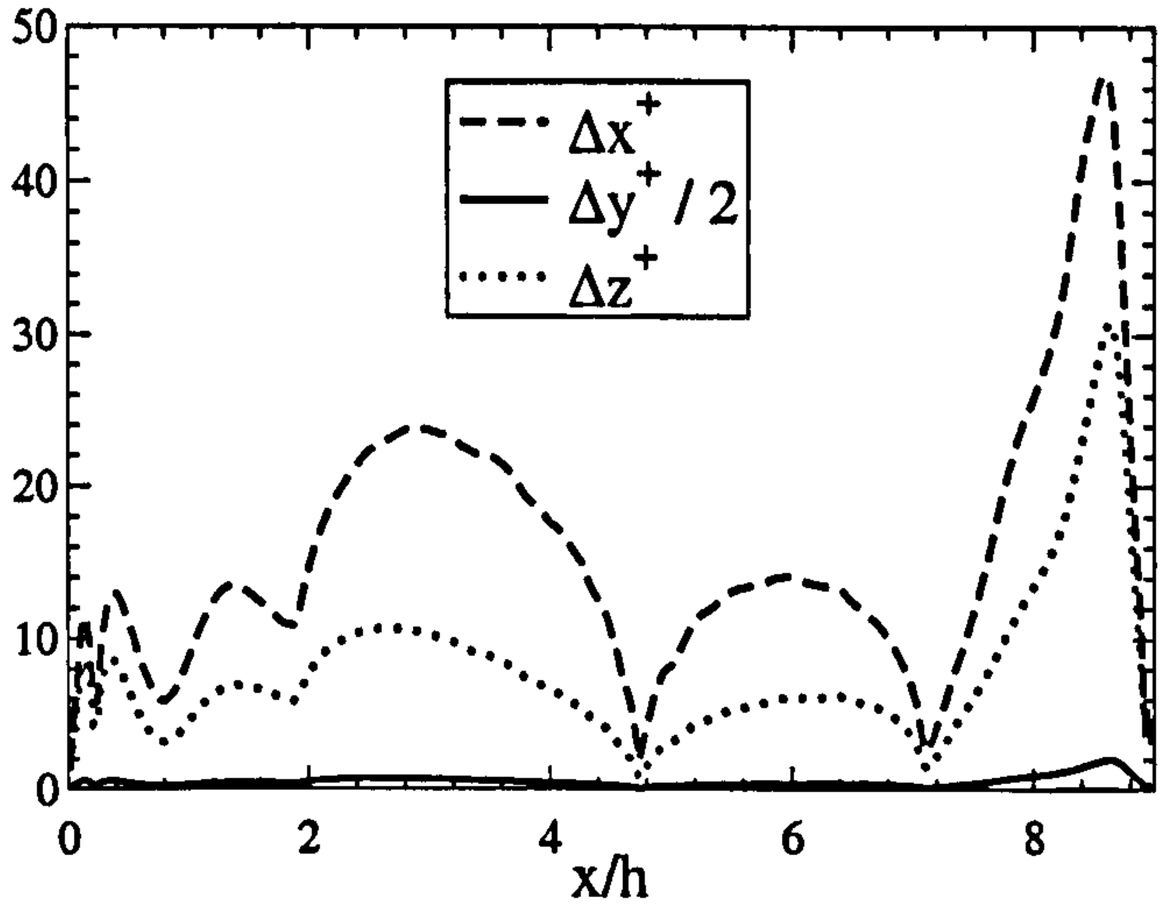

Figure 7.3: Dimensions, in wall units, of the wall-adjacent cells near the lower wall.

$$\eta = \left(\frac{\nu^3}{\epsilon}\right)^{1/4} \tag{7.1}$$

The dissipation rate ϵ was computed as part of the turbulence–energy budget during the present simulation and is presented and discussed in Section 7.3.5. Figure 7.4 shows cross-flow profiles of the ratio Δ/η at various streamwise locations. The value of η is a conservative estimate, as it is mostly biased toward the lowest end of the scale range. Strictly, Equation (7.1) is a scale relation and should not be interpreted as providing an actual eddy dimension. Considering isotropic turbulence and a carefully devised model spectrum, Pope [180] shows that the maximum dissipation takes place at a wave number of $0.26/\eta$, corresponding to a length scale of about 24η. Accounting for the need to discretise an eddy by at least two grid points thus yields a required grid spacing of 12η. With such a grid, the major part of the dissipation is resolved. Figure 7.4 shows that this level of discretisation is achieved with $\Delta/\eta < 12$ over most of the domain except near the upper wall where the resolution is intentionally coarse. The present assessment therefore indicates that most of the flow is highly resolved.

Another indication of the resolution is provided by the ratio of SGS and fluid viscosity values ν_t/ν. Figure 7.5 shows profiles of this ratio (time-averaged) at two streamwise locations, indicating that about half of the dissipation results from the SGS model, while the remainder is associated with the fluid viscosity. This again

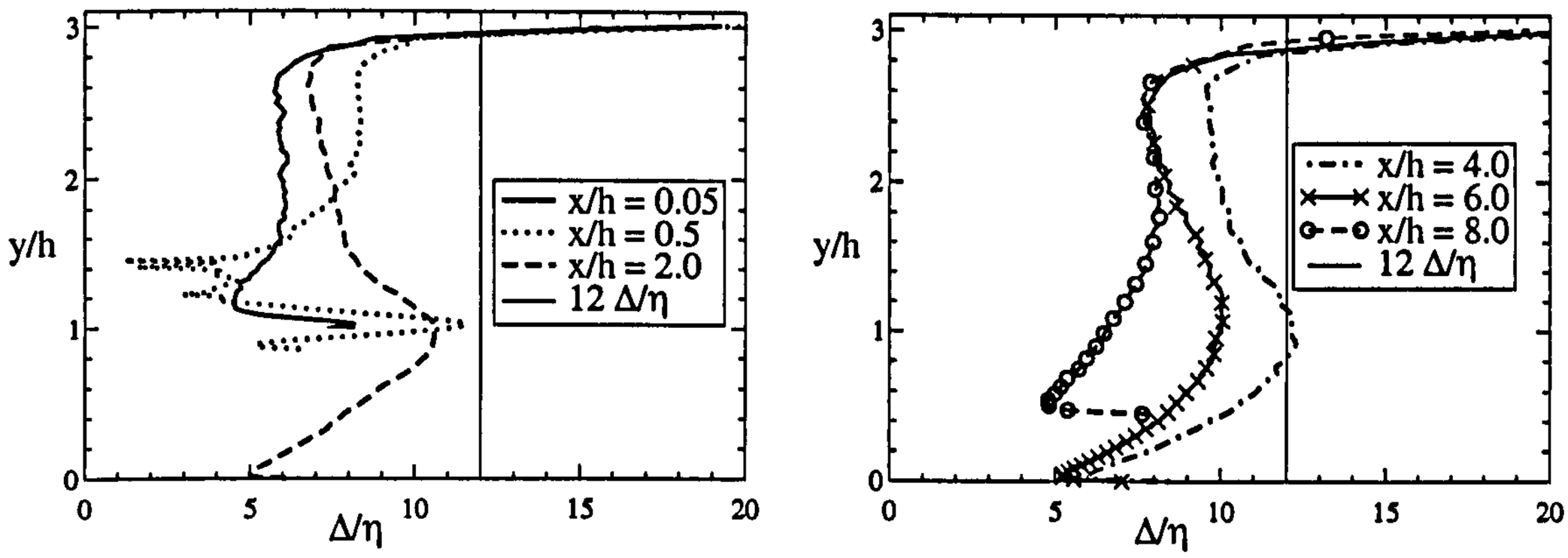

Figure 7.4: Profiles of the ratio Δ/η at six streamwise locations.

indicates a high resolution quality. The computation by Mellen et al [150] returned a SGS viscosity which was larger than the present one. The agreement between the two computations is nevertheless close, as will be shown in Subsection 7.3.4. This demonstrates the low contribution of the SGS model to the present computation, in terms of the ratio of modelled-to-resolved stresses.

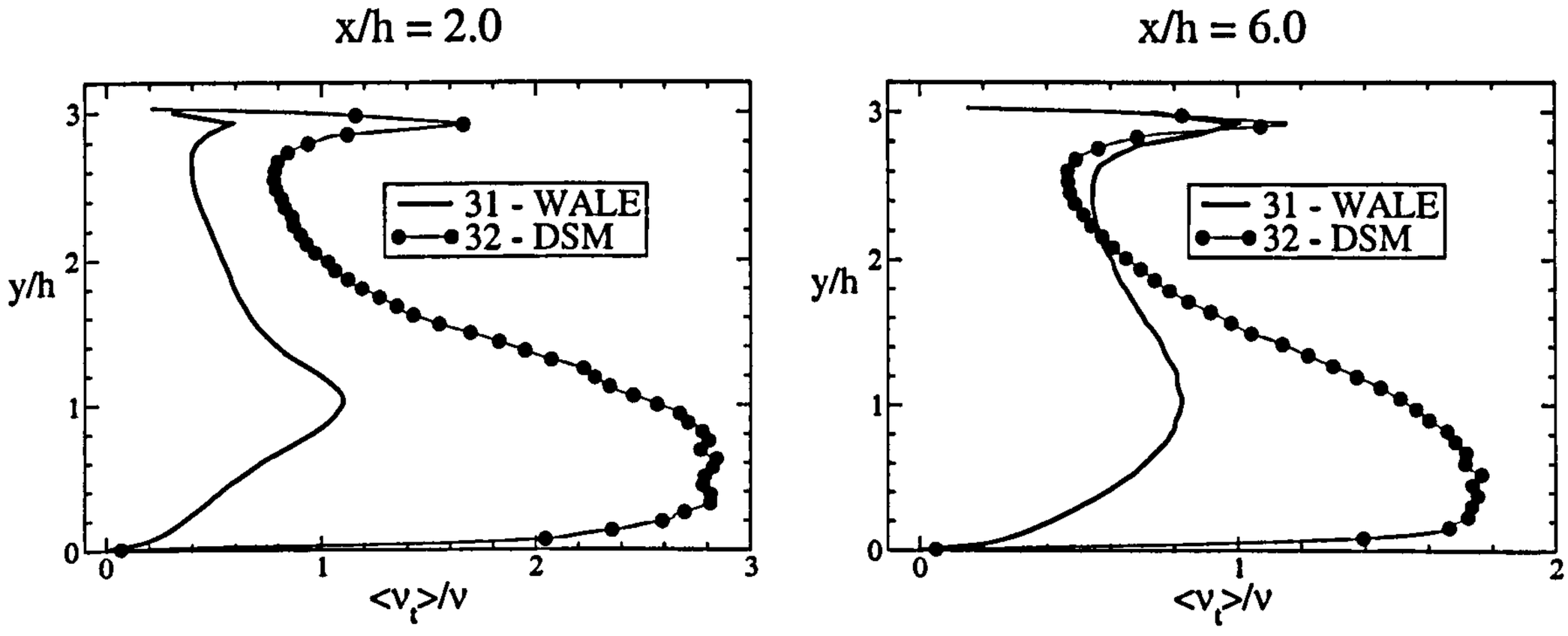

Figure 7.5: Profiles of subgrid-scale viscosity obtained with the WALE model and the DSM model (simulation of Mellen et al [150]) at two different streamwise locations.

The above results indicate that the most critical area, in terms of resolution, is the shear layer separating from the hill and entering the region where the grid gradually coarsens (see Figure 7.2).

Spectra can be used as a further indication of resolution. These have been computed in characteristic regions of the flow and are reported in Subsection 7.3.6

and indicate the resolution to be good for the grid and method employed.

7.3.3 Extent of computational domain

In 2D separated flows, which are statistically homogeneous in the spanwise direction, structures with exceptionally large scales may exist (Zdravkovich [244]) in that direction. A computation performed on a domain for which the spanwise extent is smaller than these scales, would then wrongly represent them and introduce errors. The issue of the adequacy of the spanwise extent $4.5h$ was studied by Mellen et al [150] on a somewhat coarser grid than the reference one, for reasons of economy, by performing two computations, one with a spanwise extent of $4.5h$, and the other with $9h$, all other parameters remaining unchanged. The sensitivity of the results to this change was minimal and far lower than that associated with the grid. Mellen et al [150] also computed two-point correlations for the velocity fluctuations at different locations in their computation with a spanwise extent of $9h$. The two-point correlations give an indication of the size of the structures, this size being about twice the distance between the origin of the correlation (the point at which the distance between the two points is zero), and the point where the correlations level off to zero. The domain is considered large enough if all two-point correlations effectively vanish at half the domain width. Mellen et al [150] showed that around the separation point, the correlations reached zero over small distances, indicating that the spanwise structures were also small. Downstream of the separation point, they observed a pronounced negative trough in the correlations at a two-point distance of about $2h$, which was due to the formation of streamwise vortices discussed later. Based on their studies, Mellen et al [150] concluded that a spanwise separation of $2.25h$ (half the domain size of the simulations presented here) is not quite sufficient to ensure that the correlations vanish in all regions of the flow and that a spanwise extent of $6-7h$ would have been preferable. This introduces a modest degree of uncertainty, as the largest scales cannot be fully represented in the simulation. Mellen et al [150] found this error to be marginal.

The streamwise extent of the computational domain was selected to be one inter-

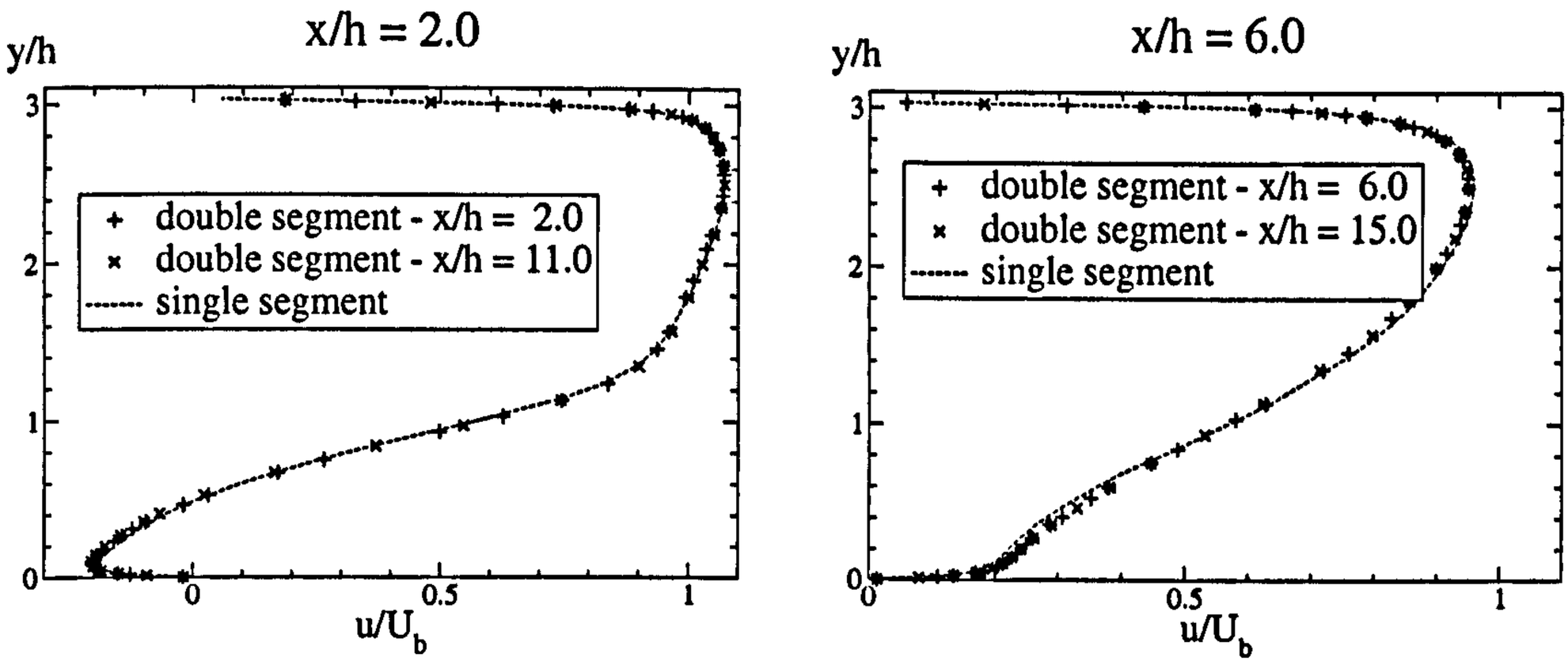

Figure 7.6: Velocity profiles at two streamwise locations for domains made of single and double hill-periods.

hills distance (9 h), and this choice is justified by several factors. For wavy simulations, Henn and Sykes [84] and Calhoun [26] demonstrated that a domain extending to two periods of the sinusoidal wall was sufficient. In the present computation, the inter-hills distance is substantially larger while the channel height has been reduced. In addition, the analysis of the spectra and the instantaneous flow reported in Subsections 7.3.6 and 7.3.7, respectively, shows that the low-frequency contributions result from the return time of the periodic flow rather than from the streamwise size of the structures. Finally, the adequacy of the choice of the streamwise extent was confirmed by computations performed on a grid of $112 \times 64 \times 56$ per period with the computational domain doubled in the streamwise direction. This is illustrated in Figure 7.6 which shows velocity profiles at two streamwise locations for two computations performed on a single and double hill–to–hill domain.

7.3.4 Comparison of solutions from highly-resolved simulations

The present section intends, first, to give an overall description of the mean flow, and, second, to compare the results of the present simulation with those of Mellen et al [150]. Table 7.1 shows the mean locations of the separation and reattachment points. An overall view of the mean flow is presented in Figure 7.7 in which the

streamlines are plotted. The dashed vertical lines indicate streamwise locations at which profiles of various quantities were extracted from the data set while the points correspond to positions where temporal signals were recorded. As expected, the flow presents a significant recirculation zone which reattaches at about half the length of the geometry, leaving some space for the recovery process to take place prior the flow reaccelerating over the windward side of the r.h.s. hill. Table 7.1 shows predictions of the separation and reattachment points arising from both simulations to be close to each other. Differences are due, in part, to the different SGS models that were used with the present simulation using the WALE model, while Mellen et al [150] choose to use the dynamic Smagorinsky model. Both models returned significantly different levels of SGS viscosity as it is shown in Figure 7.5. The effects of these differences were minor, however.

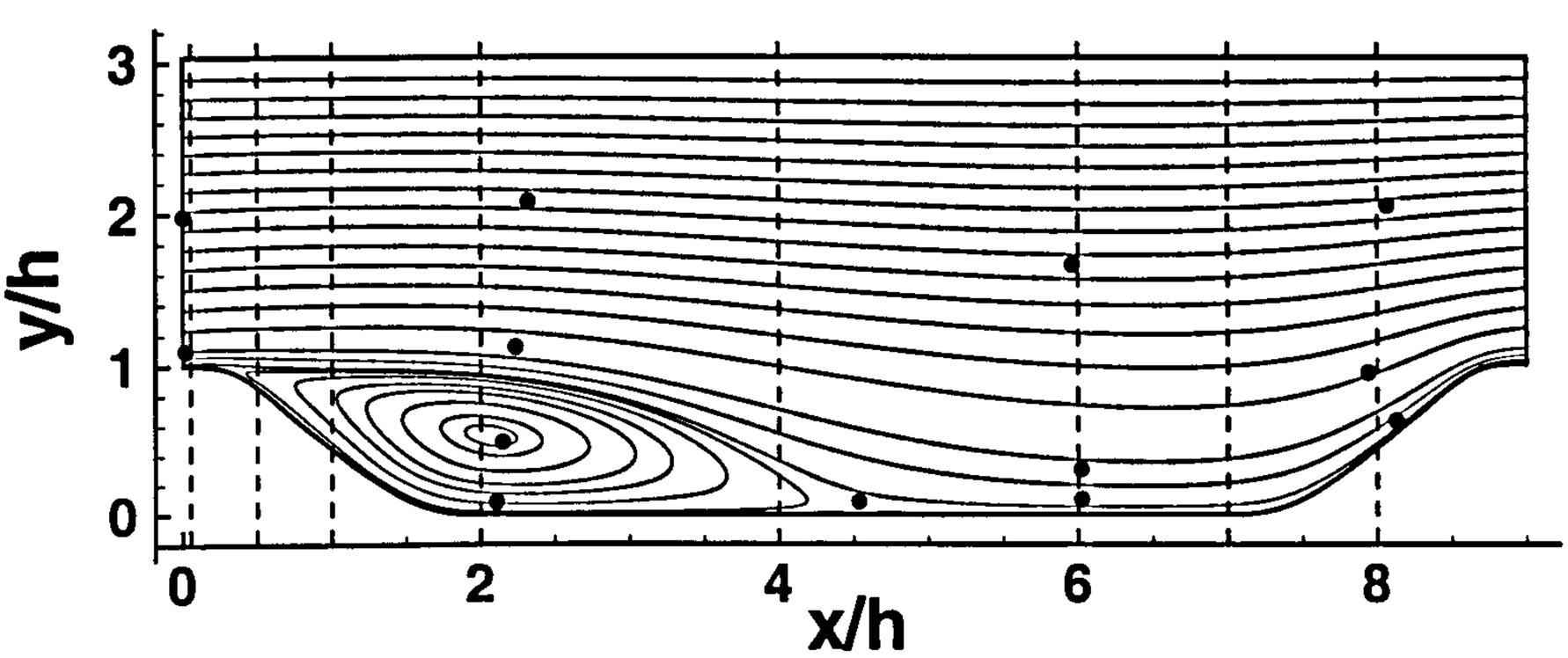

Figure 7.7: Time-averaged streamlines for the highly-resolved simulation. The dashed vertical lines indicate streamwise locations at which profiles are extracted. The points indicated the locations at which time signals were recorded.

The distribution of the pressure coefficient along the lower and upper walls, defined as $C_p =< p > /\rho U_b^2/2$, is shown in Figure 7.8. Figure 7.9 gives, for the lower wall, the distribution of the friction coefficient $C_f =< \tau_w > /\rho U_b^2/2$. Predictions from both simulations agree well. Around $x/h = 0.2$, the flow separates from the curved surface of the hill and forms a recirculation region bordered by a shear layer until the flow reattaches at $x/h \approx 4.7$. Between these two points, along the

lower wall, the friction coefficient C_f is negative in the reverse-flow region. In the same region, the pressure coefficient C_p remains, first, broadly constant between the separation point and $x/h = 2.0$, this position corresponds to the end of the hill slope, then starts to rise as the outer flow expands in the channel. Along the upper wall, at the same location, the pressure coefficient also rises, but to a lesser extent. After reattachment, a boundary layer develops along the lower wall under the influence of an adverse pressure gradient which extends to the next hill. The flow strongly accelerates over this hill, resulting in a sharp rise of the friction coefficient, while the pressure coefficient drops rapidly. In this region, the thickness of the boundary layer also decreases from $0.2h$ at the end of the plane region to about $0.08h$ at the hill crest. At the windward base of the hill, Mellen et al [150] noted the existence of a small recirculation zone (the friction coefficient presents a weakly negative value at that point), a feature not observed in the present simulation, although the dip in friction coefficient is very similar. Above the recirculation zone, the flow velocity remains fairly constant. Along the upper wall, the flow behaves as a flat–plate boundary layer subject to deceleration and then, reacceleration, the latter following reattachment.

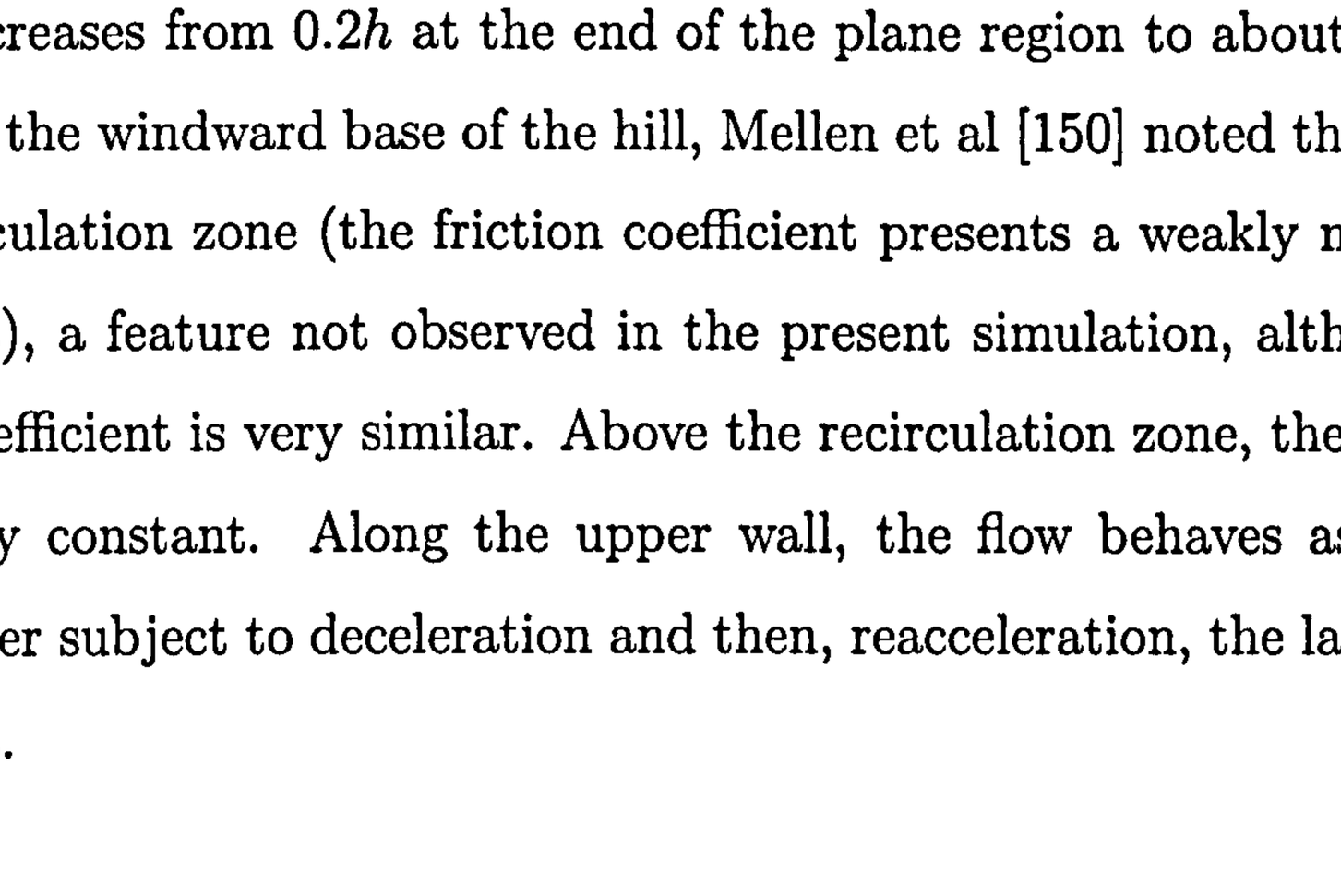

Figure 7.8: Distribution of pressure coefficient C_p along the lower and upper walls for the highly–resolved simulation.

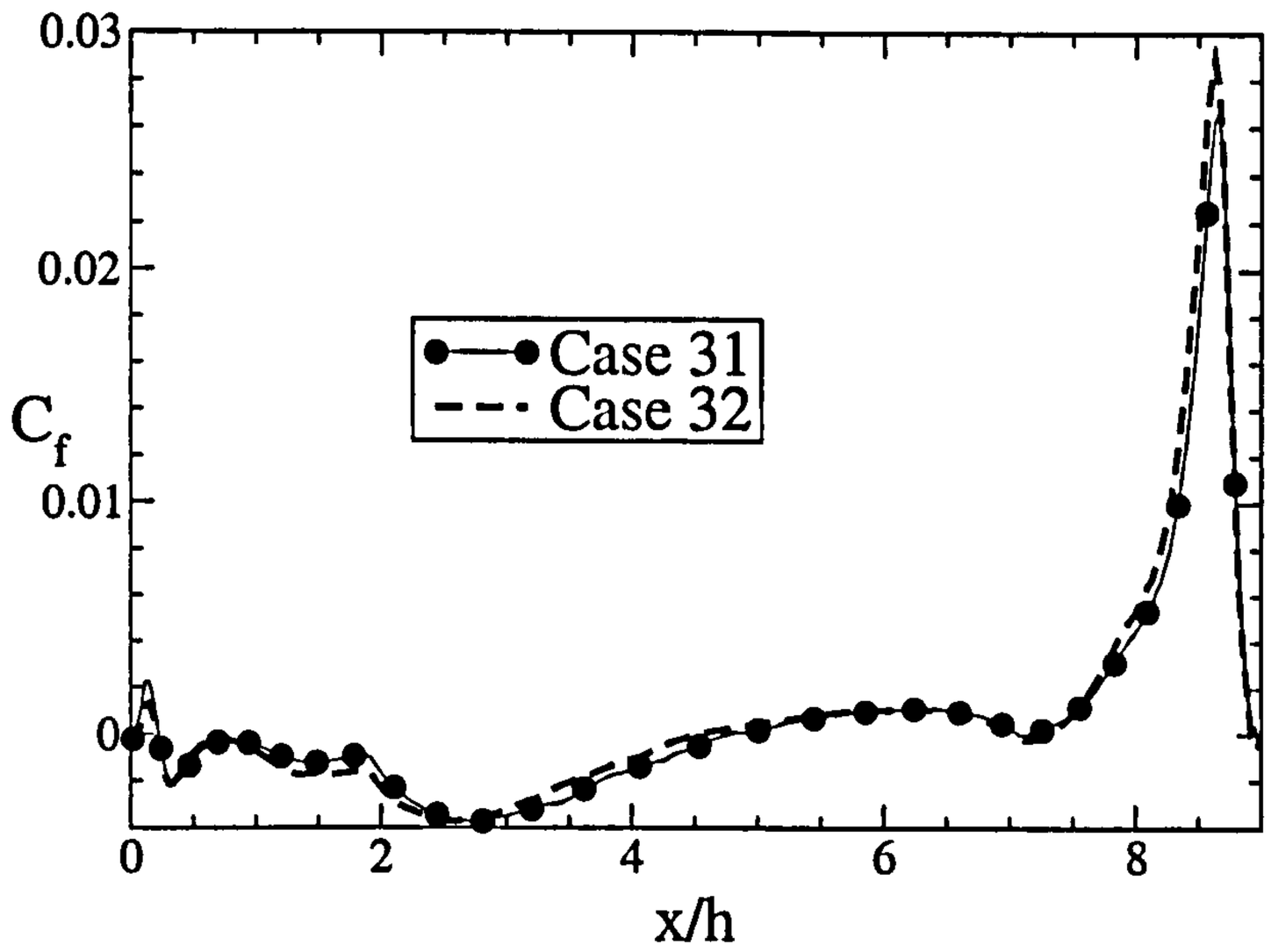

Figure 7.9: Distribution of friction coefficient C_f along the lower wall for the highly–resolved simulation.

The level of agreement between the two highly-resolved solutions is further illustrated in Figures 7.10, 7.11, 7.14, 7.17 and 7.18 which show, respectively, profiles of mean velocity, normal and shear stresses and turbulence energy, at five different streamwise locations indicated by the vertical lines in Figure 7.7. Overall, the agreement between the present simulation and the one of Mellen et al [150] is good. The velocity profiles are clearly very close, although small differences in stresses and turbulence energy are observed. In part, this is due to differences in the level of the respective SGS viscosity shown in Figure 7.5. A more detailed discussion of these results, alongside the budgets for the normal stresses, shear stress and turbulence energy is provided in the next subsection.

The above comparisons should suffice to demonstrate the essential validity of the claim that the highly-resolved simulation provides a secure foundation for evaluating the accuracy of RANS model and coarse-grid LES predictions. Indeed, since the data were generated, they have been exploited by several researchers (see Jang et al [91], Wang et al [229] and De Langhe et al [48]). The data were also made available to the turbulence community through the ERCOFTAC database (Case C81 at `http://cfd.me.umist.ac.uk/ercoftac/`).

7.3.5 Discussion of statistical properties

In what follows, profiles of mean-velocity components, turbulent stresses, turbulence energy and budgets for the stresses and energy at the streamwise stations indicated in Figure 7.7 are presented and discussed. The stations were chosen so as to present the flow regions featuring particular characteristics or behavioural features. The profiles of velocities and stresses are given over the full height of the channel from the lower to the upper wall, while the budgets profiles are only given for the lower portion of the flow, extending over a distance of $2h$ from the lower wall in which all the physical processes of prime interest occur. To enhance clarity and facilitate the discussion, the profiles of the stresses and contributions to the associated budgets close to the lower wall are presented, additionally, in magnified plots. Profiles of mean velocity, turbulent stresses and turbulence energy are included from both simulations and, thus, compared.

The budgets arise from the various terms contributing to the transport equation for the Reynolds stresses $\langle u_i' u_j' \rangle$ for which a complete description is given in Section 5.4. All the terms forming Equation (5.10) were determined explicitly, except ϵ_{ij} which was obtained as the imbalance of the other terms. An explicit evaluation of ϵ_{ij} yielded approximately 50 to 70% of the value obtained from the balance, a level regarded as reasonable in view of the fact that the ratio of grid distance to Kolmogorov length was of order 10. The budget for the turbulence energy $\langle k \rangle = 0.5 \langle u_i' u_i' \rangle$ (see Equation (5.17)) follows from contracting the set of stress equations, i.e. from half of the sum of the equations for each normal stress. In this, the pressure-strain term should vanish, and this has been confirmed to be closely correct by summing up the pressure-strain contributions to the normal-stress budgets.

Position $x/h = 0.05$

This section is located at a short distance beyond the hill crest. Profiles of velocity, Reynolds stresses and turbulence energy at this position are given in Figure 7.10. Budgets, while available, are not included here because the extremely high gradients and rates of change of the flow variables very close to the wall pose uncertainties in

relation to the accuracy of the higher-order moments contributing to the budgets.

The boundary layer is very thin (about $0.1h$) and the streamwise velocity features a near-wall peak. Both are due to the preceding acceleration along the windward slope of the hill. There is also a slight upward motion associated with the flow along the steeply inclined windward hill face. The shear stress $\langle u'v' \rangle$ reaches a first minimum value in the boundary layer and then declines to virtually zero, where the velocity component $\langle u \rangle$ reaches a maximum. Beyond this location, the velocity gradient reverses sign, while the shear stresses does not. The lowest $\langle u'v' \rangle$ value occurs around $y/h = 1.6$ at a local minimum in $\langle u \rangle$, and this indicates substantial stress-transport effects (unless $\partial \langle v \rangle / \partial x$ is important, which is not the case). The velocity then rises to a second maximum toward the upper wall, and $\langle u'v' \rangle$ decreases, changing sign roughly at the location of this maximum and reaching a peak value in the boundary layer near the upper wall.

The normal stresses are remarkable primarily in so far as their respective maxima occur at very different positions, giving rise to very high local levels of anisotropy. $\langle u'u' \rangle$ has a strong peak close to the lower wall, reflecting intense generation by the high shear strain in the boundary layer. As expected, $\langle w'w' \rangle$ is lower and $\langle v'v' \rangle$, the lowest. However, their maxima occur well outside the boundary layer, suggesting a dominant history effect from upstream locations. In the boundary layer, the anisotropy is unusually intense, with the ratio of $\langle u'u' \rangle$ and $\langle v'v' \rangle$ reaching a value of order 20 and indicating the approach to two-component turbulence, which necessarily prevails close to the wall due to the wall blocking effect. The very high near-wall level of $\langle u'u' \rangle$ is also due to intense streamwise fluctuations associated with intermittently high positive and negative velocities that arise as the separation point moves at a high rate over a substantial proportion of the surface around the hill crest. The high level of $\langle w'w' \rangle$, at around $y/h = 1.5$, is linked, as shown in Subsection 7.3.7, to an amplification of this component upstream of the hill crest by the action of *splatting* and the subsequent transport of this component towards the crest region. Away from the lower wall, in the weak and zero-shear regions, the normal stresses and the turbulence energy are maintained at fairly high levels, again indicating intense turbulence transport from the highly disturbed upstream region.

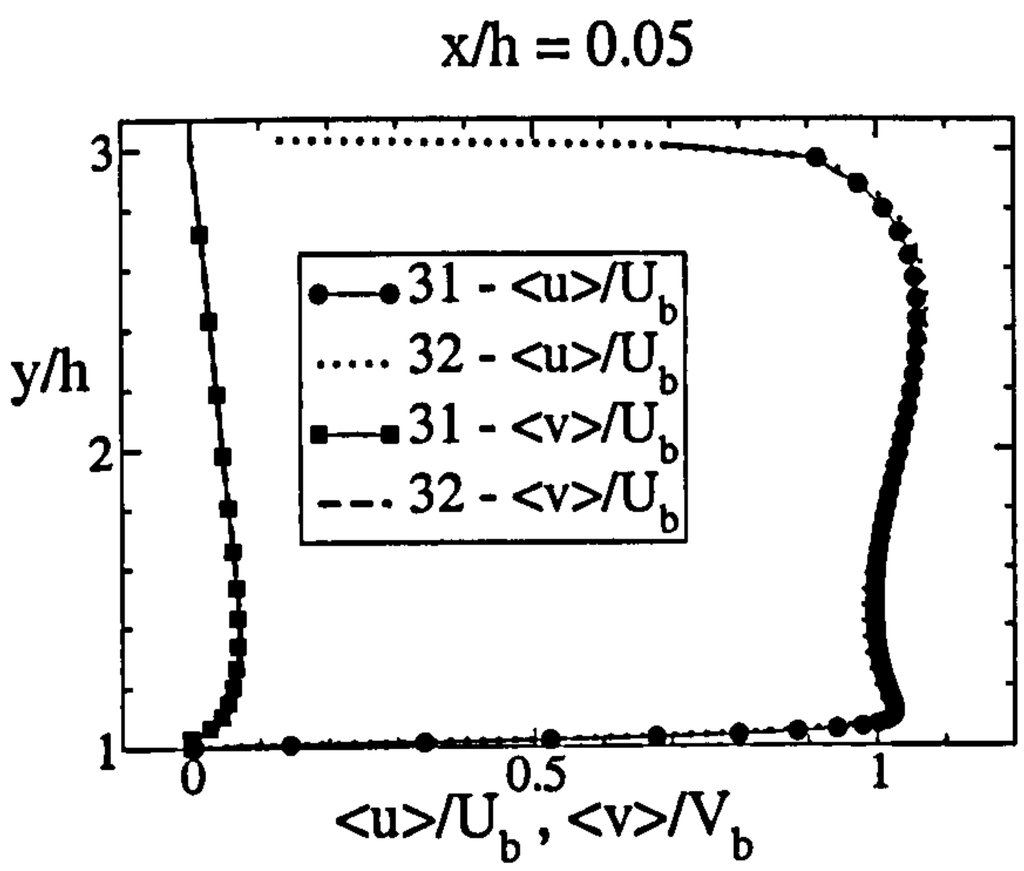

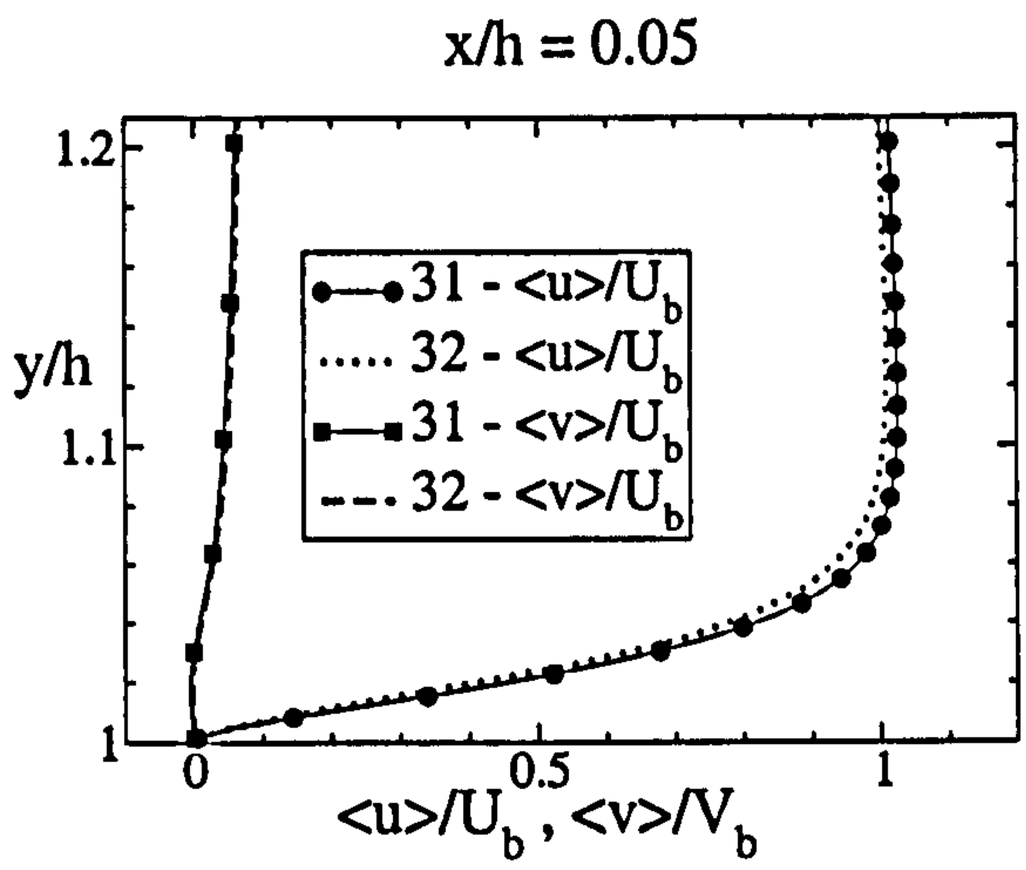

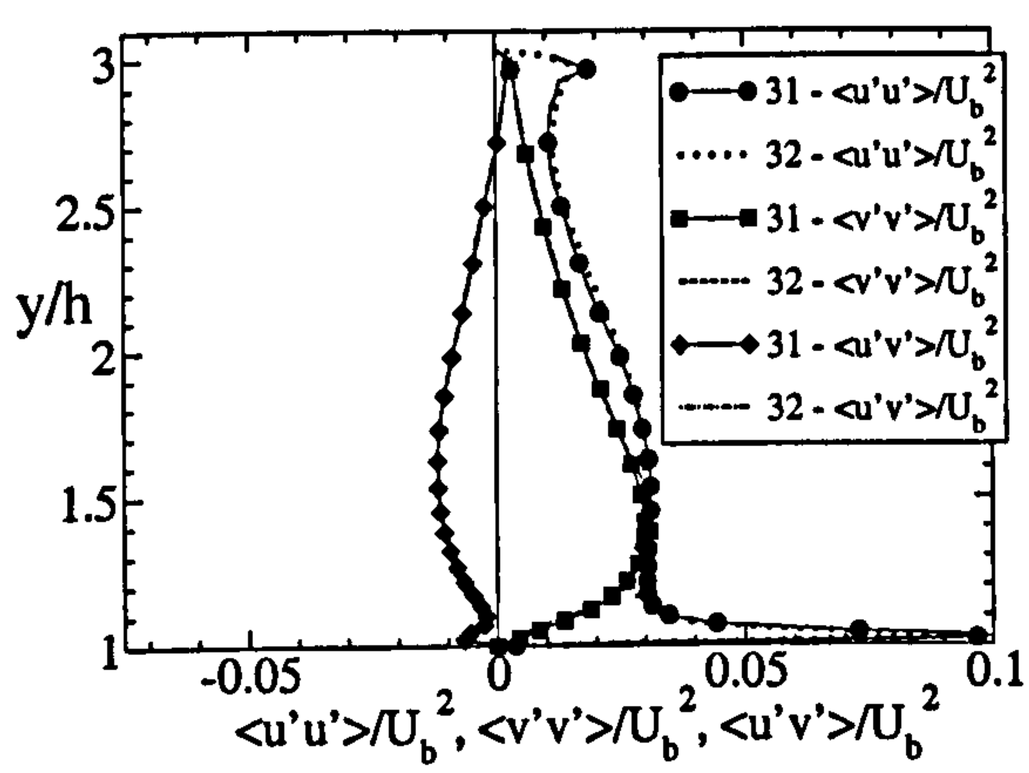

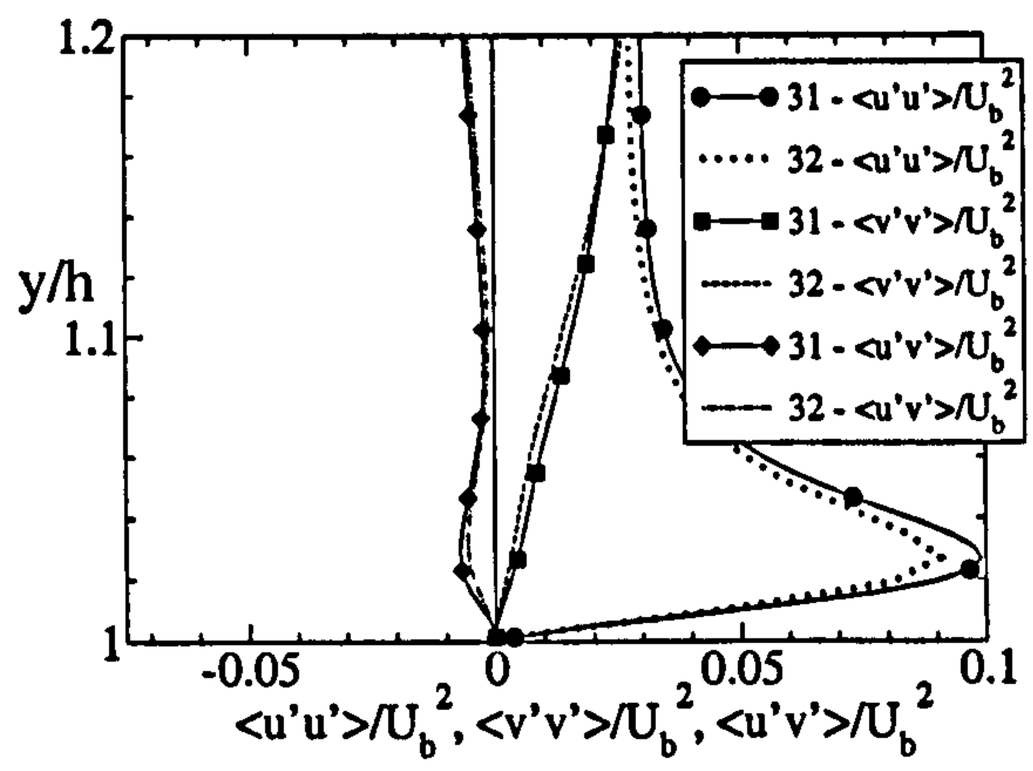

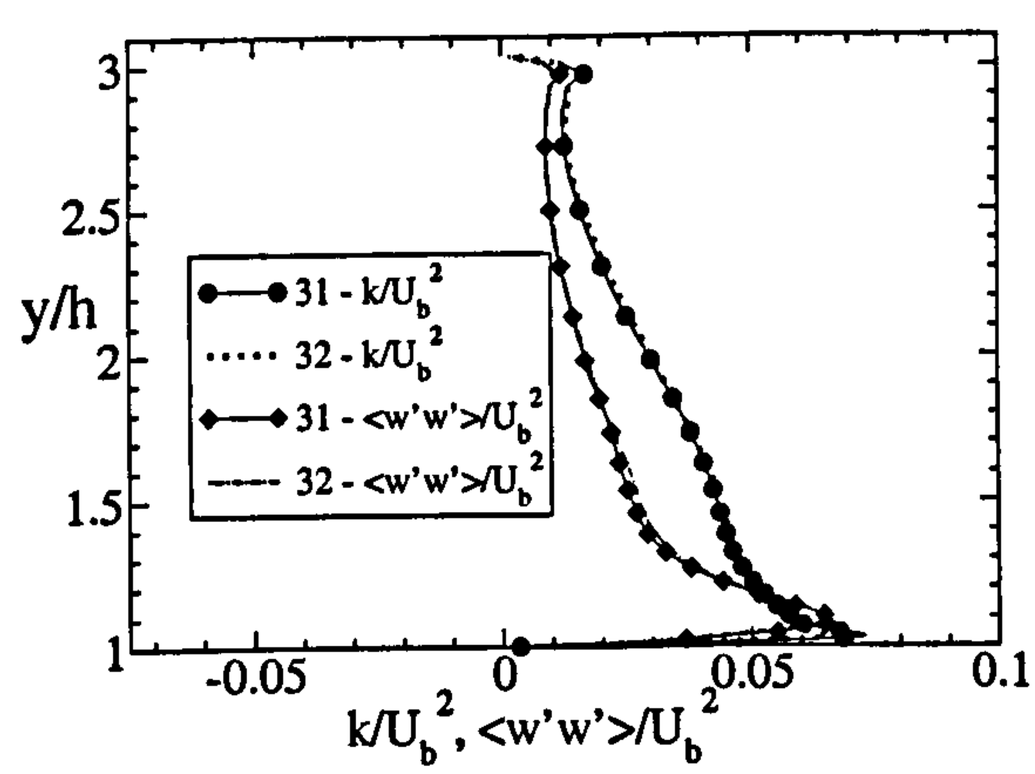

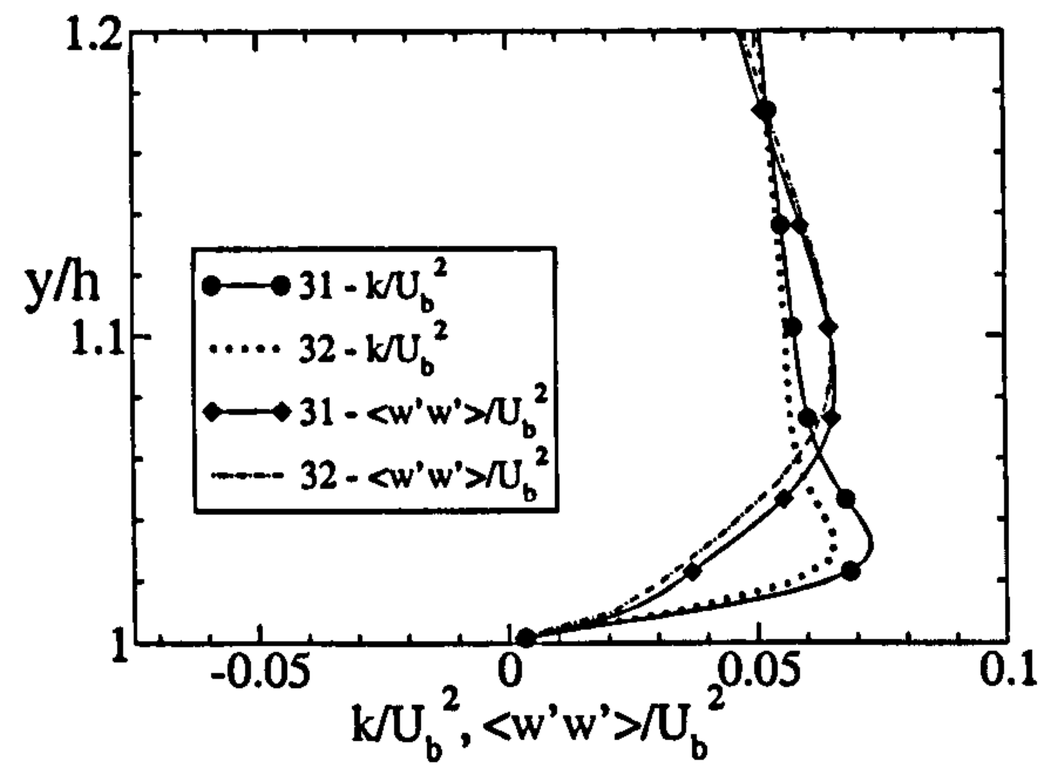

Figure 7.10: Velocity, normal and shear stresses and turbulence energy profiles at $x/h = 0.05$ for the highly resolved simulation.

Position $x/h = 2.0$

This section, located in the middle of the recirculation region, is especially interesting because it combines three interacting layers: a highly disturbed reverse flow, combining a boundary layer and a mixing layer formed from the fluid originating from the separated shear layer above it, and the upper free shear layer itself, which separates from the hill crest. Profiles pertaining to this section are included in Figures 7.11, 7.12 and 7.13, the last two figures containing the budgets.

The velocity profiles are unremarkable and show the expected reverse flow in the lower portion, the shear layer above it and the boundary layer at the upper wall, with the slight glitch in $\langle u \rangle$ originating from the application of the power-law-based wall law. This is confirmed by noting that, for the $\langle u \rangle$ profiles presented in Figure 7.6 where a wall-resolved mesh was also used on the upper side of the channel, this glitch is not present. $\langle v \rangle$ is insignificant, as this section is effectively in the streamwise centre of the recirculation bubble. The Reynolds stresses in the shear layer conform to expectations: $\langle u'v' \rangle$ is negative, and all stresses reach a peak in the location of maximum shear strain. Of the normal stresses, $\langle u'u' \rangle$ is the highest, while both $\langle v'v' \rangle$ and $\langle w'w' \rangle$ are lower and of very similar shape and magnitude, indicating that, in the absence of significant wall influences, the pressure-strain process is unbiased in respect of these two stresses. The anisotropy is significant, but not intense, with the ratio $\langle u'u' \rangle / \langle v'v' \rangle$ of order 1.3 and the ratio $\langle u'v' \rangle / k$, about 0.3.

In the reverse-flow layer, $0 < y/h < 0.5$, the most interesting feature, returned by both simulations, is the distinctive rise of $\langle w'w' \rangle$, relative to the other two normal stresses, leading to a virtual equality of $\langle w'w' \rangle$ and $\langle u'u' \rangle$ close to the wall. A similar behaviour will be shown later to occur at $x/h = 6$, and this is claimed to be due to *splatting* effects around the reattachment region, which are then carried over to neighbouring locations by transport. Splatting will also be seen later to be an exceptionally influential process in the accelerating–flow portion above the windward face of the r.h.s. hill. In contrast, $\langle v'v' \rangle$ declines steadily as the wall is approached, a behaviour anticipated due to wall blocking. A feature not foreseen is the reversal in the streamwise-velocity gradient close to the lower wall, at $y/h = 0.1$, which is

not accompanied by a corresponding reversal in the shear stress, expected on the basis of the eddy-viscosity concept. It follows that the turbulent shear stress cannot support the negative wall shear stress in this region which must exist due to the reverse motion, as seen in Figure 7.9 (note that correlation $\langle u'v' \rangle$ and the shear stress $\langle \tau \rangle$ have opposite signs). Hence, the viscous stress must dominate in this region. As will be demonstrated later upon a consideration of the budgets, the processes in the near-wall layer under consideration differ drastically from those in a conventional boundary layer. For example, although there is a sign reversal in the production of the shear stress, in line with the sign reversal in the shear strain, other contributions to the shear-stress balance conspire to maintain $\langle u'v' \rangle$ at a positive level. Moreover, the elevation of the turbulence energy and the wall-parallel normal stresses, due to a combination of production, splatting-related phenomena and convective transport, leads to very high levels of near-wall anisotropy and ratio $\langle u'v' \rangle / k$, even outside the buffer layer, the position of which corresponds to $y/h = 0.05$ at $x/h = 2$, i.e. well below the position of minimum reverse velocity.

The budgets of all stresses and turbulence energy are given in Figures 7.12 and 7.13. They cover only the lower region, roughly to the upper edge of the separated shear layer, as this region is of primary interest. The shear-stress budget shows the usual behaviour in the separated shear layer of a near-balance between pressure-strain and production, with the remaining terms being subordinate. As the wall is approached, but outside the viscous sublayer ($y/h > 0.05$), the influence of production diminishes, the pressure-strain term becomes negative and is increasingly balanced by the positive pressure diffusion. As the position of peak negative streamwise velocity is traversed, the production reverses sign, but remains low relative to pressure diffusion, a condition that prevents the shear stress from changing sign, as noted earlier. As the viscous sublayer is entered, the production reaches a weak maximum, but this is insufficient to affect the rapidly declining shear stress, which thus remains positive. Within the viscous sublayer, pressure strain rises strongly together with a corresponding drop in pressure diffusion, with both essentially balancing each other. At the wall itself, neither is constrained to vanish, because one constituent in both involves the correlation of pressure fluctuation and wall-normal

gradient of the streamwise-velocity fluctuation, neither of which asymptotes to zero at the wall.

The turbulence–energy budget shows that production is highest in the separated shear layer, thus causing a maximum in $\langle k \rangle$. The ratio of production to dissipation is of the order of 2 where the production reaches a maximum. Turbulent diffusion accounts for most of this imbalance, transporting energy from the production region to the reverse-flow region and to the edge of the shear layer. This explains the elevated values of $\langle k \rangle$ in the outer region despite the low velocity gradient and hence low production therein. Convection is also significant at the edges of the shear layer. At the outer edge, it removes energy to regions further downstream, while, in the reverse-flow region energy, is gained through convective transport from the reattachment region. Above the boundary layer, production is low in the reverse flow region, with positive convection and turbulence transport balanced by dissipation and pressure diffusion. Hence, the characteristics of this region are very different from those in a conventional mixing layer. As is the case with shear-stress production, that of turbulence energy also rises to a weak maximum very close to the wall, but its contribution to the balance is generally small. Within the viscous sublayer, pressure diffusion and viscous diffusion become the dominant gain terms, while dissipation becomes the dominant sink. As expected, the balance asymptotes to viscous diffusion being cancelled by dissipation, with all other terms vanishing at the wall.

The budget for $\langle u'u' \rangle$ shares a number of features with the budget for $\langle k \rangle$. The productions give similar profiles, with that of $\langle u'u' \rangle$ having a level about twice that of $\langle k \rangle$, since the production of $\langle w'w' \rangle$ is zero, while that of $\langle v'v' \rangle$ is negligible. On the other hand, the dissipation levels of all three normal stresses in the shear layer are similar, consistent with the concept of isotropy in the smallest scales. The imbalance between production and dissipation is compensated mainly by the pressure-strain term, which extracts energy from the $\langle u'u' \rangle$ component and transfers this to the other normal stresses, the balance of which thus feature positive pressure-strain contributions. In the near-wall region, outside the viscous sublayer, the budget of $\langle w'w' \rangle$ is dominated by positive convection and negative dissipation and pressure

strain. The positive convection reflects the transport of high levels of $\langle w'w' \rangle$ from the impingement zone in which splatting is an important mechanism. As shown earlier, the consequence is a sharp increase in $\langle w'w' \rangle$, which reaches a level very close to that of $\langle u'u' \rangle$. It is this process that causes a reversal in the pressure-strain contribution, with both $\langle u'u' \rangle$ and $\langle w'w' \rangle$ transferring energy to $\langle v'v' \rangle$. As the wall is approached, within the thin boundary layer, $\langle v'v' \rangle$ has to decay rapidly, and this is effected by a reversal in the pressure strain, which now transfers energy from $\langle v'v' \rangle$ to $\langle u'u' \rangle$ and $\langle w'w' \rangle$. Positive convective transport remains an important contributor to $\langle w'w' \rangle$, keeping this stress relatively high in the boundary layer. As the viscous sublayer is traversed, viscous diffusion tends to balance dissipation, as is the case with $\langle k \rangle$, while in the case of $\langle v'v' \rangle$, in which viscous diffusion is necessarily negligible and dissipation approaches zero as turbulence, including the smallest scales, tends toward a two-component state, the balance is dominated by pressure strain, which has to diminish $\langle v'v' \rangle$ at a rate proportional to y^4, and pressure diffusion.

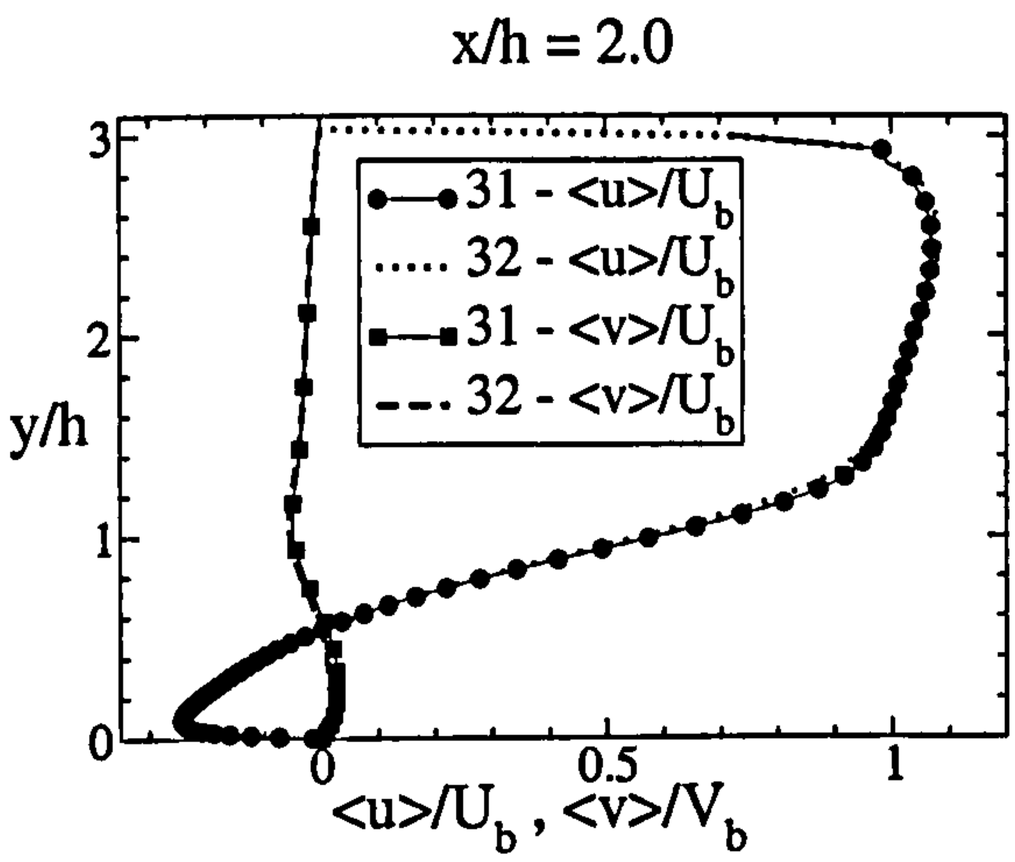

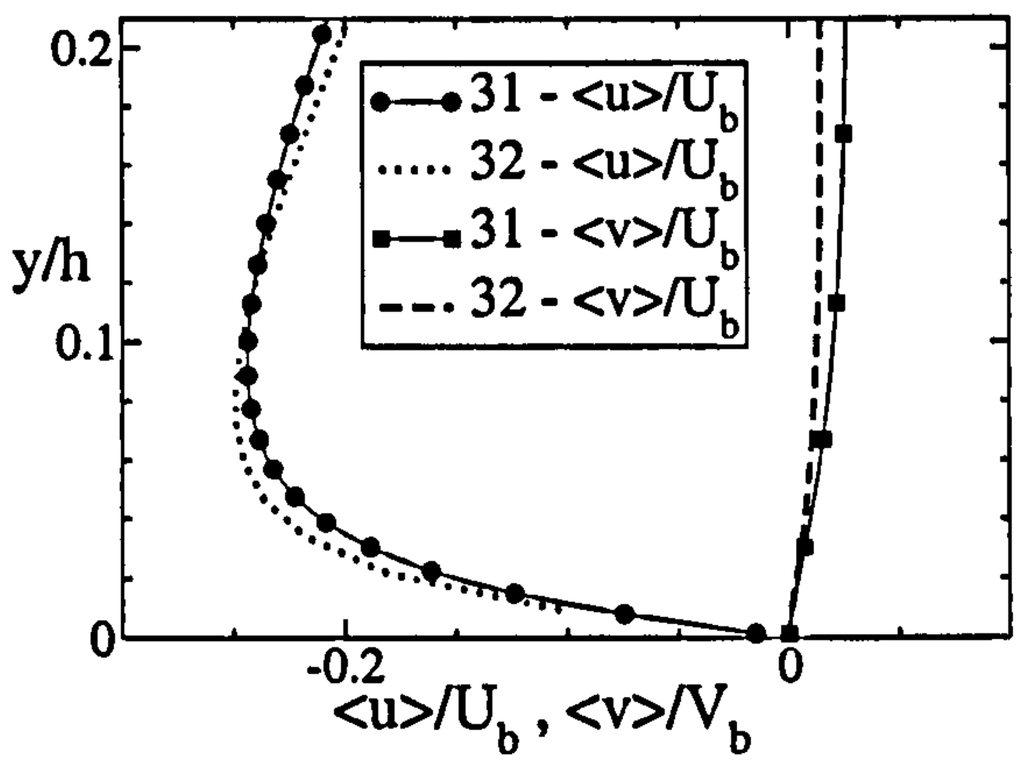

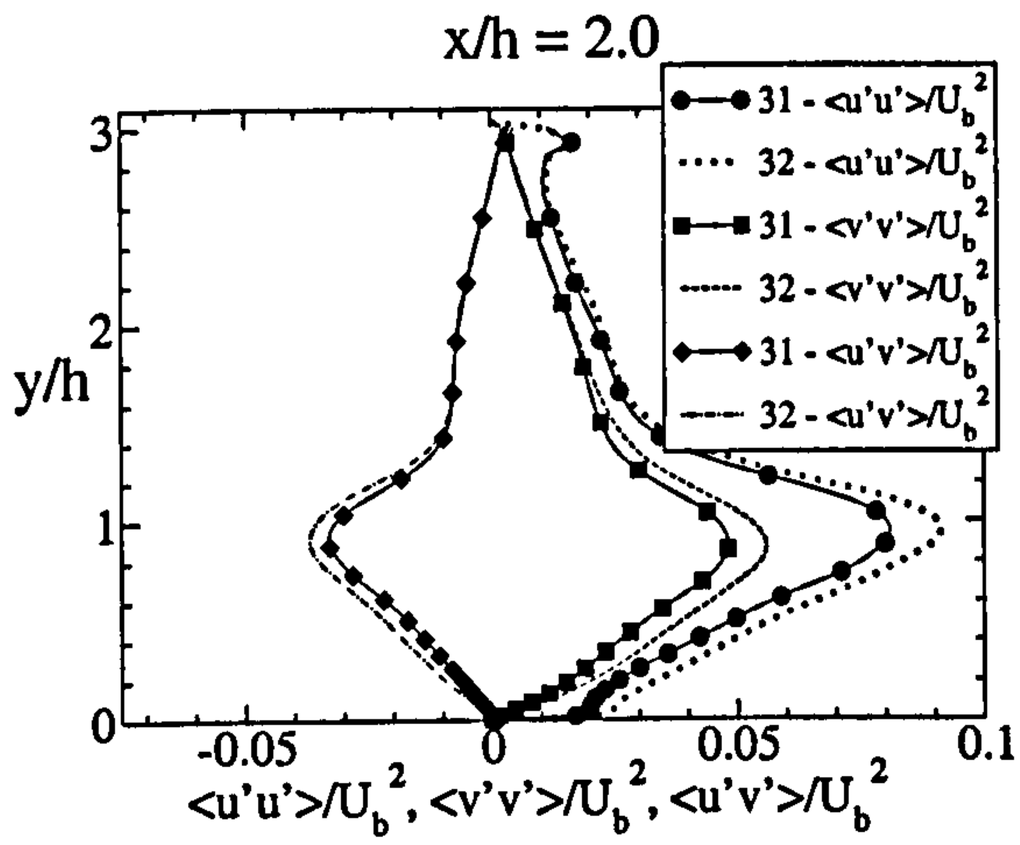

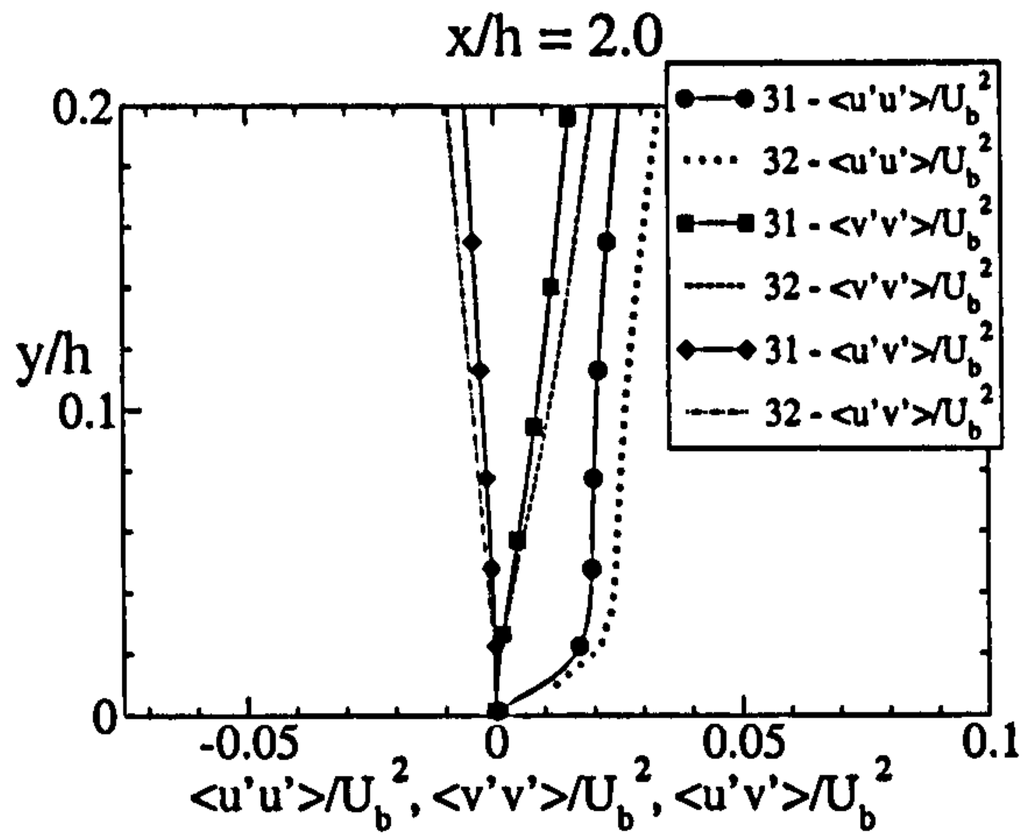

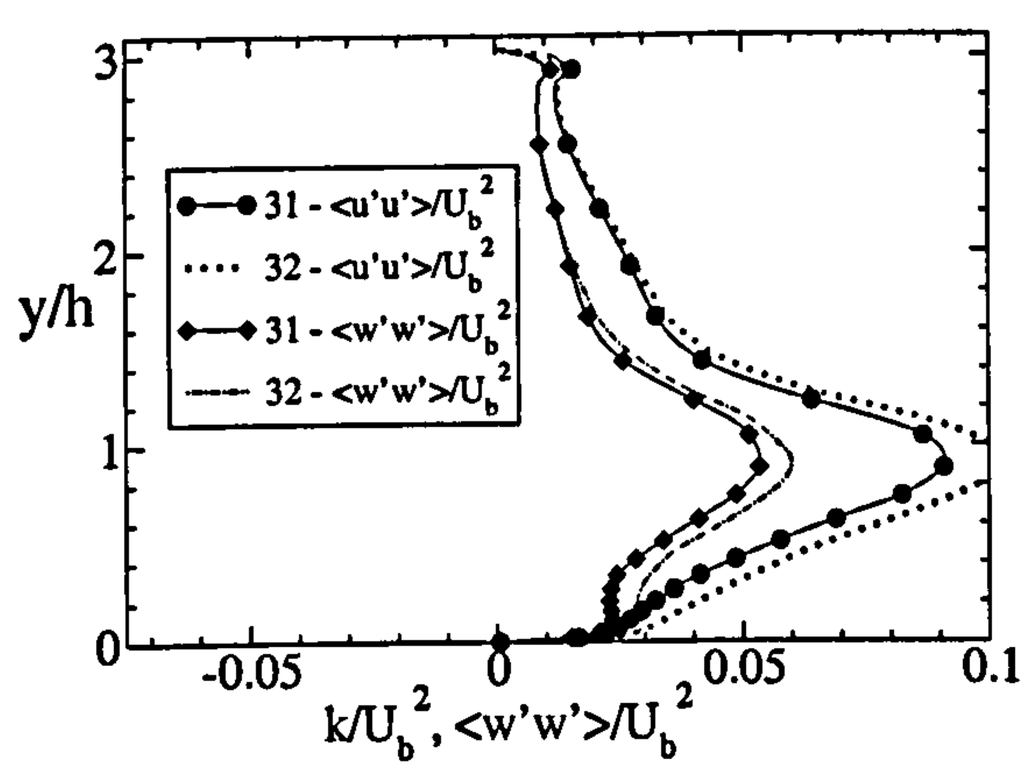

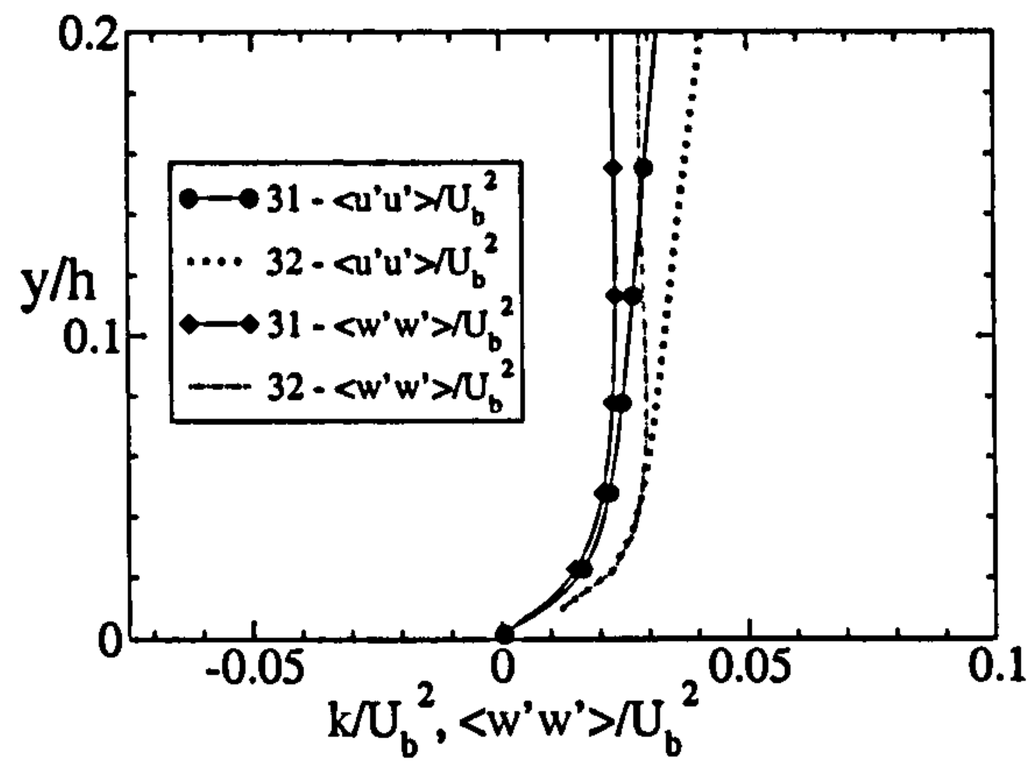

Figure 7.11: Velocity, normal and shear stresses and turbulence energy profiles at $x/h = 2.0$ for the highly resolved simulation.

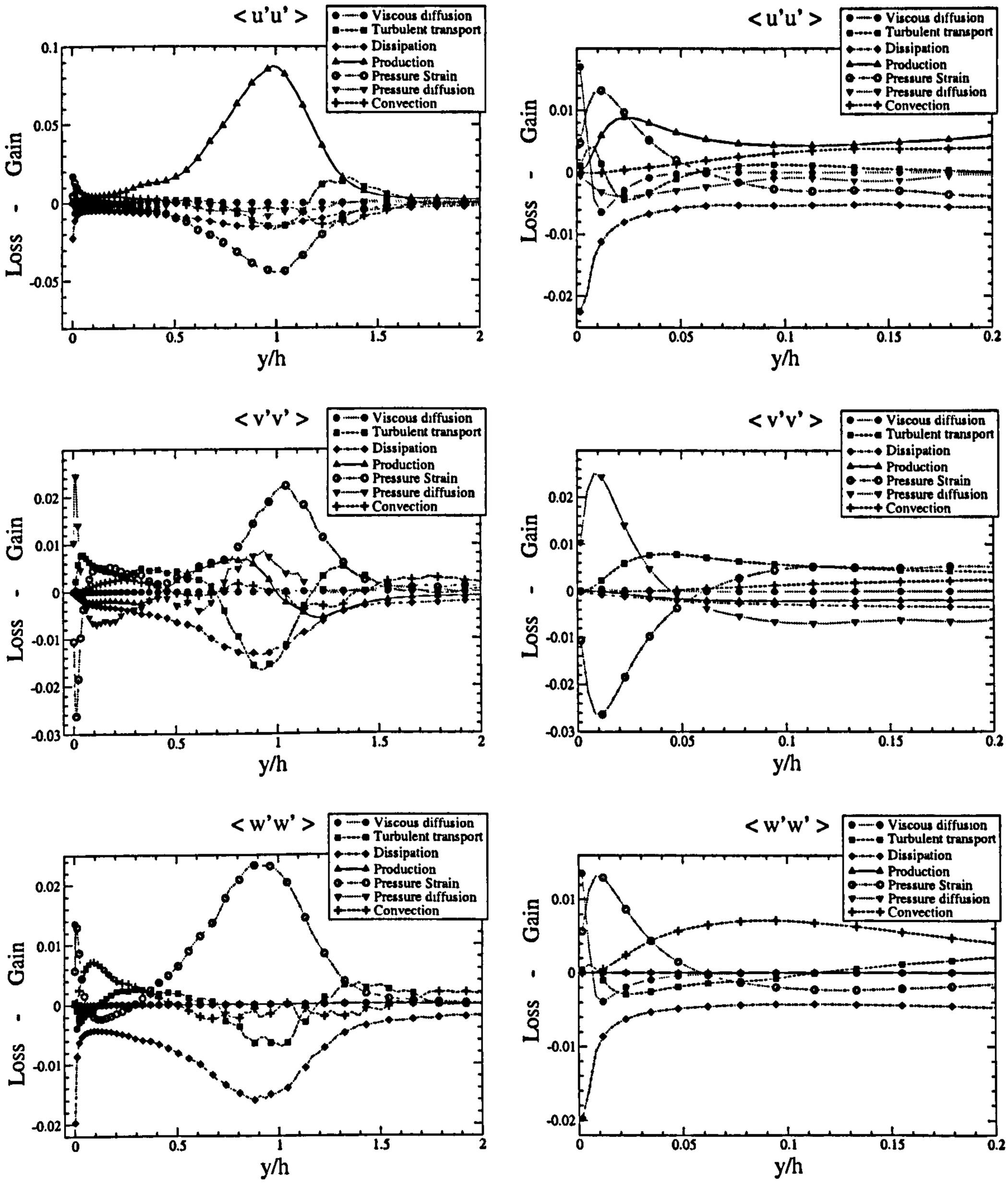

Figure 7.12: Budgets of the normal stresses at $x/h = 2.0$ for the highly resolved simulation. The left plots show the principal part of the channel and the right zoom around the bottom wall.

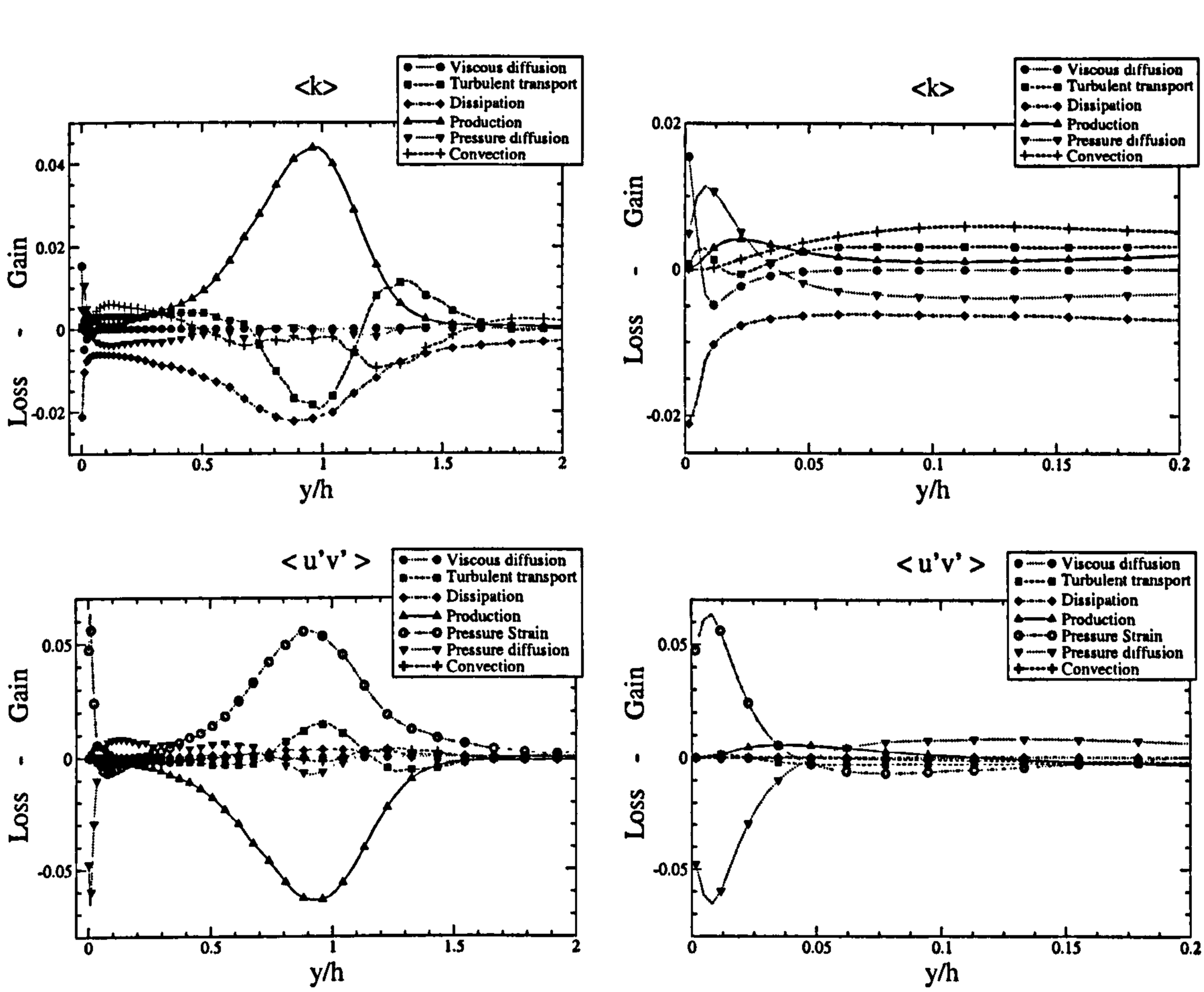

Figure 7.13: Budgets of the shear stress and turbulence energy at $x/h = 2.0$ for the highly resolved simulation. The left plots show the principal part of the channel and the right zoom around the bottom wall.

Position $x/h = 6.0$

This position is within the post-reattachment region, half way between reattachment and the foot of the next hill. The flow here consists of a boundary layer developing from the reattachment point with, above it, a wake originating from the separated shear layer further upstream. It is thus characterised by flow components with very different scales and history, which interact to form a flow recovering towards a fully-developed channel flow. It is well known that most statistical closures do not represent this recovery process well. Hence, the features discussed in this section are of particular interest to modellers.

Profiles of velocity and second moments are shown in Figure 7.14. The boundary layer, of thickness $y \approx 0.2h$, is bordered by a region of nearly constant velocity gradient, reflecting an ongoing recovery of the reattached shear layer. As seen from Figure 7.8, the flow develops against an adverse pressure gradient, caused by the outer flow decelerating mildly as fluid is being transported downward to fill the wake. The boundary layer at the upper wall is much thicker, of order $y = 0.6h$, and its structure is expected to conform to that of other boundary layers subjected to a mild adverse pressure gradient.

Although the flow in this section is drastically different from that at $x = 2h$, the turbulence field is characterised by qualitatively similar features, although the intensity of turbulence is now much reduced as the strain diminishes and the flow *tends* to approach a state of equilibrium. Thus, the stresses and turbulence energy reach maxima within the high-strain region of the mixing layer, the ratio $\langle u'v' \rangle / \langle k \rangle$ being close to 0.3, and $\langle u'u' \rangle$ exceeding $\langle w'w' \rangle$ by a factor of approximately 1.4. Some points of difference, pertaining to the flow above the boundary layer include a more distinctive separation between (the lower) $\langle v'v' \rangle$ and (the higher) $\langle w'w' \rangle$, with the ratio being typically 1.1 to 1.2, and the considerably broader region in which the stresses and turbulence energy are elevated, as a consequence of the positive shear strain and thus higher turbulence production occupying a correspondingly wider portion of the flow. Thus, with the boundary layer at the lower wall set aside, the distributions of second moments do not contain features not observed in other shear

layers. In the boundary layer, the most distinctive feature, also observed previously at $x/h = 2$, is a marked elevation of $\langle w'w' \rangle$, and this is again attributed to the splatting effect around reattachment, which causes large pressure fluctuations, in combination with convective transport from the reattachment region toward the location being considered. $\langle u'u' \rangle$ is observed to develop a local maximum in the boundary layer, but this is mainly due to production associated with the shear strain in the thickening boundary layer, although splatting may here too be a contributory process. The simultaneous elevation of $\langle u'u' \rangle$ and $\langle w'w' \rangle$ in the boundary layer is then responsible for the high level of $\langle k \rangle$ at around $y/h = 0.15$. As the shear stress remains low, for reasons clarified below by reference to the budgets, the ratio $|\langle u'v' \rangle|/\langle k \rangle$ reaches very high values, of order 10, well outside the semi-viscous near-wall region.

Figures 7.15 and 7.16 show the budgets for this location. In the shear-layer region, the budget for $\langle u'v' \rangle$ is similar to that at $x/h = 2.0$. However, the magnitude of the terms is now considerably smaller, because the velocity gradient and thus production are lower. In contrast to $x/h = 2.0$, turbulent diffusion plays a more important role in balancing production in combination with the more dominant pressure-strain process. The former transports shear stress away from the region where it is produced toward the wall and the edge of the sheared layer. At this station, production and pressure strain do not change sign, as expected for positive and substantial shear straining across the lower flow portion. The latter develops a near-wall minimum in a region in which pressure diffusion rises and balances the negative turbulence transport and production. Thus, the tendency for production to elevate the magnitude of the shear stress is counteracted by pressure-related turbulence transport away from the boundary layer, keeping the shear stress relatively low and resulting in the previously observed high levels in the ratio $|\langle u'v' \rangle|/\langle k \rangle$. As the wall is approached, through the viscous sublayer, the budget is dictated by a balance between very high pressure-strain and pressure-diffusion contributions. This is a rather surprising observation, but not an unrealistic one, as pressure fluctuations are high in this region and evidently correlate with $\partial u'/\partial y$, which is non-zero at the wall.

The budget for $\langle k \rangle$ shows a significant level of production in the broad shear-layer region, but this is much lower than at $x/h = 2.0$. Also, in contrast to $x/h = 2.0$, it is not much larger than dissipation, the ratio being about 1.2, so that turbulence is here closer to local equilibrium. Alongside dissipation, turbulent transport plays an important role in this layer, transporting turbulence energy away from the region of production toward the wall and the outer region of the sheared flow. Convection too makes an important contribution by transporting high levels of energy from upstream regions, (see the budget for $x/h = 2.0$) to the section being considered and hindering the approach toward turbulence equilibrium. In the boundary layer, the balance is dictated by turbulent transport and dissipation, the former transporting energy from the outer shear layer into the boundary layer. This interaction is very different from that in an ordinary boundary layer bordering a free stream, in which the balance is mainly between production and dissipation. As the wall is approached, pressure diffusion is the main opponent of dissipation. As will be shown below, this gain is attained through pressure fluctuations, probably elevated by splatting at the impingement region, correlated with v-fluctuations. At the wall itself, all terms but viscous diffusion and dissipation tend to vanish, as required by kinematic constraints.

As in the budget for $\langle k \rangle$, the production of $\langle u'u' \rangle$ is now much lower than at $x/h = 2.0$ and so is the pressure-strain term, which is here too the largest sink in the shear-layer region. Also, as in the case of $\langle k \rangle$, convection from upstream regions increases $\langle u'u' \rangle$ and turbulent diffusion decreases the stress by lateral transport away from the central portion of the shear layer. Over most of the boundary layer, dissipation is again balanced mainly by turbulent diffusion transporting energy from the shear layer towards the wall. As the wall is approached, pressure-strain rises and, aided by (relatively weak) production, balances dissipation. The presence of positive pressure-strain reflects the need to drain energy from $\langle v'v' \rangle$ as turbulence approaches a two-component state by wall-blocking, and this energy is transferred to both $\langle u'u' \rangle$ and $\langle w'w' \rangle$. However, the bulk of the pressure-strain-effected transfer will be seen to be to $\langle w'w' \rangle$, and this is probably associated with splatting. At the wall, there is the usual balance between dissipation and viscous diffusion, also observed in the budgets for $\langle k \rangle$ and $\langle w'w' \rangle$.

The budget for $\langle v'v' \rangle$ in the shear-layer region is dominated by dissipation and turbulent transport balanced mainly by a positive pressure-strain contribution, which is derived from $\langle u'u' \rangle$. The most interesting processes pertain to the near-wall region. Here, positive turbulence transport balances the negative pressure-strain contribution, the latter reflecting the process that is required to diminish this component through wall blocking. As the wall is approached, the balance is increasingly dominated by negative pressure-strain and positive pressure diffusion. Both reflect the high level of pressure fluctuations and the interaction of these with velocity and strain perturbations. It is the high level of pressure diffusion in the budget of $\langle v'v' \rangle$ which balances the dissipation of $\langle k \rangle$. Importantly, the near-wall dissipation of $\langle v'v' \rangle$ is low and quickly diminishes as the wall is approached, reflecting the trend toward a two-component state of the small-scale fluctuations contributing to dissipation. Hence, the near-wall dissipation is highly anisotropic.

The most noteworthy features in the budget of $\langle w'w' \rangle$ are again to be found in the near-wall region. Production is necessarily absent, and the near-wall balance is dominated by negative dissipation and a high positive pressure-strain contribution. The strongly preferential transfer of energy from $\langle v'v' \rangle$ to $\langle w'w' \rangle$ is important to highlight, and this is taken to signify the contribution of splatting associated with reattachment, a process that extends over a substantial proportion of the horizontal channel wall. As a consequence of this elevation in $\langle w'w' \rangle$, negative turbulent diffusion arises, transporting $\langle w'w' \rangle$ away toward the wall and to the outer part of the boundary layer in which all normal stresses feature positive turbulent transport supplying the boundary layer with energy components from the outer shear layer.

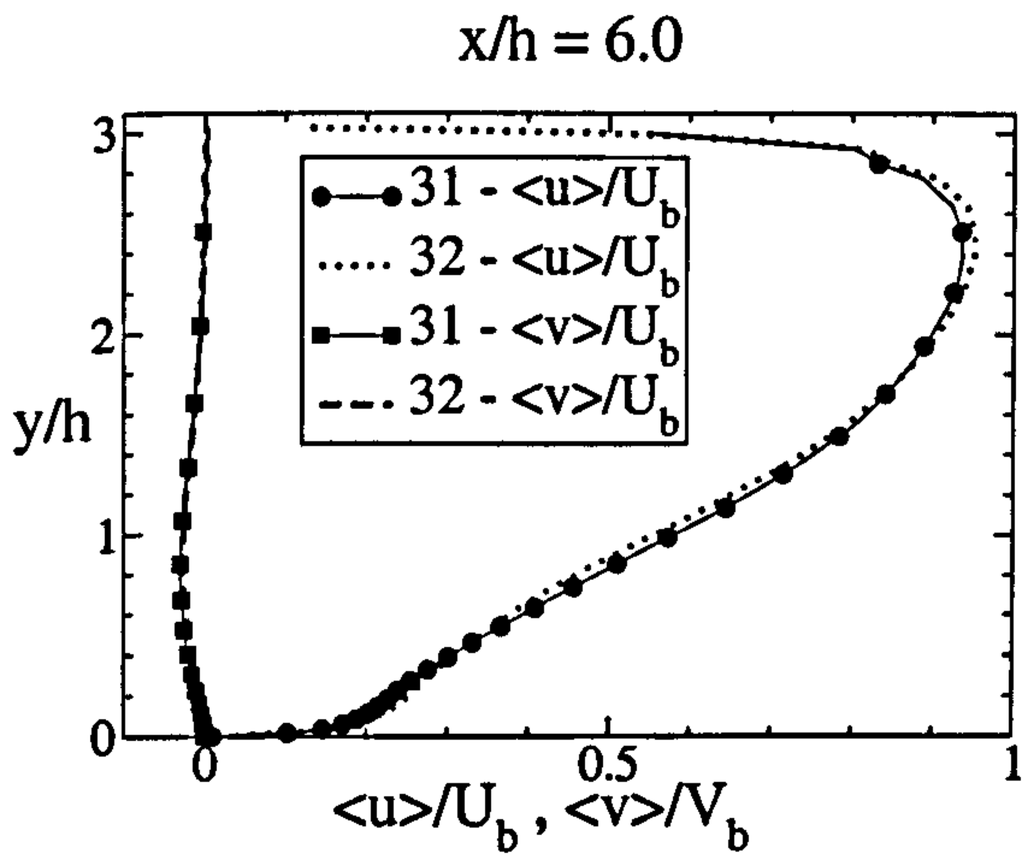

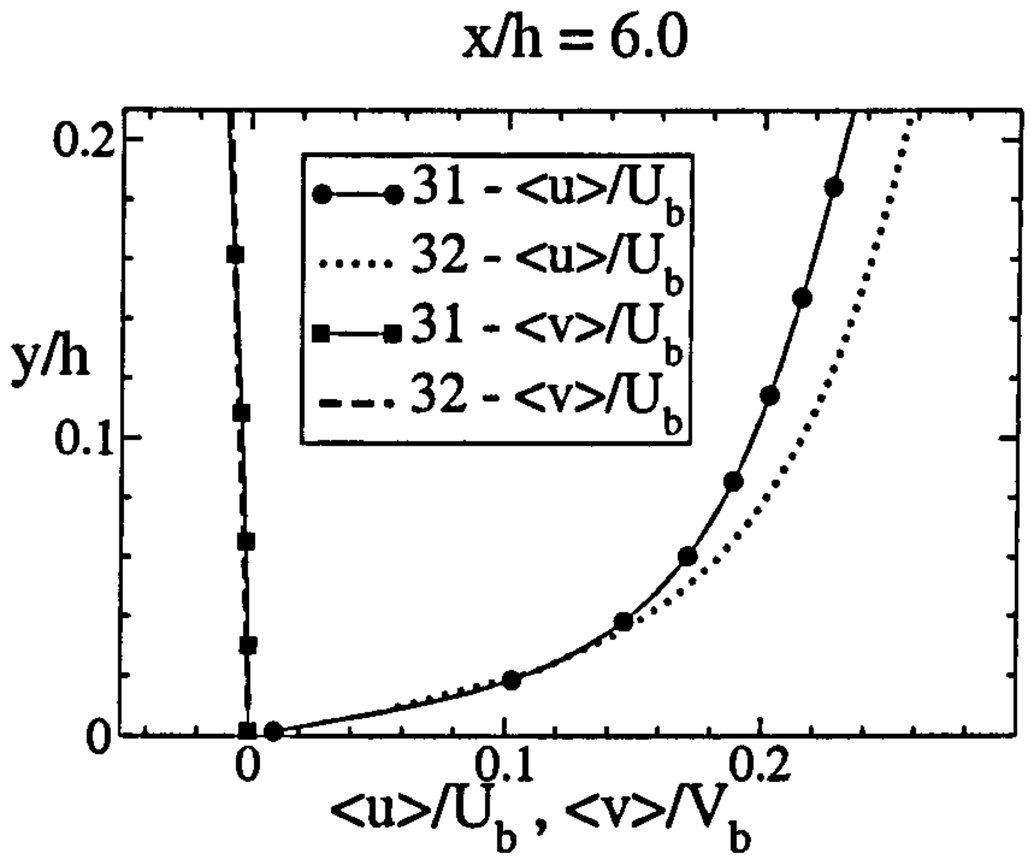

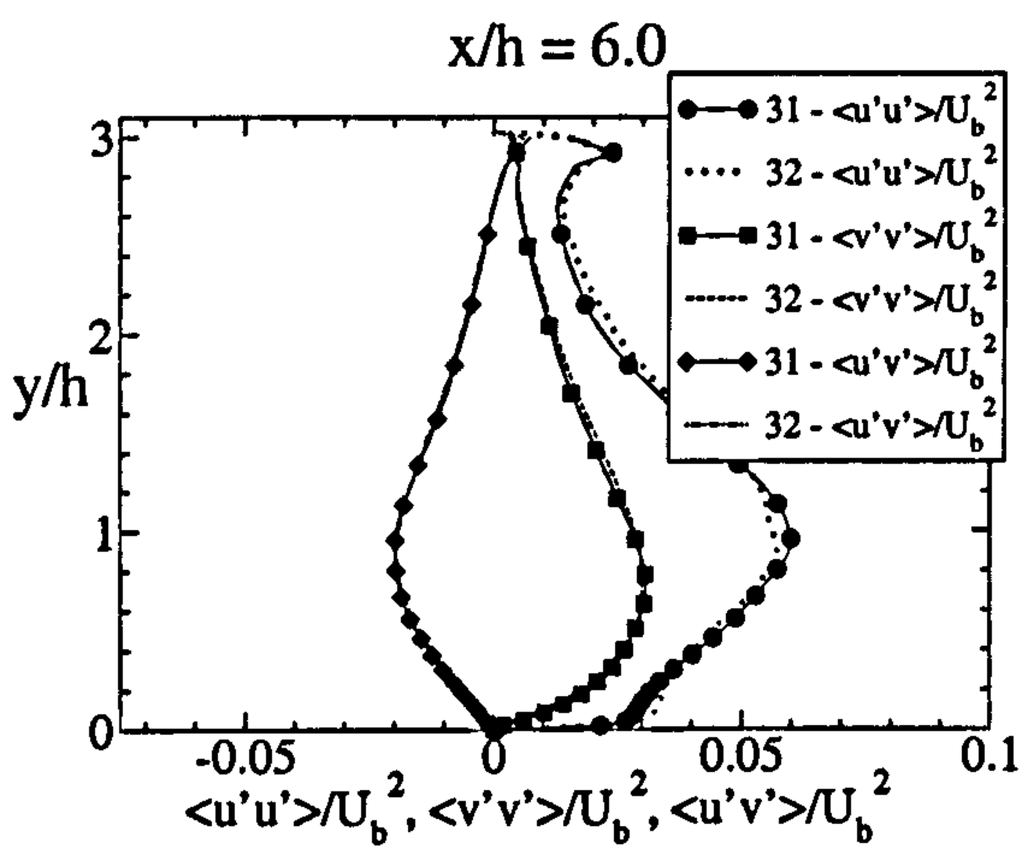

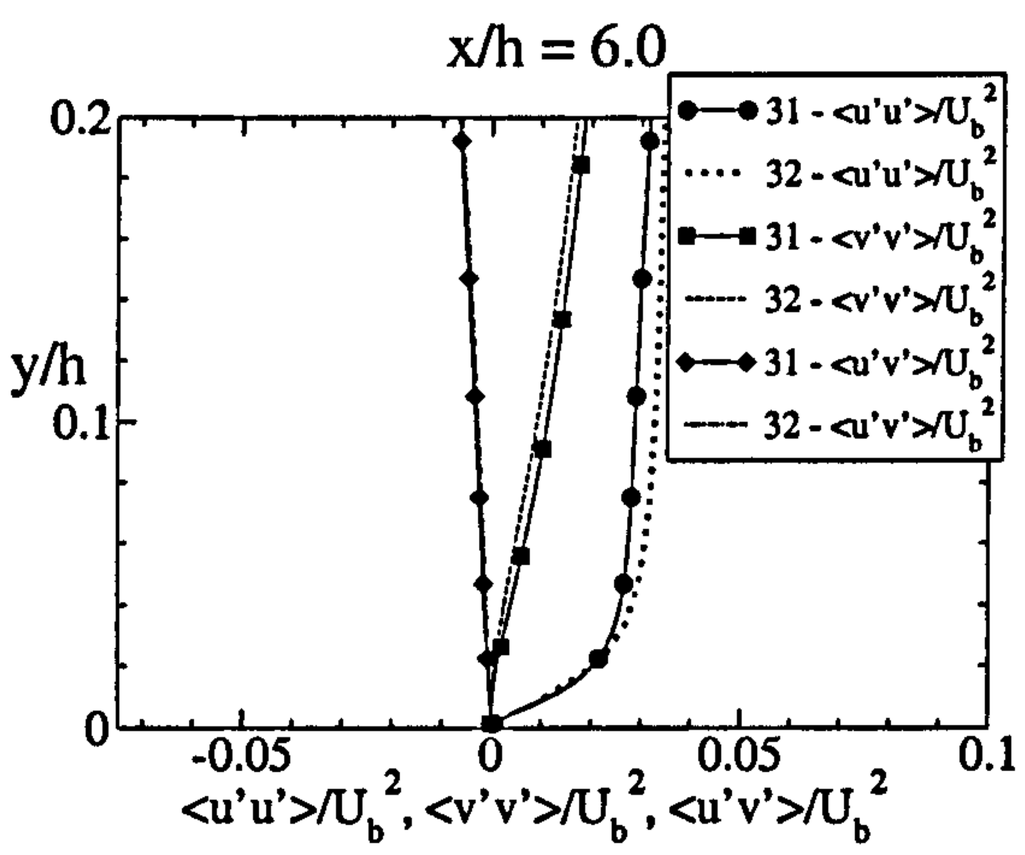

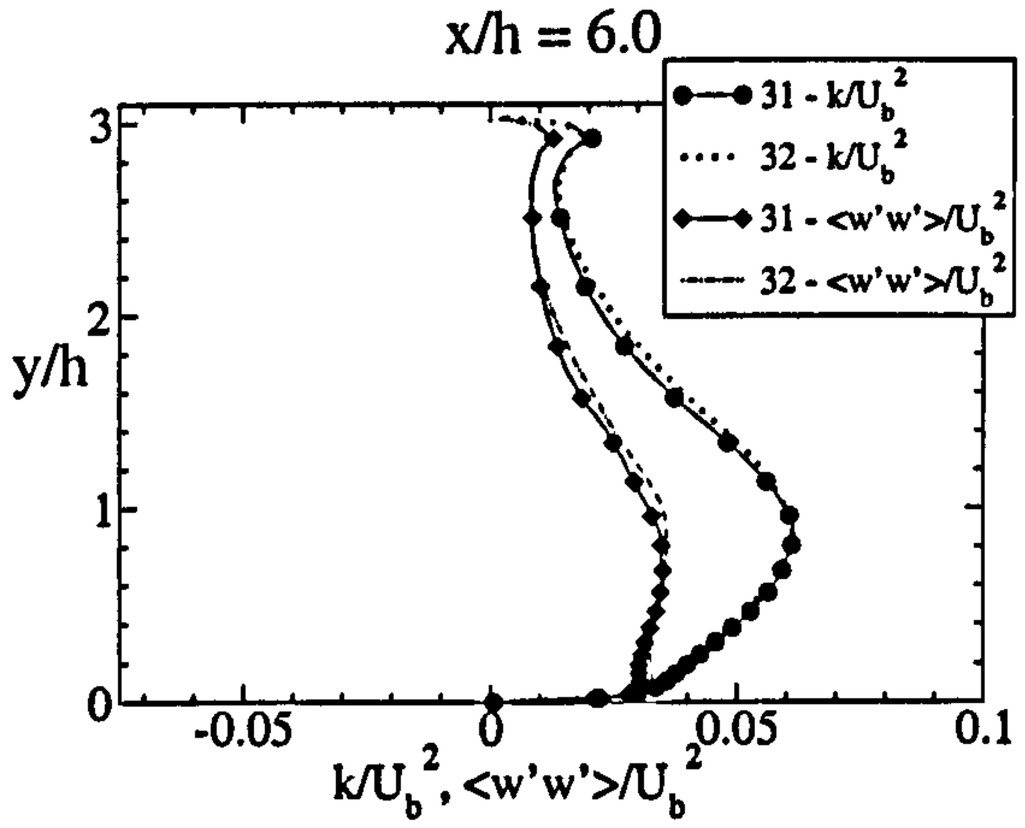

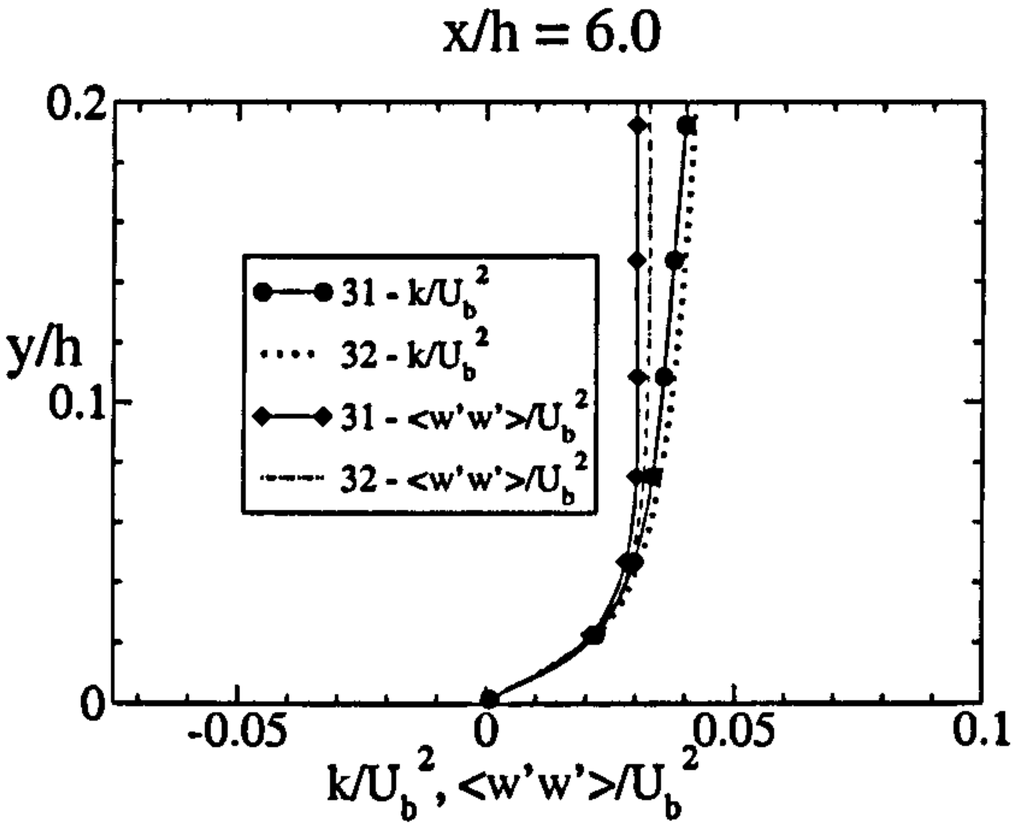

Figure 7.14: Velocity, normal and shear stresses and turbulence energy profiles at $x/h = 6.0$ for the highly resolved simulation.

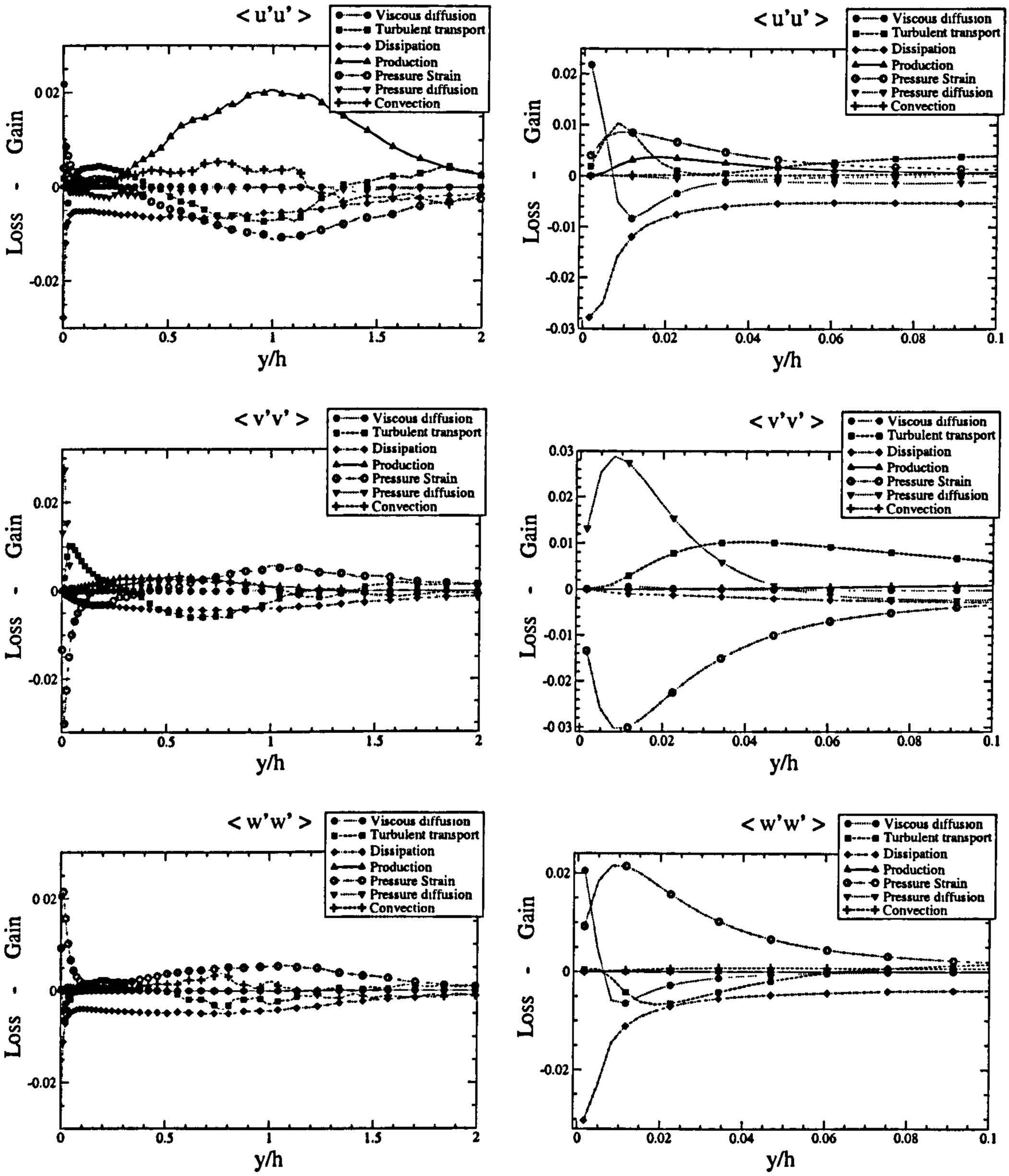

Figure 7.15: Budgets of the normal stresses at $x/h = 6.0$ for the highly resolved simulation. The left plots show the principal part of the channel and the right zoom around the bottom wall.

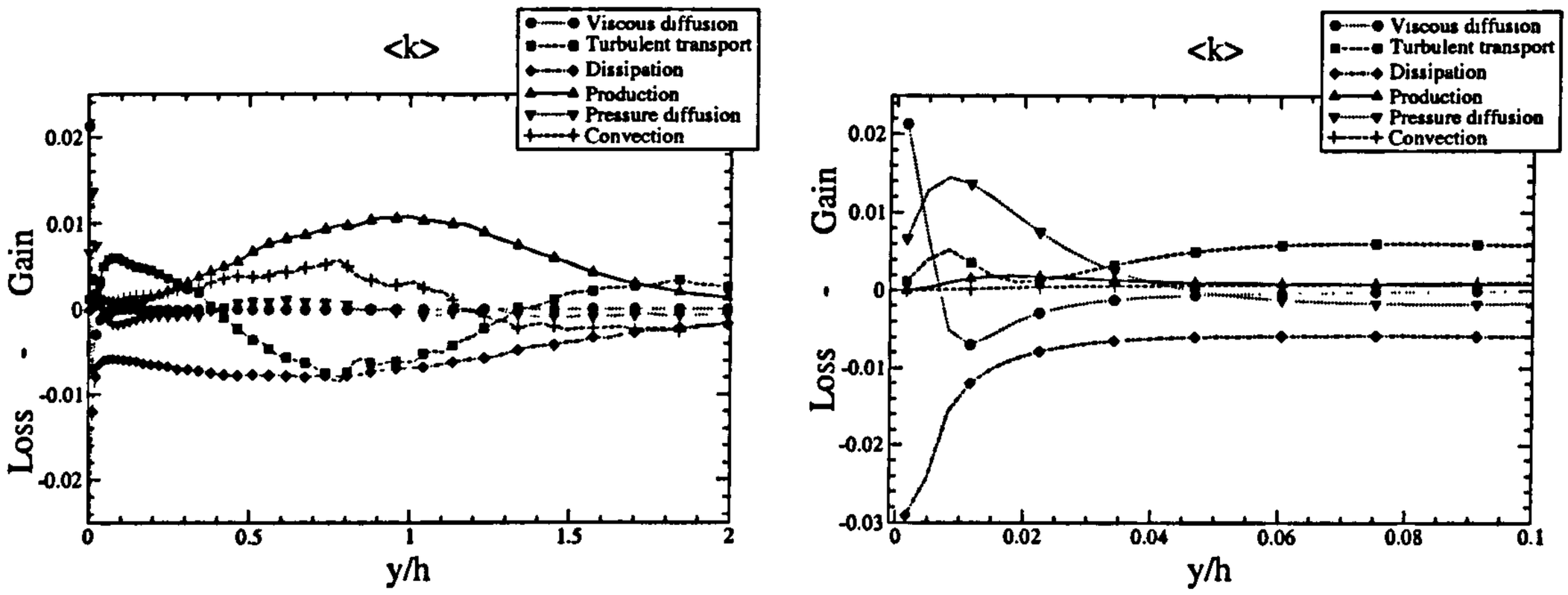

Figure 7.16: Budgets of the shear stress and turbulence energy at $x/h = 6.0$ for the highly resolved simulation. The left plots show the principal part of the channel and the right zoom around the bottom wall.

Position $x/h = 8.0$

This position lies in the windward portion of the hill where the flow is subjected to strong acceleration. Profiles of mean velocity and Reynolds stress components in $x, y-$coordinates are given for the complete cross-section in Figure 7.17. Near the lower wall, which is inclined at an angle of 38° at $x/h = 8$ from the horizontal axis, they do not lend themselves to a physically transparent interpretation and discussion, since u and v are not tangential and normal to the wall, respectively. Hence, in the near-wall region, up to a wall distance of about $0.2h$, profiles of the wall tangential (t) and normal (n) components are also provided in Figures 7.18, albeit not along a line normal to the wall but along a vertical line.

From Figure 7.17, it can be seen that the overall behaviour of the $u-$velocity is similar to that at $x/h = 6$, but due to the acceleration, the velocity is larger near the wall and the boundary layer is thinner (only about $0.05h$). Except near the lower wall, the distribution of Reynolds stresses over the full channel height, as plotted in Figure 7.17, is also very similar to $x/h = 6$. However, close to the wall, the stresses and the corresponding budgets present some exceptional features not seen at $x/h = 6$ which merit closer consideration. As is seen from Figures 7.17 and 7.18, one such feature is an extremely high level of $\langle w'w' \rangle$ relative to the $\langle u'u' \rangle$ and $\langle v'v' \rangle$ in the (x, y) plane. This statement retains its validity whether made by reference to the (x, y) or the (t, n) decomposition. The main difference between the two is that the wall-oriented decomposition highlights the very rapid decay of v-fluctuations, as is expected to occur due to wall blocking. While these stresses in the (x, y) plane depend on the orientation of the frame of reference, their sum does not, and it is advantageous therefore to consider the distribution of $\langle u'u' + v'v' \rangle/2$, included in Figure 7.17, and later also the budget for this quantity rather than the budgets for the individual components $\langle u'u' \rangle$ and $\langle v'v' \rangle$. For that same reason, the budget for the shear stress is not presented here. As seen, $\langle w'w' \rangle$ is also extremely high relative to this sum. Moreover, $\langle k \rangle$ shows a distinct near-wall peak, which is evidently a consequence of the very high near-wall level of $\langle w'w' \rangle$.

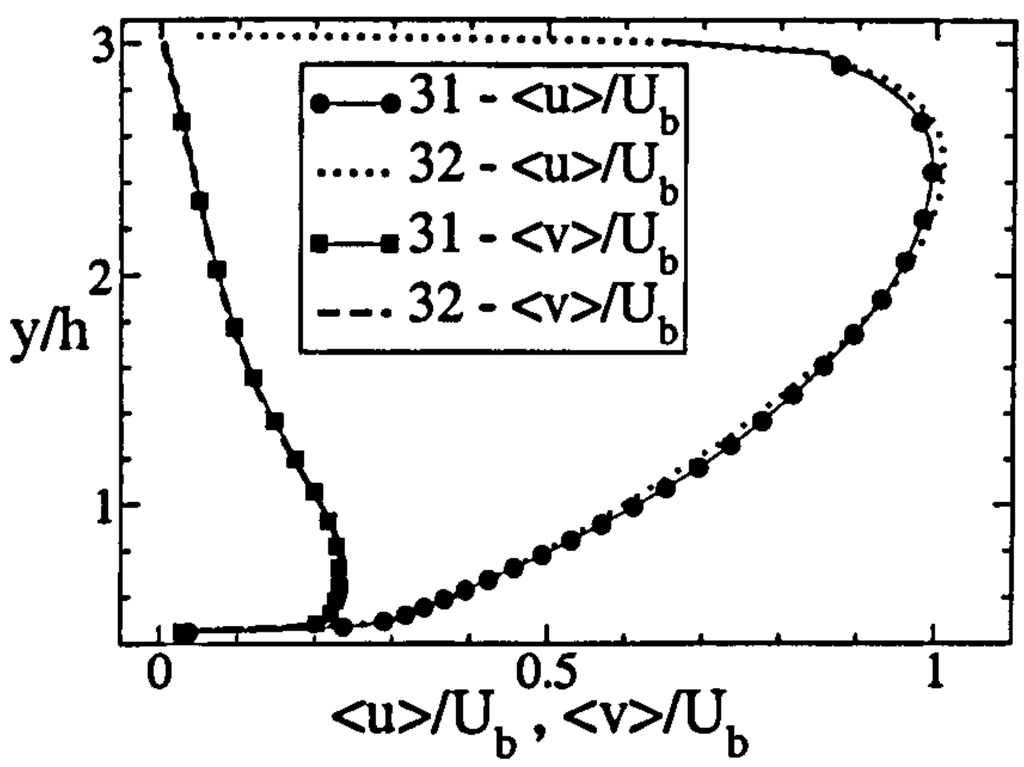

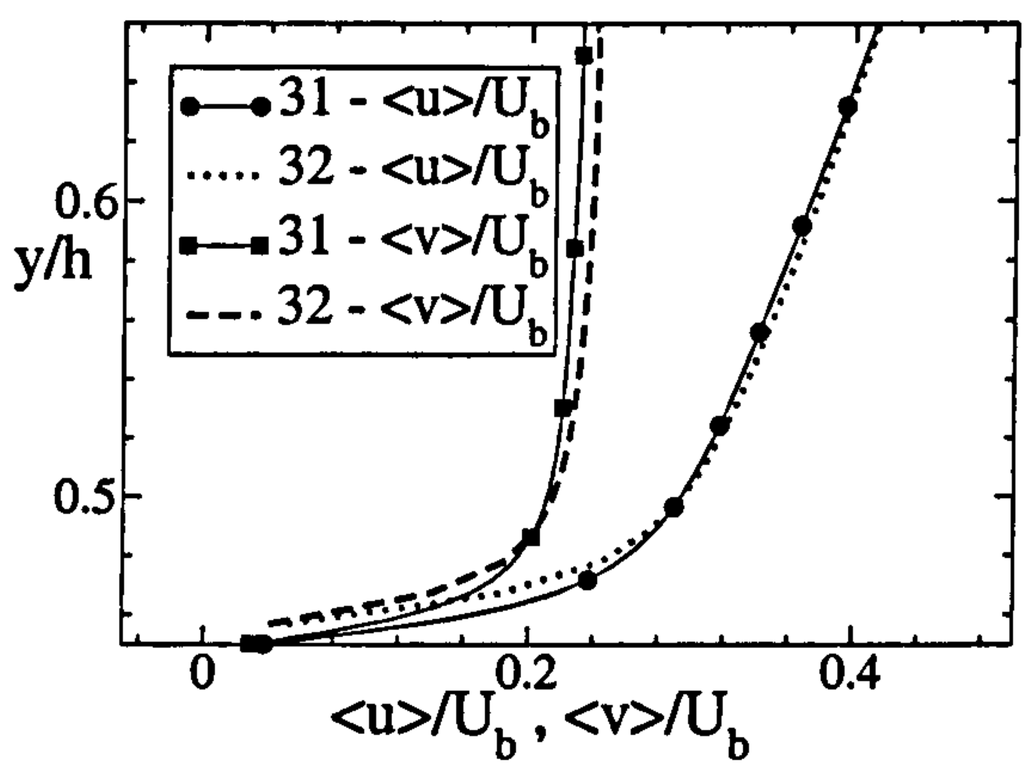

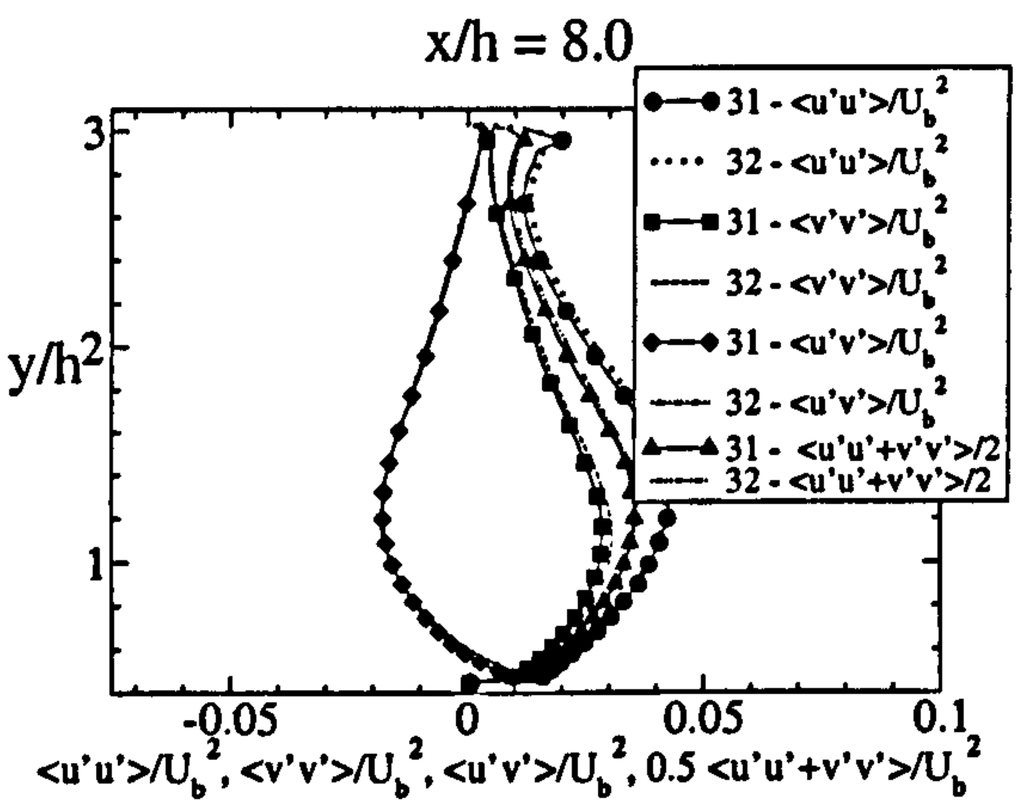

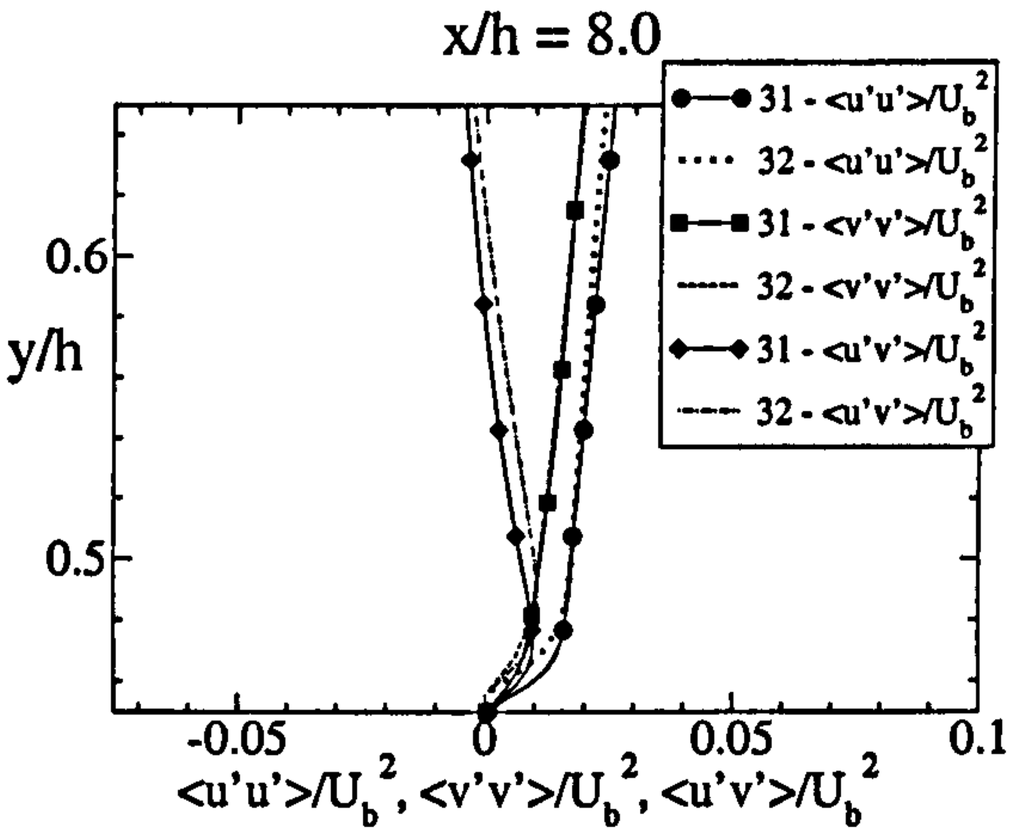

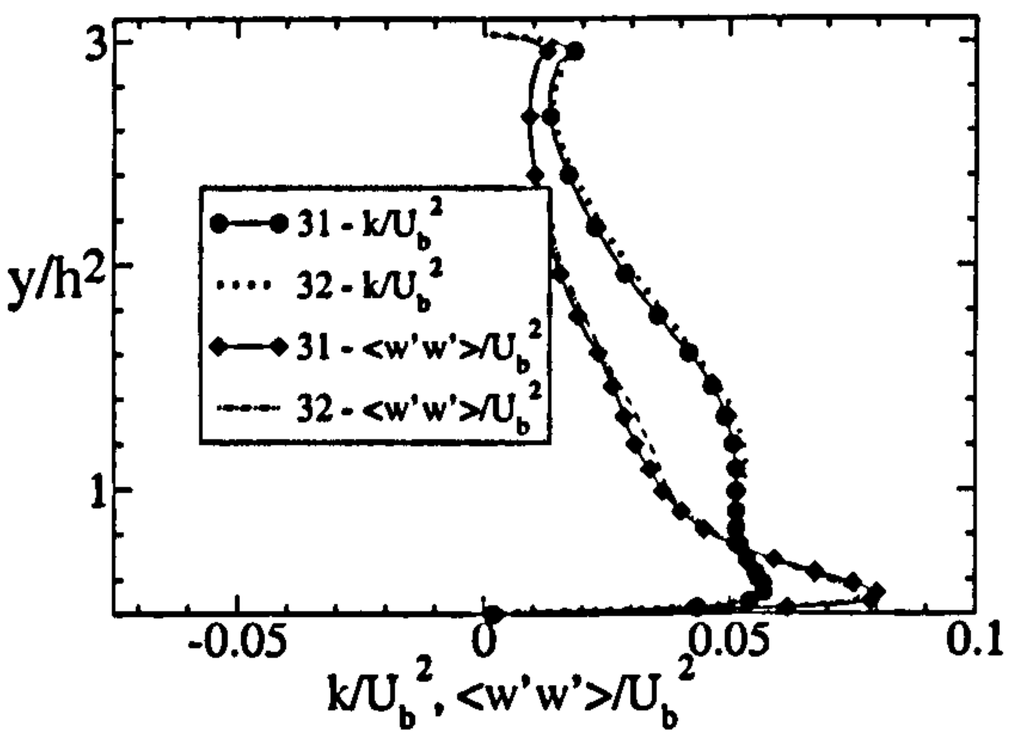

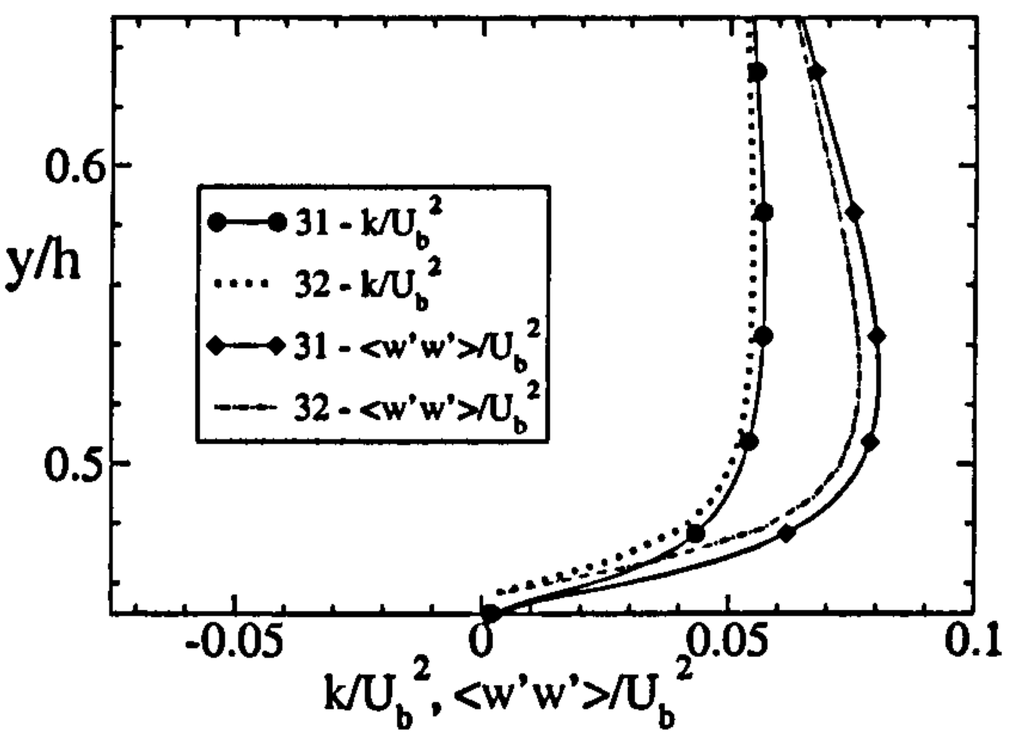

Figure 7.17: Velocity, normal and shear stresses and turbulence energy profiles at $x/h = 8.0$ for the highly resolved simulation.

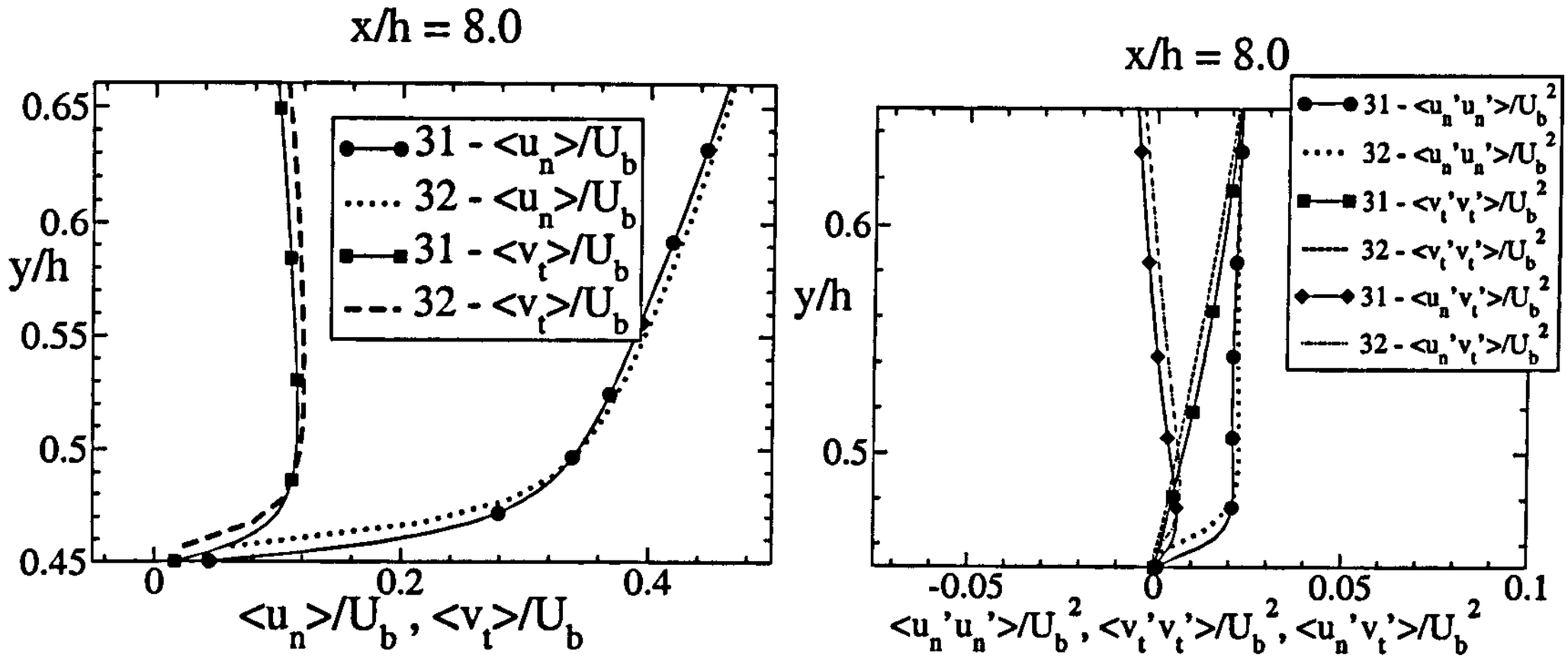

Figure 7.18: Velocity, normal and shear stresses and turbulence energy profiles at $x/h = 8.0$ for the highly resolved simulation. These profiles are converted into the wall normal system of coordinates at this particular location.

This extreme behaviour is not observed in other locations although, at $x/h = 7$ (not shown here), $\langle w'w' \rangle$ was already found to exceed $\langle u'u' + v'v' \rangle/2$ very near the wall, indicating that the flow is about to undergo some drastic modification further downstream. At this location, the lower wall is still horizontal although very close to the foot of the hill.

In order to investigate the anomalous behaviour of the $w-$fluctuations from a statistical point of view, the focus is now set on the turbulence-energy budgets for $x/h = 7$ and $x/h = 8$ presented in Figures 7.20 and 7.21, respectively. It must be noted that the location $x/h = 7$ is very close to the foot of the hill with the lower wall still horizontal. While the budgets at both locations are qualitatively similar, they present significant quantitative differences. In both cases, dissipation is balanced, substantially, by viscous diffusion close to the wall. A significant difference between the budgets lies in the substantially higher contribution of pressure diffusion to the budget at $x/h = 8$, which is balanced by increased dissipation and viscous diffusion.

Figure 7.21 shows the budgets for $\langle w'w' \rangle$ and $\langle u'u' + v'v' \rangle$ at $x/h = 8$. The comparison leads to the conclusion that the increase in $\langle w'w' \rangle$ is due to energy being extracted from the latter components and fed to $\langle w'w' \rangle$ by pressure-strain interaction. This is curious as $\langle w'w' \rangle$ is already higher than $\langle u'u' + v'v' \rangle$. This observation,

thus, contradicts the established concept of pressure-strain interaction acting to isotropize the Reynolds-normal stresses. Hence, models based on this concept must fail here. Importantly, this mode of transfer, albeit much less pronounced, is also observed at $x/h = 7$. It may therefore be claimed that this process is physically significant, unless the spanwise constraint, noted above in relation to the spanwise length scale, introduces some drastic limitations to the flow.

Reference to the budget for $\langle w'w' \rangle$ shows production and pressure diffusion to be zero, as is required by physical constraints. As noted already, pressure-strain is a major source of gain for $\langle w'w' \rangle$. Another is viscous diffusion, the high level of which is consistent with the requirement that viscous turbulence-energy diffusion should balance dissipation at the wall. Away from the wall, viscous diffusion reverses and becomes negative, due to the reversal of the gradient of $\langle w'w' \rangle$. This and turbulence transport largely balance the pressure-strain term.

The loss of $\langle u'u' + v'v' \rangle$ by the action of pressure-strain interaction, shown in Figure 7.21, has already been noted. This loss is seen to be largely compensated by pressure diffusion, except very close to the wall, where the balance is increasingly dominated by dissipation and viscous diffusion, as it does in the case of $\langle k \rangle$. Thus, here, more than in other sections through the flow, the message that is emerging is that the split of the pressure-fluctuation-containing term into pressure-strain and pressure diffusion is somewhat synthetic and not necessarily a good basis for constructing closures at second-moment level. A similar mode of compensation is also observed at $x/h = 7$, although the magnitude of the contributions is significantly lower. It is interesting to observe here that the budgets for $\langle u'u' \rangle$ and $\langle v'v' \rangle$, separately, at $x/h = 8$ display extremely large and opposite levels of pressure diffusion and pressure-strain, rendering other contributions to the budget almost insignificant. This is quite different to the budgets of these two stresses at $x/h = 6$ and $x/h = 7$, but this difference is due to the Cartesian decomposition relative to the inclined wall at this location. Hence, it is difficult to provide insightful interpretations for these stresses individually, and this is the reason for focusing on their sum in the above discussion.

At this stage, it seems hard to provide an unambigous proof about the precise

mechanisms responsible for the anisotropization of the Reynolds stresses at the bottom wall and the windward face of the hill. Apart from the present statistical analysis, a detailed analysis of instantaneous structures has been performed and is reported in Subsection 7.3.7. All information available points to a dominance of a splatting effect. This is further supported by results from Perot and Moin [171] who investigated near–wall flows with DNS. Their analysis of turbulent budgets near a solid wall without mean flow also features an anisotropization in the budget of the tangential Reynolds stress via the pressure–strain term. To some extent, the present interpretation is also supported by results of simulations of reattaching backward-facing-step flows (Le and Moin [117]) which also feature large spanwise stress levels, exceeding the streamwise stress. In the present case, the effect may have been accentuated by the high streamwise velocity in the acceleration region along the windward face of the hill.

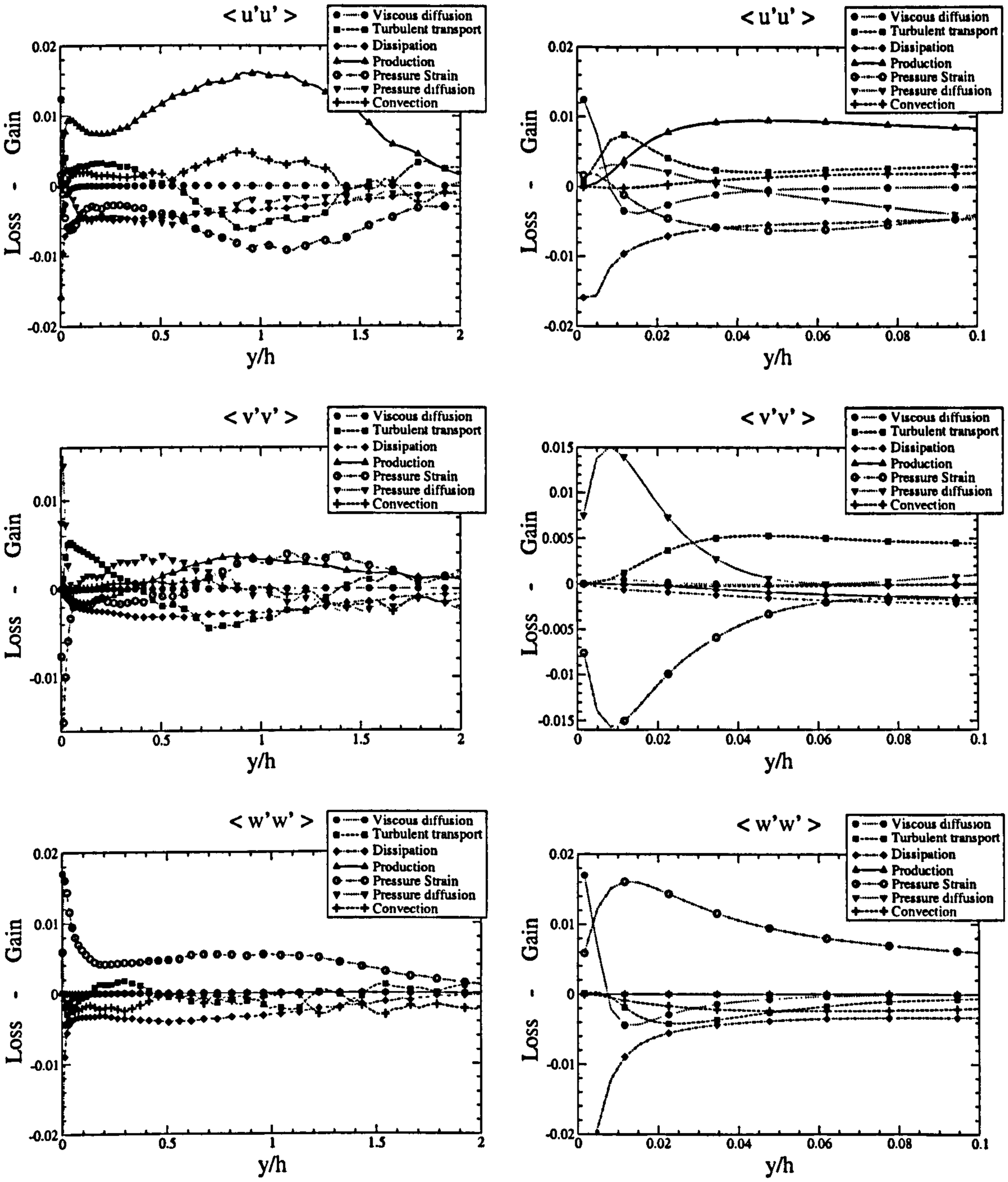

Figure 7.19: Budgets of the normal stresses at $x/h = 7.0$ for the highly resolved simulation. The left plots show the principal part of the channel and the right zoom around the bottom wall.

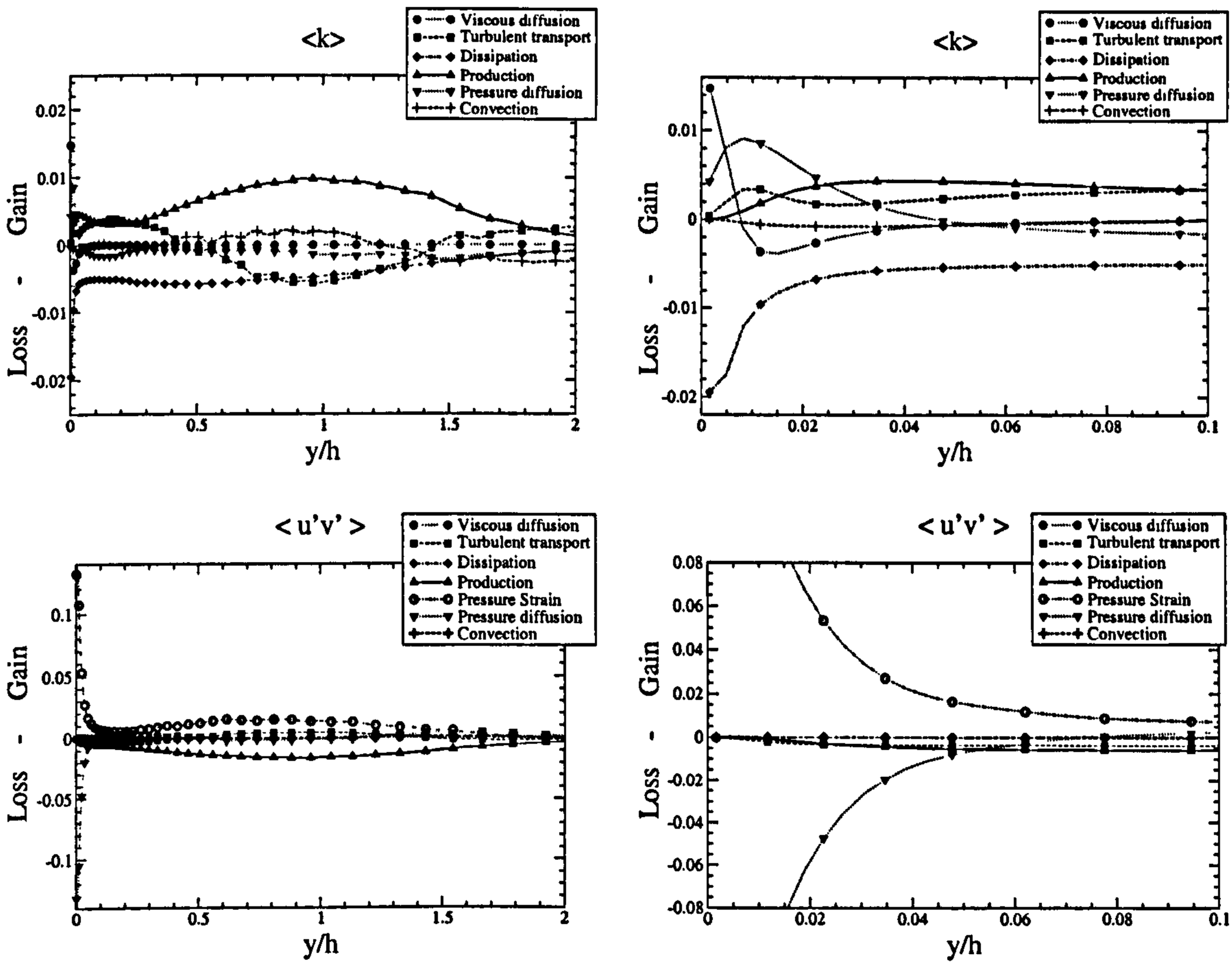

Figure 7.20: Budgets of the shear stress and turbulence energy at $x/h = 7.0$ for the highly resolved simulation. The left plots show the principal part of the channel and the right zoom around the bottom wall.

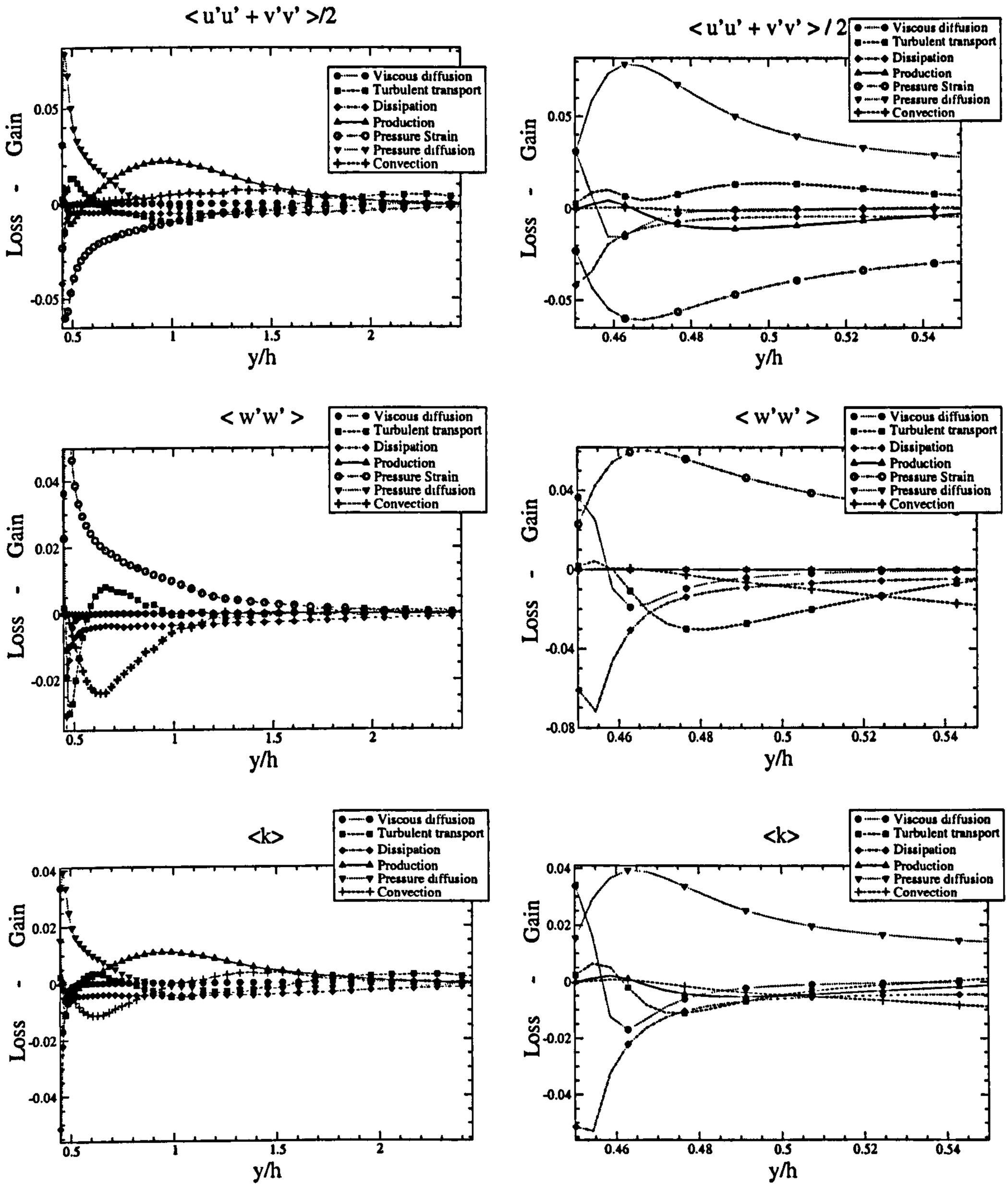

Figure 7.21: Budgets of the half sum of the streamwise and vertical stresses, spanwise stress and turbulence energy at $x/h = 8.0$ for the highly resolved simulation. The left plots show the principal part of the channel and the right zoom around the bottom wall.

Anisotropy of the flow

The Lumley triangle [133], introduced in Section 5.5 and shown in Figure 7.22, is used here to analyse the state of turbulence in characteristic regions of the flow. Fundamental considerations aside, this representation is useful to turbulence modellers attempting to construct anisotropy-resolving closures. These closures indeed make uses of the anisotropic Reynolds stress second and third invariants, defined in Section 5.5 and designed by II and III, respectively, and also the Flatness parameter, defined in Equation (5.26). In Subsection 6.6.2, such a map for the turbulent channel flow is presented and discussed.

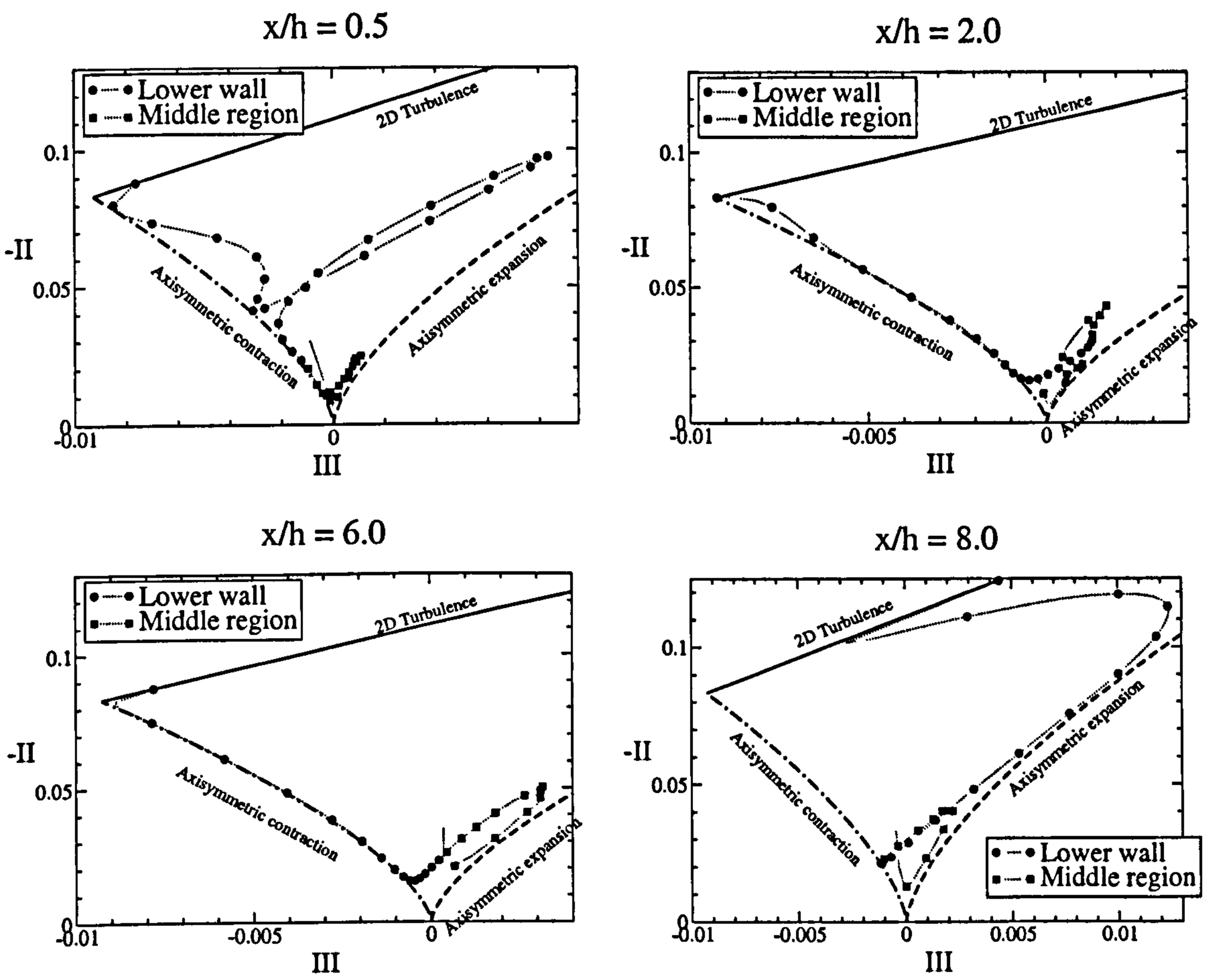

Figure 7.22: Invariant maps along vertical lines at four streamwise locations.

Figure 7.22 shows the loci in Lumley's triangle associated with traverses across four streamwise locations, while Figure 7.23 gives the corresponding profiles for the flatness parameter A. Variations of II and III are not shown here but can be found

in Jang et al [91]. The traverses in Figure 7.22 stop short of the layer closest to the upper wall, as the turbulence structure is not well resolved in this region. A first observation is that all states indeed lie within the triangle, as is required by realisability constraints. In the central region of the channel, covering 80% of the flow and identified by the solid squares, the flow is not drastically anisotropic, as also shown by a value of A around 0.8. Excluding the axisymmetric-expansion line, it corresponds, broadly, to the behaviour observed in the log-region of a channel. As the region close to the lower wall is traversed, turbulence is seen to approach the two-component state in all four sections. However, the manner in which this approach takes place varies greatly. Within the separation zone and marginally beyond the reattachment point, the approach occurs, however, at $x/h = 0.5$, and this corresponds to the sharp dip in A at around $y/h = 1$, as seen in Figure 7.23. To appreciate the origin of this feature, attention needs to be directed to the map for $x/h = 8$ where the *II-III* locus covering the near-wall layer shows a trend towards that characteristic of a log-law region, reflecting the partial recovery of the flow allowed by the stretch between reattachment and the following hill. The state of the near-wall layer around $x/h = 0$ is closely linked to that at $x/h = 8$. The flow then separates slightly further downstream, and, at $x/h = 0.5$, it contains the separated shear layer that is associated with the attached boundary layer just upstream of that location. Thus, the excursion at $x/h = 0.5$ appears to the footprint of the attached boundary layer prior to separation.

The proximity of the *II-III* locus to the axisymmetric contraction line, especially at $x/h = 2$ and $x/h = 6$, is reminiscent of that seen in a developed free shear (mixing) layer (Bell and Mehta [15]). While the present near-wall flow is clearly not a mixing layer, it is akin to a wall jet which combines a thin boundary layer with a much thicker outer free shear layer that is only weakly affected by the wall. This equivalence, albeit qualitative, provides an explanation for the behaviour observed in Figure 7.22. A point of difference is, however, that the anisotropy in a free shear layer is considerably lower than that in a near-wall layer, so that the former never approaches the two-component state. In the present case, in contrast, the shear layer above the lower wall merges into a thin boundary layer, and thus the flow has

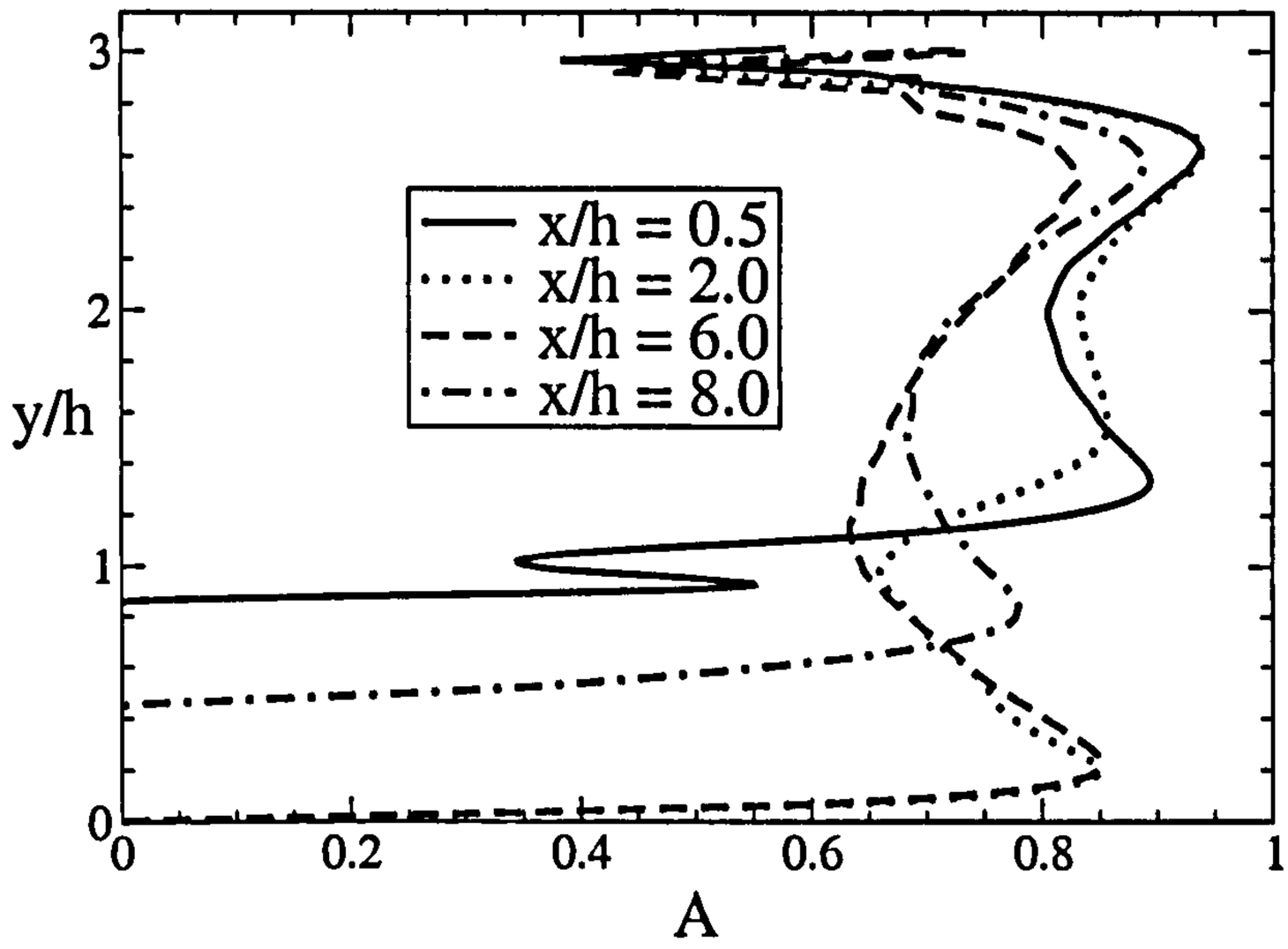

Figure 7.23: Distribution of the flatness parameter A at different streamwise locations.

to approach the two-component limit at the wall.

Velocity behaviour in the lower near-wall region

It is often instructive to consider the velocity in terms of universal wall scaling, especially during the assessment of the performances of near-wall approximations. Five velocity profiles, taken at different streamwise locations, are shown in Figure 7.24 in comparison with the standard log-law. The profiles are seen to be remote from the log-law, and this provides an early indication of the difficulties faced in using log-law based wall-laws in recirculating flows. The absence of a log-law in the separated region is, in itself, not surprising. However, Figure 7.24 also demonstrates that no part of the reattached-flow beyond $x/h = 4.7$ conforms to the log-law either. Further downstream, there is a trend toward the re-establishment of the log-law, but this ceases when the flow accelerates strongly on the windward slope of the next hill. The flow is, thus, clearly highly-disturbed, and the near-wall layer is not given the opportunity to recover to a near-universal state, a condition aggravated by the relatively low Reynolds number for which the semi-viscous sublayer is relatively thick.

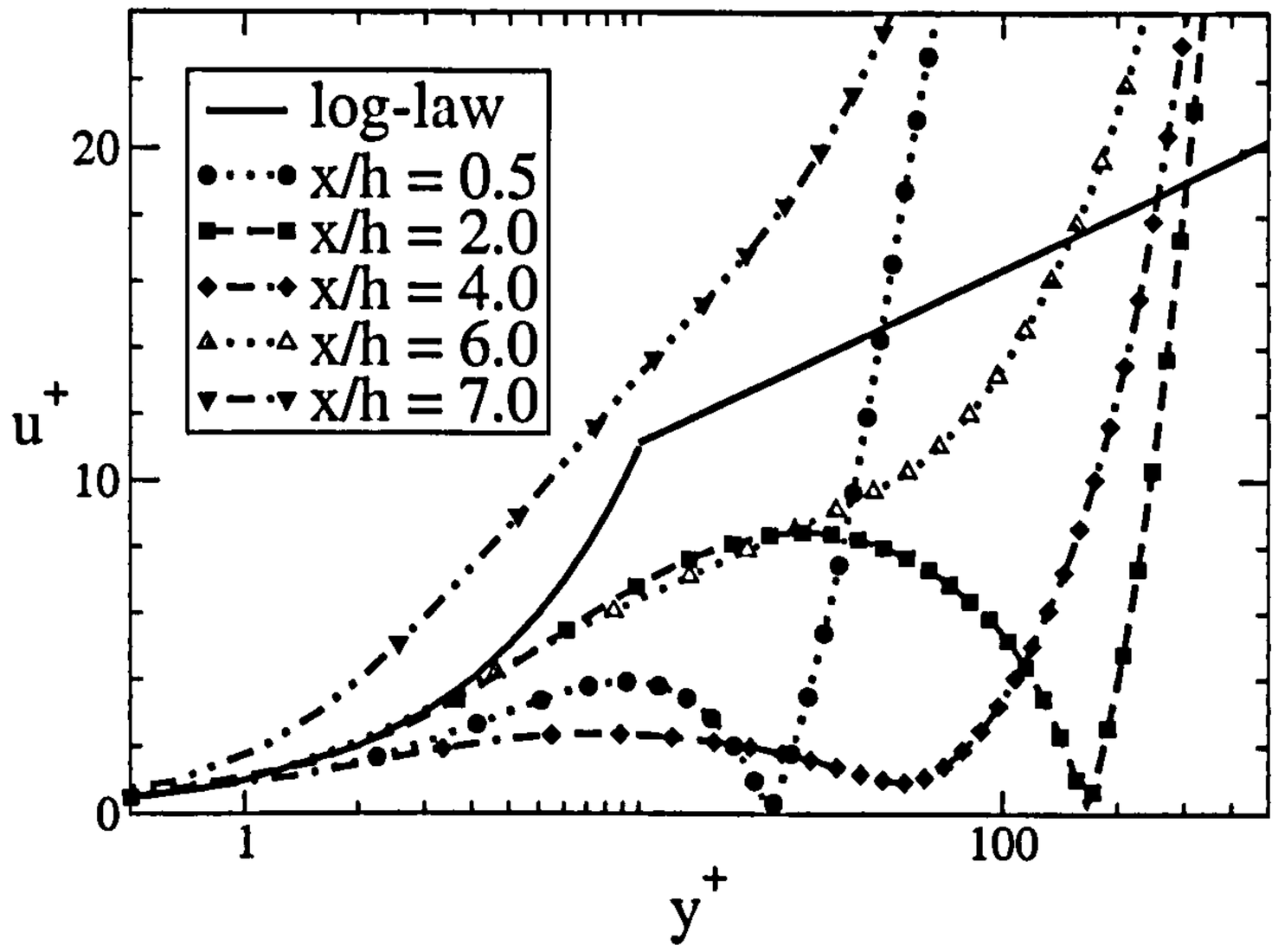

Figure 7.24: Near-wall velocity profiles at five streamwise locations derived from the highly-resolved simulation.

7.3.6 Spectral analysis

Inner flow

Time signals have been recorded at numerous locations, but only those at the points shown in Figure 7.7 are discussed here. The duration of the sampling is 33.25 non-dimensional units ($t_{ref} = h/U_b$), corresponding to 29596 time steps of $\Delta t = 1.123 \cdot 10^{-3}$ non-dimensional time-unit and 3.7 times the nominal flow-through period of L_x/U_b.

The analysis was performed using a windowed Fourier transform with a Hanning window and segments of length 2^{14} samples, i.e. spanning a period of 18.4 time units. The full signal was decomposed into four such overlapping segments over which averaging was performed. Furthermore, signals were recorded for each (x, y) position at 11 different $z-$locations and, thus, additional averaging was performed in that direction. These parameters were selected so as to obtain a reasonable compromise between the smoothness of the spectrum and the width of the frequency window covered.

The first issue discussed here concerns numerical resolution, which has already

been considered in Subsection 7.3.2. Figure 7.25 displays the power-spectrum density at two points with different characteristics. Both spectra were recorded around $x/h = 2$: one is in the centre of the recirculation region, while the other is in the shear layer. For the former, $\langle u \rangle \approx \langle v \rangle \approx 0$, whereas $\langle u \rangle = 0.73$ for the latter. These spectra exhibit several distinct ranges: low-frequencies around the inverse of the flow-through time, at around 0.1; a central region of regular decay; and a high-frequency region of stronger decay. Except for some near-wall spectra discussed in what follows, it has been verified that all other spectra computed at the points shown in Figure 7.7 have characteristics similar to the two given in Figure 7.25. All components show the same spectrum, reflecting an isotropic distribution of the spectral energy, except at very low frequency.

In the spectrum of Figure 7.25a, a regular decay of slope close to $-5/3$ is observed over more than one decade in f. This is indicative of an inertial sub-range, a necessary condition for the flow conform to fully-developed turbulence. At higher frequencies, a smooth transition to a faster decay is observed. This decay is related to the effective filter of the LES. In most circumstances, Taylor's hypothesis permits the time and spatial spectra to be related. This is, however, only possible when the mean velocity is significantly larger than the fluctuations.

The second spectrum, shown in Figure 7.25b, exhibits the same type of ranges discussed above. In contrast, however, a pronounced change of slope is observed at $f = 4.7$. This can be explained by the characteristics of the second–order central scheme employed for the convective term in this simulation. The scheme has a modified wave-number $\xi_{eff} = \sin(\pi\xi/\xi_{max})$ in space, exhibiting a maximum at $\xi_{max}/2 = 1/(4\Delta_x)$ (Ferziger and Perić [59]). Any contribution with spatial wave-number larger than this value is not adequately transported in space. Using Taylor's hypothesis for this point is possible, subject to uncertainty arising from the relatively low mean velocity: $\langle u \rangle / \langle u'u' \rangle^{1/2} \approx 3$. Hence, the critical frequency in time is $f_{CDS} = \langle u \rangle / (4\Delta_x)$, which is 4.7 in the present case. f_{CDS} is indicated by a short vertical line in Figure 7.25b. The physically meaningful range of the spectrum therefore extends up to f_{CDS} in this spectrum. These observations are similar to those of Schmitt et al [201]. An approximate relationship to the Kolmogorov length (relation

(7.1)) can be established. Indeed, the maximum resolvable spatial wavelength generates the temporal frequency $f_\Delta = \langle u \rangle / (2\Delta_x)$ and, at the present point, $\Delta/\eta \approx 10$. The temporal frequency related to η would then be around 94.

The most important criterion for assessing the quality of resolution in a simulation is the ratio between the energy content of the most energetic modes and the ones with the highest physically meaningful frequency. In the present simulation, this ratio is about two decades in the most critical area near the crest of the hill, and this, therefore, indicates a good resolution by the grid and method employed.

Attention is turned next to the low frequencies in the spectra. Two representative time signals are displayed in Figure 7.26. They were recorded in the outer flow at a streamwise distance of $6h$ on the same average streamline and at the same spanwise location. Slow undulations are visible in these signals. Animations of the whole flow field show that, at certain instances, turbulent fluctuations *accumulate* in some regions before being *swept* away. The overall mass flux, however, is constant because it is so prescribed by the code, so that local modifications in the streamwise velocity are compensated for by a corresponding change in other points. On the other hand, the two-point correlation coefficient R_{11} between the two $u-$signals is low. For the signals displayed, R_{11} is only -0.085, a value very similar to those observed at other locations. This demonstrates that the strong fluctuations are of substantially smaller size than the distance between these points. Hence, the low frequencies, at around 0.1, are principally due to the return time of the periodic flow, as illustrated by the limiting case of frozen turbulence advected in a plane channel. Therefore, the streamwise length L_x of the domain is sufficient, because the spatial size of the dominating vortical structures is substantially smaller than L_x.

Near-wall spectra

Based on the spectra shown in Figure 7.27, further insight can be gained into the Reynolds–stress anisotropy observed at $x/h = 8$ close to the wall. The figure displays spectra at four near-wall locations, at about $x/h = 0, 4.5, 6, 8$ and a distance of $0.09 - 0.1h$ from the wall. The fourth was selected to be somewhat closer to the wall at a wall-normal distance of $0.06h$, because of the reduced thickness of the boundary

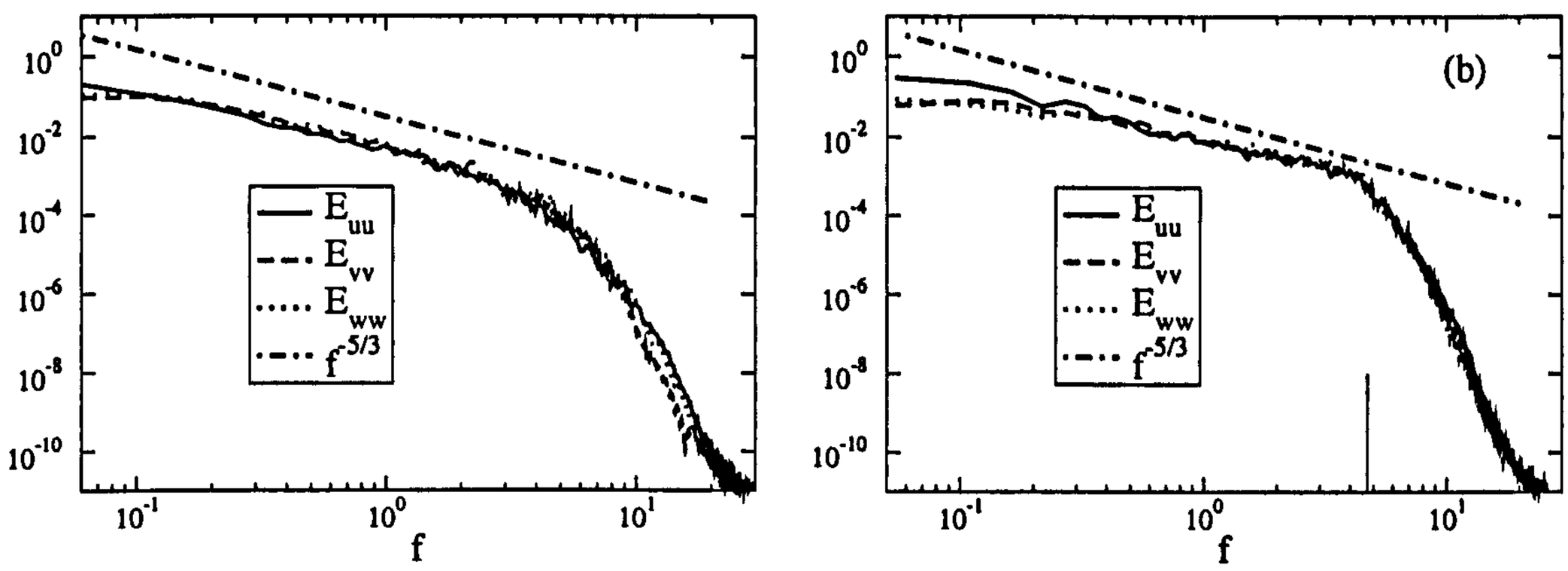

Figure 7.25: Power spectrum density in the centre of the recirculation zone at $x/h = 2.15$, $y/h = 0.49$ (a) and in the centre of the shear layer at $x/h = 2.23$, $y/h = 1.13$ (b) (see Figure 7.7). The dashed line has a slope of $f^{-5/3}$. The small vertical line in the right graph is at $f_{CDS} = 4.7$ as discussed in the text.

layer at this location. The limiting frequency f_{CDS} is relevant only for Figure 7.27a, where $\langle u \rangle = 1.07$. At the other locations, the streamwise velocity is substantially smaller.

Figure 7.27 shows that all temporal fluctuations with frequency larger than 1.0 feature similar, isotropic decay in their power spectrum. The most interesting range is that of the low frequencies. At $x/h = 4.5$, these components are large with equal energy for u and w, while small for v. Further downstream, at $x/h = 6$ and $x/h = 8$, a substantial level of anisotropy gradually develops for frequencies in the decade, $f = 0.06 - 0.6$. The energy content in the w–fluctuations increases compared to the other two components, reaching a ratio of up to 10 at $x/h = 8$ for $f = 0.1$. The anomaly in the spectrum persists until the crest of the hill as shown in Figure 7.27a. The frequency range and the difference in energy content have become somewhat smaller, but are still visible to some extent. Due to the pronounced acceleration, the energy in the u–component increases compared to that at the location on the windward slope of the hill, while it diminishes slightly in the w- and more strongly in the v–component. Downstream of the crest, the dominance of the w–fluctuations in the frequency range considered vanishes, as revealed by the spectra at $x/h = 2$ in the

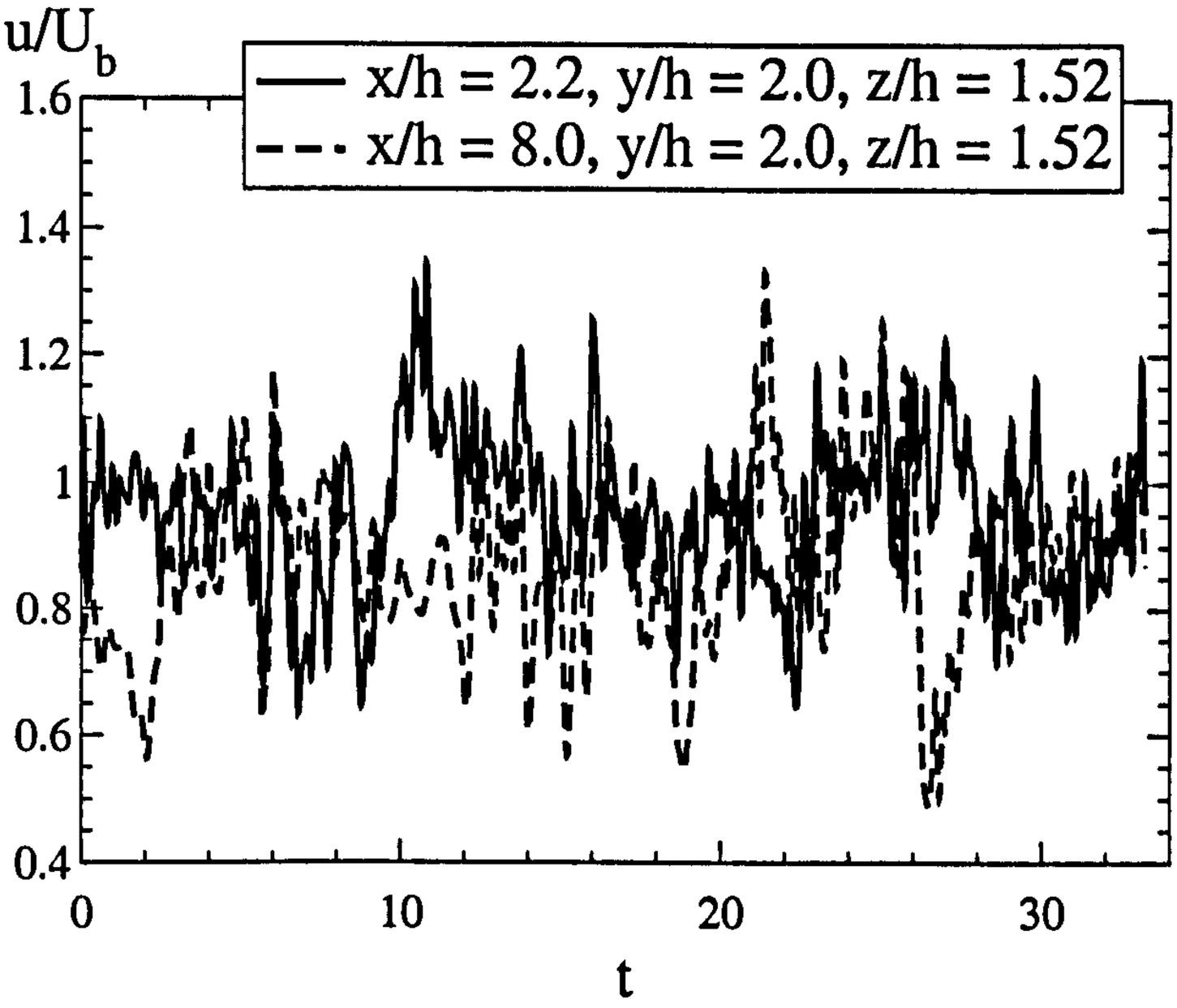

Figure 7.26: Two $u-$signals in the outer flow at $y/h = 2$ and the same $z-$location, one at $x/h = 2.2$, the other at $x/h = 8.0$.

shear layer displayed in Figure 7.25b. The near-wall spectra at this $x-$position (not included here) do not show this feature either. These observations support the earlier discussion. Furthermore, the spectra show that the dominance of $w-$fluctuations is a comparatively slow effect. It is related to temporal periods of, typically, 5 to 10 time units.

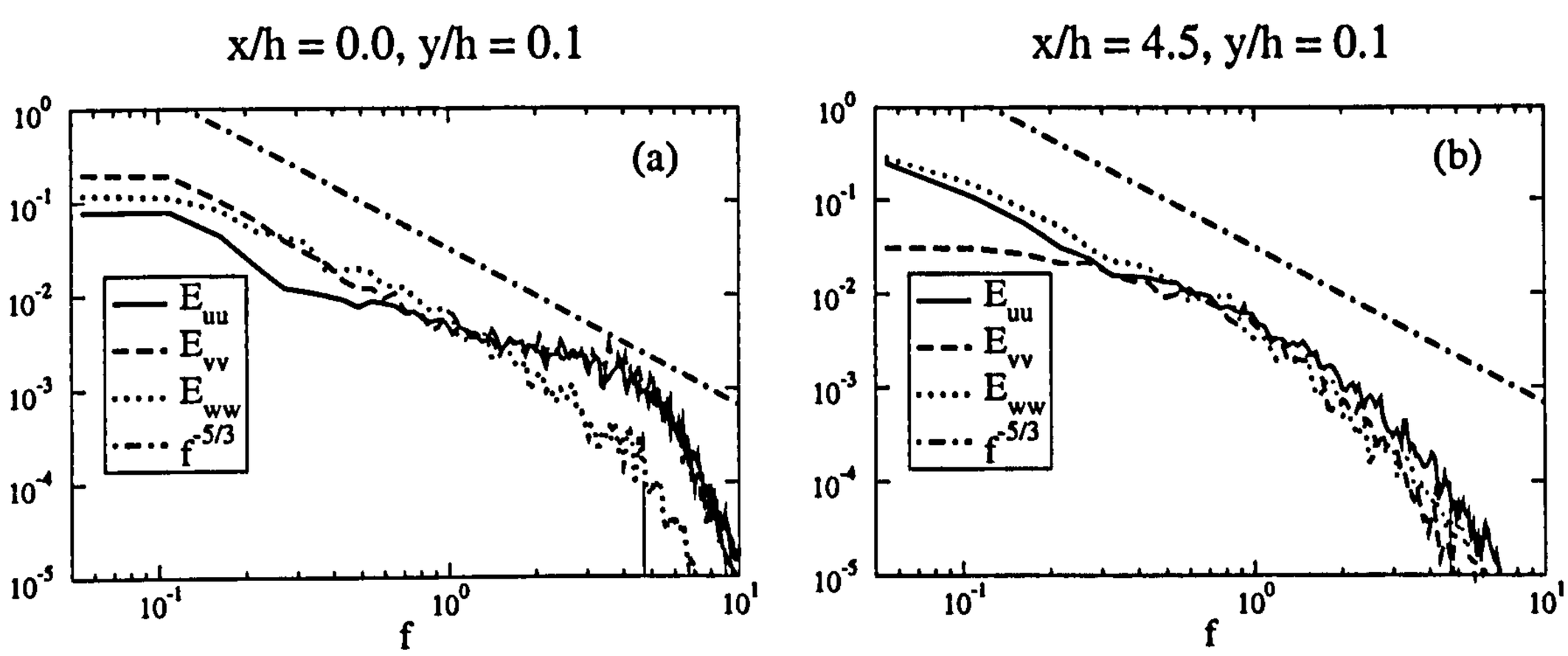

Figure 7.27: Power spectrum density at several near-wall locations: $x/h = 0, 4.5, 6, 8.1$ at a distance of about $0.09 - 0.1h$ from the wall for the first three and about 0.06 for the fourth (see Figure 7.7). The dashed line has a slope of $f^{-5/3}$.

7.3.7 Instantaneous structural aspects of the flow

General aspects

A description of the instantaneous and structural aspects of the flow allows better insight to be gained into some aspects of the flow behaviour observed during the analysis of the statistical quantities reported in Subsection 7.3.5. In particular, vortex systems are identified using a variety of criteria that are applied to several instantaneous flow realisations.

Figure 7.28 shows an instantaneous snapshot in which the flow is represented by two-dimensional streamtraces in a $x - y$ plane. This figure, if compared with Figure 7.7, provides a graphic illustration of the complexity introduced by the high level of turbulence, especially the large-scale dynamics induced by separation. The level of unsteadiness is especially evident in the lower part of the flow, with a chaotic succession of circulating and attached features. The resulting high irregularity of the flow presents a substantial challenge to its analysis and the extraction of meaningful ordered structures. In both, the reattachment region and ahead of the upslope of the hill, a substantial proportion of high-velocity fluid is directed toward the wall. The strong acceleration along the upslope results in a very thin boundary layer and the velocity overshoot near the crest shown in Figure 7.10.

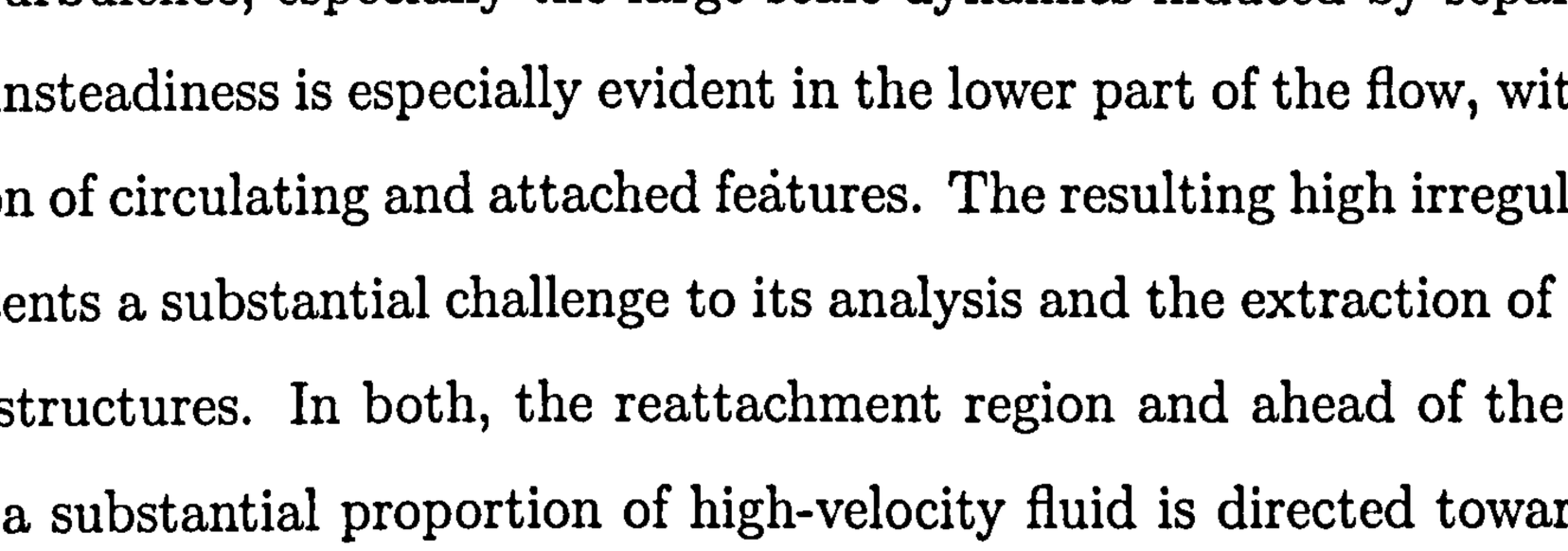

Figure 7.28: Vertical cut showing two-dimensional instantaneous streamtraces.

The irregularity of the flow illustrates the fact that the concept of a line of separation or reattachment, while pertinent to the average flow, is meaningless for

the instantaneous flow separating from a smooth wall, also pointed out by Na and Moin [164]. Figure 7.29 demonstrates this by way of the instantaneous streamwise velocity in the near-wall cells along the bottom wall, while Figure 7.30 gives the contours of instantaneous wall shear stress. The removal of negative values in Figure 7.29 (white regions) shows that forward and backward flows occur in a highly irregular fashion. Substantial backflow is observed beyond the average reattachment point and instantaneous forward flow is seen within the recirculation region. Local backflow can occur almost everywhere in the domain, except in the upper half of the hill's windward face. A pronounced reattachment line cannot be identified as is illustrated in Figure 7.30. A similar picture to that of Figure 7.29, although less irregular, is obtained on grid planes further away from the wall (not shown here). Animations reveal that the locations of forward and backward flow change with corresponding irregularity in time. Instantaneous separation is confined to a much smaller region than that of the reattachment, due to the shape of the constriction, but the separation location still moves over a streamwise distance of about $0.7h$ along the leeward hill face.

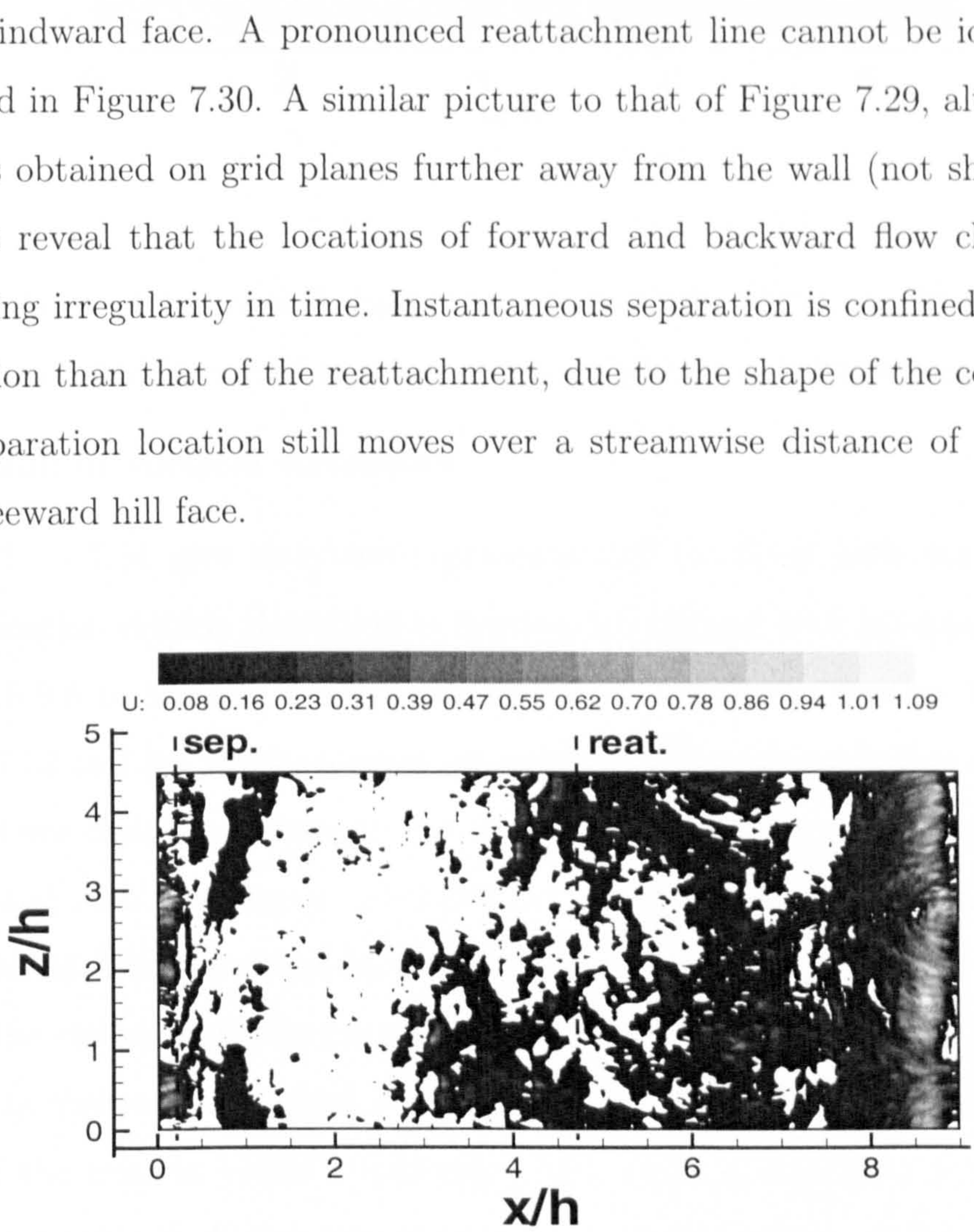

Figure 7.29: Instantaneous positive streamwise velocity along the lower wall of the hill flow. The dashed lines indicate the separation and reattachment mean locations.

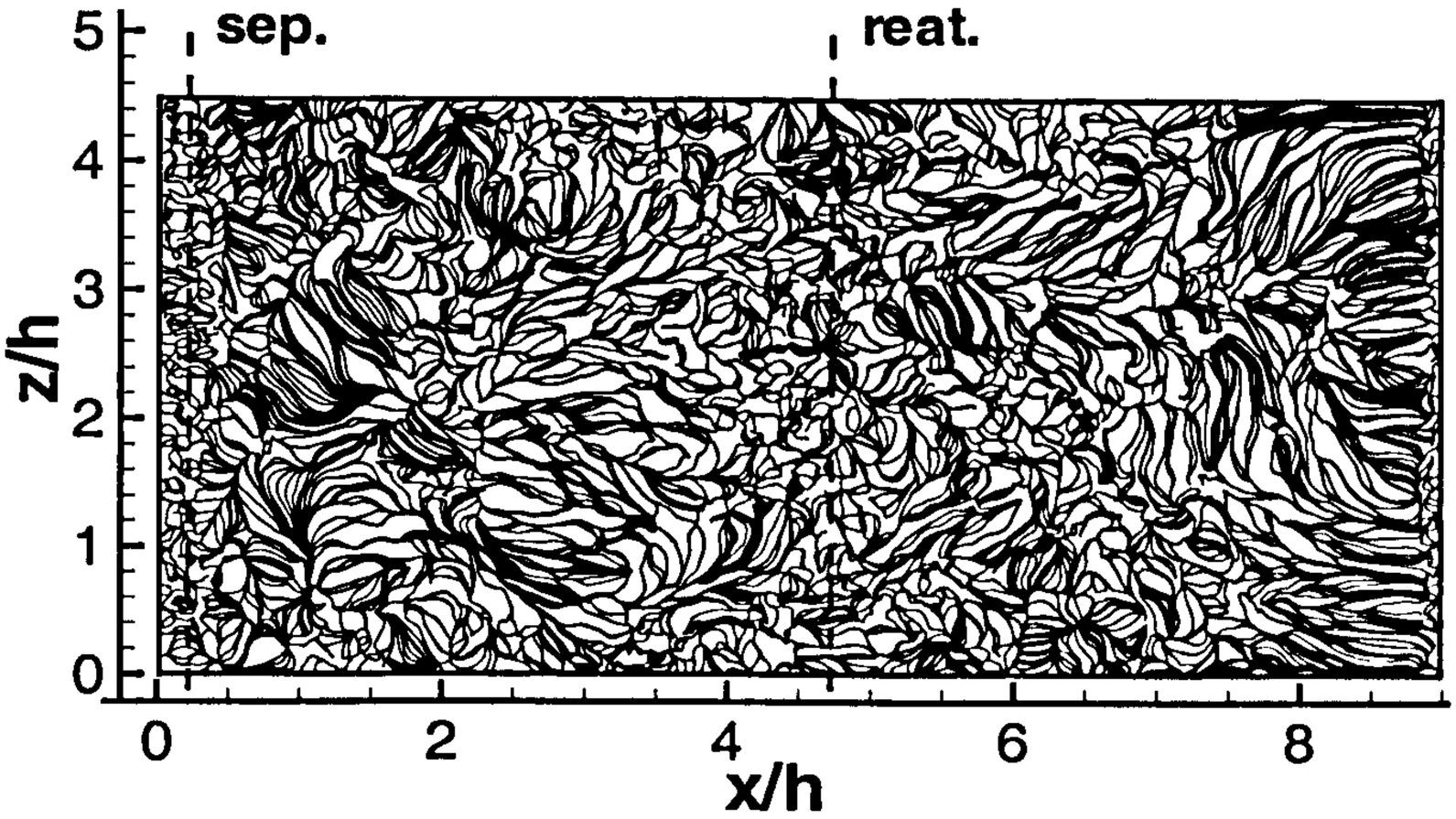

Figure 7.30: Iso-contours of wall shear stress at the lower wall for the highly-resolved hill flow. The dashed lines indicate the separation and reattachment mean locations.

Identification of vortical structures

Figures 7.31 to 7.34 give structure representations obtained with the four different identification criteria described in Section 5.8. These were previously used in Subsection 6.6.6 to identify coherent structures in a channel flow at $Re_\tau = 180$. In Figures 7.32 to 7.34, the structures are only plotted over one half of the channel depth. This was done for reasons of economy, in view of the very high computational cost associated with this type of visualisation. As the structures obtained are fine, this limitation is of little consequence. In contrast, Figure 7.31 covers the full domain depth, as the iso-pressure-fluctuation contours tend to identify larger, smoother structures, as observed in Lesieur et al [123] and also shown Subsection 6.6.6.

None of the criteria yields a representation which is especially revealing. To a large degree, this is due to the streamwise periodic nature of the flow, which favours the presence of wide-spectrum, established turbulence. Figure 7.31, and other like it but not included, suggests the formation of spanwise vortices following separation. These vortices, which may originate from Kelvin-Helmholtz instabilities, thus denoted KH, grow as the flow progresses downstream, and the inspection of

time-resolved visualisation movies reveal these to persist right up to the next hill. The structures arising from Figures 7.32 to 7.34 are much more fine-grained with all criteria yielding similar views.

This type of highly fragmented structures has been observed in the shear layer of other separated flows, such as that behind a backward-facing step (Kaltenbach [101]) or in a separated turbulent boundary layer (Chong et al [35]). As seen in Figure 7.31, the coherent spanwise vortices are quickly disrupted by break-up and by streamwise vortices swept over the hill crest. Further downstream, these vortices fragment due to secondary instabilities in a similar fashion to that behind bluff bodies (Zdrakovich [244]) or the backward facing-step (Kaltenbach [101]). Other vortices are occasionally found between the spanwise rollers visible in Figure 7.31, and also in Figure 7.1. These vortices (HP) are related to the helical pairing of the large spanwise vortices.

As the flow curves upwards over the downstream hill, concave curvature might be expected to be the source of Görtler instabilities and of organised streamwise vortices. Such vortices have not been observed, at least not unambiguously, in the visualisations performed. Another interpretation can, however, be given.

As already mentioned, the spanwise Kelvin-Helmholtz-type vortices in the shear layer yield streamwise vortices through secondary instabilities. These vortices, denoted by S in Figure 7.31, are aligned towards the streamwise direction and are inclined in that direction, as shown in Figure 7.35. Downstream of $x/h \approx 3$, these structures evolve mostly under the influence of the mean strain $\partial u/\partial y$. which exhibits a strong vertical gradient. A consequence of this gradient is the existence of a strong mean negative spanwise vorticity all over the domain, except near the upper wall. Consequently, the streamwise structures, highlighted in Figure 7.35 by the straight lines, tend to turn in the clockwise direction. Their lower end is trapped in the low-speed region and can even be transported upstream by the reverse flow of the recirculation zone.

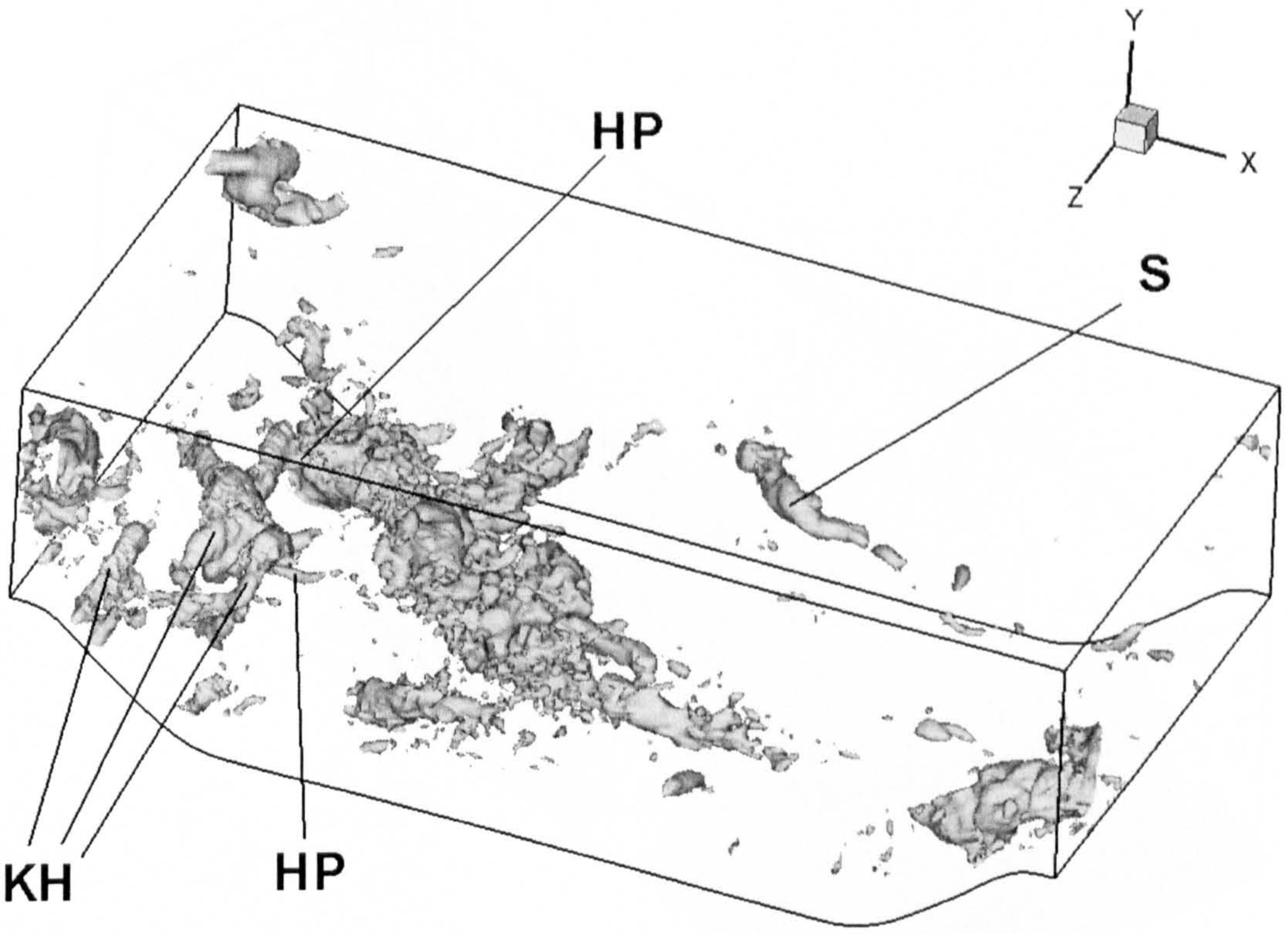

Figure 7.31: Iso-contour of the pressure fluctuation for the highly-resolved hill flow.

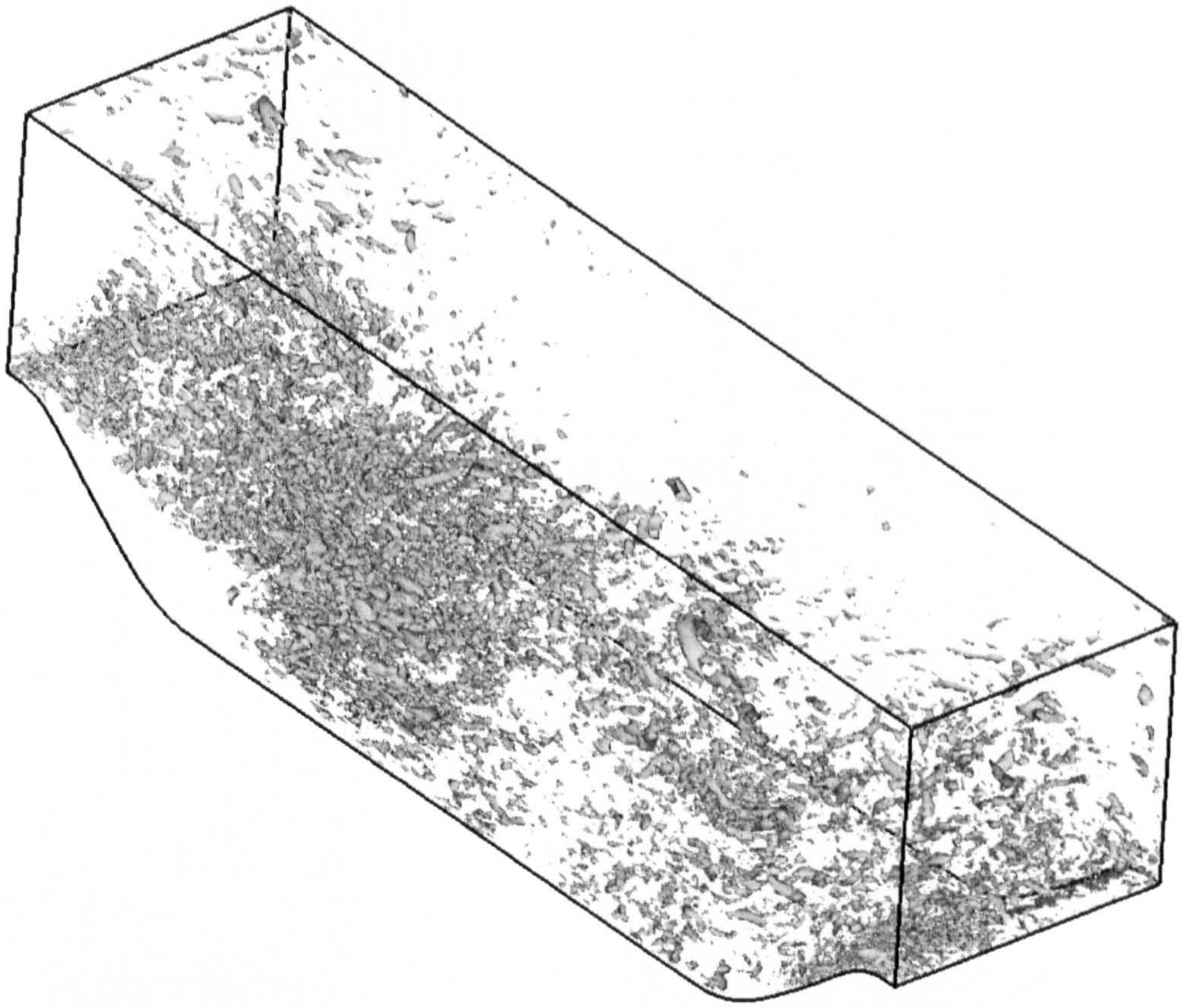

Figure 7.32: Iso-contour of λ_2 for the highly-resolved hill flow.

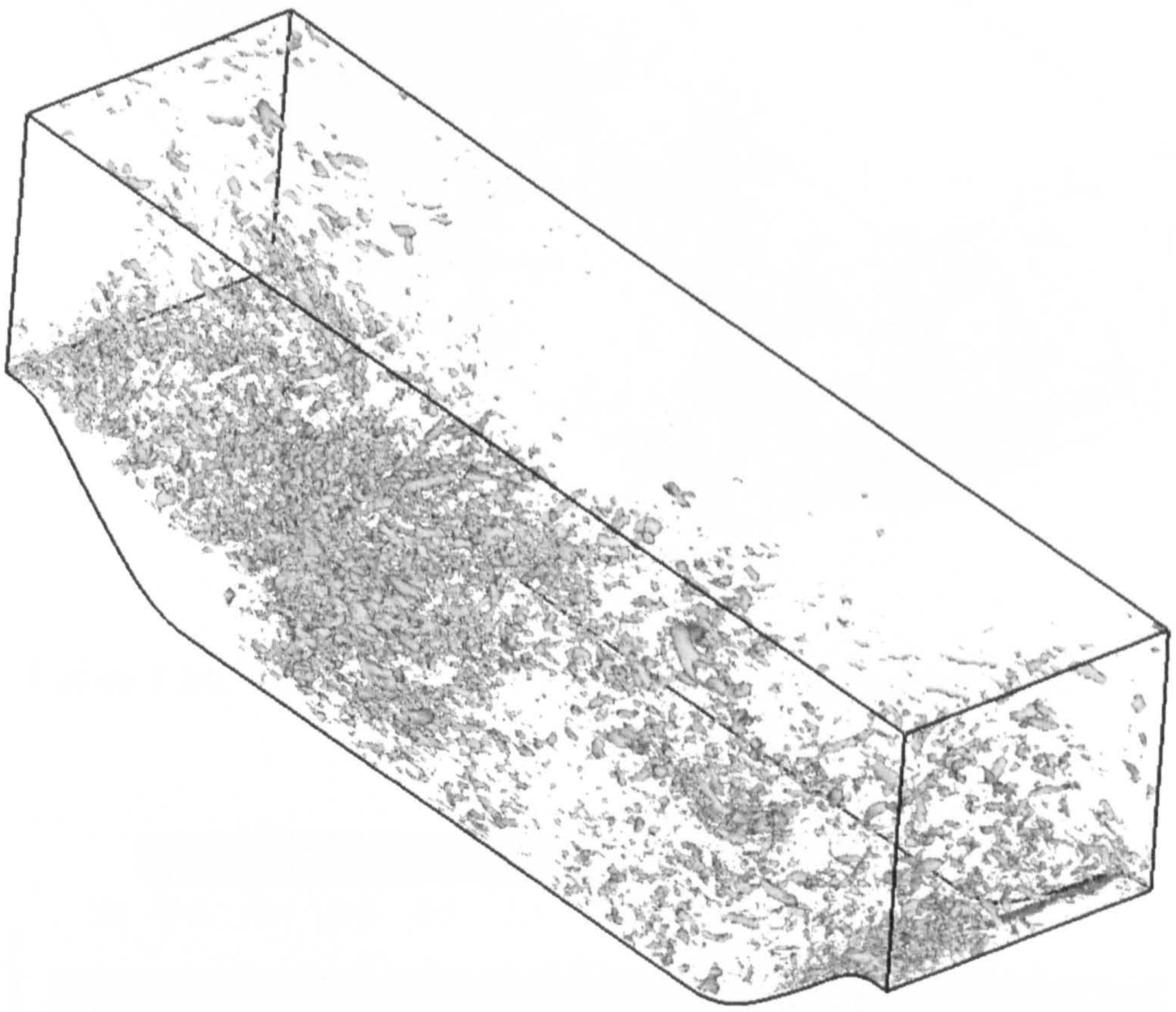

Figure 7.33: Iso-contour of Q for the highly-resolved hill flow.

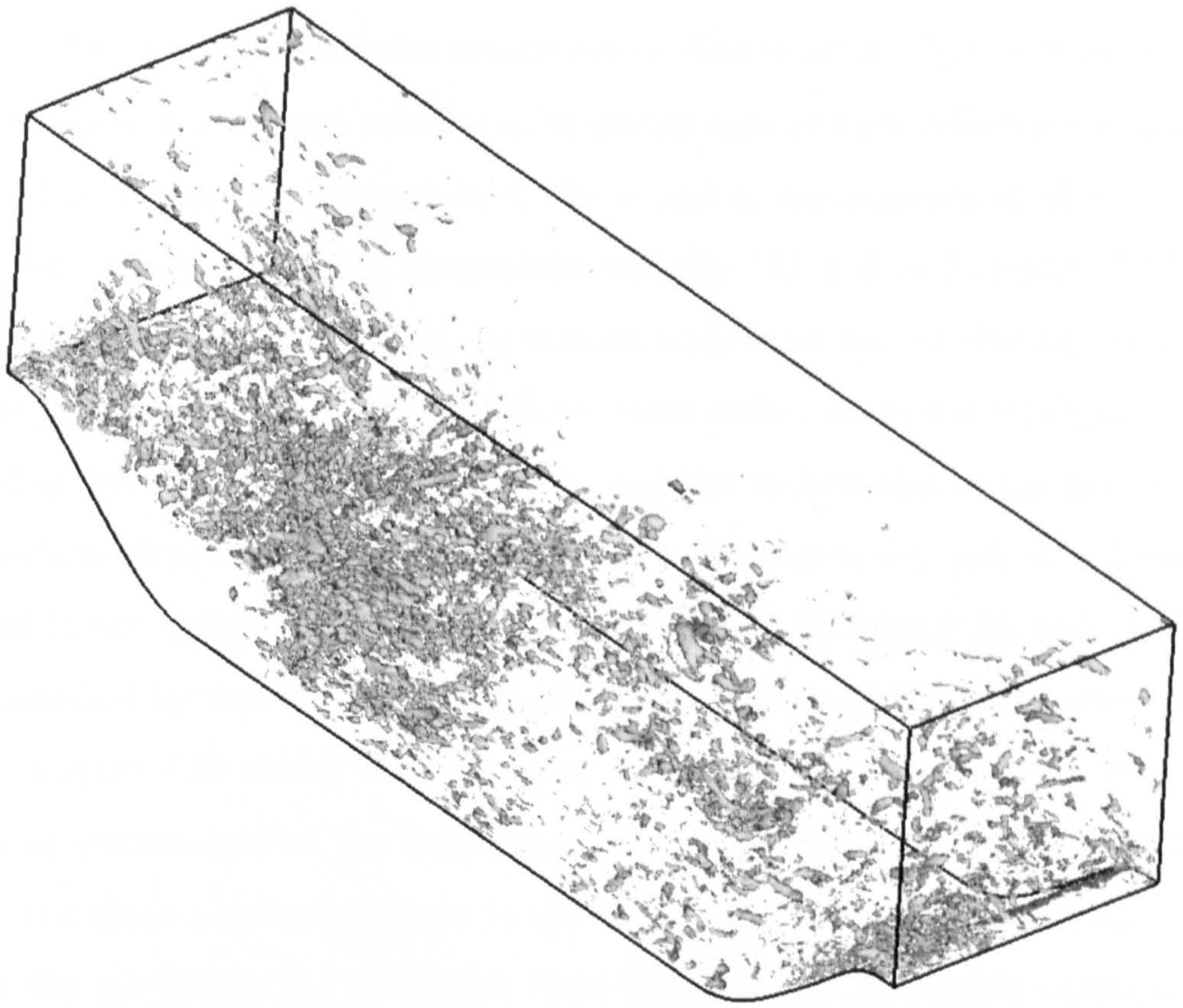

Figure 7.34: Iso-contour of Δ for the highly-resolved hill flow.

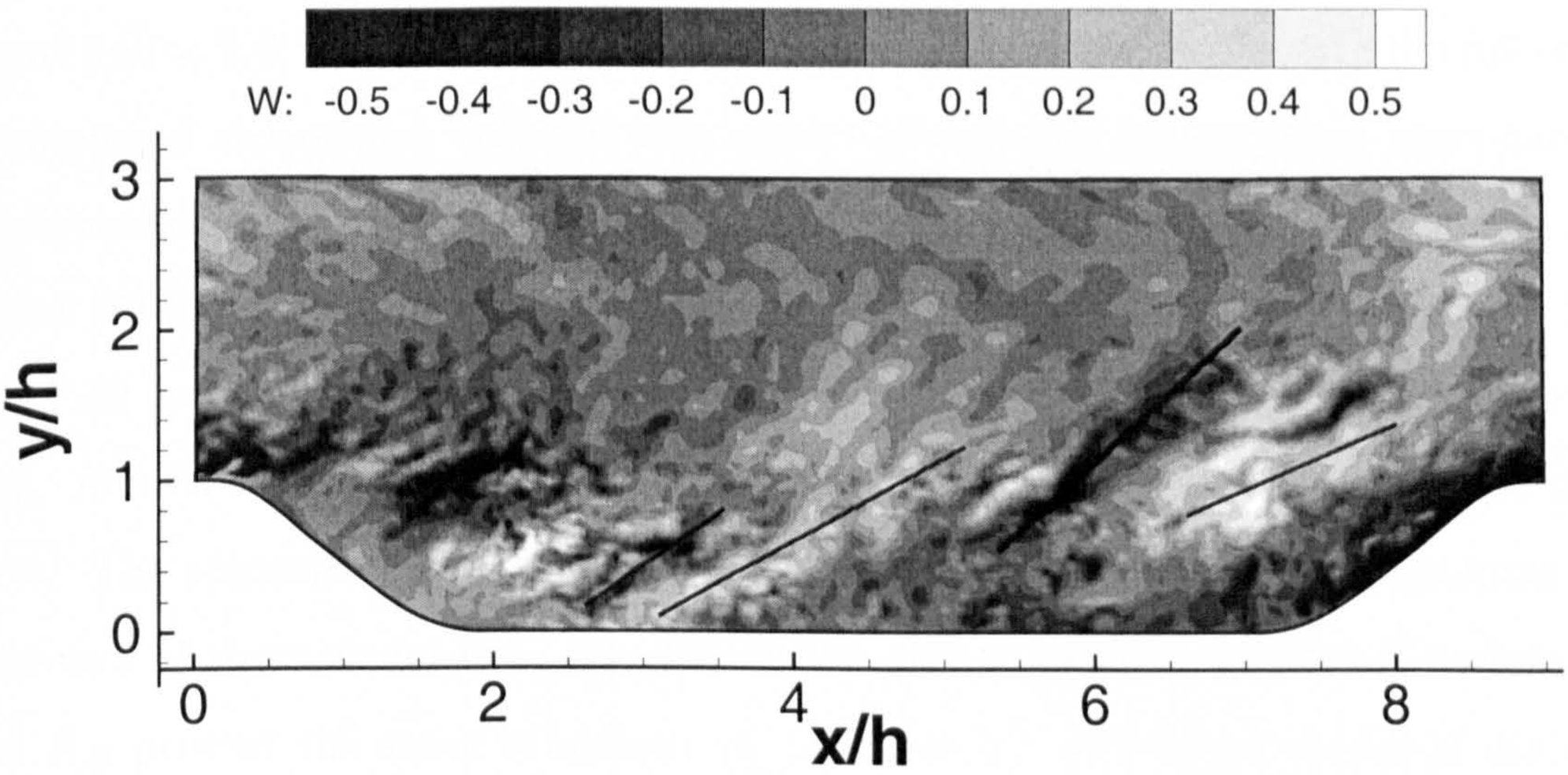

Figure 7.35: Iso-contours of instantaneous spanwise fluctuations in a $x-y$ plane for the highly-resolved hill flow.

Streamwise structures

The nature of near-wall streamwise structures is illustrated in Figures 7.36 to 7.39, which show the instantaneous velocity in spanwise cuts at four different streamwise locations. The vectors are formed from the v and w components of the velocity, while the contours represent the streamwise velocity. At $x/h = 2$ (Figure 7.37), in the middle of the recirculation zone, no ordered structures can be distinguished, although the pressure-fluctuation fields indicate some order. At $x/h = 6$ (Figure 7.38), high-speed and low-speed regions are visible, and the vectors hint at the presence of ordered vortical structures. These are confined to the region $0 \leq y/h \leq 1$, however, and extend in the spanwise direction over a distance of between $0.5h$ and $1h$. This can be quantified by considering the spanwise correlations at the same streamwise locations. Figure 7.40 shows the two-point correlations in the spanwise direction for the three components of the fluctuating velocity at four different vertical locations. For the three nearest locations to the wall, up to $y/h \approx 0.22$, the correlation length for the v-velocity R_{22} is smaller than those for the two other components. The u-correlation R_{11} is the largest and increases with distance from the wall. The w-correlation R_{33} is small at the wall, but increases away from it to become similar to R_{11} beyond $y/h \approx 0.22$. At this location, the correlation width is about $1h$.

Figure 7.35 shows the streamwise–oriented, inclined structures to extend up to about $y/h = 2.0$. In fact, this behaviour even extends to the region over the hill crest. Pronounced streamwise vortices were observed over the hill crests in wavy-terrain configurations at low Reynolds number by Calhoun and Street [27] and Zedler and Street [245], and, at higher Reynolds number, by Salvetti et al [195]. Figures 7.38 and 7.39 provide a reasonable view of these streamwise structures away from the wall. At $x/h = 2$ (Figure 7.37), the highly vigourous flow activity prevents a clear view. The spanwise correlations at $x/h = 6, y/h = 1$ in Figure 7.40 confirms the existence of these structures. R_{22} declines to zero at around $\Delta z/h \approx 0.7$ while R_{11} and R_{33} present the same behaviour up to $\Delta z \approx 0.7$. For larger values of Δz, R_{11} becomes negative around -0.2 while R_{33} levels off to zero. The u-fluctuations are thus larger in extent than those of the two other components, while, as shown in

Figure 7.14, they are twice as strong. The presence of streamwise-oriented streaks above the hill crests was also reported recently in a experimental study by Günther and von Rohr [76] for a wavy-terrain configuration, further supporting the present findings.

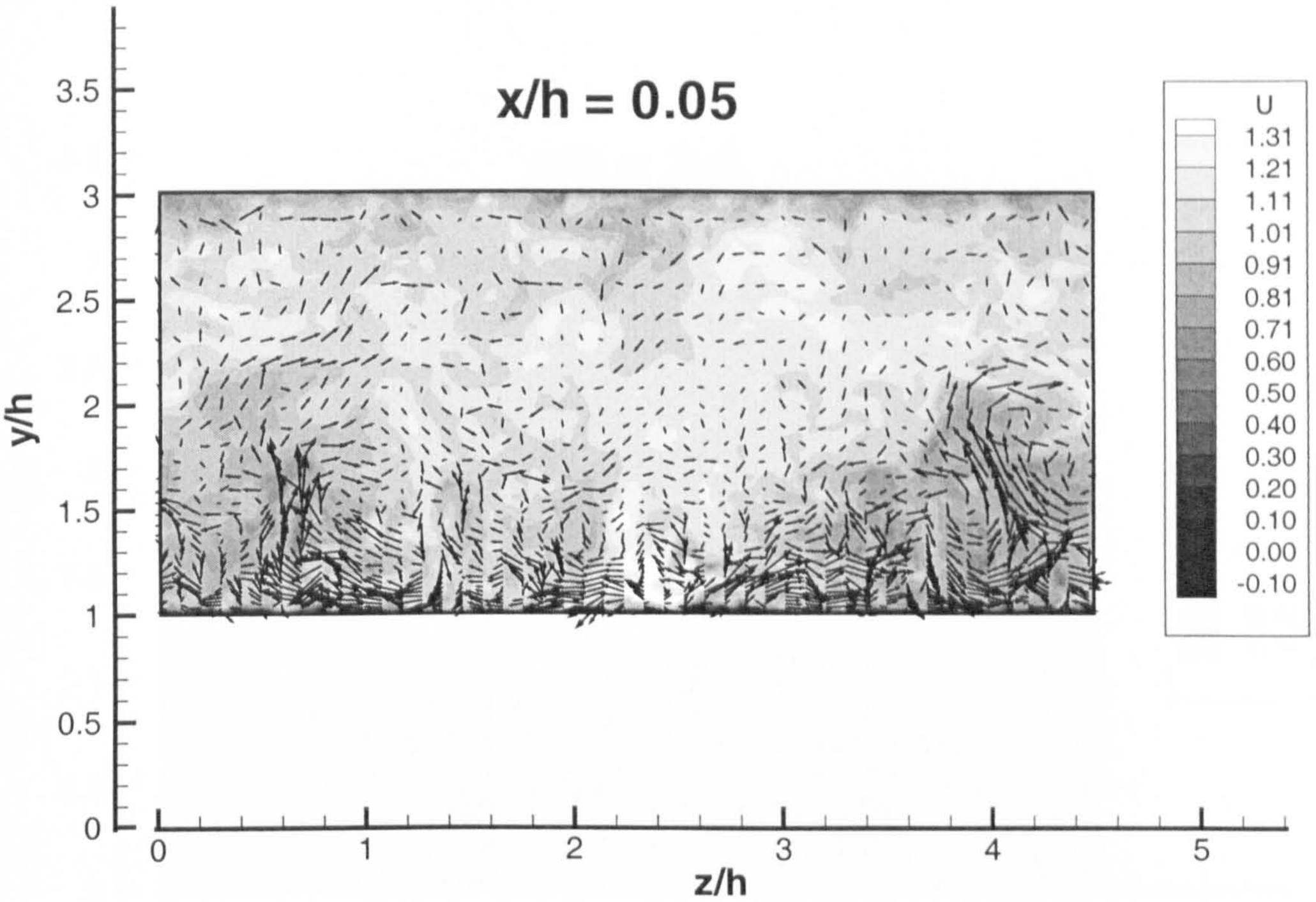

Figure 7.36: Instantaneous velocity in the y-z plane at $x/h = 0.05$. The streamwise velocity is indicated by the contours while the vectors shows the transverse velocity, made from the vertical and spanwise components v and w of the velocity vector. Note that only every fifth vectors are plotted.

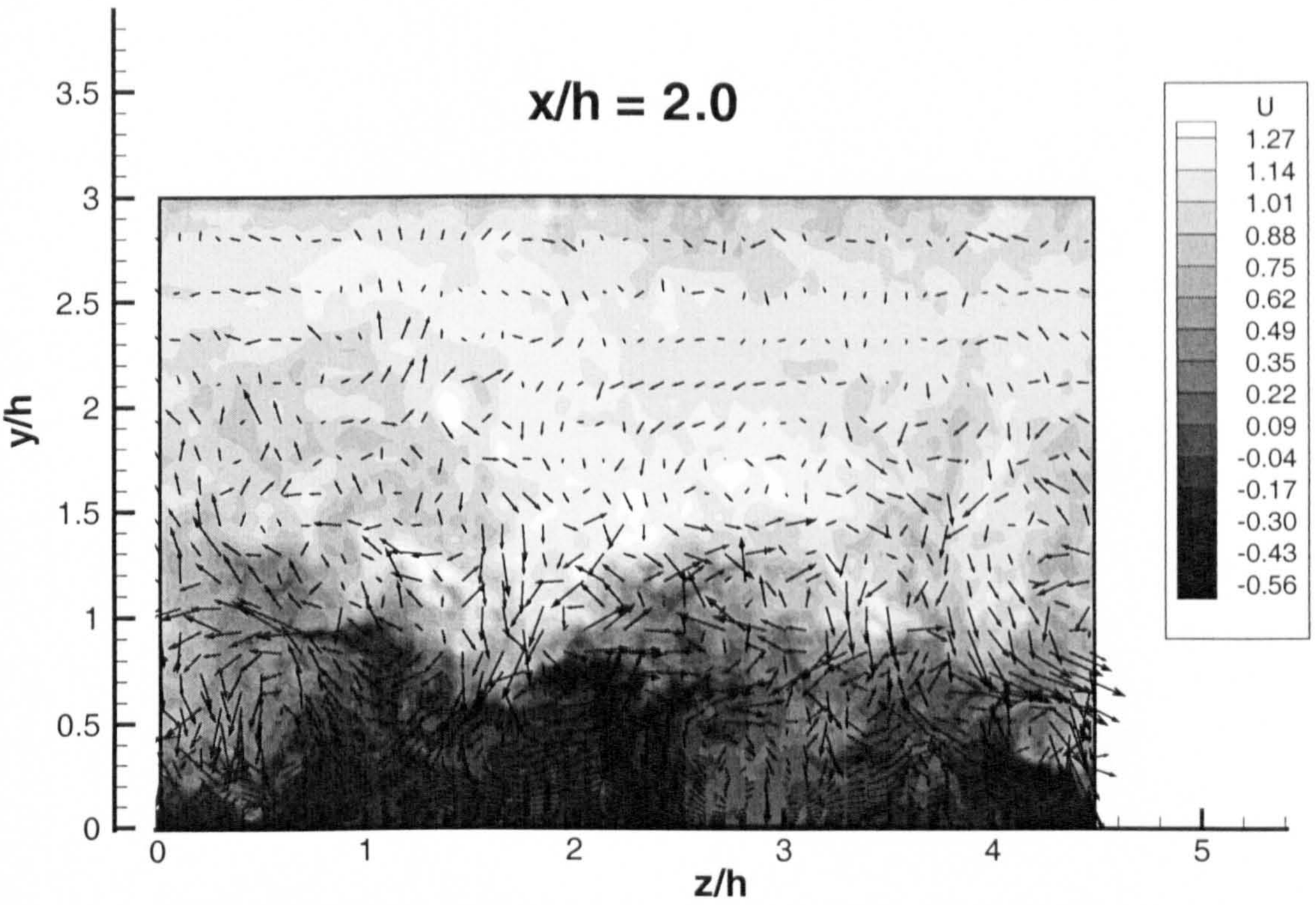

Figure 7.37: Instantaneous velocity in the y-z plane at $x/h = 2$. The streamwise velocity is indicated by the contours while the vectors shows the transverse velocity, made from the vertical and spanwise components v and w of the velocity vector. Note that only every fifth vectors are plotted.

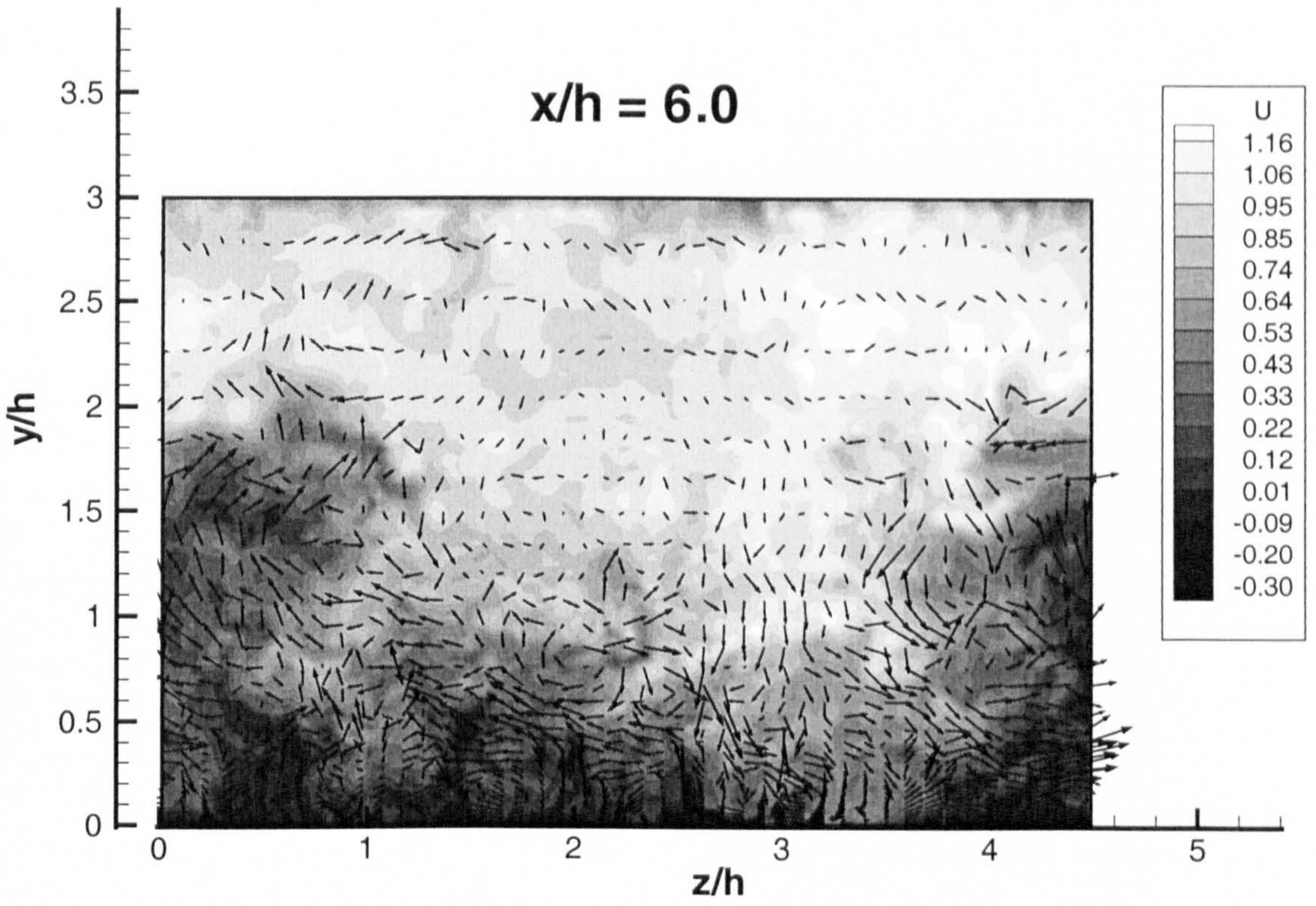

Figure 7.38: Instantaneous velocity in the y-z plane at $x/h = 6$. The streamwise velocity is indicated by the contours while the vectors shows the transverse velocity, made from the vertical and spanwise components v and w of the velocity vector. Note that only every fifth vectors are plotted.

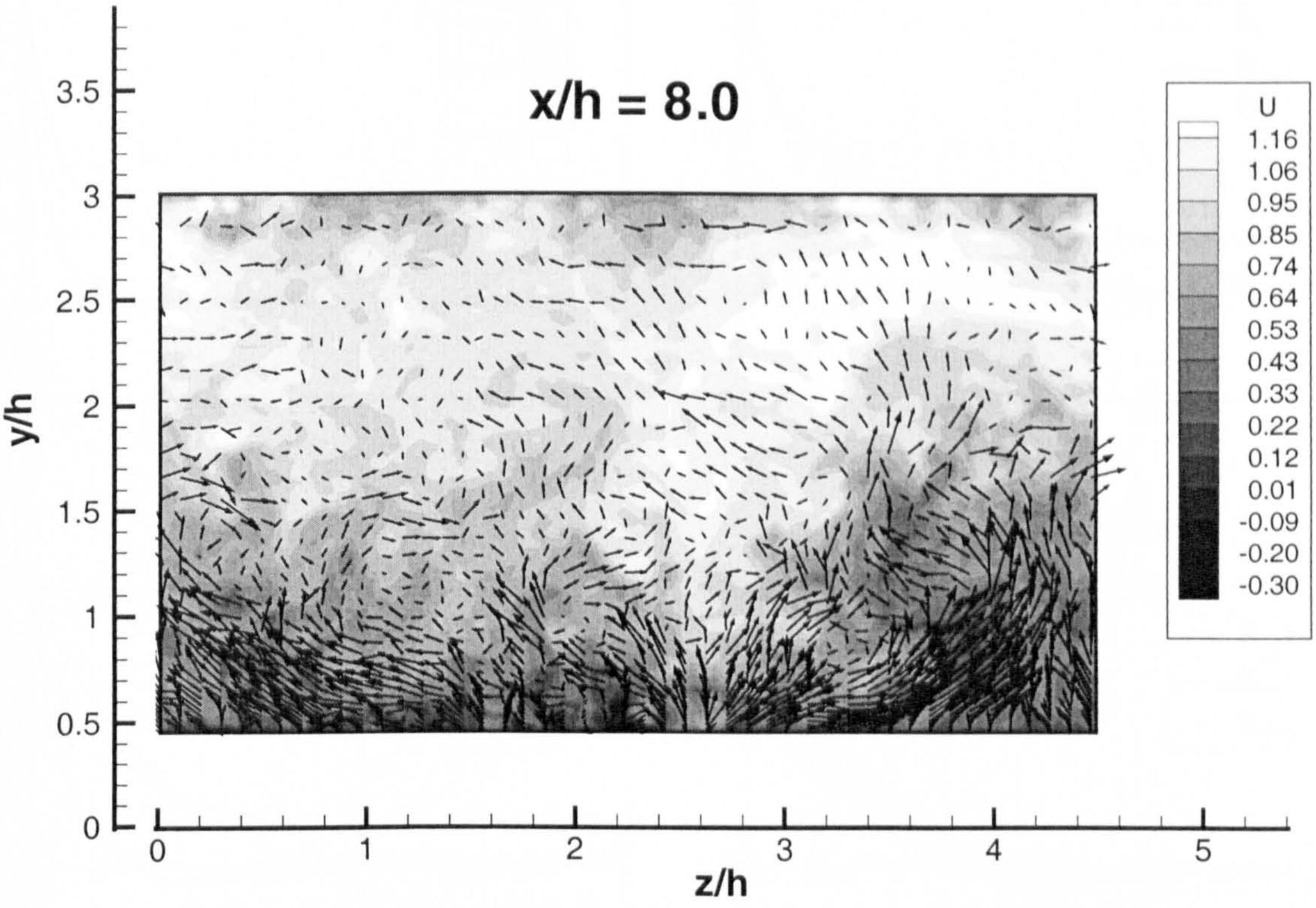

Figure 7.39: Instantaneous velocity in the y-z plane at $x/h = 8$. The streamwise velocity is indicated by the contours while the vectors shows the transverse velocity, made from the vertical and spanwise components v and w of the velocity vector. Note that only every fifth vectors are plotted.

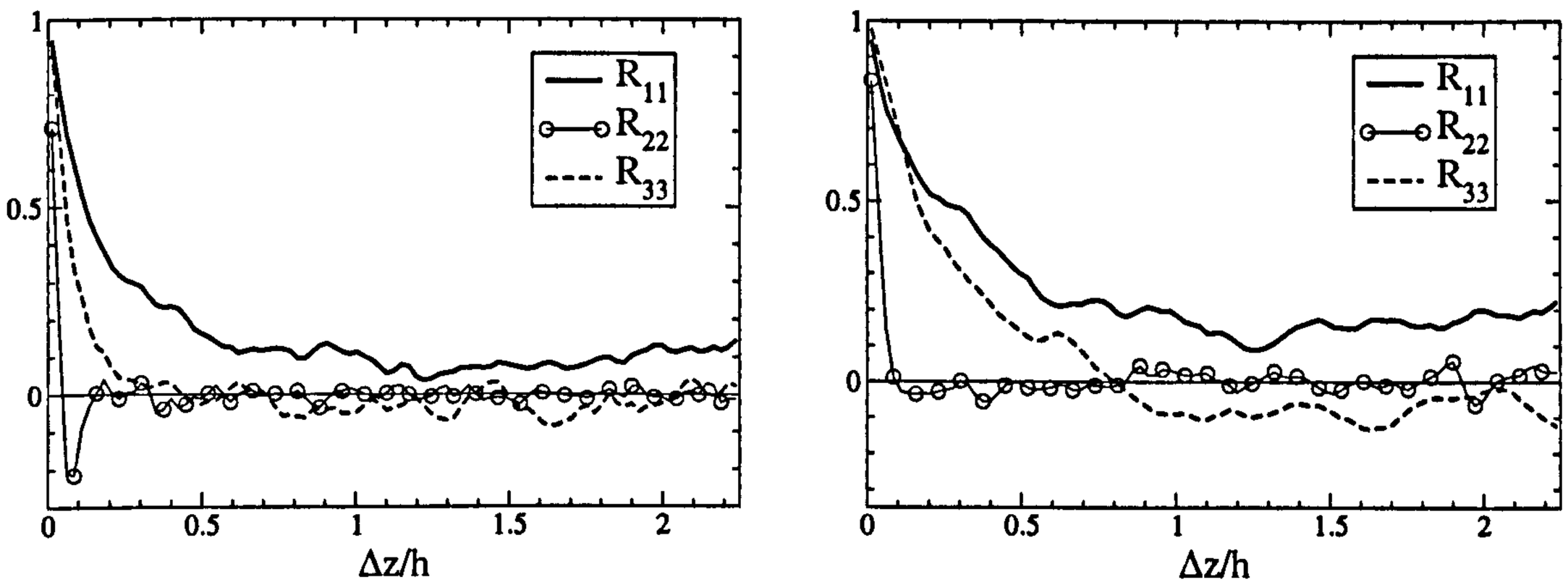

Figure 7.40: Spanwise auto-correlations for the three velocity fluctuations near the bottom wall at $x/h = 6$.

Structures near the windward face

The budgets of the Reynolds stresses at $x/h = 8$, shown in Figure 7.21, reveal the dominance of spanwise velocity fluctuations which are associated with a transfer of energy from the two other components by the pressure-strain term. A first sign of this is already visible at $x/h = 6$ (see Figure 7.15) where, at $y/h \approx 0.01$, the pressure-strain term dominates for $\langle v'v' \rangle$ and $\langle w'w' \rangle$. The transfer of energy through the pressures-strain becomes then stronger at $x/h = 7$, as seen in Figure 7.19 before reaching the high level shown in Figure 7.21. The objective, here, is to explain these observations and link them with the structural features of the flow.

It has been observed that streamwise elongated structures, such as the one indicated by S in Figure 7.31, occur and *collide* with the windward face of the hill. However, their cross-section being roughly circular, they are not likely to be at the origin of the dominant w-fluctuations. On the other hand, by considering the correlations and instantaneous transverses pictures of the flow, it was shown that broad streaks interact with the windward slope of the hill. These streaks then generate strong spanwise motions on both sides of the contact point over a large distance. One such event is shown in Figure 7.41 by the contiguous region of positive and negative w-fluctuations. The region of negative spanwise w-fluctuation is indicated by S. This event is known as a *splat* (Perot and Moin [171]) and is defined as a local region of stagnating flow resulting from the fluid impingement on the wall. Figure 7.42 gives another view of this event by showing the horizontal components of the instantaneous velocity vector. The region inside the circle is where such an event is visible, with the circle centre roughly corresponding to the impingement point. Because of the presence of the wall, the impinging fluid is obliged to change direction, so creating a lateral motion such that energy is transferred from the normal component of the fluctuations to the wall-tangential ones. Because of continuity, so-called *anti–splats* are created that transport fluid back into the core of the flow, and these are also visible in Figure 7.39. Animations of such transversal cuts have shown these conditions to prevail over a period of up to 0.5 flow-through-time, because of the large streamwise length of these streaks. Perot and Moin [171] investigated these

events in details for a free shear layer and a solid wall in the absence of a mean flow. Here, the circumstances are more complicated, because of the curvature of the wall and the resulting strong streamwise acceleration. This explain the strong inequality of the w-fluctuations and the u-fluctuations or, where the wall is inclined, the streamwise tangential component of the fluctuations.

The previous observations are further supported by Figure 7.43 which shows the two-point correlations for all three components of the velocity fluctuations at $x/h = 8$. The correlation R_{11} and R_{22} have very similar shapes and decay to zero within $\Delta z/h = 1$ without presenting any negative values. R_{11} and R_{22} are strongly related because u is not oriented with the streamlines and v is not normal to them. R_{33} is substantially different and exhibits a large correlation distance which varies from $0.65h$ to $0.95h$ as the distance to the wall increases. In addition, the negative values at the large spanwise distance become more and more pronounced. Comparing Figure 7.43 to Figure 7.40, it appears that observations made at $x/h = 6$ are precursors to the present observations.

Beyond $x/h = 8$, the flow further accelerates along the hill slope. Just beyond the hill crest, at $x/h = 0.05$, Figure 7.36 shows some vortical activities. Because of the small thickness of the boundary layer at this location (about 0.05% of L_y), it is almost impossible to distinguish the phenomena that are taking place here.

A possible source for those large spanwise fluctuations could have been streamwise Görtler vortices, generated by the high degree of concave curvature imposed by the hill slope to the streamlines, alongside the strong acceleration due to the adverse pressure gradient. This however can be ruled out by qualitative arguments, as also argued by Gong et al [73] and Phillips et al [172, 173]. Because the cross-section of Görtler vortices is broadly circular, they would not be associated with the spanwise fluctuations of the magnitude observed here. In addition, in the present case, the large streamwise structures observed appear well ahead of the hill, as shwon in Figure 7.35, and, thus, far from the high concave curvature. Finally, a Görtler instability would be aligned with the flow direction and not at a significant angle. Hence, this mechanism can be ruled out as the source of these streamwise structures in the inner flow.

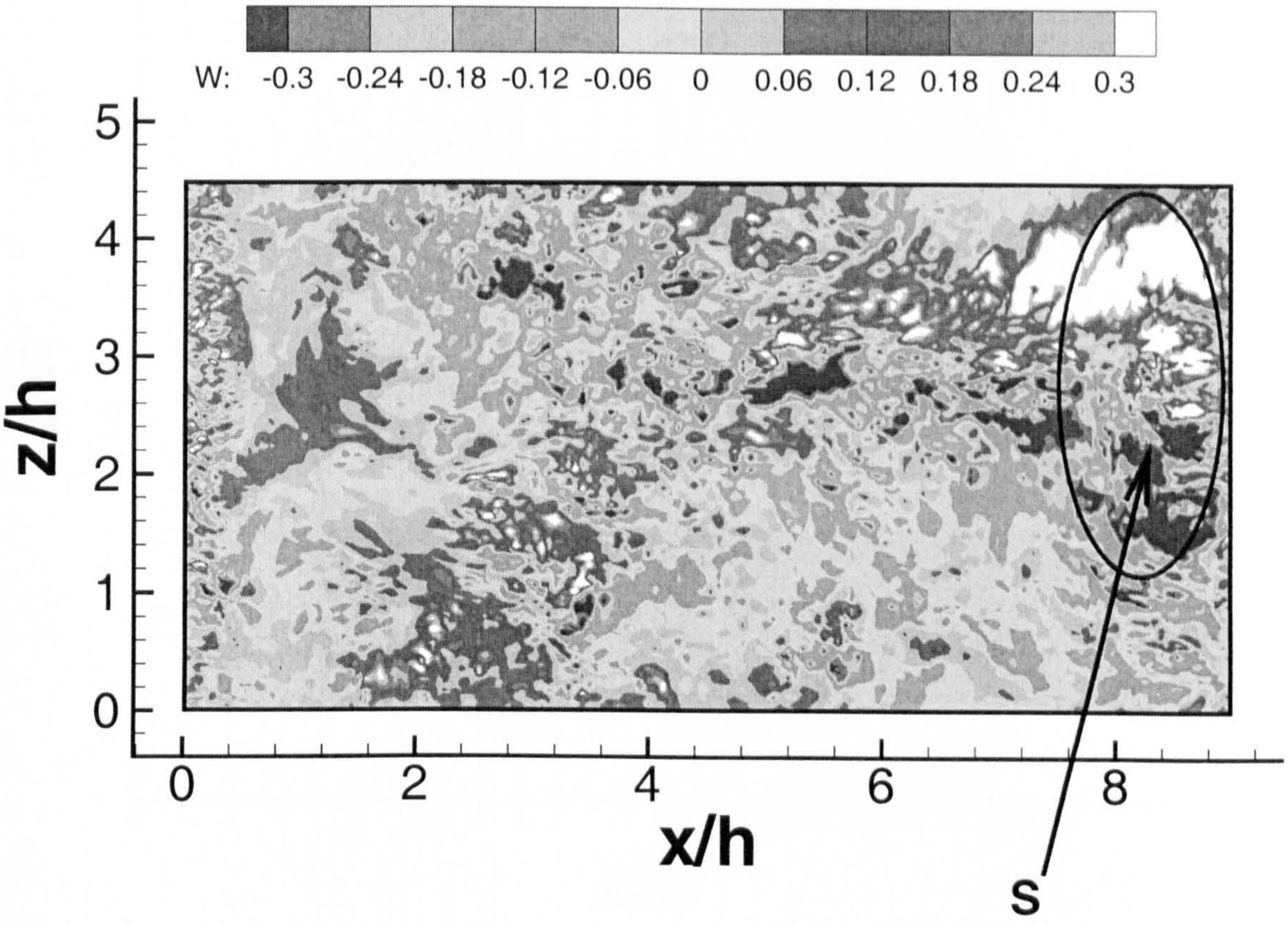

Figure 7.41: Instantaneous w-fluctuating velocity along the lower wall of the hill flow.

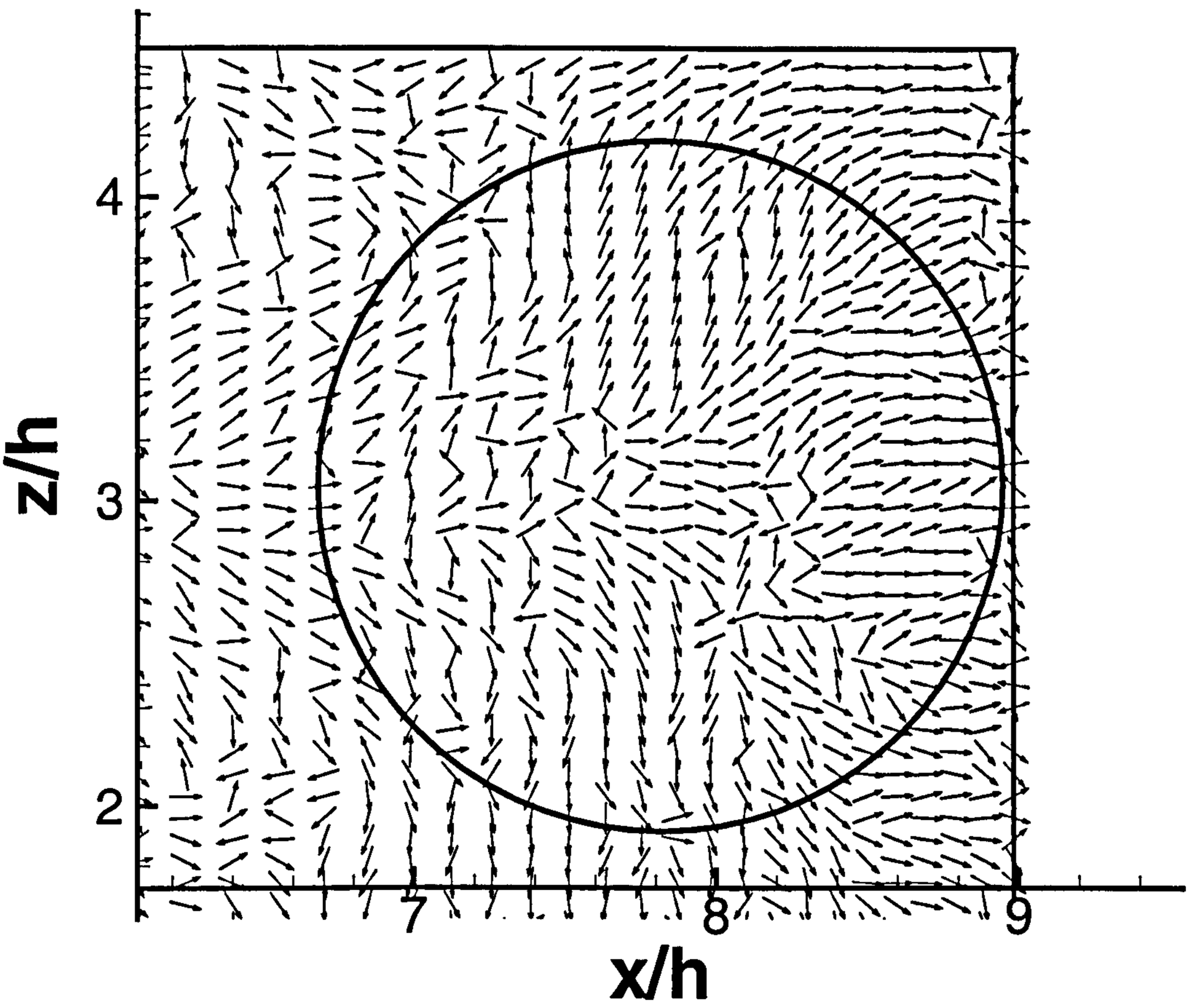

Figure 7.42: Instantaneous velocity vector along the lower wall of the hill flow on the windward face of the hill.

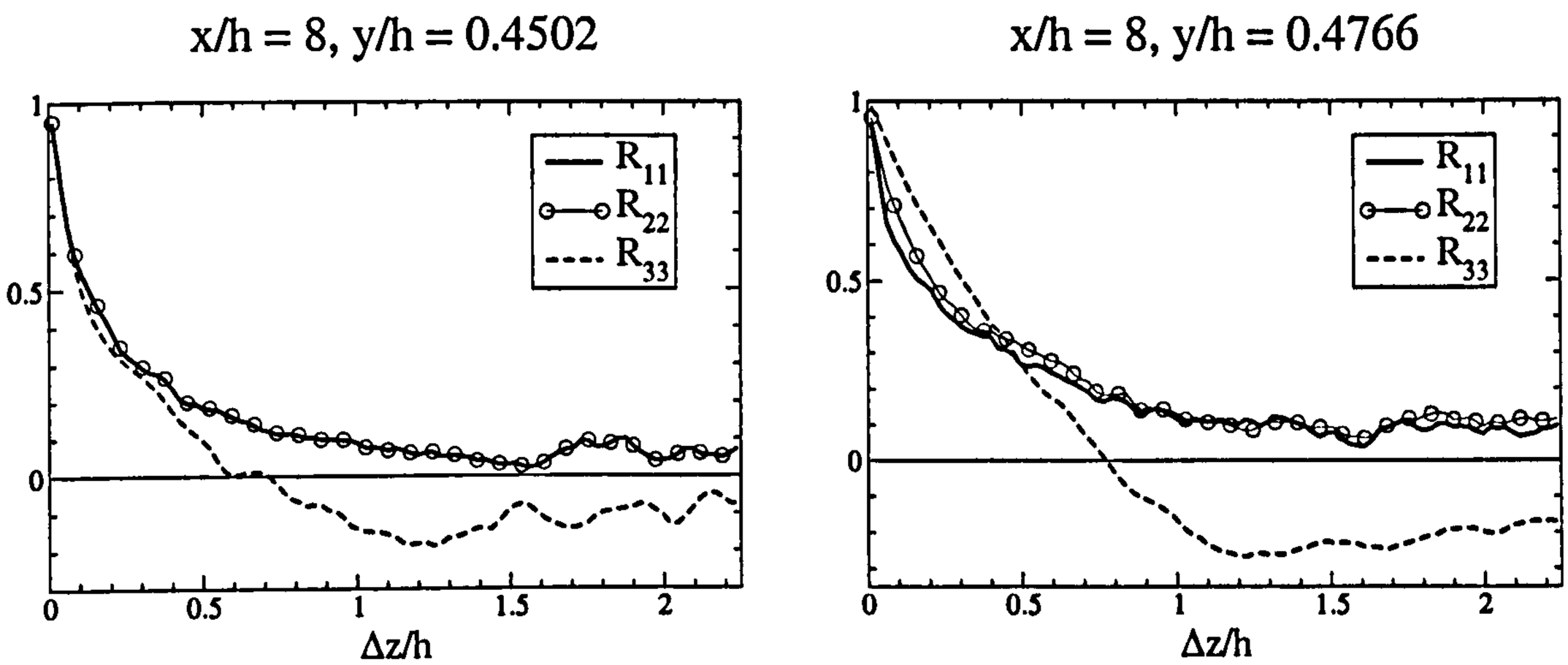

Figure 7.43: Spanwise auto-correlations for the three velocity fluctuations at $x/h = 8$ and four different vertical locations.

7.4 Coarse-grid LES with near-wall approximations

7.4.1 Overview

The principal purpose of the study reported in this section is to convey insight into the predictive accuracy that can be achieved by simulations of flow separating from curved surfaces with grids, such as those shown on Figures 7.44 and 7.45 and deemed *economically tenable* in a practical environment. Although the separated flow under consideration is challenging, its Reynolds number is still relatively low in comparison to a separated wing flow at a typical Reynolds number of 10^7. Real engineering flows are much more demanding, and the sensitivity levels reported below are likely to be considerably more severe in practice.

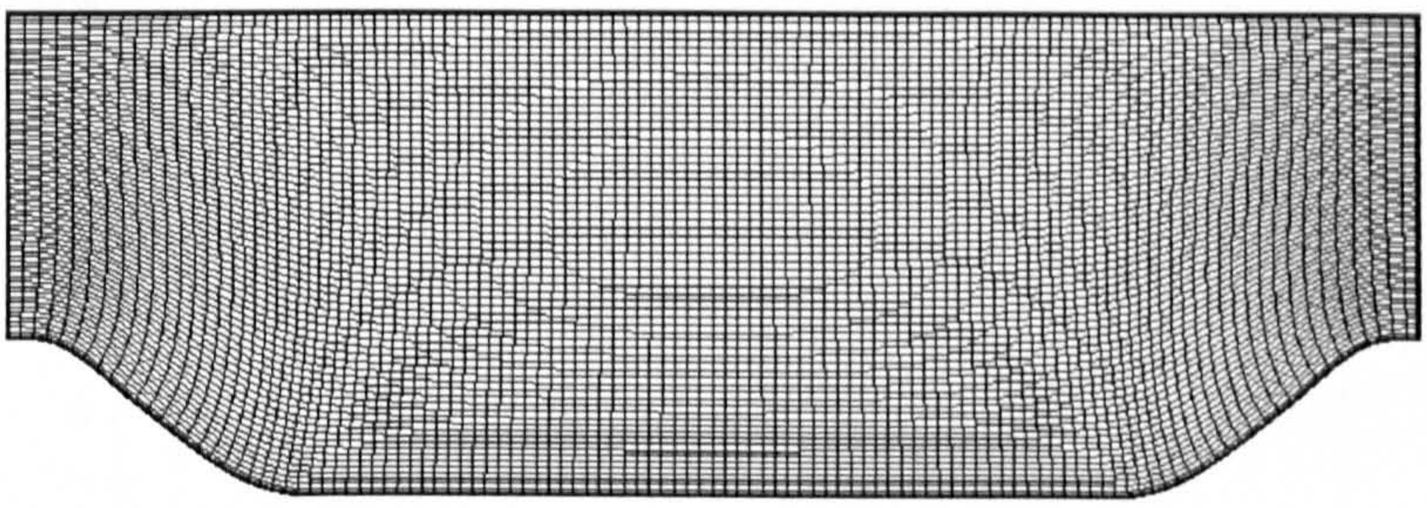

Figure 7.44: Cut in the $x - y$ plane through the coarse grid (Grid 1) made of $112 \times 64 \times 92 \approx 0.66 \cdot 10^6$ cells.

The range of simulations undertaken is summarised in Table 7.2. These simulations were conducted along three parametric *axes* intended to allow the contribution of resolution, SGS modelling and near-wall approximation to be separated, at least qualitatively. Simulations $1 - 11$ have been performed on Grid 1 made of $0.66 \cdot 10^6$ interior cells. Of these, simulations $1 - 7$, all done with the WALE SGS model, are designed to convey the sensitivity of the solution to the near-wall treatment, including the two implementation options explained in Subsection 3.3.3, while simulations $8 - 11$, all undertaken with the Werner-Wengle wall function (WW), are intended to bring out the dependence of the solution on SGS modelling for that grid.

Simulations $21 - 23$ form a selection from set $1 - 10$ for the finer Grid 2 ($1.04 \cdot 10^6$ interior cells). Finally, case 31 identify the highly-resolved simulation which was the subject of Section 7.3.

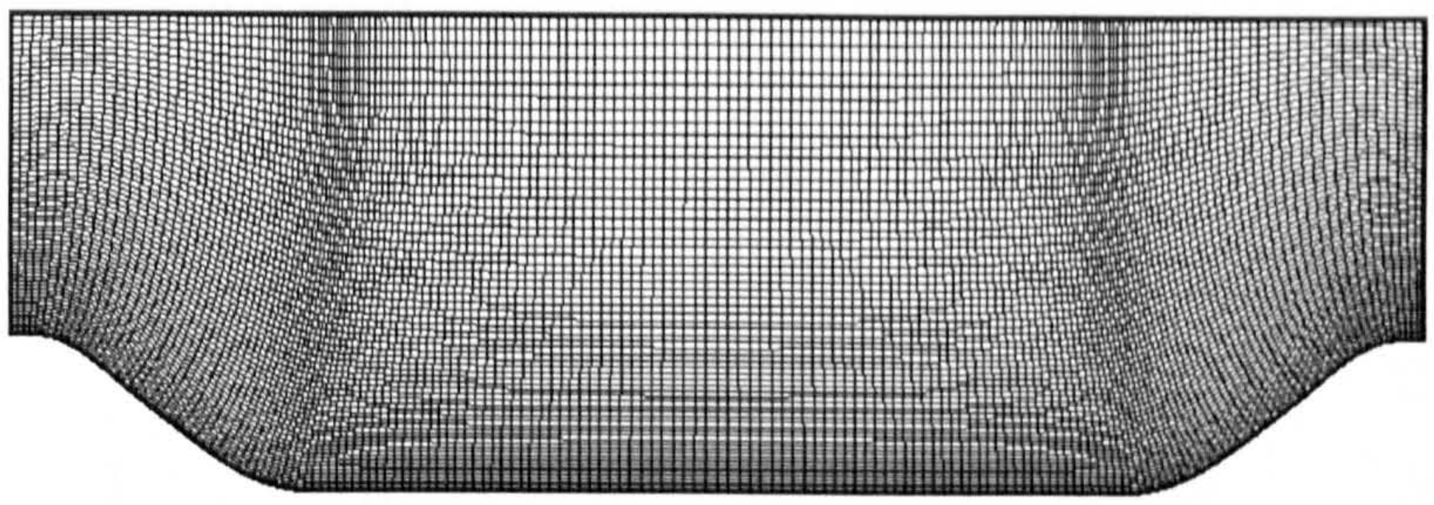

Figure 7.45: Cut in the $x - y$ plane through the coarse grid (Grid 2) made of $176 \times 64 \times 92 \approx 1.04 \cdot 10^6$ cells.

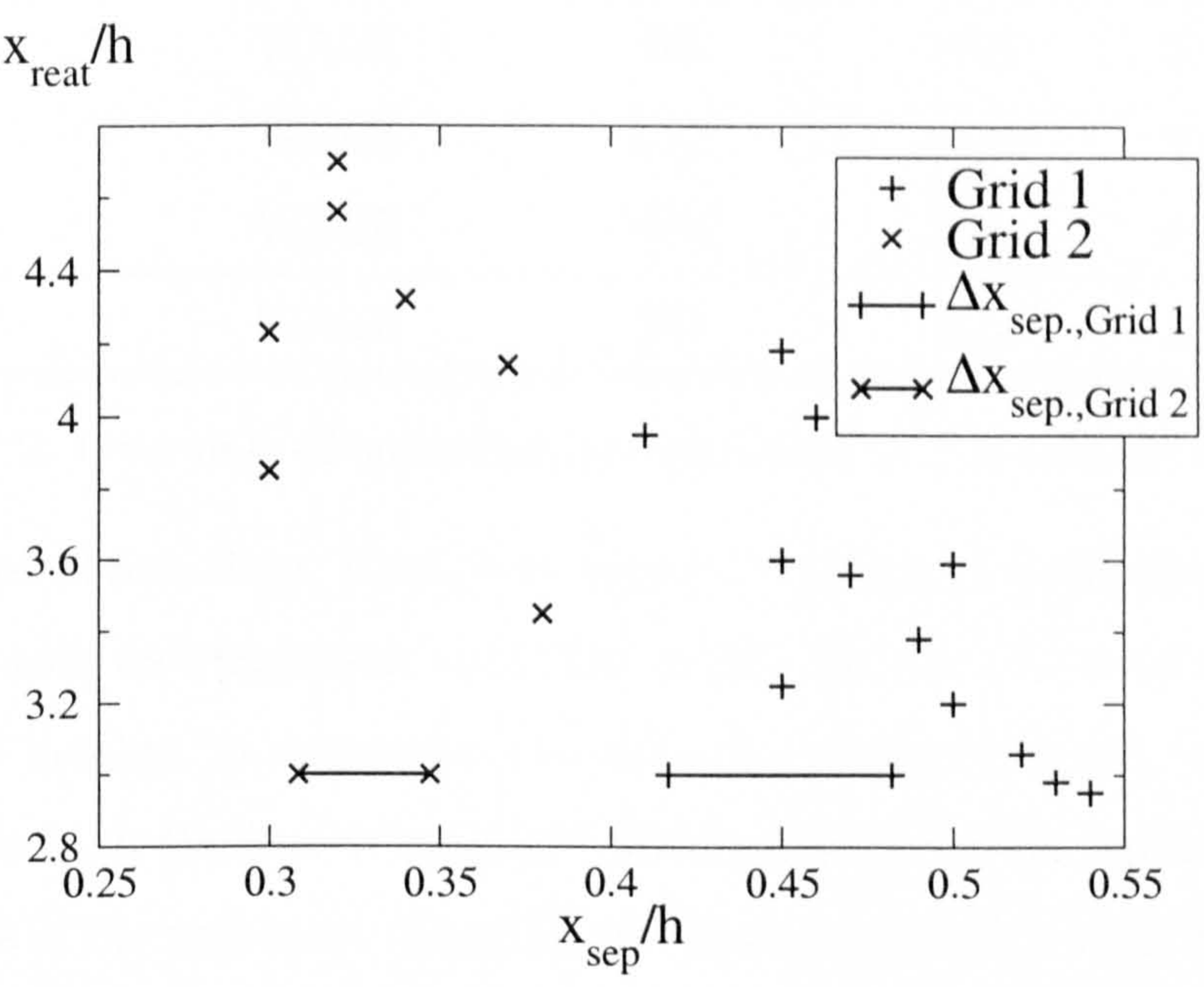

Figure 7.46: Correlation between separation and reattachment locations, + identifies data obtained with Grid 1, X identifies data obtained with Grid 2. The lines indicate the streamwise internodal distance (normalised by h) in the separation region.

In Table 7.2, the two right-most columns give the predicted time-mean separation and reattachment locations, obtained upon integration over at least 55 flow-through times. These allow a number of interesting points to be highlighted, ahead of the de-

Case	Grid	SGS model	Wall treatment	$(x/h)_{sep}$	$(x/h)_{reat}$
1	1	WALE	NS	1.12	2.17
2	1	WALE	WW	0.46	4.00
3	1	WALE	WW-p	0.52	3.059
4	1	WALE	LL2	0.54	2.95
5	1	WALE	LL2-i	0.41	3.95
6	1	WALE	LL3	0.53	2.98
7	1	WALE	LLK	0.49	3.38
8	1	SM + WD2	WW	0.50	3.59
9	1	MSM	WW	0.45	4.18
10	1	DSM	WW	0.47	3.56
11	1	LDSM	WW	0.47	3.56
21	2	WALE	NS	0.38	3.45
22	2	WALE	LL3	0.34	4.32
23	2	WALE	WW	0.32	4.56
31	3	WALE	NS	0.22	4.72

Table 7.2: Overview of computations discussed in the present section.

tailed discussion of field data. First, it is observed that the recirculation length varies greatly with mesh, wall treatment and SGS model: the shortest recirculation length is about 2 hill heights, in comparison to $4.5 - 4.7$ returned by the highly-resolved simulations. Second, the flow is evidently fairly sensitive to the implementation details of any one of the wall-laws. Thus, the simulation pairs (2,3)=(WW,WW-p) and (4,5)=(LL2,LL2-i) demonstrate a consistent difference between the integrated and point-wise implementations, defined earlier in Section 3.3, with the former practice yielding a significantly longer recirculation zone, in better accord with the highly-resolved solution. Finally, as shown in Figure 7.46, there is a fairly strong correlation between the separation and reattachment locations: typically, a forward shift of the separation point by 0.15 hill heights results in a shortening of the recirculation zone by one hill height, a causal relationship which will be revisited below. This brings

out an important difference between simulating a flow in which separation is fixed by edges, relative to one in which separation occurs from a continuous surface, especially when reattachment is not enforced by a geometric feature or blockage causing early re-acceleration.

7.4.2 Effects of resolution

Compared to the dense Grid 3, used for the highly-resolved simulation 31 in Table 7.2, two substantially coarser grids have been used to investigate issues of resolution and modelling. The coarsest Grid 1 ($0.66 \cdot 10^6$ cells, see Figure 7.44) has a fairly uniform density over the domain. The medium Grid 2, shown in Figure 7.45 is moderately finer ($1.04 \cdot 10^6$ cells), but the refinement was introduced preferentially around the hill crest, and the nodes were redistributed in the y-direction so as to achieve a better resolution at the lower wall.

Case	$\frac{x_{sep}}{h}$	$\frac{x_{reat}}{h}$	Grid size $(N_X \times N_Y \times N_Z)$	$\frac{\Delta x_{sep}}{h}$	$\frac{\Delta x_{crest}}{h}, \frac{\Delta y_{crest}}{h}, \frac{\Delta z_{crest}}{h}$
1	1.12	2.17	$112 \times 64 \times 92$	0.065	0.08, 0.032, 0.049
21	0.38	3.45	$176 \times 64 \times 92$	0.039	0.04, 0.02, 0.049
31	0.22	4.72	$196 \times 128 \times 186$	0.032	0.032, 0.0033, 0.024

Table 7.3: Sensitivity of separation and reattachment locations to grid parameters at the hill crest.

An impression of the difficulties that are posed by using *coarse* grids for separated flow is conveyed by Table 7.3 and Figures 7.46 and 7.47. Figure 7.47 shows profiles of velocity, (resolved) streamwise normal stress and shear stress at two locations, $x/h = 2$ and $x/h = 6$, i.e. within the separation bubble and after reattachment. Results are compared for the three grids employed using the same SGS model (WALE) and the same no-slip (NS) wall condition. This boundary condition might appear inappropriate for the coarsest grid, although it has been used with considerably coarser meshes in wavy-wall simulations (e.g. Salvetti et al [195]). However, as is

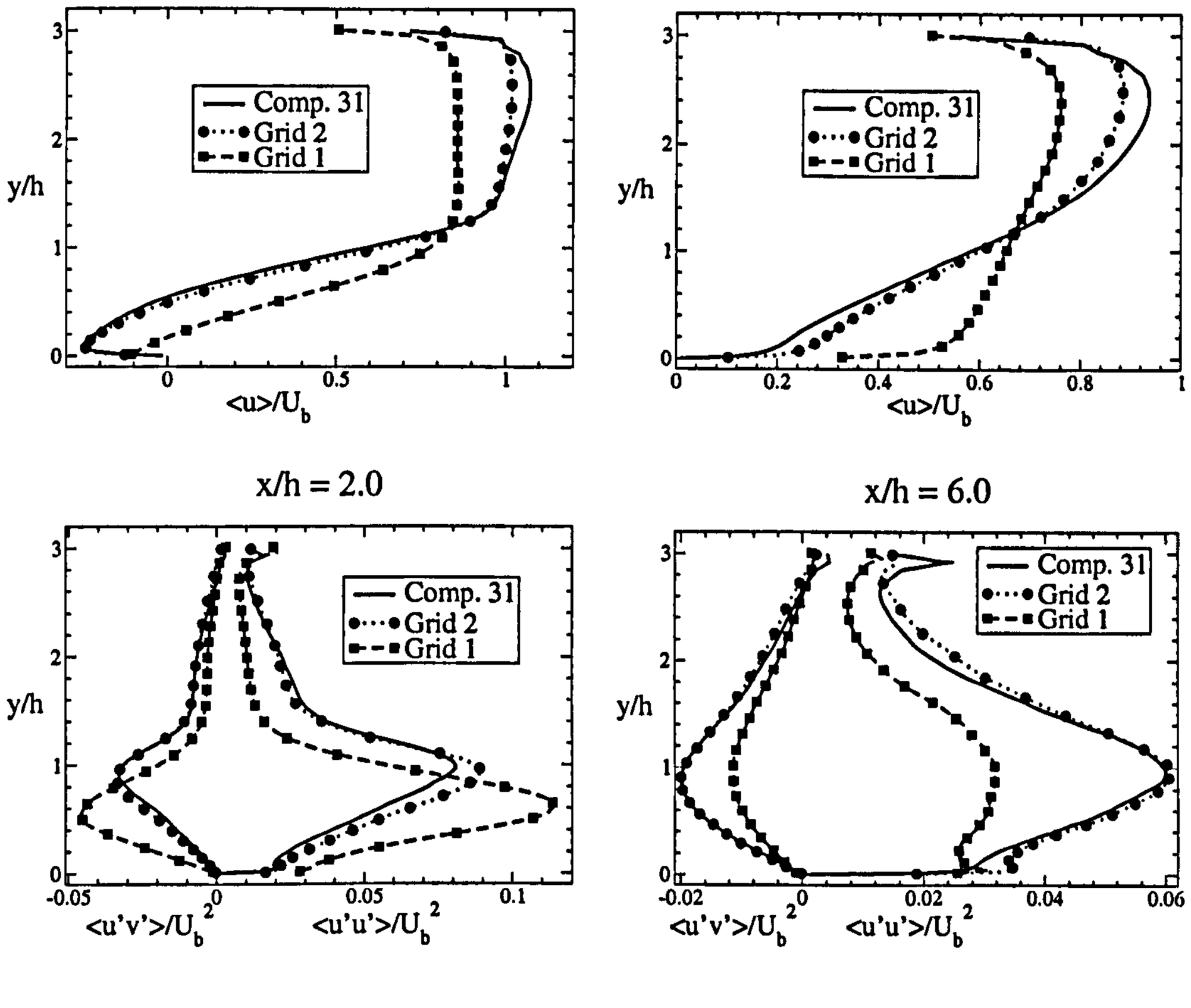

Figure 7.47: Streamwise velocity, resolved streamwise stress and resolved shear stress at $x/h = 2$ and $x/h = 6$ for Grids 1, 2 and 3, the WALE model and the no-slip (NS) wall condition have been used in all cases.

evident from Figure 7.48, the time-averaged y^+-values corresponding to the distance between the lower wall and the first grid plane are mostly below 8; the peak value of 14 arises at the crest of the hill, following the strong acceleration on the windward side. Thus, while a no-slip condition is undoubtedly a poor approximation, it might not be expected to be disastrously poor. However, when this condition is used in combination with poor resolution around the separation point, it leads to a serious misrepresentation of the entire flow, principally because of the substantial downstream shift in the separation point. As the wall shear strain is evaluated, in this case, using a linear approximation to the near-wall velocity, the resulting shear stress is underestimated relatively to both the real value and that arising from a log-law-based wall function. Hence, following acceleration, flow-retardation by wall

shear is inhibited, and separation is thus delayed. Since the separation bubble is much shorter, the $\langle u \rangle$–profile at $x/h = 6$ is much fuller, the substantially lower shear strain at that location being compatible with a much lower level of turbulence intensity and shear stress. Upstream of reattachment, at $x/h = 2$, the separated shear layer returned by the coarsest grid is significantly lower and more turbulent than the highly-resolved layer, as is reflected by the higher fluctuation intensity and shear stress. This higher level of turbulence intensity is consistent with the smaller distance between the separation point and the profile location in question ($x/h = 2$), together with the fact that the turbulence intensity reaches a maximum a short distance downstream of the separation location. Hence, it seems clear that the realism of the solution in the vicinity of the separation location is crucially important. An inappropriate downstream shift gives the wrong (mean) separation height and angle, and this, coupled with strong mixing immediately following separation, encourages rapid reattachment.

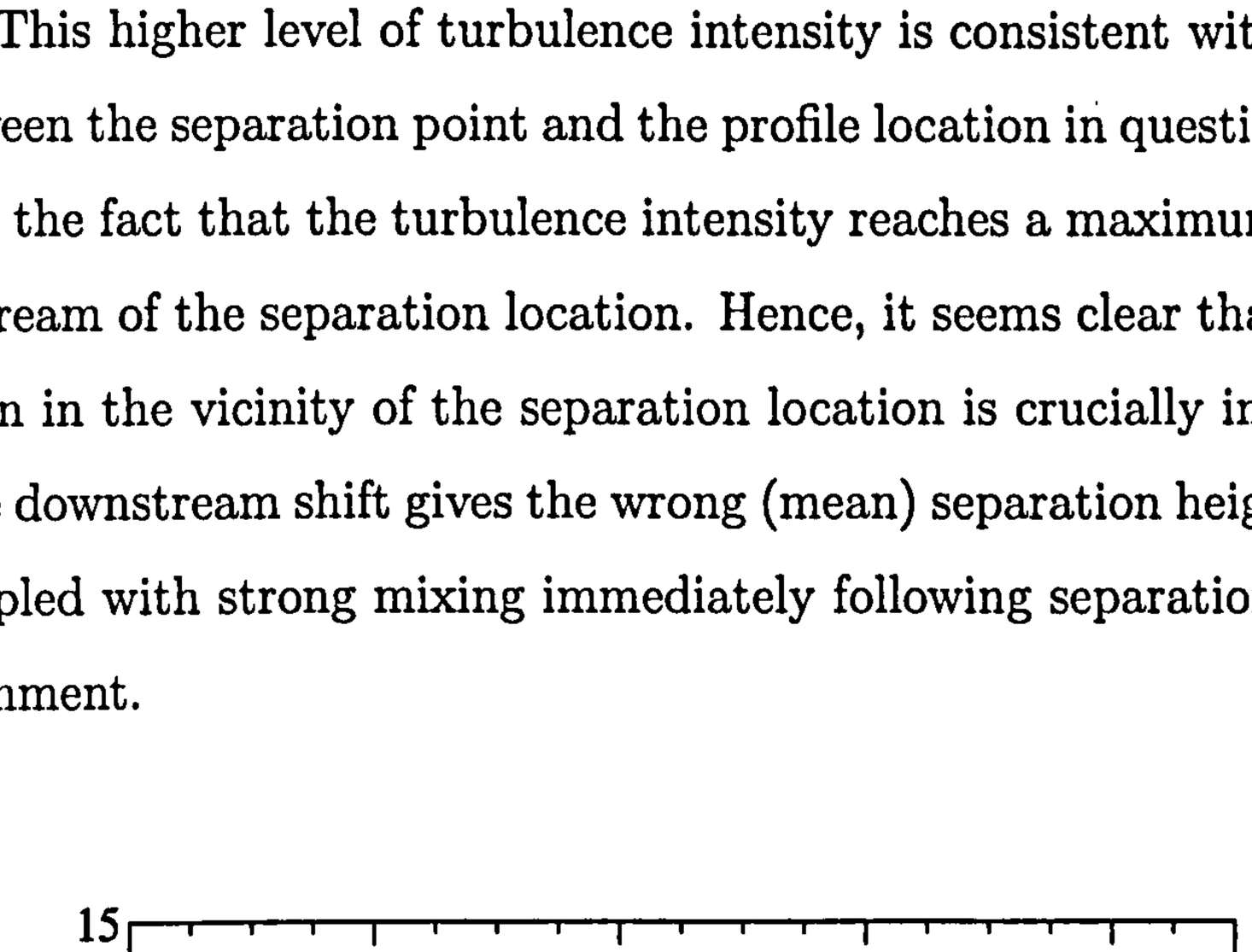

Figure 7.48: Universal wall-distance along the line passing through the centre of the wall-adjacent cells close to the lower walls; from simulations 1 and 21 using the WALE SGS model and NS.

Evidently, the grid resolution around the hill crest, where separation occurs, is

highly influential. Table 7.3 gives, for the 3 grids employed, the value of streamwise cell length Δx around the time-mean separation point and the cell dimensions just above the hill-crest (see also the horizontal line segments in Figure 7.46). Although the position of the separation line varies in time within the wide range of $-0.05h$ and $0.7h$, the expectation must be that the separation point cannot be determined to a precision substantially better than the cell length, $0.08h$, in the case of Grid 1. The associated margin in the reattachment location, implied by Figure 7.46, is of order $0.5h$, and such a shift results in a substantial change to the entire flow. Thus, subject to uncertainties arising from the crude no-slip condition used here, it may be stated that grid resolution around the separation location is especially important and, potentially, of major consequence to the predicted gross-flow features. As the instantaneous position of separation shifts across a significant portion of the hill surface, adequate grid density must be provided over the entire region in which separation is expected to occur.

7.4.3 Sensitivity to near-wall modelling on the coarsest grid

Although the streamwise resolution around the separation point is evidently a key factor, the near-wall treatment can also be expected to be a major contributor to predictive accuracy, if only because the near-wall y^+-value in the hill-crest region is high and the separation point is clearly sensitive to the details of the flow conditions in this region.

An overall view of the dependence of the flow on the near-wall approximation, on the coarsest grid, is given in Table 7.2, Cases $1-7$. All simulations were performed with the WALE model. Clearly, the separation characteristics are highly sensitive to the near-wall approximation, and this is brought out especially well relative to the no-slip implementation. In all cases, separation is delayed and reattachment is early. While the latter is linked to the former (see Figure 7.46), as discussed in the previous subsection, it is evident that the near-wall approximation also has a direct influence on the reattachment location. This fact is implied, albeit qualitatively, by the scatter in Figure 7.46.

Profiles of velocity, streamwise normal stress and shear stress, obtained with the various near-wall approximations, are shown in Figure 7.49. All three log-law-based approximations, when implemented in their standard (point-wise) form, return solutions which are better than that obtained with the no-slip condition, but which are nevertheless far from the highly-resolved simulation, especially in the post-reattachment region. In contrast, the default (cell-integrated) Werner-Wengle approximation (WW) returns a much better solution, which is remarkably close to the highly-resolved simulation. As will be demonstrated below, this is mainly the consequence of the cell-integrated implementation. Of the three log-law approximations, that using $\langle k \rangle$ as the velocity scale in the log-law (LLK) offers a modest advantage in terms of the separation and reattachment locations, but not in respect of other quantities. It should be noted that this variant differs fundamentally from the other two in its use of a time-averaged rather than instantaneous velocity scale in the log-law. This effectively established, for any one near-wall cell, a linear relationship between the near-wall velocity and the shear velocity, in the same sense as that established by Schumann's wall law [200]. Moreover, a significant uncertainty with this variant arises from the inaccuracy in determining the near-wall turbulence energy on the coarsest grid used. This is especially problematic in the vicinity of the separation point.

As is the case with the no-slip implementation, late separation is accompanied by higher turbulence activity in the separated shear layer (at a given x/h location), early reattachment and lower post-reattachment turbulence activity. Although, as argued earlier, a forward shift in the separation location is associated with an increase in turbulence levels at given streamwise x/h positions, this causal relationship is not firm, for some simulations show significant differences in maximum turbulence levels in the shear layer together with quite similar separation locations. This suggests that, at least with the coarse grid used here, separation and post-separation behaviour is sensitive to the structure of the boundary layer as it approaches separation and, arising from this, also to structural features in the separated shear layer itself. The boundary layer is, in turn, materially influenced by the near-wall treatment, especially in the hill-crest region where y^+ values along the wall-nearest

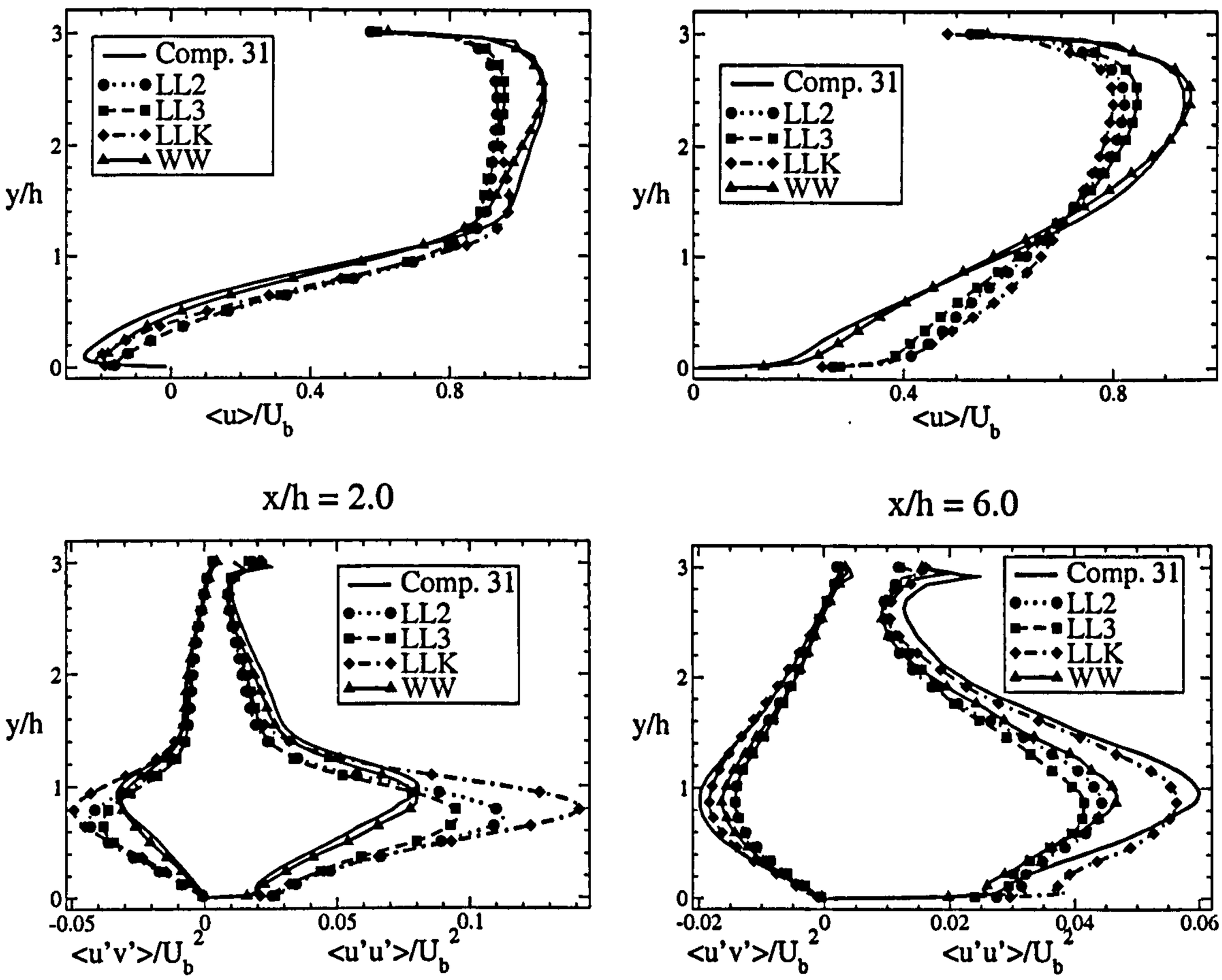

Figure 7.49: Streamwise velocity, resolved streamwise stress and resolved shear stress at $x/h = 2$ and $x/h = 6$ using 4 wall-treatments and the WALE model on the coarsest grid.

grid-line are high.

Figure 7.1 demonstrates, by way of pressure contours, that the shear layer contains a coherent motion associated with vortices associated with the Kelvin-Helmholtz-like instability, a process identified most clearly in animations performed for this flow. This organised motion contributes directly to the turbulence level in the shear layer, as well as interacting sensitively with the temporal variation of the separation process. The details of the coherent component are, however, influenced by the near-wall treatment, and this link is thus one potential source for the variability in the statistical behaviour observed in Figure 7.49.

Figure 7.50 conveys the fact that the exceptional behaviour of the WW wall

law displayed in Figure 7.49 is not essentially due to the different velocity profile forming the basis of that wall law, but arises, primarily, from the nature of its implementation. The figure compares four solutions, two obtained with the point-wise and two with the cell-integrated implementations of the wall laws LL2 and WW. As seen, there is fairly close correspondence between the two point-wise forms (LL2 and WW-p) and similarly close agreement between the two cell-integrated variants. The latter pair gives solutions which are significantly closer to the highly-resolved simulation. This level of sensitivity to the implementation details is remarkable, and is most likely linked to influential differences in the level of the wall-shear stress returned by the two implementations. A-priori studies on plane, fully-developed channel flow, in which DNS velocity profiles were fed into both implementations of the LL2 and WW wall-functions, have shown that both integrated forms give consistently higher wall-shear values than the point-wise forms, the latter returning values that are closer to the DNS level when the wall-nearest node is beyond $y^+ = 16$. A higher wall-shear stress level (traction) just upstream of the separation point encourages, all other conditions being unchanged, a slightly earlier separation, apart from possibly influencing the organised behaviour in the shear layer, via the mechanism considered earlier.

The overall conclusions emerging from the above results is, therefore, that even relatively minor variations in the near-wall treatment can have major effects on the separation behaviour and the structural features in the separated layer, thus materially affecting gross flow features if the streamwise resolution is coarse, especially around the separation point.

7.4.4 Sensitivity to SGS models on the coarsest grid

An overall view of the sensitivity of the solution to SGS modelling, on the coarsest grid, is conveyed in Table 7.2, Cases 2 and 8-11. In general, the coarser the grid, the more influential the SGS model is expected to be. Hence, it is of interest to undertake a study of the sensitivity to SGS modelling on Grid 1, even if this grid is known to offer relatively poor resolution in the separation region. All simulations

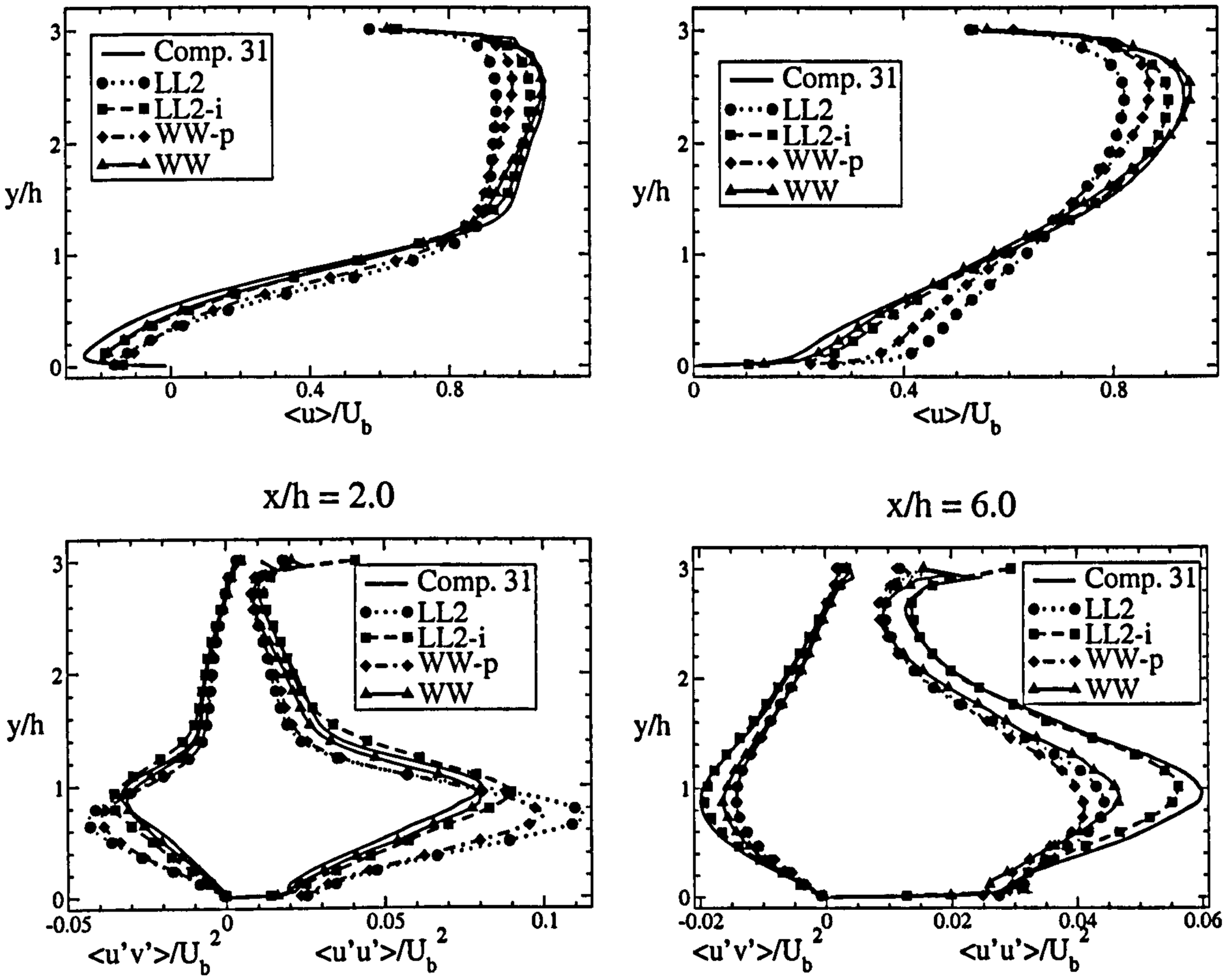

Figure 7.50: Streamwise velocity, resolved streamwise stress and resolved shear stress at $x/h = 2$ and $x/h = 6$ using the point-wise and cell-integrated forms of LL2 and WW wall-treatments and the WALE model on the coarsest grid.

were performed with the default (cell-integrated) form of the Werner-Wengle wall law (WW), shown earlier to give, alongside LL2-i, the most favourable agreement with the highly-resolved simulation.

Reference to Table 7.2 and to Figures 7.51 and 7.52, the latter showing mean-velocity and turbulent-stress profiles, allows the overall observation that sensitivity to SGS modelling, even on the coarsest grid, is not especially pronounced, and this reinforces the comments made earlier about the importance of the near-wall approximation as the major source of variability among simulations on the coarsest grid.

The separation point is seen to be rather insensitive to the SGS model, while

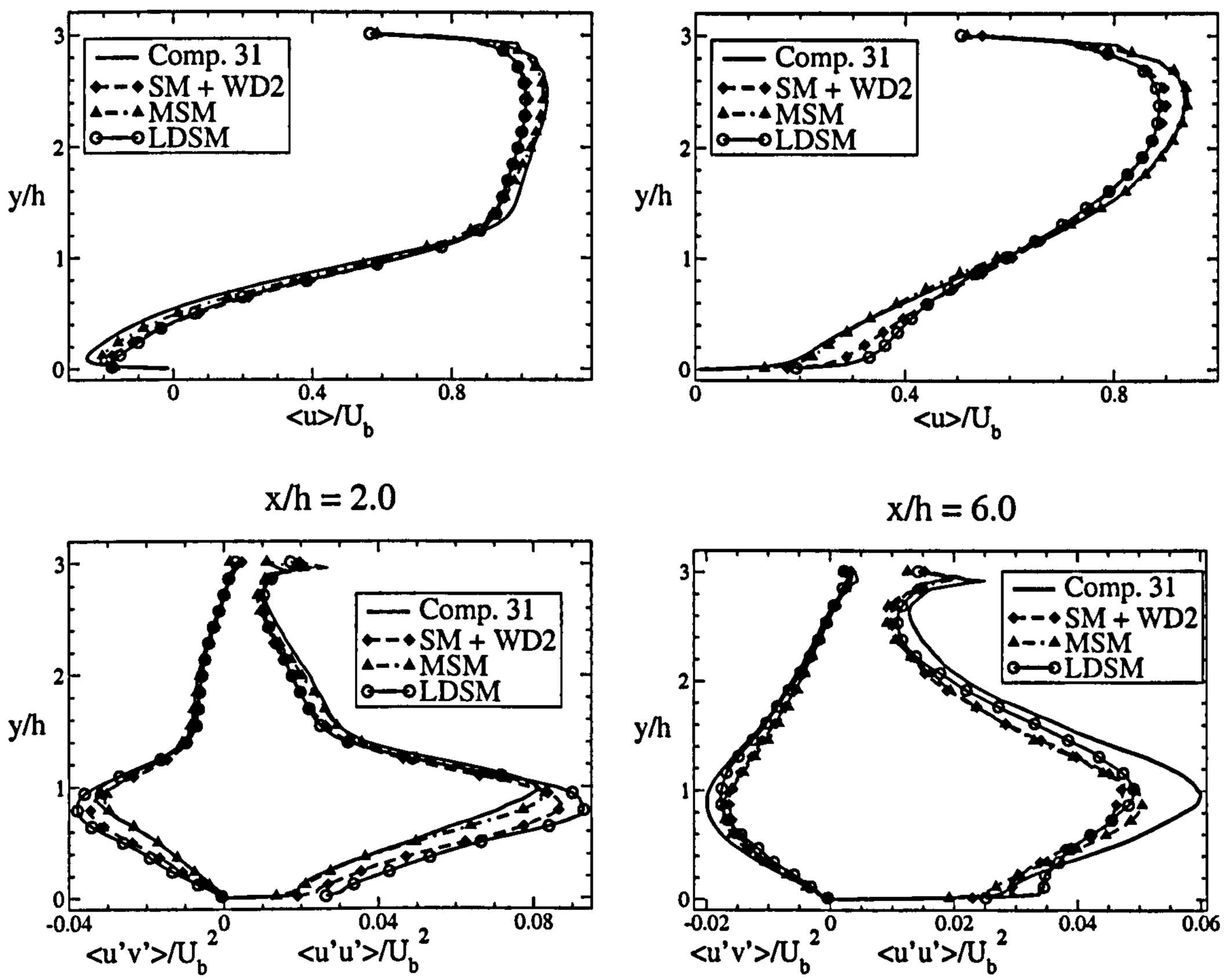

Figure 7.51: Streamwise velocity, resolved streamwise stress and resolved shear stress at $x/h = 2$ and $x/h = 6$ using 3 SGS models together with the WW wall function on the coarsest grid.

the reattachment point is somewhat more sensitive. This is a consequence of the dependence of the former primarily on the upstream near-wall flow, while the latter responds to both the separation point and the processes in the post-separation shear layer which are likely to be sensitive, to a greater extent, to SGS modelling. Among the SGS models, the WALE model and the mixed-scale model (MSM) give the longest recirculation length, closest to the reference. The dynamic models (DSM and LDSM), on the other hand, tend to return the shortest recirculation region.

Since the SGS model affects the simulated solution via the introduction of an SGS viscosity, and hence SGS stresses, it is instructive to examine the level of viscosity returned by different models. To this end, profiles of the time-averaged

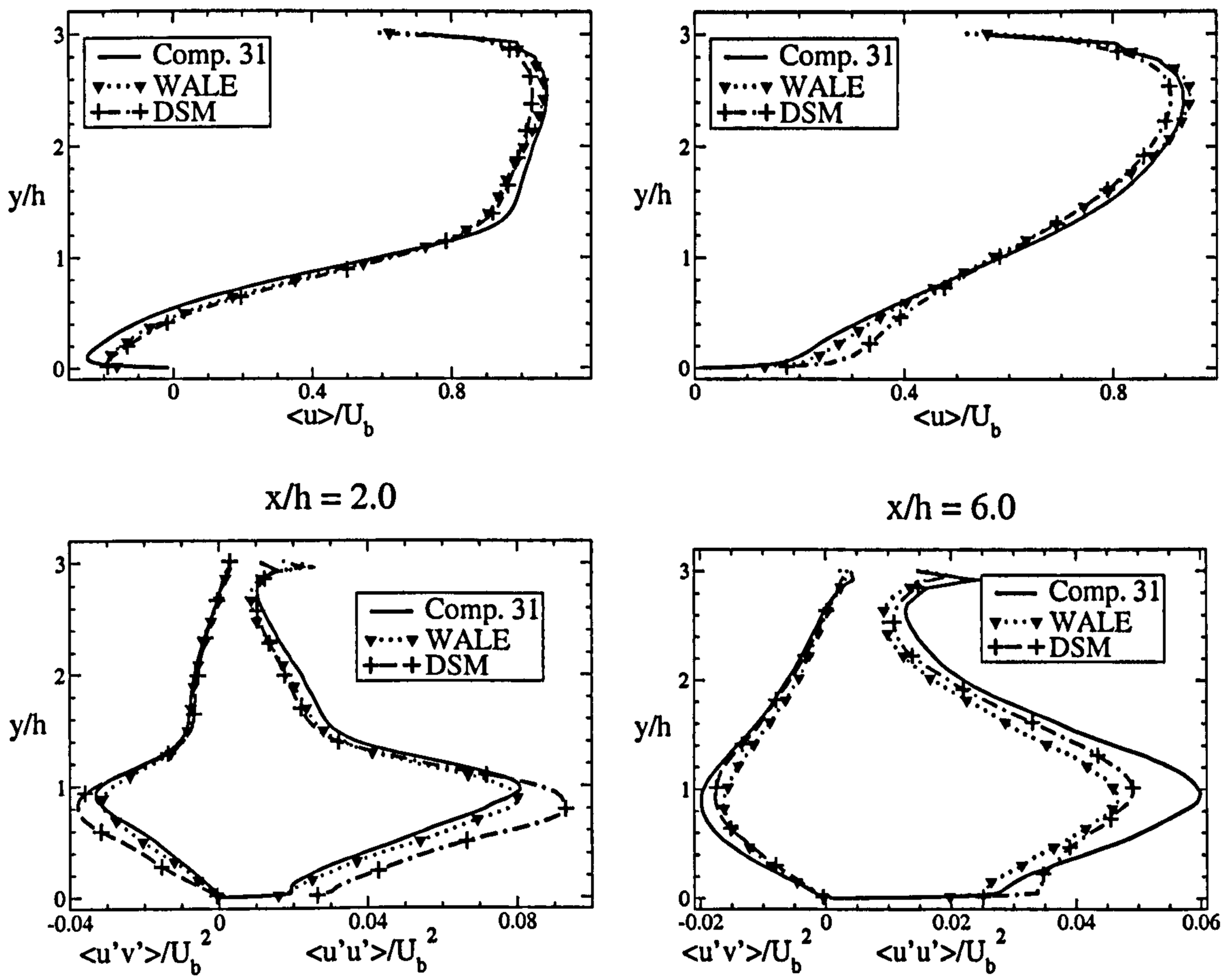

Figure 7.52: Streamwise velocity, resolved streamwise stress and resolved shear stress at $x/h = 2$ and $x/h = 6$ using the WALE and the DSM model together with the WW wall function on the coarsest grid.

SGS viscosity at the locations $x/h = 2$ and $x/h = 6$ are given in Figure 7.53. As seen, the SGS viscosity level varies between approximately 1 and 4 times the fluid viscosity, with the mixed-scale and damped Smagorinsky models giving low values, the dynamic model giving high levels and the WALE model being in the middle of the range. While Table 7.2 suggests an association between low levels of SGS viscosity and long recirculation zones, and hence improved agreement with the reference simulation, this association is not unambiguous, as is exemplified by the result with the damped Smagorinsky model. Broadly consistent with the above trend is the observation, from Figures 7.51 and 7.52, that models returning relatively low values of SGS viscosity (MSM, WALE, SM+WD2) also give rise to lower values

of resolved turbulent stresses and closer agreement with the reference simulation.

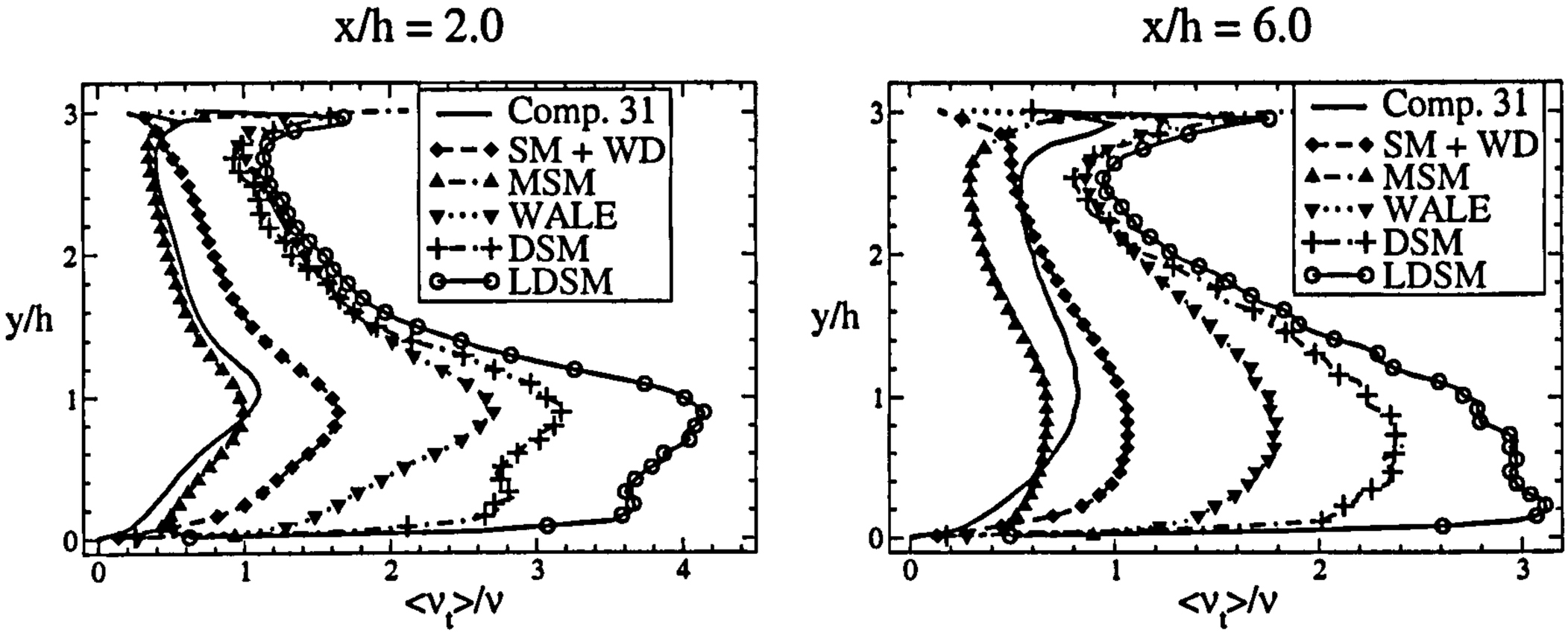

Figure 7.53: SGS viscosity at $x/h = 2$ and $x/h = 6$ using 5 SGS models and the WW wall function on the coarsest grid.

This is not a behaviour that concurs with initial expectations: a high SGS viscosity is expected to cause smoothing (damping) of the resolved scales close to the wave-number cut-off, and thus to lead to a reduction in the resolved stresses. The opposite would then be expected to occur when the SGS viscosity decreases. However, this line of reasoning is based on a consideration of isotropic turbulence, with the cut-off located well within the inertial range, not far from the dissipative limit. The present flow, in contrast, exhibits significant anisotropy in the resolved motion at the cut-off, due to the coarseness of Grid 1, and hence different energy-transfer characteristics across the large-scale part of the spectrum. This applies, in particular, to the post-separation shear layer. As noted earlier, by reference to Figure 7.1, the shear layer contains anisotropic coherent structures with relatively large spanwise extent. Animations reveal that the vortices undergo fairly pronounced helical pairing, whilst breaking up as they are convected downstream. Higher viscosity slows down this process, tending to reduce the generation of spanwise fluctuation by a dynamic redistribution of kinetic energy. This encourages the persistence of the large-scale two-dimensional anisotropic features, which then tend to result in elevated levels of resolved fluctuations, as is observed in other configurations (Mellen et al [151]).

7.4.5 Comparisons for the medium Grid 2

In accord with expectation, refinement of the grid results in an improvement in the predicted flow, both in respect of the separation and the reattachment positions. At the same time, the dependence on the near-wall approximation declines, as is seen from Figure 7.54. It is recalled, however, that the refinement is highly localised and selective, involving mainly an increase in the streamwise grid density in the vicinity of the hill crest. The result is a more accurate resolution of the separation process. The importance of this specific aspect of the simulation has been highlighted already by reference to the coarse-grid results. Evidently, it is this improvement which is principally responsible for the substantial overall improvement in the predicted flow field. Thus, the streamwise resolution, especially around the separation location, is clearly as influential as the near-wall approximation, if not more so. Reference to Figure 7.54 shows that, among the wall treatments, the no-slip condition remains poor, while the Werner-Wengle approximation performs best, as it did with the coarse grid. In fact, the departure of the WW solution from the highly-resolved simulation is almost insignificant in respect of both the mean flow and turbulence quantities. This simulation, Case 23 in Table 7.2, also gives separation and reattachment points close to those of the highly-resolved solution.

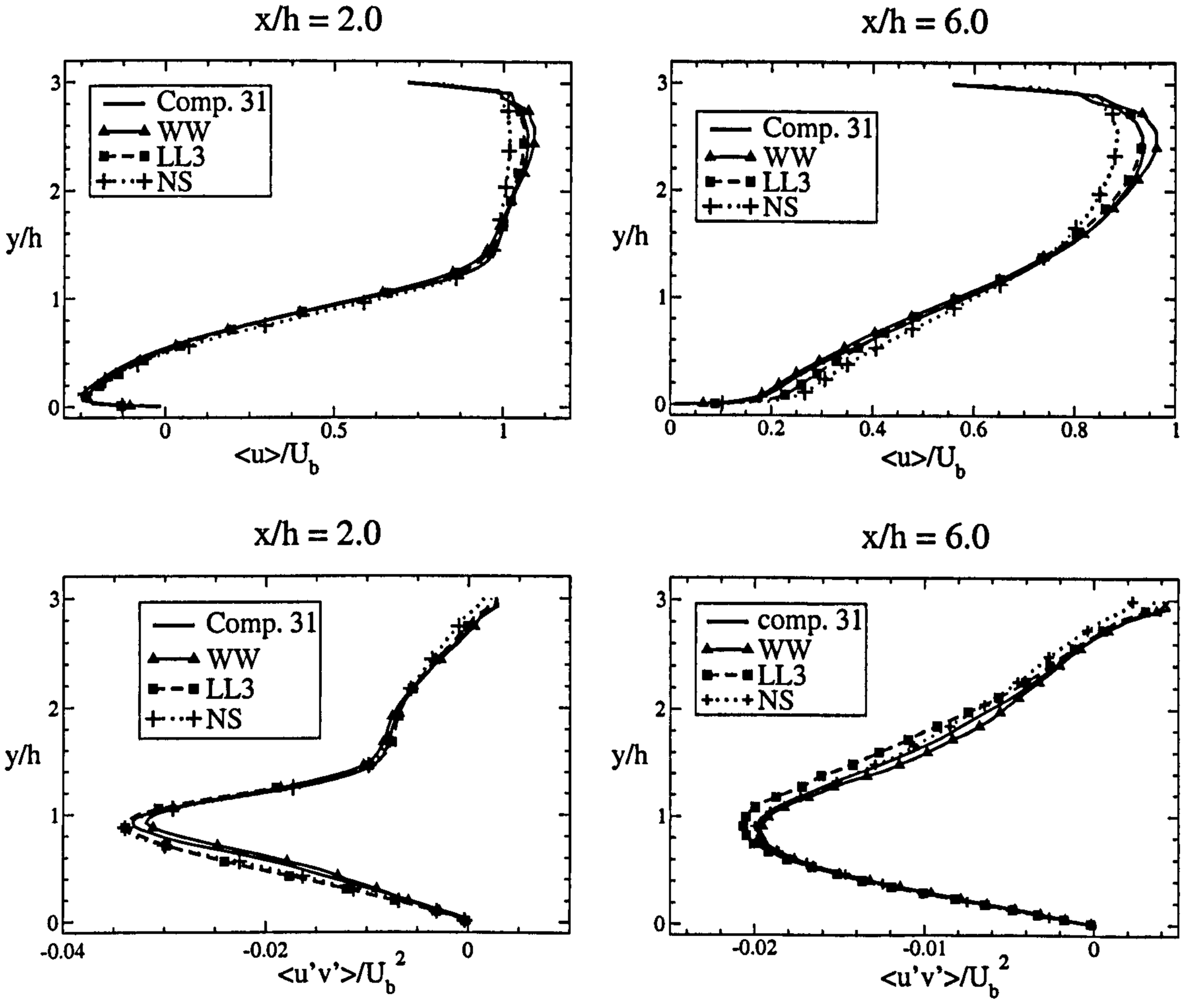

Figure 7.54: Streamwise velocity and resolved shear stress at $x/h = 2$ and $x/h = 6$ using 3 near-wall approximations together with the WALE model on Grid 2.

7.5 Concluding remarks

Large eddy simulations of a fully turbulent flow separating from a curved wall in a periodic channel have been presented. In the first part of this chapter, a test case was constructed for which data were generated and subjected to an in-depth study of the turbulence phenomena taking place in the flow. The data were carefully cross-checked by reference to another simulation performed contemporaneously on the same grid by Mellen et al [150], enhancing the confidence in the results. In the second part, the emphasize has been on investigating the influence of resolution, SGS modelling and near-wall modelling on the accuracy of the simulation.

The generation by LES of reliable data for a flow separating from a curved surface was made possible by carefully selecting the characteristics of the geometry and flow conditions, i.e. a flow which is periodic in the streamwise and spanwise directions with a Reynolds number and computational domain for which an highly-resolved LES computation remained affordable. In addition, the flow was designed to present a separation that occurred somewhere on the curved surface, while reattachment was on the horizontal plane, sufficiently far from the downstream constriction, allowing a significant recovery to take place. The complexity of the flow, alongside the availability of a reliable set of data, made it an attractive test case for researchers to develop and validate RANS and LES methods and, thus, the data were made available to the turbulence community through the ERCOFTAC website.

The data generated included mean velocities and stress profiles, turbulence energy and Reynolds-stress budgets and a significant amount of instantaneous data. The constrast projected by the instantaneous against the mean data highlighted the rather chaotic behaviour of the instantaneous flow. This is very well illustrated by the absence of clear lines of separation and reattachment. Indeed, these locations vary substantially in time, and the flow is observed to be attached and detached over most parts of the lower wall, except on the windward part of the hill where the flow is subjected to a strong acceleration due to the raising slope and, therefore, remains attached.

The most intriguing phenomena was the large excess of the spanwise normal

Reynolds stress over the other components, especially on the windward side of the hill. The transfer of energy among these stresses was shown to occur through the pressure-strain interaction and was linked to *splatting*. This process occurred due to large streamwise-oriented structures impinging on the windward side of the hill, generating substantial transverse motions. This splatting effect was observed to occur at a range of locations on the wall, although its most marked manifestation was on the windward side of the hill. In the shear layer, rollers extending over a significant spanwise extent were observed. These originate from a Kelvin-Helmholtz instability. Between these rollers, streamwise vortices created by helical pairing were also found. Following the break-up of the spanwise rollers, large streamwise-oriented inclined structures were sometimes observed and seen to transport over the downstream hill. A representation of the velocity profiles in wall units underlined the absence of an universal law of the wall at all locations and, in the recirculating region, in particular.

Simulations on a coarse grid have highlighted the outstanding importance of an adequate streamwise resolution of the flow in the vicinity of the separation line. This importance arises from the fact that the reattachment position is highly sensitive to that of separation, and so is the entire flow. Although the separation line varies in time over a substantial region around the mean location, the precision with which the latter is predicted is, at best, of the order of the local mesh size. In specific terms, a streamwise resolution of $0.08h$ around the mean separation location can be expected to produce an error margin in the reattachment position of order $0.5h$. Indeed, the present study suggests that this is a rather optimistic estimate.

The dependence of the solution on different practices of near-wall and SGS modelling has been investigated on two grids and compared to the highly-resolved reference simulation. The results have been found to be surprisingly sensitive to the nature of the numerical implementation of the wall laws, rather than to the precise assumptions of the velocity profiles underpinning them. The best performance was obtained with cell-integrated implementations of either the log-law or the Werner-Wengle approximation. The differences between the point-wise and cell-integrated implementations is due to the latter returning higher levels of wall-shear stress than

the former, all other conditions being the same. This encourages earlier separation and hence better correspondence with the highly-resolved simulation.

It must be acknowledged that the relatively low Reynolds-number of the flow led to the wall-nearest computational point lying within the semi-viscous wall layer over most of the lower wall bordering the separation zone. Also, a-priori studies, exploiting the highly-resolved simulation data, have demonstrated that the near-wall flow did not conform to the velocity profiles underpinning the wall laws. This inevitably limits the generality of the conclusions derived in respect of near-wall modelling.

The sensitivity of the solution to SGS modelling has been found to be weaker than to variations in resolution and near-wall treatment. Of the SGS models examined, the WALE and the mixed-scale (MSM) models performed best, in so far as the related coarse-grid solutions came closest to the highly-resolved simulation. Both models returned relatively low levels of SGS viscosity, although the latter was shown to give an incorrect wall-asymptotic viscosity variation in wall-resolved channel-flow simulations.

Further studies are clearly needed for flows at higher Reynolds numbers, but this poses the problem of generating sufficiently detailed and accurate benchmark data at tolerable cost. The present study at least suggests that resolution parameters are likely to be especially critical in other flows involving separation from gently curved surfaces, such as highly-loaded aerofoils and blades. Configurations of this type arguably require preferential attention to identify the capabilities of LES cases such as the one examined in the following chapter.

Chapter 8

Flow around a high-lift aerofoil near stall

8.1 Introduction

Chapters 6 and 7 considered, respectively, a periodic channel flow and a separated flow over a periodic hill. These studies demonstrated the validity of the present method, its capabilities and characteristics, and they also helped to identify some *best practices*. Issues considered included the modelling of the subgrid–scale processes, the approximate representation of under–resolved near–wall flow, the role played by the grid resolution and the influence of the numerical method. In the present chapter, a final case is considered, which may be claimed to be at the very limit of the current capabilities of LES. This case is a high–lift aerofoil at near–stall condition at high Reynolds number. Based on the experience gathered in the previous chapters, the computation of such a flow was expected to be feasible, while indicative of the current capabilities and limits of LES in conditions that approach those in aeronautical practice.

The geometry under consideration is the *Aérospatiale* single–element aerofoil, denoted A-aerofoil and shown in Figure 8.1. The aerofoil is just beyond stall condition, at an incidence angle of 13.3^o and a Reynolds number of $2.1 \cdot 10^6$, based on the free stream velocity U_o and the chord length c. The present case is especially

challenging because of the variety of phenomena taking place at scales which differ by orders of magnitude. These include, successively, a laminar separation bubble, located on the suction side near the leading edge, a transitional reattachment caused by the strong acceleration of the flow, a turbulent boundary layer subjected to a strong adverse pressure gradient, which causes separation near the trailing edge and, finally, separation extending to the wake. This test-case was selected because of the availability of recent, well–regarded experimental data, which have been used extensively over the last 10 years for the development and validation of numerical codes and RANS techniques, especially within two European projects EUROVAL [77] and ECARP [78]. The conclusions of these projects indicated that very few RANS models, mostly those based on second–moment closure, reproduced well the experimental results. In addition, transition on the suction side of the aerofoil had to be artificially triggered.

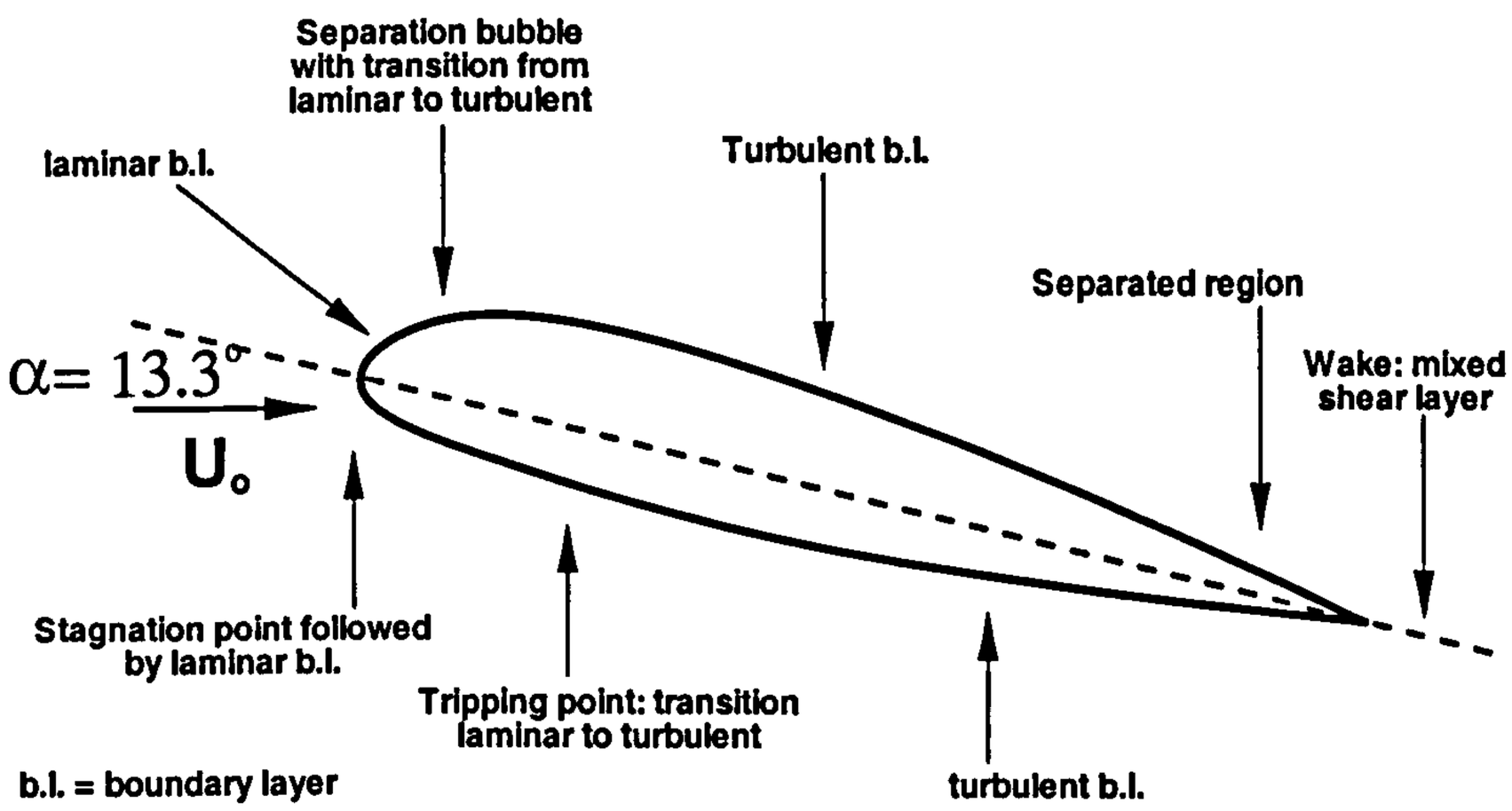

Figure 8.1: The A-aerofoil profile and flow regions around it.

The first attempts to compute moderately detached flows around aerofoils at high Reynolds numbers with LES are due to Kaltenbach and Choi [102] on structured meshes, and to Jansen [92, 93] on an unstructured mesh. The case considered was a NACA 4412 profile at maximum lift for a Reynolds number of $1.54 \cdot 10^6$, based on chord length and freestream velocity. This flow is similar to the present one in terms of the challenge it poses. Jansen [92, 93] and Kaltenbach and Choi [102]

demonstrated that such computations were feasible, although at a very high cost because of the high mesh density and the relatively small time-steps that had to be prescribed. Major problems encountered included the difficulty of correctly predicting the transition, aided by a triggering technique, and the presence of spurious waves responsible for the creation of unphysical wiggles which were indistinguishable from turbulence in some regions. The spanwise extent, limited to a few percent of the chord length for economical reasons, was a source of substantial uncertainty in respect of the realism of the simulations.

More recently, the LESFOIL project [45] focused on the present A-aerofoil. Just prior to this project, Weber et al [233] attempted to compute this particular flow, but their effort was unsuccessful and hinted at the difficulties that would be encountered in trying to achieve a successful simulation of this flow. Of all contributors to the LESFOIL project, only Mary and Sagaut [142] succeeded in matching the experimental data. However, their simulation employed a $2D/3D$ patching technique with the $3D$ patches only covering a small portion of the domain, a very dense mesh and a very small spanwise extent of 1.2% of chord. Some of the simulations reported in this chapter were also performed as part of the LESFOIL project in which the author participated.

The remainder of the chapter is organised in five parts. Section 8.2 describes in details the aerofoil and the reference data. In Section 8.3, results of computations performed on *coarse* grids are presented and discussed. These attempts aimed at identifying the role played by the subgrid-scale model, the wall treatment, the numerical scheme, the mesh and the outflow boundary condition. Based on the observations made in Section 8.3, further simulations were performed, and these are presented in Section 8.4. Finally, Section 8.5 summarises the findings derived from the simulations in this investigation and draw conclusions on the feasibility and limitations of LES for high–Reynolds–numbers near–wall flows undergoing marginal separation.

8.2 Test–case description: the A-aerofoil

Figure 8.1 gives an overall view of the phenomena encountered in the flow. On the suction side of the aerofoil, a laminar boundary layer undergoes natural transition in an essentially laminar separation bubble, ending by turbulent reattachment at $x/c = 0.12$. The boundary layer then develops and grows until it detaches at $x/c = 0.83$, beyond which a small recirculation zone forms. The reverse flow extends to $y/c = 0.016$ from the wall. The transition on the pressure side was triggered at $x/c = 0.3$ in the experiments. The experimental geometry had a blunt trailing edge of approximatively $5\%\, c$ thickness. However, for reasons of simplicity, and based on the experience derived from the EUROVAL [77] and ECARP [78] projects, a sharp trailing edge was prescribed in the simulations. Mary and Sagaut [142] demonstrated this simplification to be of no consequence.

The experimental data were obtained in the ONERA–F1 [86] and ONERA–F2 [71] wind–tunnels, with respective test sections having the dimensions of $3.5m \times 1.5m$ and $1.8m \times 1.4m$, where the first dimension refers to the height of the section and the second to its width. The Mach number was 0.15 and the flow can thus be assumed to be incompressible. Measurements of the drag, lift and skin friction coefficients, C_d, C_l and C_f, respectively, were performed in the F1 tunnel. In the F2 tunnel, detailed measurements of the boundary layer and wake were made using LDA. The drag and lift coefficients were again measured. The aerofoil tested had a chord length of 0.6 m and was identical in the two wind–tunnels, except for its spanwise extent which was slightly different. The F1 tunnel featured minimal blockage effect. Slight corrections of less than 1% were nevertheless applied to the lift coefficient and incidence angle. A system designed to enhance two–dimensionality was also used in the F1 tunnel. In the smaller F2 tunnel, blockage effects were higher and corrections were of the order of $2-3\%$. No specific measures were taken in the F2 tunnel to maintain two–dimensionality of the flow, and this may be the source for the slight differences in drag and lift coefficients between the two sets of data. In addition, C_d and C_l were measured using different techniques. Nevertheless, at the angle of incidence of 13.3^o, the contamination of the flow by three-dimensional

features remained relatively small. In what follows, predicted C_d and C_l should be compared principally with the measurements originating from the F1 tunnel. However, the data from the F2 tunnel are also included.

The exact description of the A-aerofoil profile can be found in the CD-ROM enclosed in Haase et al [78]. The computational domain extends outwards over 10 chord lengths. The geometry being homogeneous in the spanwise direction, all meshes presented here and in the following sections are effectively two–dimensional. The third dimension is obtained by repeating this mesh in the spanwise direction as many times as the discretisation chosen required it over the selected spanwise domain size. All grids considered are of the C-type, and the code used here is able to deal with this topology (see Subsection 4.8.6 for more details on this capability).

In the present study, a total of eight different meshes are used. The first and most used grid, referred to as *Mesh 1* and shown in Figure 8.2a, is made of 320×64 cells with 40 cells located in the wake, 120 cells located on the suction side and 120 cells on the pressure side. Six of the remaining meshes are evolutions of this Mesh 1 and will therefore be described in the following sections as they are being used. The last mesh, referred to as *Mesh 2* and shown in Figure 8.2b, was generated by Dahlström and Davidson [45], to allow all members of the LESFOIL consortium to perform computations on a common grid. It is made of 360×64 cells, 56 of them in the wake and the remaining equally distributed on the pressure side and the suction side, respectively. While Mesh 2 possesses a similar number of cells to Mesh 1, the repartition and shape are slightly different, especially at the domain borders where this mesh is highly non–orthogonal. This later characteristic has a strong negative impact on the convergence of the pressure solver and forced the setting of the over–relaxation coefficient to a value of 1, leading thus to an increase of the number of multi–grid cycles needed per iteration, contributing to a significant increase in the computational cost.

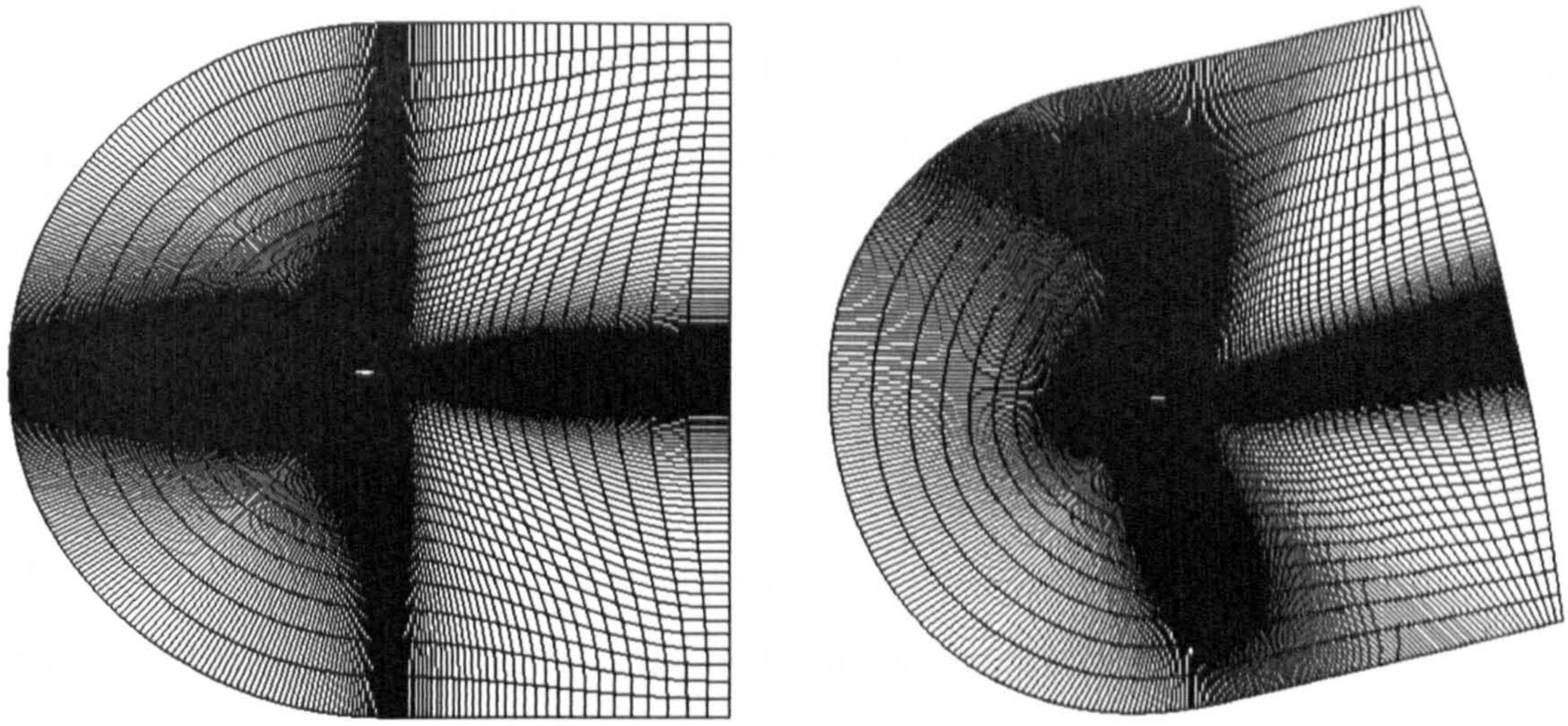

(a) (b)

Figure 8.2: Coarse meshes for the aerofoil. (a): Mesh 1; (b): Mesh 2.

8.3 Preliminary computations

8.3.1 Introducting comments

The present section contains results from a series of computations performed with the aim of gaining insight into the influence of a range of parameters and practices. These include subgrid-scale modelling, the representation of the near-wall region, the extent of the computational box in the spanwise direction, the effect of the grid resolution and the role played by the numerical scheme.

The computational domain is periodic in the spanwise direction. The spanwise extent for the computations presented in this section was 12% of chord, unless otherwise stated. This was deemed to be large enough to ensure spanwise decorrelation. All the computations were started from a potential–flow solution as the initial state and then run over a period corresponding to the time taken by the flow to traverses 5 chords before statistics were collected over a further period corresponding to 5 chords.

8.3.2 Influence of modelling

In this first set of simulations, summarised in Table 8.1, the objective was to evaluate the influence of the outflow boundary condition, the role played by the representation of the near–wall layer and the choice of subgrid–scale model. All computations were performed on Mesh 1 described in Section 8.2 with a spanwise extent of 12% of chord covered by 32 grid planes.

Table 8.2 compares the lift and drag coefficients derived from the simulations, while Figures 8.3 to 8.7 show, respectively, the distribution of the pressure coefficient along the aerofoil, the distribution of the friction coefficient along the suction side of the aerofoil, and four profiles of the streamwise mean velocity, the r.m.s. streamwise velocity fluctuations and the shear stress. Of the four positions considered, three are located along the suction side of the aerofoil, the profiles being along lines in the wall-normal direction. The fourth profile is taken in the wake, along a direction normal to the free–stream velocity.

Table 8.2 shows that both the computed drag and lift coefficients are mostly higher than the corresponding measurements. The pressure coefficient, shown in Figure 8.3, is fairly well reproduced, except at the leading and trailing edges. Figure 8.4 conveys substantial differences among the predicted skin friction values and also relative to the measured value. Transition, which manifests itself by the presence of a sudden dip in the skin-friction curve, is clearly absent in the present computations. Neither is the laminar separation bubble predicted. Most seriously, the separation towards the trailing edge is missed. Consistently, none of the present simulations returns the correct distribution of the mean streamwise velocity (Figure 8.5) and r.m.s. velocity fluctuations (Figure 8.6) at any of the locations considered. The wake is predicted to be much too weak, due to the absence of the upstream recirculation zone. In fact, all these profiles indicate that the predicted boundary layer is far too turbulent upstream of the experimental separation point. Hence, the boundary layer remains attached, and the whole flow is misrepresented at the trailing edge and beyond. An important point to highlight in Figure 8.6 is the excessive level of the fluctuating velocity away from the wall in what should be

the freestream. This is caused by numerical oscillations induced by the combination of the second-order centred scheme and large cells, which then lead to even-odd oscillations, a phenomenon described in Section 2.7. Figure 8.7 shows, however, that the predicted shear stress is not affected by the presence of numerical oscillations, signifying that the oscillations do not mimic cross–correlated fluctuations.

Overall, the simulations presented here are poor and unable to reproduce the experimental behaviour. In addition, any changes in the parameters or practices did not bring about any evident improvement or resulted in trends that could be interpreted as being physically meaningful.

Comp.	Numerical scheme	SGS model	Wall treatment	Outflow boundary
1	CDS	SMA+WD2	NS	zero gradient
2	CDS	SMA+WD2	NS	convective
3	CDS	SMA+WD2	WW	convective
4	CDS	WALE	WW	convective

Table 8.1: Description of the preliminary aerofoil computations: influence of the modelling.

Comp.	C_l	C_d
Exp. - F1	1.56	0.0204
Exp. - F2	1.515	0.0308
1	1.72	0.0348
2	1.682	0.0404
3	1.682	0.0301
4	1.646	0.0506

Table 8.2: Lift and drag coefficients predicted for the preliminary aerofoil computations (see Table 8.1 for a description of the computations).

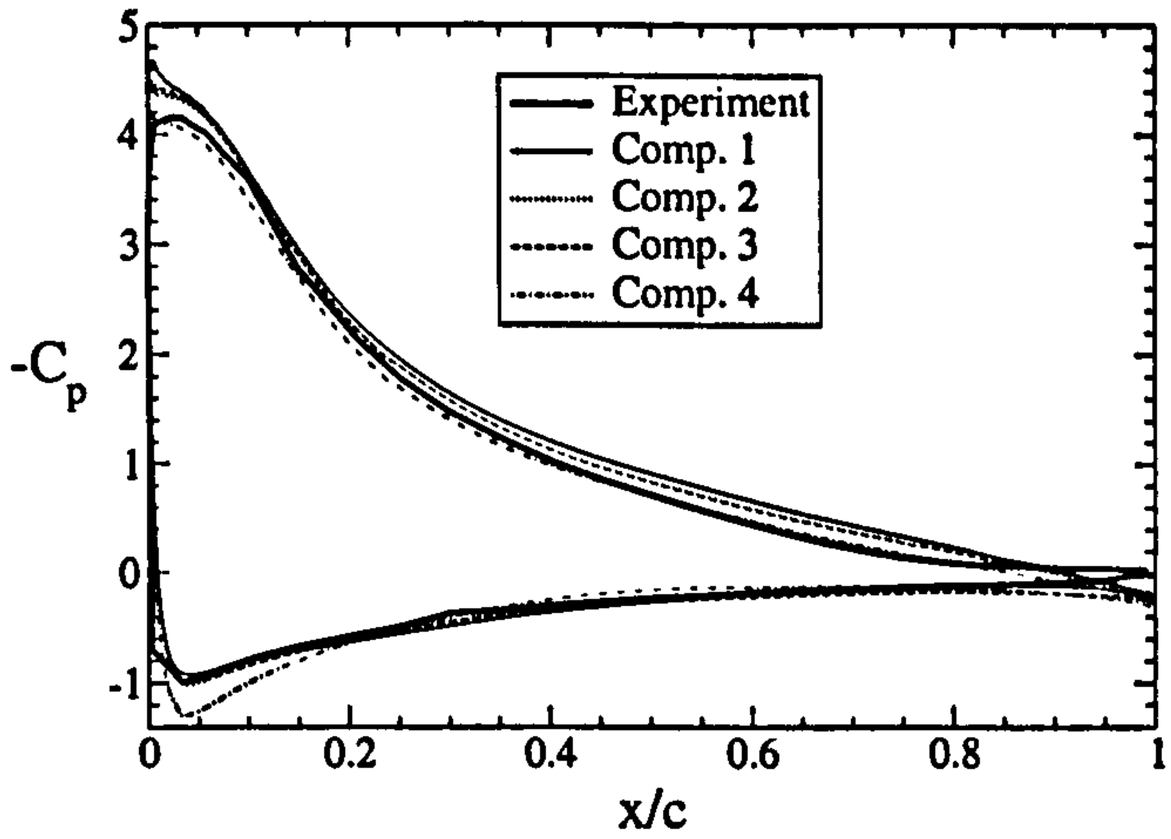

Figure 8.3: Pressure coefficient along the aerofoil for the preliminary computations (see Table 8.1 for a description of the computations).

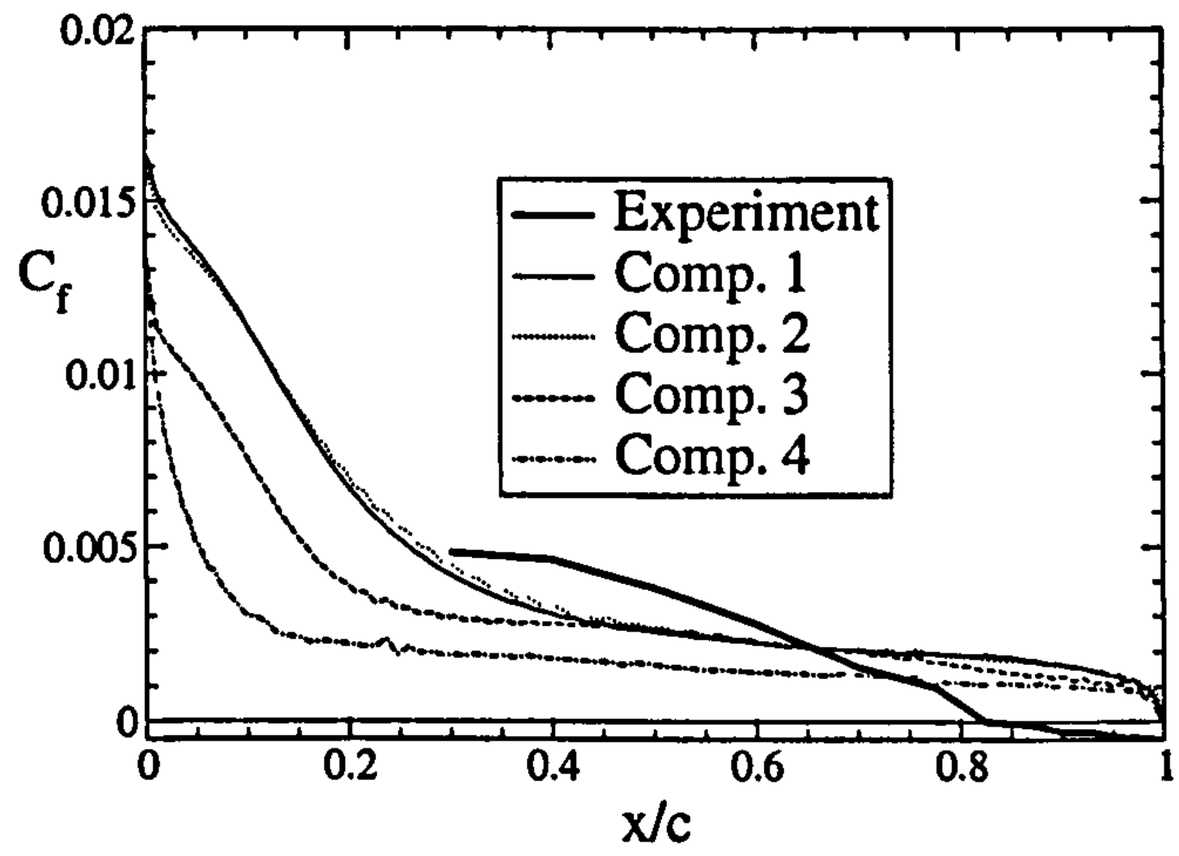

Figure 8.4: Friction coefficient along the aerofoil suction side for the preliminary computations (see Table 8.1 for a description of the computations).

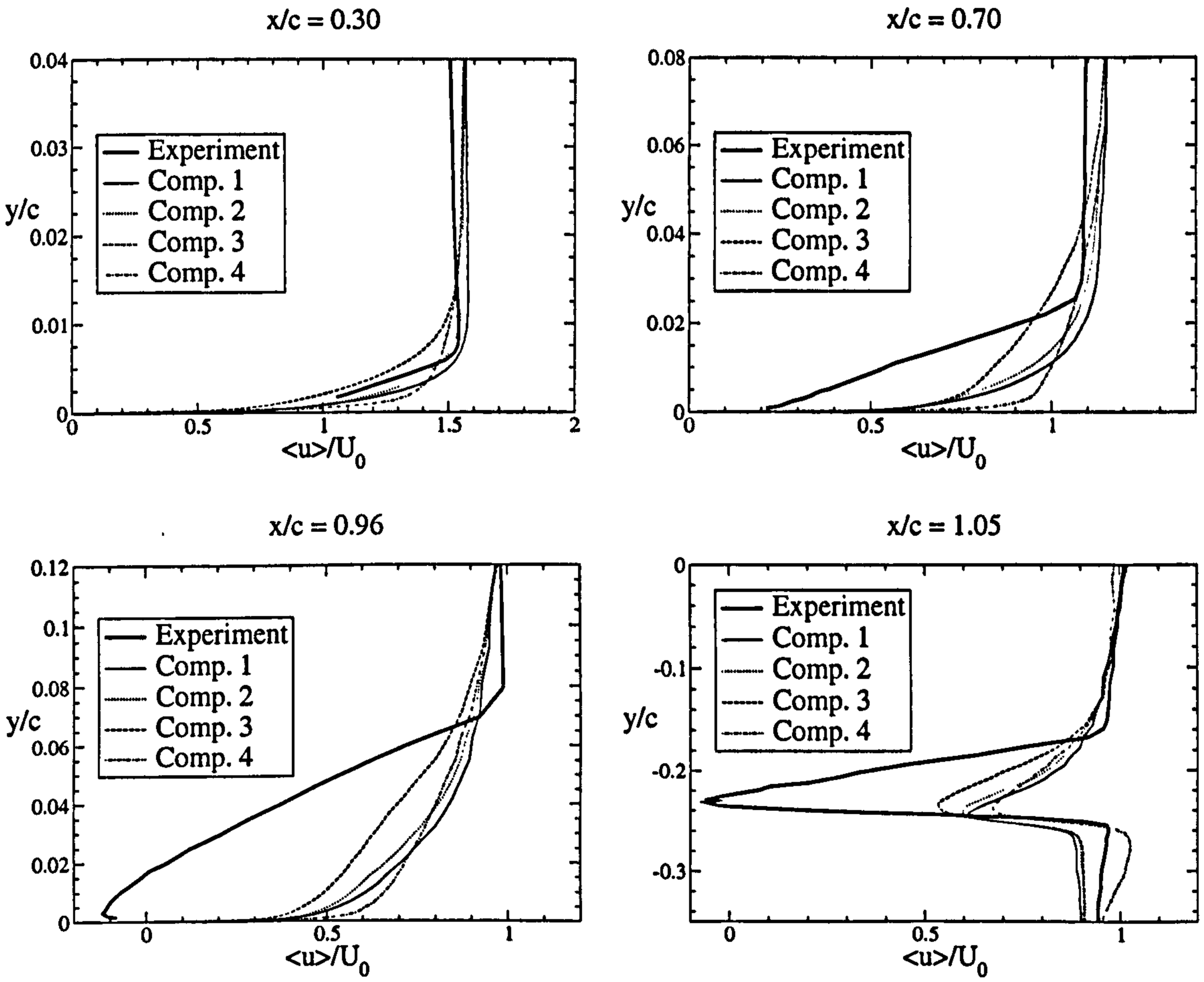

Figure 8.5: Profiles of mean streamwise velocity at four streamwise locations for the preliminary computations (see Table 8.1 for a description of the computations).

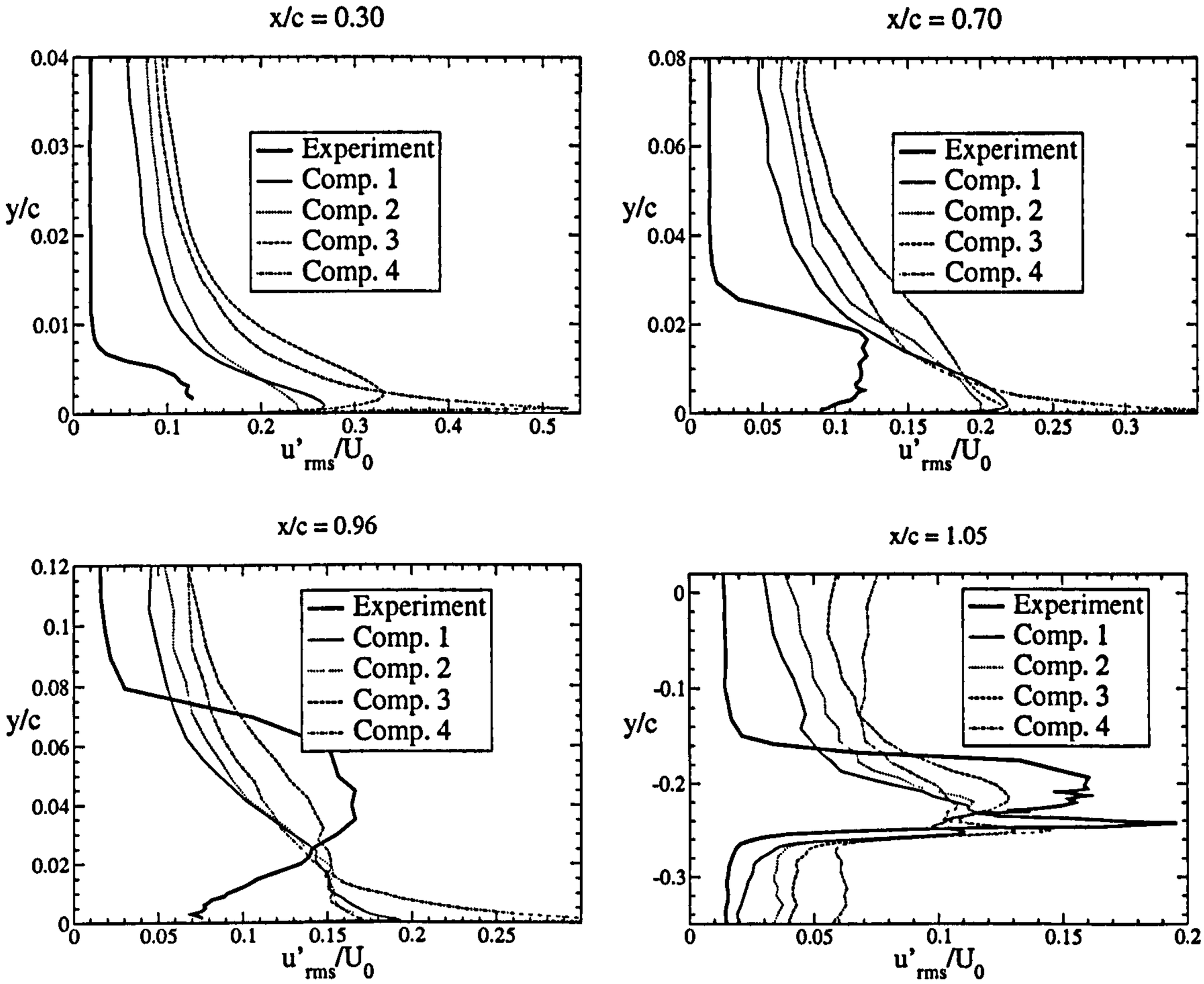

Figure 8.6: Profiles of r.m.s. streamwise turbulence intensity at four streamwise locations for the preliminary computations (see Table 8.1 for a description of the computations).

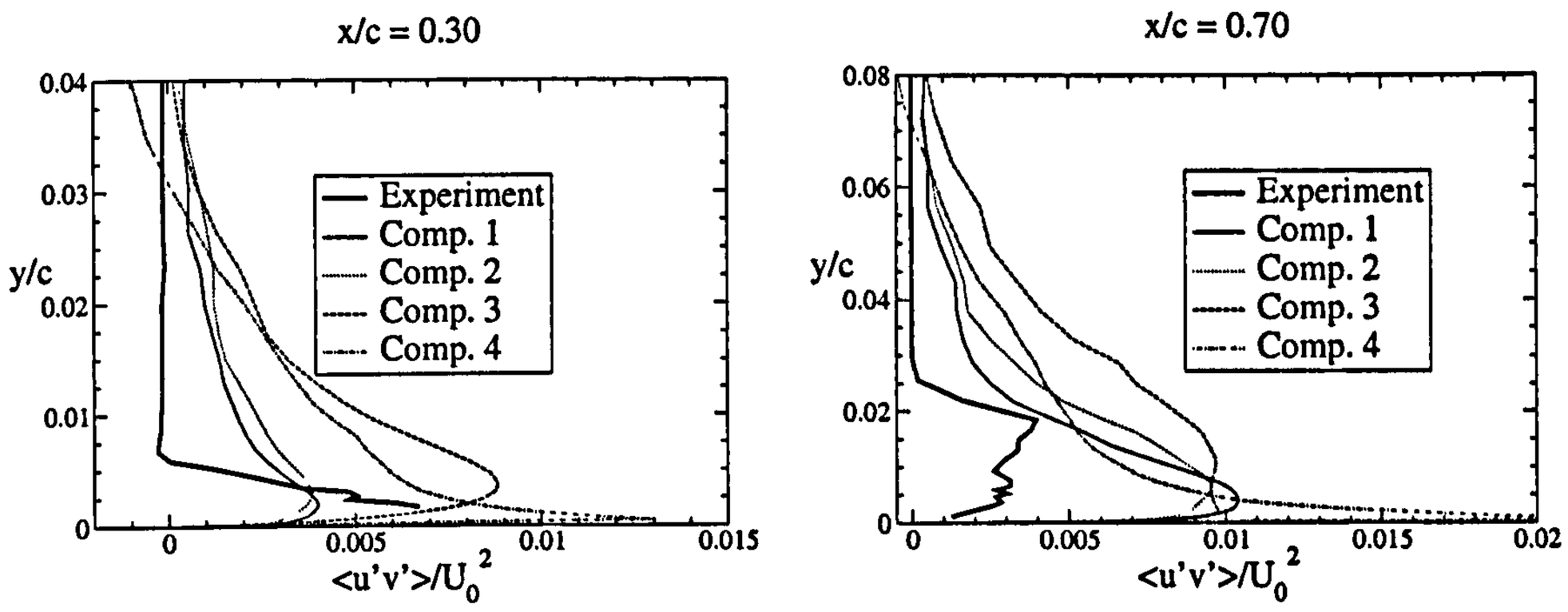

Figure 8.7: Mean shear stress profiles at four streamwise locations for the preliminary computations (see Table 8.1 for a description of the computations).

8.3.3 Effect of the spanwise extent

Previous simulations were performed with a constant spanwise extent of 12% of chord. This was deemed to be the minimum necessary to capture the post-separation, spanwise structures of the flow with any degree of realism. The successful simulation of Mary and Sagaut [142] used a spanwise extent as low as 1.2% of chord. Hence, the influence of the spanwise extent on the solution needs to be examined to determine whether the simulated flow changes drastically as the spanwise extent is reduced.

In this section, four computations, listed in Table 8.3, were performed on Mesh 1 (see Section 8.2 for more details) for spanwise domains of 12%, 6%, 3% and 1.5% of chord, keeping the spanwise resolution invariant, i.e. the spanwise interplane distance. A detrimental consequence of this invariant resolution is that the number of spanwise planes was reduced to four for the smallest spanwise slab. This raises serious doubts about the ability of this particular simulation to capture $3D$ turbulence properly. However, maintaining the spanwise resolution invariant seems to be the appropriate route to take in an exercise directed towards identifying the sensitivity to spanwise box size. It may be argued that the observation of a major dependence of the flow features on the spanwise extent provides, even at this low resolution, an indication that this distance is too low.

As is demonstrated by the results in Figures 8.8 to 8.10, there appears to be a substantial dependence of the predicted flow on the spanwise distance below 6% of chord. This sensitivity must be viewed against the background of no separation being predicted. Had separation been resolved, the sensitivity might have been significantly more pronounced, as the scales of the influential structures rise rapidly with the onset of separation and the detachment of eddies. The simulations also indicate that the tendency towards separation grows as the spanwise extent is reduced to a level at which the simulation becomes almost two-dimensional in nature.

Comp.	Mesh N_z	L_z	Numerical scheme	SGS model	Wall treatment
5	32	$12\%c$	CDS	SMA+WD2	LL3
6	16	$6\%c$	CDS	SMA+WD2	LL3
7	8	$3\%c$	CDS	SMA+WD2	LL3
8	4	$1.5\%c$	CDS	SMA+WD2	LL3

Table 8.3: Description of the computations preformed for different spanwise extents.

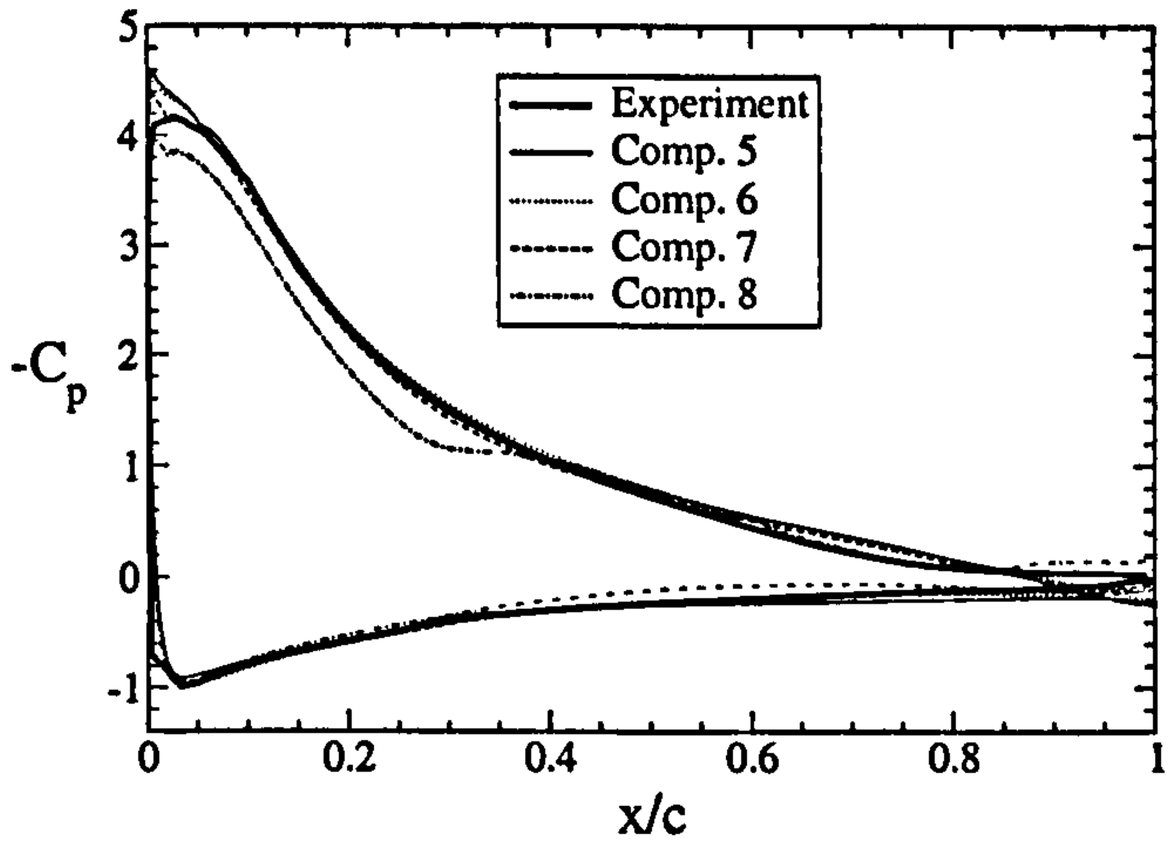

Figure 8.8: Pressure coefficient along the aerofoil for different spanwise box sizes (see Table 8.3 for a description of the computational parameters).

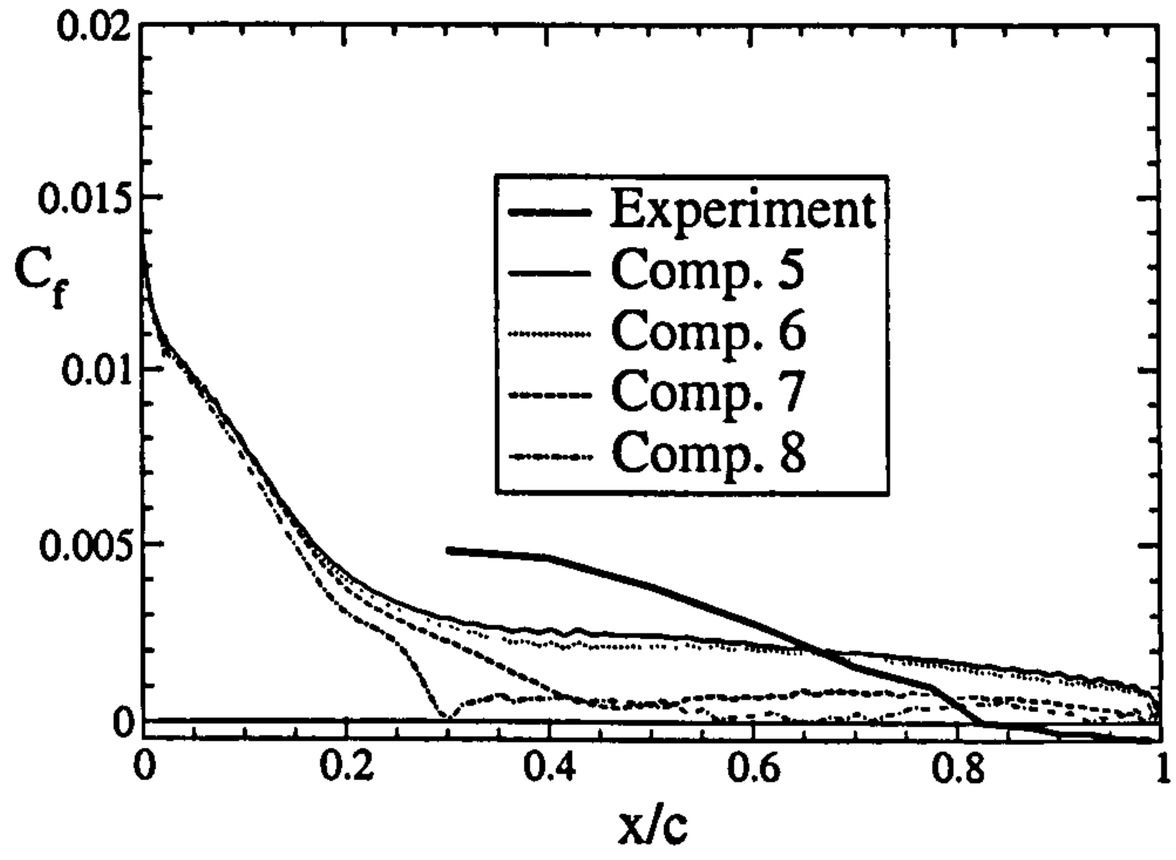

Figure 8.9: Friction coefficient along the aerofoil suction side for different spanwise box sizes (see Table 8.3 for a description of the computational parameters).

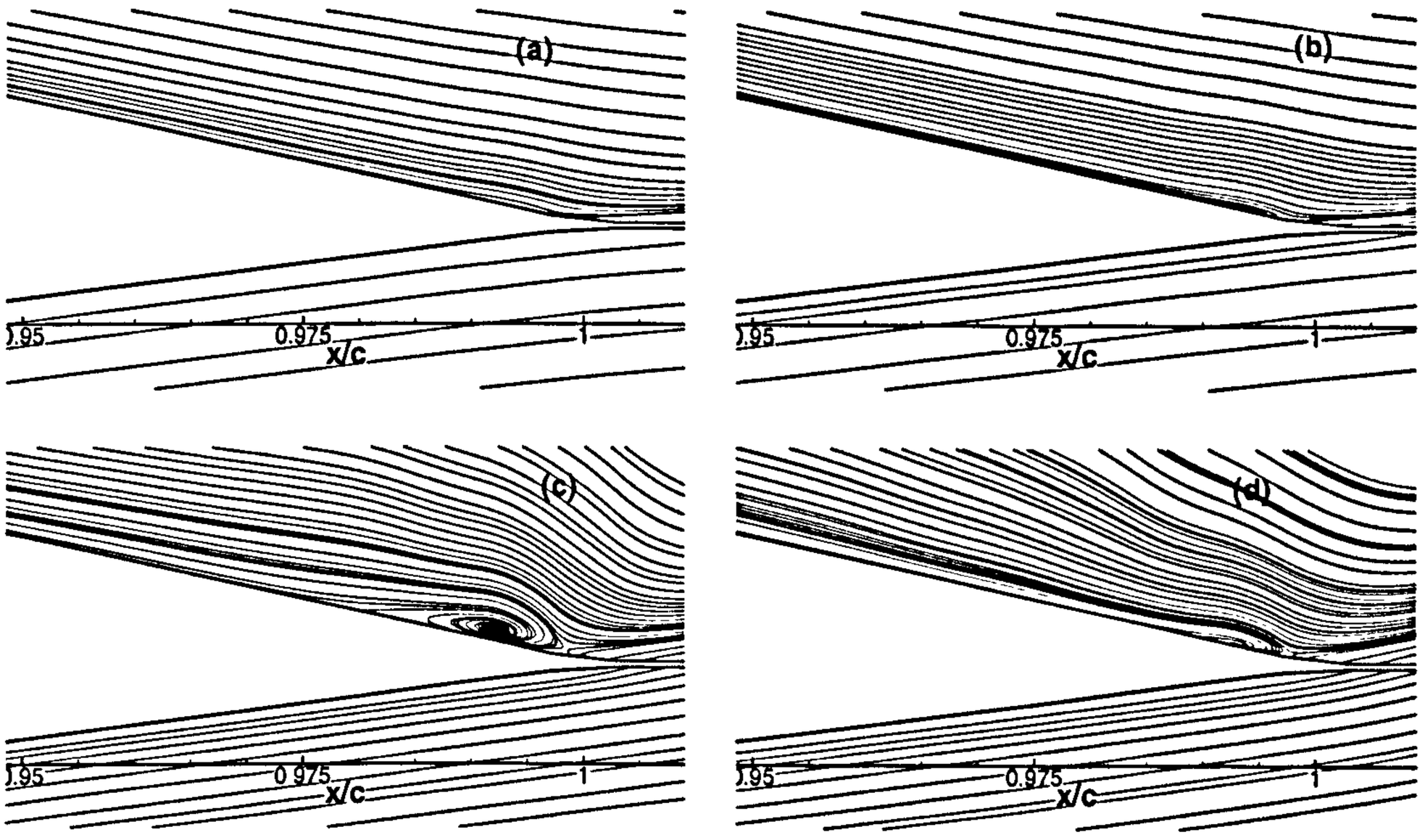

Figure 8.10: Mean streamlines at the trailing edge for the four different spanwise box sizes: $L_z = 12\%\,c$ (a); $L_z = 6\%\,c$ (b); $L_z = 3\%\,c$ (c); $L_z = 1.5\%\,c$ (d) (see Table 8.3 for a description of the computational parameters).

8.3.4 Influence of the mesh density

The computations presented so far were all performed on Mesh 1, shown in Figure 8.2a and containing 320×64. In this section, all computations but one use selective refinements of this mesh. Table 8.4 summarises the computational details of the simulations. The mesh used in computation 13 is Mesh 2 described in Section 8.2 and shown in Figure 8.2b. Table 8.5 gives the maximum cell sizes in all three dimensions, expressed in wall units, while Figure 8.11 shows the variation of the near-wall cell dimensions along the aerofoil suction side, expressed in wall units.

In previous computations, it was noted that the use of central differencing gave rise to numerical oscillations. These manifested themselves in pseudo–turbulent normal stresses (but not shear stress) outside the boundary layer. The severity of these oscillations greatly depends on the grid density, with the normal–to–surface density being especially influential. Figure 8.12 illustrates this by way of instantaneous streamwise velocity on the grids investigated and noted in Table 8.4. The lowest level of oscillations arose from computations 10 and 12, both containing 128 wall-normal grid lines.

Results for pressure coefficient, skin-friction coefficient, velocity and the r.m.s. of the streamwise velocity fluctuation are given in Figures 8.13 to 8.16, respectively, while Table 8.6 provides additional data for the lift and drag coefficients in comparison with the experimental data from both wind–tunnels F1 and F2. As seen from Figure 8.16, all five grids mimic *numerical turbulence* (albeit uncorrelated) outside the boundary layer. The lowest level tends to be produced by the grids with the highest wall-normal density, at least upstream of $x/c = 0.7$, and this is consistent with the behaviour displayed in Figure 8.12. The densest grid, used in computation 12, gives the lowest r.m.s. level outside the boundary layer throughout the flow domain. Moreover, only the meshes with the highest wall-normal resolution, 128 lines, show evidence of transition around $x/c = 0.2–0.3$. The results for computation 13 are included in Figure 8.13 to 8.16 and Table 8.6, and this did not yield better results than the others.

It is thus evident from the above figures that none of the simulations comes close

to giving a satisfactory representation of either the mean flow or the turbulence field. In particular, Figure 8.15 shows that all simulations fail to predict separation, although there is a gradual approach towards the experimental behaviour as the grid is refined, especially in the wall-normal direction. The lift coefficient is rather insensitive to the state of the boundary layer, in contrast to the drag coefficient, the value of which depends primarily on the skin friction as well as on the structure of the turbulent layer on the suction side. There is no systematic relationship between the predicted value of this coefficient and the grid, and the fairly close agreement achieved with computations 3 and 9, depending upon whether experiment F1 or F2 is used as the basis for comparison, is fortuitous.

The trends displayed by the various grids provide some indications that an appropriate resolution might be achieved with a grid of order $1200 \times 240 \times 120 \approx 35 \times 10^6$ nodes. The simulations also point to the impossibility of investigating here, with any degree of confidence, the effectiveness of alternative SGS models or near-wall treatment, except in terms of indicating sensitivity in a qualitative sense.

Comp.	$N_x \times N_y$	Mesh N_z	L_z	Numerical scheme	SGS model	Wall treatment
9	576×64	32	$12\,\%\,c$	CDS	SMA+WD2	WW
10	320×128	32	$12\,\%\,c$	CDS	SMA+WD2	WW
11	Mesh 1	64	$12\,\%\,c$	CDS	SMA+WD2	WW
12	768×128	64	$12\,\%\,c$	CDS	SMA+WD2	WW
13	Mesh 2	32	$12\,\%\,c$	CDS	SMA+WD2	WW

Table 8.4: Description of the computations performed for different grid resolutions.

Comp.	$max(\Delta x^+)_{ss}$	$max(\Delta y^+)_{ss}$	$max(\Delta z^+)_{ss}$
3	999	41.2	613
9	525	45.7	676
10	1335	27.0	803
11	1075	43.5	321
12	518	26.8	400
13	1003	42.5	619

Table 8.5: Maximum cell size (in wall units) for Comp. 3 and 9 to 13 (SS = suction side) (see Table 8.4 for a description of the computations).

Comp.	C_l	C_d
Exp. - F1	1.56	0.0204
Exp. - F2	1.515	0.0308
9	1.755	0.0189
10	1.475	0.0383
11	1.550	0.0646
12	1.553	0.0437
13	1.64	0.0429

Table 8.6: Lift and drag coefficients predicted for different grid densities (see Table 8.4 for a description of the computations).

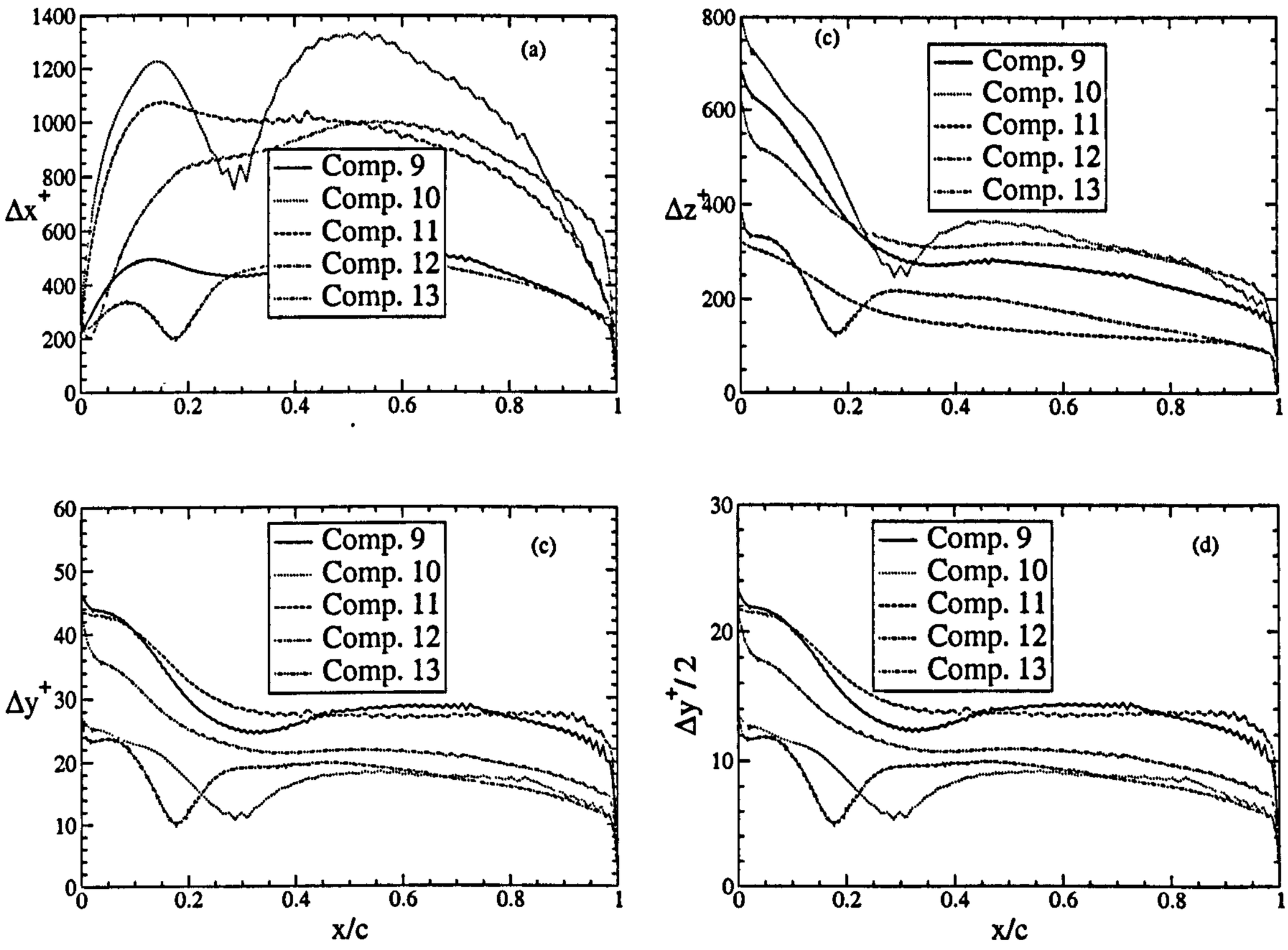

Figure 8.11: Size of the first cell along the suction side of the aerofoil expressed in wall units: (a) streamwise dimension; (b) spanwise dimension; (c) wall-normal dimension; (d) location of the first cell-centre in the wall-normal direction (see Table 8.4 for a description of the computations).

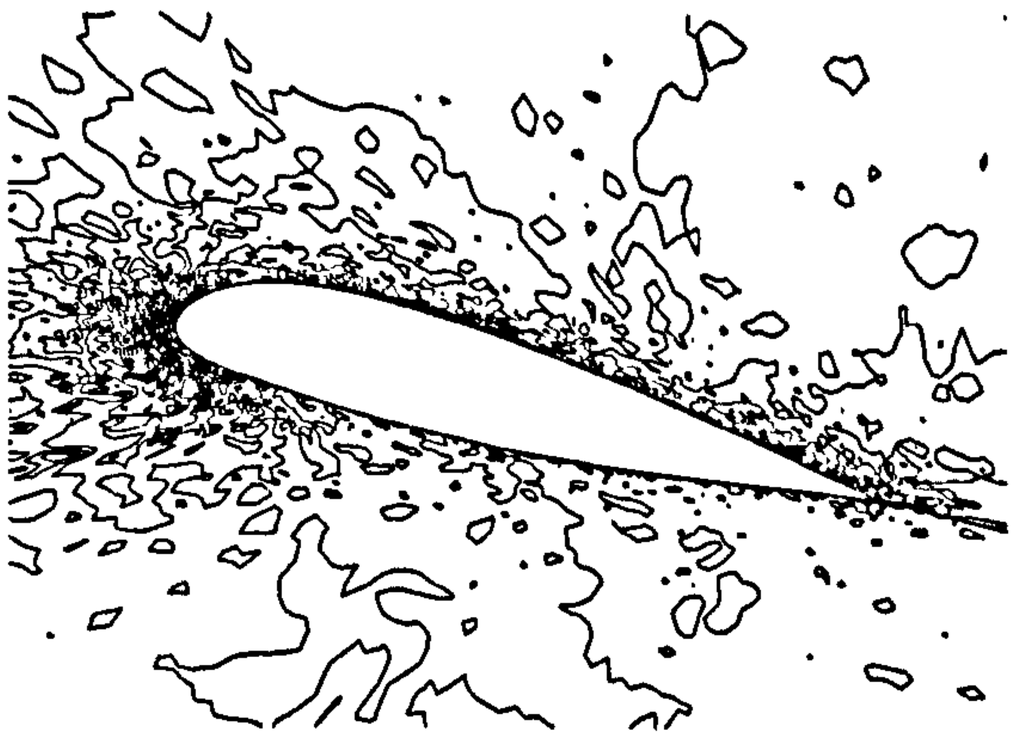

Comp. 3

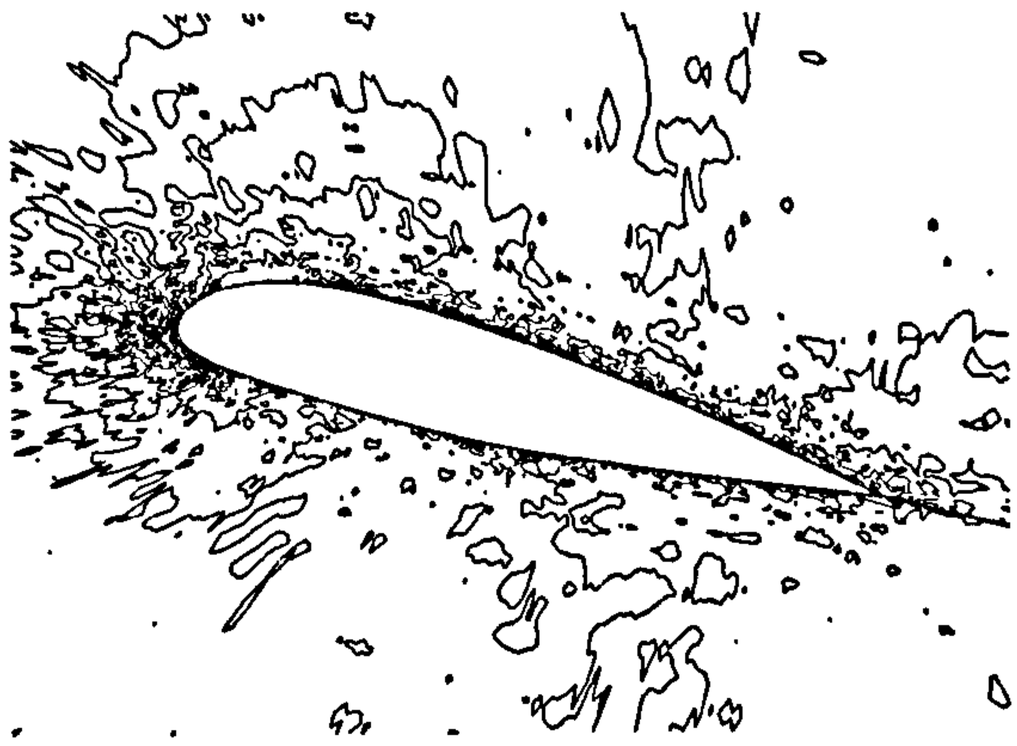

Comp. 9

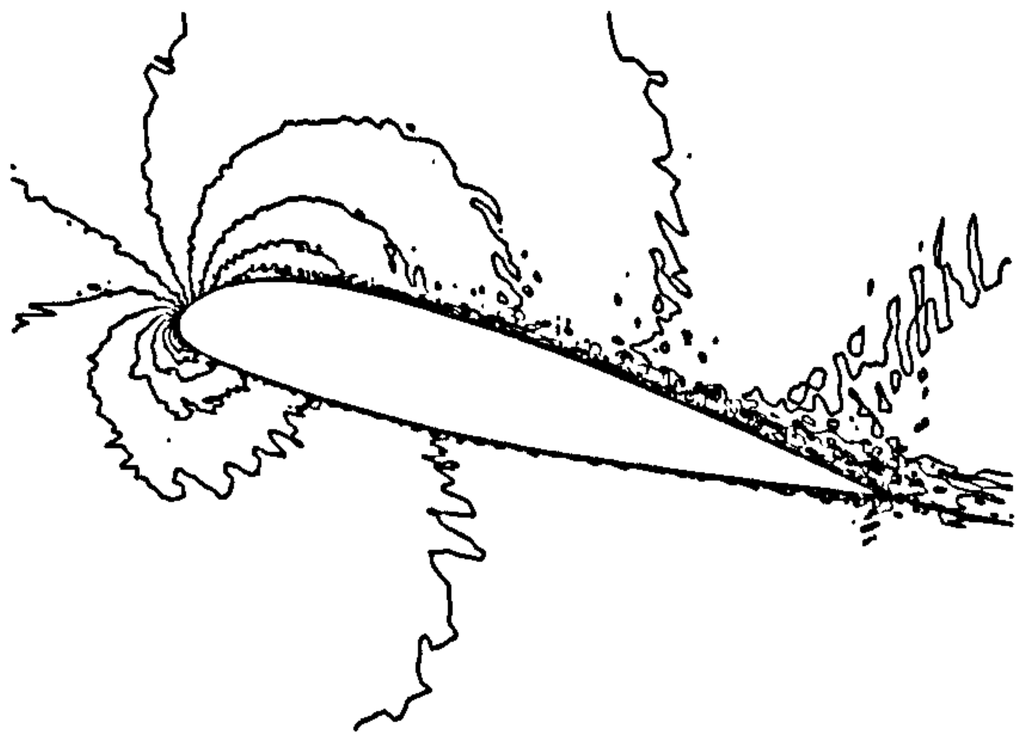

Comp. 10

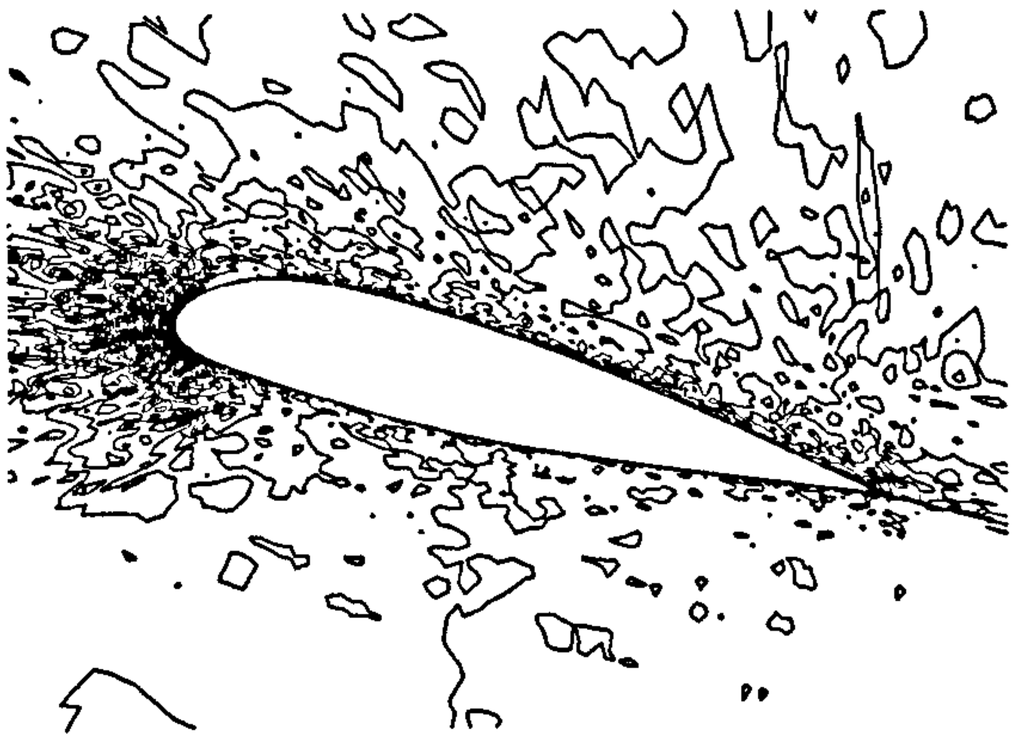

Comp. 11

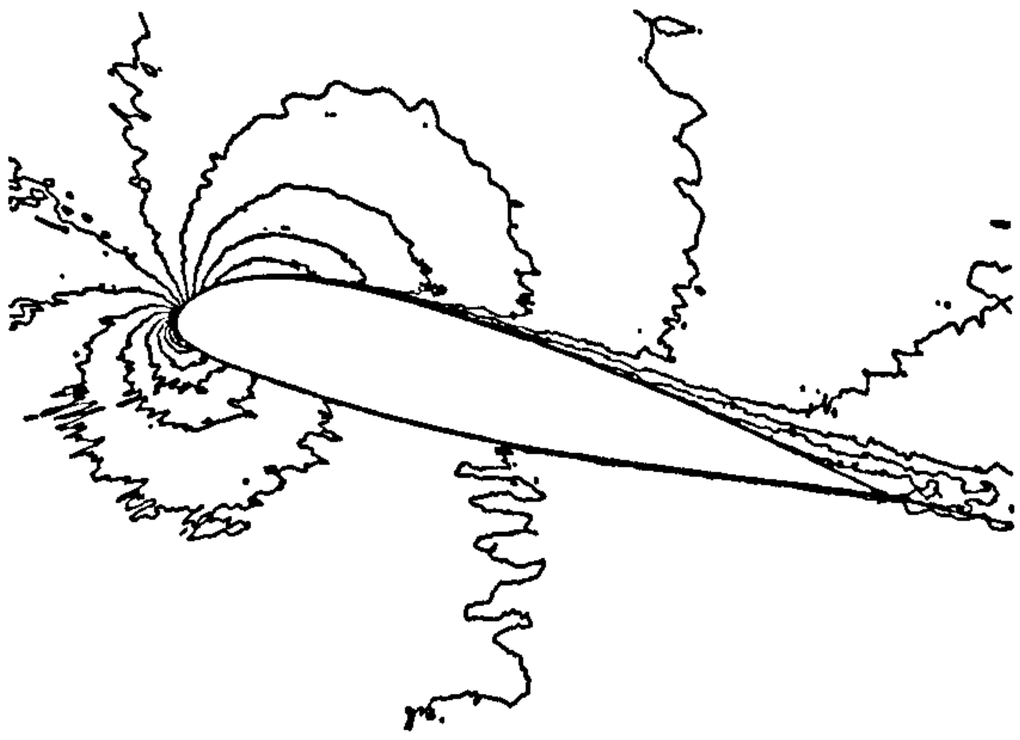

Comp. 12

Figure 8.12: Instantaneous streamwise velocity fields for five different grids (see Table 8.4 for a description of the computations).

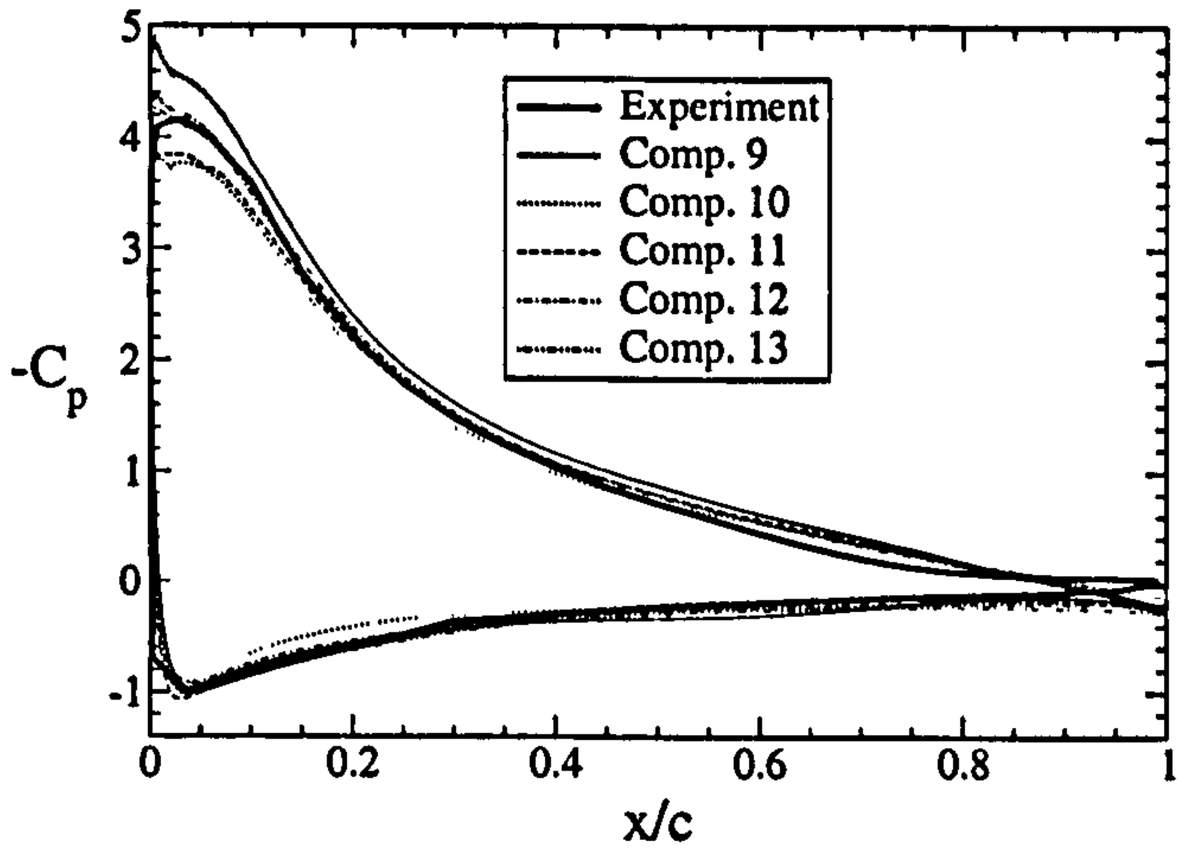

Figure 8.13: Pressure coefficient along the aerofoil for five different grids (see Table 8.4 for a description of the computations).

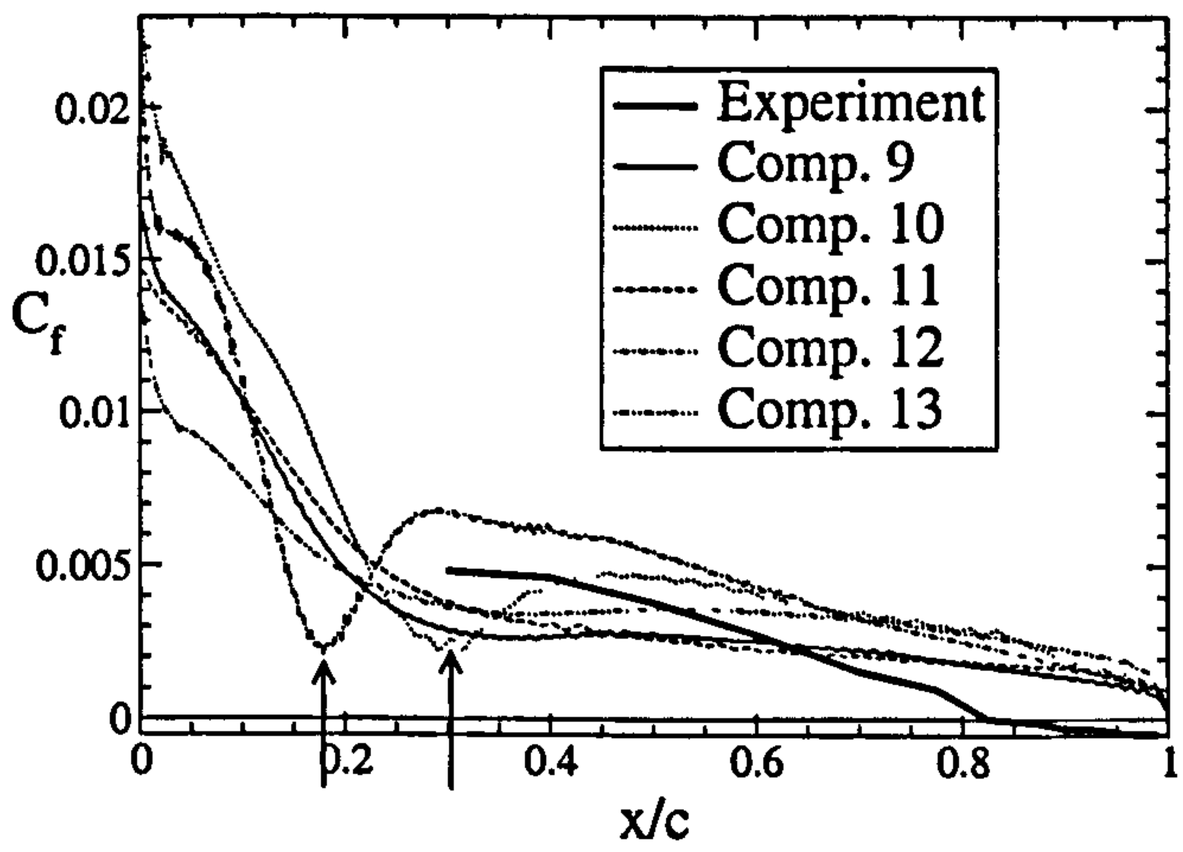

Figure 8.14: Skin friction coefficient along the aerofoil suction side for five different grids. The arrows indicate locations where transition is predicted to occur (see Table 8.4 for a description of the computations).

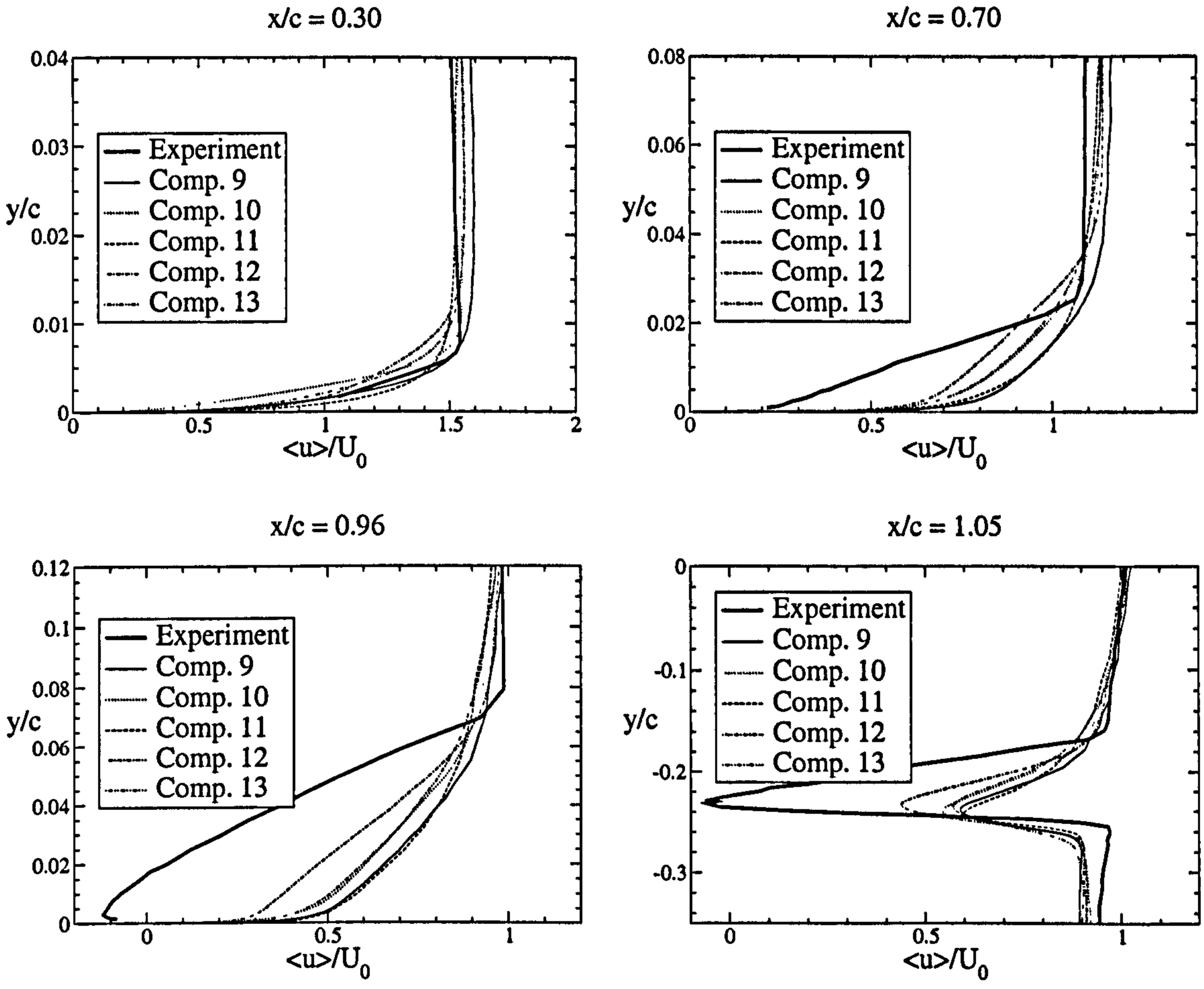

Figure 8.15: Profiles of mean streamwise velocity at four different locations for five different grids (see Table 8.4 for a description of the computations).

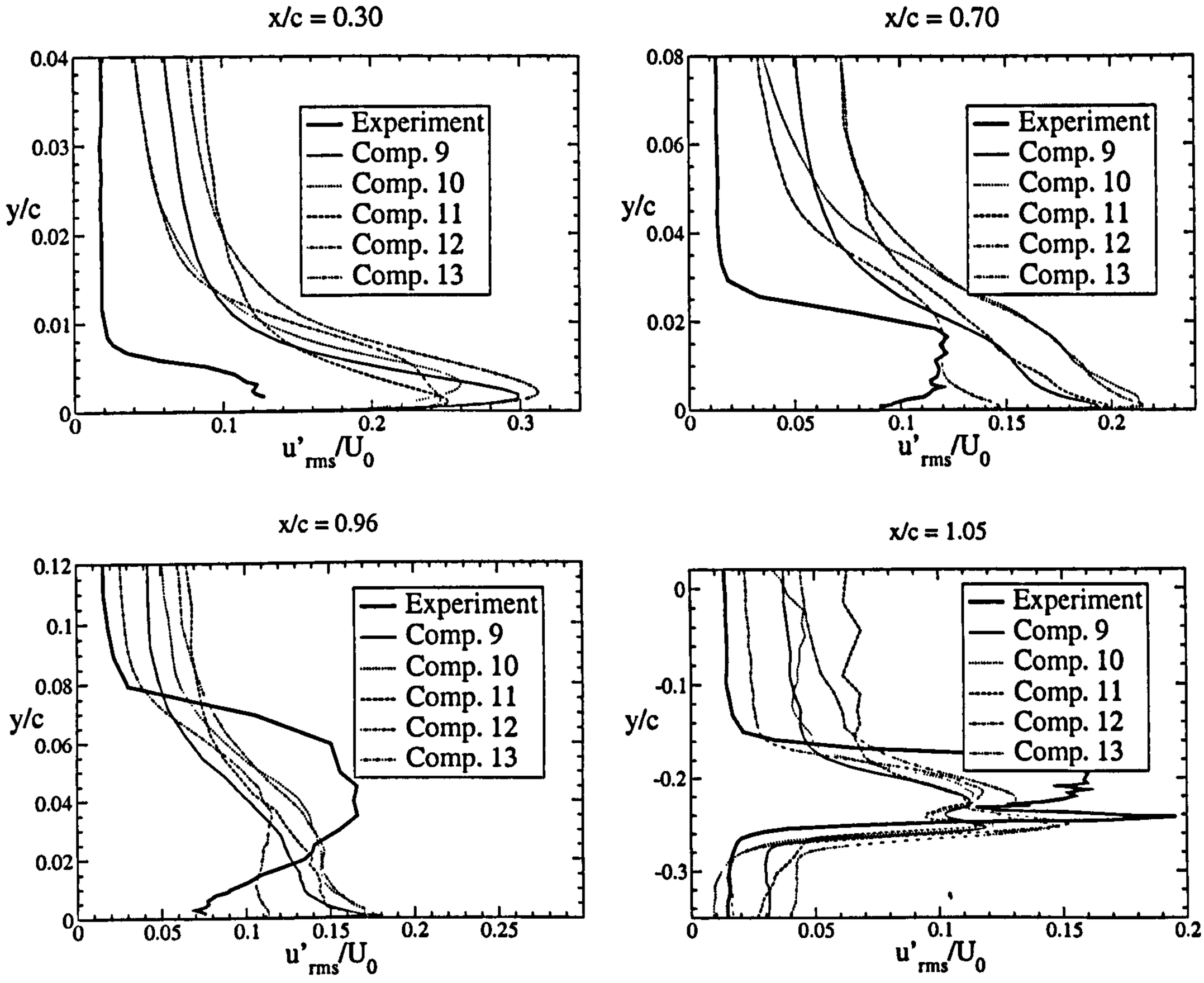

Figure 8.16: Profiles of r.m.s streamwise velocity fluctuations at four different locations for five different grids (see Table 8.4 for a description of the computations).

8.3.5 Influence of the numerical scheme and oscillation control

This section describes attempts made to control the numerical oscillations outside the boundary layer by blending central differencing in the near-wall region with second-order upwinding in the irrotational outer region. This practice has also been investigated by others for the present flow (see Dahlström and Davidson [43], Mellen et al [149], Mary and Sagaut [142]).

Blending was effected here through:

$$\phi = \beta \times \phi_{CDS} + (1 - \beta) \times \phi_{UPWIND} \tag{8.1}$$

where β is selected to lie between 0 and 1 and ϕ represents the convected variable. Evidently, $\beta = 1$ gives the fully centred scheme (CDS), while $\beta = 0$ gives the upwind scheme (UPWIND). Two alternative practices were tested:

- Blending 1: the β coefficient value is controlled by the local Reynolds number $Re_l = u\Delta x/\nu$:

$$\begin{cases} Re_l \leq 10 & \Longrightarrow \beta = 0 \\ 10 < Re_l \leq 30 & \Longrightarrow \beta = Re_l/20 - 0.5 \\ Re_l > 30 & \Longrightarrow \beta = 1 \end{cases} \tag{8.2}$$

- Blending 2: β is a function of the geometric coordinates, as illustrated in Figure 8.17.

The simulations discussed here are summarised in Table 8.7. They were all performed on Mesh 1 (see Section 8.2) for a spanwise extent of 12% of chord, discretised by 32 cells. As illustrated by Figures 8.18 and 8.19, the two blending practices give very different results. Reynolds-number-based blending results in massive separation due to a failure to trigger turbulence, a behaviour similar to that observed by use of second-order upwinding throughout the domain as seen in Figure 8.20. In contrast, geometric blending is considerably better in terms of predictive realism,

but fails, as is evident from Figure 8.17, to eliminate the oscillatory behaviour in the outer irrotational region. It alleviates it, however.

Overall, the introduction of artificial damping via upwinding cannot be regarded as a tenable practical approach, at least in the form attempted here. While it does have a stabilising effect on the computation, detrimental effects are difficult to avoid, and the precise details of the blending practice can strongly influence the physical realism of the solution. In addition, oscillations in the shear layer, from which damping is excluded, may be hidden by physical turbulence.

Mixing central and second-order upwind differencing, in a weighted–average sense, across the whole solution domain was found to be very effective, even with a 95%/5% relative weighting, but poses uncertainty in respect of numerical damping of turbulence in the shear layer. A more appropriate approach might be the use of a *wiggle detector*, such as that implemented by Mary and Sagaut [142]. This would remove the arbitrariness of the present approach. However, a problem is here that the distinction between numerical wiggles and turbulent fluctuations is not clear. Whatever scheme is adopted, artificial dissipation is likely to remain a problem, and the only realistic solution is to substantially increase the grid density.

Comp.	Numerical scheme	SGS model	Wall treatment
14	Blending 1	SMA+WD2	WW
15	Blending 2	SMA+WD2	WW
16	Upwind	SMA+WD2	WW

Table 8.7: Description of the computations performed for the different blending practices

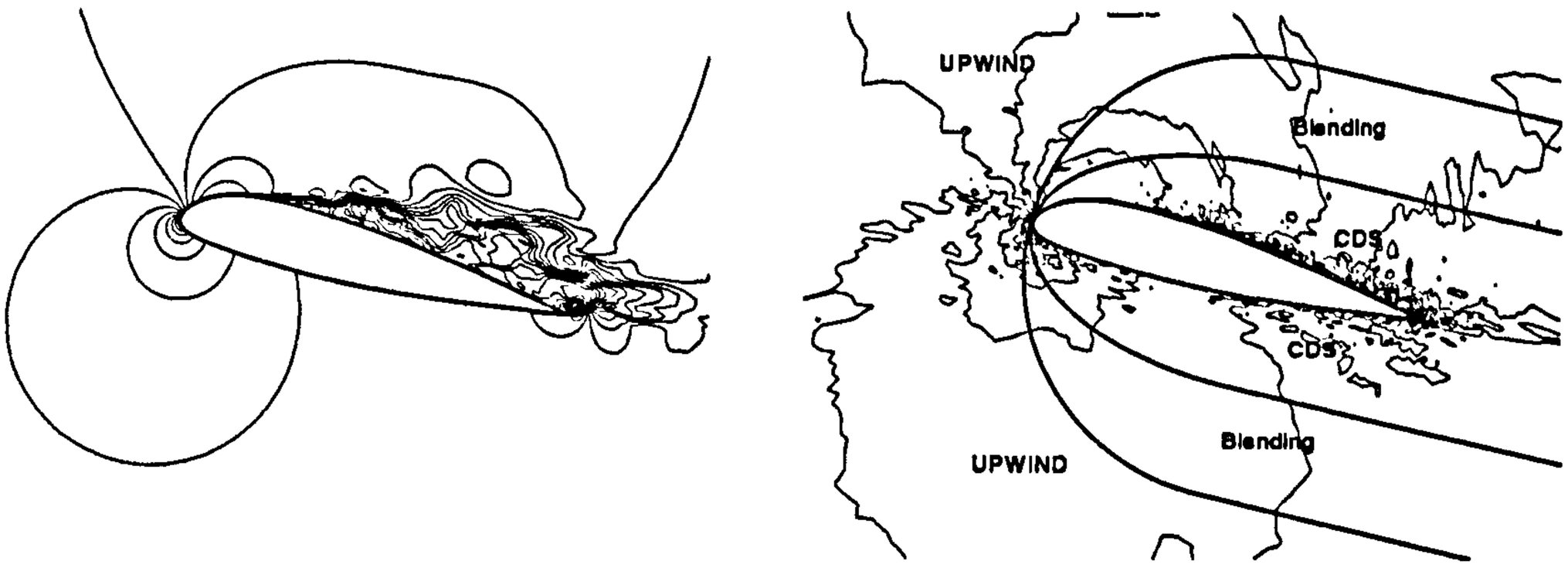

Figure 8.17: Instantaneous streamwise velocity contours around the A-aerofoil for Blending 1 (left) and Blending 2 (right) (see Table 8.7 for a description of the computations).

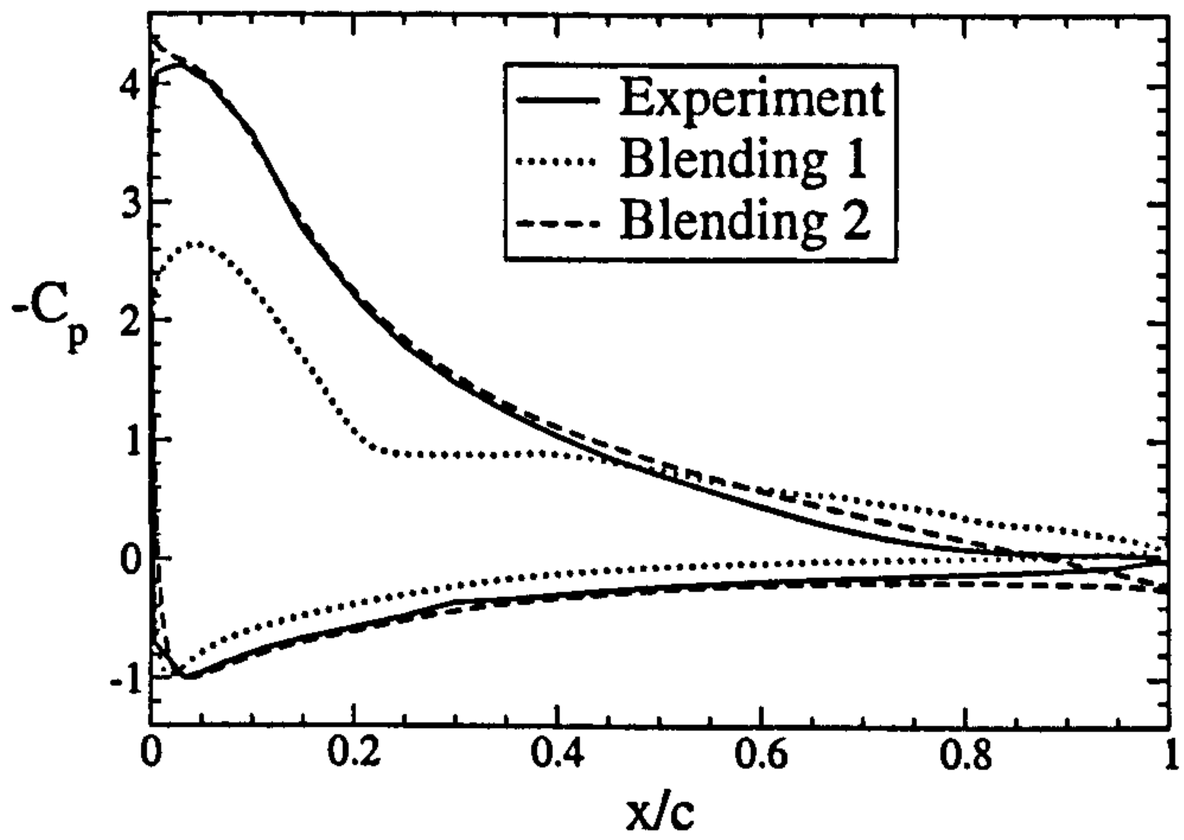

Figure 8.18: Pressure coefficient obtained with two different blending practices (see Table 8.7 for a description of the computations).

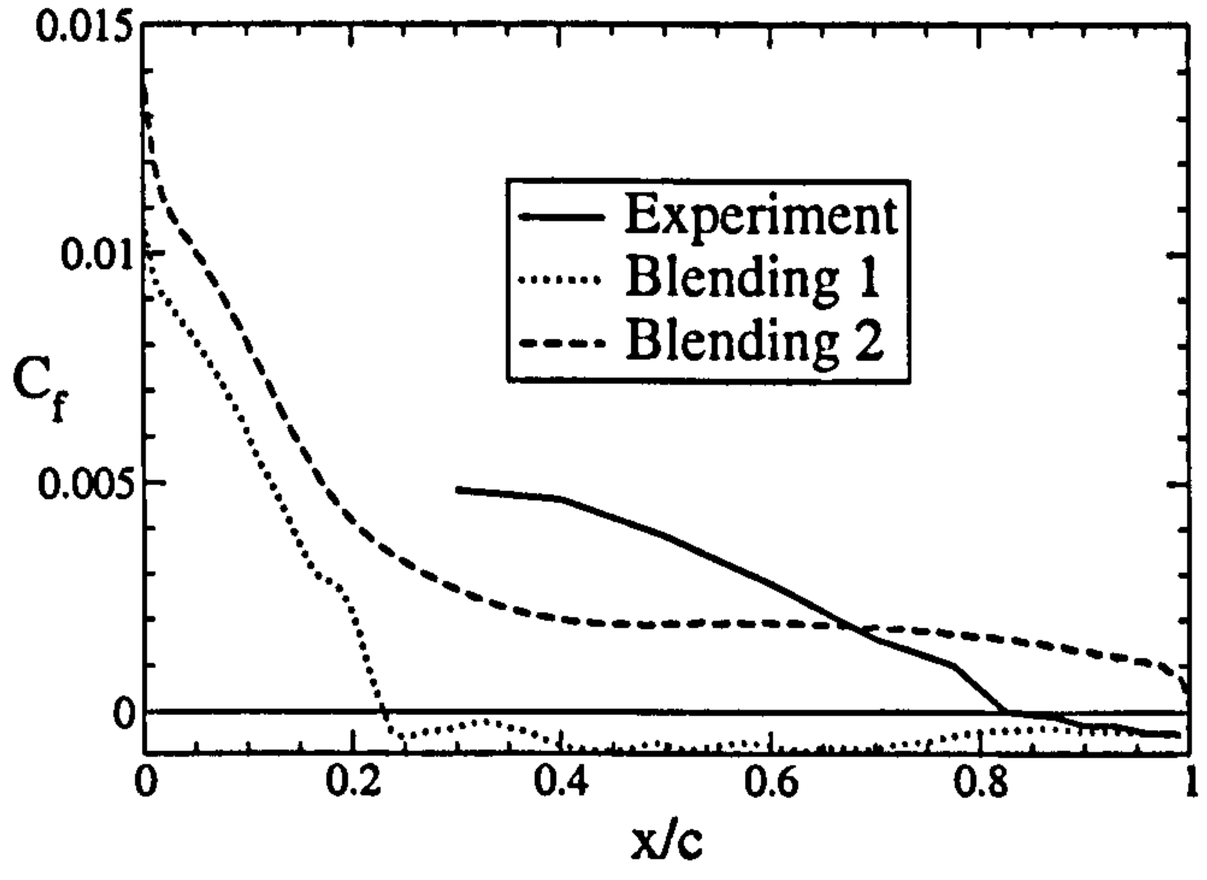

Figure 8.19: Friction coefficient obtained with two different blending functions (see Table 8.7 for a description of the computations).

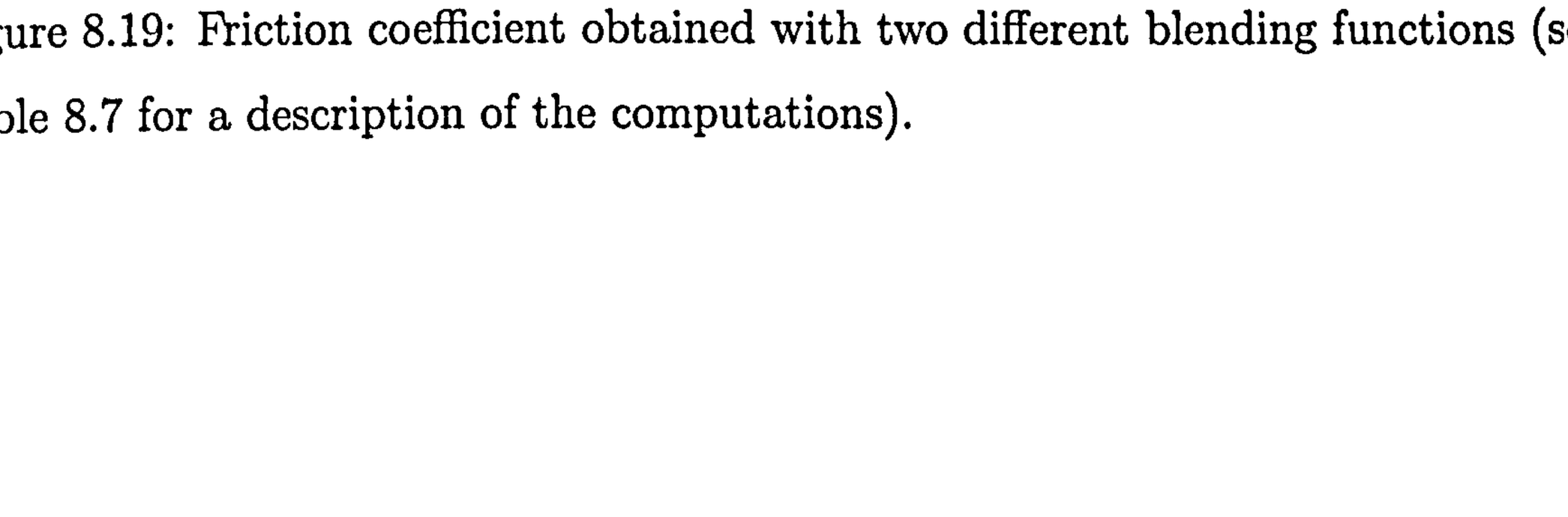

Figure 8.20: Instantaneous streamwise velocity contours around the A-aerofoil for the central scheme (left) and the upwind scheme (right) (see Table 8.7 for a description of the computations).

8.4 Final aerofoil computations

Section 8.3 described the role played by a range of numerical issues on the results for the A-aerofoil. Among these, the most influential were the grid and the ability to control numerical oscillations. In addition, the role played by the spanwise extent was also shown to be important. Indications were provided that a spanwise extent of 6% of chord was sufficient to allow the $3D$ nature of turbulence to be properly represented. This observation is of considerable importance in term of computational economy if finer grids are to be used to achieve better resolution as is done in the final part of the aerofoil study.

Three additional computations, performed on successively denser meshes over a spanwise distance of 6% of chord, are presented in this section. Table 8.8 provides details of the number of cells involved. The columns headed N_{wake}, N_{SS} and N_{PS} give the number of cells which cover the length of the wake region, the suction side and the pressure side, respectively. Figures 8.21 to 8.26 show the meshes around the whole profile and give magnified views of the cell distributions around the leading and trailing edges. All these meshes are evolutions of Mesh 1 described in Section 8.2. In computation 17, the cell number has been doubled in the streamwise and spanwise directions, while in the wall–normal direction, the number was increased by 50%. The distribution was chosen so as to achieve a nearly wall–resolving mesh. Computation 18 uses twice as many nodes as computation 17, the increases arising from the addition of lines in the streamwise direction. Essentially, each cell in computation 17 is replaced by 2.5 cells. The wall–normal distribution was not modified, however. In the wake, the cell distribution was adapted to maintain a gentle variation of the cell sizes in the trailing edge region. In the mesh used in computation 19, the number of cells in the wake has been doubled. In the wall–normal direction, there are 33% more nodes, distributed in a similar manner to that of computation 18. No changes were made in the spanwise direction. In the streamwise direction, the discretisation is organised as follows: 1904 cells are located on the suction side of the aerofoil, nearly four times the number used in computation 18; 560 cells are distributed along the pressure side, this distribution is very similar to that of com-

putation 18. The above choice is justified by two arguments. First, the successful computation of Mary and Sagaut [142] use a similar streamwise cell distribution. Second, the computations performed in Subsection 7.4.2 for the periodic hill on various grids indicated an especially high sensitivity to streamwise discretisation for the prediction of separation. Last, the boundary layer on the pressure side remains laminar due to a favourable pressure gradient as demonstrated by Weber et al [233] and Mary and Sagaut [142], so only requires moderate discretisation.

Figure 8.27 provides information on the cell dimensions, expressed in wall units, in the layer adjoining the suction side. Figure 8.27d indicates that all computations, while not fully wall–resolving, are not very far from it with $\Delta y^+/2 \approx 5$ (i.e. the first computational node is located at $y^+ \approx 5$). In the spanwise direction, cell sizes are of the order of 100 wall–units for all three computations. This is three to four times larger than usually used for a wall–resolved LES in a channel flow, say. The streamwise cell dimensions are below 800 for computation 17, below 400 for computation 18 and around 50 wall units for computation 19, the last figure being regarded as adequate in channel–flow computations.

Table 8.9 contains details of the computational parameters. All computations started from a potential–flow solution. Computations 17 and 18 ran over a period corresponding to 5 chords before statistics were recorded for a further 2 chords. Although some computations recorded in reference [45] used as little as 2.5 chords prior to starting the collection of statistics, the present choice is regarded as a safer option as it gives more time for the flow to reach a developed state. The averaging period could have been longer, and would have resulted in smoother profiles. However, these computations were extremely costly, and economy was again the limiting factor. The computations were run on a Origin 3000 parallel computer instead of the previously used Cray T3E. The speed gain resulting from this switch of machines was of the order 4 to 5.5, depending on the size of the problem considered and the partitioning used. Estimates of the computational cost are given in Table 8.9. For obvious reasons, the cost increases with the mesh density. Typically, 100000 iterations were necessary to advance the flow in time over one chord, at $CFL \approx 0.03$. The limitation in the time–step results from the use of the Adams-Bashfort time–

marching scheme. A switch to a Runge-Kutta schemes could have allowed the use of significantly higher time–steps of $O(10^{-4})$, instead of $O(10^{-5})$ with a computational cost increase per step of the order of $2-3$, eventually leading to a significant reduction in the global computational cost of the simulations.

The use of denser and denser meshes necessitated a reduction in the convergence criterion for the pressure solver (see Subsection 4.6.3 for the definition of this criterion). This had to be set to values of order 10^{-15} in the present computations compared to 10^{-9} for computation 3, i.e., individual cell residuals were close to the zero machine. This then resulted in a significant further increase in the computational cost as the number of multigrid cycles required per iteration increased.

Control and suppression of numerical oscillations was achieved by the use of a zonal approach. Figure 8.28 illustrates how this was implemented in computation 19. From the aerofoil surface and up to a wall–normal distance of approximately 0.5 c, central differencing was used. Further away, where the flow is essentially irrotational, a second–order upwind scheme was used to introduce numerical dissipation to prevent contamination of the solution by unphysical wiggles resulting from the presence, in these regions, of high–aspect–ratio cells. A similar zonal approach was previously used in computations 17 and 18.

Statistical results for the first two computations are presented in Table 8.10 and Figures 8.30 to 8.35. Statistical data for computation 19 are not included, except in one plot, because the duration of the averaging period and the time at which it was started were inadequate to obtain converged data. However, some instantaneous visualisations for this computation will be shown as they permit some useful observations to be made.

Table 8.10 compares the lift and drag coefficients. The lift coefficient predicted by computations 17 and 18 agree broadly with the experiments, while the drag is wrongly predicted. Figure 8.29 shows instantaneous streamlines around the trailing edge for computation 19. While a large separation bubble is clearly absent, the flow features small recirculating bubbles along the wall. Figure 8.30 shows the distribution of pressure coefficient distribution along the aerofoil. Computations 17 and 18 agree reasonably well with the experiment data, except, as in the previous

cases, at the leading and trailing edges. The distribution of the friction coefficient along the suction side of the aerofoil is presented in Figure 8.31. Computations 17 and 18 show a dip, hinting at the presence of a laminar–to–turbulent transition. For computation 17, this dip is located at $x/c \approx 0.16$ while, for computations 18, it is located at $x/c \approx 0.12$. This latter value corresponds to the location at which transition occurs in the experiment. However, none of these minima reach negative values that would have indicated the presence of the transitional bubble. The tails of the profiles indicate the absence of a predicted trailing–edge separation bubble.

Figures 8.32 to 8.35 show, respectively, profiles of mean streamwise velocity, the r.m.s. of streamwise velocity, the r.m.s. of the cross–stream velocity and the shear stress, the last three terms consisting of the resolved components. From Figure 8.32, it is evident that computation 18 gives the best results obtained so far in the present research. This is confirmed when considering the other quantities in Figures 8.33 to 8.35. Interestingly, computation 19 turned out to yield the best velocity profile at $x/c = 0.3$. At this location, conditions in the boundary are dictated by small–scale activity, the resolution of which requires a relatively short integration time. Hence, it is possible that, had this computation been pursued to its end, good agreement with the experiment may have been obtained. Figures 8.33 and 8.34 indicate the absence of numerical oscillations in the region above the boundary layer. This demonstrates the effectiveness of the present strategy employed to control the numerical oscillations. This is further illustrated in Figures 8.36 to 8.38 in which contours of instantaneous streamwise velocity are shown. The fields appear smooth, except perhaps around the location where the switch from one numerical scheme to the other occurs. Indeed, this switch can itself create artificial wiggles. This does not, however, seem to have had any influence on the predictions presented here. It is also relevant to mention that the switch from one numerical scheme to another was used by Mellen et al [151] to artificially trigger transition in some of their aerofoil computations.

In the course of computation 18, time–signals for the three components of the velocity were recorded for the duration of the averaging processes at the 12 locations shown in Figure 8.39. Points 1, 3 and 5 are located inside the boundary layer, while

points 2, 4 and 6 are at its edge. The six remaining points are located in the wake. For each of these locations, 64 signals were recorded, each corresponding to a spanwise location, over a period corresponding to 2.1 chords at a sampling rate $\Delta t = 10^{-4}$. Each of the signals is made up of 21702 samples.

Figures 8.40 and 8.41 show the energy spectra for all 12 positions, while Figures 8.42 and 8.43 present the spanwise correlations at these locations. The spectral analysis was performed using a Hanning window with the full signal being decomposed into four overlapping elements over which averaging was performed. As signals were recorded 64 different spanwise positions at each of the (x, y) locations considered, additional averaging was also performed in that direction. The top four plots shown in Figure 8.40 highlight the inadequacy of the mesh resolution in the boundary layer. The energy drain from the small scales is not properly captured, and an energy pile–up is observed near the cut–off frequency. This pile–up is especially well illustrated in the plot showing the spectra for point 2. The remaining two plots in this figure indicate that as the rear, thicker portion of the boundary layer is reached, resolution improved drastically, with the spectra assuming a shape much more similar to those observed for the other turbulent flows considered earlier in the present efforts. Furthermore, no pile–up is observed in the spectra shown in Figure 8.41. A point to note from this figure is the presence of peaks at low frequencies in some of the spectra shown. This points to the presence of regularly convected structures, possibly due to a mechanism similar to vortex shedding.

Figures 8.42 and 8.43 show the spanwise two–point correlations for all three components of velocity extracted at the locations shown in Figure 8.39. Along the aerofoil, all correlations shown in Figure 8.42 diminish to zero. The flow is thus decorrelated, and this indicates that the spanwise extent of 6% is, indeed, large enough. The rate at which the correlations decrease to zero diminishes, however, as the location considered is closer and closer to the trailing edge. As shown in Figure 8.43, it appears that the flow in the wake is not decorrelated either. Hence, in that region, the spanwise distance of 6% of chord is clearly not large enough. This is consistent with the expected presence of large structures in this region, which also occupy a significant spanwise extent.

Figure 8.44 shows iso–contours of instantaneous spanwise velocity for computation 18, while Figure 8.45 presents the same contours for computation 19. Iso–pressure–fluctuation contours for computation 19 are shown in Figure 8.46. The last figure, in the aerofoil wake, features large spanwise rollers which occupies the complete width of the computational domain. This explains the lack of decorrelation in this region observed in Figure 8.43. These large spanwise rollers, also observed in Figure 8.45, result from a Kelvin-Helmholtz instability arising from the mixing of the lower and upper boundary layers with different speeds at the trailing edge. Careful observations of this flow region also reveal the presence of streamwise vortices due to helical pairing. As these rollers are convected downstream, beyond the trailing edge, they break down in the flow and lose their structure. On the aerofoil, the process of transition is marked by the progressive appearance of structures followed by a build–up of a turbulent boundary layer and its progressive thickening as the flow develops.

Comp.	Mesh						SGS
	$N_x \times N_y$	N_z	N_{wake}	N_{SS}	N_{PS}	N_{tot}	model
17	640×96	64	80	240	240	$3.9 \cdot 10^6$	SMA+WD2
18	1280×96	64	80	560	560	$7.8 \cdot 10^6$	SMA+WD2
19	2836×128	64	176	1904	560	$23.2 \cdot 10^6$	WALE

Table 8.8: Meshes used for the final aerofoil simulations (SS = suction side; PS = pressure side).

Comp.	Wall treatment	N_{CPU}	Total run time	Averaging time	CPU cost (Green)	Time-step
17	NS	64	$7\,c$	$2\,c$	≈ 12000 h	$\approx 8.2 \cdot 10^{-6}$
18	NS	64	$7\,c$	$2\,c$	≈ 23000 h	$1 \cdot 10^{-5}$
19	NS	128	$2.1\,c$	$0.2\,c$	≈ 30600 h	$1 \cdot 10^{-5}$

Table 8.9: Description of the computations for the final aerofoil simulations.

Comp.	C_l	C_d
Exp. - F1	1.56	0.0204
Exp. - F2	1.515	0.0308
17	1.496	0.0622
18	1.612	0.0602

Table 8.10: Lift and drag coefficients predicted for the final aerofoil computations (see Tables 8.8 and 8.9 for a description of the computations).

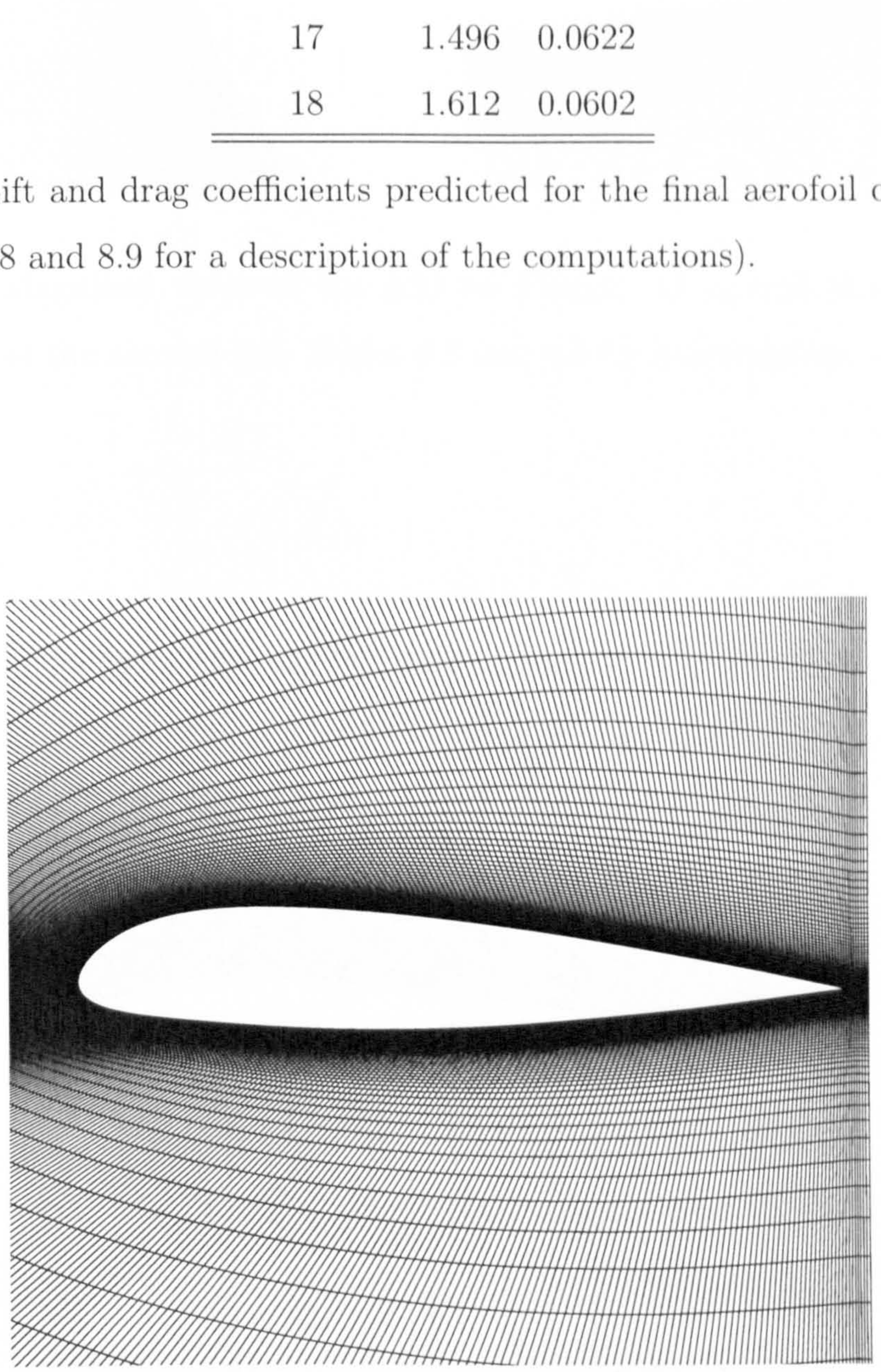

Figure 8.21: Grid around the aerofoil for Comp. 17 (see Tables 8.8 and 8.9 for a description of the computations).

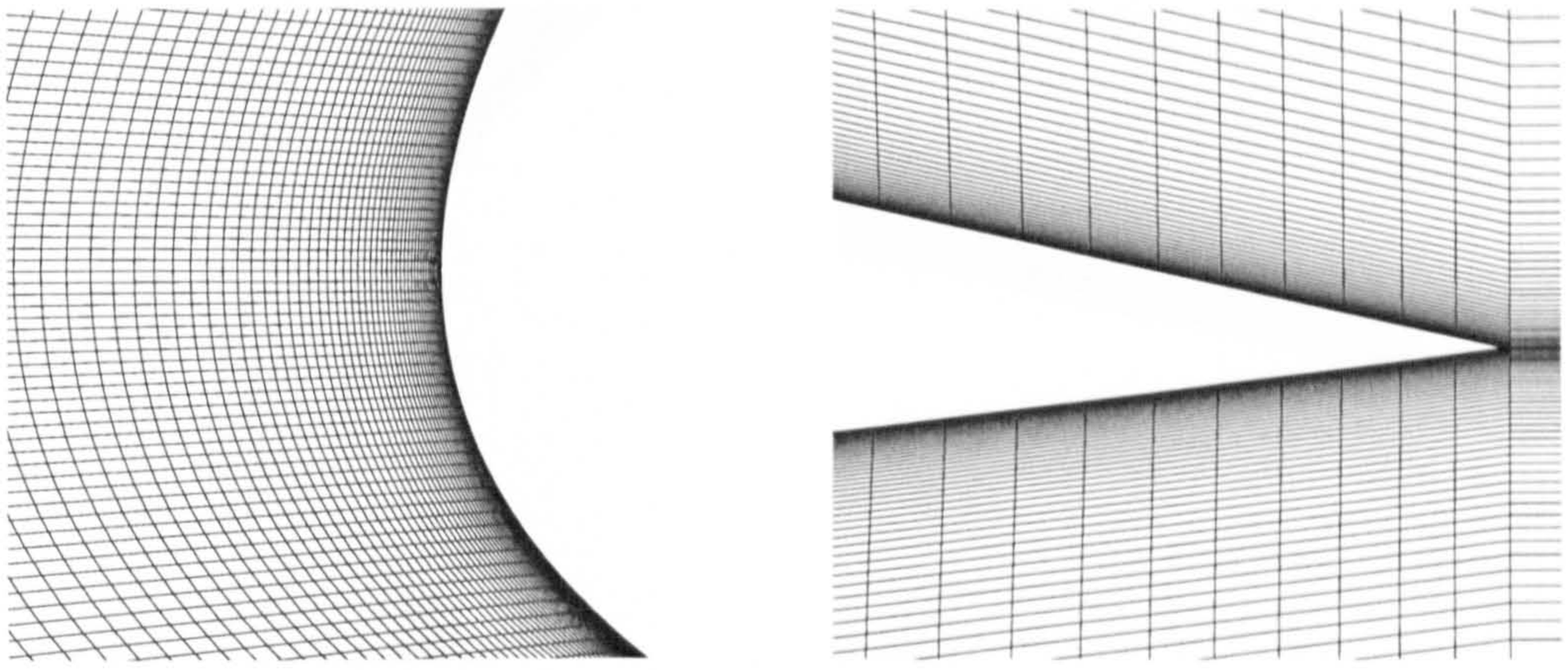

Figure 8.22: Magnified views of the grid for Comp. 17 around the leading and trailing edges of the aerofoil (see Tables 8.8 and 8.9 for a description of the computations).

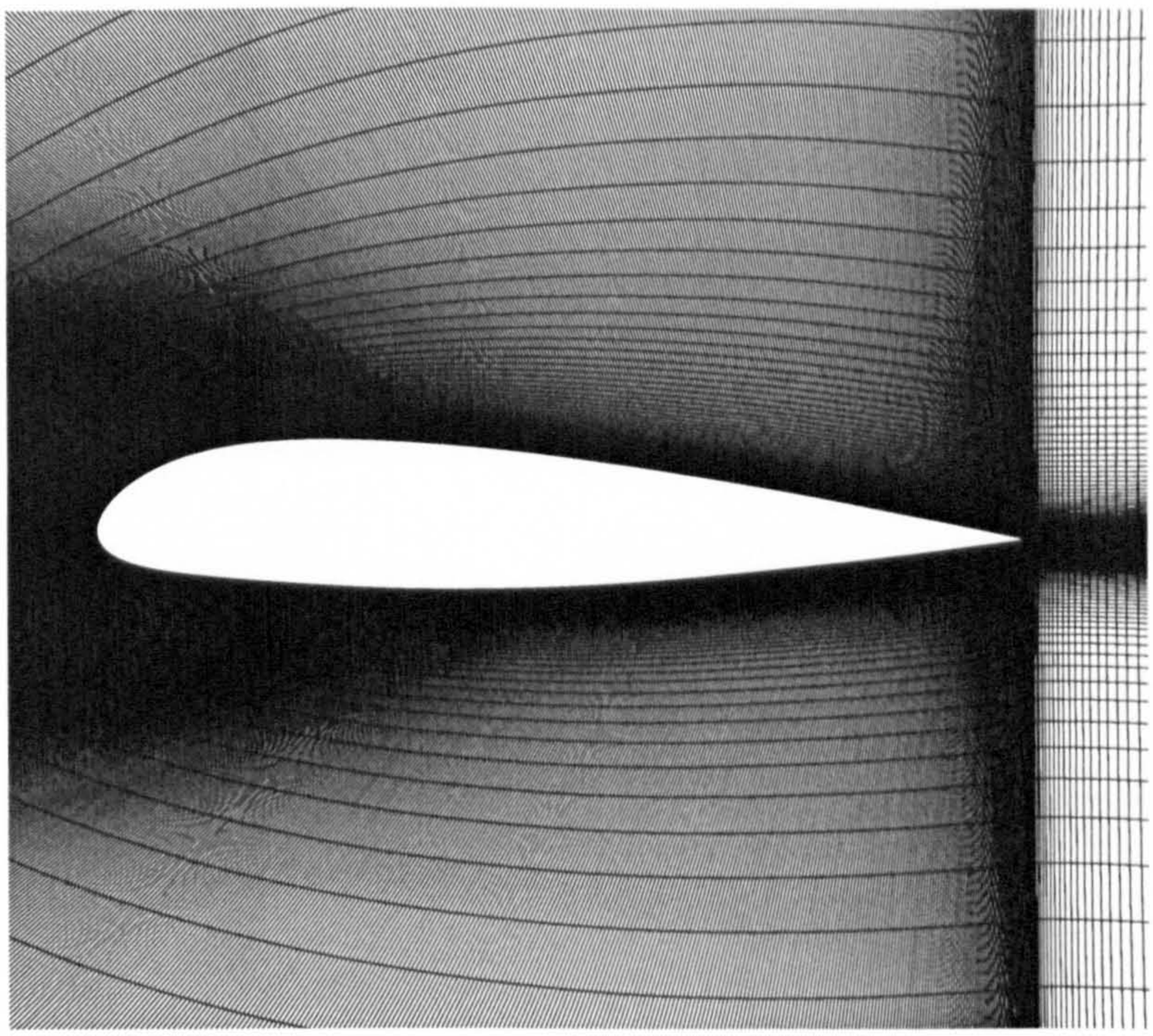

Figure 8.23: Grid around the aerofoil for Comp. 18 (see Tables 8.8 and 8.9 for a description of the computations).

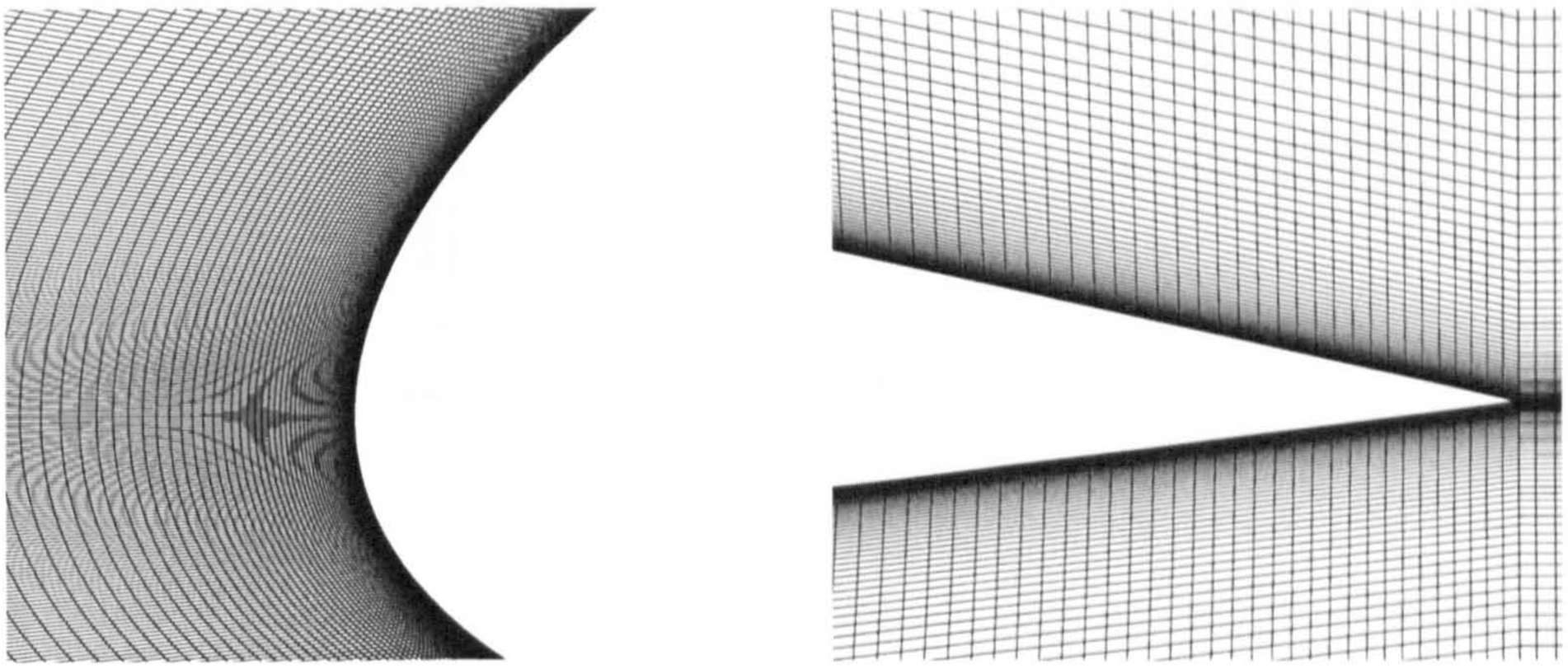

Figure 8.24: Magnified views of the grid for Comp. 18 around the leading and trailing edges of the aerofoil (see Tables 8.8 and 8.9 for a description of the computations).

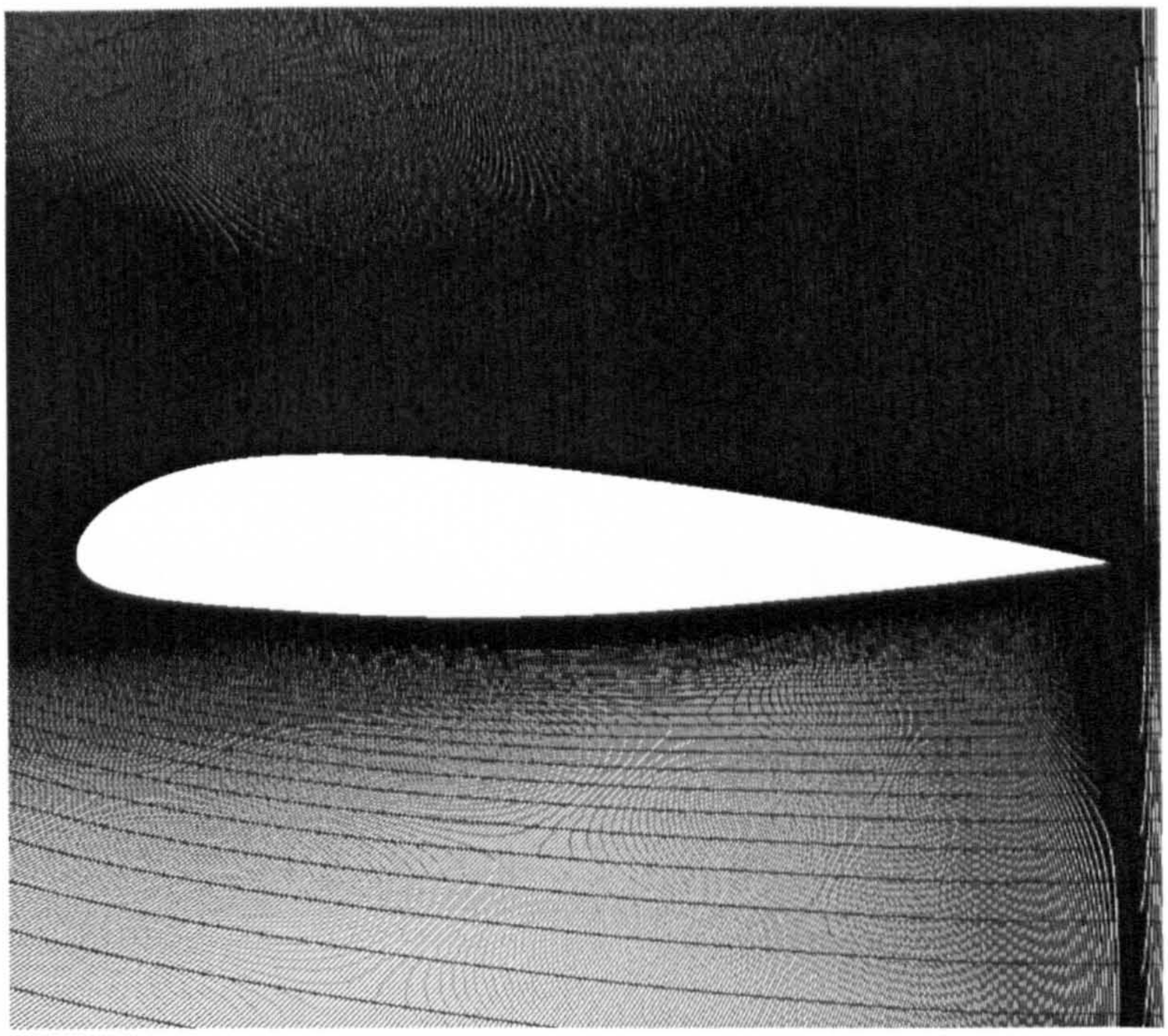

Figure 8.25: Grid around the aerofoil for Comp. 19 (see Tables 8.8 and 8.9 for a description of the computations).

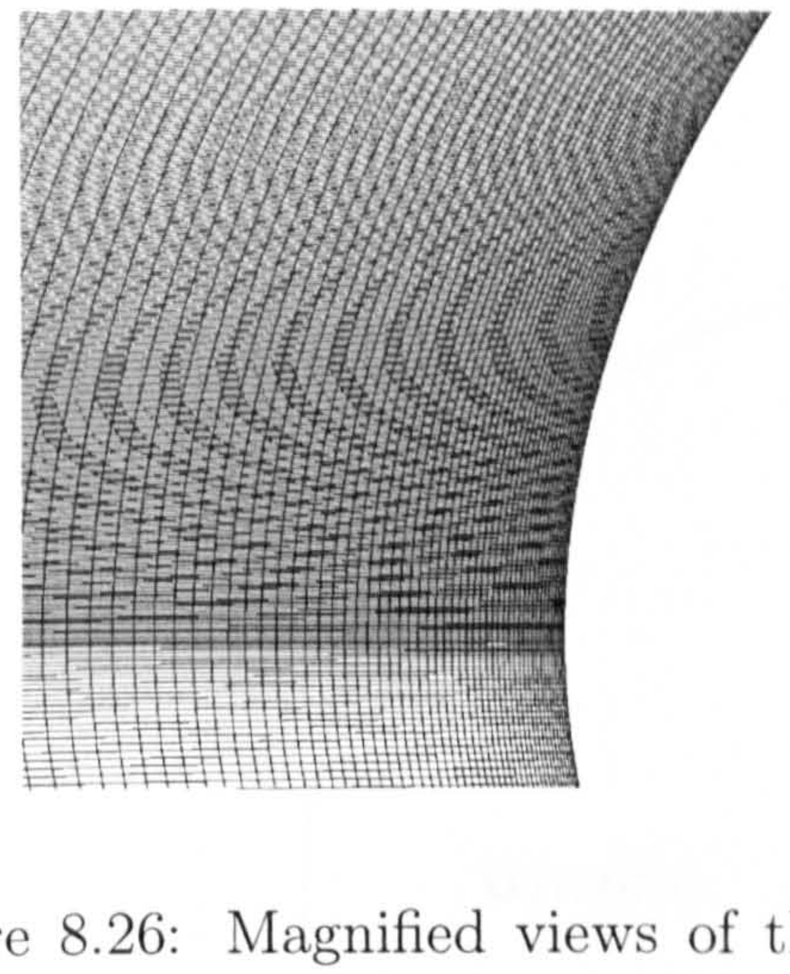

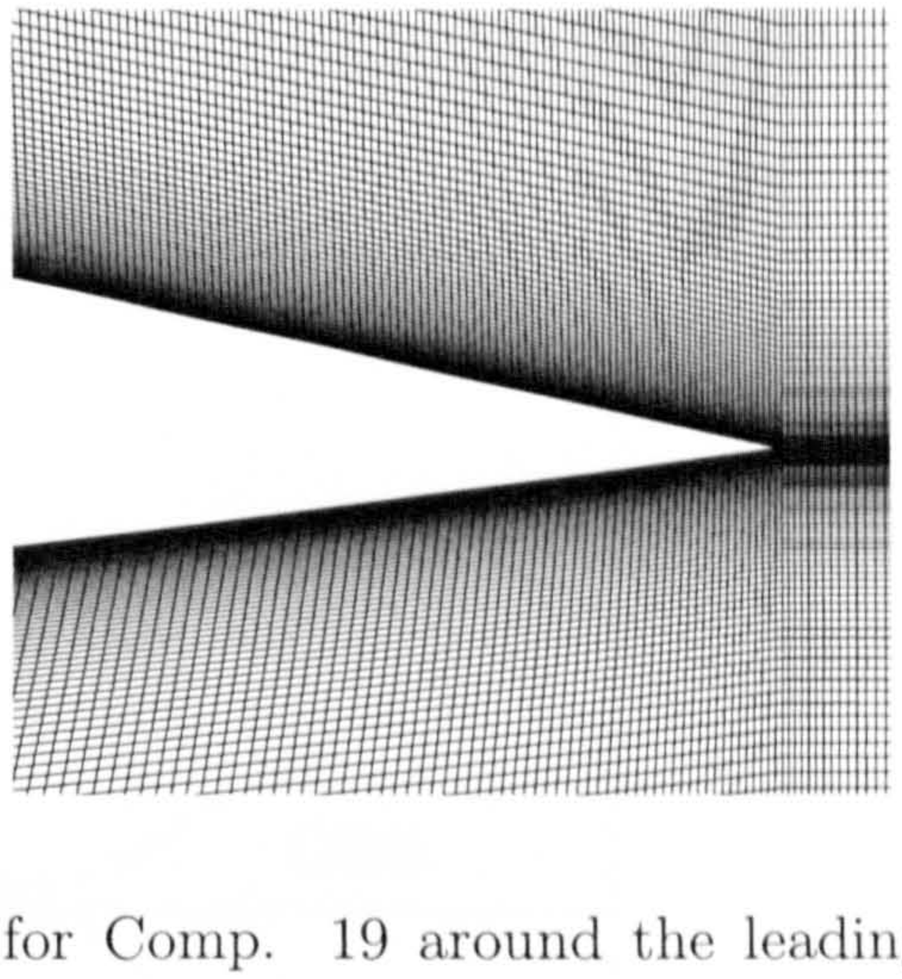

Figure 8.26: Magnified views of the grid for Comp. 19 around the leading and trailing edges of the aerofoil (see Tables 8.8 and 8.9 for a description of the computations).

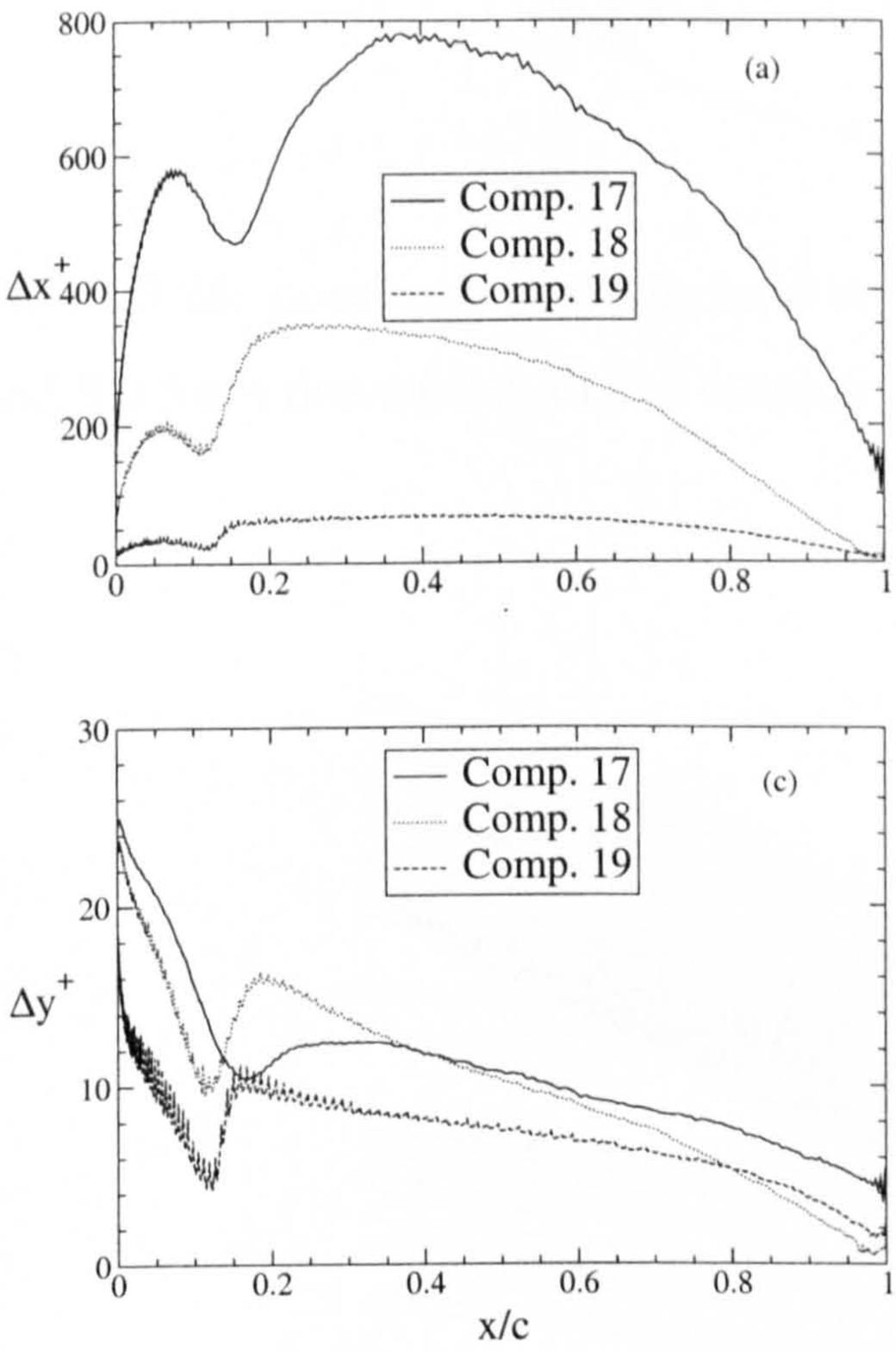

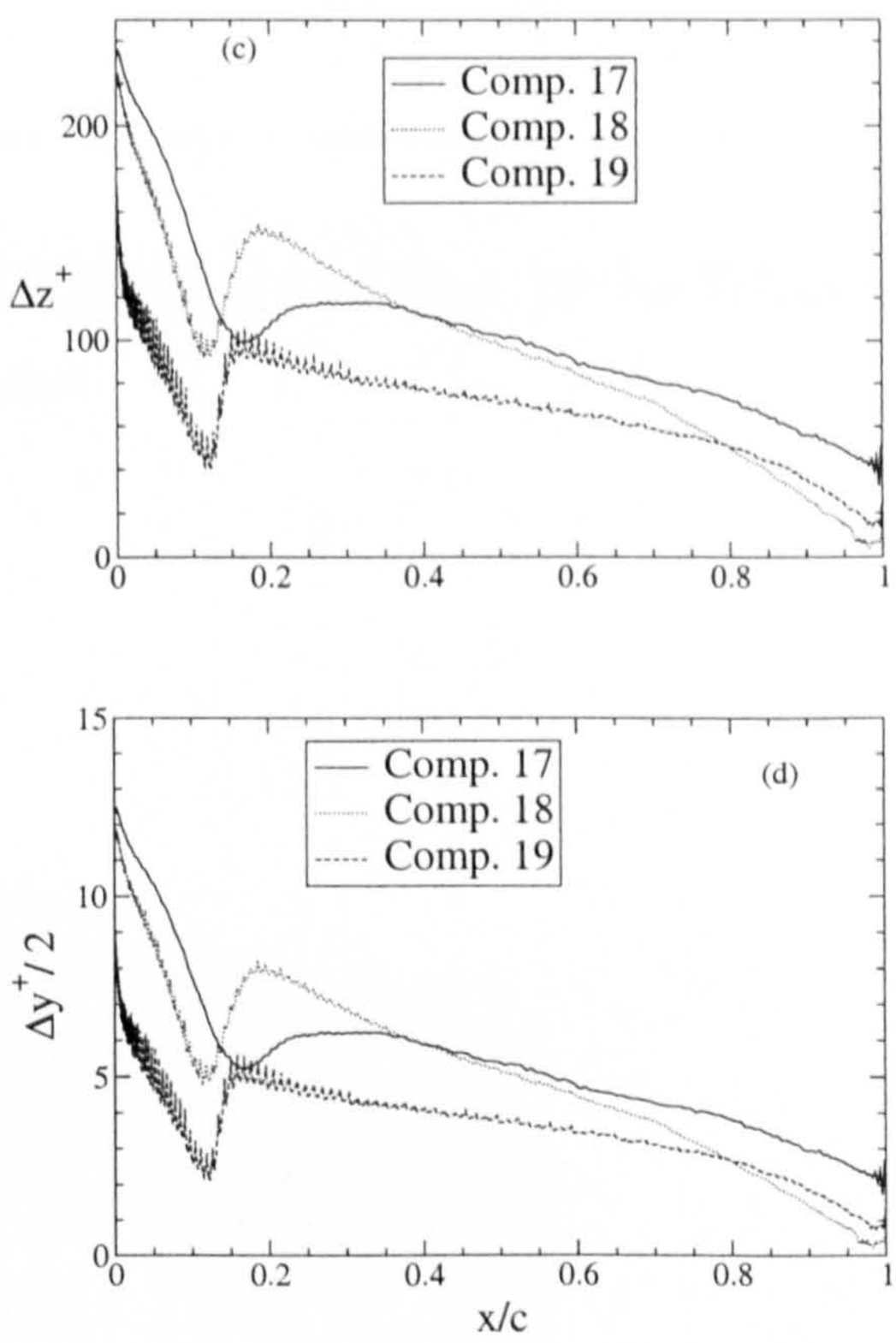

Figure 8.27: Distribution of the near–wall cell dimensions expressed in wall units along the suction side of the aerofoil for the final computations: (a) streamwise dimension; (b) spanwise dimension; (c) wall-normal dimension; (d) location of the first cell-centre in the wall-normal direction (see Tables 8.8 and 8.9 for a description of the computations).

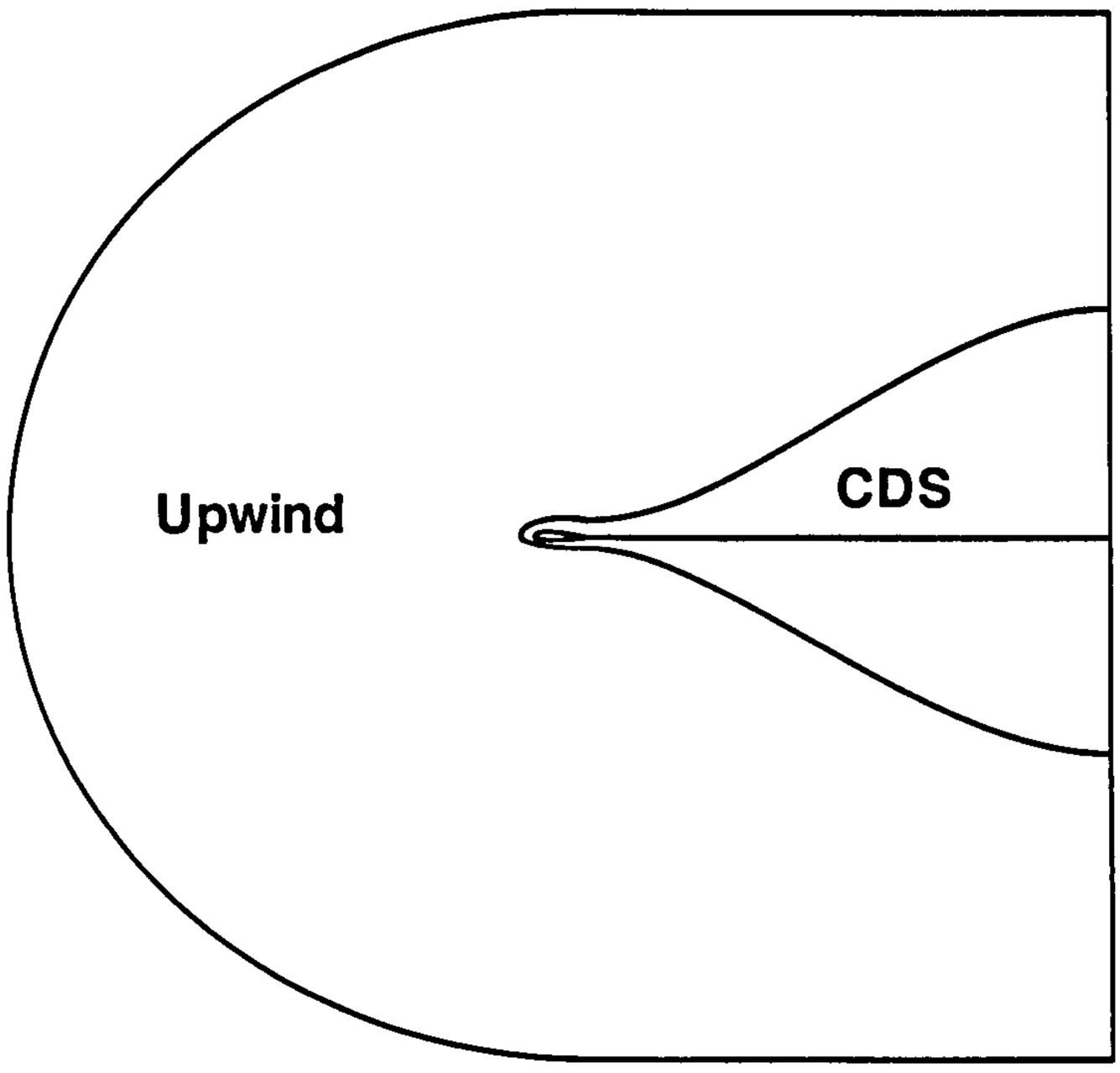

Figure 8.28: Locations of the upwind and CDS regions for Comp. 19 (see Tables 8.8 and 8.9 for a description of the computations).

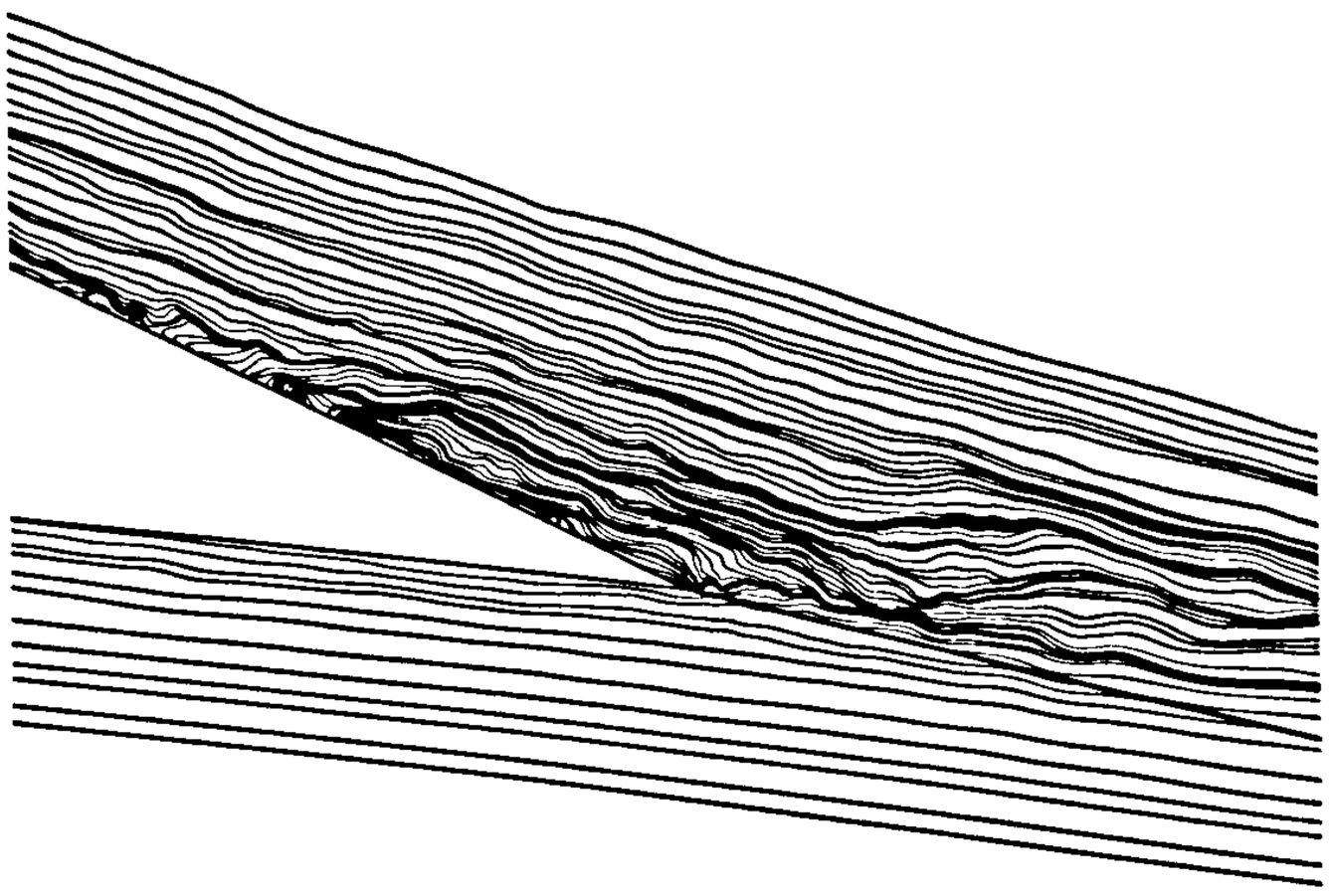

Figure 8.29: Instantaneous streamlines around the trailing edge for Comp. 19 after 2.1 dimensionless time–units (see Tables 8.8 and 8.9 for a description of the computations).

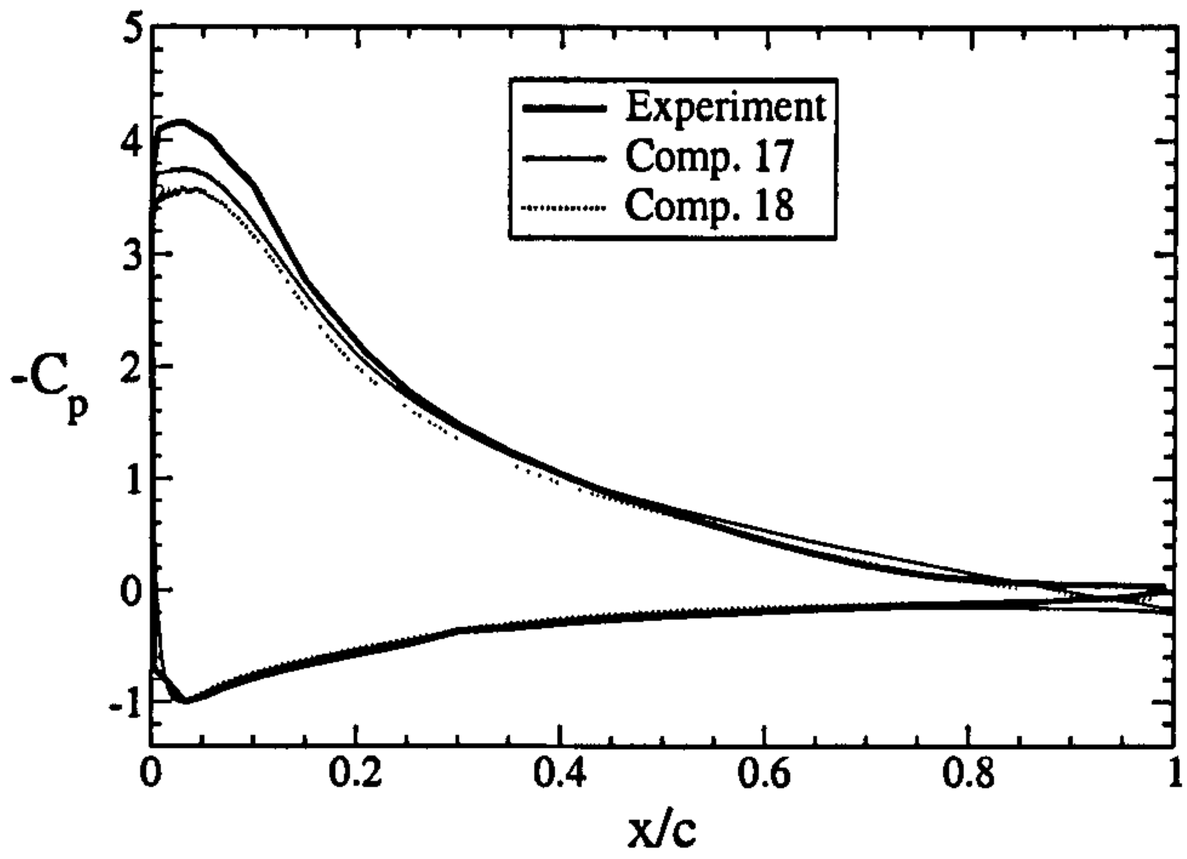

Figure 8.30: Pressure coefficient along the aerofoil for the final aerofoil computations (see Tables 8.8 and 8.9 for a description of the computations).

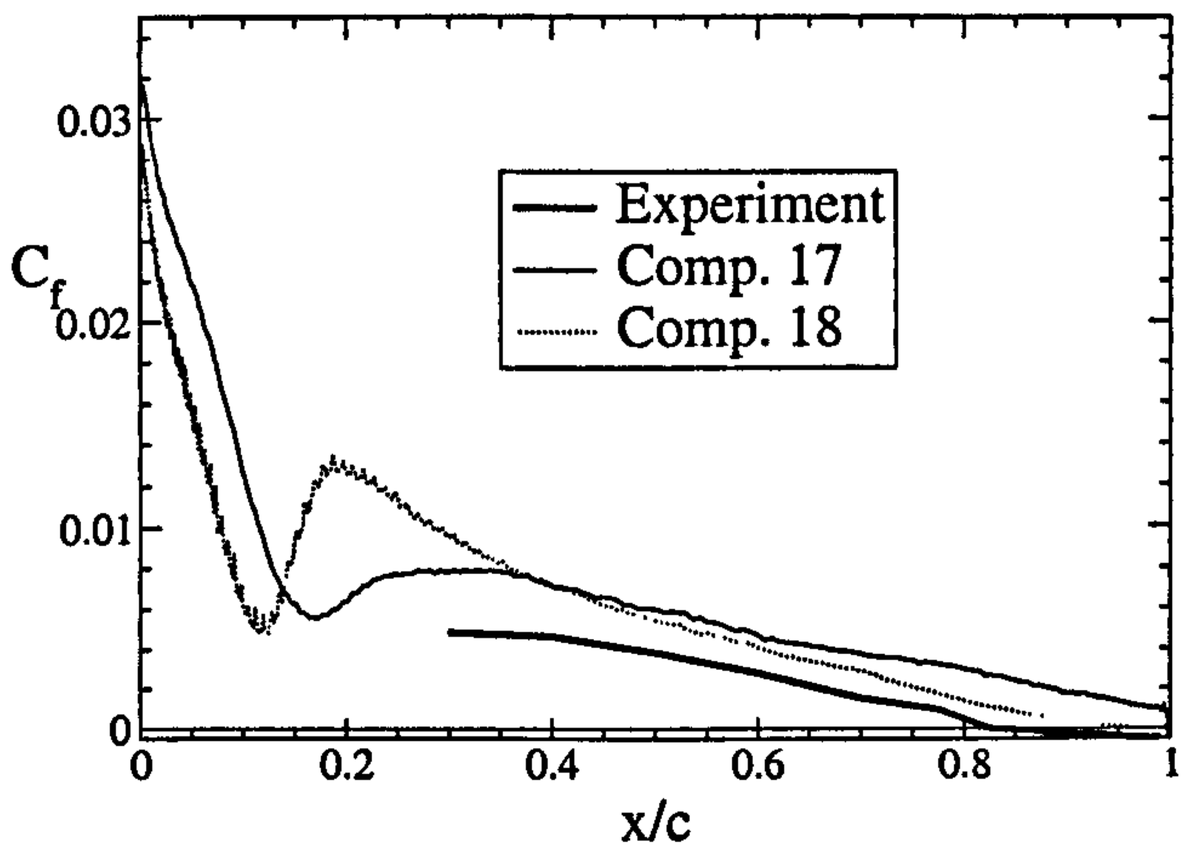

Figure 8.31: Friction coefficient along the aerofoil suction side for the final aerofoil computations (see Tables 8.8 and 8.9 for a description of the computations).

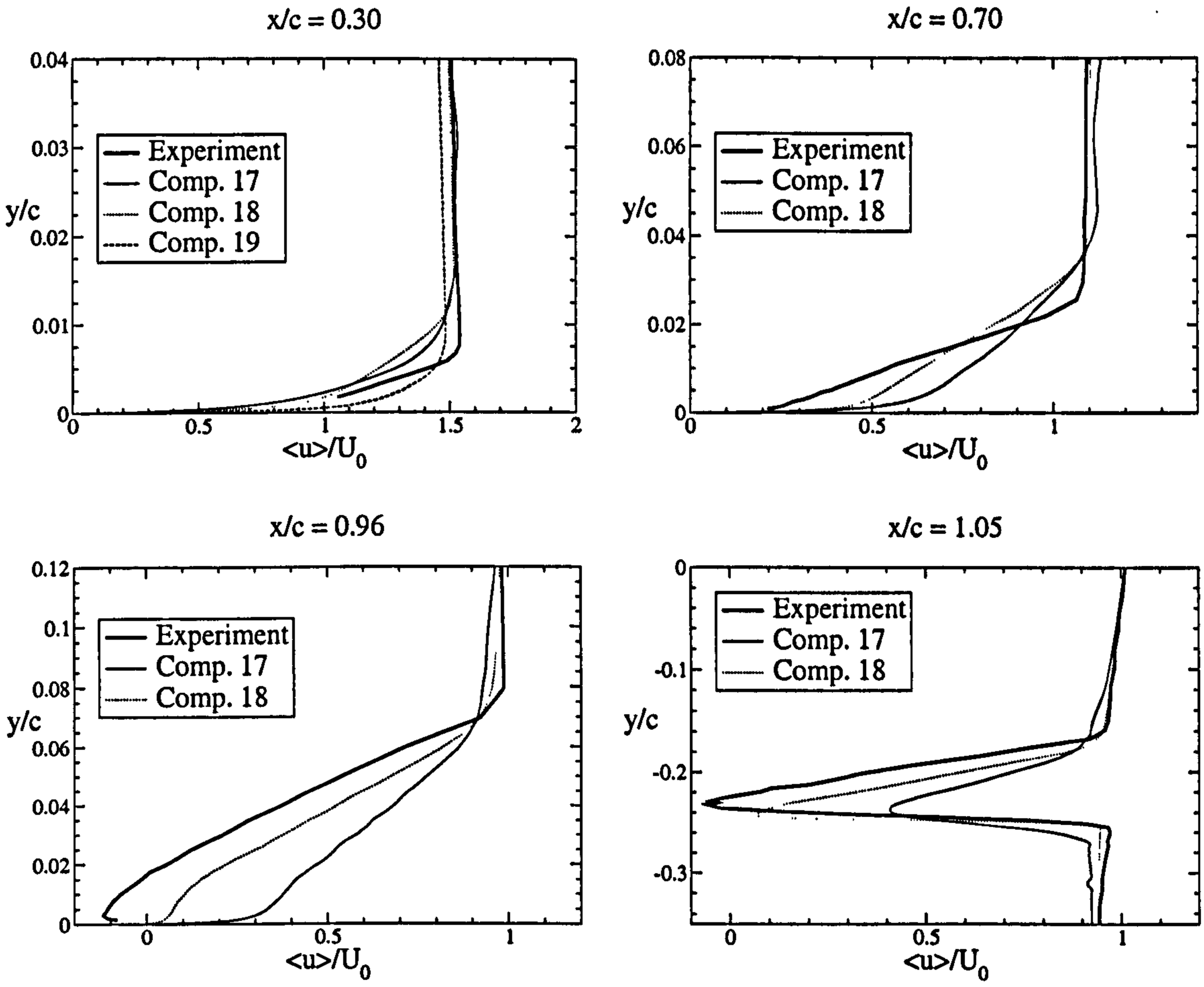

Figure 8.32: Averaged streamwise velocity profiles at four different locations for the final aerofoil computations (see Tables 8.8 and 8.9 for a description of the computations).

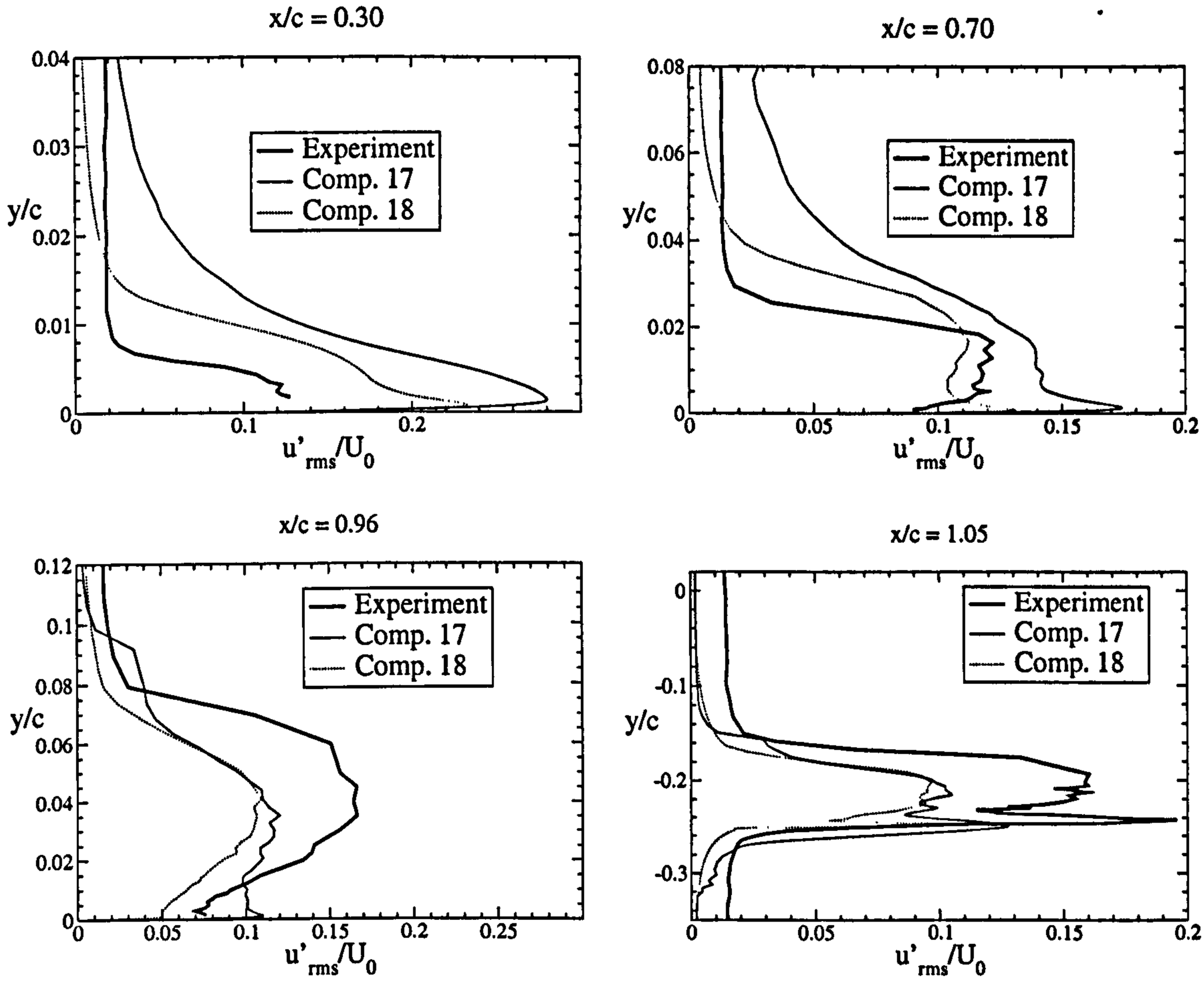

Figure 8.33: Averaged streamwise turbulence intensity profiles at four different locations for the final aerofoil computations (see Tables 8.8 and 8.9 for a description of the computations).

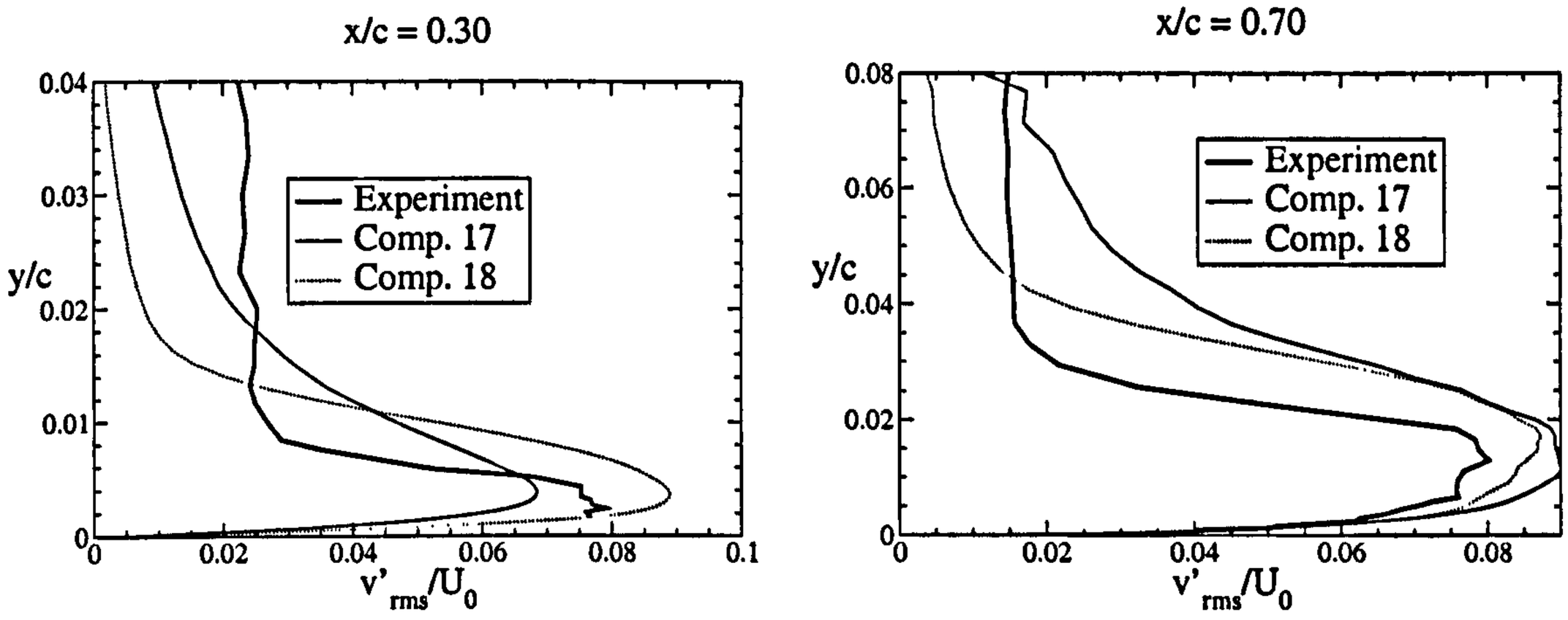

Figure 8.34: Averaged vertical turbulence intensity profiles at four different locations for the final aerofoil computations (see Tables 8.8 and 8.9 for a description of the computations).

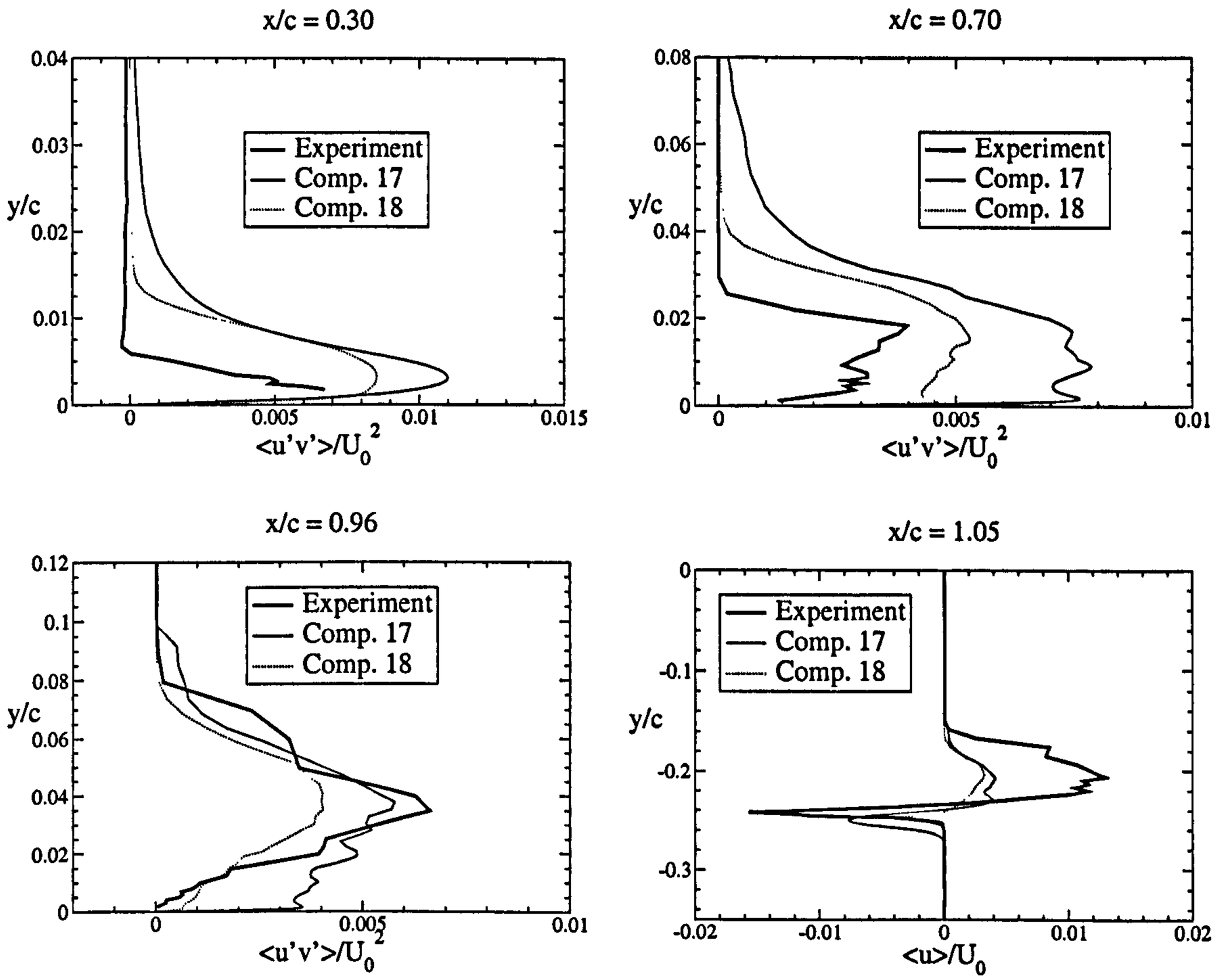

Figure 8.35: Averaged shear stress profiles at four different locations for the final aerofoil computations (see Tables 8.8 and 8.9 for a description of the computations).

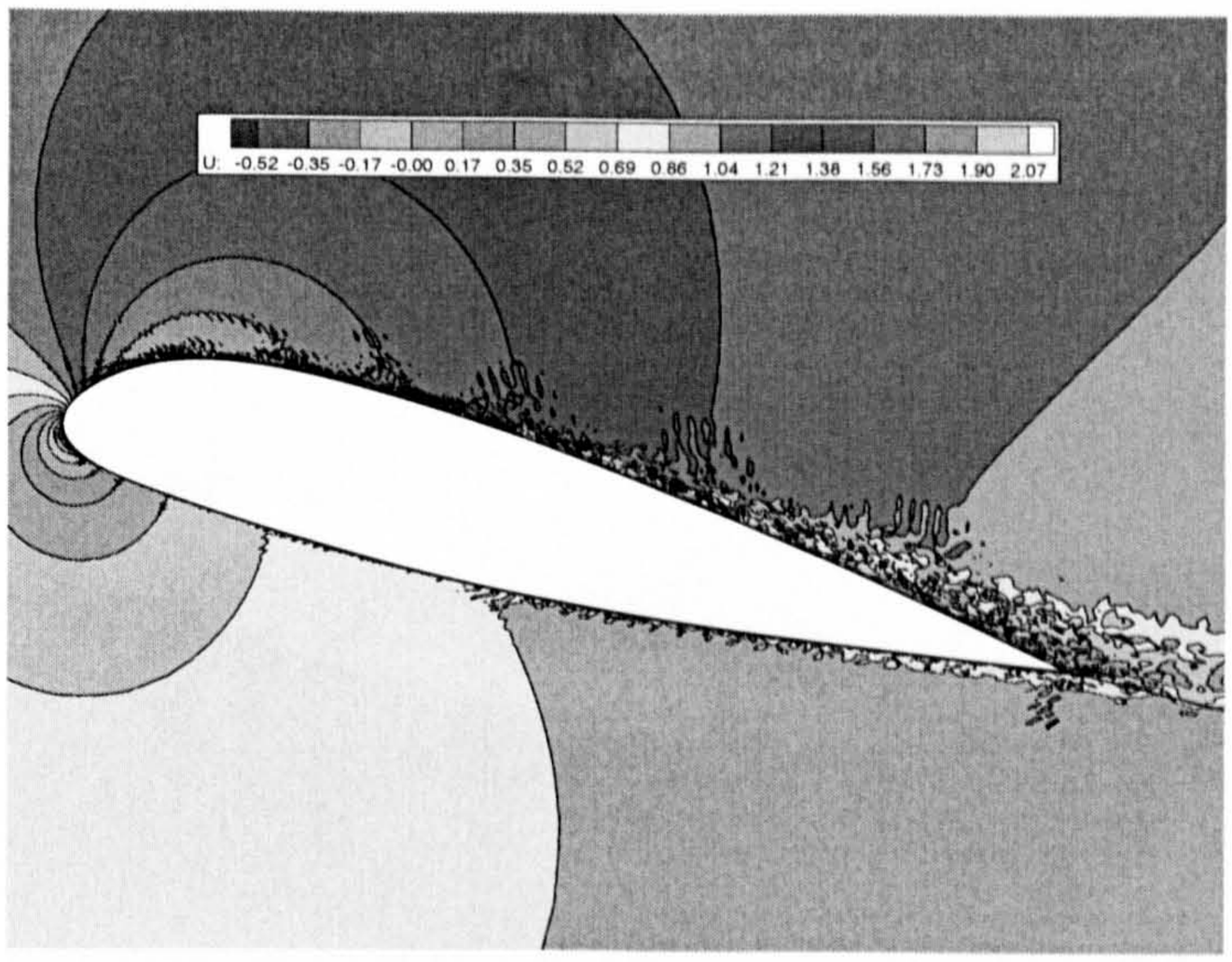

Figure 8.36: Instantaneous streamwise velocity contours for Comp. 17 (see Tables 8.8 and 8.9 for a description of the computations).

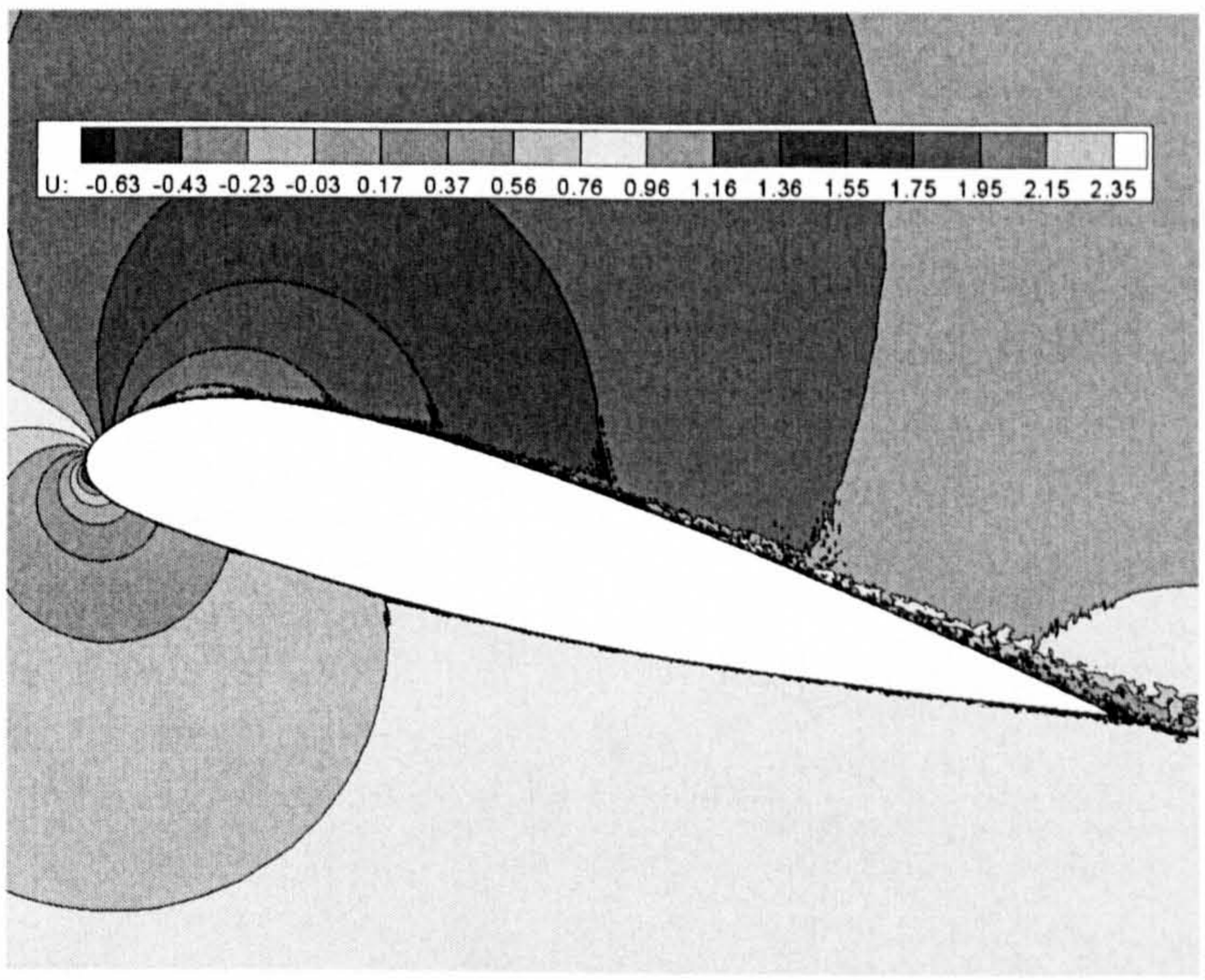

Figure 8.37: Instantaneous streamwise velocity contours for Comp. 18 (see Tables 8.8 and 8.9 for a description of the computations).

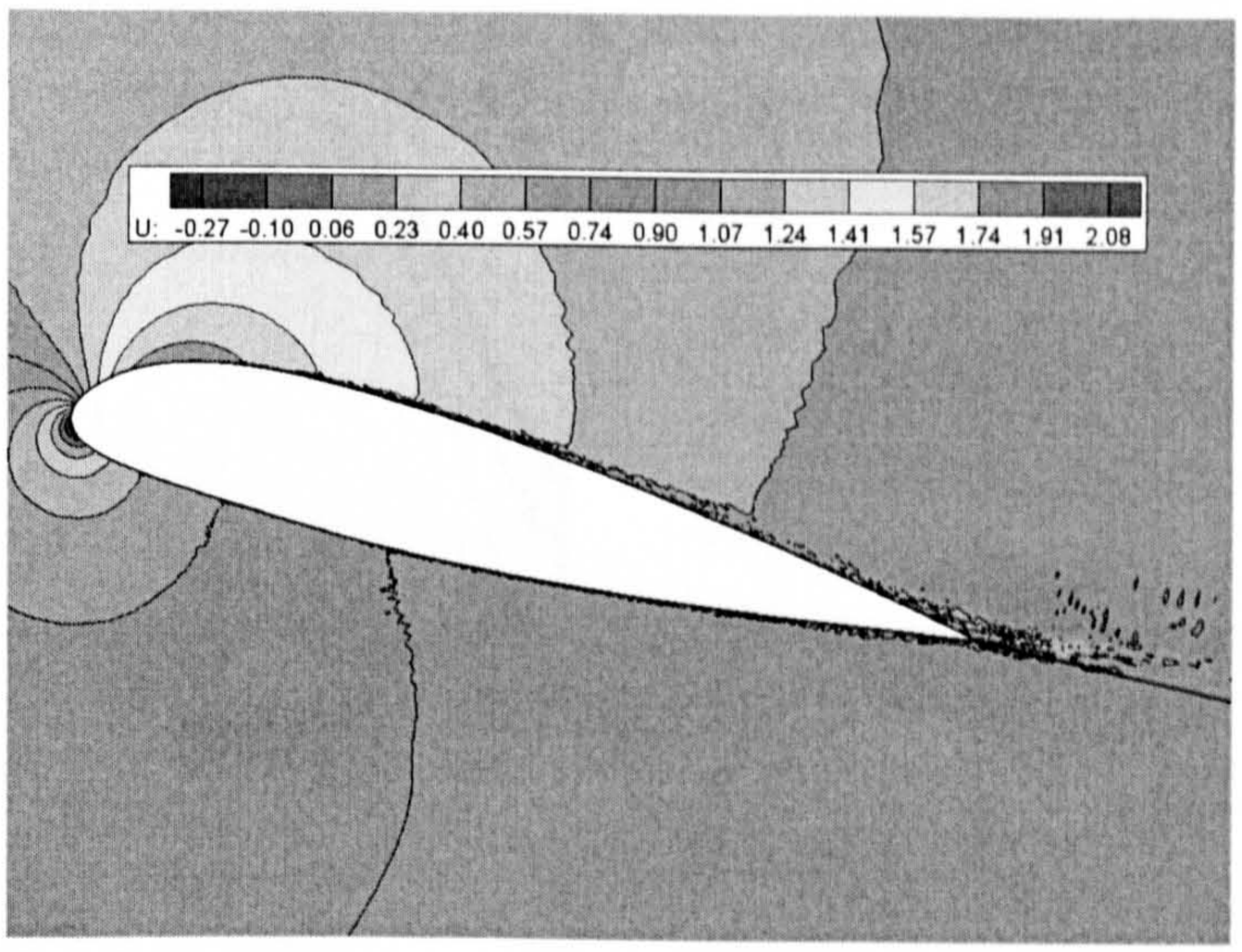

Figure 8.38: Instantaneous streamwise velocity contours for Comp. 19 (see Tables 8.8 and 8.9 for a description of the computations).

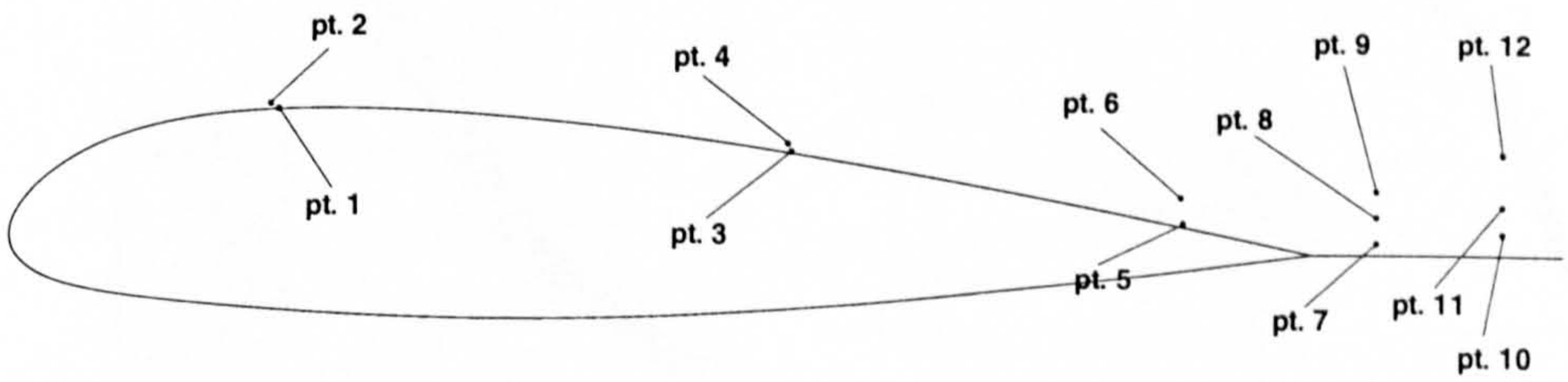

Figure 8.39: Locations of the recording points for the time–signals extracted from Comp. 18 (see Tables 8.8 and 8.9 for a description of the computations).

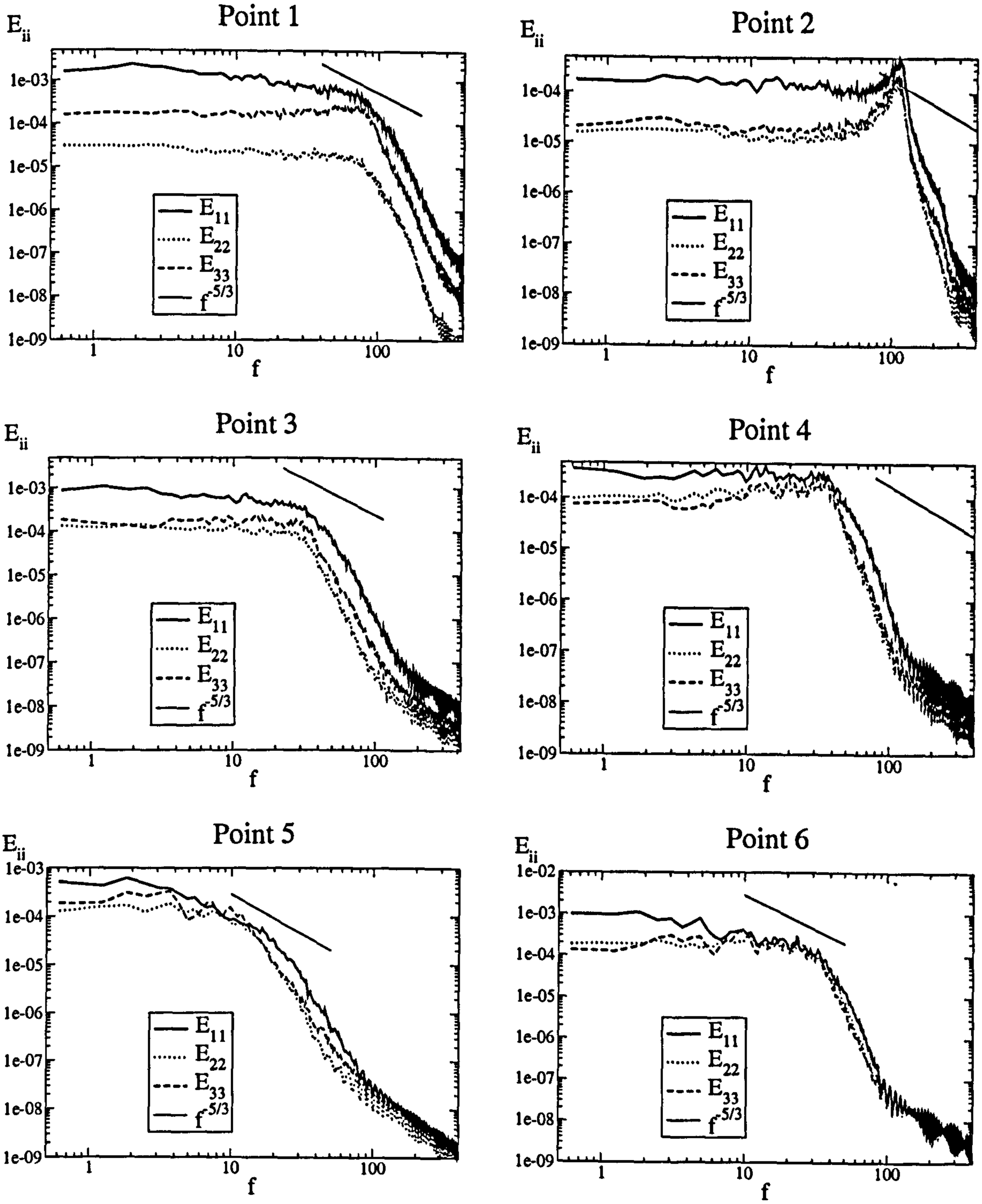

Figure 8.40: Spectra at locations 1 to 6 (see Figure 8.39) for Comp. 18 (see Tables 8.8 and 8.9 for a description of the computations).

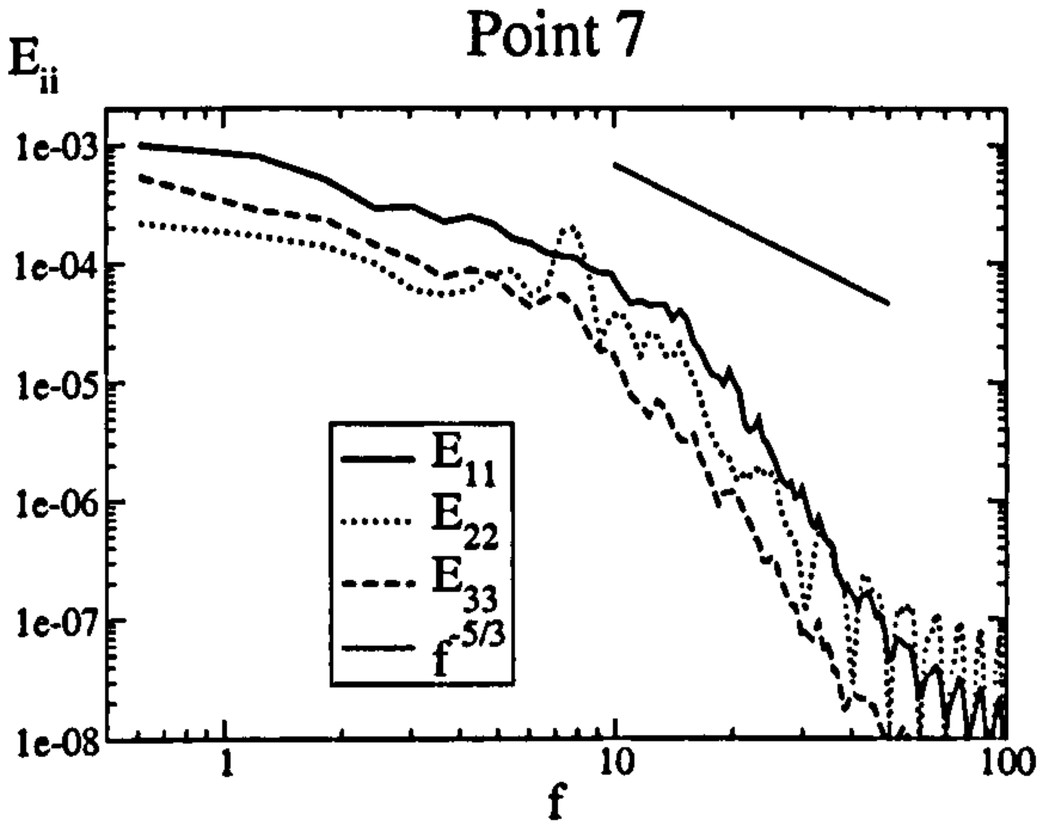

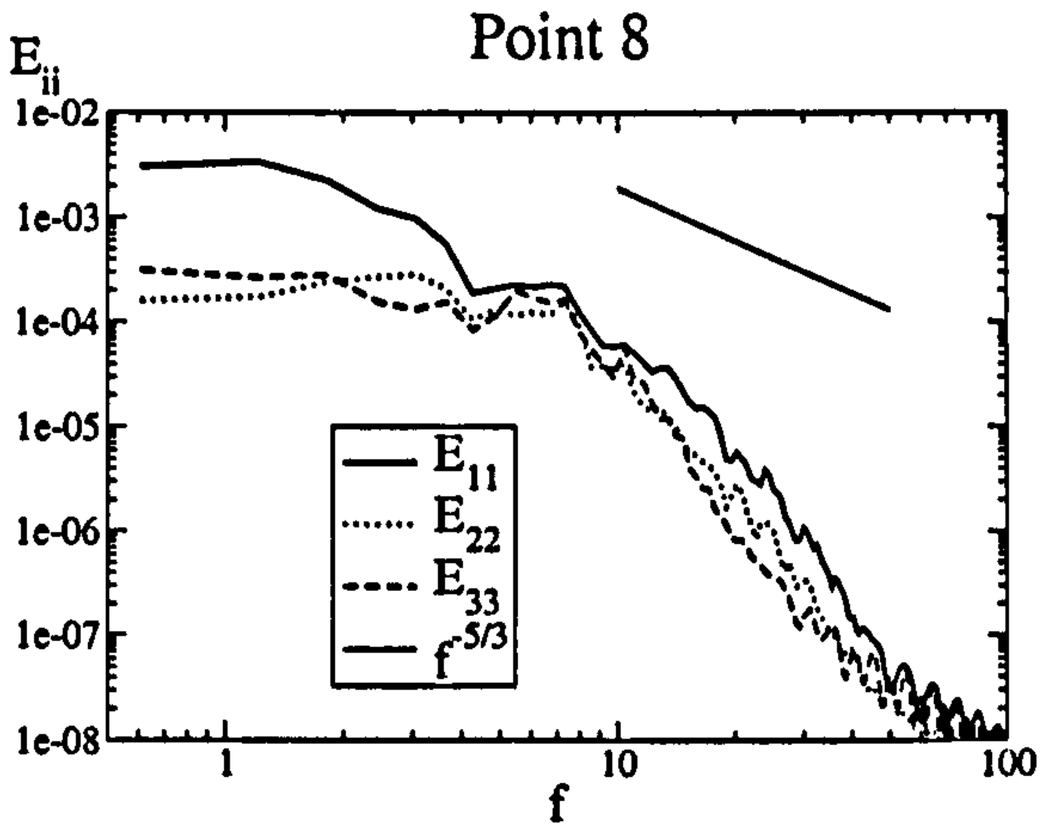

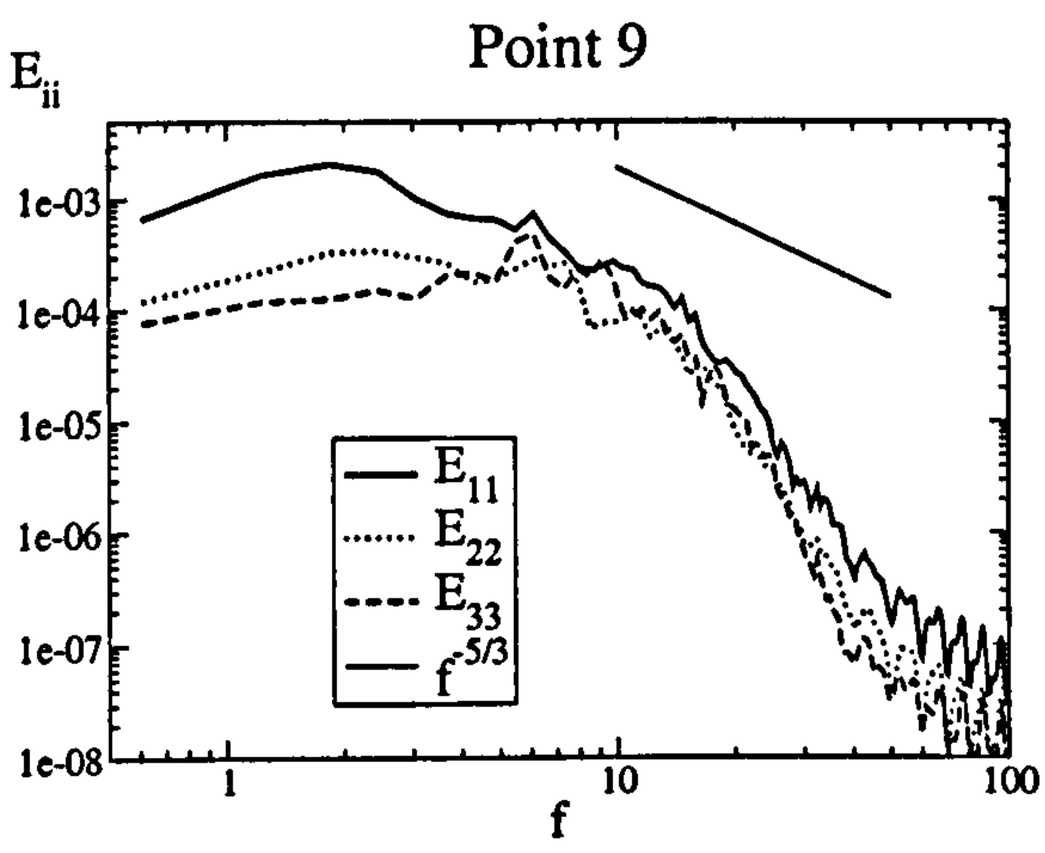

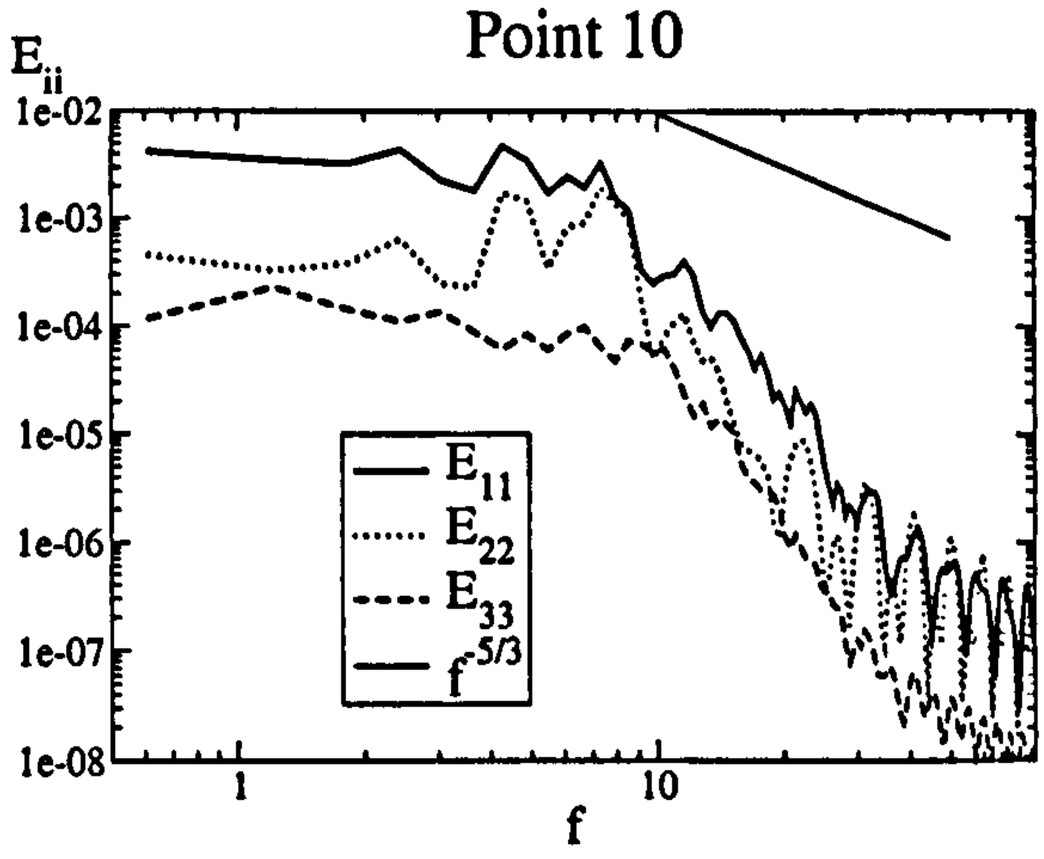

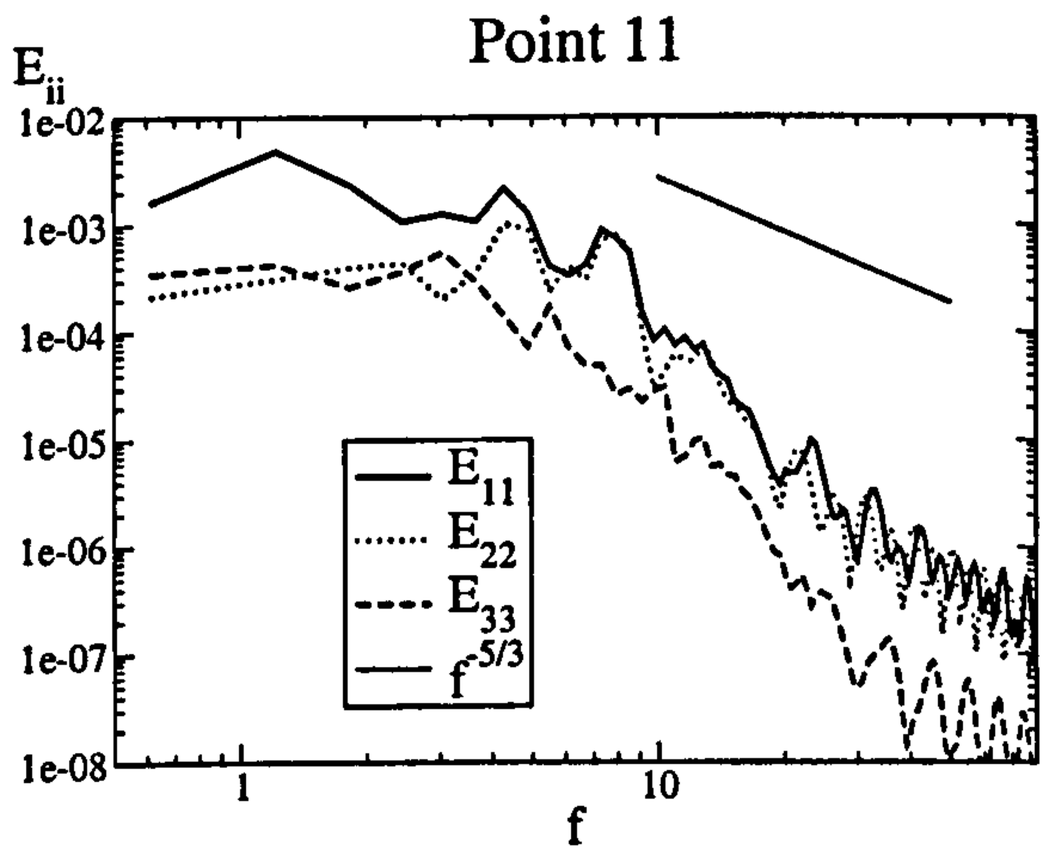

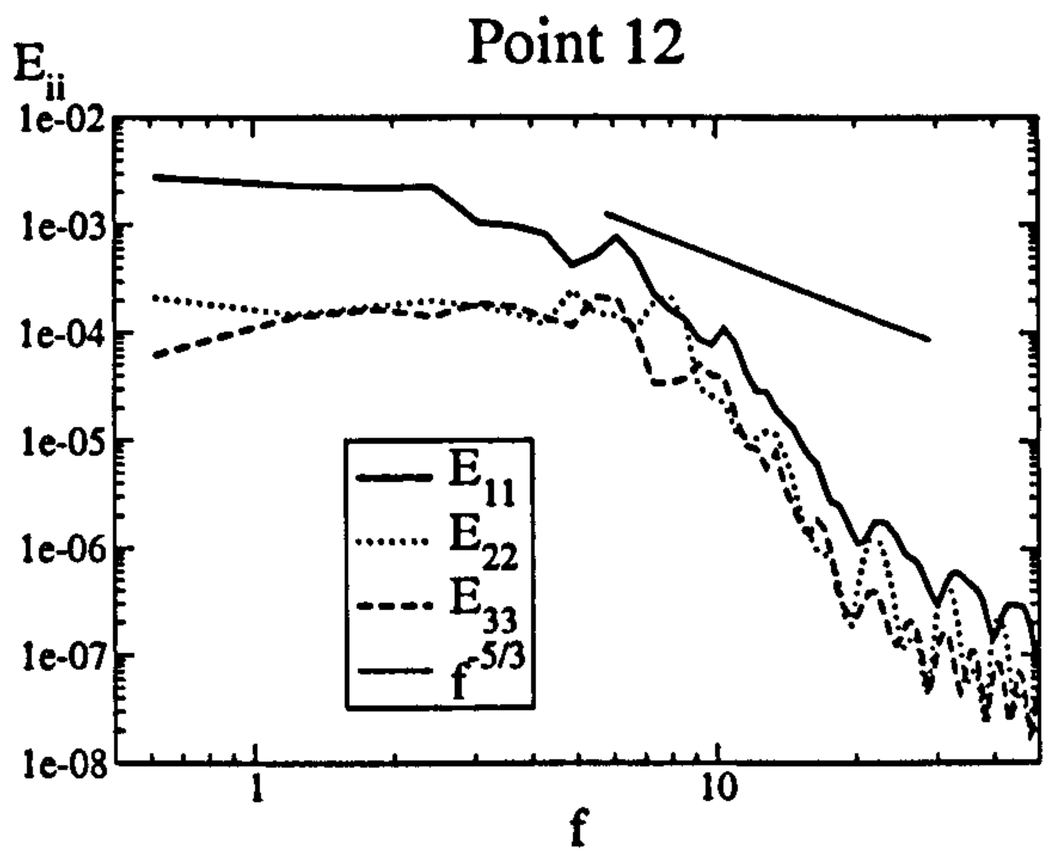

Figure 8.41: Spectra at locations 7 to 12 (see Figure 8.39) for Comp. 18 (see Tables 8.8 and 8.9 for a description of the computations).

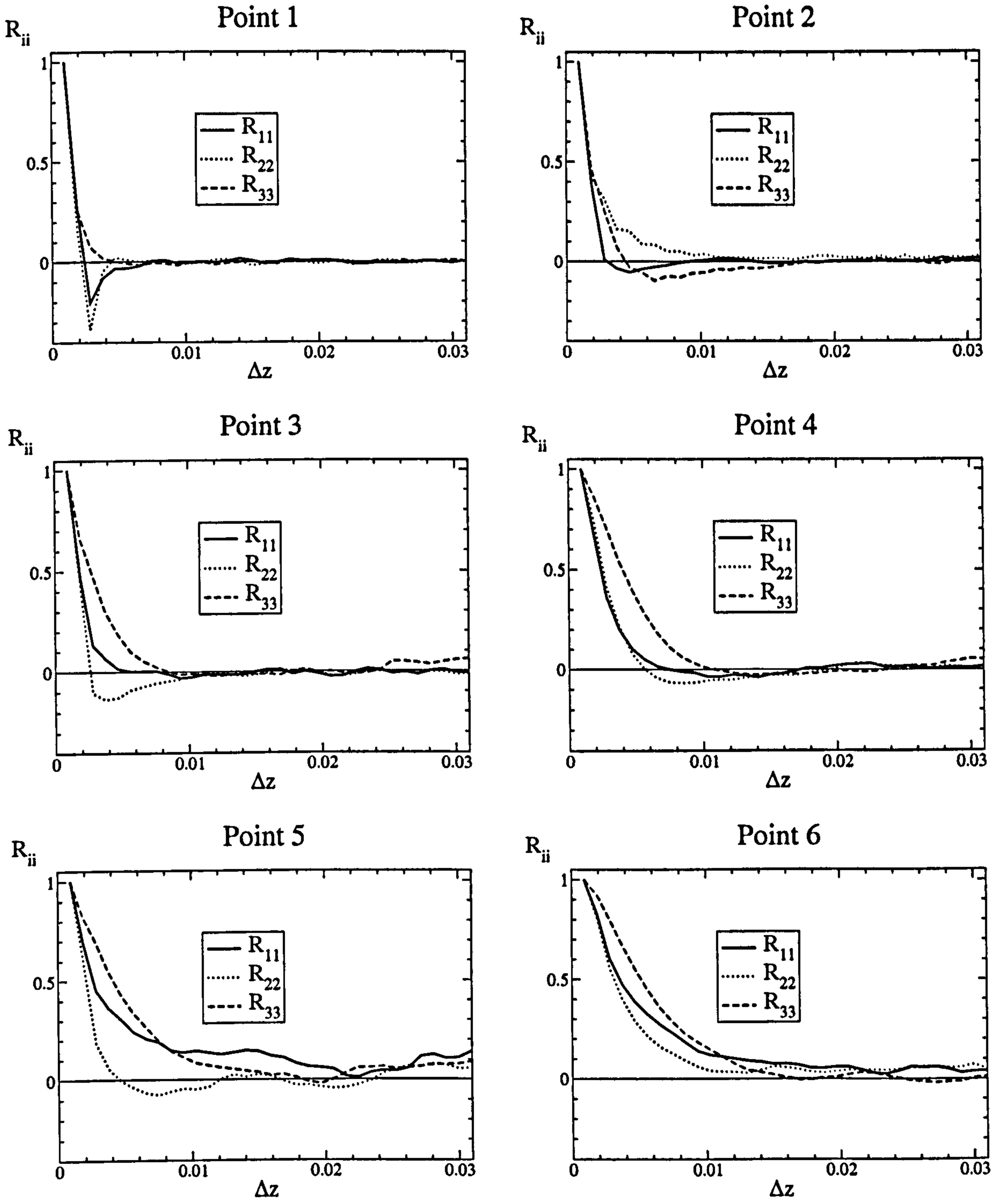

Figure 8.42: Spanwise two-point correlations at locations 1 to 6 (see Figure 8.39) for Comp. 18 (see Tables 8.8 and 8.9 for a description of the computations).

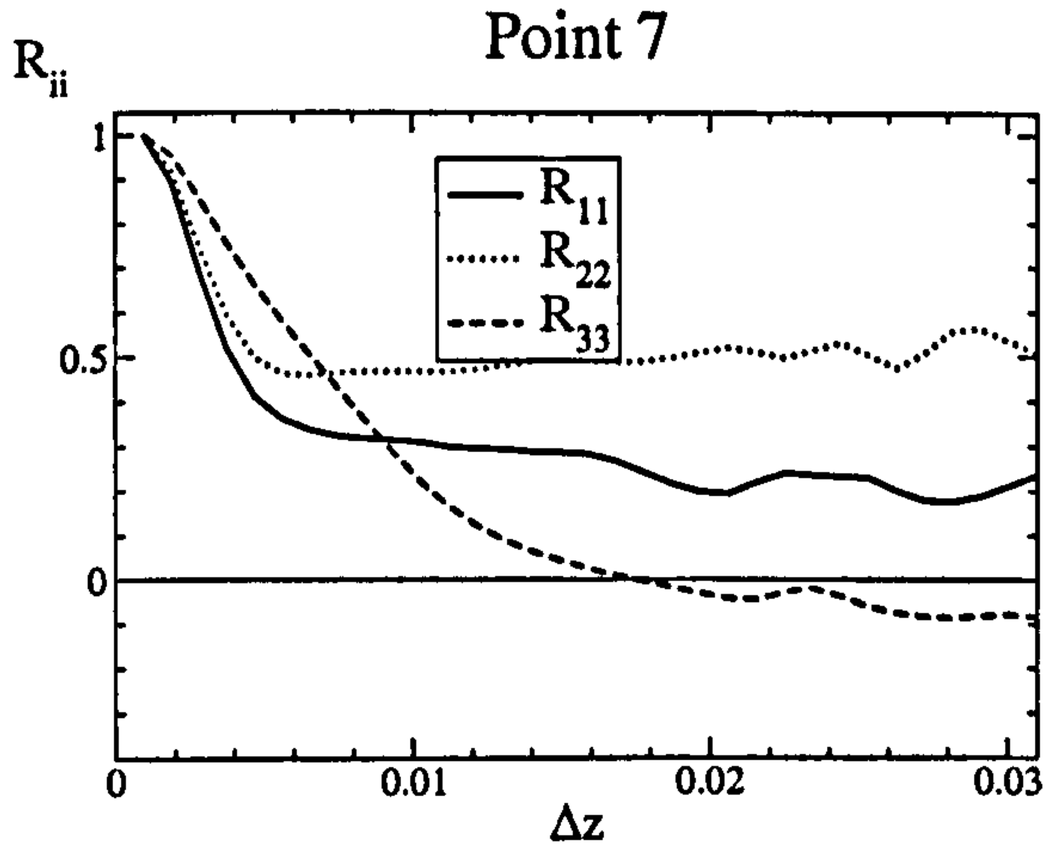

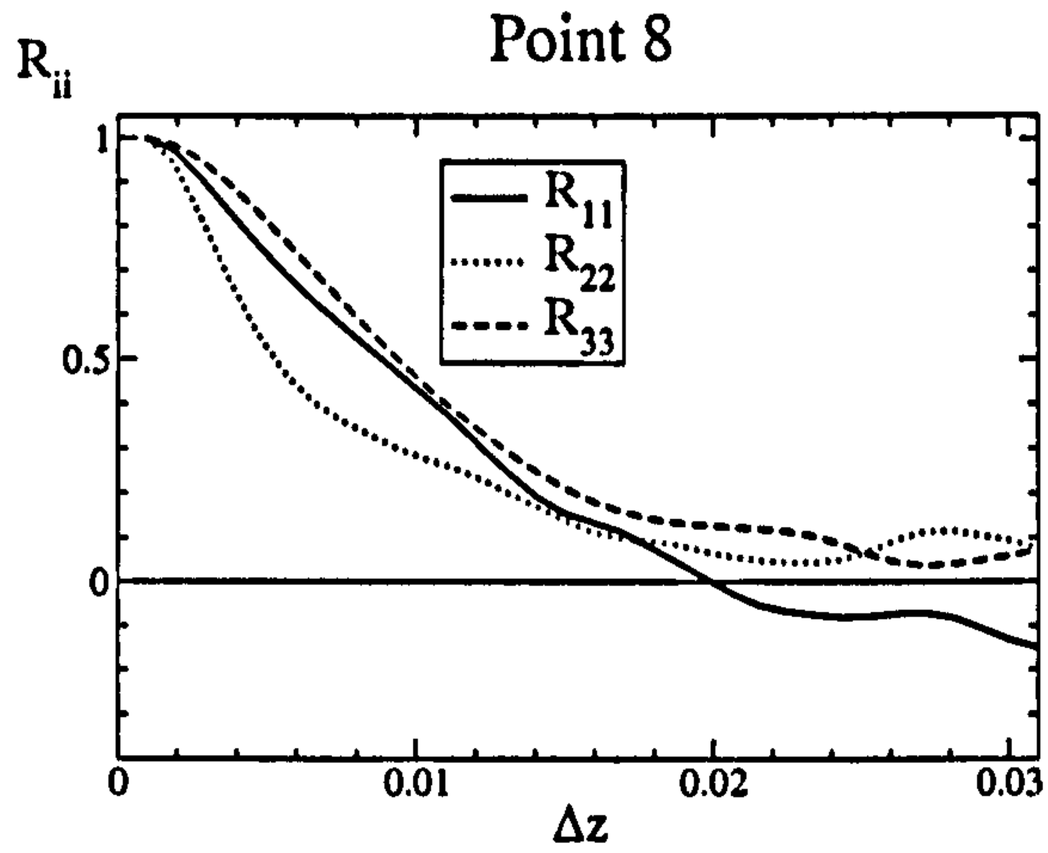

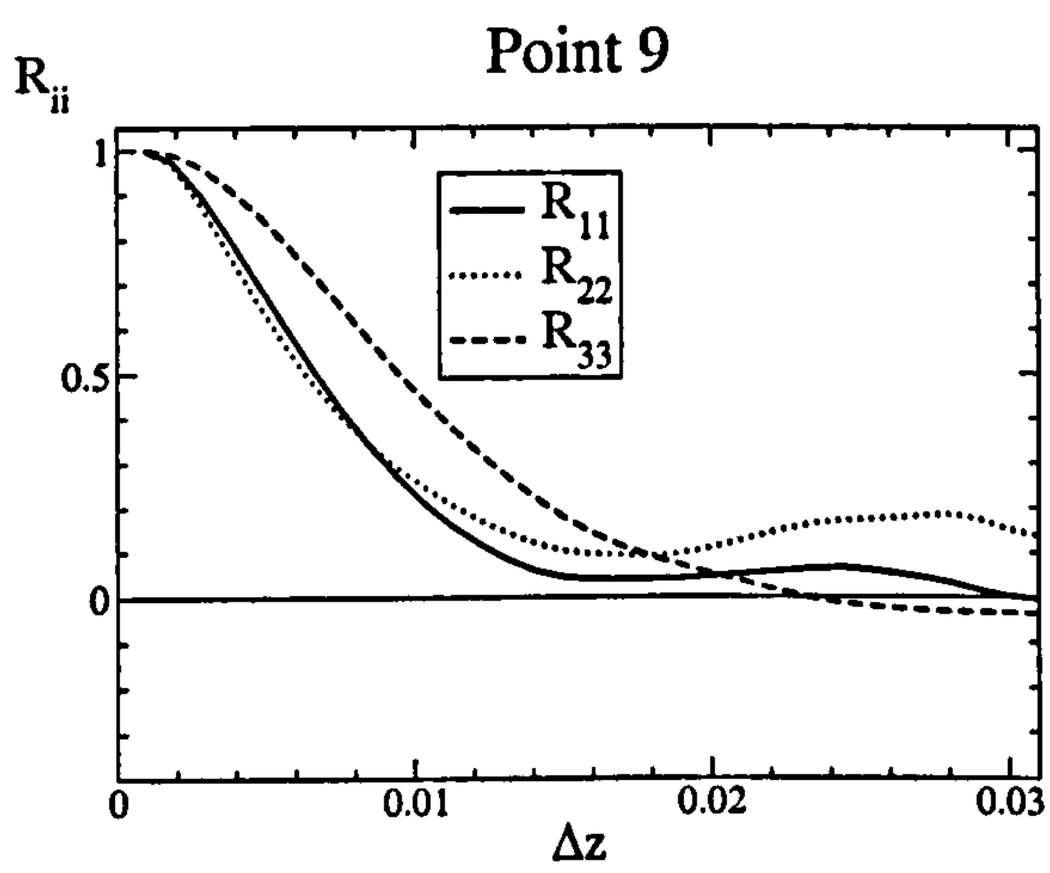

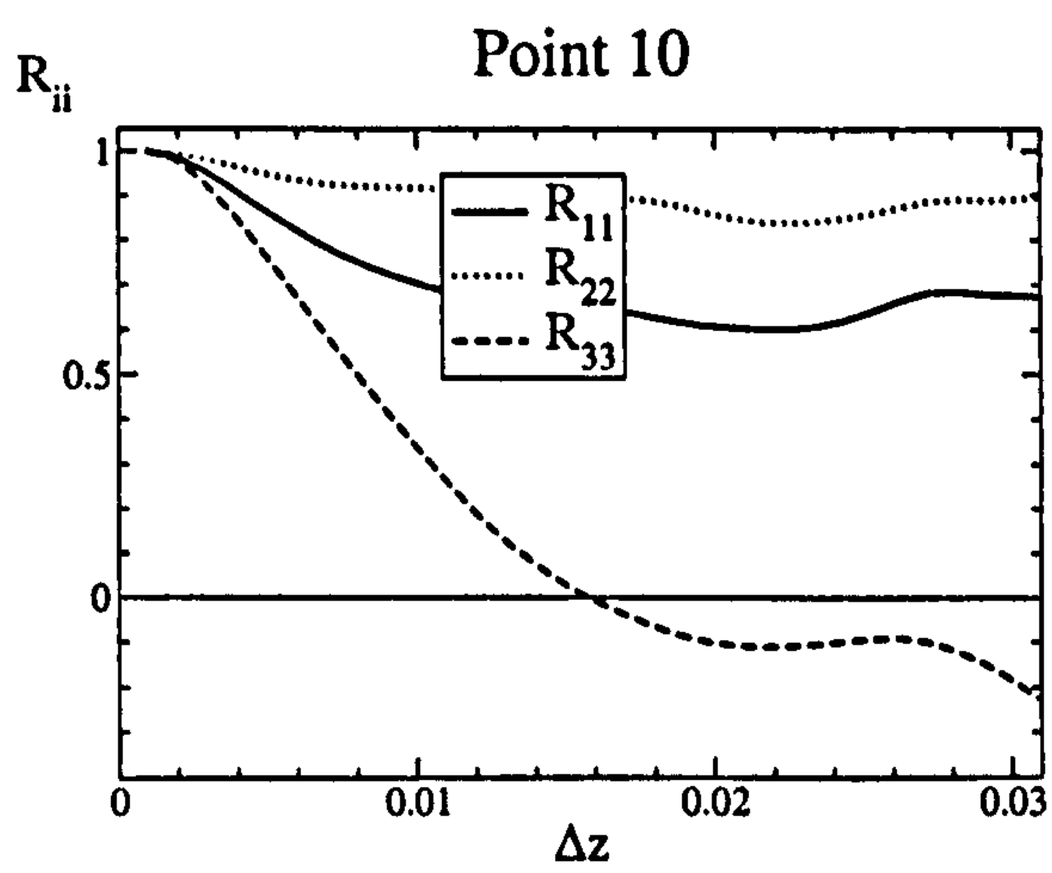

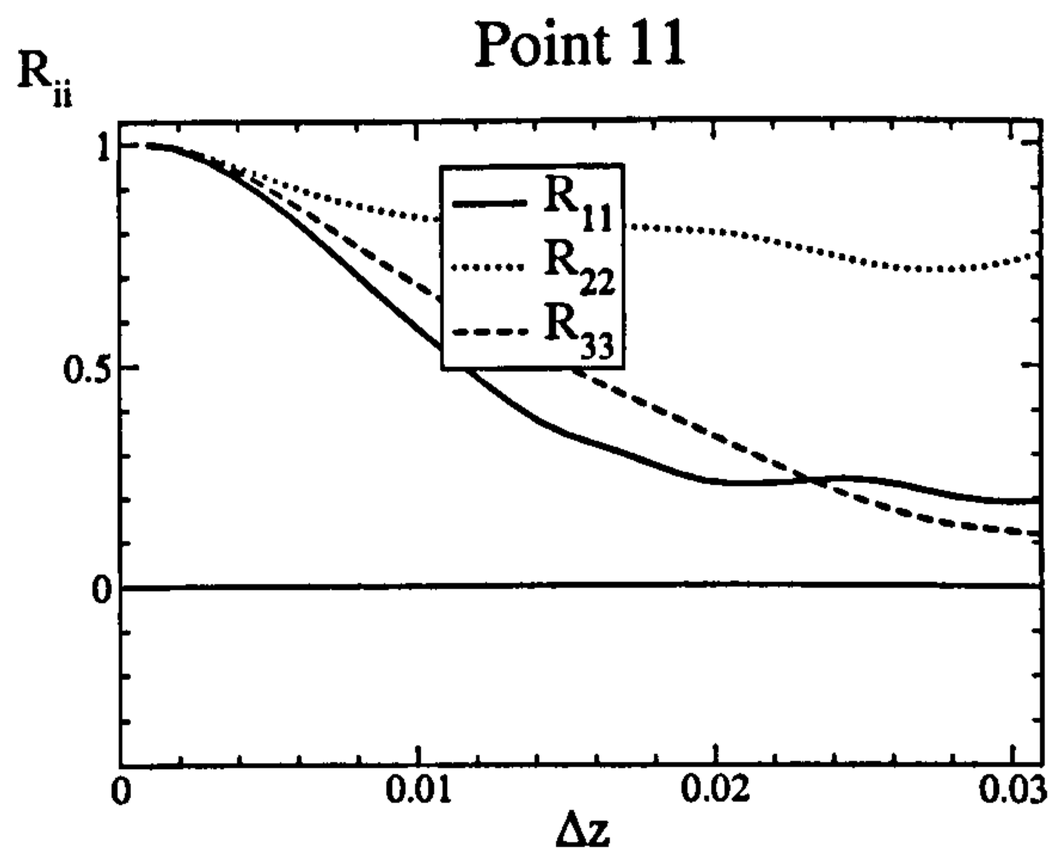

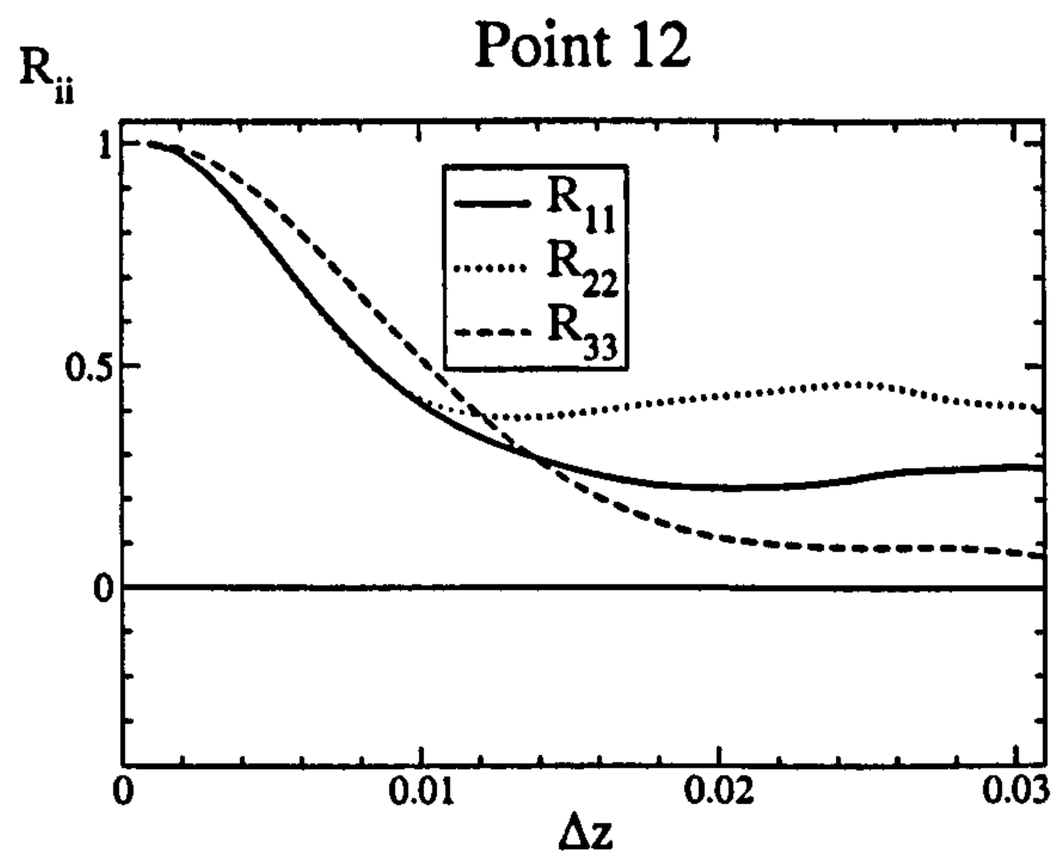

Figure 8.43: Spanwise two-point correlations at locations 7 to 12 (see Figure 8.39) for Comp. 18 (see Tables 8.8 and 8.9 for a description of the computations).

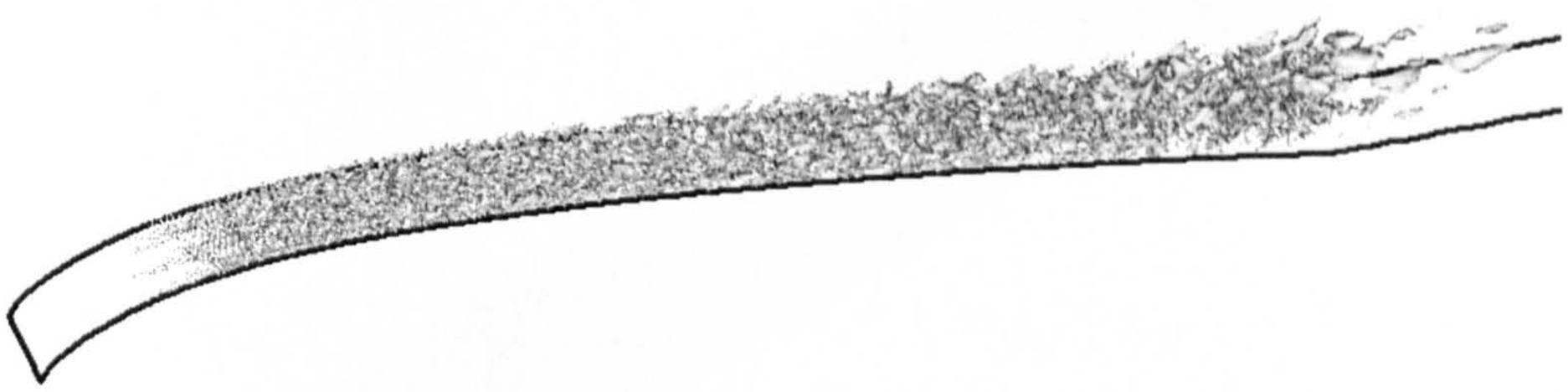

Figure 8.44: Iso–contours of spanwise fluctuations ($w' = -0.07$) for Comp. 18 (see Tables 8.8 and 8.9 for a description of the computations).

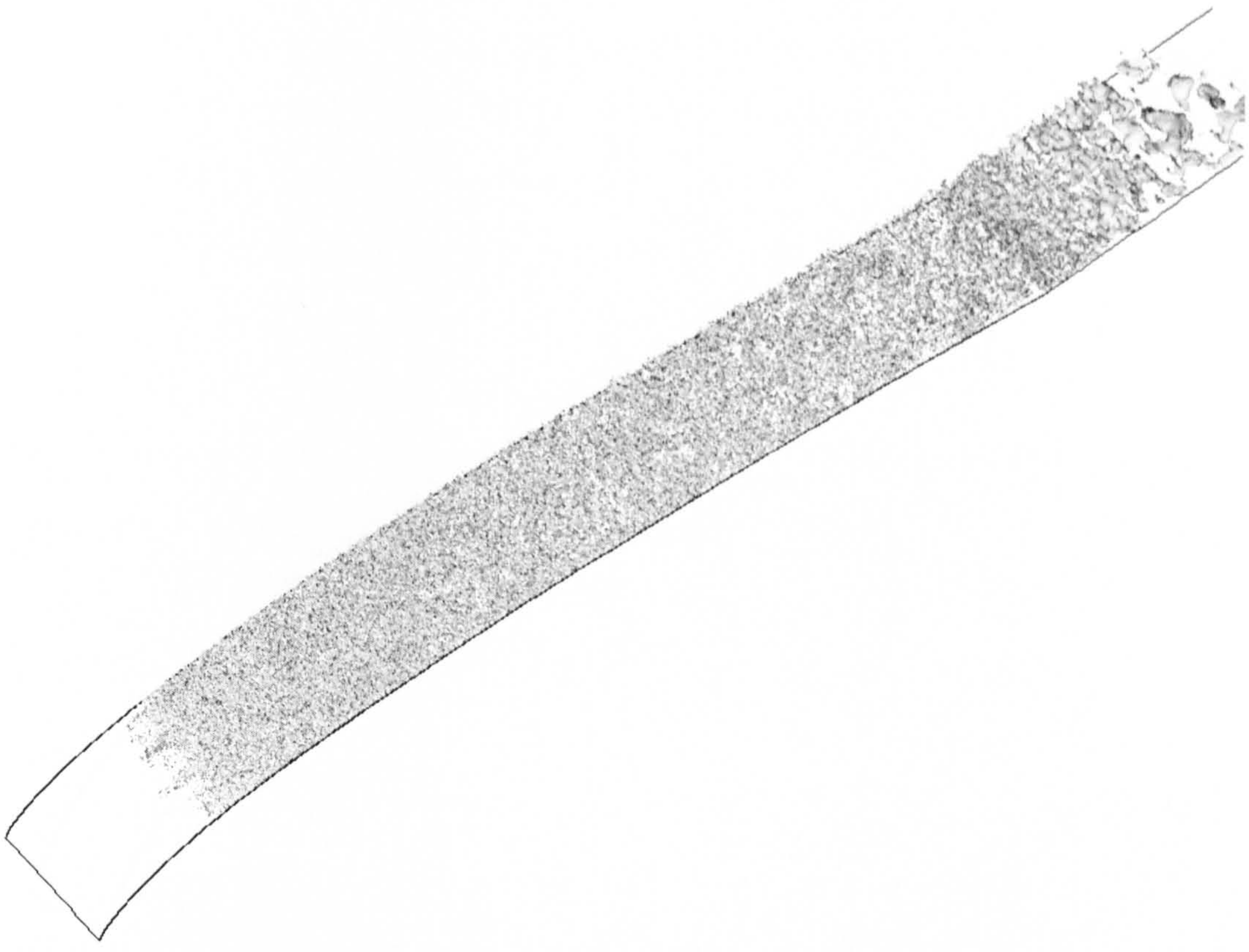

Figure 8.45: Iso–contours of spanwise fluctuations ($w' = -0.07$) for Comp. 19 (see Tables 8.8 and 8.9 for a description of the computations).

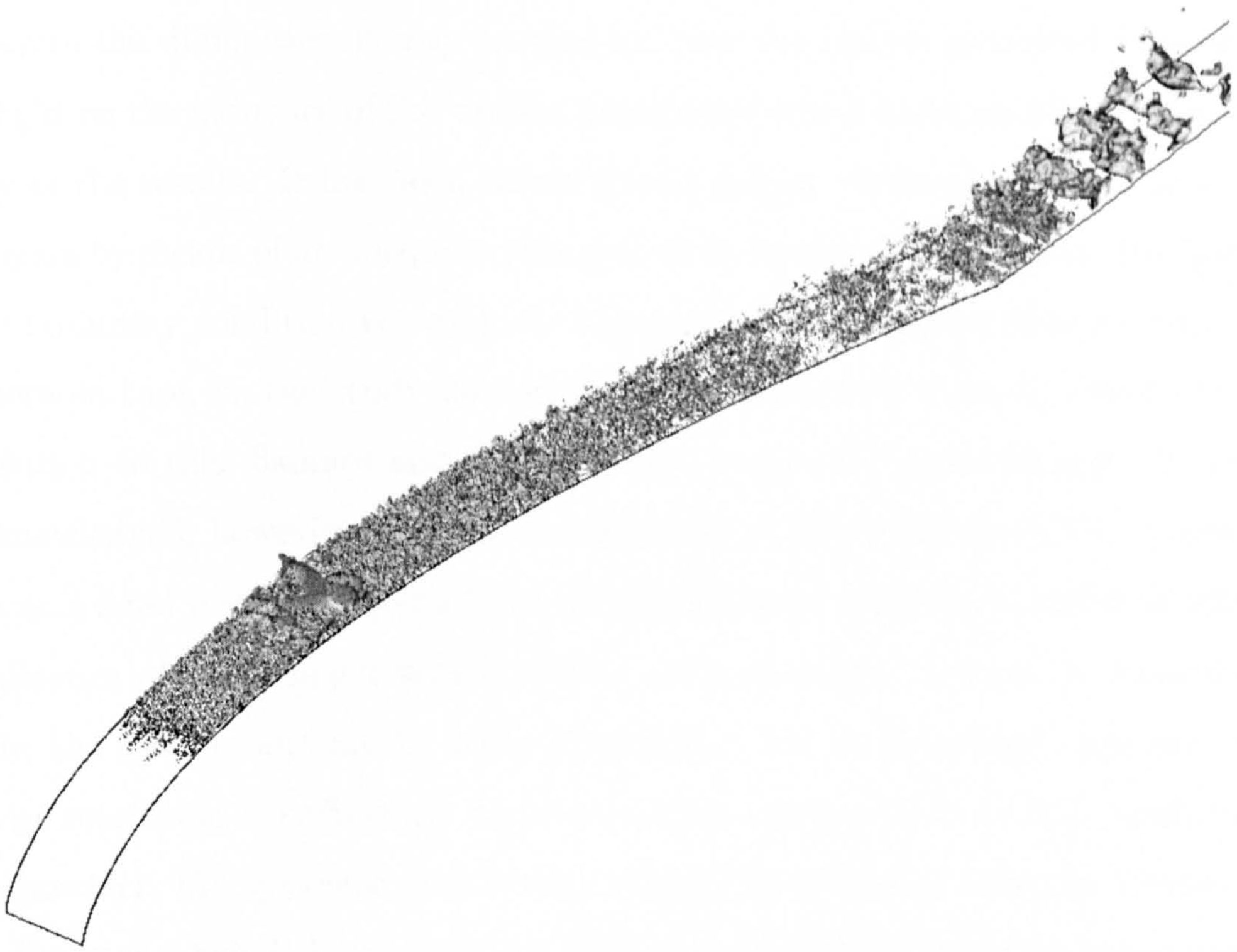

Figure 8.46: Iso–contours of pressure fluctuations ($p' = -0.021$) for Comp. 19 (see Tables 8.8 and 8.9 for a description of the computations).

8.5 Concluding remarks

Overall, the results achieved have been disappointing. The main obstacles appear all to be due to insufficient resolution, including the presence of numerical oscillations. Although the introduction of artificial dissipation reduces the level of oscillations, the manner in which damping is introduced has been observed to exert a very strong influence on the predicted flow features, and the practice must, therefore, be viewed with considerable suspicion.

Despite the difficulties, it may be claimed that the results presented have shed some light on the influence of the various parameters which exert an influence on the quality of the results. It has been shown that a proper representation of the near-wall region by means of an adequate grid and/or by means of an adequate treatment of wall boundary condition is extremely important. The spanwise distance requires considerable care, as the study has provided indications of a strong sensitivity of the solution to this distance and the resolution within the spanwise slab. It must be acknowledged, however, that the investigation of the influence of the spanwise extent at a fixed resolution needs to be accompanied by additional studies in which the influence of increasing resolution for a given spanwise distance is quantified. Strictly, the former can only be safely identified if, for each spanwise distance, the spanwise resolution is sufficiently high to eliminate dependence on that resolution. Since, however, the spanwise grid density cannot be separated from the density in other directions, this is bound to be a difficult undertaking requiring many costly simulations.

The last simulation presented in this chapter was performed on a grid of $2816 \times 128 \times 64 \approx 23 \cdot 10^6$ cells. This very large computation, while not executed to its end, gives a graphic indication of the challenges that are faced when simulating such flows. While the present x–grid probably needs very few modifications to be completely adequate for a highly–resolved LES, the near–wall cell size in the y–direction need to be reduced so that $y^+ = O(1)$. The spanwise discretisation should be three to four times finer than the present level. This grid could not be afforded in the present study. Even with such a fine grid, success would rely on state–of–the–art

numerical schemes in conjunction with advanced modelling of the subgrid scales and of the wall regions and advanced numerical strategies such as unstructured meshes or zonal approaches to limit the computational expense to an affordable level.

The present chapter thus demonstrates the limits of LES as an engineering tool in aeronautical flows. At high Reynolds numbers, it will remain a research tool for some time to come. At the industrial level, it is unlikely that it will ever become a design tool although it may well find, and indeed it has done already, a niche for research and development for flows in which unsteadiness is the driving force behind the phenomena studied, for example aero–acoustics.

Chapter 9

Conclusions and outlook

The main objective of the present research was to identify the capabilities and limitations of LES as a means of predicting separation from curved surfaces at high Reynolds numbers, the ultimate practical focus being the onset of stall on high–lift aerodynamics. The route taken was to investigate a rational sequence of flows, starting from fully–developed–channel flow and ending in a single–element aerofoil at high incidence and high Reynolds number. Questions needed to be answered about the resolution level and the nature of the approximations that could be tolerated to achieve a correct representation in applying LES to complex separated flows. These investigations were carried out using a highly–efficient parallel LES algorithm into which a wide range of models and numerical practices were introduced.

In the first part of the research, a range of subgrid–scale models and near–wall approximations, based on wall functions, were investigated in fully–developed channel flows at a range of Reynolds numbers, Re_τ, up to 1050. The objective was to select practices that would be applied in the following stages of the study in which separated flows were considered. Apart from quantifying performance by comparisons of the solutions obtained to available benchmark data, an analysis was undertaken to quantify the relative contributions of numerical and subgrid–scale–modelling errors. The investigation revealed substantial differences among a variety of subgrid–scale models, both in terms of the level of the SGS viscosity in the flow away from the wall and the asymptotic variation of the viscosity at the wall. Of

the models investigated, the dynamic Smagorinsky and the WALE models were shown to distinguish themselves by their correct asymptotic behaviour. However, the latter tended to give viscosity levels by up to one order of magnitude lower than the former variants. Overall, the WALE model was judged to perform best, in terms of the accuracy it yielded and its simplicity. The error analysis, carried out for the Smagorinsky model, first in its original form and then with the addition of a damping function, provided indications that modelling and numerical errors tended to partially cancel each other, thus reducing the overall error.

The study demonstrated further that, in channel flow, near–wall approximations, based on wall function, yielded substantial savings in computer resources and did not degrade dramatically the ability of LES to return both the mean flow and the second moments in the inner region of the channel flow. Similarly, the wall functions gave credible levels of wall shear stress. However, the resolution of the flow structure close to the wall was obviously affected. Of the near–wall approximations, one particular form, proposed by Werner and Wengle [235], was found to give the best results, and was judged the most promising for further application in more complex conditions. The study clarified that, whatever model or approximation is adopted, mesh resolution remained a critical issue. In particular, the cell–aspect ratio must be chosen so that it allows the adequate resolution of the structures in the near–wall region. Insufficient resolution was demonstrated to lead to a degradation in the distribution of the turbulence energy among the normal stresses, resulting in an excessively strong streamwise component at the expense of the other two components. None of the subgrid-scale models tested were able to compensate for this lack of resolution.

The second part of the research focused on a massively separated flow in a channel with periodically arranged curved constrictions on one wall. The choice of a confined case was motivated by the wish to study the flow, especially the separation process, in great detail, but at tenable resource requirements. The absence of extensive and reliable data which could be used as a reference to study the effectiveness of the approximations and the response to variable resolution prompted the generation of these data as part of this study. The data were obtained from a highly–resolved

LES with a mesh containing 4.6 millions nodes, with the region at the lower wall resolved almost to DNS level. The results of this simulation were shown to agree closely with those of Mellen et al [150], thus inspiring confidence in their validity. Apart from providing the reference data, this simulation offered the opportunity to undertake an in–depth study of the physics of the separation and reattachment processes. Thus, budgets for the second moments as well as much flow–structure information were extracted.

The simulation revealed substantial spatial and temporal variations in the location of both the separation and reattachment lines. The near–wall flow, whether in the separated region or following reattachment, was found not to adhere even remotely to the log law, pointing to the likely difficulties in using near–wall approximations based on this law. Large streamwise–oriented structures were seen to impinge on the windward side of the hill. This effect, known as *splatting*, was responsible for the energy transfer from the streamwise to the spanwise normal stress, giving rise to very high levels of the latter. This energy transfer was shown to take place through the pressure–strain interaction. In the shear layer bordering the upper part of the recirculation region, a succession of large rollers, formed through Kelvin–Helmholtz instability and separated by streamwise vortices originating from helical pairing, were found. These structures were convected beyond the recirculation zone before breaking up. Large streamwise–oriented, inclined structures were also observed beyond reattachment that tended to be transported over the downstream hill.

A second and important part of the investigation of this separated flow was concerned with the study of influence of the near–wall approximations, subgrid–scale models and grid resolution by reference to the newly produced data. These simulations, performed on coarser grids than the one used for the highly–resolved LES, highlighted the importance of an adequate streamwise resolution, especially in the region of separation where the streamwise cell size effectively limited the accuracy of the prediction. The results were found equally sensitive to the details of the numerical implementation of the wall laws, rather than to the precise shape of the velocity profiles upon which these approximations were formulated. Overall, the

best performance was obtained using the Werner–Wengle formulation. The influence of the subgrid–scale models was found to be relatively weak, with the WALE and the Mixed–Scale models giving the best results.

The third and final case considered was the flow around an aerofoil at near–stall conditions at a Reynolds number of $2.1 \cdot 10^6$, based on chord length and freestream velocity, at an angle of attack of 13.3^o. This case turned out to be extremely challenging, arguably beyond current capabilities. A wide range of phenomena occurs in this flow at disparate scales, including transition and separation. This particular configuration was selected because it was judged to be representative of cases to which LES would need to be applied in the context of practical aerodynamics, and because of the availability of well–regarded experimental data.

The results obtained for this flow were rather disappointing, the main obstacles being the lack of sufficient resolution and the presence of numerical oscillations which required control by introducing artificial dissipation. Although a sequence of extremely fine grids were used, none gave a satisfactory representation. While transition was resolved with the finest grid, no simulation resolved the separation on the rear suction side.

Due to the difficulty of reproducing the essential features of the experimental results, simulations in which a range of different parameters were tested could only provide qualitative indicators of their influence. Among these parameters, the spanwise extent was observed to be very influential. On the one hand, a spanwise box of less than 6% of chord was found to generate solutions which were highly dependent on this extent. On the other hand, a large spanwise box, coupled with the need to maintain acceptable grid–aspect ratio, tended to push computer resources to unacceptable heights.

With the use of wall–function–based near–wall approximations initially discounted, if only because of the importance of resolving transition, the final simulation performed for this configuration indicated that, for a spanwise extent of 6% of chord, a mesh of about 80 millions nodes would be required to obtain a satisfactory solution that might match the experimental results. In addition to the fact that there is no certainty that such a simulation would actually match the experiment, a computa-

tion of this magnitude, in terms of the resources needed, was unaffordable. The only hope of achieving adequate resolution at affordable expense rests on the combined use of superior numerical schemes and approaches such as zonal and/or unstructured meshing strategies that would permit a flexible concentration of the cells in specific regions of interest, i.e. at the wall on the suction side of the aerofoil.

This last test–case thus demonstrated the limits of LES as an engineering tool in aerodynamics. At high Reynolds numbers, it will, for the time being, remain a research aid, and it is unlikely that it will become a design tool for aeronautical applications for many years, if ever. It may however find, and indeed it has already found, a niche in research and development for the study of particular aspects such as aero–acoustics and aero–elasticity, where unsteadiness is the driving force behind the phenomena of interests.

More generally, while it seems that LES has reached a certain degree of maturity at low and relatively moderate Reynolds numbers, it is clearly not the case for higher Reynolds numbers, especially in complex geometries where phenomena with a wide range of scales occur. Several aspects still need further development before LES for such flows become routinely feasible. A much better control of the cell distribution across the domain is highly desirable, as this is crucial to reducing the computational cost. Zonal strategies, unstructured grids and adaptive meshing are all techniques that can achieve this. While these are available in most commercial CFD software, they are not often applied in research because the accuracy they offer is often inadequate for LES applied to flows which are very sensitive to near-wall processes. More accurate, energy–conserving schemes that can easily be implemented in the framework of complex geometries are thus needed to reduce the level of errors and suppress the numerical oscillations similar to those seen in the aerofoil study.

Another route to the reduction of computational costs is through the use of sophisticated wall treatments able to deal with complex near–wall phenomena, such as separation, through a combination of better numerical techniques, adequate hybrid RANS/LES methods and higher computing power. Finally, there exists a need for further reliable data sets for flows at moderately high Reynolds numbers, featuring complex physical phenomena in relatively simple geometries that can be simulated

with sufficiently high resolution to yield reference data. Examples include separated aerofoils at Reynolds numbers of order 10^5 and highly $3D$ flows around curved obstacles, again at Reynolds number of order 10^4-10^5. Such data will allow approximations to be studied at lower resolution, as done in the case of the hill flow in the present study, with much greater confidence that can be attained for the high–lift A-aerofoil at the Reynolds number of $2.1 \cdot 10^6$.

Appendix A

Filters in large eddy simulation

In LES, three different filters are commonly used:

- the Top-Hat Filter known also as the Box filter:

$$\text{in physical space} \qquad G(x-x') = \begin{cases} \frac{1}{\Delta} & \text{if} \quad |x-x'| \leq \frac{\Delta}{2} \\ 0 & \text{otherwise} \end{cases} \tag{A.1}$$

$$\text{in spectral space} \qquad \widehat{G}(k) = \frac{sin\left(k\frac{\Delta}{2}\right)}{k\frac{\Delta}{2}} \tag{A.2}$$

- the Gaussian filter:

$$\text{in physical space} \qquad G\left(x-x'\right) = \sqrt{\frac{6}{\pi\Delta^2}} exp\left(-\frac{6\left(x-x'\right)^2}{\Delta^2}\right) \tag{A.3}$$

$$\text{in spectral space} \qquad \widehat{G}(k) = exp\left(-\frac{k^2\Delta^2}{24}\right) \tag{A.4}$$

- the Sharp Fourier Cut-Off filter:

$$\text{in physical space} \qquad G\left(x-x'\right) = \frac{sin\left(k_c\left(x-x'\right)\right)}{k_c\left(x-x'\right)} \quad \text{with} \quad k_c = \frac{\pi}{\Delta} \tag{A.5}$$

$$\text{in spectral space} \qquad \widehat{G}(k) = \begin{cases} 1 & \text{if} \quad k \leq \frac{\pi}{\Delta} \\ 0 & \text{otherwise} \end{cases} \tag{A.6}$$

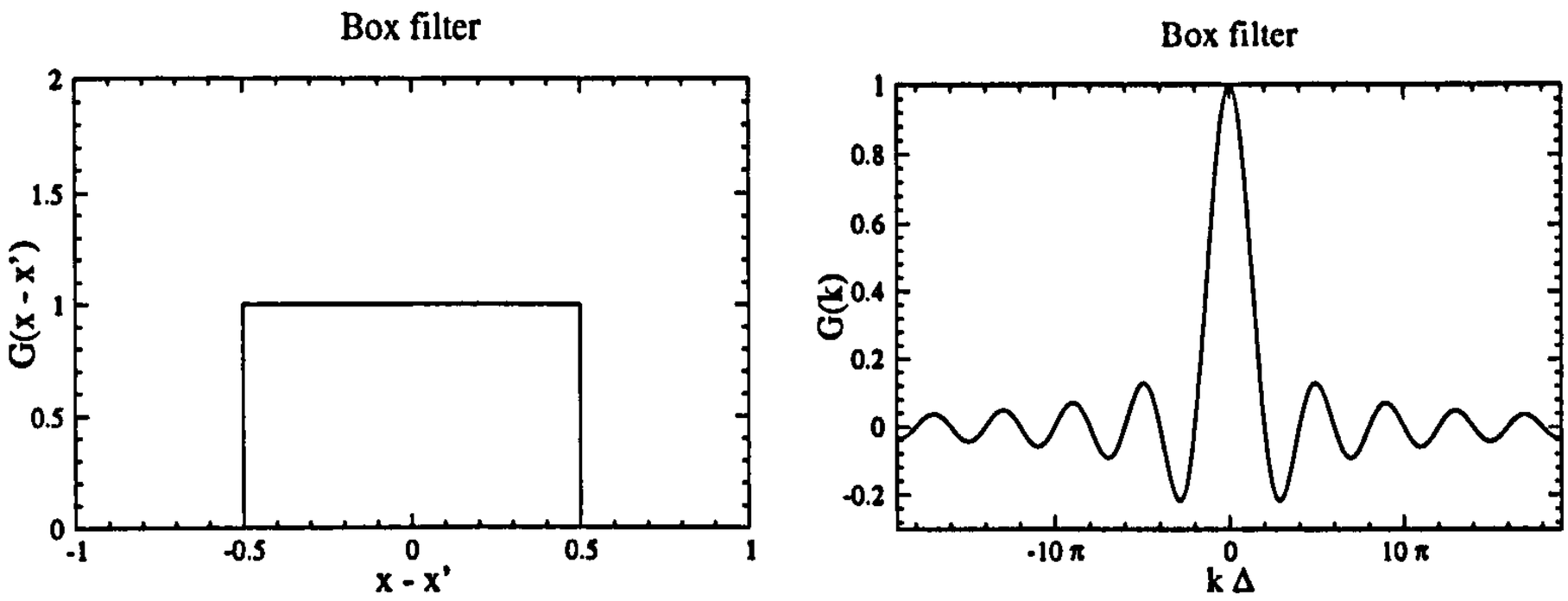

Figure A.1: The Box Filter: left: in physical space; right: in spectral space.

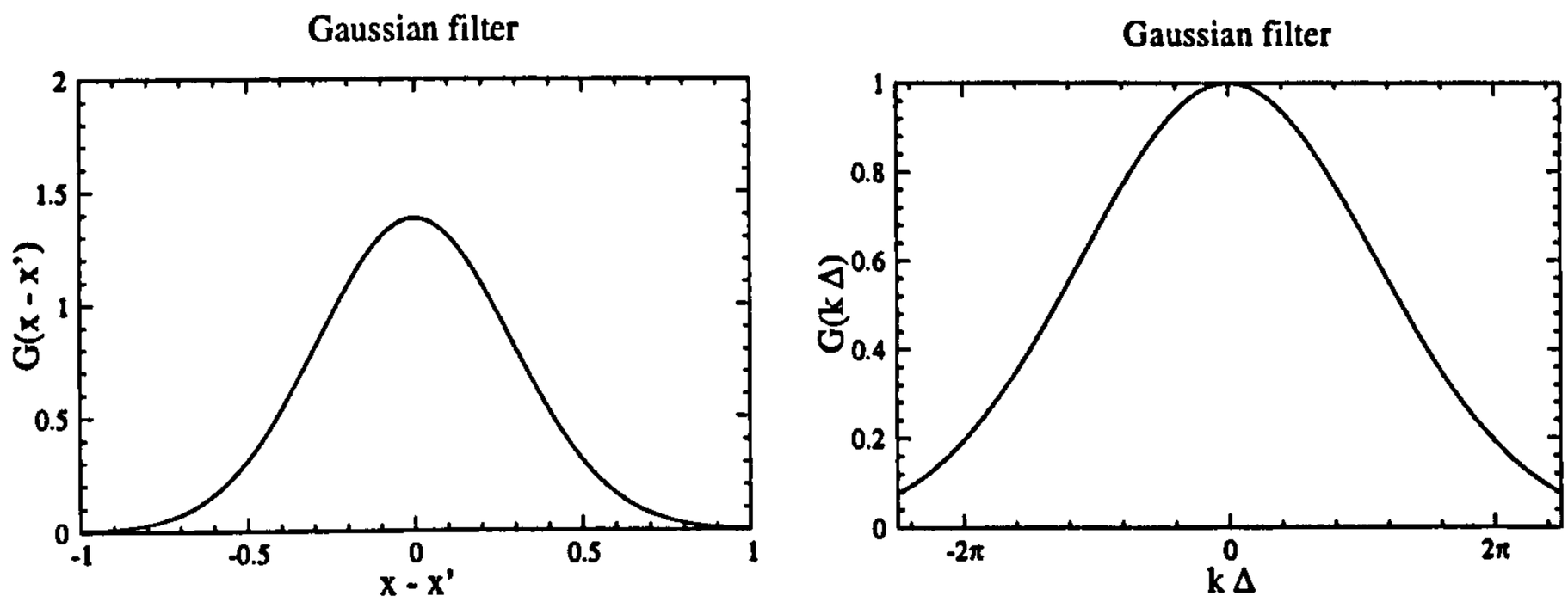

Figure A.2: The Gaussian Filter: left: in physical space; right: in spectral space.

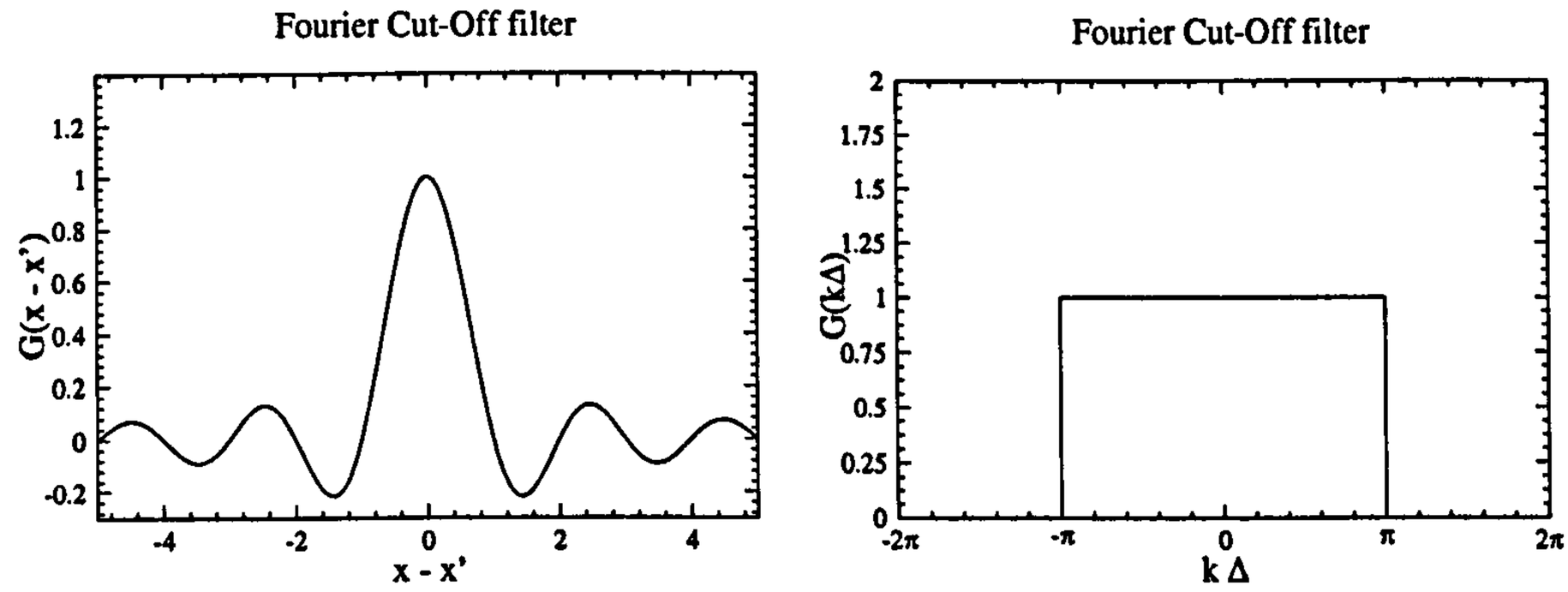

Figure A.3: The Fourier Cut-Off Filter: left: in physical space; right: in spectral space.

Appendix B

Methods for the resolution of numerical systems

B.1 Eigenvalues and eigenvectors for partial diagonalisation

If it is assumed that the discretised Poisson problem is written as:

$$a_i x_{i-1} + b_i x_i + c_i x_{i+1} = S_i \qquad i = 1 \ldots n \tag{B.1}$$

and periodic boundary conditions are used:

$$\begin{cases} x_0 = x_n \\ \\ x_{n+1} = x_1 \end{cases} \tag{B.2}$$

Then, the eigenvalues associated to System (B.1) are:

$$\begin{cases} \lambda_1 = 0 \\ \\ \lambda_{2i} = \lambda_{2i+1} = -4\, sin^2 \frac{i\pi}{n} \quad \text{if n is even} \\ \\ \lambda_n = -4 \end{cases} \tag{B.3}$$

where $i = 1 \ldots \frac{n-1}{2}$.

The corresponding eigenvectors are:

$$\begin{cases} r_j^1 = 0.5 & j = 1, n \\ r_j^{2i} = cos\frac{2ij\pi}{n} & j = 1 \ldots n \quad i = 1 \ldots \frac{n}{2} - 1 \\ r_j^{2i+1} = sin\frac{2ij\pi}{n} & j = 1 \ldots n \quad i = 1 \ldots \frac{n}{2} - 1 \\ r_j^n = \frac{1}{2}(-1)^j & j = 1 \ldots n \end{cases} \tag{B.4}$$

The solution writes as:

$$x_j = \frac{1}{2}\hat{x}_1 + \sum_{i=1}^{n/2-1} \left[\hat{x}_{2i}\, cos\frac{2ij\pi}{n} + \hat{x}_{2i+1}\, sin\frac{2ij\pi}{n} \right] + \frac{1}{2}\hat{x}_n\,(-1)^j \tag{B.5}$$

which is a Fourier serie expansion whose coefficients are corresponding to the eigenvectors (B.4) of System (B.1).

B.2 Method of Samarskii and Nikolaev

Say that the discrete system is;

$$a_i\phi_{i-1} + b_i\phi_i + c_i\phi_{i+1} = S_i \qquad \text{with} \quad i = 1 \ldots n \tag{B.6}$$

If the system is periodic, then:

$$\begin{aligned} a_i &= a_{i+n} & b_i &= b_{i+n} \\ c_i &= c_{i+n} & S_i &= S_{i+n} \end{aligned} \tag{B.7}$$

and the solution will also be periodic:

$$\phi_n = \phi_{n+1} \tag{B.8}$$

The system writes:

$$\begin{bmatrix} b_1 & c_1 & & \dots & a_1 \\ a_2 & b_2 & c_2 & \dots & \\ & \dots & & \dots & \\ & \dots & a_{n-1} & b_{n-1} & c_{n-1} \\ c_n & & \dots & a_n & b_n \end{bmatrix} \begin{bmatrix} \phi_1 \\ \phi_2 \\ \\ \phi_{n-1} \\ \phi_n \end{bmatrix} = \begin{bmatrix} S_1 \\ S_2 \\ \\ S_{n-1} \\ S_n \end{bmatrix} \tag{B.9}$$

If the system has one solution, it is a linear combination of two functions u_i and v_i such that:

$$\phi_i = u_i + \phi_1 v_i \qquad i = 1 \dots n+1 \tag{B.10}$$

where u_i is the solution of:

$$\begin{cases} a_i u_{i-1} + b_i u_i + c_i u_{i+1} = S_i \qquad i = 2 \dots n \\ u_1 = 0 \\ u_{n+1} = 0 \end{cases} \tag{B.11}$$

and v_i, the solution of:

$$\begin{cases} a_i v_{i-1} + b_i v_i + c_i v_{i+1} = 0 \qquad i = 2 \dots n \\ v_1 = 0 \\ v_{n+1} = 0 \end{cases} \tag{B.12}$$

and ϕ_1 is determined from $i = 1$:

$$a_1 (u_n + \phi_1 v_n) + b_1 phi_1 + c_1 (u_2 + \phi_1 v_2) = S_1 \tag{B.13}$$

Appendix C

Assembling the turbulence energy and Reynolds-stress budgets

The energy and Reynolds stress budgets presented in Section 5.4 contain a large number of terms and, when the need to evaluate each of these terms is faced, a large number of quantities has to be recorded. The object of this appendix is to list the quantities that require recording and highlight some simplifications that can be taken advantage of mainly because the flows studied in this work are homogneous in the spanwise direction z. The collection of these data and the time-averaging procedure (denoted by $< \cdot >$) are performed as the computation goes on. Once the end of the computation is reached, the terms of the budgets are then assembled on a $2D$ plan using the quantities recorded. Spatial derivatives are evaluated through a second-order centred colocated finite-volume approximation.

Spanwise homogeneity means that:

$$\frac{\partial \langle \cdot \rangle}{\partial z} = 0 \tag{C.1}$$

The quantities recorded in the course of the computation, are thus:

$$< u > , < v > , < w > , < p > \tag{C.2}$$

$$
\begin{array}{c}
< uu > , < vv > , < ww > , \\
< uv > , < uw > , < vw > , \\
< up > , < vp > , < wp >
\end{array}
\tag{C.3}
$$

$$
< uuu > , < vvv > , < www > , < uuv > , < uuw > , < uvw > , \\
< uvv > , < uww > , < vvu > , < vvw > , < wwu > , < wwv >
\tag{C.4}
$$

$$
\begin{array}{c}
< p\frac{\partial u}{\partial x} > , < p\frac{\partial u}{\partial y} > , < p\frac{\partial u}{\partial z} > , \\
< p\frac{\partial v}{\partial x} > , < p\frac{\partial v}{\partial y} > , < p\frac{\partial v}{\partial z} > , \\
< p\frac{\partial w}{\partial x} > , < p\frac{\partial w}{\partial y} > , < p\frac{\partial w}{\partial z} >
\end{array}
\tag{C.5}
$$

$$
\begin{array}{c}
< \frac{\partial u}{\partial x}\frac{\partial u}{\partial x} > , < \frac{\partial u}{\partial y}\frac{\partial u}{\partial y} > , < \frac{\partial u}{\partial z}\frac{\partial u}{\partial z} > , \\
< \frac{\partial v}{\partial x}\frac{\partial v}{\partial x} > , < \frac{\partial v}{\partial y}\frac{\partial v}{\partial y} > , < \frac{\partial v}{\partial z}\frac{\partial v}{\partial z} > , \\
< \frac{\partial w}{\partial x}\frac{\partial w}{\partial x} > , < \frac{\partial w}{\partial y}\frac{\partial w}{\partial y} > , < \frac{\partial w}{\partial z}\frac{\partial w}{\partial z} >
\end{array}
\tag{C.6}
$$

$$
\begin{array}{c}
< \frac{\partial u}{\partial x}\frac{\partial v}{\partial x} > , < \frac{\partial u}{\partial y}\frac{\partial v}{\partial y} > , < \frac{\partial u}{\partial z}\frac{\partial v}{\partial z} > , \\
< \frac{\partial u}{\partial x}\frac{\partial w}{\partial x} > , < \frac{\partial u}{\partial y}\frac{\partial w}{\partial y} > , < \frac{\partial u}{\partial z}\frac{\partial w}{\partial z} > , \\
< \frac{\partial v}{\partial x}\frac{\partial w}{\partial x} > , < \frac{\partial v}{\partial y}\frac{\partial w}{\partial y} > , < \frac{\partial v}{\partial z}\frac{\partial w}{\partial z} >
\end{array}
\tag{C.7}
$$

Appendix D

Description of the hill shape

The present appendix contains the mathematical description of the shape of the hill employed in the geometry studied in Chapter 7. This shape is identical to the one used by Almeida et al [5], and its description of this shape can also be found in the Ercoftac database, at `http://fluindigo.mech.surrey.ac.uk/database/`.

The functions describing half the hill are given in Table D.1 in which all dimensions are quoted in mm. The hill height is equal to 28 mm while its half-basis has a length of 54 mm. The half hill is represented in Figure D.1.

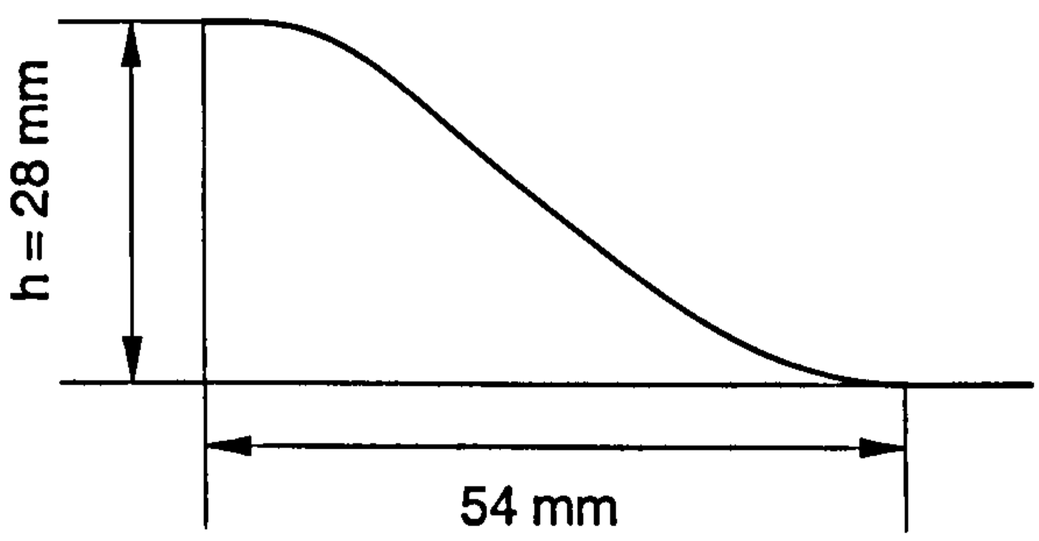

Figure D.1: Representation of an half hill.

x_{start}	x_{stop}	a_0	a_1
0	9	$2.8 \cdot 10^{1}$	0
9	14	$2.507355893131 \cdot 10^{1}$	$9.754803562315 \cdot 10^{-1}$
14	20	$2.579601052357 \cdot 10^{1}$	$8.206693007457 \cdot 10^{-1}$
20	30	$4.046435022819 \cdot 10^{1}$	-1.379581654948
30	40	$1.792461334664 \cdot 10^{1}$	$8.743920332081 \cdot 10^{-1}$
40	54	$5.639011190988 \cdot 10^{1}$	-2.010520359035

x_{start}	x_{stop}	a_2	a_3	$h(x)$
0	9	$6.775070969851 \cdot 10^{-3}$	$-2.124527775800 \cdot 10^{-3}$	$min(28, h_1(x))$
9	14	$-1.016116352781 \cdot 10^{-1}$	$1.889794677828 \cdot 10^{-3}$	h_1
14	20	$-9.055370274339 \cdot 10^{-2}$	$1.889794677828 \cdot 10^{-3}$	h_1
20	30	$1.945884504128 \cdot 10^{-2}$	$-2.070318932190 \cdot 10^{-4}$	h_1
30	40	$-5.567361123058 \cdot 10^{-2}$	$6.277731764683 \cdot 10^{-4}$	h_1
40	54	$1.644919857549 \cdot 10^{-2}$	$2.674976141766 \cdot 10^{-5}$	$max(0, h_1(x))$

Table D.1: Spline describing the hill shape ($h_1(x) = a_0 + a_1x + a_2x^2 + a_3x^3$).

Bibliography

[1] ABBA, A., CERCIGNIANI, C., VALDETTARO, L., AND ZANINI, P. LES of turbulent thermal convection. In *Direct and Large Eddy Simulations II* (1997), J.-P. Chollet, P. Voke, and L. Kleiser, Eds., Kluwer Academic, pp. 147–156.

[2] AKSELVOLL, K., AND MOIN, P. Large eddy simulation of a backward facing step flow. In *Engineering Turbulence Modelling and Experiments 2* (1993), W. Rodi and F. Martelli, Eds., Elsevier Science, pp. 303–314.

[3] AKSELVOLL, K., AND MOIN, P. Large eddy simulation of turbulent confined coannular jets and turbulent flow over a backward facing step. Tech. Rep. TF-63, Department of Mechanical Engineering, Stanford University, 1995.

[4] AKSELVOLL, K., AND MOIN, P. Large-eddy simulation of turbulent confined coannular jets. *J. Fluid Mech. 315* (1996), 387–411.

[5] ALMEIDA, G. P., DURÃO, D. F. G., AND HEITOR, M. V. Wake flows behind two-dimensional model hills. *Experimental Thermal and Fluid Science 7*, 1 (1993), 87–101.

[6] ARMENIO, V., AND PIOMELLI, U. A Lagrangian mixed subgrid–scale model in generalized coordinates. *Flow, Turb. and Combust. 65*, 1 (2000), 51–81.

[7] AVITAL, E. Direct and large-eddy simulations of compressible open cavity flows. In *Direct and Large-Eddy Simulation IV* (2001), B. Geurts, R. Friedrich, and O. Métais, Eds., Kluwer Academic, pp. 213–220.

[8] BAGGET, J., JIMÉNEZ, J., AND KRAVCHENKO, A. Resolution requirements in large-eddy simulations of shear flows. In *Annual Research Briefs* (1997), CTR, Stanford, USA, pp. 51–66.

[9] BALARAS, E., AND BENOCCI, C. Subgrid-scale models in finite difference simulations of complex wall bounded flows. In *Applications of Direct and Large Eddy Simulation* (1994), AGARD, pp. 2–1 – 2–6.

[10] BALARAS, E., BENOCCI, C., AND PIOMELLI, U. Two-layer approximate boundary conditions for large-eddy simulations. *AIAA J. 34*, 6 (1996), 1111–1119.

[11] BARAKOS, G., AND DRIKAKIS, D. Unsteady separated flows over manouvring lifting surfaces. *Phil. Trans. Royal Soc. Lond. A 358* (2000), 3279–3291.

[12] BARDINA, J., FERZIGER, J., AND REYNOLDS, W. Improved subgrid-scale models for large-eddy simulations. AIAA Paper 80-1357, 1980.

[13] BARON, F., AND LAURENCE, D. Large eddy simulation of a wall-bounded turbulent jet flow and of a homogeneous shear flow. In *Turbulent Shear Flows 4* (1984), D. Durst and B. Launder, Eds., Springer-Verlag, pp. 4.7–4.12.

[14] BEHZADI, S., AND WATKINS, A. Flow and turbulence modeling in a motored reciprocating engine using a k-ϵ turbulence model. In *Proc. 4th Int. Symp. on Engineering Turbulence Modeling and Measurement* (1999), W. Rodi and D. Laurence, Eds., Elsevier, pp. 279–288.

[15] BELL, J., AND MEHTA, R. Development of a two-stream mixing layer from tripped and untripped boundary. *AIAA J. 28*, 12 (1990), 2034–2042.

[16] BERNARD, R., AND KAPITZA, H. How to discretize the pressure gradients for curvilinear mac grids. *J. Comp. Phys. 99* (1992), 288–298.

[17] BLACKBURN, H., MANSOUR, N., AND CANTWELL, B. Topology of fine-scale motions in turbulent channel flow. *J. Fluid Mech. 310* (1998), 269–292.

[18] BORIS, J., GRINSTEIN, F., ORAN, E., AND KOLBE, R. New insights into large eddy simulation. *Fluid Dynamic Research 10* (1992), 199–228.

[19] BOSCH, G., AND RODI, W. Simulation of vortex shedding past a square cylinder with different turbulence models. *Int. J. Num. Meth. Fluids 28* (1998), 601–616.

[20] BRADBROOK, K., LANE, S., RICHARDS, K., BIRON, P., AND ROY, A. Large eddy simulation of periodic flow characteristics at river channel confluences. *J. of Hydraulic Research 38* (2000), 207–215.

[21] BREUER, M. Large eddy simulation of the subcritical flow past a circular cylinder: numerical and modeling aspects. *Int. J. Numer. Meth. Fluids 28*, 9 (1998), 1281–1302.

[22] BREUER, M. A challenging test case for large eddy simulations: high reynolds number circular cylinder flow. In *Proc. of the 1st Int. Symp. Turb. Shear Flow Phen. I* (1999), S. Banerjee and J. Eaton, Eds., Begell House, pp. 735–740.

[23] BREUER, M., AND RODI, W. Large eddy simulation of turbulent flow through a straight square duct and a 180° bend. In *Direct and Large Eddy Simulation I* (1994), P. Voke, R. Kleiser, and J. Chollet, Eds., vol. 26 of *Fluid Mech. and its Appl.*, Kluwer Academic, pp. 273–285.

[24] BREUER, M., AND RODI, W. Large eddy simulation of complex turbulent flows of practical interest. In *Flow simulation with high performance computers II*, E. Hischel, Ed., vol. 52 of *Notes on numerical fluid mechanics*. Vieweg, 1996, pp. 258–274.

[25] CABOT, W., AND MOIN, P. Approximate wall boundary conditions in the large-eddy simulation of high reynolds number flow. *Flow, Turb. and Combust. 63* (2000), 269–291.

[26] CALHOUN, R. *Numerical investigations of turbulent flow over complex terrain.* PhD thesis, Stanford University, 1998.

[27] CALHOUN, R., AND STREET, R. Turbulent flow over a wavy surface: Neutral case. *Journal of Geophysical Research - Part C - Oceans 106* (2001), 9277–9294.

[28] CARETTO, L., GOSMAN, A., PATANKAR, S., AND SPALDING, D. Two calculation procedures for steady, three dimensional flows with recirculation. In *Proc. 3rd Int. Conf. Numer. Methods Fluid. Dyn.* (1972), Springer-Verlag, pp. 60–68.

[29] CEBECI, T., AND SMITH, A. *Analysis of turbulent boundary layers.* Academic Press, 1974.

[30] CHALOT, F., MARQUEZ, B., RAVACHOL, M., AND DUCROS, F. A consistent finite element approach to large eddy simulation. AIAA Paper 98-2652, 1998.

[31] CHAMPAGNE, F., FRICHE, C., LARUE, J., AND WYNGAARD, J. Flux measurements, flux estimation techniques, and fine-scale turbulence measurements in the unstable surface layer over land. *J. Atmos. Sci. 34* (1977), 515–530.

[32] CHERUKAT, P., NA, Y., HANRATTY, T., AND MCLAUGHLIN, J. Direct numerical simulation of a fully developed flow over a wavy wall. *Theoret. Comput. Fluid Dynamics 11*, 2 (1998), 109–134.

[33] CHOI, H., AND MOIN, P. Effects of the computational time step on numerical solutions of turbulent flow. *J. Comp. Phys. 113* (1993), 1–4.

[34] CHONG, M., PERRY, A., AND CANTWELL, B. A general classification of three-dimensional flow fields. *Phys. Fluids A2*, 5 (1990), 765–777.

[35] CHONG, M., SORIA, J., PERRY, A., CHACIN, J., CANTWELL, B., AND NA, Y. Turbulence structures of wall-bounded shear flows found using dns data. *J. Fluid Mech. 357* (1998), 225–247.

[36] CHORIN, A. A numerical method for solving incompressible viscous flow problems. *J. Comp. Phys. 2* (1967), 12–26.

[37] CHORIN, A. Numerical solution of the navier-stokes equations. *Mathematical Computations 22* (1968), 745–762.

[38] CHUNG, Y., TUCKER, P., AND LUO, K. Large-eddy simulation of complex internal flows. In *Direct and Large-Eddy Simulation IV* (2001), B. Geurts, R. Friedrich, and O. Métais, Eds., Kluwer Academic, pp. 373–380.

[39] CLARK, R., FERZIGER, J., AND REYNOLDS, W. Evaluation of subgrid-scale models using an accurately simulated turbulent flow. *J. Fluid Mech. 91* (1979), 1–16.

[40] CONSTANTINESCU, G., MAHESH, K., APTE, S., IACCARINO, G., HAM, F., AND MOIN, P. A new paradigm for simulation of turbulent combustion in realistic gas turbine combustor using les. In *Proc. of ASME Turbo Expo 2003 Power for Land, Sea, and Air* (2003), vol. 2, ASME, pp. 259–272.

[41] COOK, A., AND RILEY, J. A subgrid scale model for equilibrium chemistry in turbulent flows. *Phys. Fluids 6*, 8 (1994), 2868–2870.

[42] CRAFT, T., AND LAUNDER, B. A reynolds stress closure designed for complex geometries. *Int. J. Heat Fluid Flow 17*, 3 (1996), 245–254.

[43] DAHLSTRÖM, D., AND DAVIDSON, L. Chalmers 30-month report, LESFOIL: a Brite-Euram project. Technical report, Chalmers, Göteborg, Sweden, 2000.

[44] DAHLSTRÖM, S., AND DAVIDSON, L. Large eddy simulation of the flow around an Aérospatiale A-aerofoil. In *ECCOMAS 2000, European Congress on Computational Methods in Applied Sciences and Engineering* (2000).

[45] DAVIDSON, L., COKLJAT, D., FRÖHLICH, J., LESCHZINER, M., MELLEN, C., AND RODI, W., Eds. *LESFOIL: Large Eddy Simulation of Flow Around a High Lift Airfoil. Results of the Project LESFOIL Supported by the European Union 1998-2001*, vol. 83 of *Notes on Numerical Fluid Mechanics and Multidisciplinary Design (NNFM)*. Springer, 2003.

[46] DAVIDSON, L., AND PENG, S.-H. A hybrid LES-RANS model based on a one-equation SGS model and a two-equation $k - \omega$ model. In *The Second International Symp. on Turbulence and Shear Flow Phenomena* (2001), E. Lindborg, A. Johansson, J. Eaton, J. Humphrey, N. Kasagi, M. Leschziner, and M. Sommerfeld, Eds., vol. 2, pp. 175–180.

[47] DE ANGELIS, V., LOMBARDI, P., AND BANERJEE, S. Direct numerical simulation of turbulent flow over a wavy wall. *Phys. Fluids 9*, 8 (1997), 2429–2442.

[48] DE LANGHE, C., MERCI, B., LODEFIER, K., AND DICK, E. Very-large-eddy simulation subgrid modelling using the statistical mechanics renormalization group. In *3rd International Symposium on Turbulence and Shear Flow Phenomena* (2003), N. Kasagi, J. Eaton, R. Friedrich, J. Humphrey, M. Leschziner, and T. Miyauchi, Eds., vol. 2, pp. 657–661.

[49] DEARDORFF, J. A numerical study of three-dimensional turbulent channel flow at large reynolds number. *J. Fluid Mech. 41* (1970), 481–507.

[50] DEARDORFF, J. The use of subgrid transport equations in a three-dimensional model of atmospheric turbulence. *J. Fluids Eng. 95* (1973), 429–438.

[51] DEJOAN, A. *Simulations de grandes échelles turbulentes en écoulement de canal plan soumis à des perturbations instationnaires.* PhD thesis, Université de la Méditerranée, Aix-Marseille II, 1998.

[52] DOMARADZKI, J., AND LOH, K.-C. The subgrid-scale estimation model in the physical space representation. *Phys. Fluids 11*, 8 (1999), 2330–2342.

[53] DUCROS, F., COMTE, P., AND LESIEUR, M. Large-eddy simulation of transition to turbulence in a boundary layer developing spatially over a flat plate. *J. Fluid Mech. 326* (1996), 1–36.

[54] DUCROS, F., FERRAND, V., NICOUD, F., WEBER, C., DARRACQ, D., GACHERIEU, C., AND POINSOT, T. Large-eddy simulation of the shock/turbulence interaction. *J. Comp. Phys. 152* (1999), 517–549.

[55] DUCROS, F., NICOUD, F., AND POINSOT, T. Wall-adapting local eddy-viscosity models for simulations in complex geometries. In *6th ICFD Conference on numerical methods for fluid dynamic* (1998), M. Baines, Ed., ICFD, pp. 293–300.

[56] ESFAHANI, A. *Numerical study of laminar transitional and turbulent flow past rectangular cylinders.* PhD thesis, Chalmers University, Göteborg, Sweden, 1998.

[57] FAN, S., AND LAKSHMINARAYANA, B. Computation and simulation of wake-generated unsteady pressure and boundary layers in cascades: Part 1 - description of the approach and validation. *J. Turbomachinery 118*, 1 (1996), 96–108.

[58] FERZIGER, J., MEHTA, U., AND REYNOLDS, W. Large eddy simulation of homogeneous isotropic turbulence. In *Symp. Turbul. Shear Flows* (1977).

[59] FERZIGER, J., AND PERIĆ, M. *Computational methods for fluid dynamics.* Springer Verlag, 1996.

[60] FLETCHER, R. Conjugate gradient methods for indefinite systems. In *Lecture Notes in Mathematics*, vol. 506. Springer-Verlag, 1976, pp. 73–89.

[61] FRÖHLICH, J., AND RODI, W. Introduction to large eddy simulation of turbulent flows. In *Closure strategies for turbulent and transitional flows*, B. Launder and N. Sandham, Eds. Cambridge University Press, 2002, pp. 267–298.

[62] FUREBY, C., TABOR, G., WELLER, H., AND GOSMAN, A. A comparative study of subgrid scale models in homogeneous isotropic turbulence. *Phys. Fluids 9*, 5 (1997), 1416–1429.

[63] FUREBY, C., TABOR, G., WELLER, H., AND GOSMAN, A. Differential subgrid stress models in large eddy simulations. *Phys. Fluids 9*, 11 (1997), 3578–3580.

[64] GAO, F., AND O'BRIEN, E. A large eddy simulation scheme for turbulent reacting flows. *Phys. Fluids A 5*, 6 (1993), 1282–1284.

[65] GERMANO, M., PIOMELLI, U., MOIN, P., AND CABOT, W. A dynamic subgrid-scale eddy viscosity model. *Phys. Fluids A 3*, 7 (1991), 1760–1765.

[66] GEURTS, B., AND LEONARD, A. Is LES ready for complex flows? In *Closure strategies for turbulent and transitional flows*, B. Launder and N. Sandham, Eds. Cambridge University Press, 2002, pp. 721–739.

[67] GHOSAL, S. An analysis of numerical errors in large-eddy simulations of turbulence. *J. Comp. Phys. 125* (1996), 187–206.

[68] GHOSAL, S. Mathematical and physical constraints on large-eddy simulation. *AIAA J. 37*, 4 (1999), 425–433.

[69] GHOSAL, S., LUND, T., MOIN, P., AND AKSEVOLL, K. A dynamic localization model for large-eddy simulation of turbulent flows. *J. Fluid Mech. 286* (1995), 229–255.

[70] GHOSAL, S., AND MOIN, P. The basic equations for the large eddy simulation of turbulent flows in complex geometry. *J. Comp. Phys. 118* (1995), 24–37.

[71] GLEYZES, C. Opération décrochage - résultats de la 2ème campagne d'essais à F2 - mesures de pression et vélocimétrie laser. Tech. Rep. RT-DERAT 55/5004, ONERA, 1989.

[72] GOLUB, G., AND VAN LOAN, C. *Matrix computations.* John Hopkins University Press, 1990.

[73] GONG, W., TAYLOR, P., AND DÖRNBRACK, A. Turbulent boundary-layer flow over fixed aerodynamically rough two-dimensional sinusoidal waves. *J. Fluid Mech. 312* (1996), 1–38.

[74] GRÖTZBACH, G. Direct numerical and large eddy simulation of turbulent channel flows. *Encyclopedia of Fluid Mechanics 6* (1987), 1337–1391.

[75] GRÖTZBACH, G., AND SCHUMANN, U. Direct numerical simulation of turbulent velocity-, pressure-, and temperature-fields in channel flows. In *Symposium on Turbulent Shear Flow 1* (1979), F. Durst, B. Launder, F. Schmidt, and J. Whitelaw, Eds., Springer-Verlag, pp. 370–385.

[76] GÜNTHER, A., AND VON ROHR, P. Large-scale structures in a developed flow over wavy terrain. *J. Fluid Mech. 478* (2003), 257–285.

[77] HAASE, W., BRADSMA, F., ELSHOLZ, E., LESCHZINER, M., AND SCHWAMBORN, D., Eds. *EUROVAL - An European Initiative on Validation of CFD Codes*, vol. 43 of *Notes on Numerical Fluid Mechanics.* Vieweg Verlag, 1993.

[78] HAASE, W., CHAPUT, E., ELSHOLZ, E., LESCHZINER, M., AND MÜLLER, U., Eds. *ECARP - European Computational Aerodynamics Research Project: Validation of CFD Codes and Assessment of Turbulence Models*, vol. 58 of *Notes on Numerical Fluid Mechanics.* Vieweg Verlag, 1997.

[79] HANJALIĆ, K., AND JAKIRLIĆ, S. Contribution towards the second-moment closure modelling of separating turbulent flows. *Comp. & Fl. 27*, 2 (1998), 137–156.

[80] HANJALIĆ, K., AND KENJEREŠ, S. Reorganization of turbulence structure in magnetic Rayleigh-Bénard convection: a T-RANS study. *Journal of Turbulence 1* (2000), 1–22.

[81] HANJALIĆ, K., AND KENJEREŠ, S. 'T-RANS' simulation of deterministic eddy structure in flows driven by thermal buoyancy and lorentz force. *Flow, Turb. and Combust. 66*, 4 (2001), 427–451.

[82] HAWORTH, D., AND JANSEN, K. Large-eddy simulation on unstructured deforming meshes: towards reciprocating IC engines. *Comp. & Fl. 29*, 5 (2000), 493–524.

[83] HELD, J., AND FUCHS, L. LES of shock induced separation. In *Direct and Large-Eddy Simulation III* (1999), P. Voke, N. Sandham, and L. Kleiser, Eds., Kluwer Academic Publishers, pp. 111–122.

[84] HENN, D. S., AND SYKES, R. I. Large-eddy simulation of flow over wavy surfaces. *J. Fluid Mech. 383* (1999), 75–112.

[85] HIRSCH, C. *Numerical computation of internal and external flows: Fundamental of numerical discretisation, Vol. 1.* John Wiley, 1988.

[86] HUDDEVILLE, R., PICCIN, O., AND CASSOUDESALLE, D. Opération décrochage - mesures de frottements sur profiles AS 239 et A240 à la soufflerie F1 du CFM. Tech. Rep. RT-OA 19/5025 (RT-DERAT 19/5025 DN), ONERA, 1987.

[87] HUDSON, J., DYKHNO, L., AND HANRATTY, T. Turbulence production in flow over a wavy wall. *Experiments in Fluids 20* (1996), 257–265.

[88] HUNT, J., WRAY, A., AND MOIN, P. Eddies, stream and convergence zones in turbulent flows. Tech. Rep. CTR-S88, Center for Turbulence Research, Stanford, USA, 1988.

[89] HUSER, A., BIRINGEN, S., AND HATAY, F. Direct simulation of turbulent flow in a square duct: Reynolds-stress budgets. In *Applications of Direct and Large Eddy Simulation.* AGARD, 1994, pp. 12–1 – 12–12.

[90] ISSA, R. Solution of implicitly discretised fluid flow equations by operator-splitting. *J. Comp. Phys. 62* (1986), 42–65.

[91] JANG, Y., LESCHZINER, M., ABE, K., AND TEMMERMAN, L. Investigation of anisotropy-resolving turbulence models by reference to highly-resolved LES data for separated flow. *Flow, Turb. and Combust. 69*, 2 (2002), 161–203.

[92] JANSEN, K. Preliminary large-eddy simulations of flow around a NACA 4412 airfoil using unstructured grids. In *Annual Research Briefs* (1995), CTR, Stanford, USA, pp. 61–72.

[93] JANSEN, K. Large-eddy simulations of flow around a NACA 4412 airfoil using unstructured grids. In *Annual Research Briefs* (1996), CTR, Stanford, USA, pp. 225–232.

[94] JEONG, J., AND HUSSAIN, F. On the identification of a vortex. *J. Fl. Mech. 285* (1995), 69–94.

[95] JEONG, J., HUSSAIN, F., SCHOPPA, W., AND KIM, J. Coherent structures near the wall in a turbulent channel flow. *J. Fl. Mech. 332* (1997), 185–214.

[96] JIMÉNEZ, J. Computing high-Reynolds number channels: Will DNS ever substitute experiments? In *Engineering Turbulence Modelling and Experiments V* (2002), W. Rodi and N. Fueyo, Eds., Elsevier, pp. 17–27.

[97] JIMÉNEZ, J., AND MOIN, P. The minimal flow unit in near-wall turbulence. *J. Fluid Mech. 225* (1991), 213–240.

[98] JONES, W., AND WILLE, M. Large eddy simulation of a plane jet in a cross-flow. *Int. J. Heat and Fluid Flow 17*, 3 (1996), 296–306.

[99] JONES, W., AND WILLE, M. Large eddy simulation of a round jet in a cross-flow. In *Engineering Turbulence Modelling and Experiments - 4* (1996), W. Rodi and G. Bergeles, Eds., Elsevier Science, pp. 199–208.

[100] JORDAN, S. A large-eddy simulation methodology in generalized curvilinear coordinates. *J. Comp. Phys. 148* (1999), 322–340.

[101] KALTENBACH, H. The effect of sweep-angle variation on the turbulence structure in a separated, three-dimensional flow. *Theoret. Comput. Fluid Dynamics 16* (2003), 187–210.

[102] KALTENBACH, H., AND CHOI, H. Large-eddy simulation of flow around an aerofoil on a structured grids. In *Annual Research Briefs* (1995), CTR, Stanford, USA, pp. 50–60.

[103] KALTENBACH, H., FATICA, M., MITTAL, R., LUND, T., AND MOIN, P. Study of flow in a planar asymmetric diffuser using large-eddy simulation. *J. Fluid Mech. 390* (1999), 151–185.

[104] KASAGI, N., SUMITANI, Y., SUZUKI, Y., AND LIDA, O. Kinematics of the quasi-coherent vortical structure in near-wall turbulence. *Int. J. Heat and Fluid Flow 16*, 1 (1995), 2–10.

[105] KIM, J. The effect of rotation on turbulence structure. In *Proc. 4th Symposium on Turbulent Shear Flows* (1984), F. Durst and B. Launder, Eds., Springer-Verlag, pp. 6.14–6.19.

[106] KIM, J., MOIN, P., AND MOSER, R. Turbulence in channel flow at low reynolds number. *J. Fluid Mech. 177* (1987), 133–166.

[107] KIM, W.-W., AND MENON, S. An unsteady incompressible navier-stokes solver for large-eddy simulation of turbulent flows. *Int. J. Numer. Meth. Fluids 31*, 6 (1999), 983–1017.

[108] KOLMOGOROV, A. The local structure of turbulence in incompressible viscous fluid for very large reynolds number. *Dokl. Akad. Navsk. SSSR 30*, 4 (1941), 9–13. Reprinted in *Proc. R. Soc. Lond. A (434)* (1991), 9–13.

[109] KOSOVIĆ, B., PULLIN, D., AND SAMTANEY, R. Subgrid-scale modeling for large-eddy simulations of compressible turbulence. *Phys. Fluids 14*, 4 (2002), 1511–1522.

[110] KRAVCHENKO, A., AND MOIN, P. On the effect of numerical errors in large eddy simulations of turbulent flows. *J. Comp. Ph. 131* (1997), 310–322.

[111] KRAVCHENKO, A., AND MOIN, P. Numerical studies of flow over a circular cylinder at $Re_D = 3900$. *Phys. Fluids 12*, 2 (2000), 403–417.

[112] KRAVCHENKO, A., MOIN, P., AND MOSER, R. Zonal embedded grid for numerical simulations of wall-bounded turbulent flows. *J. Comp. Ph. 127* (1996), 421–423.

[113] LARDAT, R. Private communication, 1999.

[114] LARDAT, R., AND LESCHZINER, M. A Navier-Stokes solver for LES on parallel computers. Internal report, UMIST, Manchester, UK, 1998.

[115] LAUNDER, B., REECE, G., AND RODI, W. Progress in the development of a reynolds-stress turbulence closure. *J. Fl. Mech. 68* (1975), 537–566.

[116] LAUNDER, B., AND SPALDING, D. The numerical computation of turbulent flows. *Comp. Meth. in Ap. Mech. and Eng. 3* (1974), 269–289.

[117] LE, H., AND MOIN, P. An improvement of fractional step methods for the incompressible Navier–Stokes equations. *J. Comput. Phys. 92* (1991), 369–379.

[118] LE, H., MOIN, P., AND KIM, J. Direct numerical simulation of turbulent flow over a backward-facing step. *J. Fluid Mech. 330* (1997), 349–374.

[119] LEE, S., LELE, S., AND MOIN, P. Simulation of a spatially evolving turbulence and the applicability of Taylor's hypothesis in compressible flow. *Phys. Fluids A 4*, 7 (1997), 1521–1530.

[120] LEONARD, A. Energy cascade in large-eddy simulations of turbulent fluid flows. *Adv. Geophys. 18A* (1974), 237–248.

[121] LEONARD, B. A stable and accurate convection modelling procedure absed on quadratic upstream interpolation. *Comput. Methods Appl. Mech. Engrg. 19* (1979), 59–98.

[122] LESCHZINER, M. Statistical turbulence modelling for the computation of physically complex flows. In *New trends in turbulence*, M. Lesieur, A. Yaglow, and F. David, Eds. Springer, 2000, pp. 187–258.

[123] LESIEUR, M., BEGOU, P., COMTE, P., AND MÉTAIS, O. Vortex recognition in numerical simulations. *Ercoftac Bulletin 46* (2000), 25–28.

[124] LESIEUR, M., AND MÉTAIS, O. New trends in large-eddy simulations of turbulence. *Ann. Rev. Fluid Mech. 28* (1996), 45–82.

[125] LESIEUR, M., AND ROGALLO, R. Large eddy simulation of passive scalar diffusion in isotropic turbulence. *Phys. Fluids A 1*, 4 (1989), 718–722.

[126] LI, N., BALARAS, E., AND PIOMELLI, U. Inflow conditions for large-eddy simulations of mixing layers. *Phys. Fluids 12*, 4 (2000), 935–938.

[127] LILEK, Z., AND PERIĆ, M. A fourth-order finite volume method with colocated variable arrangement. *Comp. & Fl. 24*, 3 (1995), 239–252.

[128] LILLY, D. Proceedings of the IBM Scientific Computing Symposium on Environmental Science. IBM Form 320-1951, 1967.

[129] LILLY, D. A proposed modification of the Germano subgrid-scale closure method. *Phys. Fluids A4*, 3 (1992), 633–635.

[130] LIU, S., MENEVEAU, C., AND KATZ, J. On the properties of similarity subgrid-scale models as deduced from measurements in a turbulent jet. *J. Fluid Mech. 275* (1994), 83–119.

[131] LONGATTE, E., LAURENCE, D., BARRE, F., AND LEDAC, P. Applications of large eddy simulation to a flow induced vibration problem. In *ASME-PUBLICATIONS-PVP (Pressure Vessel and Piping Conference)* (2001), M. Pettigrew, Ed., vol. 420, ASME, pp. 81–88.

[132] LUGT, H. The dilemna of identifying a vortex. In *Recent developments in theoritical and experimental fluid mechanics*, U. Müller, K. Roesner, and B.Schmidt, Eds. Springer, 1979, pp. 309–321.

[133] LUMLEY, J. Computational modeling of turbulent flows. *Advances in Applied Mechanics 18* (1978), 123–176.

[134] LUMLEY, J., AND NEWMAN, G. The return to isotropy of homogeneous turbulence. *J. Fl. Mech. 82* (1977), 161–178.

[135] LUND, T. On the use of discrete filters for large eddy simulation. In *Annual Research Briefs* (1997), CTR, Stanford, USA, pp. 83–95.

[136] LUND, T., WU, X., AND SQUIRES, K. On the generation of turbulent inflow conditions for boundary layer simulations. In *Annual Research Briefs* (1996), CTR, Stanford, USA, pp. 281–295.

[137] MAHESH, K., CONSTANTINESCU, G., AND MOIN, P. Large-eddy simulation of gas turbine combustors. In *Annual Research Briefs* (2000), CTR, Stanford, USA, pp. 219–228.

[138] MANKBADI, R., HAYER, M., AND POVINELLI, L. Structure of supersonic jet flow and its radiated sound. *AIAA J. 32*, 5 (1994), 897–906.

[139] MANNA, M., Ed. *Introduction to the modelling of turbulence.* VKI Lecture Series 1997-03. von Karman Institute for Fluid Dynamics, Belgium, 1997.

[140] MANSOUR, N., KIM, J., AND MOIN, P. Reynolds-stress and dissipation-rate budgets in a turbulent channel flow. *J. Fl. Mech. 194* (1988), 15–44.

[141] MARGOLIN, L., AND RIDER, W. A rationale for implicit turbulence modelling. *Int. J. Numer. Meth. Fluids 39*, 9 (2002), 821–841.

[142] MARY, I., AND SAGAUT, P. Large eddy simulation of flow around an airfoil near stall. *AIAA J. 40*, 6 (2001), 1139–1145.

[143] MASON, P., AND CALLEN, N. On the magnitude of the subgrid-scale eddy coefficient in large-eddy simulations of turbulent channel flow. *J. Fluid Mech. 162* (1986), 439–462.

[144] MCMILLAN, O., AND FERZIGER, J. Direct testing of subgrid-scale models. *AIAA J. 17* (1979), 1340–1346.

[145] MCMILLAN, O., FERZIGER, J., AND ROGALLO, R. Tests of subgrid-scale models in strained turbulence. AIAA Paper 80-1339, 1980.

[146] MEINKE, M., AND KRAUSE, E. Applications of LES to jets and internal turbulent flows. In *Advanced Turbulent Flow Computations* (1998), R. Peyret and E. Krause, Eds., Springer-Verlag, pp. 155–208.

[147] MELANDER, M., AND HUSSAIN, F. Polarized vortical dynamics on a vortex column. *Phys. Fluids A5*, 8 (1993), 1992–2000.

[148] MELLEN, C., FRÖHLICH, J., AND RODI, W. Interim LESFOIL report: 18 months. Tech. rep., Karlsruhe University, Germany, 1999.

[149] MELLEN, C., FRÖHLICH, J., AND RODI, W. Chalmers 30-month report, LESFOIL: a Brite-Euram project. Technical report, Chalmers, Göteborg, Sweden, 2000.

[150] MELLEN, C. P., FRÖHLICH, J., AND RODI, W. Large eddy simulation of the flow over a periodic hill. In *16th IMACS World Congress 2000* (2000).

[151] MELLEN, C. P., FRÖHLICH, J., AND RODI, W. Lessons from the European LESFOIL project on LES of flow around an airfoil. AIAA Paper 2002-0111, 2002.

[152] MENEVEAU, C. Statistics of turbulence subgrid-scale stresses: necessary conditions and experimental tests. *Phys. Fluids 6*, 2 (1994), 815–833.

[153] MENEVEAU, C., LUND, T., AND CABOT, W. A Lagrangian dynamic subgrid-scale model of turbulence. *J. Fl. Mech. 319* (1996), 353–385.

[154] MENON, S., YEUNG, P.-K., AND KIM, W.-W. Effect of subgrid models on the computed interscale energy transfer in isotropic turbulence. *Comp. & Fl. 25* (1996), 165–180.

[155] MITTAL, R., AND BALACHANDAR, S. Direct numerical simulation of flow past elliptic cylinders. *J. Comp. Phys. 124*, 2 (1996), 351–367.

[156] MITTAL, R., AND MOIN, P. Suitability of upwind-biased finite-difference schemes for large-eddy simulation of turbulent flows. *AIAA J. 35*, 8 (1997), 1415–1417.

[157] MOIN, P. Towards large eddy and direct simulation of complex turbulent flows. *Comp. Meth. in App. Mech. and Eng. 87* (1991), 329–334.

[158] MOIN, P. Numerical and physical issues in large eddy simulation of turbulent flows. *JSME International Journal, Series B 41*, 2 (1998), 454–463.

[159] MOIN, P., AND KIM, J. Numerical investigation of turbulent channel flow. *J. Fluid Mech. 118* (1982), 341–377.

[160] MOIN, P., AND MAHESH, K. Direct numerical simulation: a tool in turbulence research. *Ann. Rev. Fluid Mech. 30* (1998), 539–578.

[161] MOSER, R., KIM, J., AND MANSOUR, N. Direct numerical simulation of turbulent channel flow up to $Re_\tau = 590$. *Phys. Fluids 12*, 7 (1999), 943–945.

[162] MURAKAMI, S., MOCHIDA, A., AND HIBI, K. Three-dimensional simulation of air flow around a cubic model by means of large-eddy simulation. *J. Wind. Eng. Ind. Aerodyn. 25* (1987), 291–305.

[163] MURAKAMI, S., MOCHIDA, A., RODI, W., AND SAKAMOTO, S. Large eddy simulation of turbulent vortex shedding flow past 2D square cylinders. In *Engineering applications of large eddy simulations*, S. Ragab and U. Piomelli, Eds., vol. 162 of *ASME - Publications - FED*. ASME, 1993, pp. 113–120.

[164] NA, Y., AND MOIN, P. Direct numerical simulation of a separated turbulent boundary layer. *J. Fluid Mech. 374* (1998), 379–405.

[165] NAJJAR, F., AND TAFTI, D. Study of discrete test filters and finite difference approximations for the dynamic subgrid-scale stress model. *Phys. Fluids 8*, 4 (1996), 1076–1087.

[166] NEUMANN, J., AND WENGLE, H. Active control of turbulent separated flows using large-eddy simulation. In *Direct and Large-Eddy Simulation IV* (2001), B. Geurts, R. Friedrich, and O. Métais, Eds., Kluwer Academic, pp. 427–434.

[167] NICOUD, F., AND DUCROS, F. Subgrid-scale stress modelling based on the square of the velocity gradient tensor. *Flow, Turb. and Combust. 62*, 3 (1999), 183–200.

[168] OLSSON, M., AND FUCHS, L. Large eddy simulations of a forced semiconfincd circular impinging jet. *Phys. Fluids 10*, 2 (1998), 476–486.

[169] PATANKAR, S. *Numerical heat transfer and fluid flow.* Series in computational methods in mechanics and thermal sciences. McGraw-Hill, 1980.

[170] PAULEY, L., MOIN, P., AND REYNOLDS, W. The structure of two-dimensional separation. *J. Fluid Mech. 220* (1990), 397–411.

[171] PEROT, J., AND MOIN, P. Shear-free turbulent boundary layers. Part 1. Physical insights into near-wall turbulence. *J. Fluid Mech. 295* (1995), 199–227.

[172] PHILLIPS, W., AND WU, Z. On the instability of wave-catalysed longitudinal vortices in strong shear. *J. Fluid Mech. 272* (1994), 235–254.

[173] PHILLIPS, W., WU, Z., AND LUMLEY, J. On the formation of longitudinal vortices in a turbulent boundary layer over wavy terrain. *J. Fluid Mech. 326* (1996), 321–341.

[174] PIERCE, C., AND MOIN, P. Large eddy simulation of a confined coaxial jet with swirl and heat release. AIAA Paper 98-2892, 1998.

[175] PIOMELLI, U. High reynolds number calculations using the dynamic subgrid-scale stress model. *Phys. Fluids A5*, 6 (1993), 1484–1490.

[176] PIOMELLI, U., AND CHASNOV, J. Large-eddy simulations: theory and applications. In *Turbulence and Transition Modelling*, M. H. et al, Ed. Kluwer Academic, 1996, pp. 269–331.

[177] PIOMELLI, U., FERZIGER, J., MOIN, P., AND KIM, J. New approximate boundary conditions for large eddy simulations of wall-bounded flows. *Phys. Fluids A 1*, 6 (1989), 1061–1068.

[178] PIOMELLI, U., AND LIU, J. Large-eddy simulation of rotating channel flows using a localized dynamic model. *Phys. Fluids 7*, 4 (1995), 839–848.

[179] POINSOT, T., AND LELE, S. Boundary conditions for direct simulations of compressible viscous flows. *J. Comp. Phys. 101* (1992), 104–129.

[180] POPE, S. *Turbulent Flows.* Cambridge University Press, 2000.

[181] PORTELA, L., AND OLIEMANS, R. Direct and large-eddy simulations of particle-laden flows using the point-particle approach. *In Direct and Large-Eddy Simulation IV* (2001), B. Geurts, R. Friedrich, and O. Métais, Eds., Kluwer Academic, pp. 453–460.

[182] PRANDTL, L. Über die ausgebildete turbulenz. *ZAMM 5* (1925), 136–139.

[183] RAVERDY, B., MARY, I., SAGAUT, P., AND LIAMIS, N. Large-eddy simulation of the flow around a low pressure turbine blade. In *Direct and Large-Eddy Simulation IV* (2001), B. Geurts, R. Friedrich, and O. Métais, Eds., Kluwer Academic, pp. 381–388.

[184] REVEILLON, J., AND VERVISCH, L. Response of the dynamic LES model to heat release induced effects. *Phys. Fluids 8*, 9 (1996), 2248–2250.

[185] REYNOLDS, W. The potential and limitations of direct and large-eddy simulations. In *Whither Turbulence? Turbulence at the Crossroads*, J. Lumley, Ed. Springer-Verlag, 1990, pp. 313–342.

[186] RHIE, C., AND CHOW, W. Numerical study of the turbulent flow past an airfoil with trailing edge separation. *AIAA J. 21*, 11 (1983), 1525–1532.

[187] ROBINSON, S. Coherent motions in the turbulent boundary layer. *Annu. rev. Fluid Mech. 23* (1991), 601–639.

[188] RODI, W., BONNIN, J., AND BUCHAL, T., Eds. *ERCOFTAC workshop on data bases and testing of calculation methods for turbulent flows.* University of Karlsruhe, Germany, 1995.

[189] ROGALLO, R., AND MOIN, P. Numerical simulation of turbulent flows. *Annu. Rev. Fluid Mech. 116* (1984), 99–137.

[190] ROGERS, M., AND MOSER, R. Direct simulation of a self-similar turbulent mixing-layer. *Phys. Fluids 6*, 2 (1994), 903–923.

[191] ROLLET-MIET, P., LAURENCE, D., AND FERZIGER, J. LES and RANS of turbulent flow in tube bundles. *Int. J. Heat and Fluid Flow 20*, 3 (1999), 241–254.

[192] SAGAUT, P. Simulations of separated flows with subgrid models. *La Recherche Aérospatiale 1* (1996), 51–63.

[193] SAGAUT, P. *Introduction à la simulation des grandes échelles pour les écoulements de fluide incompressible.* Mathématiques et Applications. Springer, 1998.

[194] SAGAUT, P., AND GROHENS, R. Discrete filters for large eddy simulations. *Int. J. Num. Meth. in Fluids 31*, 8 (1999), 1195–1220.

[195] SALVETTI, M. V., DAMIANI, R., AND BEUX, F. Three-dimensional coarse large-eddy simulations of the flow above two-dimensional sinusoidal waves. *Int. J. Num. Meth. in Fluids 35*, 6 (2001), 617–642.

[196] SAMARSKII, A., AND NIKOLAEV, E. *Numerical methods for grid equations. Volume I.* Birkhäuser, 1989.

[197] SAMARSKII, A., AND NIKOLAEV, E. *Numerical methods for grid equations. Volume II.* Birkhäuser, 1989.

[198] SANDHAM, N. Introduction to direct numerical simulation. In *Closures strategies for turbulent and transitional flows*, B. Launder and N. Sandham, Eds. Cambridge University Press, 2004, pp. 248–266.

[199] SCHMITT, L., AND FRIEDRICH, R. Large-eddy simulation of turbulent backward facing-step flow. In *Proc. of the 7th GAMM-Conference on Numerical Methods in Fluid Mechanics* (1988), Vieweg, pp. 335–362.

[200] SCHUMANN, U. Subgrid scale models for finite difference simulations of turbulent flows in plane channels and annuli. *J. Comp. Phys. 18* (1975), 376–404.

[201] SCHUMANN, U., AND FRIEDRICH, R., Eds. *Large-eddy simulation of turbulent boundary layer and channel flow at high Reynolds number* (1986), vol. 15 of *Notes on Numerical Fluid Mechanics*, Vieweg.

[202] SCHUMANN, U., AND SWEET, R. Fast Fourier transforms for direct solution of Poisson's equation with staggered boundary conditions. *J. Comp. Phys. 75* (1988), 123–137.

[203] SCOTTI, A., MENEVEAU, C., AND LILLY, D. Generalised Smagorinsky model for anisotropic grids. *Phys. Fluids A 5*, 9 (1993), 2306–2308.

[204] SEROR, C., SAGAUT, P., BAILLY, C., AND JUVÉ, D. On the radiated noise computed by large-eddy simulation. *Phys. Fluids 13*, 2 (2001), 476–487.

[205] SHAH, K., AND FERZIGER, J. Stimulated small scale SGS model and its application to channel flow. In *11th Symposium on Turbulent Shear Flows* (1997), pp. 16–1–16–6.

[206] SHUR, M., SPALART, P., STRELETS, M., AND TRAVIN, A. Detached-eddy simulation of an airfoil at high angle of attack. In *Engineering Turbulence Modelling and Experiments 4* (1999), W. Rodi and D. Laurence, Eds., Elsevier Science, pp. 669–678.

[207] SILVEIRA-NETO, A., GRAND, D., MÉTAIS, O., AND LESIEUR, M. A numerical investigation of the coherent vortices in turbulence behind a backward-facing step. *J. Fluid Mech. 256* (1993), 1–25.

[208] SMAGORINSKY, J. General circulation experiments with the primitive equations. I. The basic experiment. *Monthly Weather Review 91* (1963), 99–163.

[209] SNIR, M., OTTO, S., HUSS-LEDERMAN, S., WALKER, D., AND DONGARRA, J. *MPI: the complete reference.* MIT Press, 1996.

[210] SPALART, P. Strategies for turbulence modeling and simulations. *Int. J. Heat and Fluid Flow 21*, 3 (2000), 252–263.

[211] SPALART, P., AND ALLMARAS, S. A one-equation turbulence model for aerodynamic flows. *La Recherche Aérospatiale 1* (1994), 5–21.

[212] SPALART, P., JOU, W.-H., STRELETS, M., AND ALLMARAS, S. Comments on the feasibility of LES for wings and on the hybrid RANS/LES approach. In *Advances in DNS/LES* (1997), C. Liu, Z. Liu, and L. Sakell, Eds., Greden Press, pp. 137–148.

[213] SPEZIALE, C. Galilean invariance of subgrid-scale stress models in the large-eddy simulation of turbulence. *J. Fluid Mech 156* (1985), 55–62.

[214] SPEZIALE, C., SARKAR, S., AND GATSKI, T. Modelling the pressure-strain correlation of turbulence: an invariant dynamical systems approach. *J. Fl. Mech. 227* (1991), 245–272.

[215] SQUIRES, K., AND PIOMELLI, U. Dynamic modelling of rotating turbulence. In *Proc. 9th Symp. Turb. Shear Flows* (1995), F. Durst, Ed., Springer-Verlag, pp. 71–84.

[216] STOLZ, S., AND ADAMS, N. An approximate deconvolution procedure for large-eddy simulation. *Phys. Fluids 11*, 7 (1999), 1699–1701.

[217] STONE, H. Iterative solution of implicit approximations of multidimensional partial differential equations. *SIAM J. Numer. Anal. 5* (1968), 530–558.

[218] TEMMERMAN, L., LESCHZINER, M., AND HANJALIĆ, K. A-priori studies of a near-wall RANS model within a hybrid LES/RANS scheme. In *Engineering Turbulence Modelling and Experiments V* (2002), W. Rodi and N. Fueyo, Eds., Elsevier, pp. 317–326.

[219] TEMMERMAN, L., LESCHZINER, M., MELLEN, C. P., AND FRÖHLICH, J. Investigation of wall-function approximations and subgrid-scale models in

large eddy simulation of separated flow in a channel with streamwise periodic constrictions. *Int. J. Heat and Fluid Flow 24*, 2 (2003), 157–180.

[220] THOMPSON, K. Time dependent boundary conditions for hyperbolic systems. *J. Comp. Ph. 68* (1987), 1–24.

[221] VAN DEN VORST, H. BI-CGSTAB: a fast and smoothly converging variant of BI-CG for the solution of non-symmetric linear systems. *SIAM J. Sci. Stat. Comput. 13* (1992), 631–644.

[222] VAN DRIEST, E. On turbulent flow near a wall. *Journal of the Aeronautical Sciences 23* (1956), 1007–1011.

[223] VASILYEV, O., LUND, T., AND MOIN, P. A general class of commutative filters for LES in complex geometries. *J. Comp. Phys. 146* (1998), 82–104.

[224] VERZICCO, R., IACCARINO, G., FATICA, M., AND ORLANDI, P. Flow in an impeller stirred tank using an immersed boundary method. In *Annual Research Briefs* (2000), CTR, Stanford, USA, pp. 219–228.

[225] VERZICCO, R., MOHOD-YUSOF, J., ORLANDI, P., AND HAWORTH, D. LES in complex geometries using body forces. In *Annual Research Briefs* (1998), CTR, Stanford, USA, pp. 171–186.

[226] VREMAN, A. *Direct and large-eddy simulation of the compressible mixing layer.* PhD thesis, Twente Universiteit, The Netherlands, 1995.

[227] VREMAN, B., GEURTS, B., AND KUERTEN, H. A priori tests of large eddy simulation of the compressible mixing layer. *Journal of Engineering Mathematics 29* (1995), 299–327.

[228] VREMAN, B., GEURTS, B., AND KUERTEN, H. Comparison of numerical schemes in large-eddy simulation of the temporal mixing layer. *Int. Journal for Num. Meth. in Fluids 22*, 4 (1996), 297–311.

[229] WANG, C., JANG, Y., AND LESCHZINER, M. Modelling 2D and 3D separation from curved surfaces with anisotropy-resolving turbulence closures.

In *3rd International Symposium on Turbulence and Shear Flow Phenomena* (2003), N. Kasagi, J. Eaton, R. Friedrich, J. Humphrey, M. Leschziner, and T. Miyauchi, Eds., vol. 1, pp. 257–262.

[230] WANG, M., AND MOIN, P. Computation of trailing-edge flow and noise using large-eddy simulation. *AIAA J. 38*, 12 (2000), 2201–2209.

[231] WASISTHO, B. *Spatial direct numerical simulation of compressible boundary layer flow.* PhD thesis, Universiteit Twente, Enschede, The Netherlands, 1997.

[232] WEBER, C., AND DUCROS, F. Large eddy and reynolds-averaged navier-stokes simulations of turbulent flow over an airfoil. *Int. J. Comp. Fluid Dyn. 13*, 4 (2000), 327–356.

[233] WEBER, C., DUCROS, F., AND CORJON, A. Large eddy simulation of complex turbulent flows. AIAA Paper 98-2651, 1998.

[234] WERNER, H., AND WENGLE, H. Large-eddy simulation of turbulent flow over a square rib in a channel. In *Advances in Turbulence II* (1989), H. Fernholz and H. Fiedler, Eds., Springer Verlag, pp. 418–423.

[235] WERNER, H., AND WENGLE, H. Large-eddy simulation of turbulent flow over and around a cube in a plate channel. In *8th Symposium on Turbulent Shear Flows* (1991), F. D. et al, Ed., Springer, pp. 155–168.

[236] WILCOX, D. *Turbulence Modeling for CFD.* DCW Industries, 1993.

[237] WILLE, M. *Large-eddy simulation of jets in cross-flows.* PhD thesis, Imperial College London, University of London, UK, 1997.

[238] WU, X., AND SQUIRES, K. Numerical investigation of the turbulent boundary layer over a bump. *J. Fluid Mech. 362* (1998), 229–271.

[239] YANG, K.-S., AND FERZIGER, J. Large-eddy simulation of turbulent obstacle flow using a dynamic subgrid-scale model. *AIAA J. 31*, 8 (1993), 1407–1413.

[240] YOSHIZAWA, W. Statistical theory for compressible shear flows with the application of subgrid modelling. *Phys. Fluids 29*, 7 (1986), 2152–2164.

[241] ZANG, T. On the rotation and skew-symmetric forms for incompressible flow simulations. *Appl. Numer. Math. 7* (1991), 27–40.

[242] ZANG, Y., STREET, R., AND KOSEFF, J. A dynamic mixed subgrid-scale model and its application to turbulent recirculating flows. *Phys. Fluids A 5*, 12 (1993), 3186–3196.

[243] ZANG, Y., STREET, R., AND KOSEFF, J. A non-staggered grid, fractional step method for time-dependent incompressible navier-stokes equations in curvilinear coordinates. *J. Comp. Phys. 114* (1994), 18–33.

[244] ZDRAVKOVICH, M. *Flow Around Circular Cylinders.* Oxford University Press, 199).

[245] ZEDLER, E., AND STREET, R. Large-eddy simulation of sediment transport: currents over ripples. *J. Hydr. Engrg. 127*, 6 (2001), 444–452.